Development of an Aeroprediction Method for Slender Bodies Including Aeroelastic Effects Using Euler-Based Local Piston Theory

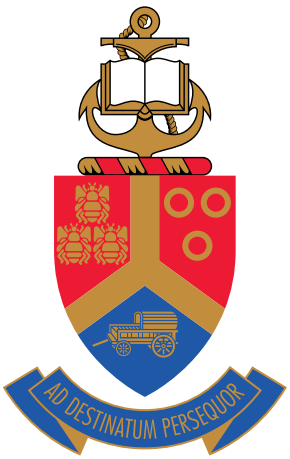

Marius-Corné Meijer

Department of Mechanical and Aeronautical Engineering

University of Pretoria

This dissertation is submitted for the degree of

Doctor of Philosophy

Pretoria, South Africa January 2019

Abstract

Euler-based local piston theory (LPT) has received significant interest in recent literature. The method utilizes a simple, algebraic relation to predict between perturbation pressures directly from local surface deformation and from the local fluid conditions obtained from a steady Euler solution. Early applications of Euler-based LPT to simple, non-interfering geometries and flows yielded the accurate ($< 5\%$ error) prediction of unsteady pressures at orders-of-magnitude lower computational expense compared to unsteady CFD. These successes led to the broader application of Euler-based LPT to more complex scenarios, such as full-vehicle geometries and interference flows. However, a degradation in the prediction accuracy was noted. This motivated the present work, in which the suitability of Euler-based LPT as an aeroprediction method for slender bodies with aeroelastic effects is assessed.

An extensive and thorough review of the literature revealed that no investigation into higher-order terms in the pressure equation of LPT had been made. More significantly, the mathematical basis for LPT had yet been developed. Finally, no controlled numerical investigation into the application of Euler-based LPT under aerodynamic interference associated with cruciform control surfaces on slender bodies could be found in the literature.

The present work addresses the above gaps in the literature. The first is addressed analytically, and shows that second-order LPT provides a non-zero contribution to aerodynamic stiffness. To address the second gap, a derivation of LPT from the 3D unsteady Euler equations is presented, with an in-depth discussion of the required assumptions. A number of significant conclusions regarding the validity of Euler-based LPT are drawn. It is argued that the method will be in significant error when applied in regions involving, amongst others, viscous boundary-layers, concentrated vorticity, transonic or embedded subsonic flows, sharp curvature, wing-body junctions, subsonic leading-edges, wing-tips, and trailing-edges. Furthermore, it is argued that Euler-based LPT will be in error when applied to mode-shapes of deformation involving localized bending and camber or point-local deformations. Finally, it is stressed that an algebraic pressure equation in LPT cannot account for flowfield interaction, which may be significant in the aforementioned scenarios. These conclusions are supported by a numerical investigation performed in the present work, which addresses the third gap in the literature.

Declaration

I hereby declare that except where specific reference is made to the work of others, the contents of this thesis are original and have not been submitted in whole or in part for consideration for any other degree or qualification in this, or any other University. This thesis is the result of my own work and includes nothing which is the outcome of work done in collaboration, except where specifically indicated in the text.

Marius-Corné Meijer
January 2019

Acknowledgements

The financial support of the work conducted towards the completion of this thesis by the Fluxion / Ledger grant of Armaments Corporation of South Africa is gratefully acknowledged.

The road from the start to the completion of this work brought many interesting people, experiences, and opportunities across my path. I would like to extend my gratitude to (and for) a number of these.

I would like to thank Prof. Robert Dominy of the University of Northumbria and all those involved behind the scenes for affording me the opportunity to "occupy some space" in the postgrad offices as a "visiting researcher" of sorts in the final stages of my work. The possibility to walk down the hall and consult with my supervisor face-to-face was certainly of value in this vital stage of the research.

I would also like to thank Dr. Sergei Serokhvostov of the Department of Aeromechanics and Flight Engineering of Moscow Institute of Physics and Technology, as well as all others involved in the processes behind enabling me to attend a semester internship at the institute. It was an enriching experience, and further afforded me the opportunity to consult with experts in the field in the early stages of my research.

One such expert was Prof. Petr Georgiyevich Karkle. His encouragement, engagement, and support for the research in its early stages were of immense value to me. Furthermore, his kindness and friendly demeanour made a significant impression upon me. His passing was a great loss both to the scientific community in general and to those who had the honour of knowing him. Thank you, Prof. Karkle.

I sincerely believe that the computational portion of the research would have been significantly more frustrating were it not for the support of Dr. Johan Heyns, whom I would like to thank here. Aside from providing access to and support with the `HiSA` solver for `OpenFOAM`, his interest in and support for my research were of great value.

My penultimate thanks is extended to my supervisor, Prof. Laurent Dala. Prof, I could probably write a "thank you" as long as this thesis, but after the work of reading through my thesis in its various revisions, I am not sure you will ever want to read something of mine again! Thank you for the opportunities you helped to create for me and for your

encouragement to pursue them. I honestly could not ask for a better supervisor. I deeply appreciate the freedom you gave me in how I approached the research, and for allowing me to “make it my own,” while still providing foresight and guidance. Thank you for letting me chase the rabbit down the rabbit hole, and for pulling me out by the feet the times that I did not catch the rabbit. Repaying your patience with bottles of wine would put me in crippling financial debt. You, Liam, and Valerie, are very dear to me.

My final thanks goes out to my loving parents. I wish that I had introduced you to some of the classics of www.phdcomics.com, so that it could communicate some aspects of the PhD experience that I felt I could not. Thank you for standing by me from start through finish, through the highs and the lows, and for your continued patience, love, and support.

To my parents

Table of contents

List of figures

List of tables

Nomenclature

Roman Symbols

a dimensional speed of sound in the fluid, or cylinder radius

AR aspect ratio

c chord length

c_1, c_2, c_3 coefficients in piston-theory pressure equation

C_l rolling-moment coefficient about the x-axis

$C_{l(W)}$ rolling-moment coefficient about the x-axis of the wing in isolation

$C_{l(W(B))}$ rolling-moment coefficient about the x-axis of the wing in the presence of the body

C_m pitching-moment coefficient about the y-axis

C_N normal-force coefficient

C_{N_B}, $C_{N(B)}$ normal-force coefficient of the body in isolation

$C_{N_{B(W)}}$, $C_{N(B(W))}$ increment to body normal-force coefficient due to wing interference

C_{N_F} force-coefficient normal to the control fin

C_{N_W}, $C_{N(W)}$ normal-force coefficient of the wing in isolation

$C_{N_{W(B)}}$, $C_{N(W(B))}$ normal-force coefficient of the wing in the presence of the body

C_p pressure coefficient

$C_{p_{cyl}}$ pressure coefficient based on the un-perturbed reference pressure in cylinder

C_Y side-force coefficient

$C_{Y(W)}$ side-force coefficient of the wing in isolation

$C_{Y(W(B))}$ side-force coefficient of the wing in the presence of the body

d body diameter or transverse length

e dimensional specific internal-energy of the fluid

F_N normal force

F_Y side force

h dimensional specific-enthalpy of the fluid

K hypersonic similarity parameter, $K = M_\infty \delta$

k reduced frequency of oscillation, $k = \frac{\omega c}{V_\infty}$

k reduced frequency

K_B body carryover-factor

K_W wing carryover-factor

L body length

M_c crossflow Mach number

M_{cyl} un-perturbed Mach number in cylinder

M_∞ freestream Mach number

p_m local mean-steady pressure in cylinder

M_N Mach number normal to the leading edge

$\hat{\mathbf{n}}$ unit normal-vector of the local structural surface following a perturbation

n_i i-th component of the surface unit normal-vector

p fluid pressure

p_{cyl} un-perturbed reference pressure in cylinder

q_∞ freestream dynamic pressure

Re Reynolds number

r_N nose radius

s dimensional specific-entropy of the fluid

s_m wing semi-span or span of single panel

T fluid temperature

t dimensional time

v_i i-th component of the dimensional fluid-velocity vector

$\mathbf{V_b}$ velocity vector of the local structural surface

$\mathbf{V_b}$ velocity vector of local body surface

v_{Bi} i-th component of the local dimensional surface-velocity vector

$\mathbf{V_{cyl}}$ velocity vector of cylinder advection

$\mathbf{V_f}$ velocity vector of the local flow

V_∞ dimensional freestream velocity

$\mathbf{V_m}$ velocity vector of the local mean steady flow

V_m velocity magnitude of the local mean-steady flow

w downwash velocity

x global body axis in Chapter 5

x_i i-th dimensional spatial-coordinate

x_{CP} x-location of the centre-of-pressure

x_{ref} x-location of the moment-reference centre

y global “horizontal” axis in Chapter 5

z global “vertical” axis in Chapter 5

z_{CP} z-location of the centre-of-pressure

Greek Symbols

α angle of attack

α_c inclination of the body axis to the freestream velocity vector

α_N angle of attack normal to the leading edge

β shock angle measured from the reference axis (typically the body axis)

δ body slenderness ratio, flow turning angle, or local surface inclination to the freestream; out-of-plane deflection in Chapter 5

δ_{ij} Krönecker delta

ε_{ij} fluid rate of deformation tensor

Γ fluid circulation

γ ratio of specific heats

Λ sweep angle

μ Mach angle, or dynamic viscosity

ω (circular) frequency of oscillation

ϕ roll angle, azimuth, or perturbation velocity potential

ρ fluid density

τ thickness-to-chord of ratio of a lifting surface, or more generally, a small parameter with $\tau \ll 1$

θ cylinder orientation relative to advection direction in generalized piston theory

Acronyms / Abbreviations

BC boundary condition

CFD computational fluid dynamics

CPT classical piston theory

DLM coublet-lattice method

DNS direct numerical simulation

DOF degree of freedom

$\frac{\mathrm{d}}{\mathrm{d}t}$ material derivative

FVFSM free vortex / feeding-sheet pair method

FVM free vortex method

LES large-eddy simulation

LHS left-hand side

LPT local piston theory

MDD multi-disciplinary design

MDO multi-disciplinary optimization

MVDVM multi-vortex discrete vortex method

NS Navier-Stokes

PDE partial differential equation

PNS parabolized Navier-Stokes

RANS Reynolds-averaged Navier-Stokes

RHS right-hand side

ROM reduced-order model

SA Spalart-Allmaras

SBLI shock / boundary-layer interaction

SDT small-disturbance theory

TSD transonic small-disturbance

TSL yhin shear-layer

Chapter 1

Introduction

Advances in computing power have historically enabled previously high-fidelity computational methods to find industrial use where they were once considered "prohibitively expensive" [1]. A prime example of this is the application of numerical solvers to solving the Reynolds-averaged Navier-Stokes (RANS) equations. While the time required to obtain a solution may still be perceived as prohibitively expensive for preliminary design, the resolution of the solution (whether physical or temporal) has increased drastically. This introduces the notion of the trade-off between computational cost and the fidelity of the physical (or mathematical) model.

A broad range of mathematical models for aerodynamic analysis (aeroprediction methods) exists today. These methods span the spectrum of computational expense and physical fidelity [2]. Many of the computationally inexpensive methods are rooted in mathematical approximations to the physics describing the flow [3]. These approximations often exploit some known feature of the geometry considered, such as a small ratio of body lengths [4]. This introduces the class of geometries known as slender bodies. A particularly broad range of prediction methods – many of which are semi-empirical – is intended for aerodynamic analysis and preliminary design of slender bodies [5, 6]. The majority of engineering-level (approximate, computationally inexpensive) aeroprediction methods for slender bodies are based in steady flows. While this renders them useful for preliminary design, it restricts the broader application of the methods.

As noted earlier, advances in computing power have over time rendered more computationally expensive methods feasible for use earlier in the design cycle. The associated introduction of higher modelling fidelity has facilitated the implementation of multi-disciplinary design (MDD) and optimization (MDO) [7]. This is particularly significant for slender bodies, which are susceptible to aeroelastic effects at high speeds [8]. While the cost of computational fluid dynamics (CFD) has significantly decreased, its use for MDD / MDO

early in the design cycle is still broadly considered computationally expensive. This has fueled significant interest in developing various reduced-order models (ROMs) [9–11]. These retain a high fidelity of prediction, while often being orders-of-magnitude less computationally expensive. This is of crucial importance and value in control system design. Engineers require a description of the variation in aerodynamic loading over a broad parameter space in order to design appropriate control laws. The large parameter space dictates that the ROM must supply aerodynamic information rapidly. Meanwhile, the application (namely, stability and control of the vehicle) requires that the aerodynamic information supplied by the ROM be accurate.

Reduced-order models vary significantly in their implementation. Most are *a-posteriori* reductions, in which a database of existing high-fidelity solutions are required. From this database, various numerical methods may be adopted to construct the ROM. While the computational cost associated with the use of the ROM is insignificant, the cost required to obtain (or generate) the necessary database of high-fidelity solutions is certainly not insignificant [12]. It should also be considered that a large number of solutions may be required for the database in order for the ROM to be constructed.

Approximate mathematical models of the governing physics of a flow may be viewed as *a-priori* ROMs [13]. This is in the sense that the approximation is made independent of (or prior to) an existing solution. One such method has gained significant interest in recent literature on aeroelastic analyses in supersonic / hypersonic flows. Local piston theory (LPT) utilizes an existing mean-steady flow solution, and provides a computationally inexpensive model for predicting unsteady aerodynamic pressures about this reference solution [14]. The method has yielded excellent prediction accuracy in simple flow and geometry scenarios at computational costs several orders-of-magnitude less than what would be required by unsteady CFD [14]. This renders the method particularly suitable for aeroelastic analysis and optimization [15]. The promising results of early applications of the method led to its further application to increasingly complex geometries and flows [12, 16–19]. However, this was typically accompanied by a degradation in the prediction accuracy [16].

1.1 Thesis

The recent trends in the literature on CFD-based LPT noted above prompted the following two-pronged research question:

- Can the application of Euler-based LPT to a slender-body geometry with aerodynamically-interfering, elastically-deforming control surfaces be justified from a theoretical or mathematical basis?

- Is Euler-based LPT in its present form suitable as an aeroprediction method for this class of flows / geometry?

The thesis put forward is that Euler-based LPT may be derived from the 3D unsteady Euler equations provided that appropriate ratios of directional perturbation-magnitudes and gradients exist in the flow. It is further posited that a derivation of LPT from the Euler equations will inform the prediction shortcomings of LPT that have been noted in the literature.

1.2 Outline

The outline of the present work is as follows. A broad overview of the physics typical of slender-body aerodynamics is given in Section 2.1. This is followed by a review of the prediction methods broadly used for slender bodies in Section 2.2. These establish the context for CFD-based LPT as an aeroprediction method, as summarized in Section 2.3. The focus is then shifted to literature relating to piston theory as a whole in Chapter 3. A conceptual introduction to the method in Section 3.1 is followed by a thorough review of historical developments to the method in Section 3.2. The latter establishes the recent trends in the literature and identifies a number of gaps. One such gap, specifically dealing with the role of higher-order pressure-equation terms in LPT, is addressed in Section 3.3. The other gap in the literature, namely the lack of a mathematical basis for LPT, is addressed in Chapter 4. Following a general development, the derivation of LPT from the 3D unsteady Euler equations is presented in Section 4.6. This is followed by an in-depth discussion of the scenarios under which Euler-based LPT is expected to break down in Sections 4.7 and 4.8. The mathematical basis is supplemented by a numerical investigation into the controlled application of Euler-based LPT to a slender body with control-surfaces subjected to aeroelastic deformation in Chapter 5. The key conclusions of the present body of work are presented in Chapter 6, with the novel contributions to the field listed in Chapter 7.

Chapter 2

Review of Slender Body Aerodynamics

Aerodynamics is an integral component to flight vehicle design, impacting diverse activities and disciplines. These include, but are not limited to, vehicle flight dynamics, performance, and structural design. The range of flight conditions that slender flight vehicles may operate in leads to diverse fluid dynamic features being encountered. Aeroprediction aims to replicate the physics that will be encountered in flight by the final design. The flow features and associated physics will be broadly referred to as slender body aerodynamics, and are the subject of Section 2.1. Flow features will be broadly categorized by the component of the flight vehicle that gives rise to them, namely as body-specific, wing-specific, and general flow features.

The range of prediction methods available to the engineer will be the focus of Section 2.2. These methods vary in their approach to modelling slender body aerodynamics, their complexity and the computational effort required in using them, and in their ability to accurately reproduce the physics encountered in practice (which will be referred to as the fidelity of the method). An overview of broadly-used prediction methods for slender body aerodynamics will be given, with the methods grouped into the commonly-used categories of "engineering-level", "intermediate", and "advanced" methods. These categories broadly refer to the increasing complexity and computational expense of the methods. Where appropriate, the differences in mathematical (and physical) modelling of the methods will be emphasized.

The reader that is familiar with the particulars of slender-body aerodynamics and related aeroprediction methods will be familiar with the content of Sections 2.1 and 2.2. For such readers, the abridged contextualization of piston theory in Section 2.3 may be of greater interest, as it motivates the current research and development in piston theory. This lays the basis for the detailed overview of piston theory and its variants in Chapter 3.

2.1 Experimental Observations

Extensive literature is available providing detailed overviews of slender body aerodynamics in general, as well as in-depth reviews of specific flow phenomena. The aim of this section is to provide at most an introductory overview of typical flow features that are encountered and which must be considered in aeroprediction. Examples include of flow features covered include: the development of curved shocks and associated entropy wakes; shock / boundary-layer interaction; transition and separation of the boundary-layer; the formation and breakdown of vortical structures; the local effect of aerodynamic interference between wings and bodies; interaction between upstream flow structures and control surfaces. To this end, this section provides a curation of figures from texts dedicated to visualization of flow phenomena [20, 21] and to providing a detailed overview of slender body aerodynamics [22], with the figures located at the end of each subsection.

It is worth noting that the underlying physics – viscosity, turbulence, flow rotationality, and compressibility (manifested as shock waves) – giving rise to the flow features to be discussed here is by no means particular to slender bodies. Rather, it is the vehicle geometry, which acts as the boundary conditions to the physics, which gives rise to their particularity. This section therefore loosely categorizes flow features by the vehicle component giving rise to them, and briefly notes the influence of the component geometry and of various flow conditions. The section opens with consideration of body-specific flow features, continues with wing-specific features, and closes with flow features not specific to the individual vehicle components.

2.1.1 Body-Specific Features

Flight vehicles come in a broad range of geometric configurations, such as distinct wing-body configurations, blended-wing bodies, lifting bodies, and more. The distinction between components may become blurred, particularly in the case of hypersonic vehicles featuring a high degree of component blending. In this text, the term “body” will refer to the predominantly axisymmetric or tubular portions of the flight vehicle, which will be distinct from typically planar “wings”. The focus of this subsection will be on the body-specific flow features encountered, with the key parameters governing them introduced where appropriate. Varying degrees of interaction between flow features occur; however, the individual flow features will be introduced so far as possible in isolation, with their interactions noted in due course. The features and flowfield will be discussed in the broad categories of body shocks, the body boundary-layer, and body-shed vortices.

Body Shocks

The flowfield around a body and the extent of the flowfield varies significantly from subsonic through to hypersonic speeds. An illustration of some of the changes is given in Fig. 2.1 [23] for a sharp-nosed body. A significant point to note in the transonic regime (depicted in the figure by $M_\infty < 1$ and $M_\infty > 1$) is the importance of shock / boundary-layer interaction (SBLI) in determining the flowfield structure. Also depicted are the appearance of a bow shock at the nose, a recompression shock near the base, and the decrease of the lateral extent of the flowfield at hypersonic speeds (denoted $M_\infty \gg 1$). These features as encountered in practice are illustrated in a series of shadowgraph images curated by Van Dyke [20]. The presence of Mach waves are typically quite clear in these images. Often noted in the images is the interaction between the bow shock and Mach waves incident from the body. The interaction leads to a curvature of the bow shock and reflection of the Mach waves. The reflected Mach waves influence the pressure distribution on the aft-body, as shown by the gradual pressure recovery along a similar body in Fig. 2.2 [24]. The interaction between incident waves and the bow shock is more visible in Fig. 2.3 [20], which shows the flow around a sphere at hypersonic speeds. Detail A clearly shows the reflected wave.

Figure 2.3 further serves to introduce both the role of bluntness and some features of hypersonic flows. The bluntness of the sphere causes the bow shock to detach from the body surface. This occurs because the rate of flow-turning required by the high inclination of the surface to the flow is too great. The deceleration caused by turning the flow into itself results in a rise in pressure which, when large enough, forces the shock off of the surface. The shock strength results in a region of subsonic flow between the bow shock and the body in the vicinity of the stagnation point; the transition to supersonic flow is seen by the onset of Mach waves at detail B. Detail C highlights the growth of the boundary-layer, which leads to shock-induced separation further aft, and serves as an example of SBLI at hypersonic speeds.

Aerodynamic heating at hypersonic speeds will typically result in blunting occurring on sharp-nosed bodies. This has both structural-thermal and aero-thermal causes. In the structure, corners and regions with small radii act as temperature-concentration areas. In the fluid, heat transfer is proportional to the rate of change of velocity along the boundary-layer edge [25], which is a function of the surface curvature. Hayes and Neumann [26] note stagnation-point heat-transfer models of $\dot{q} \propto r_N^{-0.5}$ for laminar flows and $\dot{q} \propto r_N^{-0.2}$ for turbulent flows, both clearly showing that heat transfer is reduced by a larger nose blunting-radius. In this sense, a degree of bluntness is unavoidable and is characteristic of bodies which fly at these speeds. Figure 2.4 [27] interprets the flowfield around a blunt-faced body, with the features clearly illustrated; prominent are the mixed subsonic-supersonic flow in the vicinity of the stagnation point, and pronounced curvature of the bow shock. The effect of the

degree of blunting is shown in Fig. 2.5 for a series of power-law nose shapes at hypersonic speeds. For the sharpest nose, shown in Fig. 2.5a, it is seen that the bow shock lies close to surface of the body. As the Mach number is increased in the hypersonic range, the bow shock will approach a limiting shape and position, with a corresponding freeze in certain nondimensional flow properties in the flowfield behind the shock. This is known as the Mach independence principle [28]. As the degree of blunting is progressively increased, increases are noted in the shock standoff distance, the bow shock curvature, and the lateral extent of the flowfield aft of the nose.

Curvature of the bow shock sets up an entropy gradient in the flow immediately aft of the shock. The nomenclature for this portion of the flow is shown in Fig. 2.6a [27]; the portion of the outer, inviscid flowfield affected by this entropy gradient and the associated flow rotationality is termed the entropy wake, while a portion of the rotational flow aft of the bow shock is convected along the body surface and is termed the entropy layer. The effect of the entropy wake on steady aerodynamic charateristics downstream of the nose is shown in Fig. 2.6b [26]. The entropy wake also plays a significant role on the unsteady aerodynamic characteristics of bodies, with Fig. 2.7 [29] showing the destabilizing effect of nose blunting on the pitching damping of a cone; accounting for the entropy wake (denoted "embedded Netwonian") when using inviscid Newton-Busemann theory is shown to given improved correspondence to experiment, highlighting the role of the inviscid entropy wake.

A component of the influence of blunting on pitch damping is due to the change of shock curvature (and subsequently, the flowfield properties behind the bow shock) with body incidence. Much of the rest of the overview of body-specific features deals with incidence-related features. As is seen in the Schlieren images of a tangent-ogive cylinder shown in Fig. 2.8 [30], both the Mach number and angle-of-attack play a role in determining the shock shape and flowfield features, typically in the form of the parameter $M_c = M_\infty \sin\alpha$, termed the crossflow Mach number. It is seen that as the crossflow Mach number increases, the lateral extent of the flowfield on the windward side of the body decreases, with the bow shock lying close to the body surface. As the body incidence approaches the semi-vertex angle of the nose, the bow shock on the leeward side becomes progressively weaker, with the lateral extent of the leeward flowfield being noticeably larger than the windward extent.

A particularly important characteristic of slender bodies is that they typically (disregarding the transonic regime) produce perturbations which have significantly smaller gradients in the axial direction than in the crossflow directions [25, 27]. This allows the three-dimensional flowfield to be visualized as a two-dimensional crossflow which changes with a parameter relating the axial position of the crossflow plane – typically, this parameter is expressed as a time variable [27]. Significant attention will be given to this method of interpreting the flow

at a later stage, while at present it will simply be referred to as the crossflow analogy. Here, it will be used to aid in interpreting the effects of the crossflow Mach number on flow features related to slender bodies at incidence.

Figure 2.9 [20] depicts the flowfield around a sphere through a range of Mach numbers. In using the visualization of flow around a sphere to interpret flows around cylindrical bodies, it is important to recall that the three-dimensionality of the sphere flow provides a pressure relief, which results in a shorter standoff distance of the bow shock and a smaller adverse pressure gradient; the latter results in later boundary-layer separation and crossflow shock formation. With this in mind, the images of Fig. 2.9 may be interpreted with the freestream Mach number understood as the crossflow Mach number. Turning to Fig. 2.9a, it is seen that SBLI is an important feature of the flow, with boundary-layer separation observed to occur around the equator and resulting in a lambda crossflow-shock forming. As the freestream Mach number increases to supersonic speeds, as in Fig. 2.9b, a detached bow shock is observed on the sphere. When using the sphere-to-cylinder interpretation, it should be recalled that the bow shock produced by the nose may lie close to the body (as seen in Fig. 2.8i) and be the equivalent to the sphere bow-shock. Boundary-layer separation is again observed in the region of the equator with oblique shocks forming at the separation point. The flow features remain essentially similar as the Mach number is increased, as in Fig. 2.9c, with the bow-shock standoff distance decreasing; the position of the crossflow shock and boundary-layer separation is not significantly affected. These images serve to underscore the importance of the boundary layer at incidence, which is the topic of the following subsection.

Body Boundary Layer

As was noted in the previous subsection, SBLI may play a significant role in the flow structure near the surface of slender bodies. This is also true for slender bodies at slight incidence, as depicted for a body at $\alpha \approx 2^\circ$ in Fig. 2.10 [27]. Detail A shows the point of laminar-to-turbulent transition of the windward boundary layer; the corresponding increase in the thickness of the boundary layer results in a shock forming, which is seen to impinge on the flare. Hayes and Probstein [27] note that laminar separation of the boundary layer occurs on the leeside at detail B, a significantly earlier axial station than the transition point on the windward side. The region of separated flow is seen to blanket the leeside of the flare. As was noted previously in conjunction with the entropy wake, these flow features have an impact on both steady and unsteady aerodynamic characteristics of the body. Figure 2.11 [28] serves to distinguish between the entropy wake, which is largely inviscid, and the entropy layer, which has been noted [27] to be ingested by the viscous boundary layer. The interaction between the boundary layer, the entropy layer, and the shock layer at hypersonic speeds,

while potentially significant, is beyond the scope of this overview. Figure 2.10 [27] has hinted at the importance of the state of the boundary layer in determining the flowfield structure, in particular due to SBLI at supersonic and hypersonic speeds. The overview in this subsection will first focus on boundary-layer related influences on slender body aerodynamics at near-zero influence. As the incidence is increased, separation of the boundary layer leads to the formation of body-shed vortices. As a consequence, the influence of the boundary layer at incidence will be considered at the end of this subsection.

Figure 2.12 [29] clearly illustrates a number of the trends noted earlier. In particular, Fig. 2.12a demonstrates the impact of the state of the boundary layer (through the Reynolds number *Re*) on the pitch damping, the pitch stiffness, and base pressure of a sharp cone for small perturbations about zero incidence. The effect of incidence on the leeward and windward locations of boundary-layer transition is shown in Fig. 2.12b, with the inset depicting the impact on the flowfield through SBLI.

The extensive collection of data discussed in [29] also covers the influence of the body shape on boundary-layer related effects. This is a broad topic, and will not be discussed here. It is merely noted that the nose shape and body length may significantly affect the dynamic aerodynamic characteristics of the body. This may occur due to the influence of the geometry on the bow shock, on the generation of an entropy layer and entropy wake, and on the boundary layer.

All of the above are often illustrated for near-zero incidence. The influence of flow incidence should also be considered. Figure 2.13 [31] depicts the influence of increasing flow incidence on the regions of laminar, transitional, and turbulent boundary-layer states on slender bodies with sharp and blunt noses. It is immediately evident that blunt-nosed bodies show significantly less variation in the location of boundary-layer transition, while also exhibiting a narrow laminar corridor between the nose and the aft-body on the windward side. On the other hand, the slender body with the tangent-ogive nose demonstrates a more varied spectrum of boundary-layer state distributions, with a larger laminar region observed on the windward side. This translates into a broader variation in surface flow patters and on separation characteristics.

As when considering flow features related to body shocks, the crossflow analogy may be utilized as an aid in understanding variations of the body boundary-layer with incidence. The transition to turbulence along cylindrical aft bodies may then be interpreted in terms of flows around two-dimensional cylinders, as depicted in Fig. 2.14 [31]. For such flows, the crossflow Reynolds number, computed using the crossflow velocity and body diameter, is one of the characteristic parameters of the flow. As the flow incidence in increased, the crossflow Reynolds number increases, and the transition point shifts closer to the windward meridian,

as was noted in Fig. 2.13. The influence of the crossflow Mach number on the sensitivity of the flowfield to the boundary-layer state is depicted through the crossflow drag-coefficient in Fig. 2.14b. The boundary-layer state is seen to have an important influence until $M_c \approx 0.5$. Around this crossflow Mach number, acceleration of the flow through transonic speeds around the cylinder results in a crossflow-shock developing on the body near an azimuth of $\phi \approx 90°$, which essentially forces transition at the shock location.

The boundary-layer on a slender body, however, is not two-dimensional, and three-dimensional effects play a significant role. This is demonstrated by the complexity of the surface-flow patterns on a tangent-ogive nose and their variation with incidence as depicted in Fig. 2.15 [32]. It is noted that at sufficiently low incidence (in this case, $\alpha \leq 10°$ at $M_\infty = 0.25$) laminar separation may occur without the formation of vortices over the nose. However, as the incidence increases, the complexity of the surface flow increases, with laminar, transitional, and turbulent, and secondary separation of the boundary layer occurring – these features are noted in the surface-flow patterns available at 20°. This flow-pattern complexity extends to the three-dimensional flow away from the surface, with the axial velocity component playing a role in the structure and stability of the flow structures formed. An example of the three-dimensional flow forming around the tangent-ogive nose is given in Fig. 2.16 [29], clearly showing the formation of primary and secondary vortices.

Body-Shed Vortices

The variation in surface-flow patterns and the three-dimensional flow structure with increasing incidence, introduced in Figs. 2.15 and 2.16, may be categorized into four different vortex-shedding regimes for slender bodies, as in Fig. 2.17 [31]. As depicted in Fig. 2.17a, these include:

- A vortex-free regime at low incidence, in which a region of reduced velocity exists on the leeside,
- Symmetrical vortex shedding, in which separation from the body feeds a vortex sheet which rolls into a primary vortex core on either side of the body, with the vortex cores positioned symmetrically about the incident flow vector,
- Asymmetrical vortex shedding, under which the vortex strength and position is asymmetric, with the dominant vortex side alternating down the length of the body,
- Cylinder-like alternate shedding of vortices, in which a vortex-street forms behind the body.

As noted earlier, the relative strength of the axial velocity component (manifested as the flow incidence) clearly plays a role in the structure of the flow resulting from boundary-layer separation. The transition between vortex-shedding regimes is influenced by a number of factors as detailed in [31], including the level of freestream turbulence, the body surface roughness and geometrical asymmetries, Reynolds number, and Mach number, and as a consequence does not exist as a hard boundary, as shown in Fig. 2.17b [33]. It is further noted that the regime of vortex shedding may vary down the length of the body if the body is sufficiently long.

The onset of asymmetrical vortex shedding represents an important phenomenon for the design of slender bodies, as the vortex shedding is unsteady and complex. This is in contrast to the steady symmetric vortices that develop at lower incidences. In the case of sharp cones, the angle-of-attack at which the onset of asymmetrical shedding occurs may be correlated to the cone semi-vertex angle, as in Fig. 2.18 [31]. The correlation is extended to tangent-ogive noses by using the semi-apex angle in place of the cone's semi-vertex angle. For somewhat blunted noses, an approximate correlation of $\alpha \approx 4.2D/L$ is suggested in [31] for the onset of asymmetric vortices from the tail of the body. Asymmetrical vortex shedding is highly sensitive to a number of parameters, notably including the nose geometry, Reynolds number, turbulence, and the crossflow Mach number. The dependency on the above is typically non-trivial, as illustrated in [31, 34], and is not discussed further in the present overview.

The difference in the vortex-shedding structures between the asymmetrical and symmetrical regimes is highlighted in Fig. 2.19 [24]. It shows the single vortex feeding-sheet and primary vortex core of the symmetrical regime contrasted with the alternating sheets and cores of the asymmetrical regime. The continuity of the feeding sheet in the symmetrical shedding regime translates to a growth in the strength of the vortex down the length of the body. The vortex strength increases with angle-of-attack. The vortex structure and strength influences the structure of the crossflow, with typical streamlines shown in Fig. 2.20. As noted earlier, the state of the body boundary-layer also has an influence of the flowfield structure. Variations in the two-vortex system are shown in Fig. 2.20a [35] and the connection of the separation points is shown in Fig. 2.20b [24].

The flow features discussed thus far have particular significance for the integration of aerodynamic control surfaces or stabilizers, as may be anticipated from Fig. 2.21 [24]. Depicted is what would essentially be an interferential sidewash distribution on a leeside control surface. The stability of these flow structures is a further consideration, with the breakdown of the body-shed vortices depicted in Fig. 2.22 [36] for both symmetrically and asymmetrically shed vortices. In closing the overview of body-specific features, a short summary of some of the key parameters associated with these features is given below.

Key Parameters

The roles of body-geometric and aerodynamic parameters have been noted in the context of specific flow features thus far. Here, the focus will be shifted to some of the key parameters, with mention made of the flow features they influence. While the body-geometric and aerodynamic parameters were previously noted in isolation (for example, through considering the influence of Mach number in shaping the flowfield around a given body), the present emphasis will be chiefly on similarity parameters, such as the crossflow Mach number and the hypersonic similarity parameter.

The extent of nose bluntness has been seen to have a significant impact on the structure of the flowfield in the vicinity of the nose, particularly through the formation of a detached bow shock: associated are the entropy gradient of the curved shock, as well as large flow gradients and the existence of mixed subsonic-supersonic regions. It has also been seen that the degree of nose bluntness has an influence on the lateral extent of the flowfield aft of the nose, while the entropy gradient has an influence on the dynamic characteristics of the aft-body. The nose bluntness may be expressed in terms of the ratio of the blunting radius to the body diameter, r_N/D, with values of $r_N/D < 0.5$ representing, e.g., spherically-blunted ogives and cones, and values of $r_N/D > 0.5$ representing blunt-faced bodies, such as the power-law bodies in Figs. 2.5c and 2.5d. This is detailed in [37]. The effective slenderness of the nose, as far as vortex shedding is concerned, may be expressed in terms of the semi-apex angle θ_A, with the similarity parameter for vortex shedding being $\tan\alpha/\tan\theta_A$ as described in [31].

Similarity for a hypersonic slender body at incidence is given by $\delta\cot\alpha$, where $\delta = D/L$ is the body slenderness ratio, and by M_c, as shown in [27]. It is noted that for a cone, the similarity parameters $\tan\alpha/\tan\theta_A$ and $\delta\cot\alpha$ are reciprocal. For a body at near-zero incidence, the hypersonic similarity parameter may be taken as $M\sin\theta_A$. The hypersonic similarity parameter, as mentioned previously, is the key parameter relating the lateral extent of the flowfield between the body and the bow shock at supersonic to hypersonic speeds. At transonic speeds, the transonic similarity parameter plays a similar role, while there is some dependence on the axial variation of the body cross-section, as described in [38].

The crossflow Mach number, M_c, not only influences the lateral extent of the windward flowfield, but also influences the formation of crossflow-shocks near the maximum lateral extent of the body, as seen in Fig. 2.9 [20]. This influences the location of boundary-layer transition and the formation of body-shed vortices. Significantly, the crossflow Mach number also represents the extent of the influence of the leeside flow structures, with the vacuum pressures being neared for $M_c > 1$ and wake perturbations not reaching the body. Conversely, at $M_c < 0.4$, the leeside flow structures are dominated by boundary-layer effects, and the role of body-shed vortices are significant. This was demonstrated in [31] through Fig. 2.14.

For these subsonic crossflow Mach numbers, the roles of the crossflow Reynolds number, $Re_D = \rho V_\infty D \sin\alpha/\mu$, and freestream turbulence are key parameters in defining the flow, as described in [31].

The slenderness ratio of the body, $\delta = D/L$, impacts the relative strength of lateral and axial perturbations, which defines extent to which three-dimensional effects may be accurately interpreted by means of the crossflow analogy, as noted in [27]. It has also been seen to influence the onset of asymmetrical vortex shedding and vortex breakdown. Significantly, the slenderness ratio plays a role in the similarity of unsteady effects, such as those due to the entropy wake, through the Strouhal number for vortex shedding, $Sh = f_V D/V_\infty \sin\alpha$ (where f_V is the shedding frequency), and the reduced frequency for pitching motions, $k = qL/V_\infty \cos\alpha$ (where q is the pitching rate). The roles of these parameters in unsteady effects are described in [27, 37].

Another important parameter cross-sectional shape of the body and its axial variation along the aft-body. This has not been covered in detail here, as most slender-body-type flow features are adequately introduced by axisymmetric bodies with constant cross-section. The cross-sectional shape and its variation does have an influence on all three categories of body-specific features that have been discussed. For example, the influence of the body cross-section on the bow shock is central to the design of waveriders. Non-axisymmetric bodies exhibit crossflow characteristics (with particular emphasis on vortex shedding) which are sensitive to parameters such as sideslip [24, 39], axial variations in cross-section [24], and changes in the cross-sectional radius of curvature [24]. As the ratio of of the cross-sectional dimensions increases, the realm of slender wings and blended wing-bodies is approached, and the categorization of the related flow-features as “body-specific” becomes an issue of semantics due to similarity of the features to those exhibited by “wings” and full-configuration flight vehicles.

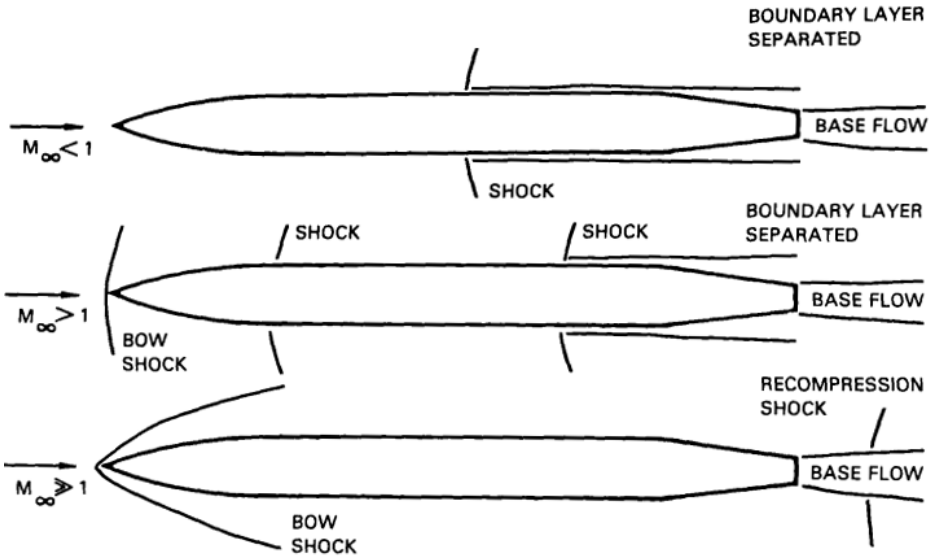

Fig. 2.1 Body shock development with increasing Mach number for a tangent-ogive [23].

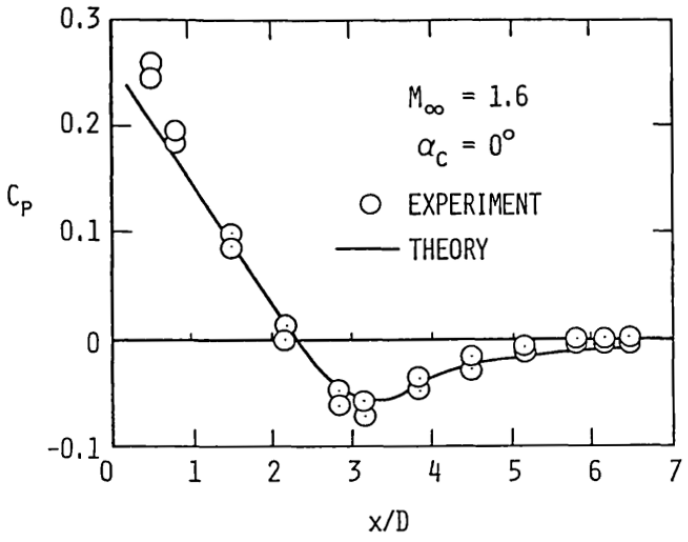

Fig. 2.2 Influence of wave-reflection from the bow shock on the aft-body axial pressure distribution along a tangent-ogive cylinder at $M_\infty = 1.6$ at zero incidence [24].

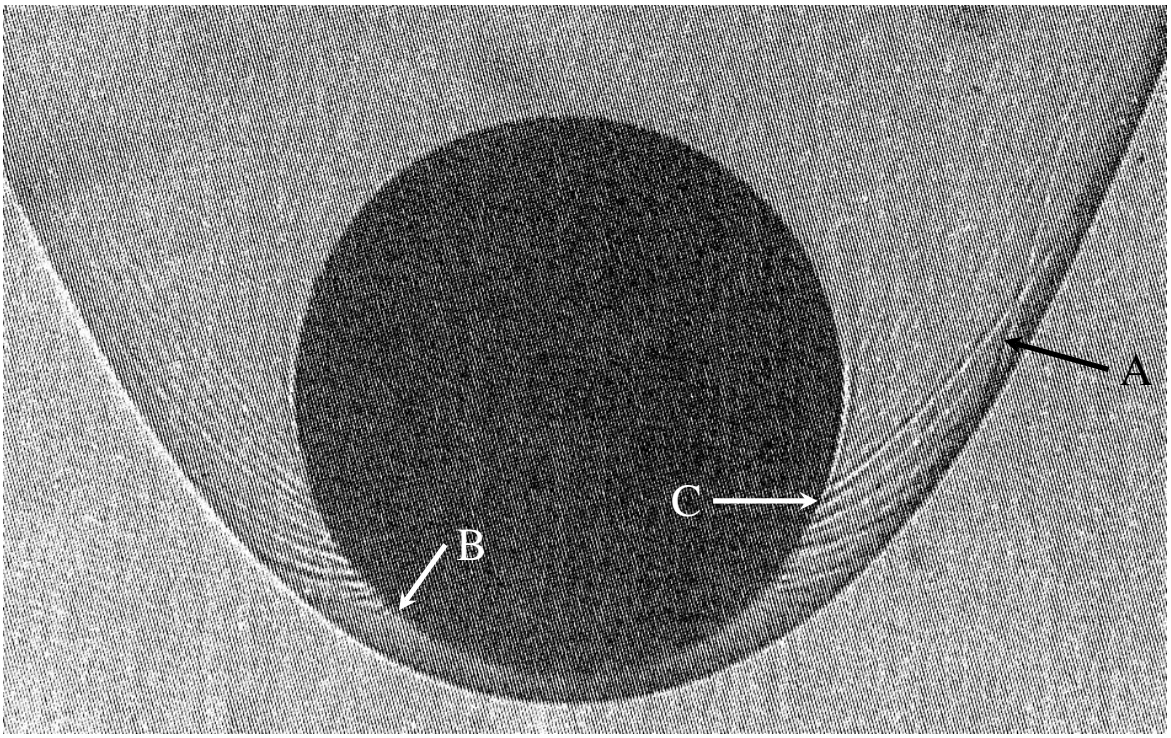

Fig. 2.3 Bow-shock wave-reflection and the development of supersonic flow behind the bow shock over a sphere at $M_\infty = 7.6$ [20].

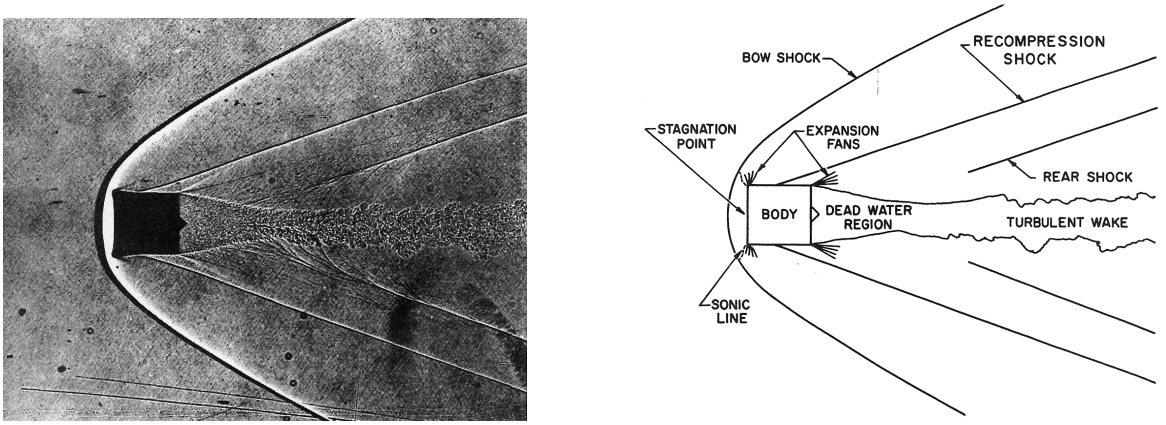

(a) Visualization (b) Interpretation

Fig. 2.4 Blunt-body flowfield interpretation [27].

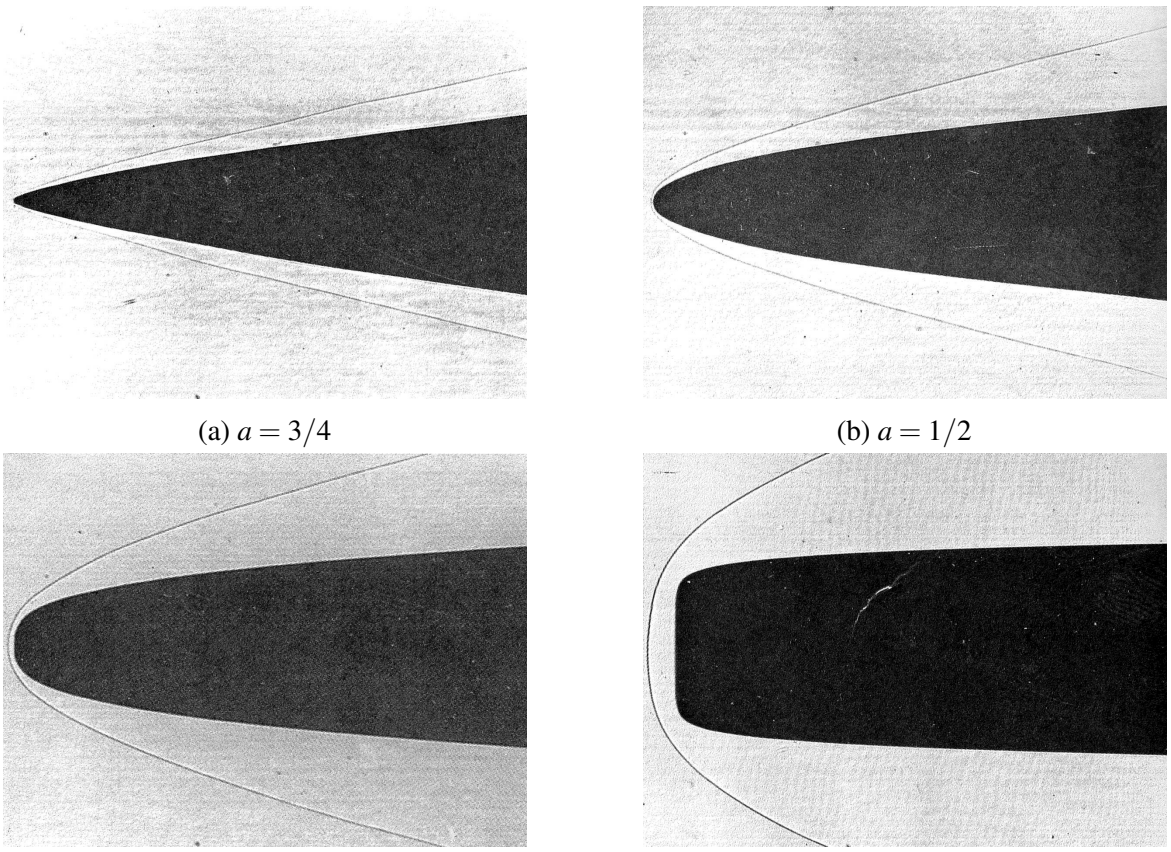

(a) $a = 3/4$ (b) $a = 1/2$

(c) $a = 1/3$ (d) $a = 1/10$

Fig. 2.5 Effect of nose bluntness on bow-shock shape for power-law ($r = x^a$) bodies at $M_\infty = 8.8$ [20].

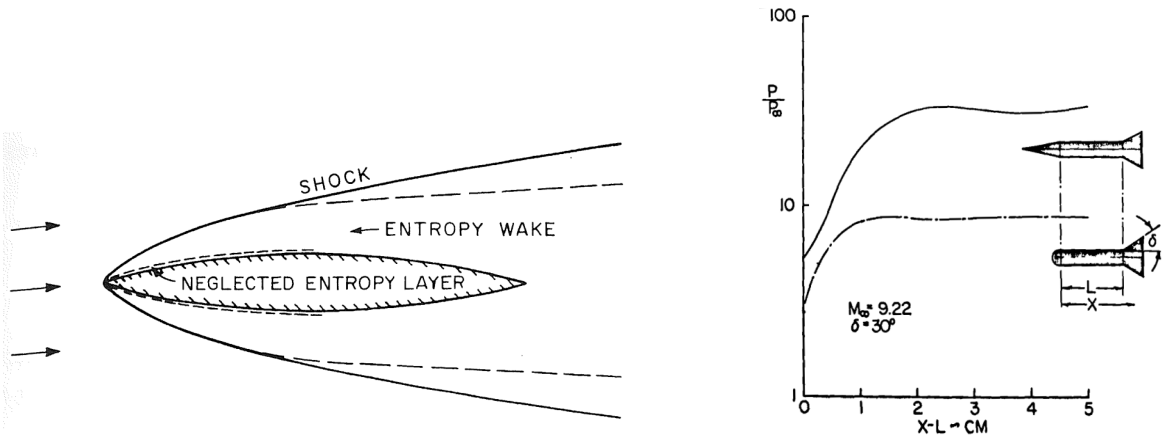

(a) Nomenclature [27] (b) Flare pressure distribution [26]

Fig. 2.6 Influence of strong shock-curvature and the associated entropy wake on steady pressure distributions downstream.

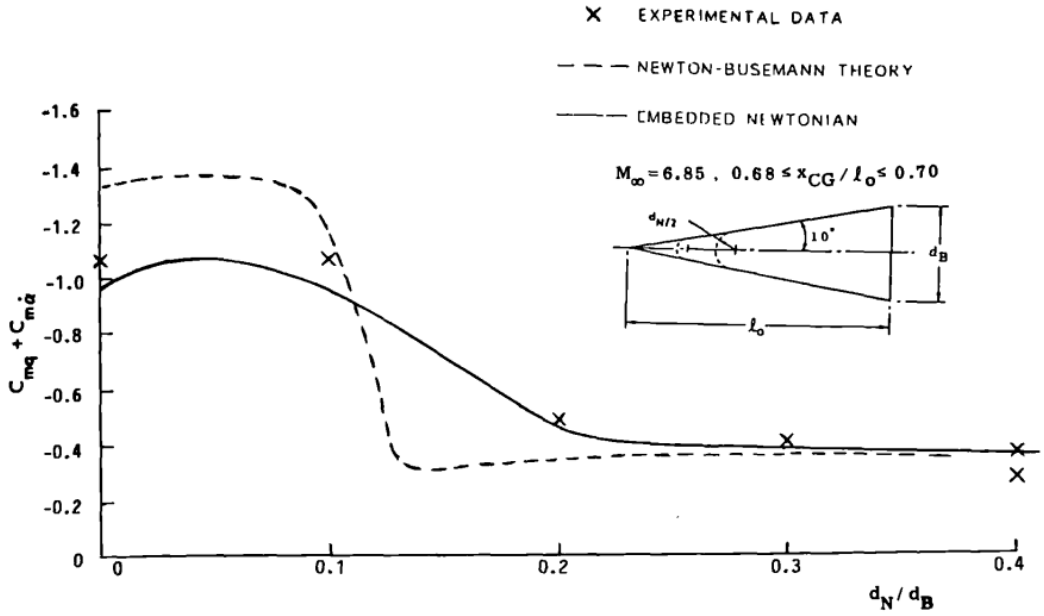

Fig. 2.7 Influence of nose blunteness and the entropy wake on pitch damping of a 10° semi-vertex angle cone at $M_\infty = 6.85$ [29].

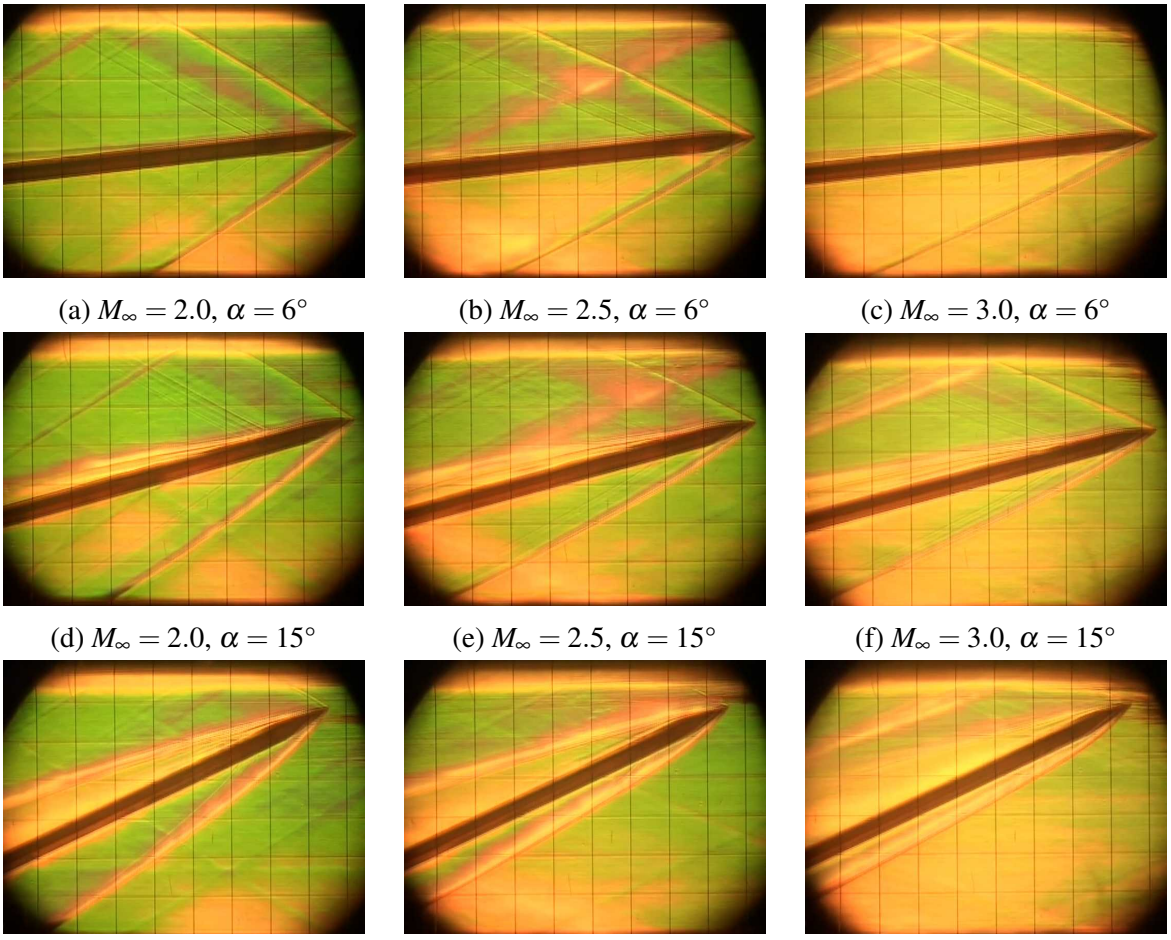

(a) $M_\infty = 2.0$, $\alpha = 6°$ (b) $M_\infty = 2.5$, $\alpha = 6°$ (c) $M_\infty = 3.0$, $\alpha = 6°$

(d) $M_\infty = 2.0$, $\alpha = 15°$ (e) $M_\infty = 2.5$, $\alpha = 15°$ (f) $M_\infty = 3.0$, $\alpha = 15°$

(g) $M_\infty = 2.0$, $\alpha = 25°$ (h) $M_\infty = 2.5$, $\alpha = 25°$ (i) $M_\infty = 3.0$, $\alpha = 25°$

Fig. 2.8 Asymptotic behaviour of the windward bow-shock shape with increasing Mach number for a tangent-ogive cylinder [30].

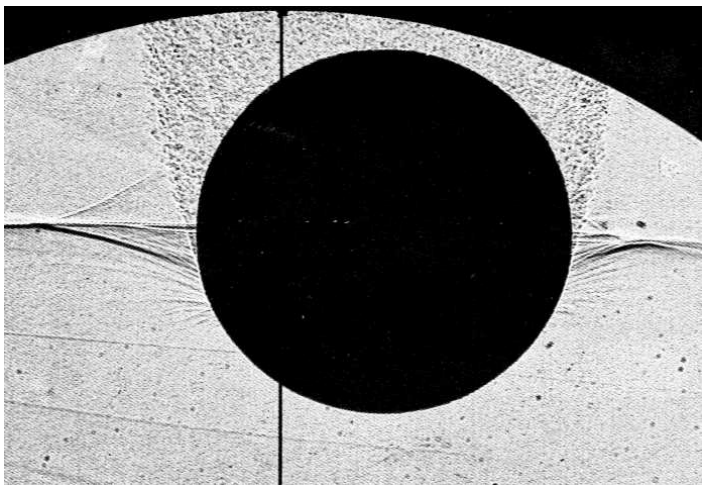

(a) $M_\infty = 0.86$

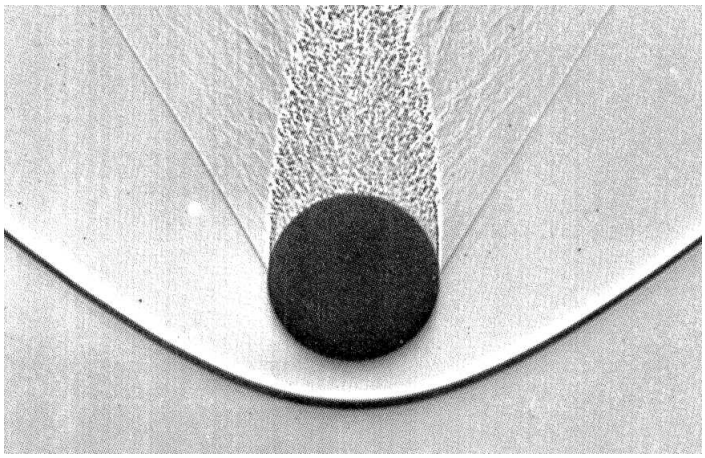

(b) $M_\infty = 1.53$

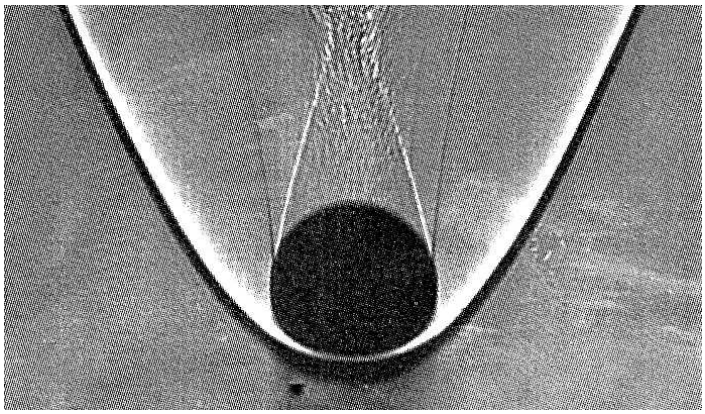

(c) $M_\infty = 4.01$

Fig. 2.9 Flowfield around a sphere at increasing Mach numbers [20].

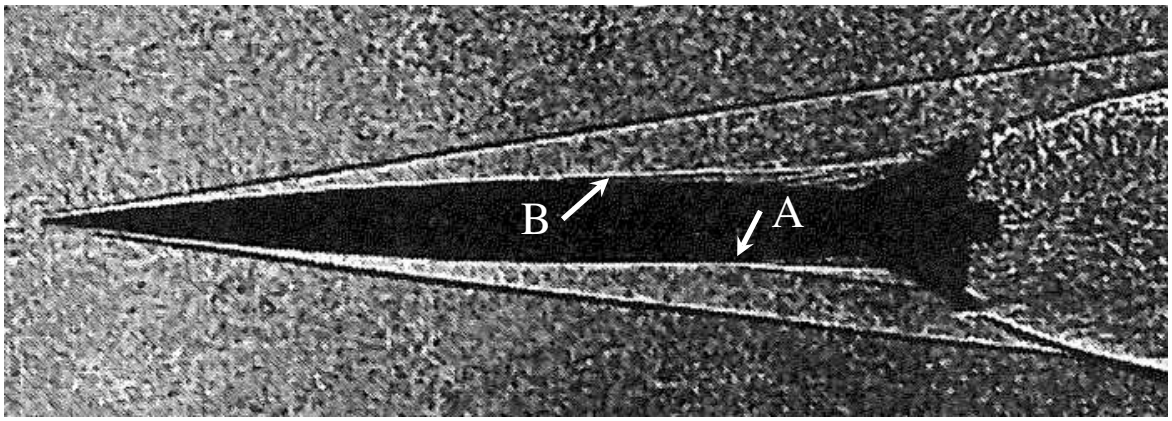

Fig. 2.10 Slender body flowfield at $M_\infty = 9.8$ at slight incidence [27].

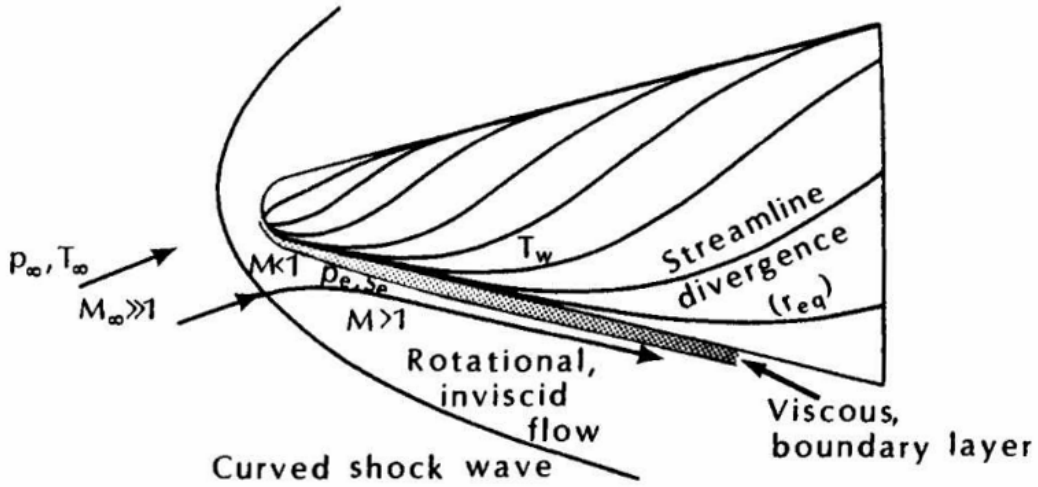

Fig. 2.11 Simplified hypersonic flowfield structure for slender bodies at incidence [28].

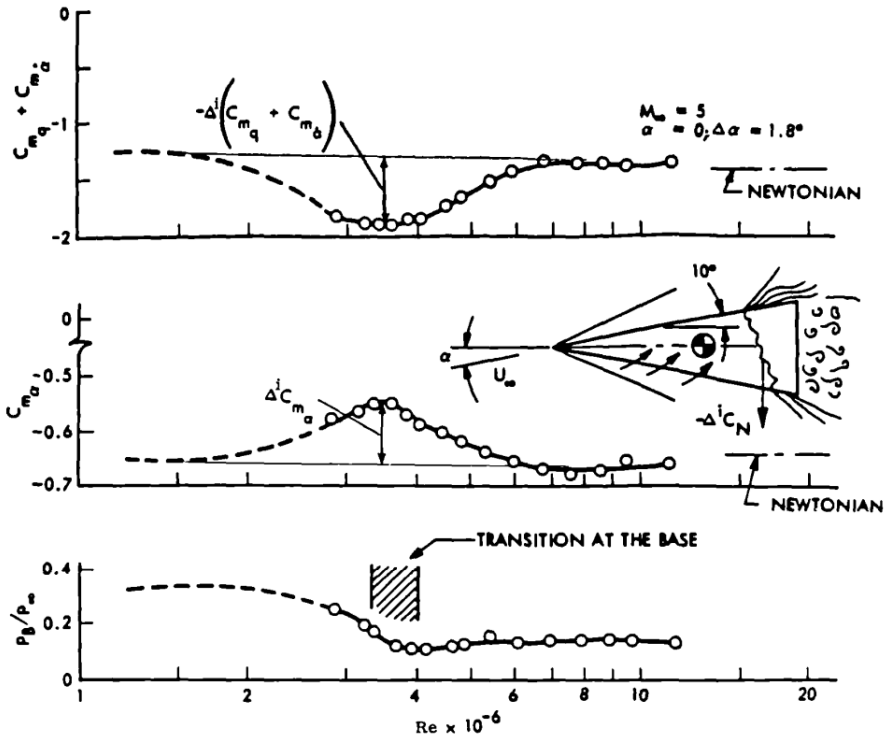

(a) Effect of Reynolds number on pitch-damping, pitch-stiffness, and base pressure

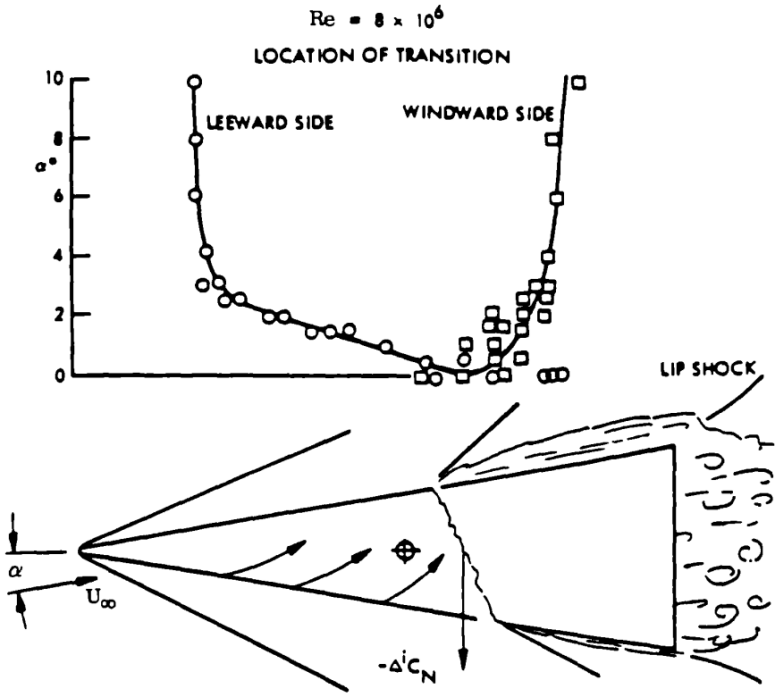

(b) Effect of incidence on transition location

Fig. 2.12 Effect of boundary-layer state on the aerodynamic characteristics of a 10° semi-vertex angle cone at $M_\infty = 5$ around $\alpha = 0°$ [29].

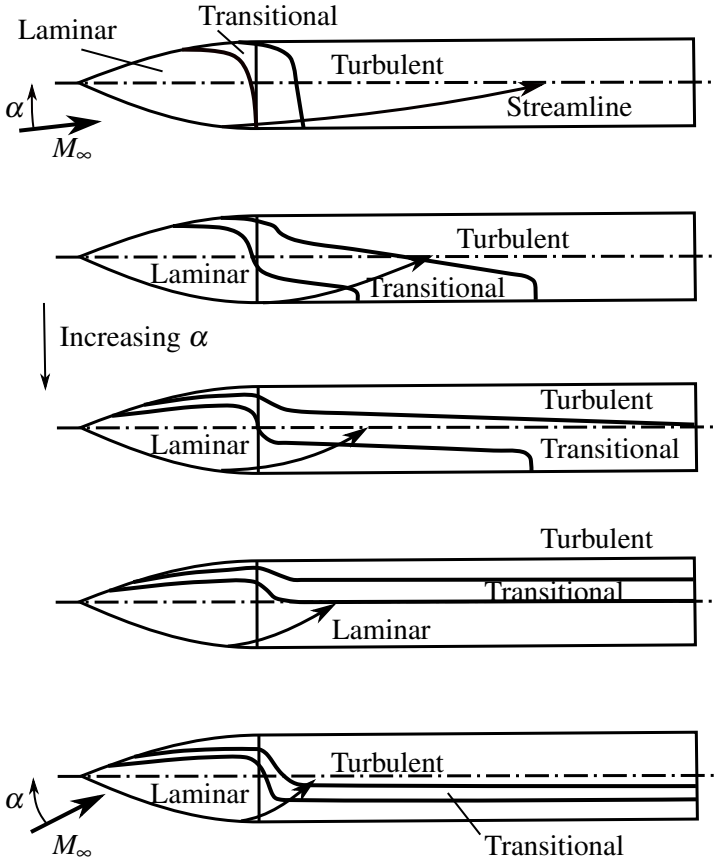

(a) Tangent-ogive cylinder

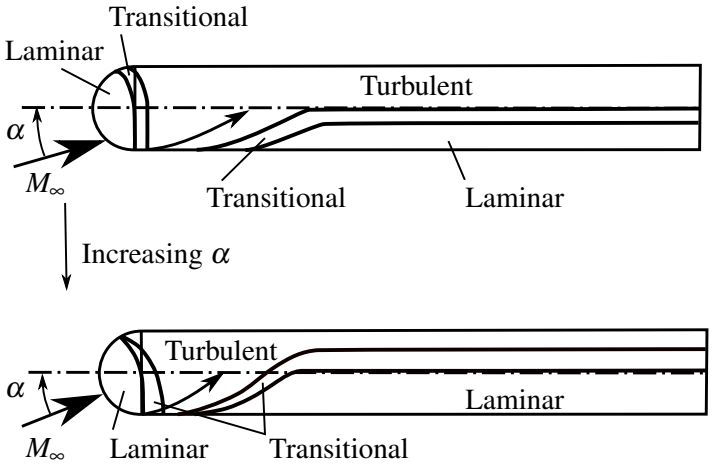

(b) Hemisphere-cylinder

Fig. 2.13 Effect of nose shape on the incidence-variation of boundary-layer transition down the length of slender bodies [31].

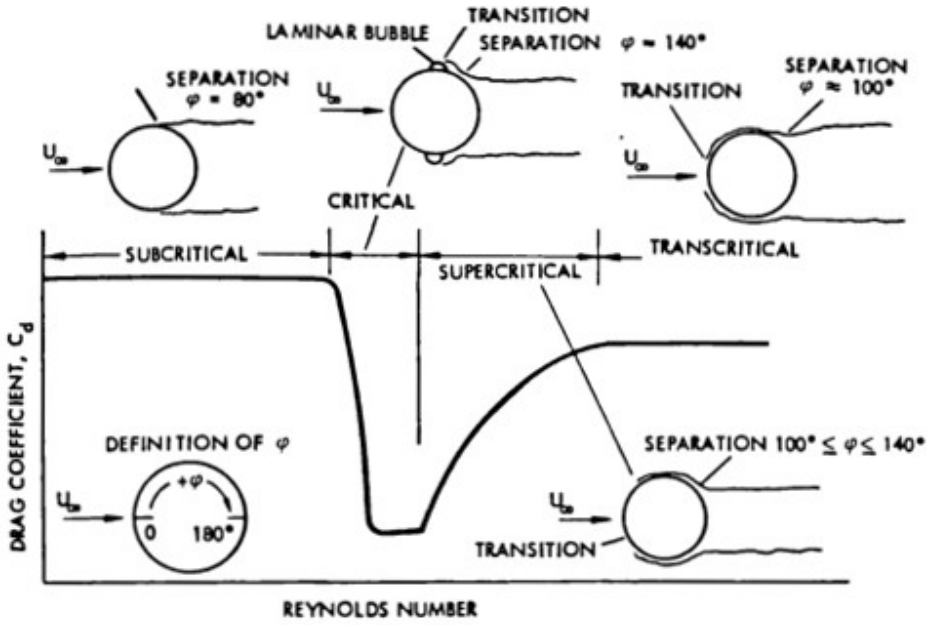

(a) Reynolds number variation

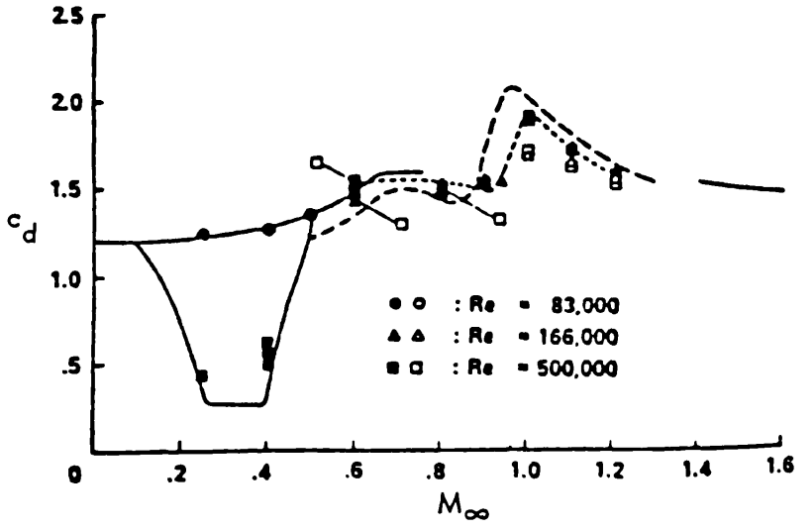

(b) Mach number variation

Fig. 2.14 Drag coefficient of a 2D cylinder as a function of boundary-layer transition and Mach number [31].

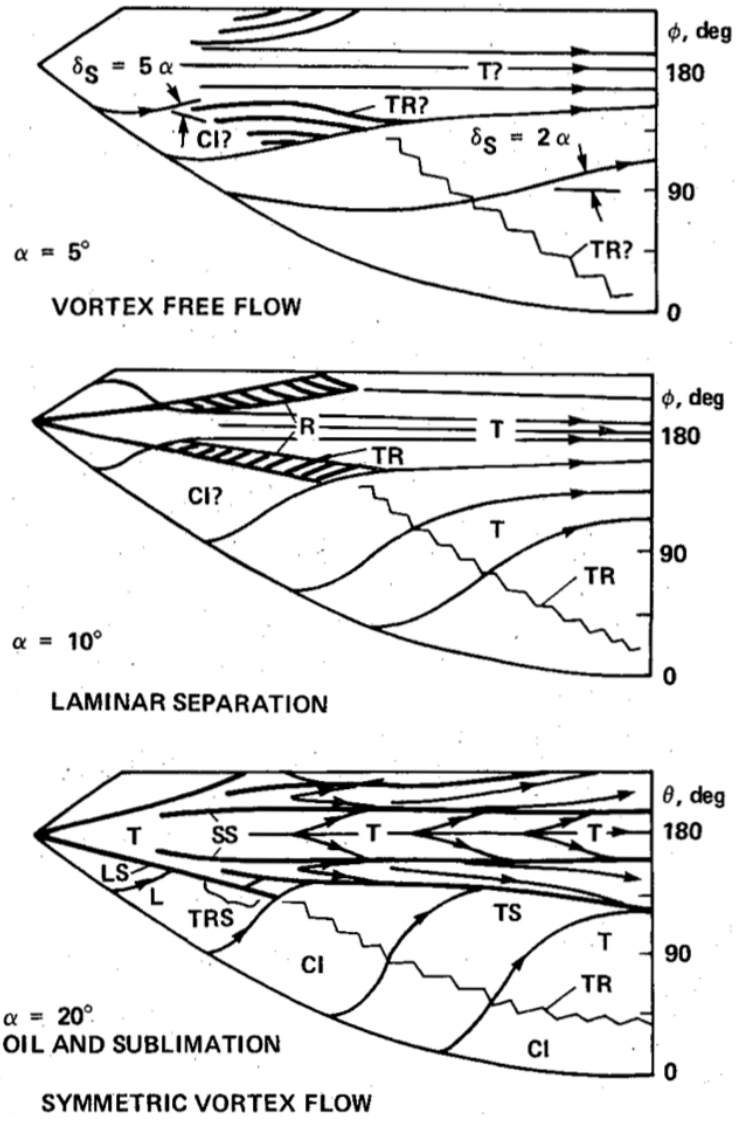

Fig. 2.15 Surface flow visualization on a 3.5 caliber tangent ogive at a transitional Reynolds number depicting boundary-layer transition regime variation with incidence [32]; $M_\infty = 0.25$, $Re = 0.8 \times 10^6$. The following abbreviations are used: L – laminar; LS – laminar separation; TR – transition; TRS – transitional separation; T – turbulent; TS – turbulent separation; SS – secondary separation; R – reattachment, CI – crossflow instability, δ_S – angle between streamline tangent and meridianal line.

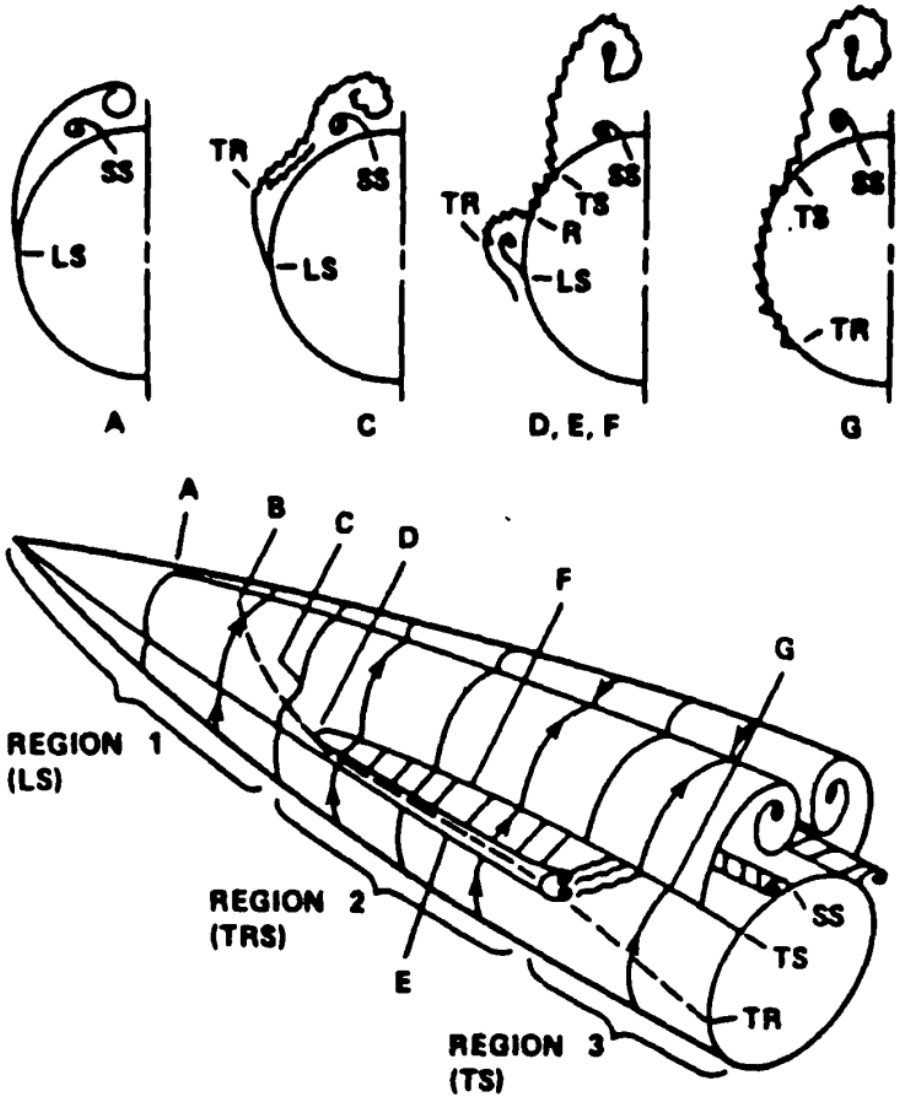

Fig. 2.16 Crossflow structures associated with boundary-layer separation regimes on a 3.5 caliber tangent ogive at a transitional Reynolds number [29]; $M_\infty = 0.55$, $Re = 0.8 \times 10^6$, $\alpha = 40°$. The following abbreviations are used: LS – laminar separation; TR – transition; TRS – transitional separation; TS – turbulent separation; SS – secondary separation; R – reattachment.

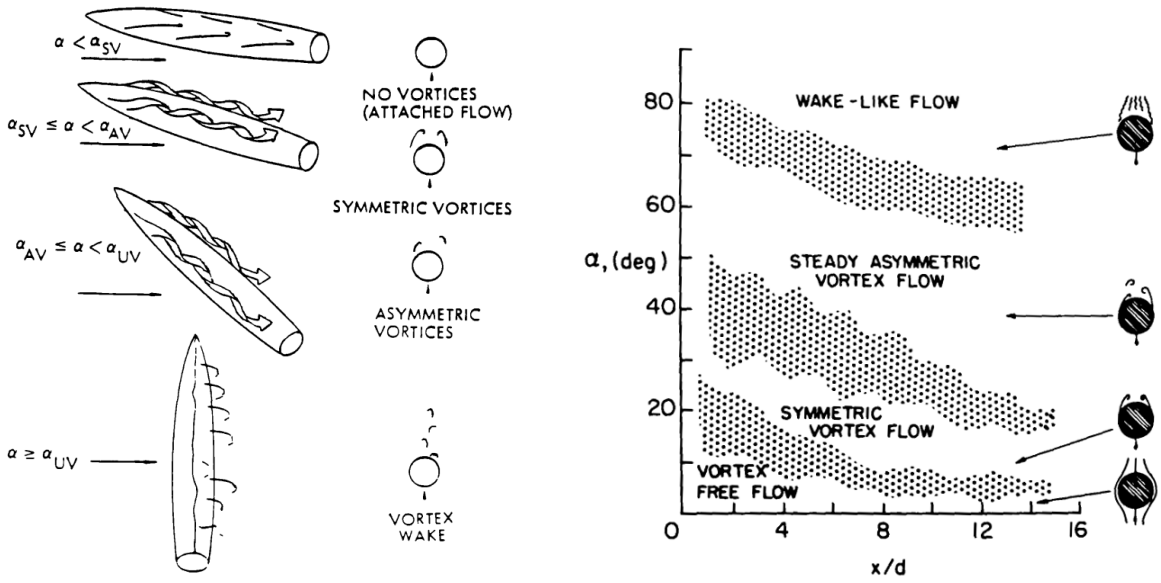

(a) Three-dimensional structure [31] (b) Approximate regime bounds [33]

Fig. 2.17 Vortex-shedding regimes for slender pointed bodies.

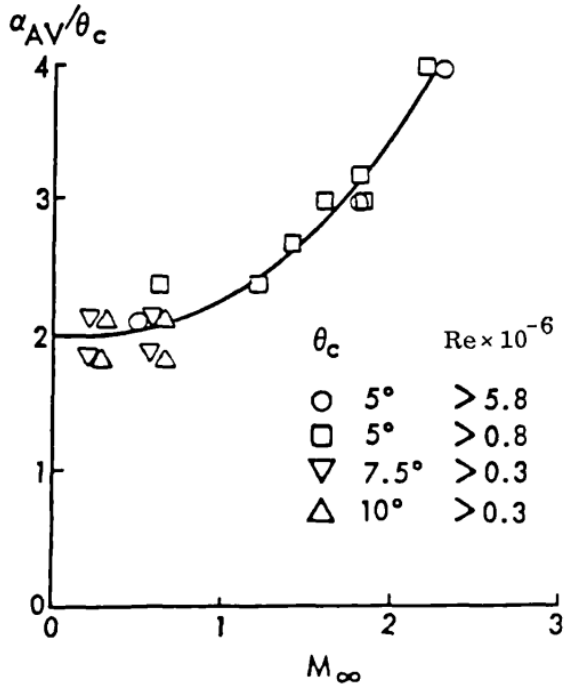

Fig. 2.18 Asymmetric-shedding onset-incidence variation with Mach number for sharp cones [31].

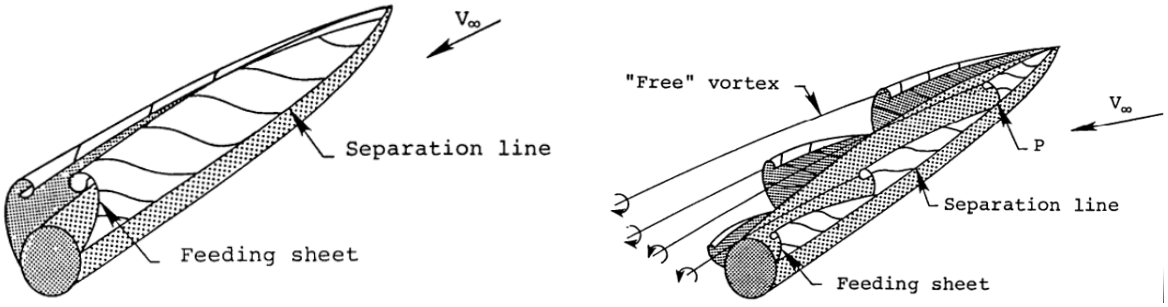

(a) Symmetrical shedding (b) Asymmetrical shedding

Fig. 2.19 Difference in three-dimensional vortical structures [24].

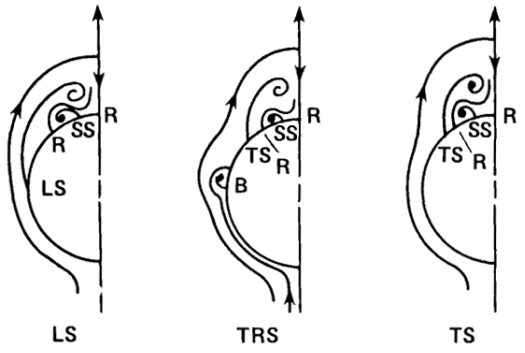

(a) Variation with separation type [35]. The following abbreviations are used: LS – laminar separation; TRS – transitional separation; TS – turbulent separation; SS – secondary separation; R – reattachment; B – bubble-type region.

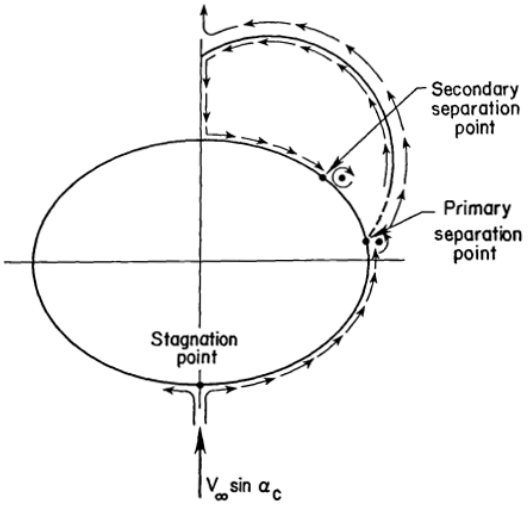

(b) Connection of primary and secondary separation points [24]

Fig. 2.20 Crossflow streamlines for symmetric vortex structures.

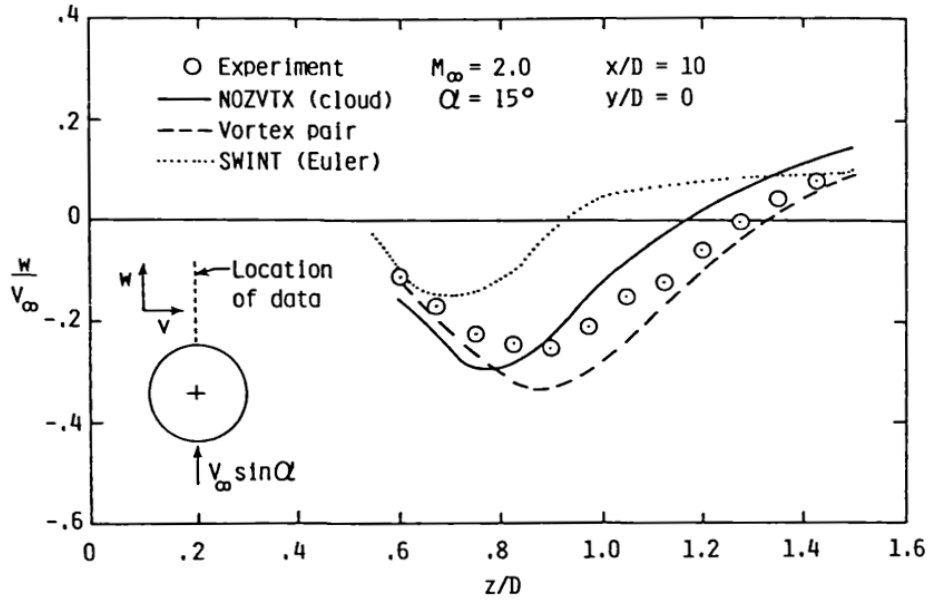

Fig. 2.21 Crossflow downwash distribution along the symmetry plane for a tangent-ogive cylinder undergoing symmetric vortex shedding [24].

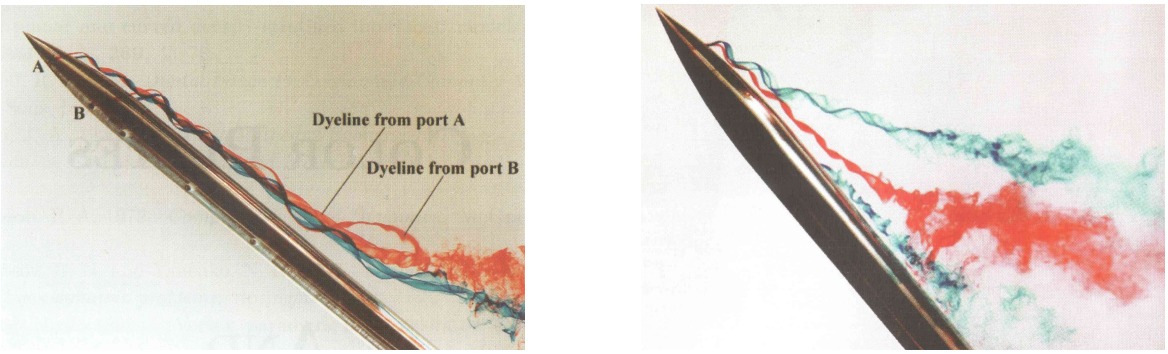

(a) Symmetric shedding

(b) Asymmetric shedding

Fig. 2.22 Breakdown of vortices shed from a tangent-ogive cylinder in a water tunnel [36].

2.1.2 Wing-Specific Features

The overview of flow features specific to the wings will be restricted to the context of typical geometries found on slender bodies. Due to the high speeds ($M_\infty > 1$) associated with typical applications, the wings encountered in practice vary from very-low aspect ratio strakes ($AR = 0.01 \sim 0.05$) through to relatively high aspect ratios (for the application) of $AR = 2 \sim 3$, and are typically of rectangular, triangular, trapezoidal, or "double-delta / cranked" planform. A qualitative comparison of the planforms is given in [8]. Other parameters of the wing profile, such as thickness, camber, and leading-edge bluntness, depend on the application: hypersonic vehicles typically featuring thicker wings with rounded leading-edges due to wing-body blending and considerations of aerodynamic heating; missiles, on the other hand, typically feature thin, symmetrical profiles with chamfered leading-edges. While leading-edge roundness does have an impact on the aerodynamic characteristics of the wing and on the structure of the flowfield, the majority of the flow features will be discussed in the context of sharp leading-edges. Due to the degree of influence of the wing planform (and leading-edge Mach number) on the character of flows around wing-like surfaces, the overview will categorize the flow features encountered according to planform type. The overview will introduce the majority of flow features in the context of delta wings, will introduce the differences observed for other planforms, and will summarize some of the key parameters associated with the features. The focus will largely be on leeside flows, which exhibit more complex flow structures.

Delta-Wing Features

The typical evolution of the flowfield with increasing Mach number around a two-dimensional airfoil at near-zero incidence, depicted in Fig. 2.23 [23], has limited relevance in the context of wing-components of slender bodies. This due to the extent to which vortical structures dominate the definition of the leeside flowfield when the wings are at incidence, as well as due to the extent of the surface subjected to end-effects as a consequence of the low aspect-ratio. Nevertheless, it is of worth to note that SBLI may still play a role in defining the flow structure, and indeed other interactions, such as shock-vortex interactions, are of importance.

A significant feature of the leading-edge sweep, Λ_{LE}, of delta wings is the formation of vortices shed from the leading-edge when the wing is at incidence. Separation of the boundary layer from the sharp leading-edge results in a sheet of rotational separated flow, which rolls up into a primary vortex core, as is seen in Fig. 2.24a [20]. These vortices have a significant influence on the structure of the crossflow flowfield, as depicted in Fig. 2.24b [40].

Also seen in Fig. 2.24b is the onset of vortex breakdown and its impact on the order of the crossflow .The breakdown of the leading-edge vortices, much like their formation, is another significant feature of flows around wings at incidence, as it has the potential to influence a significant portion of the planform, as shown in Fig. 2.25a [20]. Two types of breakdown occur, as shown in Fig. 2.25b [33]. The sudden onset of the "bubble-type" breakdown is typical of vortex-shock interactions.

The breakdown of both symmetric and asymmetric vortices shed by bodies was shown to be a feature of slender-body flows earlier in Fig. 2.22. As was noted in closing the overview of body-specific flow features, similarity in flow features is to be expected when "body" and "wing" components become geometrically similar. This is seen to be true when considering highly-swept delta wings. In particular, it is seen in [34] that the incidence at which asymmetrical vortex shedding occurs in subsonic flows may be correlated to the slenderness of both cones and highly-swept wings. However, the difference between slender-body and delta-wing flows becomes more notable as the sweep-angle decreases, as seen by how asymmetrical vortex shedding is prevented* by the onset of vortex breakdown [41]. This hints at the significance of vortex breakdown in considering wing-specific flow features. The impact of the leading-edge sweep angle on the onset-incidence of vortex breakdown is shown in Fig. 2.26 [41]. It shows the progression of the breakdown location up the chord. It is notable that relatively rapid progression with α is seen over the aft portion of the wing, and that the breakdown behaviour is sensitive to the dynamic viscosity of the fluid. As seen in Fig. 2.26b, the freestream Mach number also has an influence on the onset of vortex breakdown, although the sensitivity to Mach number is affected by the leading-edge sweep (as reflected through aspect-ratio in Fig. 2.26b).

With vortex-breakdown seen to dominate the relatively higher-incidence subsonic flows, the attention will shift to flow features occurring in the absence of vortex breakdown – namely, to the formation and structure of stable, symmetric vortices at subsonic and supersonic speeds. A typical structure of the leeside flowfield at subsonic flows is shown in Fig. 2.27. The vortices shed from the leading-edge is seen to create extra suction on the leeside surface, manifested as a nonlinear increment to the loading-curve for the wing, as shown in Fig. 2.27a [41]. Figure 2.27b [42] illustrates the structure of a two-vortex system, in which separation at the leading-edge (denoted S_1 in the figure) leads to the formation of the primary feeding-sheet (Σ_1), which rolls into the primary vortex core. Due to symmetry, the flow reattaches along the centreline (A_2), with the vortices inducing spanwise flow, which separates (S_2) into a feeding

*It is important to note that this is in the absence of sideslip, which would destroy the overall symmetry of the flowfield and result in the starboard and port leading-edges having different effective sweep angles.

sheet (Σ_2) for the secondary vortex core. The two-vortex system is one of a number [42] of flowfield structures which may occur on the leeside in subsonic flows.

The two-vortex system may also be noted in supersonic flows. This is due to the leading-edge of the delta-wing lying inside the bow shock produced by the apex. As a consequence, the same conical structure of the flow is observed. This introduces one of the key parameters characterizing delta-wing flows – the leading-edge-normal Mach number, $M_N = M_\infty \cos\Lambda_{LE}\left(1+\sin^2\alpha\tan^2\Lambda_{LE}\right)^{1/2}$ – which is accompanied by the leading-edge-normal angle of attack, $\alpha_N = \arctan\left(\tan\alpha/\cos\Lambda_{LE}\right)$. These parameters are central to determining the structure of the leeside flowfield. An example of their role and the difference between subsonic leading-edges ($M_N < 1$) and supersonic leading-edges ($M_N > 1$) is given in Fig. 2.28 [41]. The existence of attached leeside flows is noted for near-zero incidences, with a shock present on the leeside in the case of supersonic leading-edges. The previously-seen two-vortex system is noted in Fig. 2.28a, while Fig. 2.28b introduces another mechanism of vortex generation through shock-induced separation.

A range of leeside flowfield structures exist, with Fig. 2.29a [35] depicting the boundaries between them, and Fig. 2.29b [41] depicting the variation of the windward flow structure with the same parameters. It is to be noted that the boundaries between flow-structure types are affected by leading-edge bluntness. Referring to the sharp-edged flows of Fig. 2.29a, it is noted that leeside flows with no separation are only observed at essentially zero-incidence, or for low-incidence ($\alpha_N < 15°$) at supersonic leading-edge Mach number. The broad spectrum for which shocks and separation are observed underscores the role of SBLI for delta-wing flows. The flow structures depicted in Fig. 2.29a are considered as follows:

- At low incidences of $\alpha_N < 15°$, the classical two-vortex system is observed at approximately $M_N < 0.3$, with no shocks observed on the leeside. As M_N is increased, the leeside flow-structure changes. At higher subsonic M_N, a separation bubble is observed at the wing edge, reattaching further inboard. No shocks or distinct vortex cores are noted. At supersonic M_N in this range of α_N, the separation bubbles are absent. Separation-free expansion occurs around the wing edge. The inboard flow induced by this expansion passes through a shock, which is attached to the wing surface. No separation-bubble observed behind the shock,

- As α_N is increased from $\approx 15°$ at supersonic leading-edge Mach numbers, the inboard shock induces a separation bubble behind the shock. As the incidence is increased further, the separation bubble is seen to originate at the wing edge. A shock is observed to occur above the separation bubble. At even higher incidences, a primary vortex core and its feeding-sheet are observed shocks are observed on the leeside of the vortex core,

- The aforementioned classical-vortex structure with leeside shocks is observed even for subsonic M_N, provided the incidence is sufficiently high ($\alpha_N > 30°$). As M_N is reduced, the leeside flow structure becomes shock-free again.

The broader interpretation of these structures is given in Fig. 2.29b. The transition from conical flow around the leading-edge to supersonic expansion as M_N increases is highlighted. The transition from a detached to an attached bow-shock on the windward side at sufficiently high M_N is also noted. This relative simplicity in the windward flowfield is reflected in Fig. 2.30 [3]. It depicts the constant-pressure regions on the windward surface for $M_N > 1$.

While the leeside flowfield has been seen to exhibit more complex flow structures, the contribution of the leeside surface to the overall loading on the wing diminishes as the freestream Mach number increases. This is shown through numerous figures in [41]. This has a number of consequences. Leeside features such as vortices and vortex breakdown have progressively less influence on the integrated loads for the lifting surface. The windward loading-contribution is influenced in part by the aspect ratio of the surface. It may be noted [41] that an incidence exists at which a crossover occurs in the dominant factor determining the loading slope. Below this incidence, the load-slope is largely governed by aspect-ratio effects, with the slope generally decreasing with increasing Mach number. Above this incidence, the increased strength of the bow shock dominates aspect-ratio effects, and the load-slope is seen to increase with Mach number. The actual incidence at which the change in dominant contribution occurs is a function of the wing planform, as noted in [41]. These remarks regarding the windward-leeward contribution split hold true for the range of planforms and aspect ratios considered here.

Other Wing Planforms and Features

Rectangular planforms are commonly used as stabilizers in slender-body configurations, and exhibit somewhat different structures and behaviour to delta-wing planforms. Of the more notable changes is that to the leeside flow structure, as separation occurs not only at the leading-edge, but also at the tip. This results in non-trivial flow structures being observed, as illustrated in Fig. 2.31 [41]. Another notable change in the flow structure is shown in Fig. 2.32 [3], which underscores the changes brought about by end-effects and the lack of leading-edge sweep. End-effects are particularly important due to the low aspect-ratios typically encountered in the application of slender-body configurations, with end effects impacting progressively larger portions of the wing as the aspect ratio is reduced, as illustrated in Fig. 2.33 [3]. The absence of leading-edge sweep and the associated reduced pressure-relief has a notable influence on the onset of vortex-breakdown. This is typically manifested through a earlier onset of vortex-breakdown as the aspect-ratio is increased [41].

This is also reflected in the earlier breakdown (relative to the delta-wing case) observed at transonic speeds in [41]. At supersonic speeds, however, the overall loading trends for an $AR = 1$ rectangular wing are seen to be similar to those of a delta-wing, with somewhat greater Mach-sensitivity noted in the low-incidence loading slope [41].

Another commonly encountered planform is the trapezoidal wing, or clipped-delta wing, which may be viewed as an intermediate stage between rectangular and delta wings, as seen in the loading-curve in Fig. 2.34a [41]. Unsurprisingly, trapezoidal wings exhibit a combination of delta-wing and rectangular-wing features, as demonstrated through the mixture of conical-flow and tip-effected regions illustrated in Fig. 2.34b [23]. The trends observed for trapezoidal wings thus do not differ remarkably from those seen for rectangular or delta wings. The differences (in particular, the earlier onset of vortex breakdown and more pronounced Mach-sensitivity of low-incidence windward loading-slope) observed in [41] are attributable to the higher aspect-ratio of the $AR = 2$ wing. The double-delta or cranked wing configuration, on the other hand, effectively acts as a trapezoidal wing with improved vortex-breakdown characteristics. This is due to the influence of the vortex shed from the highly-swept strake. It induces a spanwise flow on the main wing which increases its effective sweep, as shown in Fig. 2.35a [41]. Interaction between the strake-shed vortex and the leading-edge vortex of the main wing, as shown in Fig. 2.35b [43], acts to delay the onset of vortex breakdown. This interaction between flow structures is an example of positive interference, which features prominently in the overview of full-vehicle features in the following subsection.

Key Parameters

Wing geometry has been seen (consider Figs. 2.28, 2.29, 2.31 and 2.35) to play a notable role in determining the qualitative characteristics of flow features, particularly in the case of leeside flows. The role of a number of parameters in defining the flow structure is not readily expressed in terms of similarity parameters – particular examples include the influence of leading-edge bluntness on the leeside structures and the influence of aspect-ratio on the loading-variation due to vortex breakdown [41]. Other parameters, such as the Reynolds number, play a relatively smaller role in determining the structure of the flowfield (except in the case of vortex breakdown). This is because structure-defining features, such as the location of flow separation or shocks, are determined more strongly by the geometry and Mach number. The role of sideslip in driving asymmetry of the flowfield is outside the scope of the introductory overview of flow features given here.

The leading-edge sweep angle, freestream Mach number, and freestream angle-of-attack have been seen to influence the flow through the key similarity parameters of the leading-

edge-normal Mach number, $M_N = M_\infty \cos\Lambda_{LE}\left(1+\sin^2\alpha\tan^2\Lambda_{LE}\right)^{1/2}$, and the leading-edge-normal angle-of-attack, $\alpha_N = \arctan\left(\tan\alpha/\cos\Lambda_{LE}\right)$. The role of these parameters in defining leeside and windward flow structures has been prominently featured in this overview. In the case of delta wings with no trailing-edge sweep, the leading-edge sweep angle and the aspect-ratio of the wing are interdependent, and M_N and α_N may be formulated in terms of AR.

More generally, the wing aspect-ratio acts as a measure of the effective slenderness of the wing, and enters both transonic and hypersonic similarity parameters, as detailed in [27, 44]. The transonic similarity parameters are given [44] as: $\chi_T = \left(1-M_\infty^2\right)/\left[(\gamma+1)M_\infty^2\delta\right]^{2/3}$, where γ and δ is the maximum thickness-to-chord ratio of the wing; the transonic aspect-ratio similarity parameter $\tilde{AR} = \left[(\gamma+1)M_\infty^2\delta\right]^{1/3}AR$; the transonic (small) incidence parameter $\tilde{\alpha} = \alpha/\delta$. The hypersonic similarity parameters [27] are seen to be simpler in form, and are given as: $K = M_\infty\delta$; the thickness-relative aspect ratio δ/AR; the hypersonic incidence parameter $\delta\cot\alpha$.

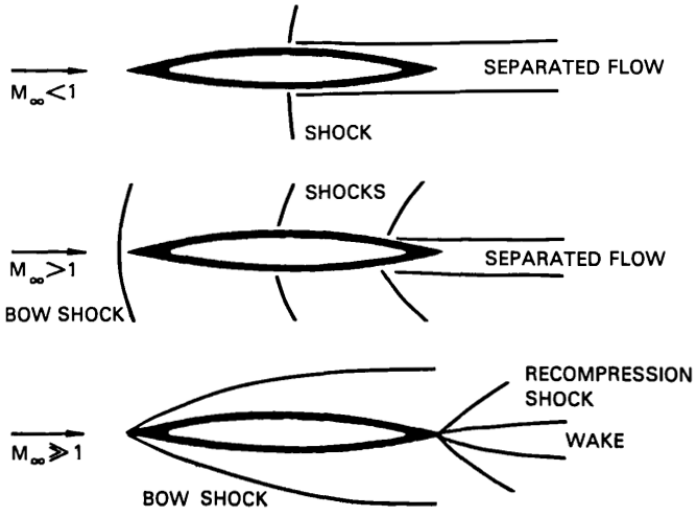

Fig. 2.23 Airfoil shock development with increasing Mach number [23].

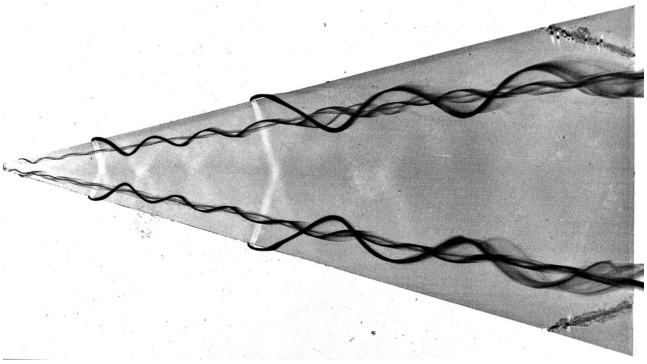

(a) Filaments of the feeding sheet and primary vortex core [20]

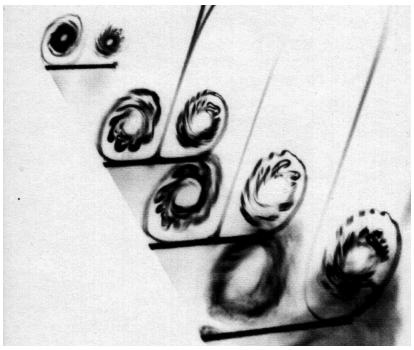

(b) Primary vortex crossflow structure and vortex breakdown [40]

Fig. 2.24 Visualization of subsonic flow over delta wings at incidence.

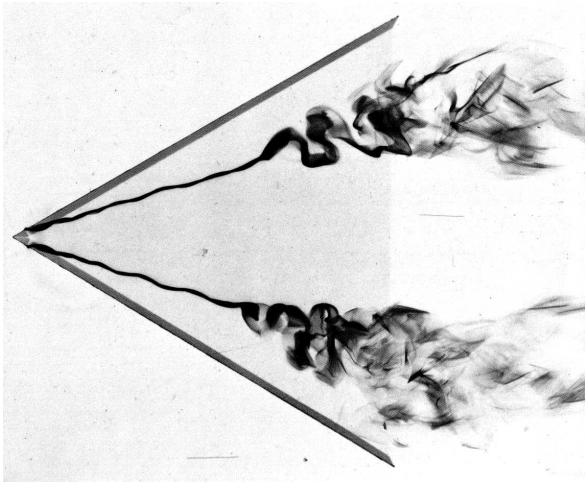

(a) Visualization of breakdown [20]

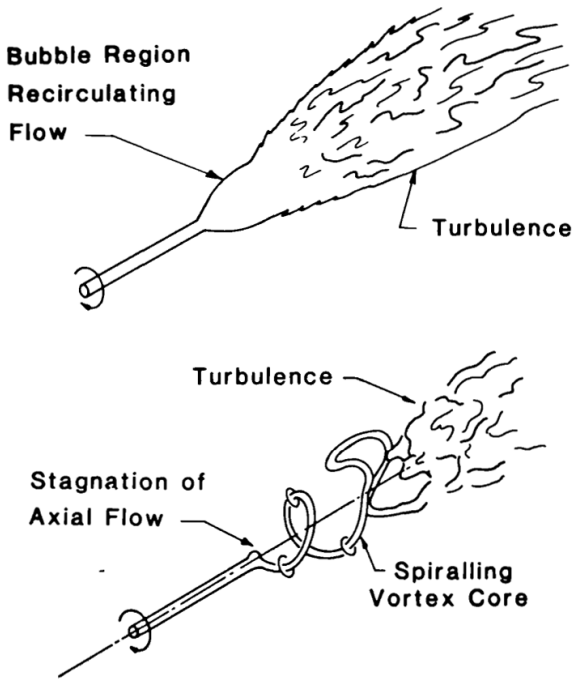

(b) Breakdown types [33]

Fig. 2.25 Vortex breakdown over delta wings in subsonic flow.

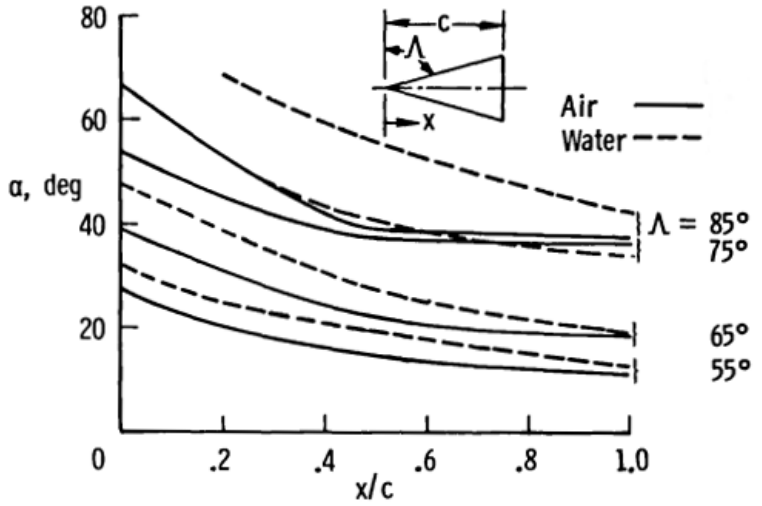

(a) Influence of leading-edge sweep

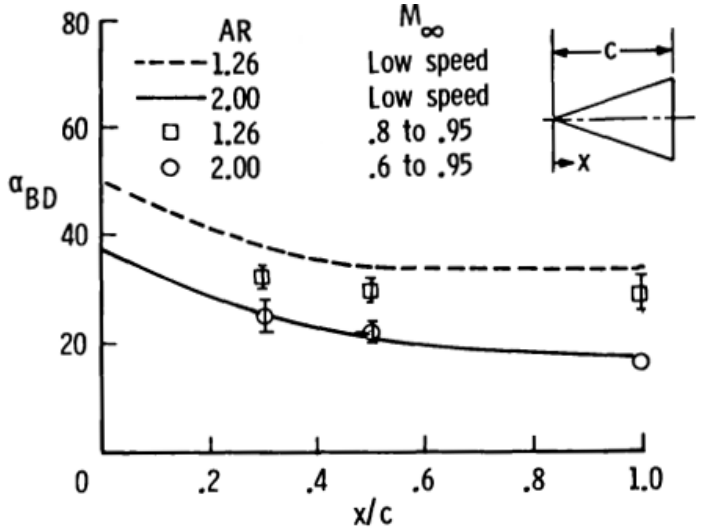

(b) Influence of Mach number

Fig. 2.26 Progression of chordwise-position of vortex-breakdown over delta wings in subsonic flows [41].

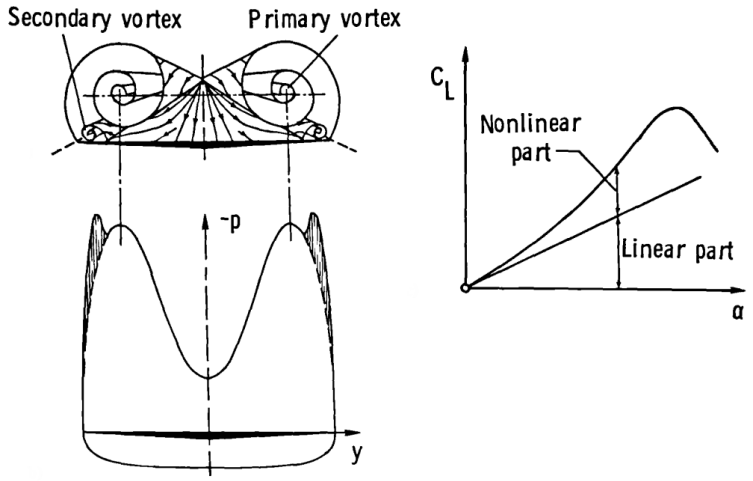

(a) Crossflow flow structures, pressure distribution, and normal force contribution [41]

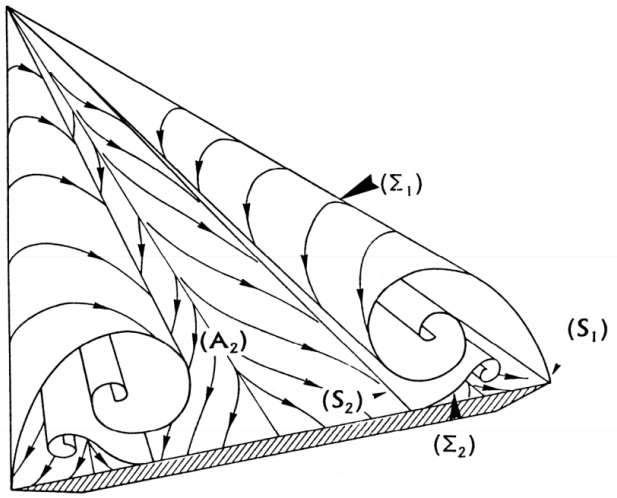

(b) Detailed description of crossflow structures [42]

Fig. 2.27 Vortex development for sharp-edged delta wings in subsonic flow.

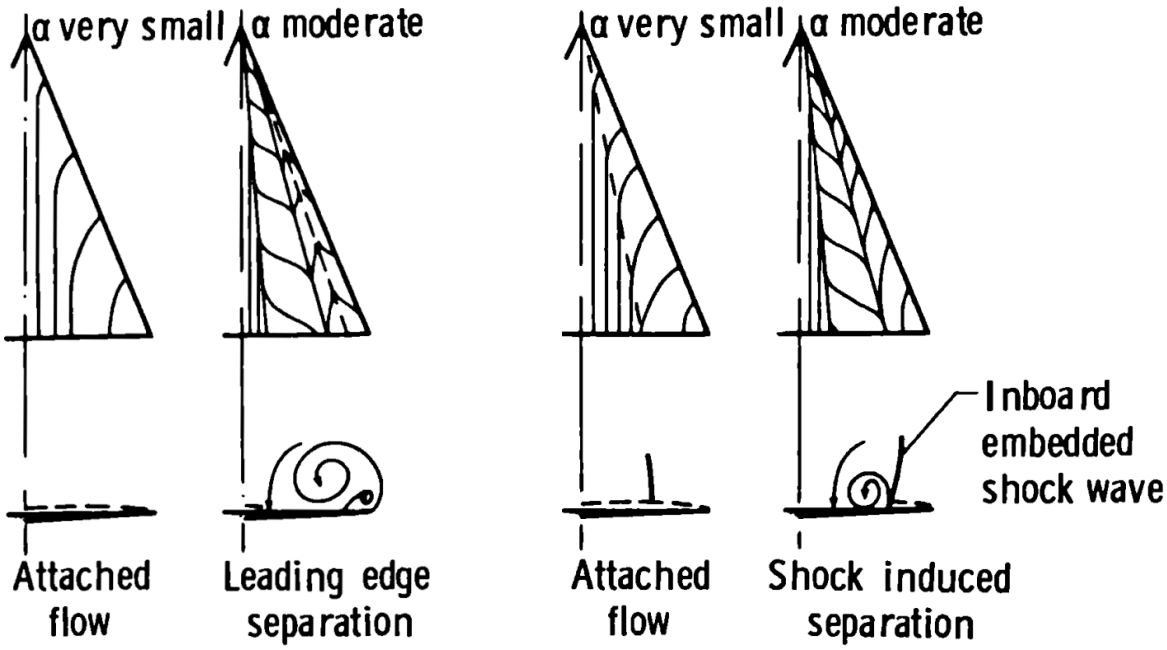

(a) Subsonic leading-edge (b) Supersonic leading-edge

Fig. 2.28 Difference in leeward delta-wing flow structures between subsonic and supersonic leading-edge flows [41].

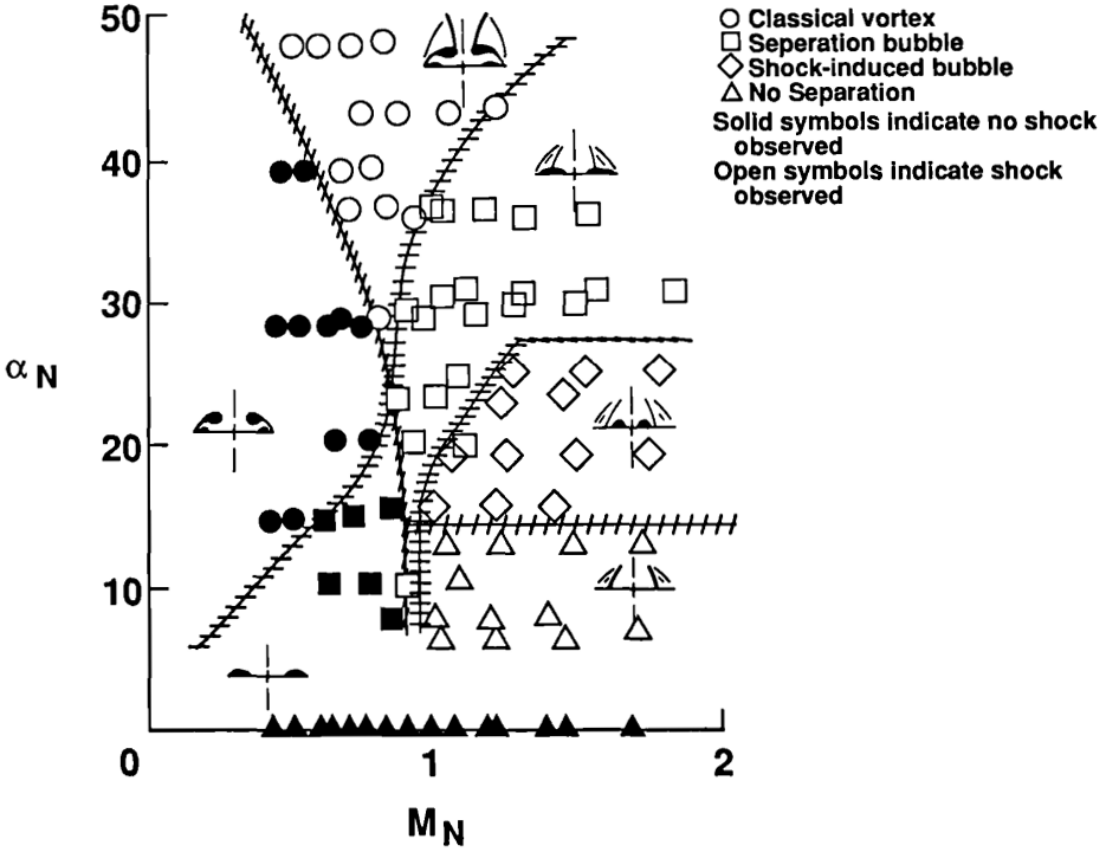

(a) Classification of leeward structures [35]

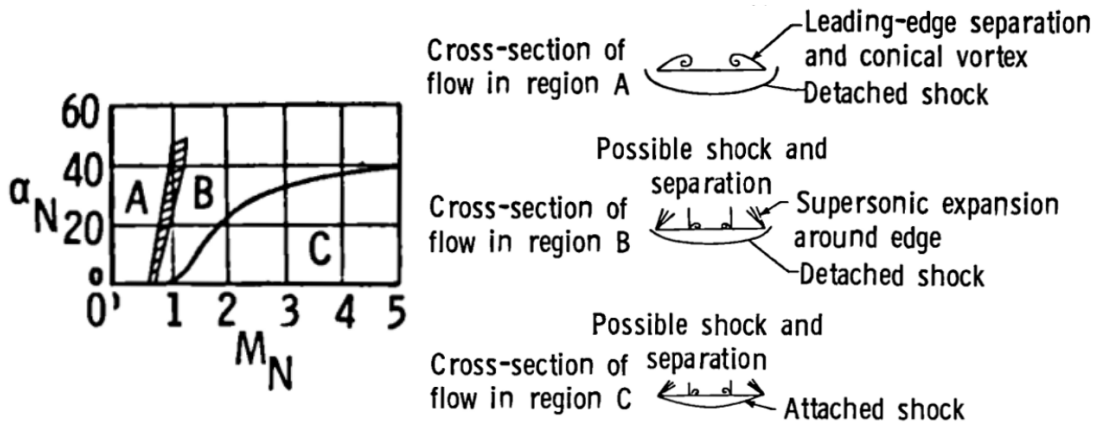

(b) Progression of windward shock position [41]

Fig. 2.29 Variation of sharp-edged delta-wing flow structures with leading-edge normal Mach number and incidence.

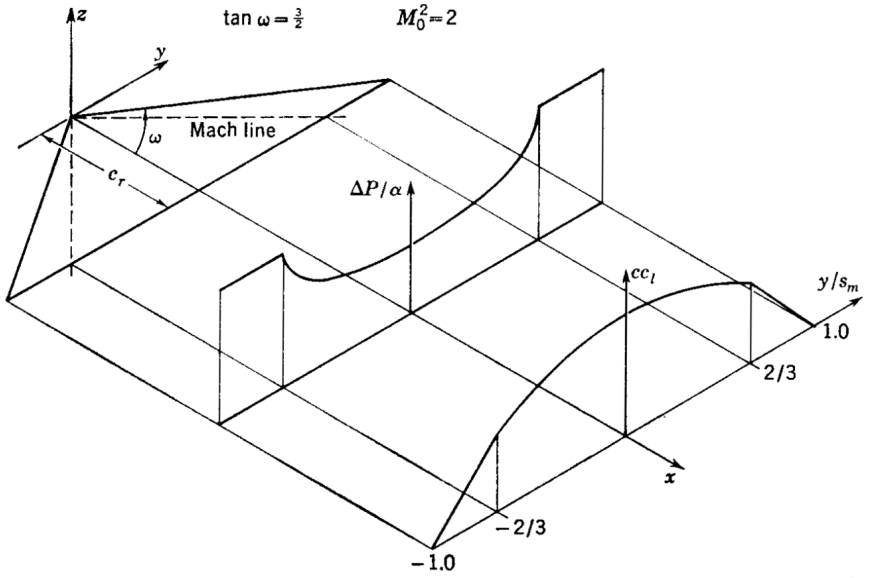

Fig. 2.30 Regions of non-constant pressure on the windward surface of a delta wing with supersonic leading edges [3].

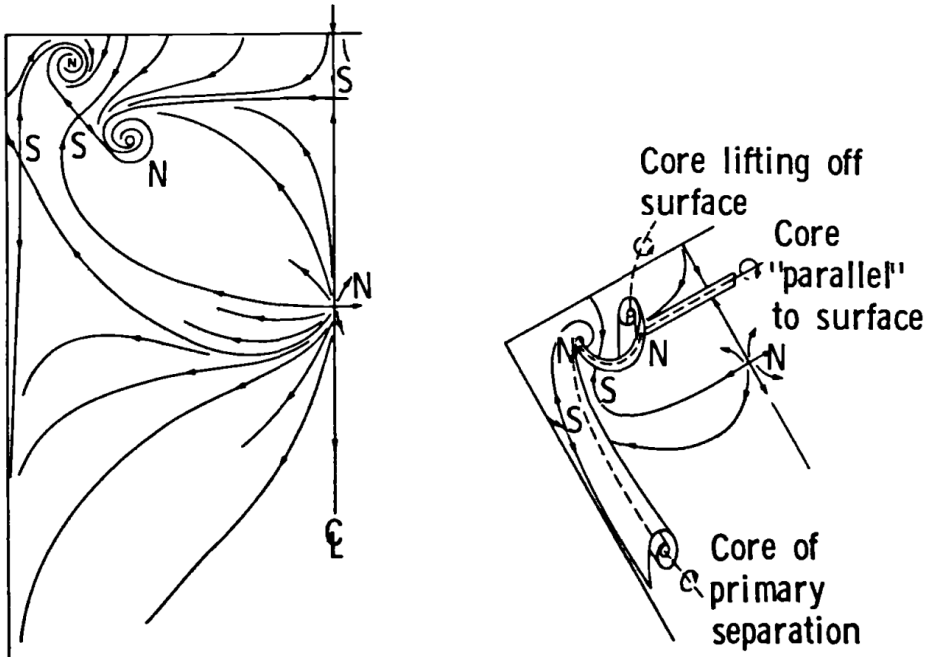

Fig. 2.31 Leeward flow structures of a low aspect-ratio rectangular wing at incidence at subsonic Mach numbers [41].

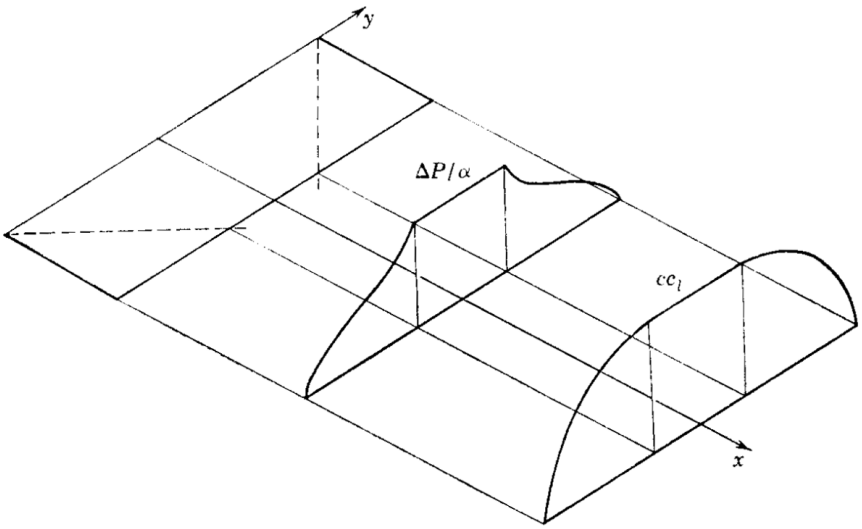

Fig. 2.32 Regions of non-constant pressure on the windward surface of a rectangular wing with supersonic leading edges [3].

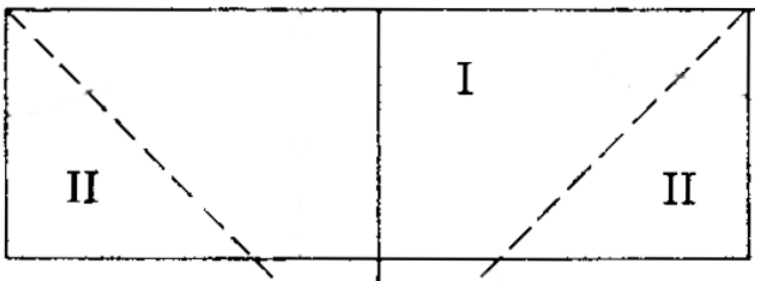

(a) $AR = 3.0$

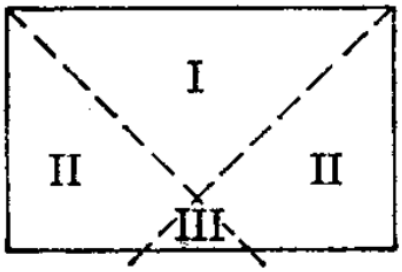

(b) $AR = 1.6$

(c) $AR = 0.6$

Fig. 2.33 Illustration of variation of regions of influence due to end-effects with wing aspect-ratio at $M_\infty = 1.4$ [3].

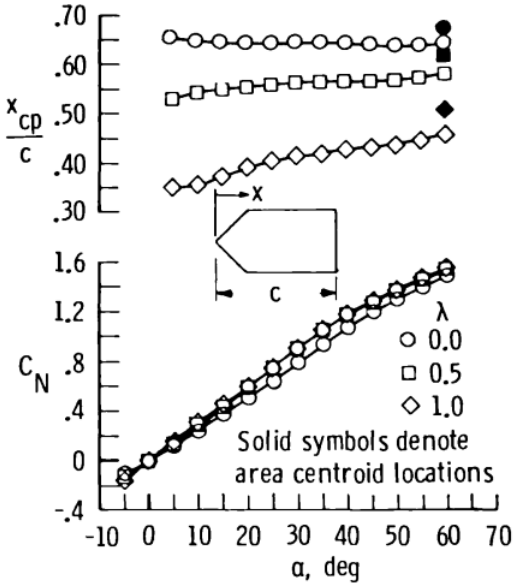

(a) Effect of taper ratio on the wing normal-force curve and center-of-pressure location; $AR = 1$, $M_\infty = 2.16$ [41]

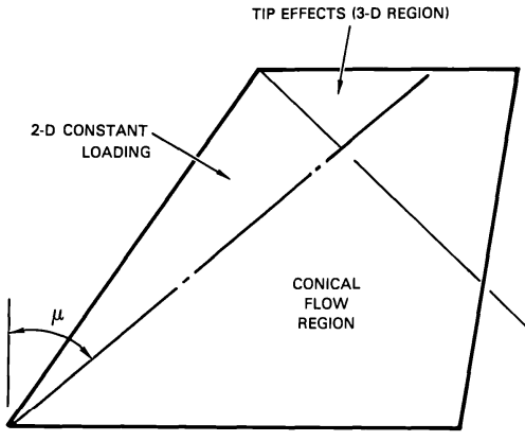

(b) Regions of influence on a trapezoidal wing with supersonic leading edges [23]

Fig. 2.34 Trapezoidal wings as a transition between rectangular and delta wings.

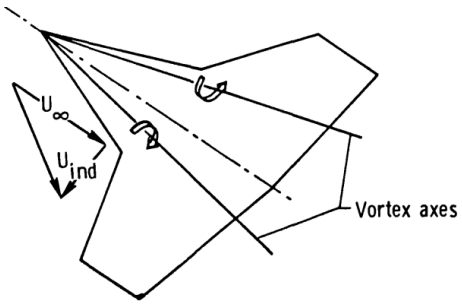

(a) Effect of strake-vortex on wing flow [41]

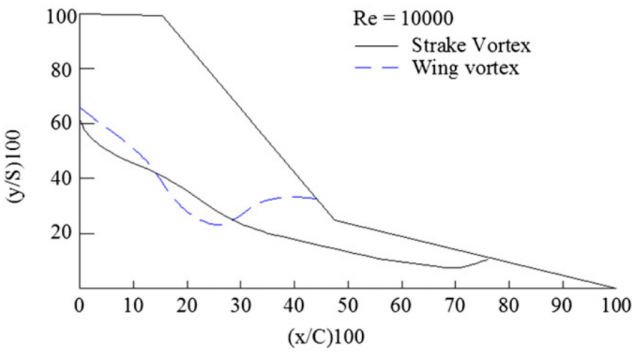

(b) Example of vortex interaction [43]

Fig. 2.35 Vortex interaction on a double-delta (or straked) wing.

2.1.3 Full-Vehicle Features

Aerodynamic interference, or the interaction of flowfields associated with vehicle components, is a characteristic feature of full-vehicle configuration aerodynamics. As illustrated in Fig. 2.36 [41], favourable interference yields improved aerodynamic characteristics. Figure 2.36a demonstrates how vortex interactions due to the adddition of a strake may delay the onset of vortex breakdown over the wing, yielding a more linear loading curve; Fig. 2.36b demonstrates that, for a similar configuration, the contribution due to interference may be highly nonlinear.

This is to be expected, as significant changes to the component-alone flowfields may occur, with complex interactions including SBLI and shock-shock interactions taking place. An example of the impact of wing-components on the flowfield around the body surface is given in Fig. 2.37 [21]. The impact of the windward-surface shock from the port-side fin on the body's surface flow is evident, as is the presence of separation on the leeside. Slightly higher, the flow-turning due to the shock from the upper fin is seen on the body surface, which hints at the complex interactions which would occur further downstream of the fin-section shown. The complexity of the surface flows extends to the flowfield, as suggested even by the simplified physics of the computed inviscid flowfield shown in Fig. 2.40 [45], and as seen in the visualization [21] of the crossflow structure behind a "$\times$" configuration finned slender-body at incidence, which depicts the interaction of the body-shed and wing-shed vortices.

The impact of these flowfield interactions on the loading of the components and of the full-vehicle is usually the quantity of interest, with the contributions generally expressed [46] as

$$C_N = C_{N_B} + C_{N_{W(B)}} + C_{N_{B(W)}} \,, \tag{2.1}$$

where in the interest of simplicity, the expression assumes the configuration is limited a single wing-set, and where C_N is the normal-force coefficient of the full-vehicle configuration, C_{N_B} is that of the body-alone (for the body in isolation), $C_{N_{W(B)}}$ is the normal-force coefficient of the wing in the presence of the body, and $C_{N_{B(W)}}$ is the increment to the body-load due to interference from the wing. For clarity, these terms are depicted in Fig. 2.38. The interference is often expressed in terms of so-called carryover factors, namely through

$$C_N = C_{N_B} + (K_W + K_B) C_{N_W} \,, \tag{2.2}$$

where C_{N_W} is the normal-force coefficient of the wing in isolation, K_W is the wing carryover-factor for the body at zero incidence, and K_B is the body carryover-factor for zero fin deflection. The variation of carryover factors with the diameter-to-span ratio of the wing-

body combination as predicted by slender body theory is shown in Fig. 2.39 [3]. The positive interference on the wing-force is seen to disappear ($K_W \to 1$) in the case of a vanishingly small body. As the wing span is decreased to the limiting case of strakes, it is seen that both the body-force and wing-force are enhanced, with $K_W \to 2$ and $K_B \to 2$. The normal forces here are defined to lie in the plane defined by the vertical fins of a "+" configuration fin-set, with the angle-of-attack similarly defined to lie in this plane.

Turning to Fig. 2.42 [45] it is seen that the addition of a tail to a slender body has a stabilizing effect (reflected in the aft shift in center-of-pressure location) which varies with both incidence and Mach number, and has in impact on the overall normal-force realized. Significantly, the increment to the normal-force is seen to diminish with increased Mach number in Fig. 2.42b. It may be seen in Fig. 2.43 [46] that the variation of the wing carryover-factor may be correlated by the crossflow Mach number, expressed in terms of the body-incidence α_c as $M_c = M_\infty \sin \alpha_c$. The positive interference on the wing-load from the body is seen in Fig. 2.43b to steadily diminish at subsonic-crossflows, with the wing-load being diminished by the body's influence at transonic-crossflows and asymptoting to a constant in the supersonic-crossflow range. The impact of the crossflow Mach number on the overall load-increment due to interference on a typical finned slender-body is shown in Fig. 2.44a [46]. The trend of diminishing contribution with increasing M_c is repeated, both for the "+" configuration (a roll angle of $\phi = 0°$) and for a roll angle of $\phi = 40°$ (close to the "×" configuration). A notable difference is that the overall contribution due to interference in the "×" configuration approaches zero, and does so by $M_c \approx 0.4$; this is also seen for the body-load increment in Fig. 2.44b and the wing-load increment in Fig. 2.44c. From the latter, it is seen that the wing-load contribution to the overall normal-force that is influenced by the body is less sensitive to roll-angle at supersonic-crossflows. This suggests the diminished influence of body vortices on interference. Conversely, the influence of the wing on the body-load increment is visibily more sensitive to the roll-angle and remains so at supersonic-crossflows. This suggests that the body-load increment is largely due to the fins creating a flow-shadow on the leeside and an over-pressure on the windward side in the "+" configuration by restricting the three-dimensional pressure relief the body would experience without fins; the rotation of the fins through to the "×" orientation restricts the body-flow to a lesser extent. This serves to introduce the roll angle as a significant parameter influencing the full-configuration flow features and interference.

The impact of component-integration has thus far been introduced in the context of its effect on the normal-force of the full-vehicle configuration (and contributions towards it). However, its effect on control-surface aerodynamics is of particularly great importance. Reduced control effectiveness and the variation of aerodynamic derivatives, as may result

from aerodynamic interference or aeroelastic effects, impacts the design requirements placed on the control surfaces, control actuators, and the control law. These are of significant consequence in the case of missile design, due to the degree of interaction between sub-systems and the sensitivity of the overall system design to sub-system changes [7]. With this in mind, the remainder of the overview will focus on the impact of full-vehicle configuration flow features and their impact on control-fin loading. This will typically be interpreted through the fin-normal force coefficient, C_{N_F}, which is oriented normal to the control surface.

The previous remarks regarding windward over-pressure and leeside shadowing in the context of wing-body interference are now revisited in the context of control-fin effectiveness. Figure 2.45 [46] shows the variation with crossflow Mach number of control-effectiveness for the windward and leeward control-fins in the "+" configuration, expressed as the ratio of the fin-normal force at incidence to that at zero-incidence for a deflected fin, both in the presence of the body. In both cases, it is noted that the crossflow Mach number is a similarity parameter. It is seen that the effectiveness of the leeward fin is progressively reduced due to shadowing by the body, with the load-ratio asymptoting to zero at supersonic-crossflows; conversely, the effectiveness of the windward fin is enhanced. A fairly smooth variation of the fin-normal loading with roll angle is observed in Fig. 2.46a [46], with a nearly linear variation with deflection angle over the majority of the windward side. The data points of Fig. 2.46a may be correlated by the equivalent angle-of-attack method [47], taking into account the variation of the body-alone flowfield averaged over the space spanned by the undeflected fin, as in shown Fig. 2.46b [46]. This shows that the scaling of fin control-effectiveness is due to the flowfield of the body. Notably, poor correlation is obtained for roll angles lying within approximately 35° of the leeward meridian [46]. This suggests the variation in fin-normal loads in this region may not be attributed solely to variations in the local flow properties, and that the interaction between the fin and body flowfields must be accounted for.

As is seen from the variation of fin-normal loads with Mach number for the undeflected fin, shown in Fig. 2.47 [45], this interaction is likely with the body-shed vortices. This is particularly evident at the lower crossflow Mach number of $M_c = 0.35$ in Fig. 2.47b, with a reversal in the force direction noted at a roll angle of approximately $\phi \approx 35°$ away from the leeward meridian. The same trend is noted for fins of a different planform at a crossflow Mach number of $M_c = 0.73$, as seen in Fig. 2.48 [45]. Also seen is the effect of fin deflection on the fin-vortex interaction, with a shift noted in the roll angle at which the local loading peaks are observed.

In closing, it is noted that more general interactions with upstream flow structures occur. Figure 2.49 [45] shows the impact on rolling moment characteristics of interaction between tail fins and canard-shed vortices, highlighting the impact of aerodynamic interference on

control design. A further example of control-related interactions is given in Fig. 2.50 [21]. It depicts shock-induced breakdown of the canard-shed vortex and the subsequent interactions which occur. The vortex breakdown changes the shock structure, strength, and the downstream flowfield. The role of further interactions, such as SBLI between various geometric components, and of lateral control jets is outside the scope of the present overview.

Key Parameters

The complexity of many of the interactions observed on full-vehicle configurations renders the identification of key parameters difficult. It may be broadly observed that the Mach number plays a key role in defining the zones of influence of upstream structures, while the vehicle geometry (and its inclination to the flow) interacts with the Mach number to determine which components are embedded in these regions of influence, as noted in [48]. This is partly observed in the diminishing of the carryover-factors that is observed with increasing Mach number, as the zones of influence between the body and wing are reduced. In the case of comparitavely local wing-body interference, as occuring over the span of a single wing-set, the ratio of the body diameter to the tip-to-tip span, D/s_m, plays a significant role [3] in determing the interference factors. As may be expected from the overview of wing-alone flow features, the aspect ratio is also significant, with very-low aspect ratio wings [30] or strakes exhibiting different interference trends to control fins. The slenderness-ratio of the body, D/L, relative placement of the wing-sets, crossflow Mach number, fin deflection, and roll angle have all been seen to be important parameters in fin-vortex interaction and indeed local wing-body carryover. The characterization of full-vehicle configuration load-variation and interference factors in terms of these parameters is the realm of aeroprediction methods, particularly of empirical and semi-empirical methods.

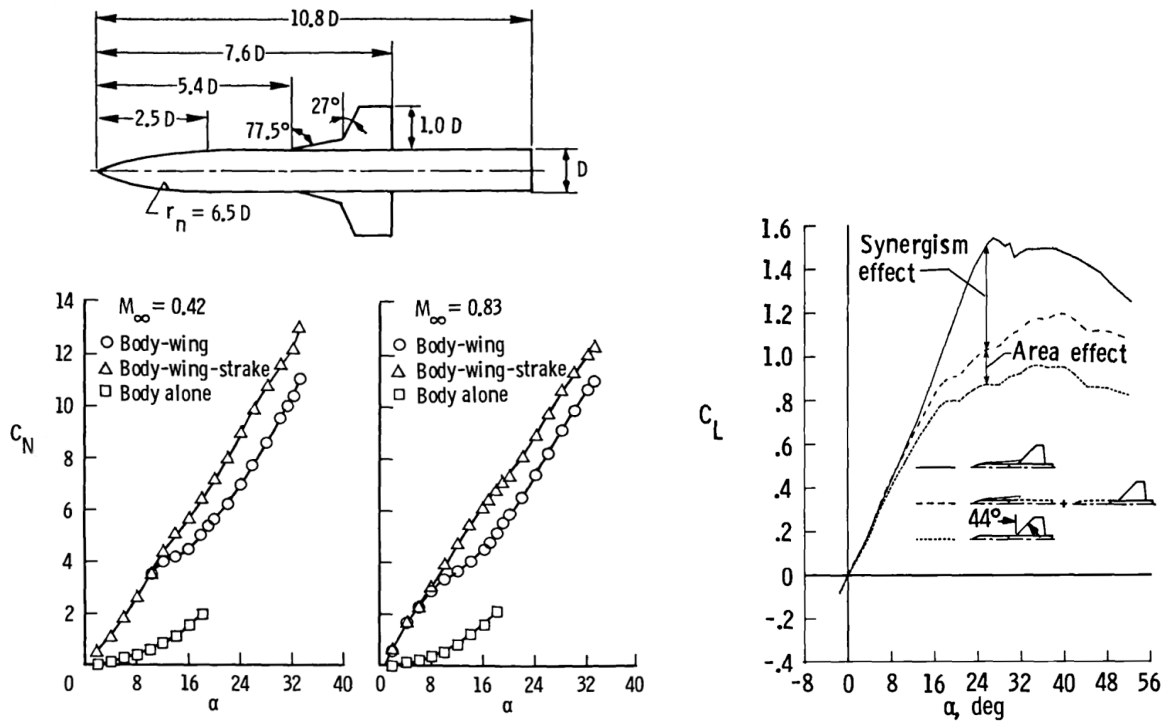

(a) Configuration 1

(b) Configuration 2, $M_\infty = 0.2$

Fig. 2.36 Enhancement of wing-body lift through interaction with a strake-vortex at subsonic speeds [41].

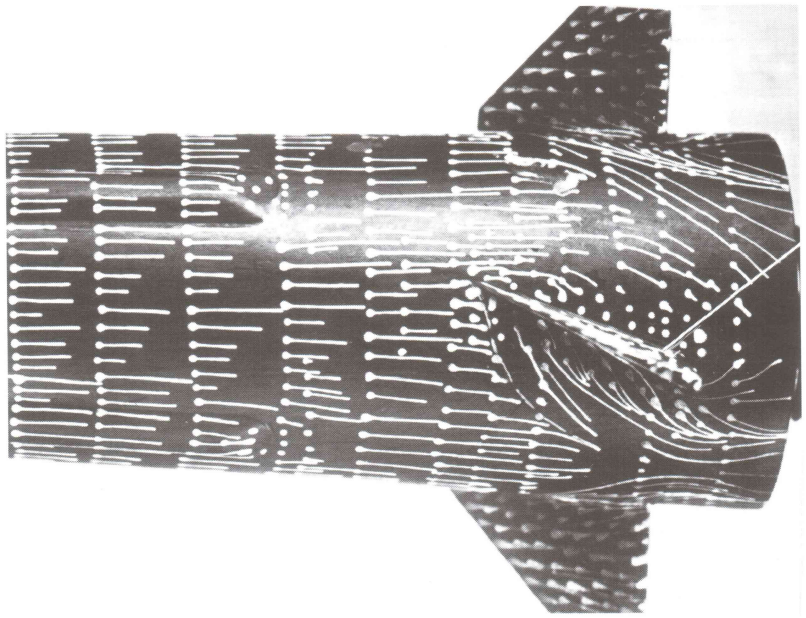

Fig. 2.37 Example of the influence of fins on the body surface flow at supersonic speeds [21].

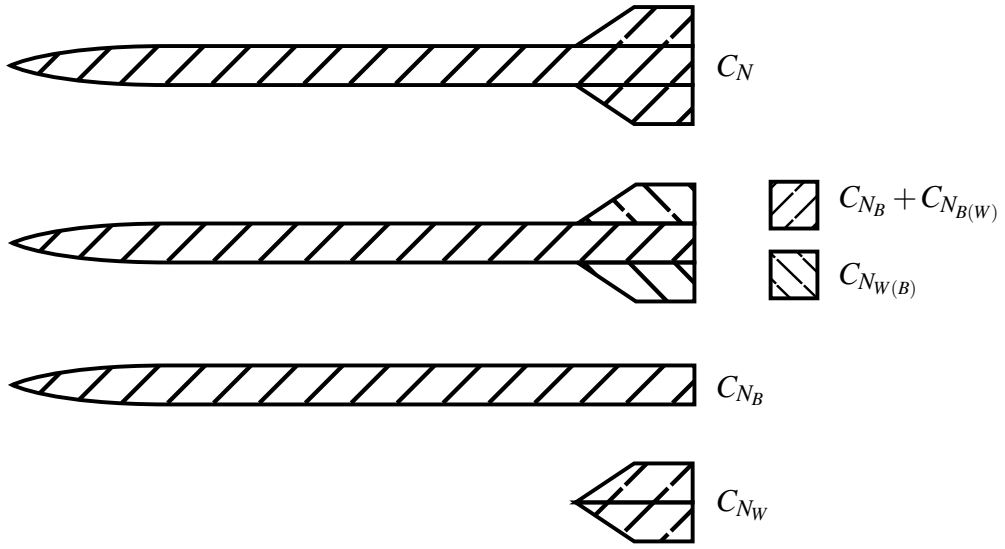

Fig. 2.38 Nomenclature for interference terms.

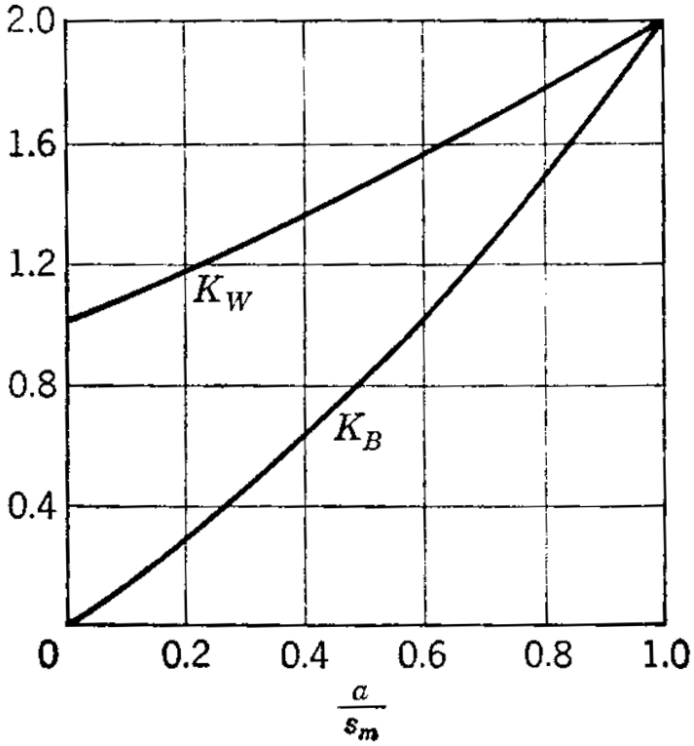

Fig. 2.39 Variation of carryover factors with diameter-to-span ratio as predicted by slender body theory [3].

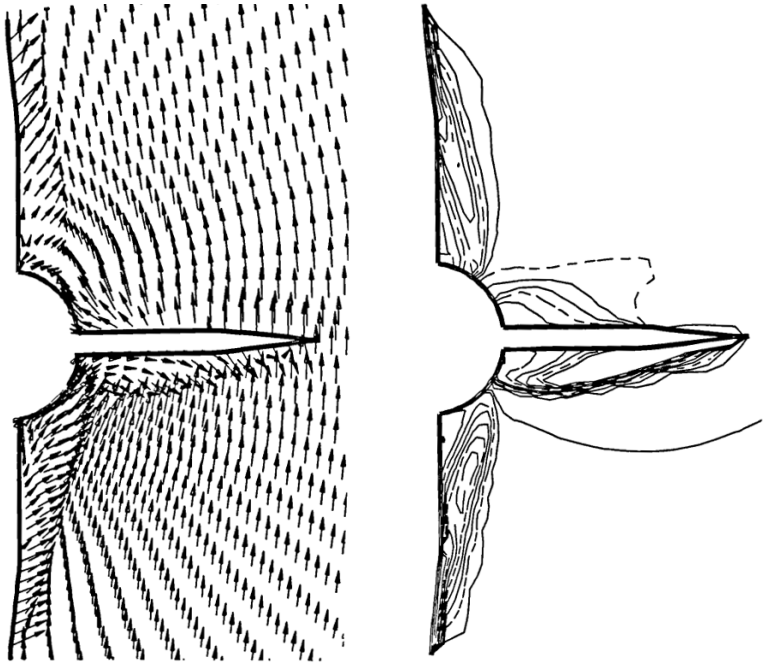

(a) Crossflow velocity (b) Pressure contours

Fig. 2.40 Computed inviscid crossflow flowfield for a finned slender body at $M_\infty = 3.7$, $\alpha = 7.8°$ [45].

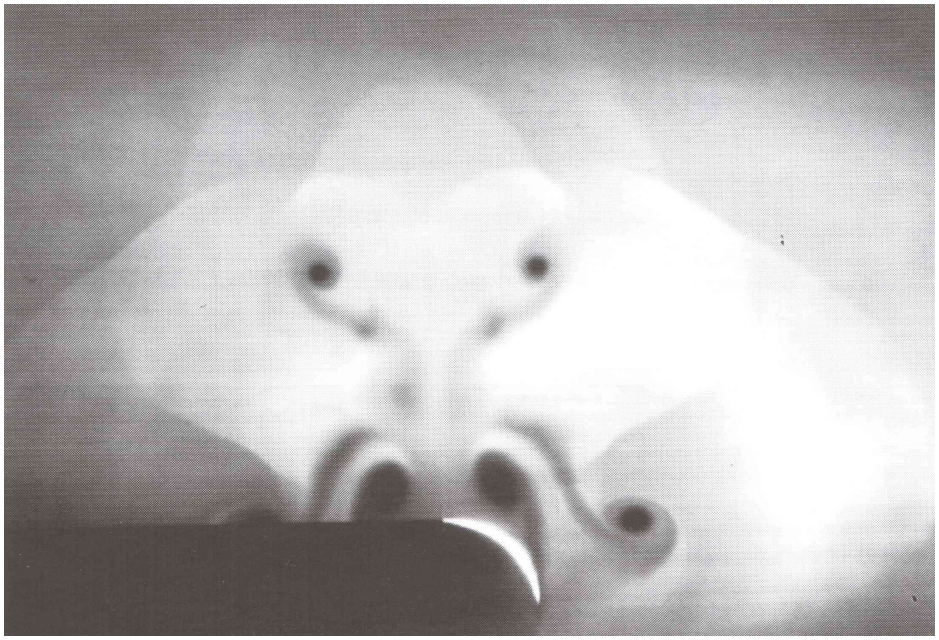

Fig. 2.41 Body and wing vortices in the crossflow plane behind a fin-section in the "×" configuration [21].

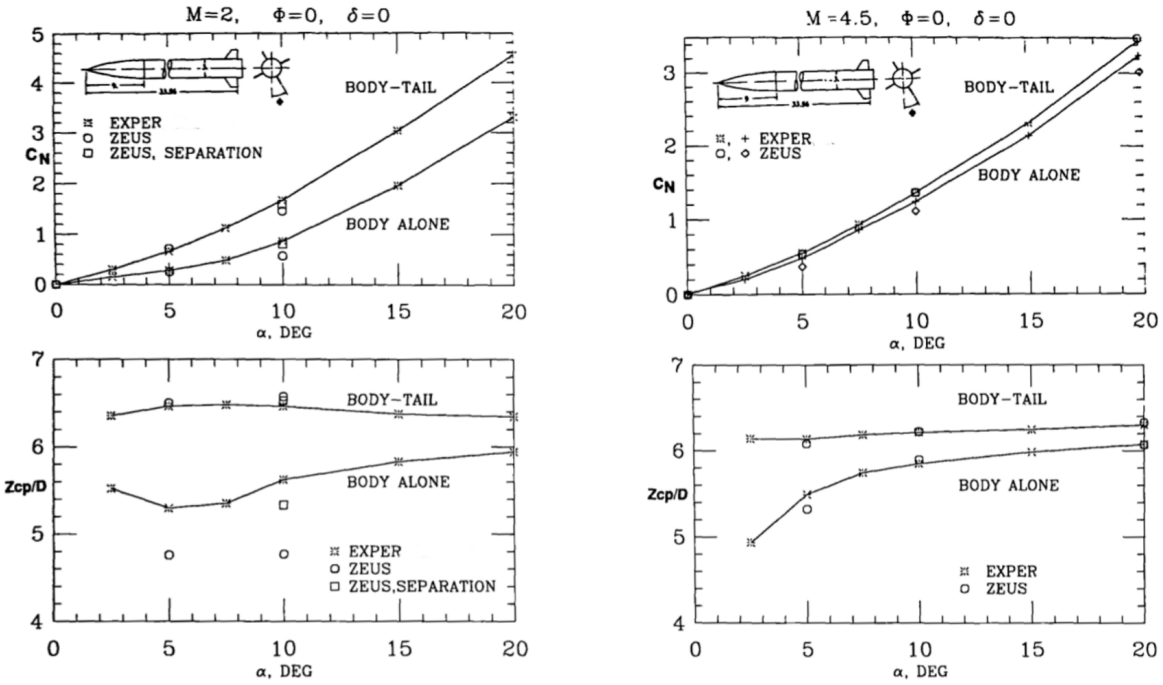

(a) $M_\infty = 2$ (b) $M_\infty = 4.5$

Fig. 2.42 Lifting characteristics of a finned slender body at supersonic speeds [45].

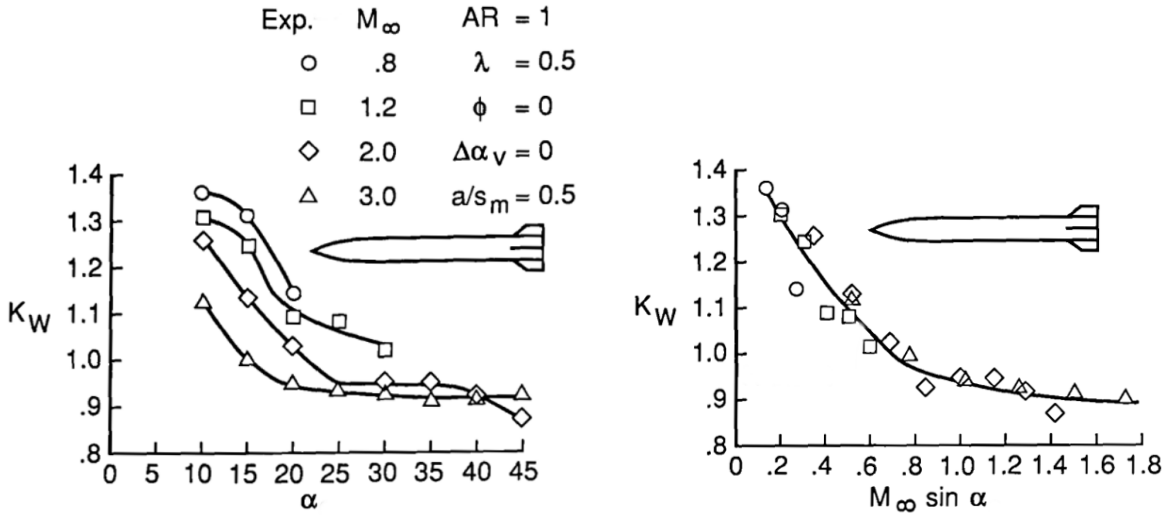

(a) Effect of freestream Mach number (b) Correlation by crossflow Mach number

Fig. 2.43 Compressibility effects on positive interference on wing lift for a finned slender body [46].

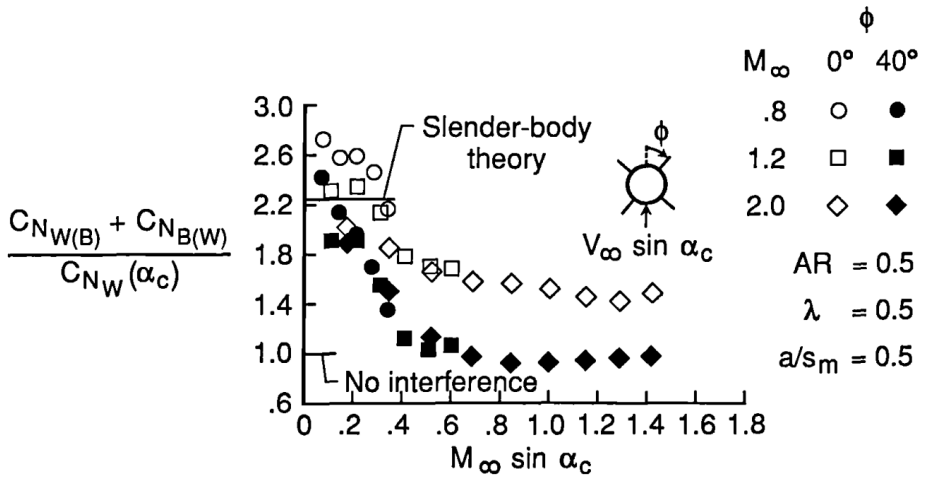

(a) Total interference

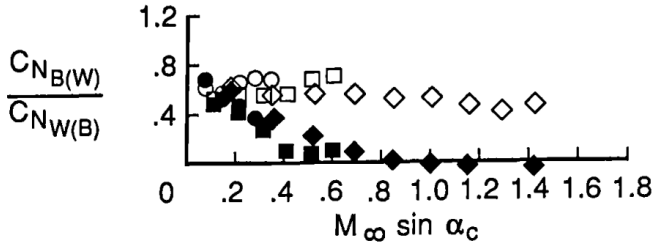

(b) Interferential increment to body load

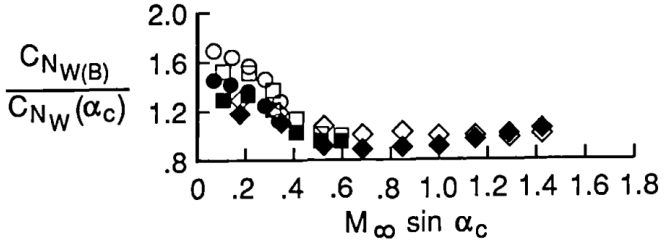

(c) Interferential increment to wings load

Fig. 2.44 Effect of roll angle on the variation of interference factors with crossflow Mach number for a finned slender body; $AR = 0.5$, $\lambda = 0.5$ [46].

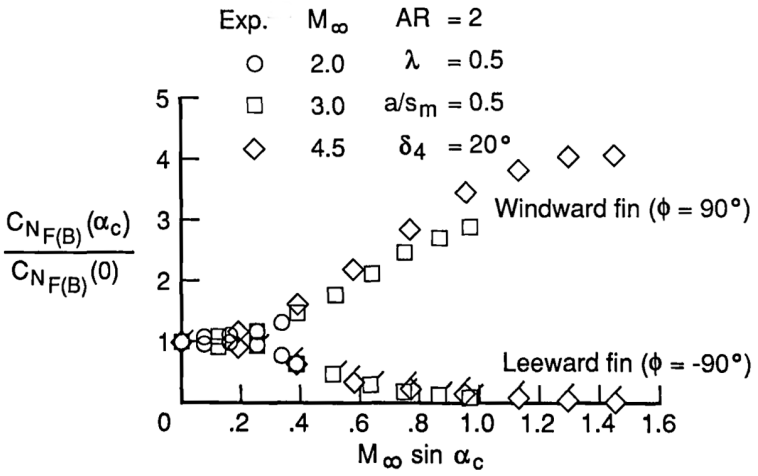

Fig. 2.45 Effect of incidence on the fin-normal force as a function of crossflow Mach number for a fin deflection of $\delta = 20°$ [46].

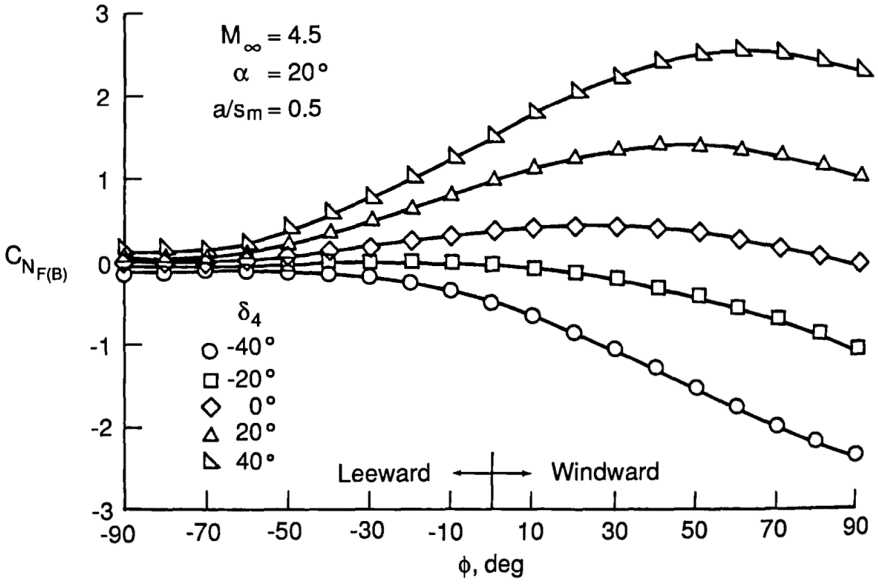

(a) Variation of fin-normal force

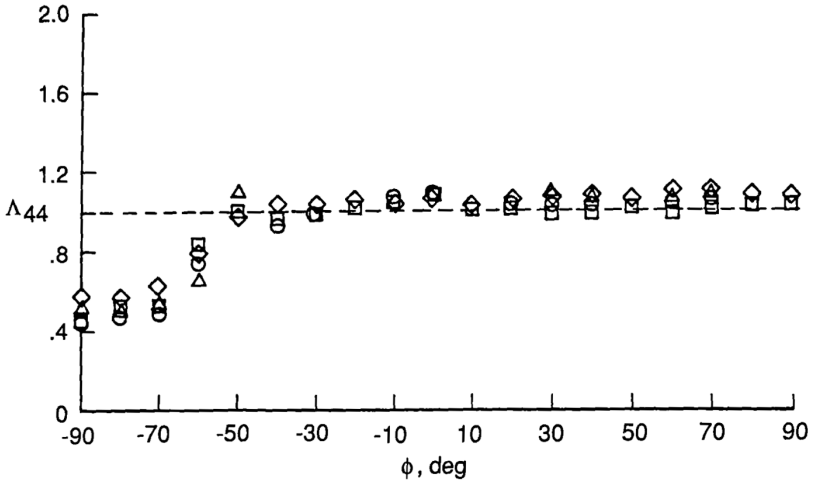

(b) Correlation of the control effectiveness parameter by the equivalent angle-of-attack method

Fig. 2.46 Control-fin effectiveness at a crossflow Mach number of 1.54 for the model from Fig. 2.45 as a function of roll angle and fin deflection [46].

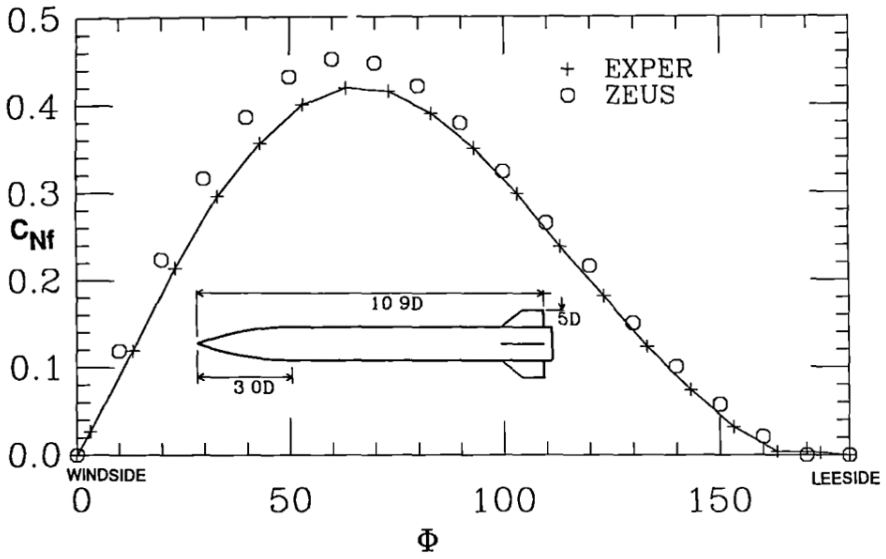

(a) $M_\infty = 4.5$, $\alpha = 20°$

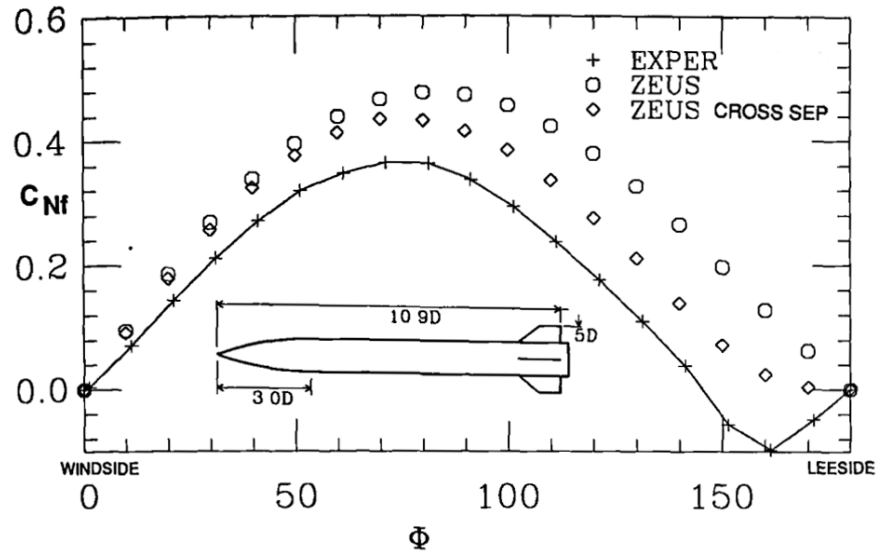

(b) $M_\infty = 2$, $\alpha = 10°$

Fig. 2.47 Variation of fin-normal force with roll angle and Mach number [45].

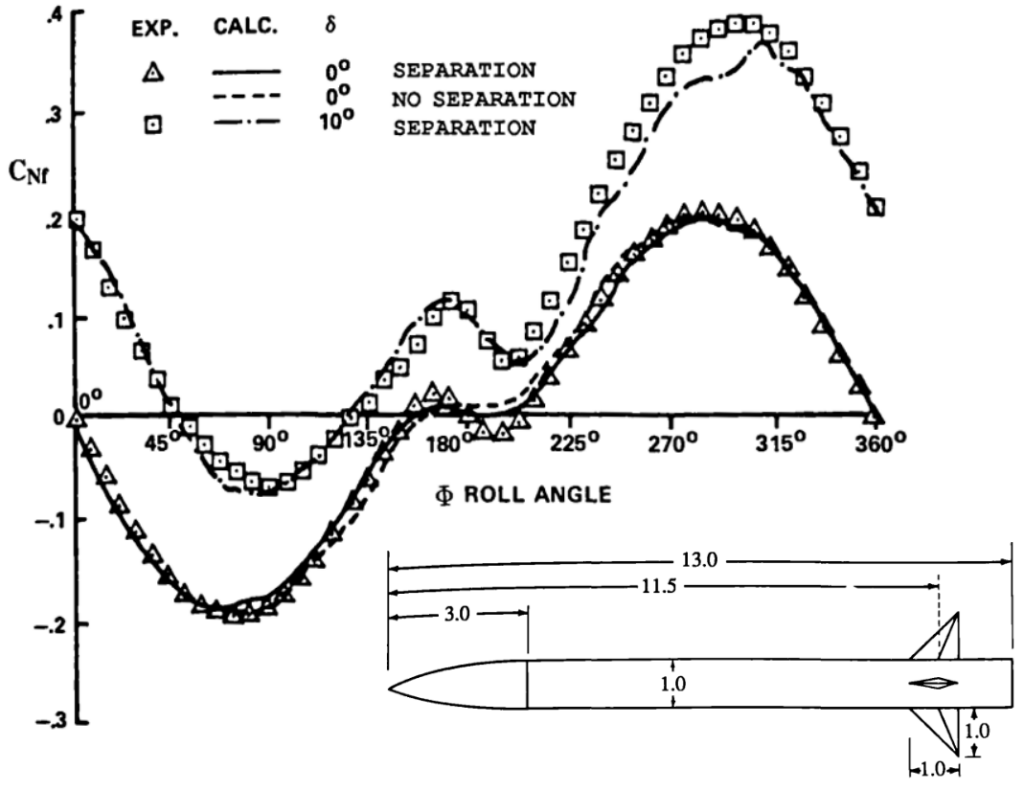

Fig. 2.48 Effect of fin deflection on the variation of fin-normal force with roll angle; $M_\infty = 3.5$, $\alpha = 12°$ [45].

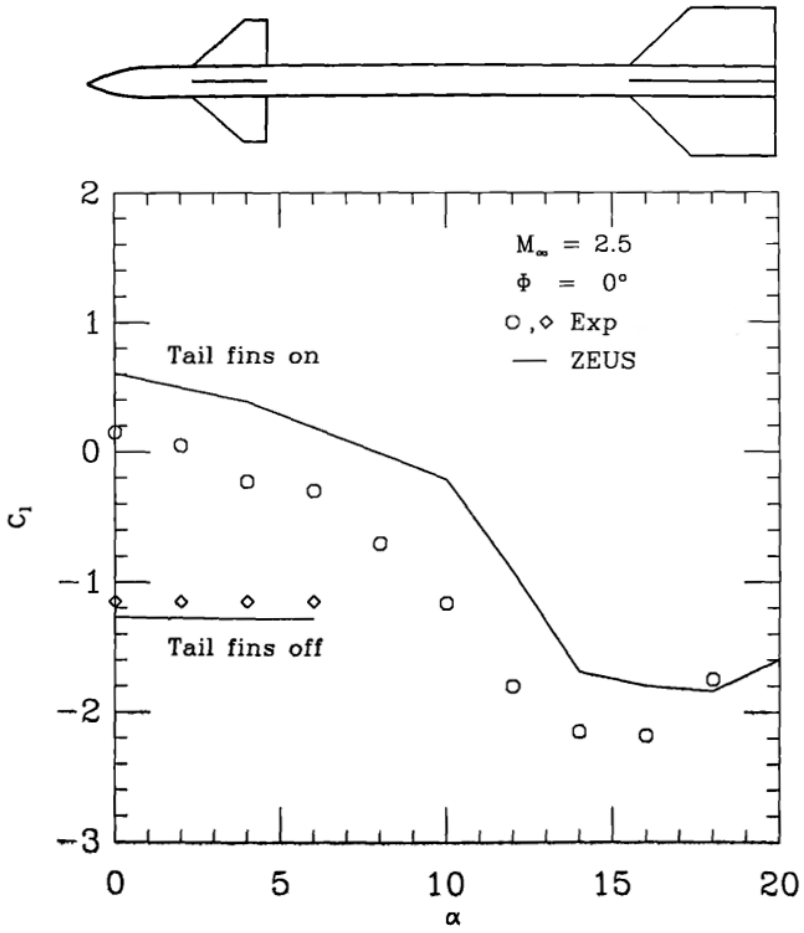

Fig. 2.49 Effect of interaction between canard-shed flowfield and tail fins on rolling moment as a function of incidence; horizontal canards have antisymmetric deflections of $\delta = 5°$ [45].

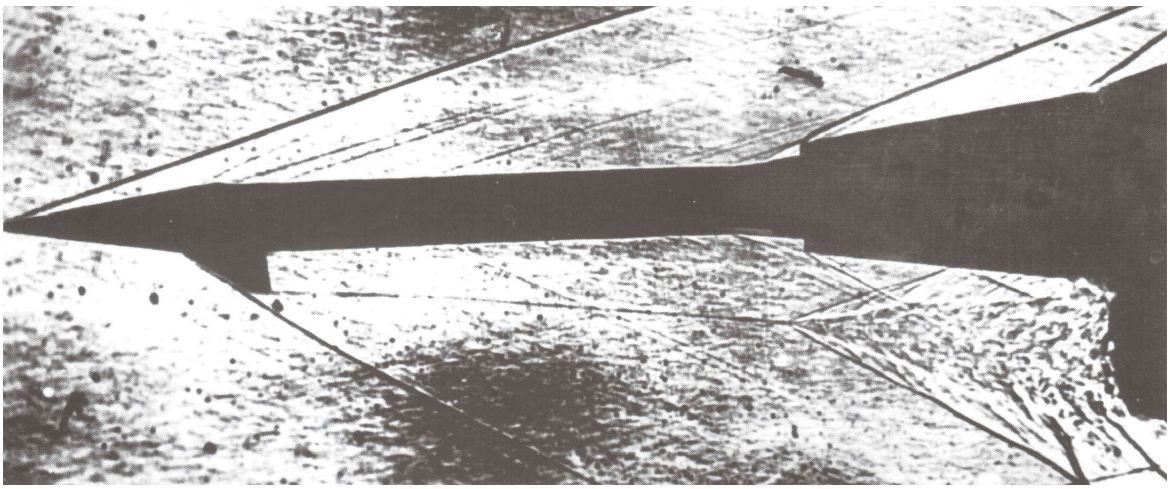

Fig. 2.50 Interaction of canard-shed vortices with a downstream shock and the subsequent vortex breakdown and shock-reduction [21].

2.2 Broadly-Used Prediction Methods

2.2.1 Introduction

The aerodynamic characteristics of a flight vehicle have broad influence [7] on the vehicle's flying characteristics and overall design, with some examples of full-vehicle aerodynamic features introduced in Section 2.1.3. The design of various vehicle sub-systems (e.g., control system, structure, and air-breathing propulsion) requires information about the vehicle aerodynamics, as discussed in [7, 8]. More detailed information about the vehicle aerodynamics is required [8, 49] as the design progresses and matures. This is illustrated in Fig. 2.51. The requirements [30] placed on aeroprediction methods as the design matures are outlined in Table 2.1 [50]. Aeroprediction methods are typically grouped [51] into three categories:

- "Engineering level",
- "Intermediate-level",
- "Advanced-level'.

These categories roughly correspond to the three tiers of requirements noted in Table 2.1, but do not have a strict definition.

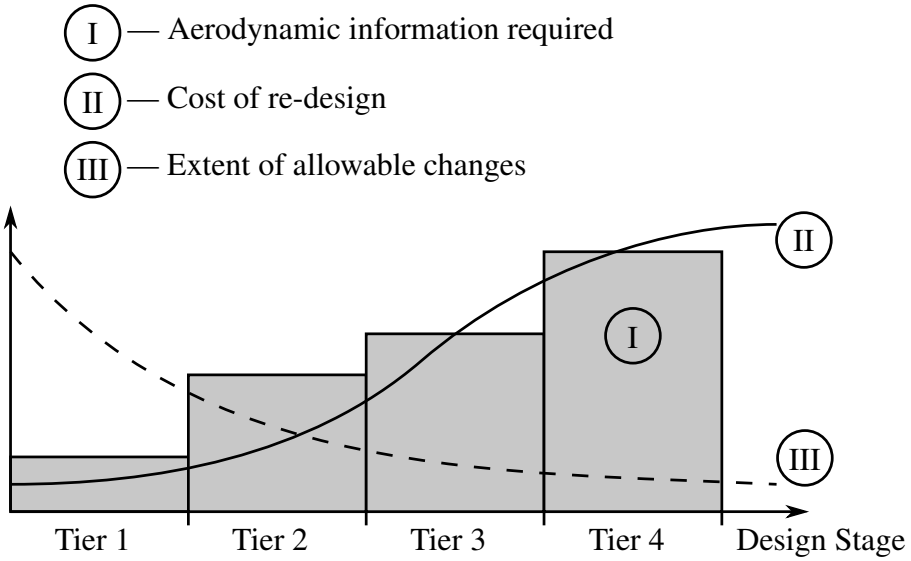

Fig. 2.51 Typical tiered-development design cycle.

In the early stages of the design cycle, in particular during conceptual design, a large number of configurations may be investigated and the time- and computational-cost of aeroprediction must be kept low. Typically [52], "engineering-level" prediction methods are

Table 2.1 Requirements from aeropredict ion methodologies in the missile design cycle [50].

Design Stage	Prediction Code Requirements	Typical Trade Studies	Aerodynamics Uses
Conceptual Design	- Robustness - Ease of use - Minimal input parameters - Extremely fast computationally - $<$ 25% error	- Engine types - Warhead types - Material requirements - Typical weights - Guidance types - Airframe control type	- Range - Maneuverability - Response time
Preliminary Design	- Blend of robustness, ease of use, and accuracy - Fast computationally - $<$ 10% error	- Structural layout (material, thickness) - Aerodynamic shape vs. engineering and guidance size - Hot vs. cold structure	- Range - Maneuverability - Miss distance (3 DOF) - Structural design
Detailed Design	- Robustness still important - Computationally affordable - $<$ 5% error	- Detailed structural design including material selection - Investigating critical problem areas	- Range - Maneuverability - Miss distance (6 DOF) - Structural design.

used in the early stages of the design, so named due to the simplicity of the methods and the often limited detail of information they provide. This category of methods encompasses methods based in interpolation from experimental databases (empirical methods), approximate analytical models which are supplemented by or derived from experimental trends (semi-empirical methods), as well as approximations to higher-order analytical models. This is detailed in [50, 52, 53].

As the design matures, more detailed aerodynamic information is required [8, 49], as may be provided by "intermediate-level" prediction methods. These methods are intermediate in the sense of providing more detail than engineering-level methods at lower time- and computational-cost than "advanced-level methods", which are typically computational fluid dynamics (CFD) codes that provide accurate, detailed information but are computationally expensive [50]. Intermediate-level methods consist of higher-order approximate models and are often supplemented by semi-empirical methods [50].

The different categories of aeroprediction methods represent the trade-off taking place between the computational cost (which is proportional to the time-cost) of the methods and the fidelity of the methods. In the present context, the fidelity of a model refers to its ability to reproduce the physics observed experimentally, rather than the accuracy of the integrated loads predicted by the model. This trade-off between physics and computational cost is depicted for analytical models in Fig. 2.52 [1]. A number of intermediate models are omitted, such as thin-layer [54] Reynolds-averaged Navier-Stokes (RANS) and the transonic small-disturbance potential equation [55]. More detail on approximations to the Navier-Stokes (NS) equations is given in [56].

For the purposes of this review, the primary factor that will be used in determining the category into which a prediction method falls will be computational cost. Empirical and semi-empirical methods are inherently low-cost, as they typically involve interpolation from an existing database or the use of simple algebraic equations. These methods do not typically provide details about the pressure distribution on the vehicle or about the flowfield. For these reasons, they are categorized as engineering-level methods. In categorizing analytical methods, the computational cost may be considered a function of the complexity and number of equations to be solved. The categorization is thus made based on the extent of spatial discretization required by the methods:

- Methods based in linear potential flows, or requiring at most boundary-discretization (panel methods) are thus categorized as engineering-level methods. Examples include slender body theory [3], the doublet-lattice method [57], first-order shock-expansion theory [58], Newtonian impact theory [27], and piston theory [59],

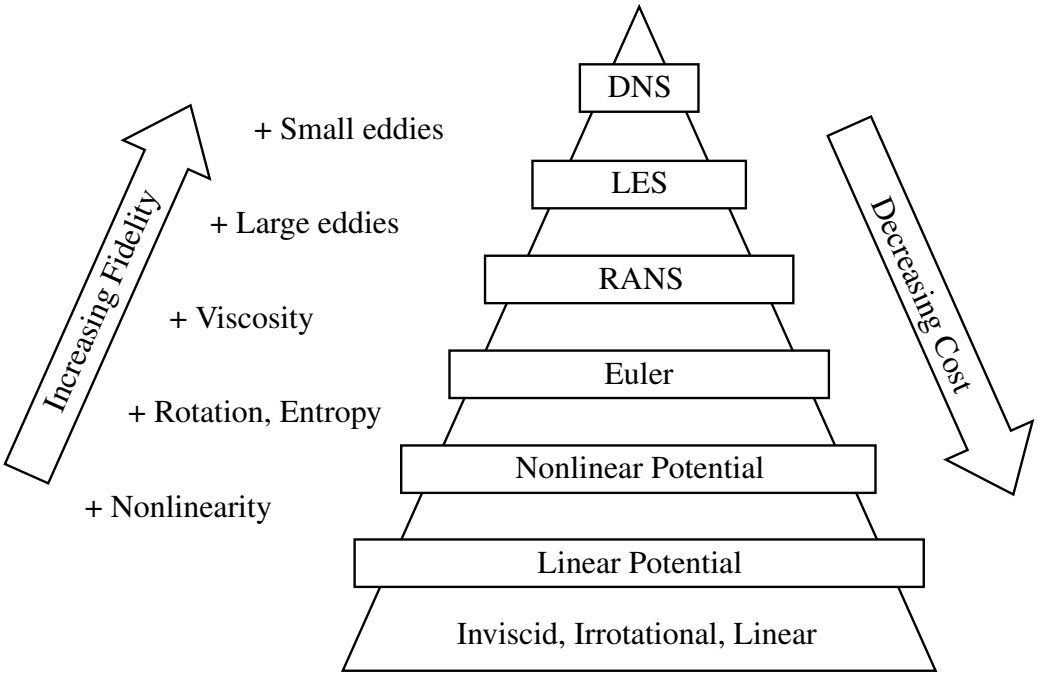

Fig. 2.52 Trade-off between physics fidelity and computational cost in analytical methods [1].

- Nonlinear inviscid methods requiring at most 2D field-discretization are considered intermediate-level methods. Examples include slender-body approximations such as hypersonic small-disturbance theory [27] and Sychev's [4] method for large-incidence hypersonic flows. The transonic small-disturbance theory [44] and the full potential equation [44], as well as CFD augmented by local piston theory [14, 18], will also be considered intermediate-level methods,
- Methods requiring 3D field-discretization are considered advanced-level methods. This encompasses various simplifications to the Navier-Stokes equations, such as thin-layer and parabolized RANS, and the Euler equations. These methods are described in [56].

The notable exceptions to the categorization rule are 3D nonlinear potential flows and CFD augmented by local piston theory. The first is categorized as an intermediate-level method due to the reduced number of equations and variables [44] relative to Euler and Navier-Stokes methods. The second is considered such due to the reduced cost of perturbation modelling relative to full unsteady CFD [14].

It is to be noted that the aeroprediction methods that will be listed in the following sections have been implemented in a range of prediction codes and analysis software. Various extensions and modifications to the basic methods are not covered, and the particulars of the methods are not entered into in great detail. Methods dealing with axial-force prediction

are not considered due to the negligible role axial-force plays in aeroelastic phenomena. The purpose of the review is to give an overview of common methods used and of their capabilities, with the view of identifying gaps in current modelling capabilities. The spectrum of methods will be approached starting with advanced-level methods, as intermediate-level and engineering-level analytical methods are in many cases mathematical simplifications of advanced-level methods. This is depicted in Fig. 2.53.

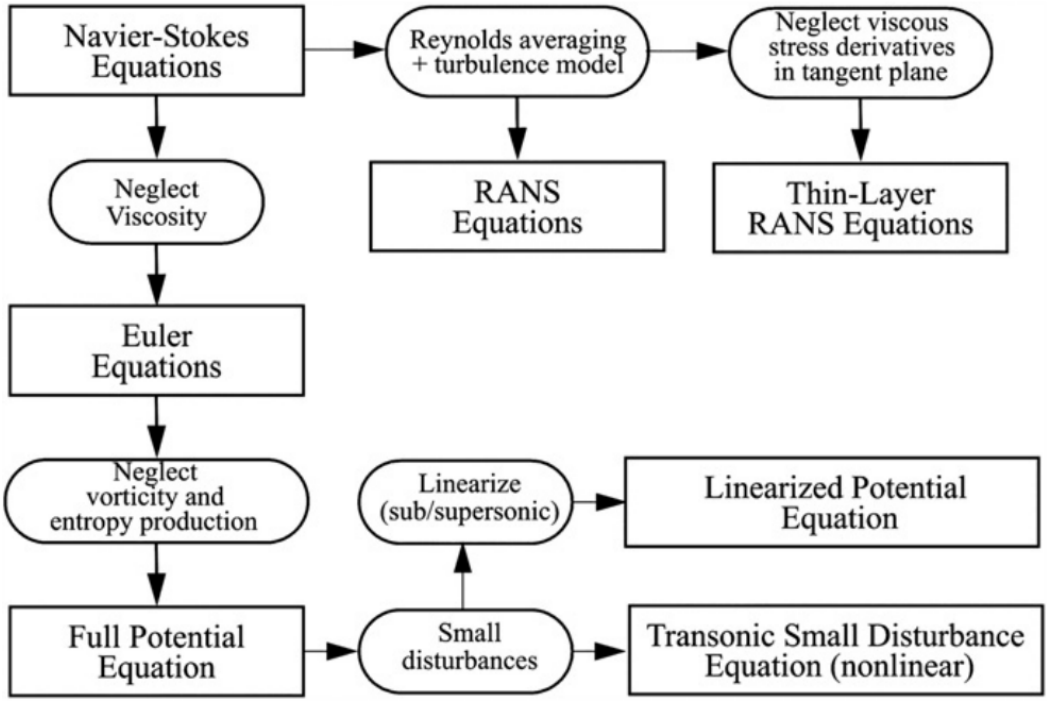

Fig. 2.53 Relationship between analytical methods of different fidelities [44].

2.2.2 Advanced-Level Methods

To accurately replicate physical flow features in a computational environment, mathematical models must be used that correctly describe the dominant flow physics. As was noted in the overview of Section 2.1, slender bodies often exhibited complex flow structures. Shock-waves, SBLI, turbulence, boundary-layer separation, and vortices were seen to play important roles in defining the flowfield. Of the spectrum of aeroprediction methods available, advanced-level methods offer the highest modelling fidelity and greatest detail. The methods considered here include the

- Reynolds-averaged Navier-Stokes equations,
- Euler equations,

- Euler equations with boundary-layer interaction.

While greater fidelity is possible with more advanced methods such as Large-Eddy Simulation [60, 61] (LES) and Direct Numerical Simulation [61] (DNS), these methods are seldom used in a design environment due to having a restrictively high computational cost. The methods outlined here are essentially control-volume-based models. Other advanced-level methods, such as the Lattice-Boltzmann method [62], are not covered here. The Lattice-Boltzmann method in particular has not been applied as widely as RANS, due in part to the lack of consensus on a consistent approach to modelling supersonic flows, as described in [62].

Viscous Formulations

The Reynolds-averaged Navier-Stokes equations will be the highest-fidelity aeroprediction method covered in this overview. The inherent assumptions in the model are that the fluid may be considered a continuum, and that the effects of turbulence may be averaged over time. Of the various aeroprediction methods covered here, RANS-based methods have the distinguishing feature of explicitly modelling viscosity and turbulence. The RANS equations will be introduced in the context of the general Navier-Stokes equations. The unsteady NS equations in Cartesian coordinates are quoted from [63] below as

$$\text{Continuity:} \quad \frac{\partial \rho}{\partial t} + \frac{\partial \rho v_i}{\partial x_i} = 0\,, \tag{2.3}$$

$$\text{Momentum:} \quad \rho \frac{\partial v_i}{\partial t} + \rho v_j \frac{\partial v_i}{\partial x_j} = \frac{\partial T_{ij}}{\partial x_j}\,, \tag{2.4}$$

$$\text{Energy:} \quad \rho \frac{\mathrm{d}e}{\mathrm{d}t} = -\frac{\partial q_j}{\partial x_j} + T_{ij} \frac{\partial v_i}{\partial x_j}\,, \tag{2.5}$$

$$\text{Surface BC:} \quad v_i = v_{Bi}\,, \tag{2.6}$$

where p is the fluid pressure, ρ is the fluid density, v_i is the i-th component of the fluid velocity vector, v_{B_i} is the i-th component of the local velocity-vector of the surface, x_i is the i-th spatial coordinate, t is time, e is the specific internal energy of the fluid, q_i is the i-th component of the fluid heat-flux vector, and T_{ij} is the Cauchy stress tensor. The material derivative is denoted $\frac{\mathrm{d}}{\mathrm{d}t}$, with

$$\frac{\mathrm{d}}{\mathrm{d}t} = \frac{\partial}{\partial t} + v_i \frac{\partial}{\partial x_i}\,. \tag{2.7}$$

The equations as they are written are unclosed, and require a constitutive equation to relate fluid shears to stresses and an equation of state. If the fluid is assumed to be Newtonian, then

the Cauchy stress tensor T_{ij} may be written in the notation of [63] as

$$T_{ij} = \left(-p + \lambda_C \frac{\partial v_k}{\partial x_k}\right)\delta_{ij} + 2\mu\varepsilon_{ij}\,, \tag{2.8}$$

where λ_C is the non-shear component of the coefficient of bulk viscosity, μ is the dynamic viscosity of the fluid, δ_{ij} is the Krönecker delta, and ε_{ij} is the fluid rate of deformation tensor. Aris [63] writes the rate of deformation tensor and the first two invariants of the Cauchy stress tensor as

$$\varepsilon_{ij} = \frac{1}{2}\left(\frac{\partial v_i}{\partial x_j} + \frac{\partial v_j}{\partial x_i}\right), \tag{2.9}$$

$$\frac{\partial \varepsilon_{ij}}{\partial x_j} = \frac{1}{2}\nabla^2 v_i + \frac{1}{2}\frac{\partial}{\partial x_i}\frac{\partial v_j}{\partial x_j}, \tag{2.10}$$

$$\Theta_C = \sum_i \varepsilon_{ii} = \frac{\partial v_i}{\partial x_i}, \tag{2.11}$$

$$\Phi_C = \frac{1}{2}\sum_{i\neq j}\left(\varepsilon_{ii}\varepsilon_{jj} - \varepsilon_{ij}\varepsilon_{ji}\right), \tag{2.12}$$

where Θ_C is the first invariant of the Cauchy stress tensor (which is equal to the divergence of fluid velocity), and Φ_C is the second invariant of the Cauchy stress tensor. Aris [63] notes that the rate at which internal forces do work in the fluid, $T_{ij}\frac{\partial v_i}{\partial x_j}$, may be split into a reversible interchange with strain energy, $-p\frac{\partial v_i}{\partial x_i}$, and an irreversible dissipation by viscous forces via Υ, written as

$$T_{ij}\frac{\partial v_i}{\partial x_j} = -p\frac{\partial v_i}{\partial x_i} + \Upsilon\,, \tag{2.13}$$

$$\Upsilon = (\lambda_C + 2\mu)\Theta_C^2 - 4\mu\Phi_C\,, \tag{2.14}$$

where Υ is the viscous dissipation function.

Alternative formulations of the NS momentum equation, Eq. (2.4), may be obtained by using Eqs. (2.9) and (2.10) in the derivative of Eq. (2.8) and substituting into Eq. (2.4). It is common to see formulations in which it is implicitly assumed that μ and λ_C may be taken as constants. Two formulations of the momentum equation are presented below with this assumption:

$$\text{Laplacian form:}\quad \rho\frac{\partial v_i}{\partial t} + \rho v_j\frac{\partial v_i}{\partial x_j} = -\frac{\partial p}{\partial x_i} + (\lambda_C + \mu)\frac{\partial}{\partial x_i}\frac{\partial v_j}{\partial x_j} + \mu\nabla^2 v_i\,, \tag{2.15}$$

$$\text{Vorticity form:} \quad \rho\frac{\partial v_i}{\partial t}+\rho v_j\frac{\partial v_i}{\partial x_j}=-\frac{\partial p}{\partial x_i}+(\lambda_C+2\mu)\frac{\partial}{\partial x_i}\frac{\partial v_j}{\partial x_j}-\mu\varepsilon_{ijk}\frac{\partial \omega_k}{\partial x_j}, \tag{2.16}$$

where ω_i is the fluid vorticity vector. In cases where it is not admissible to assume constant μ and λ_C, as in hypersonic flows with large temperature gradients and chemistry, an alternative formulation must be obtained by appropriate differentiation of Eq. (2.8), as shown in [64].

A number of alternative formulations of the NS energy equation, Eq. (2.5), may be obtained through applying assumptions about the equation of state and the heating conduction law. Without invoking these assumptions, the energy equation may be expressed in the following forms:

$$\text{Internal energy form:} \quad \rho\frac{\mathrm{d}e}{\mathrm{d}t}=-p\frac{\partial v_i}{\partial x_i}-\frac{\partial q}{\partial x_i}+\Upsilon, \tag{2.17}$$

$$\text{Enthalpy form:} \quad \rho\frac{\mathrm{d}h}{\mathrm{d}t}=\frac{\partial p}{\partial t}-\frac{\partial q}{\partial x_i}+\Upsilon, \tag{2.18}$$

$$\text{Entropy form:} \quad \rho T\frac{\mathrm{d}s}{\mathrm{d}t}=-\frac{\partial q}{\partial x_i}+\Upsilon, \tag{2.19}$$

where h is the specific enthalpy of the fluid, s is the specific entropy of the fluid, and T is the fluid temperature. Since the viscous dissipation function always has a value of $\Upsilon \geq 0$, as shown in [63], Eq. (2.19) clearly shows that a flow can only be isentropic ($\frac{\mathrm{d}s}{\mathrm{d}t}=0$) in the absence of viscosity and heat transfer.

The equations introduced thus far represent the general unsteady NS equations. The Reynolds-averaged formulation of the NS equations is essentially similar, and will not be entered into in great detail as they are covered extensively in literature, such as [64–66]. The essence of the RANS formulation lies in splitting the flow variables into two components:

- An ensemble-averaged component (denoted by a barred quantity), e.g. $\bar{v}_i$,
- A component representing the turbulent fluctuation about the average value (denoted by a dashed quantity), e.g. v'_i.

The fluid velocity, for example, would then be written as $v_i=\bar{v}_i+v'_i$. This splitting of variables is done for each flow quantity, and the resulting equations are ensemble averaged. Terms in the equations which are linear in fluctuating variables disappear when the ensemble average is taken, as it is assumed that the mean of the fluctuating quantities is zero by definition. The result is that the form of the general NS equations is retained for ensemble-averaged quantities. Additional nonlinear turbulent-fluctuation terms appear, which are interpreted as turbulent-stress terms.

The introduction of new variables (specifically, the turbulent-fluctuation terms) in the RANS formulation renders the equations unclosed. To close the equations, a turbulence model is required that relates the turbulent flow variables to the averaged flow variables. An extensive range of turbulence models are available, which will not be covered in this overview. Examples of prominent turbulence models used for external aerodynamic flows include the Spalart-Allmaras (SA) model [67–69], the k-ε model[70], and the k-ω model [71, 72]. Turbulence models are essentially semi-empirical, with recommended coefficients in the equations determined by correlation of the models to experimental data. The RANS equations themselves are limited in their modelling fidelity of highly separated or highly unsteady flows, as noted in [73]. Such flows, as may occur at very high angles of attack ($\alpha = \mathcal{O}(90°)$), are better modelled by LES. This is due to the ability of LES to model coherent instantaneous turbulent structures, which are important in these flows, as discussed in [73]. The successes and shortcomings of RANS-based methods in replicating experimental flows associated with slender bodies are covered in detail in [35, 74].

The remainder of the analytical methods that will be considered may be viewed as progressively more extensive approximations to the NS equations. Two approximations to the NS equations which retain viscosity are the so-called thin shear-layer (TSL) and the parabolized Navier-Stokes (PNS) formulations. Both approaches involve assumptions about the relative importance of various directional gradients of the viscous stress terms. In the TSL formulation, it is assumed [64] that all turbulent and viscous shear-stress terms involving gradients tangential to the surface may be neglected. In the resulting TSL-NS equations, viscous terms only appear as velocity-derivatives normal to the surface. As noted by Hirsch [64], the final formulation is similar to the boundary-layer approximation, as viscous diffusion parallel to the surface is neglected. The main difference between the boundary-layer formulation and the TSL approximation is that the latter retains the momentum equation normal to the surface, and thus permits a viscous surface-normal pressure-gradient within the shear-layer.

Hirsch [64] notes that the PNS approximation differs from the TSL formulation in two key ways:

- PNS applies only to the steady-state formulation of the NS equations,
- Surface-tangential transverse shears are not neglected.

The main assumption of the PNS approximation is that a dominant flow direction exists, and that diffusion of momentum and energy in that direction may be neglected. As a result, no viscous terms involving streamwise derivatives appear, and the PNS equations are first-order in the streamwise direction. As noted by Hirsch [64], the streamwise spatial-variable may

then be viewed as a pseudo-time variable, with the equations solved as an unsteady problem in the transverse plane. This mathematical interpretation of a steady 3D flow as an unsteady 2D flow was introduced in Section 2.1 as the viscous crossflow analogy. The mathematical interpretation will be elaborated on in Section 2.2.3 in the context of 2D inviscid methods. Moore [50] suggests that the TSL approximation is suitable for "moderate" separation, while the PNS formulation is limited to "small" separation. This is because flow reversal in the dominant streamwise direction would mean that the viscous gradients in this direction would be comparable to the transverse gradients [64], violating the underlying assumption of the PNS approximation.

Inviscid Formulations

The next level of simplification of the RANS equations is given by the Euler equations. This is achieved through neglecting the contribution of viscosity. The resulting Euler equations are given by

$$\text{Continuity:} \quad \frac{\partial \rho}{\partial t} + \frac{\partial \rho v_i}{\partial x_i} = 0\,, \tag{2.20}$$

$$\text{Momentum:} \quad \rho \frac{\partial v_i}{\partial t} + \rho v_j \frac{\partial v_i}{\partial x_j} = 0\,, \tag{2.21}$$

$$\text{Energy:} \quad \rho \frac{\mathrm{d}e}{\mathrm{d}t} = 0\,, \tag{2.22}$$

$$\text{Surface BC:} \quad v_i n_i = v_{B_i} n_i\,, \tag{2.23}$$

where n_i is the i-th component of the unit normal-vector to the surface boundary. Comparing the equations to Eqs. (2.3) to (2.6), it is noted that the right-hand-side (RHS) terms, which arise due to viscosity and heat conduction, are set to zero. This changes the set of equations to first-order partial differential equations (PDE), in contrast to the second-order Navier-Stokes equations. The surface boundary condition (BC) is also changed. A slip velocity now exists at the surface, while no velocity is permitted normal to the surface. This is termed the non-permeability condition, the non-penetration condition, or the flow tangency condition. The reduction in the mathematical complexity of the equations to be solved, as well as the reduction in the number of equations to be solved (with the turbulence models no longer being required) leads to a reduction in computational cost relative to the NS equations.

The lack of viscosity has an important influence of the flowfield structure that is modelled. This is manifested through differences how flow rotationality is modelled. The vorticity-form of the NS momentum equation, Eq. (2.16), highlights the interplay between viscosity and rotationality. Viscosity between adjacent fluid layers transforms transverse velocity gradients

into rotationality. Momentum may thus be transferred into rotationality. However, in an inviscid formulation (such as the Euler equations), rotationality can only be created by an entropy gradient as is generated by a variation in shock-wave strength (due to shock curvature, for example). This has significant implications for vortex formation. In viscous flows, vortices may be shed from the body surface through separation of the boundary layer. Rotationality inside the boundary layer is convected through the vortex sheet. In inviscid flows, vortex formation from the surface boundary may occur through one of two mechanisms:

- Crossflow shocks, which generate an entropy gradient near the surface,
- Accumulation of rotationality through the entropy-layer, as is produced by a curved bow-shock.

The lack of viscosity also has implications for the persistence of flow structures. The lack of viscous dissipation means that perturbations propagate without losing energy, and are thus modelled as persisting indefinitely. The differences in flow-feature modelling between Euler and RANS methods are qualitatively illustrated in Fig. 2.54 [35]. It depicts the parameter space of delta-wing flows for which Euler and RANS codes give similar modelling of primary flow structures. As is noted by [35], Euler codes are not able to model secondary flow-structures such as secondary vortices (which arise from boundary-layer separation along the inboard surface) or shock-induced boundary-layer separation. At intermediate incidence for supersonic leading-edges, modelling of the vortical and separated flow structures was noted by [35] to be sensitive to the boundary-layer model used.

As an intermediate approximation to the NS equations, the Euler equations may be coupled to boundary-layer equations. Such methods are termed “Euler equations with boundary-layer interaction” in this overview. A typical implementation is weak coupling of the equations. In this approach, an initial Euler solution is used as the edge conditions for the boundary-layer equations. The boundary-layer displacement thickness is then computed and used to displace the computational boundary for the Euler problem. Euler / boundary-layer coupled methods allow skin-friction and the boundary-layer thickness to be estimated, but do not resolve the flow within the boundary layer. The variation of flow variables is thus obtained for an inviscid flow around a modified geometry of “equivalent thickness”. These methods are of limited use in cases of significant boundary-layer separation, and are thus typically more suited to geometries at near-zero incidence. The development of boundary-layer interactive Euler methods suitable for slender bodies at incidence is detailed in [65].

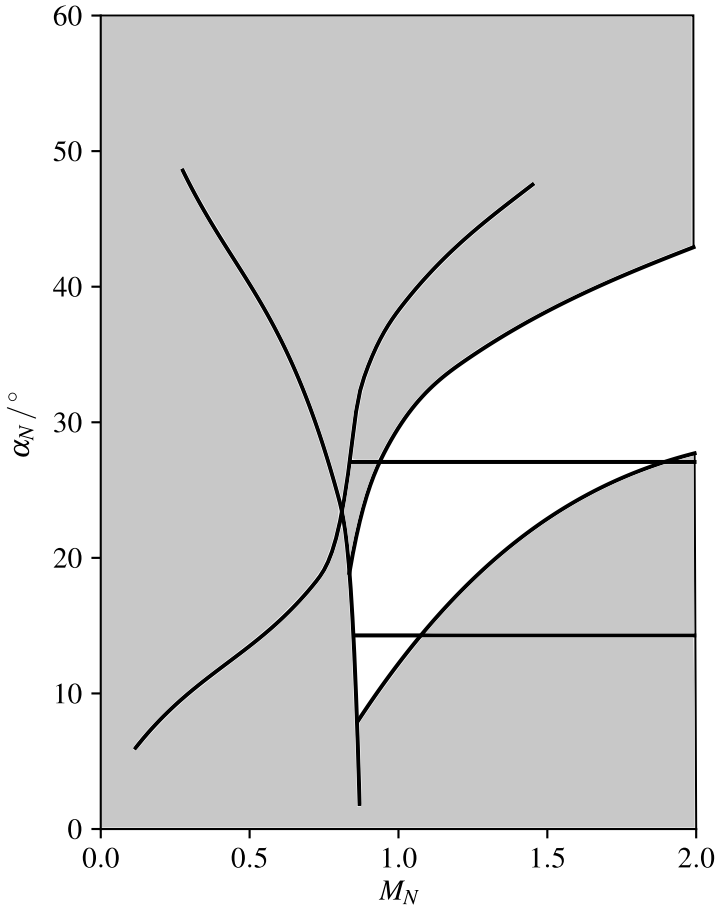

Fig. 2.54 Delta-wing flows for which Euler and RANS codes give similar modelling (shaded areas) of primary flow structures [35].

2.2.3 Intermediate-Level Methods

The remainder of the prediction methods considered are inviscid formulations, and involve further approximations to the Euler equations to reduce their computational cost. As was noted in Section 2.2.1, the intermediate-level category of prediction methods is mostly composed of nonlinear, inviscid formulations which required at-most 2D field discretization. The prediction methods in this category may be grouped into:

- Small-parameter approximations,
  - Unsteady analogy [75–77],
  - Hypersonic small-disturbance theory [27, 77, 78],
  - Sychev's method [4],

- Reduced-order perturbation modelling,
  - Euler-based local piston theory [14],
  - NS-based local piston theory [18],
  - Potential-flow perturbations to higher-fidelity solutions, as implemented in the ZAERO software suite [79]
- Nonlinear potential flows,
  - Full potential equation [44],
  - Transonic small-disturbance equation [44],
- Distributed-vorticity vortex modelling [24]

These represent different approximation philosophies. Small-parameter approximations are based in non-dimensionalization of the Euler equations. The methods covered here seek a non-dimensionalization which is uniformly valid throughout the flowfield. When one of the parameter groups in the resulting equations is significantly smaller than the others, it is typically neglected in a small-parameter approximation and the equations are simplified. In this sense, these methods involve assumptions regarding the relative importance of directional gradients. The unsteady analogy is a central component of these methods, and will be covered in depth before considering the methods categorized as small-parameter approximations.

The second philosophy is termed "reduced-order perturbation modelling". The essence of this approach lies in decoupling the mean-steady flow and variations about it. The mean-steady flow is solved using a high-fidelity model, while a computationally-inexpensive approximate method is used to model perturbations about the mean-steady conditions. This assumes that there is no interaction between the steady and the unsteady physics. This approximation is termed dynamic or time-linearization [80]. The steady solution is used as the starting conditions for the perturbation modelling, and is not updated after perturbations take place. Additional assumptions regarding neglected gradients may be made after the dynamic linearization in order to further simplify the equations.

"Reduced-order perturbation modelling" is not to be confused with so-called "a-posteriori reduced-order modelling". The former involves an a-priori approximation to the governing equations that is independent of the solution to the equations. In the latter, a reduced-order representation of the dynamical system is constructed from an ensemble of solutions to the full equations. The computational cost required to obtain the ensemble of solutions is one of the main disadvantages of a-posteriori reduced-order models (ROMs). Typically, the larger the solution set is, the greater the confidence in the accuracy of the ROM will be. However,

once the ROM is constructed, it offers high-fidelity modelling at very low computational cost. In this sense, a-posteriori ROMs straddle the space between advanced-level and intermediate-level prediction methods. They will not be considered further in this overview of prediction methods, as they do not explicitly model the flow physics in their formulation. Examples of a-posteriori ROM approaches include

- Proper orthogonal decomposition [9],
- Kriging surrogates [10],
- Dynamic mode decomposition [11].

The third approximation philosophy that will be considered involves restricting the flow kinematics. In particular, it is assumed that the flow is irrotational, which allows the velocity vector to be expressed as the gradient of a single scalar-field. This is the potential flow approximation. It reduces the computational cost by reducing the number of variables to be solved for. This approximation philosophy does not explicitly place assumptions on the geometry or perturbations involved. The assumption of irrotationality imposes restrictions on entropy generation as through shock-waves. Potential flow models involving "entropy corrections" [81] attempt to address this shortcoming in the presence of shock waves. Further approximations to the potential flow equations may be, such as neglecting certain directional derivatives or assuming small disturbances.

The final group of intermediate-level prediction methods consists of vortex-modelling methods which utilize multiple discrete vortex elements. Methods of this type are include panel-type methods as well as "vortex cloud" [24] or "multi-discrete-vortex" [30, 82] models. A detailed overview of methods in this category is given in [82]. The approximation philosophy of this category of methods lies in modelling the kinematics of vortical flows in an otherwise inviscid fluid through the use of irrotational vortices. The computational cost of methods in this category vary, depending on whether a boundary-layer model is implemented and on the number of discrete vortex elements modelled. They are categorized as intermediate-level prediction methods here due to their significantly higher computational cost relative to single-vortex methods. As noted in [82], the computational cost of multi-vortex methods rises according to $\mathcal{O}\left(N^2\right)$, where N is the number of vortex elements modelled.

The progressively more severe approximations to the Euler equations which are made in developing intermediate-level methods results in a reduction in the broad applicability of the methods. This is illustrated in Fig. 2.55 from [81]. It shows the approximate validity regions of various inviscid methods for modelling a circular cone at zero incidence. For this case, the Euler equations represent the exact solution. The narrow region of applicability of

linear potential-flow methods demonstrates the importance of nonlinear terms in modelling large perturbations. Similarly, the importance of entropy losses as hypersonic speeds are approached is illustrated by the limits of full-potential methods. The parameter space for which mixed subsonic-supersonic regions exist is denoted as "transonic flow". The influence of viscosity may become dominant in these flows, and so the region represents the approximate limits of inviscid methods in general.

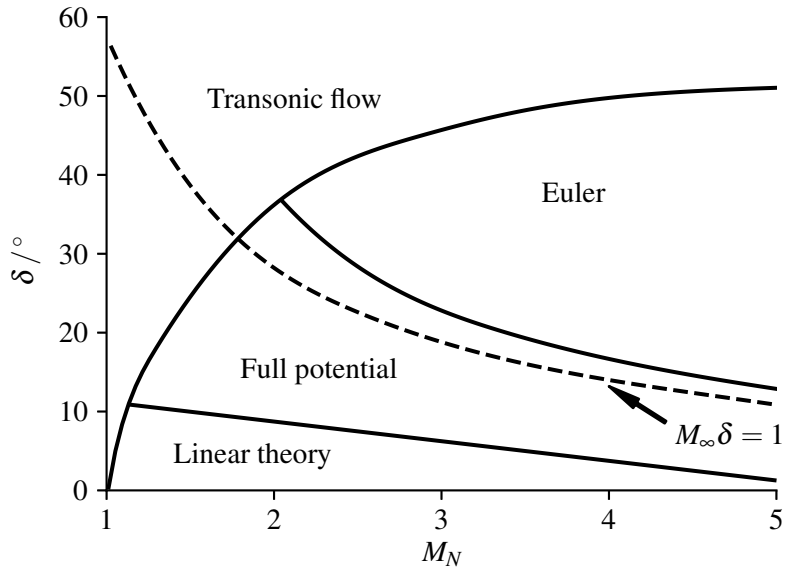

Fig. 2.55 Approximate regions of method applicability for circular cones at zero incidence [81].

Small-Parameter Approximations

The reduction in computational cost achieved by these methods stems from two sources:

- The elimination of one velocity component as a variable,
- The reduction in spatial dimensions requiring discretization from 3D to 2D.

The second source is essentially a by-product of the elimination of the velocity component in the reduced direction. This is demonstrated as follows. If the velocity component v_1 is expressed in perturbation form as $v_1 = V_1\,(1+\varepsilon_1\,u^*{}_1)$, where V_1 is a constant reference velocity and $\varepsilon_1\,u^*{}_1$ is the nondimensional perturbation velocity, then the following may be observed regarding advection:

$$v_i\frac{\partial}{\partial x_i} = V_1\,(1+\varepsilon_1\,u^*{}_1)\frac{\partial}{\partial x_1} + \sum_{i\neq 1} v_i\frac{\partial}{\partial x_i}\,,$$

$$= V_1 \frac{\partial}{\partial x_1} + \sum_{i \neq 1} v_i \frac{\partial}{\partial x_i} + V_1 \, \varepsilon_1 \, {u^*}_1 \frac{\partial}{\partial x_1} \, . \tag{2.24}$$

The advection in the x_1 direction is thus split into a contribution due to advection at a constant speed V_1 and a contribution due to perturbations to that speed. This may be exploited through considering a Galilean transformation to a frame moving at a constant speed V_1 . The relationship between variables in the frames are given as

$$t_G = t \, , \tag{2.25}$$

$$x_{1(G)} = x_1 - V_1 \, t \, , \tag{2.26}$$

$$x_{i(G)} = x_i \quad \text{for} \quad i \neq 1 \, , \tag{2.27}$$

where the subscript "(G)" denotes variables in the Galilean frame, and with the following transformations applying to partial derivatives taken in the respective frames:

$$\frac{\partial}{\partial t_G} = \frac{\partial}{\partial t} + V_1 \frac{\partial}{\partial x_1} \, , \tag{2.28}$$

$$\frac{\partial}{\partial x_{i(G)}} = \frac{\partial}{\partial x_i} \, . \tag{2.29}$$

This essentially demonstrates that spatial gradients in the direction of frame convection are perceived as temporal gradients in the convected frame. This is the essence of what is referred to as "pseudo-time" or an "alternative time variable" [76] in some literature on the unsteady analogy, and also sheds light on why it is named the "unsteady" analogy. Returning to the introduction of a nondimensional perturbation velocity $\varepsilon_1 {u^*}_1$, it is seen that the material derivative may be written as

$$\begin{aligned} \frac{\mathrm{d}}{\mathrm{d}t} &= \frac{\partial}{\partial t} + V_1 \frac{\partial}{\partial x_1} + \sum_{i \neq 1} v_i \frac{\partial}{\partial x_i} + V_1 \, \varepsilon_1 \, {u^*}_1 \frac{\partial}{\partial x_1} \, , \\ &= \frac{\partial}{\partial t_G} + \sum_{i \neq 1} v_i \frac{\partial}{\partial x_i} + V_1 \, \varepsilon_1 \, {u^*}_1 \frac{\partial}{\partial x_1} \, . \end{aligned} \tag{2.30}$$

As a final preparation to demonstrating the reduction from a 3D to a 2D spatial set of equations, it is noted that where the derivative of v_1 is taken, it reduces to the derivative of the perturbation:

$$\frac{\partial v_1}{\partial x_i} = V_1 \frac{\partial (1 + \varepsilon_1 \, {u^*}_1)}{\partial x_i} \, ,$$

$$= V_1 \frac{\partial \varepsilon_1 {u^*}_1}{\partial x_i} . \tag{2.31}$$

Substituting for v_i and Eqs. (2.24), (2.28), (2.30) and (2.31) into the Euler equations of Eqs. (2.20) to (2.23), it may be shown that the perturbation form is given by

Continuity: $$\frac{\partial \rho}{\partial t_G} + \frac{\partial \rho v_i}{\partial x_i} = -V_1 \frac{\partial \rho \varepsilon_1 {u^*}_1}{\partial x_1} \quad \text{for} \quad i \neq 1 , \tag{2.32}$$

Momentum 1: $$\rho V_1 \frac{\partial \varepsilon_1 {u^*}_1}{\partial t_G} + \rho V_1 \, v_j \frac{\partial \varepsilon_1 {u^*}_1}{\partial x_j} = -\rho {V_1}^2 \varepsilon_1 {u^*}_1 \frac{\partial \varepsilon_1 {u^*}_1}{\partial x_1} \quad \text{for} \quad j \neq 1 , \tag{2.33}$$

Momentum 2,3: $$\rho \frac{\partial v_i}{\partial t_G} + \rho v_j \frac{\partial v_i}{\partial x_j} = -\rho V_1 \, \varepsilon_1 {u^*}_1 \frac{\partial v_i}{\partial x_1} \quad \text{for} \quad i, j \neq 1 , \tag{2.34}$$

Energy: $$\rho \frac{\partial e}{\partial t_G} + \rho v_i \frac{\partial e}{\partial x_i} = -\rho V_1 \, \varepsilon_1 {u^*}_1 \frac{\partial e}{\partial x_1} \quad \text{for} \quad i \neq 1 . \tag{2.35}$$

The equations have been arranged with terms involving derivatives in x_1 placed on the RHS. The LHS of the equations then involve only time derivatives in the Galilean frame and spatial derivatives in the plane normal to x_1. For the sake of brevity, the plane normal to x_1 will be referred to as the *crossflow plane*, and x_1 will be referred to as the *convected direction*. It is noted that the RHS of the momentum and energy equations represents the x_1-advection by perturbations of velocity components and energy. The RHS of the continuity equation represents the x_1-gradient of perturbation momentum. If these RHS terms are neglected in favour of the remaining terms, the Euler equations are reduced to unsteady equations in the crossflow plane and involve only v_2 and v_3 as velocity variables. This is the mathematical basis of the unsteady analogy. The unsteady analogy thus assumes that:

- The contribution to momentum divergence from convected-direction terms is negligible relative to crossflow terms. In other words, the predominant changes to mass-flow occur in the crossflow plane,

- The advection of scalar quantities in the convected-direction is negligible relative to their advection in the crossflow plane.

These two assumptions reduce to the physical interpretation that if a flow direction exists in which a body generates significantly weaker perturbations (in comparison to the remaining directions), the 3D flow around the body may be treated as 2D flow in a plane convected in that direction. This gives rise to the unsteady analogy also being known as the “law of plane sections” [77].

The two methods that will be covered in the category of small-parameter approximations are hypersonic small-disturbance theory [27, 77, 78] and Sychev's method [4] for high incidences. Both of these methods rely on a slender-body assumption, with $\delta \equiv D/L \ll 1$, and assume hypersonic flow such that $M_\infty \delta \geq 1$. Both methods reduce the Euler equations to 2D unsteady equations in a crossflow plane, with the direction for the Galilean transform defined by the body axis. The methods will not be outlined in great detail, as the essence of the approach lies in the unsteady analogy that was detailed above. Moreover, a general approach in reducing the Euler equations will be developed in the following chapter, which will be shown to reduce to the two methods depending on the non-dimensionalization used. A range of other small-parameter approximations for specific scenarios, such as slightly-blunted cones, are reviewed in [27].

Hypersonic small-disturbance theory (SDT) is essentially a small angle-of-attack method, with $\alpha \leq \delta$. It assumes that axial perturbations are of an order $\mathscr{O}(\delta)$ smaller than lateral perturbations. In the nomenclature of Eqs. (2.32) to (2.35), this is equivalent to assuming that $\varepsilon_1 {u^*}_1 = \mathscr{O}\left(\delta^2\right)$ while $v_2/V_1 = \mathscr{O}(\delta)$. Neglecting terms of the order $\mathscr{O}\left(\delta^2\right)$ results in a first-order approximation to the Euler equations. The approximation may be interpreted by the unsteady analogy, with the convected plane swept along the body axis. In fact, for the small incidences considered, the error in considering the plane to be convected in the direction of the freestream is of the order of the neglected terms. The development and accuracy of hypersonic SDT is covered in detail in [78, 83], with a more detailed order-of-magnitude analysis of the various terms given in [77]. As noted by Van Dyke [83], the theory may be extended to supersonic Mach numbers through replacing M_∞ in similarity parameters by the factor $\sqrt{M_\infty^2 - 1}$ from linearized supersonic flow theory. Van Dyke notes that this allows the lower-limit of validity of hypersonic SDT to be extended from $1/M_\infty \delta = \mathscr{O}(1)$ to approximately $M_\infty \delta \geq 0.3$.

Sychev [4] adopted a similar approach in treating the hypersonic slender-body problem for large incidences. A characteristic feature of Sychev's analysis is that the assumption of relatively-smaller axial perturbations is dropped, with the requirement reduced to $\varepsilon_1 {u^*}_1 = \mathscr{O}(\delta)$. This is in conjunction with an assumption that the body is slender in its largest lateral dimension such that $\delta \ll 1$ applies. It is further assumed that $M_\infty \delta \geq 1$ and that $M_c = M_\infty \sin\alpha \gg 1$. Neglecting terms of order $\mathscr{O}\left(\delta^2\right)$ allows the axial-perturbation of velocity to be eliminated from the equations for larger perturbations than in hypersonic SDT. The application of the unsteady analogy sees the convected plane swept down the axis of the body. The resulting equations are governed by two similarity parameters: $\delta \cot\alpha$ and $M_\infty \sin\alpha$. Sychev noted that the resulting high-incidence theory agreed with small-incidence SDT theory in the range $\alpha = \mathscr{O}(\delta)$, and developed the theory for up to $\alpha \approx 90°$.

The similarity between hypersonic SDT and Sychev's method drew the attention of various researchers [84–86] in investigating the limits of validity of Sychev's formulation. Hemsch [85] found that Sychev's similarity parameters successfully correlated experimental results for smooth bodies and sharp wings well outside of the theoretical validity bounds put forward by Sychev. In particular, it was noted that correlation was successful at all crossflow Mach numbers, provided that the axial flow was supersonic. It was also observed that correlation was successful even for rectangular wings of aspect ratios up to $AR = 4$. This led Barnwell [84] to revisit the mathematical formulation of Sychev. Barnwell suggested that as no explicit assumptions regarding Mach number were made in obtaining the nearfield-form of the equations, their form should govern the nearfield inviscid flows at all Mach numbers. Consideration of the bow shock led Barnwell to suggest that Sychev's requirement of $M_\infty \sin\alpha \gg 1$ may be relaxed to $M_\infty \sin\alpha > 1$.

Voevodenko and Panteleev [86] investigated the accuracy of Sychev's method relative to solutions to the full Euler equations. They demonstrated that Sychev's method is an accurate approximation to the Euler equations for a wide range of crossflow Mach numbers and wing sweep angles. Significantly, Voevodenko and Panteleev investigated the accuracy in pressure distribution prediction, allowing regions in which Sychev's method is inaccurate to be identified. It was observed that the error was greatest in the vicinity of the wing edges. Another significant outcome of the investigation was the establishment of the approximate regions of validity of Sychev's theory. The conditions under which Sychev's theory reduces to other aerodynamic formulations, such as hypersonic SDT and strip theory, were identified. Finally, it was noted that for flows in which the leading-edge shocks detached (while remaining attached at the apex of the wing), Sychev's method was invalid within the entropy layer, but could be applied outside of it.

Reduced-Order Perturbation Modelling

As was noted in the introduction to Section 2.2.3, the methods that will be considered in this category do not include a-posteriori ROMs. Consideration will be limited to methods which explicitly model the flow physics. Particular attention will be given to methods utilizing local piston theory (LPT). This is due to the increased interest in Euler-based LPT [14] in recent literature and due to ongoing work to extend LPT [18]. Greater attention will be given to the development and context of LPT in Chapter 3.

Local piston theory has become a popular method for the reduced-order modelling of perturbations to Euler solutions of supersonic flows. It has been shown to offer order-of-magnitude reductions in the computational cost of predicting unsteady aerodynamic loads, as compared to the cost of unsteady Euler solutions [87]. This is cost reduction is by virtue

of the formulation for pressure in LPT, which is given by

$$p_u = p_s + \rho_s a_s w\,, \tag{2.36}$$

where the subscript "u" denotes values associated with unsteady perturbations, the subscript "s" associates terms with the mean steady flow solution, a is the speed of sound in the fluid, and w is the downwash velocity on the piston face. This latter quantity is related to the surface in motion through

$$w = -\mathbf{V_s}\cdot\hat{\mathbf{n}} + \mathbf{V_b}\cdot\hat{\mathbf{n}}\,, \tag{2.37}$$

where $\mathbf{V_b}$ is the local velocity vector of the structural surface, $\mathbf{V_f}$ is the local fluid velocity at the surface in the mean steady flow, and $\hat{\mathbf{n}}$ is the unit normal vector of the local structural surface following a perturbation. LPT thus provides a direct algebraic relationship between the local fluid pressure at the surface and the local motion of the surface. The resulting model for pressure perturbations on the structural surface is computationally inexpensive and physically intuitive.

For the purposes of determining the onset of aeroelastic instability, it is typically sufficient to consider small perturbations about the mean steady position. Most literature showcasing the application of LPT focuses on small perturbations to relatively simple geometries, such as airfoils and isolated lifting surfaces [14]. For these cases, LPT has shown to accurately predict unsteady loads, typically within 5% of the full unsteady Euler results [14]. The perturbations produced in the conditions considered in such literature correspond to subsonic piston-downwash Mach numbers ($w/a_s < 1$). This is in line with the assumption in the original piston-theory formulation that piston motion does not produce shocks [88]. The application of higher-order formulations of the pressure equation Eq. (2.36) in the context of LPT (as would be necessary when $w/a_s = \mathcal{O}(1)$) have not been noted in literature.

The successes of Euler-based LPT in modelling unsteady inviscid flows about simple geometries have led to its application to more complex scenarios. These include inviscid hypersonic flow around a highly-swept, low aspect-ratio wing-body configuration [16] and the use of LPT to model perturbations to RANS solutions [18]. In the application to the full vehicle configuration of [16], the only modification to Euler-based LPT was in the definition of the downwash term of Eq. (2.37) to include both transverse velocity components on the body. Significantly worse agreement between Euler-based LPT and the full Euler solution was noted, with up to 27% error observed in the prediction of flutter dynamic-pressure [16].

Liu et al [18] developed a method to extend the application of LPT to mean steady solutions obtained from the RANS equations. The essence of the method lies in identifying the effective thickness of the body due to momentum displacement of the boundary layer.

This effective shape is then used in place of the physical body geometry in the inviscid LPT equations of Eqs. (2.36) and (2.37). Local fluid quantities used in LPT, such as the fluid density and speed of sound, are taken at the effective shape. The procedure of the method and of similar previous work will be discussed in detail in Chapter 3. A significant shortcoming of the method proposed by [18] is that the parameters used in the procedure for effective shape determination must be tuned using an ensemble of unsteady RANS solutions. Application of the method to an airfoil and to two slender waverider configurations was demonstrated [18]. Within the range of parameters for which the model was tuned, RANS-based LPT provided good prediction of loading trends for the airfoil. The relative error for the normal-force coefficient was typically within 5% of unsteady RANS, while the pitching-moment coefficient was typically predicted within 15%. The prediction accuracy was seen to suffer somewhat when the model was applied to airfoils of a thickness different to that of the tuning-model. Nevertheless, better correlation with the unsteady RANS results was obtained that than offered by LPT applied at the physical airfoil surface.

A significant outcome of the study by Liu et al [18] was the variation in accuracy when applied to two waverider configurations. When applied to the first configuration (elliptical cross-section), noticeably better prediction of the pitching-moment coefficient was obtained by LPT applied at the effective shape, as shown in Fig. 2.56. This is in contrast to the results obtained for a similar waverider configuration with a different cross-section. Prediction of the pitch-damping of the second configuration by the method of Liu et al [18], denoted "VLPT", is seen to be in nearly comparable error as LPT applied at the physical surface of the waverider, as demonstrated in Fig. 2.57. This strongly suggests that the accuracy of the method is dependent on correct tuning of the parameters. This serves to support the conclusion from similar work using classical piston theory by [13] that the effect of viscosity on aeroelastic behaviour cannot be reliably captured using effective shape corrections.

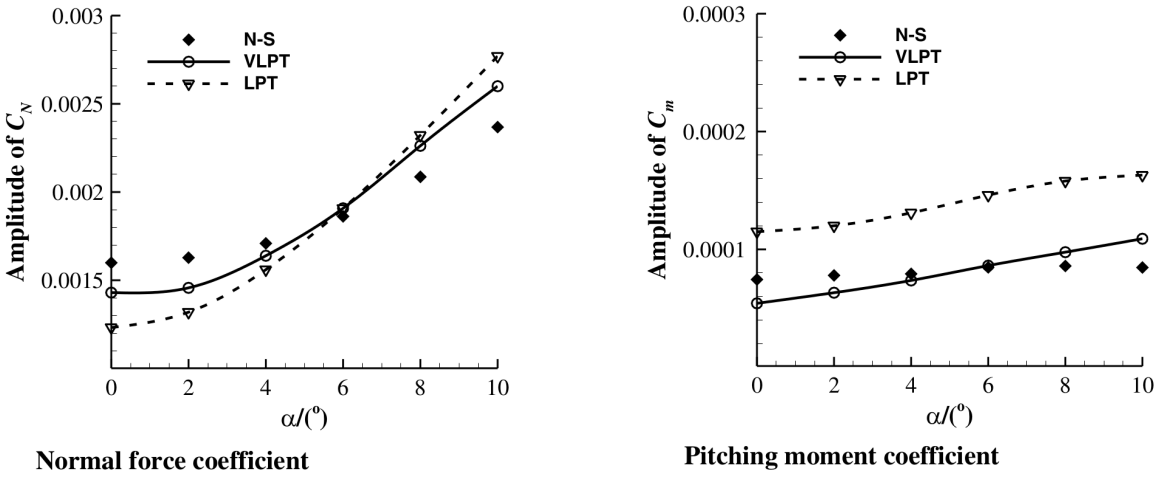

(a) Normal-force coefficient

(b) Pitching-moment coefficient

Fig. 2.56 Variation in amplitudes of loading coefficients for an elliptical cross-section waverider undergoing harmonic pitching; $M_\infty = 20$, altitude of 60 km, $k = 0.0915$, $\Delta\alpha = 1°$ [18].

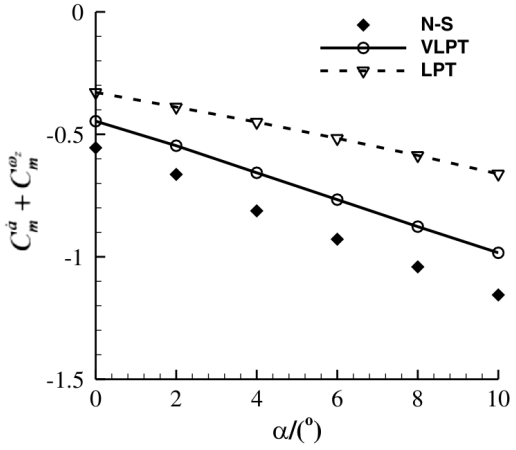

Fig. 2.57 Variation in pitch-damping coefficients for a waverider undergoing harmonic pitching; $M_\infty = 15$, altitude of 55 km [18].

Dynamic linearization was adopted extensively in the development of methods in the ZAERO suite of software [79]. Methods developed for transonic aeroelastic analysis were based in the transonic small-disturbance (TSD) potential flow equations. The common thread in the various methods employed consisted of splitting the velocity potential function into a mean steady contribution, ϕ_0, and an unsteady contribution, ϕ_1. Surface oscillations were assumed to be sufficiently small that the governing equations were linearized in terms of ϕ_1, while allowing nonlinearity in ϕ_0. A range of methods for the solution of the nonlinear mean-steady flow were proposed, including an transonic equivalent-strip theory [89] and the use of steady CFD [79]. The unsteady problem was then solved using panel methods for the linear potential flow problem in ϕ_1. Better accuracy in the unsteady pressures was obtained through this approach than through the use of steady downwash-correction or force-correction matrices, as detailed in [79]. It was also noted that a significant reduction in computational cost could be achieved relative to full nonlinear potential flow codes, potentially up to an order of magnitude [89].

Nonlinear Potential Flows

Methods based in the full potential equation or the transonic small-disturbance equations typically require 3D field discretization. Nevertheless, they are categorized as intermediate-level methods here due to the reduction in computational cost that they offer relative to the Euler equations. This is achieved by expressing the velocity vector as the gradient of a scalar function known as the velocity potential:

$$\mathbf{V} \equiv \nabla\Phi\,. \tag{2.38}$$

This reduces the number of velocity variables to be solved for from 3 to 1, but it also places a restriction on the kinematics of the flow. In particular, the flow is defined to be irrotational and isentropic. The full potential equation may be expressed in a number of forms, two of which will be given below. The vector form is given by [44] as

$$\text{Potential:} \qquad a^2\nabla^2\Phi - \mathbf{V}\cdot\nabla\left(V^2/2\right) - \frac{\partial V^2}{\partial t} - \frac{\partial^2\Phi}{\partial t^2} = 0\,, \tag{2.39}$$

$$\text{Speed of sound:} \qquad a^2 = a_\infty^2 + \frac{\gamma-1}{2}\left(V_\infty^2 - V^2 - 2\frac{\partial\Phi}{\partial t}\right), \tag{2.40}$$

$$\text{Pressure:} \qquad p = p_\infty\left(\frac{a^2}{a_\infty^2}\right)^{\frac{\gamma}{\gamma-1}}, \tag{2.41}$$

where $V^2 = \nabla\Phi \cdot \nabla\Phi$ is the square of the local flow speed. The component form of Eq. (2.39) in Cartesian coordinates will be given below in order to highlight the terms neglected in the TSD approximation and in the linear potential flow equation. A perturbation potential ϕ is introduced, such that

$$\Phi \equiv V_\infty x + \phi\,, \tag{2.42}$$

in terms of which Eq. (2.39) may be written as

$$\begin{aligned}
\left[(a_\infty^2 - V_\infty^2) - (\gamma-1)\left(eV_\infty\phi_x + \frac{e\phi_x^2}{2} + \frac{\phi_y^2}{2} + \frac{\phi_z^2}{2} + \phi_t\right)\right]\phi_{xx} \qquad & 2(V_\infty + \phi_x)\phi_{xt} \\
\left[a_\infty^2 - (\gamma-1)\left(V_\infty\phi_x + \frac{\phi_x^2}{2} + \frac{e\phi_y^2}{2} + \frac{\phi_z^2}{2} + \phi_t\right)\right]\phi_{yy} \quad = \quad & +2\phi_y\phi_{yt} \\
\left[a_\infty^2 - (\gamma-1)\left(V_\infty\phi_x + \frac{\phi_x^2}{2} + \frac{\phi_y^2}{2} + \frac{e\phi_z^2}{2} + \phi_t\right)\right]\phi_{zz} \qquad & +2\phi_z\phi_{zt} \\
-2(V_\infty + \phi_x)\phi_y\phi_{xy} - 2(V_\infty + \phi_x)\phi_z\phi_{xz} - 2\phi_y\phi_z\phi_{yz} \qquad & +\phi_{tt}
\end{aligned} \tag{2.43}$$

where subscript notation denotes partial differentiation and $e \equiv (\gamma+1)/(\gamma-1)$. The RHS of the equation consists of unsteady terms, while the LHS consists of spatial velocity gradients. The successive approximations to the full potential equation and their validity are treated in greater detail in Chapter 3. The boundary conditions may be written as

$$F_t + \nabla\Phi \cdot \nabla F = 0 \quad \text{at} \quad F(x,y,z,t) = 0\,, \tag{2.44}$$

$$\nabla\Phi = V_\infty \quad \text{at} \quad r \to \infty\,, \tag{2.45}$$

where $F(x,y,z,t) = 0$ is the function representing the surface of the body of interest, and the farfield boundary condition in supersonic flows is changed to the Sommerfeld radiation condition.

The nonlinearity of the full potential equation permits the formation of discontinuities in the flow. However, energy is not conserved across the discontinuity, and the jumps do not correspond to physical shock waves. A comparison between the isentropic "shocks" and physical shocks is given in [90]. In contrast to the modelling of physical shocks by the Euler equations, the discontinuities in the nonlinear potential equation do not give rise to rotationality. The significance of differences in physics-modelling between the Euler equations, the full potential equation, and the linear potential equation was illustrated in detail for a variety of bodies in [81]. An example of the increments between flow models is given in Fig. 2.58 from [81].

The following trends are noted from Fig. 2.58:

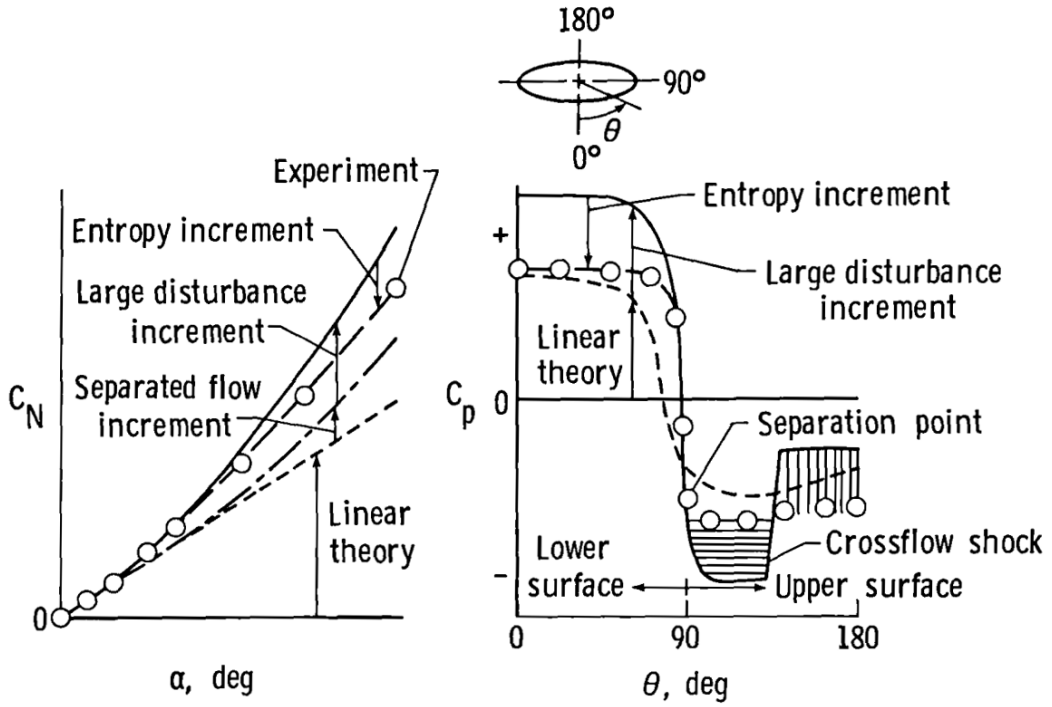

Fig. 2.58 Illustration of the role of nonlinear increments to the linear potential flow model. Large disturbance increment: linear to full potential; entropy increment: full potential to Euler [81].

- The effect of adding nonlinear potential terms is denoted “large disturbance increment”. These terms typically increase the magnitude of the pressure coefficient, leading to an increase in the integrated forces,

- The effect of accounting for entropy jumps at shocks (and the associated flow rotationality) is denoted ‘entropy increment”. As noted in [81], the effects of entropy on the pressure distribution is typically limited to the windward side of the body in flows with separation. Correctly modelling energy conservation by accounting for entropy jumps is seen to decrease the pressure magnitude relative to the isentropic full potential model. This is also manifested as a decrease in the magnitude of integrated forces,

- Pittman [81] notes that when integrating the pressure distribution predicted by inviscid methods, the contributions from inaccuracies on the leeside may cancel out, yielding good agreement with experiment in the integrated forces. This is illustrated by the hatched regions in Fig. 2.58 which are approximately equal in area.

The shortcomings in the full potential equation illustrated above led to the development of “entropy corrections” to potential flow formulations for slender bodies. The method

is outlined in [81]. Its essence lies in using the Rankine-Hugoniot equations with a bow-shock-fitting solution procedure. This allows the entropy jump across the bow shock to be modelled correctly. The entropy jump is then used in a correction to the body-surface pressures. The rationale behind the approach is that for conical flows, streamlines from the shock approach the body along radial lines and are entrained into an entropy layer near the surface. Entropy conserved along streamlines and the variation in pressure through the entropy layer is assumed negligible. This forms the basis for entropy jumps at the shock to be project radially to the body surface for use in the pressure-correction formula.

Further approximations may be made to full potential equation, with non-dominant nonlinear terms in Eq. (2.43) omitted as required. The motivation behind this is to further reduce the computational cost by reducing the number of terms in the equation. A number of different approximations may be made, resulting in a variety of formulations existing under the moniker of the "transonic small disturbance" (TSD) equation. Bendiksen [55] gives a thorough derivation of unsteady transonic similarity parameters with aeroelastic applications in mind. The derivation is based in an asymptotic development of the unsteady full potential equation. The reduction of the analysis to a number of notable transonic approximations is demonstrated, with the implicit assumptions in these approximations clarified [55]. For the sake of illustration, the form of the TSD equation with minimum complexity, derived from first principles in [91], is given here as

$$\left[\left(a_\infty^2 - V_\infty^2\right) - (\gamma+1)V_\infty\phi_x\right]\phi_{xx} + a_\infty^2\phi_{yy} + a_\infty^2\phi_{zz} = 2V_\infty\phi_{xt} + \phi_{tt}\,, \tag{2.46}$$

with the dominant nonlinear term assumed to be $(\gamma+1)V_\infty\phi_x\phi_{xx}$. As discussed by Bendiksen [55], certain unsteady terms must be retained despite their smallness, as their contribution cumulatively becomes of first-order importance over time in unsteady problems. The accuracy of the TSD equations in unsteady transonic flows are limited. This is due in part to the small-disturbance assumption, and in part due to the importance of viscosity in the transonic regime [44].

Distributed-Vorticity Vortex Modelling

A variety of formulations exist within the category of multi-vortex discrete vortex models. The variety rises from the differences in approaches to answering the following questions, quoted from [82], associated with the development and shedding of vortices:

- How is separation to be defined?
- Where are the separation lines?

- What is the rate of shedding of vorticity?
- How does the separating stream surface leave the body?
- What conditions should be satisfied at the separation lines?
- What is the relationship between the Kutta condition and separation from a smooth surface (both for steady and unsteady flows about interacting or non-interacting bodies)?

Sarpkaya [82] gives a detailed overview of the different approaches used to model the shed vortices and vortex sheets. Consequently, the mathematical details of these methods will not be entered into here. A representative example of the practical adaptation and application of these methods is given by Tuling [30], who extended the methods to flows about slender bodies with strakes. In reviewing computational methods with vortices for three-dimensional flows, Sarpkaya [82] notes that the methods may be categorized as follows:

- Two-dimensional models utilizing the unsteady analogy,
  - Multi-discrete-vortex models [24, 30],
  - Vortex-segment methods [92],
  - Panel methods [93]
- Fully three-dimensional models,
  - Vortex-lattice models [94],
  - Panel methods [95],

where so-called "two-vortex models" [82] or "single concentrated vortex" models [30] are not included here, as they are categorized as engineering-level methods in the present overview. In the above methods, vorticity is typically introduced into the interior of the flowfield at separation points along the body surface. This is either through the introduction of discrete vortices (as in multi-discrete-vortex models) or through the growth of line-vortex segments (as in vortex-segment, vortex-lattice, and panel methods). Illustrations of these methods are given in Figs. 2.59 and 2.60.

All these methods require specification of the location of separation lines. A variety of approaches may be adopted. These include empirical specification, solution of a boundary-layer model with semi-empirical separation criteria. As noted by Sarpkaya [82], determination of the separation points (when they are not fixed by sharp edges) is non-trivial, and often

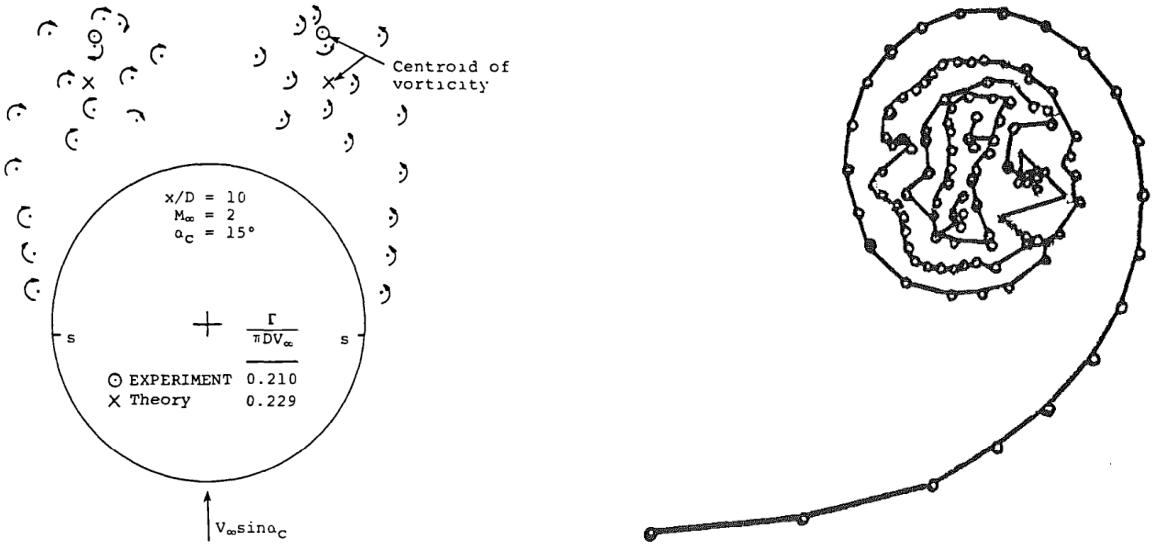

(a) Multi-discrete-vortex models [24]

(b) Vortex-segment methods [82]

Fig. 2.59 Typical 2D methods employed in distributed-vorticity modelling of vortical flows.

approximate at best. Unsteady flows present a particular challenge in the definition of separation points and also impacts the definition of vorticity production. A detailed discussion on these challenges is given in [82].

Other modelling difficulties arise in the various methods. Examples include the mutual-orbiting tendency of discrete vortices, and solution sensitivity to panelling [82]. Tuling [30] also demonstrates the numerical sensitivity of multi-discrete-vortex methods to the number of vortex elements modelled. None of the methods are able to model vortex breakdown. Sarpkaya [82] concluded that existing vortex-modelling methods were not able to accurately capture the complex, unsteady phenomena of high-incidence aerodynamics. In refining the methods, additional physics would be required to model the interaction of vortices with other flight vehicle components and with transient vortex behaviour in adverse pressure gradients [82]. As noted by [96], methods for distributed-vorticity modelling of vortical flows have been widely implemented despite these difficulties.

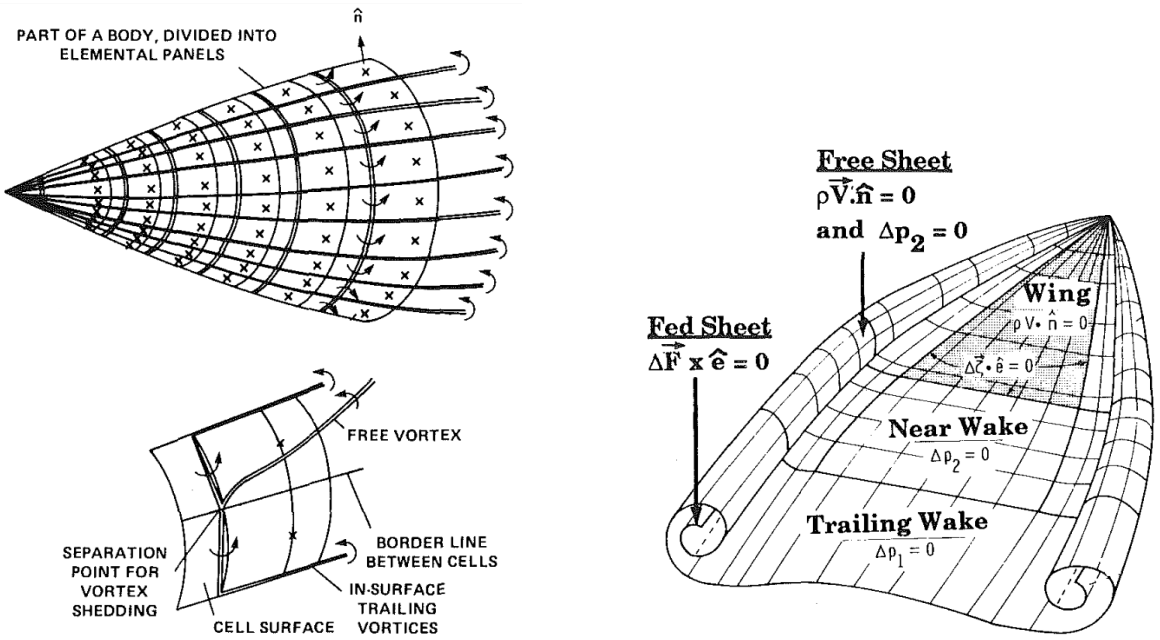

(a) Vortex-lattice models [94] (b) Panel models [82]

Fig. 2.60 Typical 3D methods employed in distributed-vorticity modelling of vortical flows.

2.2.4 Engineering-Level Methods

This category of prediction methods is characterized by the low computational cost of the methods. The emphasis is typically on predicting integrated loads or sectional loads (e.g. an axial load distribution). Engineering-level methods may be broadly sub-categorized into analytical methods and semi-empirical or empirical methods. A broad range of analytical engineering-level prediction methods are available. The low computational cost of these methods is largely due to the relative simplicity of the mathematical equations to be solved. Where solutions are not available in closed-form, they require discretization of at-most the boundary of the field-problem. The majority of these methods have a theoretical basis in linearized potential flows, as is evident in the following list of methods that will be covered:

- Concentrated-vorticity vortex modelling
  - Free vortex / feeding-sheet pair method [82, 97, 98],
  - Free vortex method [30, 99],
- Linear potential flows:
  - Slender body theory [100, 101] and strip theory [27, 100],
  - Panel methods [79, 102],
- Local-inclination methods:
  - Newtonian impact theory [25, 27],
  - Classical piston theory [88, 103],
  - Van Dyke's second-order theory [104],
  - First-order shock-expansion theory [58],
  - Donov's theory [105].

A range of prediction codes extensively utilizing experimental databases exist, with prominent examples including:

- Missile DATCOM [5],
- Naval Surface Warfare Center's Aeroprediction Code [6],
- Items in the ESDU database [106, 107],
- Codes from Nielsen Engineering and Research including MISL3 [108], MISDL [109], and their previous versions [51],

- In-house codes, such as ONERA's MISSILE [110] code,
- Supersonic / Hypersonic Arbitrary Body Program (SHABP) code [48].

The codes employ a mix of analytical, semi-empirical, and empirical methods, with proprietary experimental databases being used. A thorough overview of the various semi-empirical methods available is outside the scope of this section, and only the following representative methods will be introduced:

- Viscous-crossflow analogy [111–113],
- Equivalent angle-of-attack method [46, 47].

The methods are typically limited to predicting the integrated forces over components or the vehicle, and do not provide the pressure distribution.

Concentrated-Vorticity Vortex Modelling

One of the chief distinctions between the methods of this category and distributed-vorticity vortex modelling methods is that the former do not attempt to model the vortex feeding-sheets. Instead, the distributed vorticity is represented by a single, concentrated vortex. Many of the same modelling questions as were raised in Section 2.2.3 apply. Once again, methods in this category differ in their approaches to answering these questions. Particular distinctions arise in the approach to modelling the rate of vorticity production (shedding) and in the treatment of separation points. Two significant concentrated-vorticity vortex modelling methods will be outlined here. A high-level comparison of the modelling approaches between these methods and a representative multi-vortex method [24] will also be made.

The first method considered is referred to here as the "free vortex / feeding-sheet pair" method (FVFSM), but is also known as the "NACA vortex model" [97], Bryson's [98] method, the "two-vortex model" [82], and the "single concentrated vortex model" [30]. The number of names by which the conceptual model is referred to is indicative of the extensive adaptation and application of the method, which is fuelled by the relative simplicity of the model [82]. The elements modelled in the method are depicted for a delta wing in Fig. 2.61 from [97].

The method models shed vorticity using line vortices of varying strength that are connected to the separation lines by feeding sheets. These are represented in the crossflow plane by irrotational vortices and cuts of vanishingly small vorticity [82]. The defining feature of the method is that the net force acting on each vortex / feeding-sheet pair is assumed to be zero [98]. The force experienced by the concentrated vortex, $\mathrm{i}\rho\Gamma(W_1 - \dot{\sigma}_1)$, is balanced by

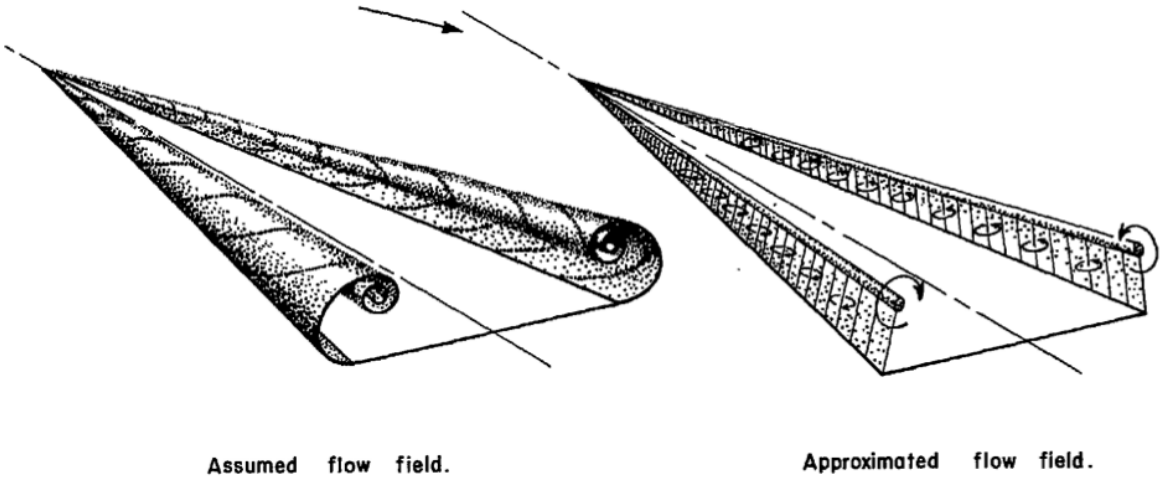

Fig. 2.61 Depiction of the modelling approach of the free vortex / feeding-sheet pair model [97].

an equal and opposite force acting on the feeding sheet, $i\rho\dot{\Gamma}(\sigma_1 - \sigma_0)$, as noted by [82]. This leads to the following relation between the vortex motion and vorticity production:

$$\dot{\sigma}_1 + (\sigma_1 - \sigma_0)\frac{\dot{\Gamma}}{\Gamma} = W_1\,, \tag{2.47}$$

where Γ is the circulation of the vortex, σ is the complex variable in the crossflow plane, W_1 is the complex crossflow velocity vector at σ_1 leaving out the velocity induced by the vortex itself, dot notation denotes time differentiation, subscript 0 denotes the separation point, subscript 1 denotes the concentrated vortex, and i is the imaginary number.

When the method is applied to cylinders, the vortex is initially shed from pre-defined separation points at a distance from the surface of $0.05a\%$ (where a is the cylinder radius) along a line at 30° to the cylinder-tangent at the separation point. This is to avoid the mathematical saddle-point at the separation point [98]. A further discussion of this decision and alternatives is given in [82]. With the (initial) position of the vortex known, its strength is determined by enforcing the Kutta condition such that the surface-tangential velocity at the separation point is zero. For a symmetrical two-vortex system, this leads to the following expression for the circulation:

$$\frac{\Gamma}{2\pi a V_\infty \sin\alpha} = \frac{(\sigma_1 - \sigma_0)(\bar{\sigma}_1 - \bar{\sigma}_0)(\sigma_1 + \sigma_0)(\bar{\sigma}_1 + \bar{\sigma}_0)}{(\sigma_1\bar{\sigma}_1 - a^2)(\sigma_1 + \bar{\sigma}_1)}\,, \tag{2.48}$$

where an overbar denotes the complex conjugate, and from which it is evident that the circulation is a function only of the position of the vortex. The position of the separation

points, σ_0 and $\bar{\sigma}_0$, are assumed to be stationary. Differentiating Eq. (2.48) yields the relation between $\dot{\Gamma}$, $\dot{\sigma}_1$, and σ_1 required to enforce the Kutta condition. Substituting for Γ and $\dot{\Gamma}$ from Eq. (2.48) (and its differentiated counterpart) into Eq. (2.47) yields a nonlinear first-order differential equation for the vortex position σ_1, as noted by Bryson [98]. In other words, simultaneously enforcing the Kutta condition and requiring a force-free vortex / feeding-sheet pair closes the system of equations and defines the vortex trajectory. A consequence of this is that the vortex is not advected by the local flow velocity (stated otherwise, the vortex is not a streamline), except in the limiting case of $\dot{\Gamma} = 0$. Various authors [30, 82, 98] have noted non-physical behaviour of the vortices associated with the vortices returning to the body and with $\dot{\Gamma} < 0$. In spite of this non-physical behaviour developing over time, good agreement with experiment was noted for the initial development of the vortices, with $t < 2.5d/V_\infty \sin\alpha$, where d is the cylinder diameter [98]. Tuling [30] noted that the method yielded good accuracy for slender bodies with strakes at low angles of attack, with $\alpha < 4°$. The cross-sectional load experienced by the body is given by the vortex impulse theorem [3] as

$$\frac{\mathrm{d}F_N}{\mathrm{d}x} - \mathrm{i}\frac{\mathrm{d}F_Y}{\mathrm{d}x} = \rho_\infty V_\infty \frac{\mathrm{d}}{\mathrm{d}x}\left[\sum_N^{j=1} \Gamma_j \left(\sigma_j - \frac{a^2}{\bar{\sigma}_j}\right)\right], \tag{2.49}$$

where F_N is the normal force, F_Y is the side force, and N is the total number of vortices (in both the left and right planes). In the free vortex / feeding-sheet model, the cross-sectional load is an implicit result of the vortex dynamics.

This is in contrast with the formulation of the free vortex method (FVM) developed in [99] and extended to slender bodies with strakes by Tuling [30]. The loading predicted by the vortex impulse theorem may be split into a contribution from vortex motion and a contribution from circulation growth:

$$\rho_\infty V_\infty \frac{\mathrm{d}}{\mathrm{d}x}\left[\sum_N^{j=1} \Gamma_j \left(\sigma_j - \frac{a^2}{\bar{\sigma}_j}\right)\right] = \frac{\mathrm{d}F_I}{\mathrm{d}x} + \frac{\mathrm{d}F_V}{\mathrm{d}x}, \tag{2.50}$$

where, as noted in [99], F_I is the loading arising from inviscid effects, and F_V is the loading associated with viscous structures such as the feeding sheet through $\dot{\Gamma}$:

$$\frac{\mathrm{d}F_I}{\mathrm{d}x} = \rho_\infty V_\infty \sum_N^{j=1} \Gamma_j \frac{\mathrm{d}}{\mathrm{d}x}\left[\left(\sigma_j - \frac{a^2}{\bar{\sigma}_j}\right)\right], \tag{2.51}$$

$$\frac{\mathrm{d}F_V}{\mathrm{d}x} = \rho_\infty V_\infty \sum_N^{j=1} \frac{\mathrm{d}\Gamma_j}{\mathrm{d}x}\left(\sigma_j - \frac{a^2}{\bar{\sigma}_j}\right). \tag{2.52}$$

The philosophy of the FVM is to prescribe the viscous cross-sectional loading, using empirical or semi-empirical methods such as Jorgensen's [113] crossflow method. From Eq. (2.52) it is seen that this defines the change in circulation of the discrete vortex, $\frac{\mathrm{d}\Gamma}{\mathrm{d}x}$, if the vortex positions are already known. The FVM assumes that the discrete vortices themselves experience no net force, and they are thus advected by the local fluid velocity [30, 99]. The vortex tracking equation for this case is given below for comparison to the more complex formulation of the FVFSM given by Eqs. (2.47) and (2.48):

$$\dot{\sigma}_j = W_j\,, \tag{2.53}$$

where as before, W_j is the complex velocity vector at the j-th vortex. Together with a prescription for $\frac{\mathrm{d}F_V}{\mathrm{d}x}$ from another method, Eqs. (2.52) and (2.53) close the system of equations for the vortex shedding and tracking. The Kutta condition is not enforced, as it is not required for equation closure. Tuling [30] notes that the free vortex method requires external input for the starting conditions. In light of the accuracy of the free vortex / feeding-sheet pair method for short nondimensional times, Tuling [30] recommends its use to generate the starting conditions for the FVM.

The FVFSM and FVM both model the shedding and viscous feeding of only two vortices. It should be noted that other vortices advected from upstream may be included in the vortex tracking scheme of the FVM. However, the circulation of these upstream vortices is modelled as remaining constant, as their feeding sheets are not included in the formulation of the FVM [99]. These methods are now compared to a representative multi-vortex discrete vortex method (MVDVM) [24]. This is a distributed-vorticity vortex modelling method, in which discrete potential vortices of constant circulation are shed from separation points at each time step. These are termed nascent vortices. The model described by [24] utilizes a boundary-layer model, with separation being predicted from semi-empirical separation criteria for a flat plate. The criteria are described as a critical pressure coefficient C_p at which separation occurs:

$$\text{Laminar:} \quad C_p^{0.5}\left(\xi\frac{\mathrm{d}C_p}{\mathrm{d}\xi}\right) = 0.087\sin\alpha\,, \tag{2.54}$$

$$\text{Turbulent:} \quad C_p\left(\xi\frac{\mathrm{d}C_p}{\mathrm{d}\xi}\right)^{0.5}\left(Re_\xi\times 10^{-6}\right)^{-0.1} = 0.35\sin\alpha\,, \tag{2.55}$$

where ξ is the distance along the surface from the stagnation point. The velocity at the edge of the boundary layer at the separation point, V_e, is used to define the rate of circulation

production as

$$\dot{\Gamma} = \frac{V_e^2}{2}\,. \tag{2.56}$$

This is used to define the strength of the nascent vortex shed at each time step. The Kutta condition is then used to position the nascent vortex [24]. Vortices are modelled as being advected by the local fluid velocity. Cross-sectional loads are obtained by integrating the pressure distribution at the surface. These modelling approaches are summarized and compared to the concentrated-vorticity vortex modelling methods in Table 2.2.

Linear Potential Flows

The linear potential equation is expressed below in vector form in an Eulerian frame as

$$a_\infty^2 \nabla^2 \Phi = \frac{\partial^2 \Phi}{\partial t^2}\,, \tag{2.57}$$

with comparison to the full potential formulation of Eq. (2.39) showing that the linear potential equation is rooted in a small-disturbance assumption. This is also clear by comparing the Cartesian component form for the perturbation potential below with Eq. (2.43):

$$\left(a_\infty^2 - V_\infty^2\right)\phi_{xx} + a_\infty^2 \phi_{yy} + a_\infty^2 \phi_{zz} = 2V_\infty \phi_{xt} + \phi_{tt}\,, \tag{2.58}$$

from which it is clear that all second-order perturbation terms are discarded in the linear formulation. The surface boundary condition of Eq. (2.44) is often linearized to be applied on some intermediate surface, such as the thickness plane of a wing rather than on the wing surface itself. The linear potential equation is equivalent to the classical wave equation in an earth-fixed frame with a moving body.

A limited number of closed-form solutions to the linear potential equation are known, such as potential flow around a cylinder or sphere. These have been extended to more practical shapes of interest, such as airfoils, through the use of mathematical transforms. These transforms map the geometry of interest in the physical space onto a cylinder in the computational space. The known solution in the computational space is then mapped back to a solution in the physical space. Other closed-form solutions include those for conical flow (as for a delta-wing) and for various slender-body assumptions (thin-airfoil theory and slender-body flows). In these methods, a continuous distribution of basic potential-flow elements (such as velocity sources and sinks) is . These solutions are covered in detail in [100].

An important subset of potential-flow solutions lie in slender body theory. A detailed mathematical development of slender body theory is given in [3, 100]. Only the salient

Table 2.2 Comparison of modelling approaches in discrete vortex modelling methods.

	FVFSM	FVM	MVDVM
No. of shed vortices:	Two	Two	Multiple
Separation point, $t = 0$:	Pre-defined	Pre-defined	BL semi-empirical
Separation point, $t > 0$:	Constant	Variable	Variable
Shed vortex strength:	Variable	Variable	Constant
Seeding position:	Explicit: empirical	Explicit: empirical	Implicit: Kutta
Seeding Γ:	Explicit: empirical	Explicit: empirical	Implicit: $\dot{\Gamma}$ marching
Shed Γ:	Explicit: Kutta	Implicit: $\dot{\Gamma}$ marching	Explicit: constant
Shed $\dot{\Gamma}$:	Explicit: force-free pair	Explicit: specified F_V	Explicit: shed $\dot{\Gamma} = 0$
Vortex velocity:	Implicit: not advected	Explicit: local advection	Explicit: local advection
Force-free elements:	Vortex / feeding-sheet pair	Vortex	Vortex
Cross-sectional load:	Implicit:	Explicit:	Implicit:
	Vortex impulse theorem	Viscous crossflow method	Surface pressure integration

points and results will be covered here. These will be outlined for a steady axisymmetric flow for brevity. The extension to general three-dimensional bodies is treated in [3, 100]. The development utilizes asymptotic expansions of the velocity potential Φ in outer-flow and inner-flow regions as follows:

$$\Phi^o = V_\infty x + V_\infty \varepsilon \phi_1^o(x,r) + V_\infty \varepsilon^2 \phi_2^o(x,r) + \dots , \tag{2.59}$$

$$\Phi^o = V_\infty x + V_\infty \varepsilon \phi_1^i(x,\bar{r}) + V_\infty \varepsilon^2 \phi_2^i(x,\bar{r}) + \dots , \tag{2.60}$$

where superscript "o" denotes the outer expansion, "i" denotes the inner expansion, and numerical subscripts denote the order of perturbation potential ϕ. The non-dimensionalization used for the inner expansion is given by

$$\bar{r} = r/\varepsilon , \tag{2.61}$$

where ε is a small parameter used to non-dimensionalize the description of the body surface $R(x)$ as

$$R(x) = \varepsilon \bar{R}(x) . \tag{2.62}$$

Through substitution of the above expansions into the nonlinear steady potential equation and matching the inner and outer asymptotic expansions, it is shown in [100] that $\phi_1^o = \phi_1^i = 0$ is required, and that the nonlinear potential equation reduces to the following equations:

$$\text{Outer expansion:} \quad \left(a_\infty^2 - V_\infty^2\right)\phi_{2xx}^o + \frac{1}{r}\phi_{2r}^o + \phi_{2rr}^o = 0 , \tag{2.63}$$

$$V_\infty \lim_{r\to 0}\left(r\phi_{2r}^o\right) = \bar{R}\bar{R}_x , \tag{2.64}$$

$$\text{Inner expansion:} \quad \phi_{2\bar{r}\bar{r}}^i + \frac{1}{\bar{r}}\phi_{2\bar{r}}^i = 0 , \tag{2.65}$$

$$\text{Surface BC:} \quad \phi_{2\bar{r}}^i(x,\bar{R}) = \bar{R}_x , \tag{2.66}$$

$$\text{Surface pressure:} \quad c_p = -\varepsilon^2\left[2\frac{\phi_{2x}^i}{V_\infty} + \frac{\left(\phi_{2\bar{r}}^i\right)^2}{V_\infty^2}\right] + \mathscr{O}\left(\varepsilon^4 \ln(\varepsilon)\right) . \tag{2.67}$$

It is evident that the above equations are linear in the perturbation potentials. The outer expansion is simply the 3D linear potential equation, while the inner expansion is the incompressible wave equation in the crossflow plane. Ashley and Landahl [100] note that the equations may be written in terms of a single nondimensional perturbation, introducing

$$\varphi \equiv \varepsilon^2 \phi_2^o / V_\infty , \tag{2.68}$$

with the outer expansion equations Eqs. (2.63) and (2.64) and the surface pressure Eq. (2.67) being written as

$$\text{Outer expansion:} \quad \left(1-M_\infty^2\right)\varphi_{xx}+\frac{1}{r}\varphi_r+\varphi_{rr}=0\,, \tag{2.69}$$

$$\lim_{r\to 0}\left(2\pi r\varphi_r\right)=S_x(x)\,, \tag{2.70}$$

$$\text{Surface pressure:} \quad c_p=-\left(2\varphi_x+\varphi_r^2\right)+\mathscr{O}\left(\varepsilon^4\ln\varepsilon\right), \tag{2.71}$$

where $S(x)\equiv\pi R^2(x)$ is the cross-sectional area of the body of revolution. In the case of axisymmetric flows, the boundary conditions must be applied on the actual body surface due to the singularity of the expression for φ_r at $r=0$. Ashley and Landahl [100] note that in the inner region, the following solution is obtained for the nondimensional perturbation potential:

$$\varphi\approx\frac{1}{2\pi}S_x(x)\ln r+g(x)\,, \tag{2.72}$$

where the first term represents the effect of local flow divergence in the crossflow plane due to the rate of change of the body cross-sectional area, and the function $g(x)$ accounts for Mach number effects and upstream / downstream influence. Ashley and Landahl [100] provide the following expressions for $g(x)$ for bodies with a sharp nose ($S_x(0)=0$), with the additional assumption of $S_x(L)=0$ in subsonic flows:

$$M_\infty<1: \quad g(x)=\frac{S_x(x)}{2\pi}\ln\frac{\sqrt{1-M_\infty^2}}{2}-\frac{1}{4\pi}\int_0^x S_{xx}(x_1)\ln(x-x_1)\mathrm{d}x_1 + \frac{1}{4\pi}\int_x^L S_{xx}(x_1)\ln(x_1-x)\mathrm{d}x_1\,, \tag{2.73}$$

$$M_\infty>1: \quad g(x)=\frac{S_x(x)}{2\pi}\ln\frac{\sqrt{M_\infty^2-1}}{2}-\frac{1}{2\pi}\int_0^x S_{xx}(x_1)\ln(x-x_1)\mathrm{d}x_1\,, \tag{2.74}$$

where x_1 is a running variable. The influence from upstream and downstream enters through the integrals. It is to be noted that in this derivation, it was assumed that the body is sufficiently smooth. Investigation of the relation for φ in Eq. (2.72) shows that for terms such as φ_{xx} to be well defined, the body must be smooth such that $S_x(x)$ is at least C^2-continuous.

The essence of slender body theory in separating the 3D flow problem into a compressible non-lifting problem and an incompressible crossflow problem has been widely exploited. Typical exploitations make use of conformal mappings to transform the body cross-section to a cylinder or flat plate in the computational plane [3, 100]. Analytical solutions for incompressible cylinder or plate flow are then transformed back to the physical plane to give the crossflow solution around the body cross-section. Slender body theory is the basis for

the Pitts-Nielsen-Kaattari [101] method for computing wing-body interference. The normal force predicted for a representative wing-body configuration is given by [3] as

$$\frac{F_N}{q_\infty} = 2\pi\alpha s_m^2\left(1 - \frac{a^2}{s_m^2} + \frac{a^4}{s_m^4}\right), \tag{2.75}$$

where F_N is the total normal force including the inviscid forebody loads, a is the radius of the body, s_m is the semi-span of the wing at the trailing edge (including the body radius), and $q_\infty = \rho_\infty V_\infty^2/2$ is the freestream dynamic pressure. As noted in [100], this equation contains as special cases the normal force predicted by slender body theory of a body in isolation as

$$\frac{F_{N_B}}{q_\infty} = 2\pi a^2\alpha\,, \tag{2.76}$$

where the normal force is due to the inviscid force arising from changes in body cross-sectional area. Equation (2.75) also contains the normal force predicted by slender body theory of a wing alone as

$$\frac{F_{N_W}}{q_\infty} = 2\pi\alpha(s_m - a)^2\,, \tag{2.77}$$

where $(s_m - a)$ is the exposed semi-span of wing panel. Integration of the pressure on the wing panels and substitution of Eq. (2.77) gives the following relation for the wing carryover-factor, quoted from [3] as

$$\begin{aligned} K_W &\equiv \frac{F_{N_{W(B)}}}{F_{N_W}}\,, \\ &= \frac{1}{\pi(\lambda-1)^2}\left[\frac{\pi}{2}\left(\frac{\lambda^2-1}{\lambda}\right)^2 + \left(\frac{\lambda^2+1}{\lambda}\right)^2 \sin^{-1}\left(\frac{\lambda^2-1}{\lambda^2+1}\right) - \frac{2\left(\lambda^2-1\right)}{\lambda}\right], \end{aligned} \tag{2.78}$$

where $\lambda = s_m/a$ is the span-to-diameter ratio. The body carryover-factor is then found as

$$K_B = \left(1 + \frac{a}{s_m}\right)^2 - K_W\,. \tag{2.79}$$

The modification of these parameters for various wing shapes and afterbody lengths is described in [3, 101].

The approach adopted in the development of slender body theory may be adapted to thin wings of high aspect ratio. In the resulting non-dimensionalization, the small parameter is $1/AR$, and the 3D flow problem is reduced to 2D flow in the incidence plane. This reduction is known as strip theory [27].

The linearity in terms of the velocity potential of Eqs. (2.57) and (2.58) allows the solution of the flow around a body to be constructed from a summation of the solutions to elementary flow elements, such as velocity potential sources, sinks, doublets, irrotational vortices, and uniform flow. This is implicitly utilized in the solutions to slender body theory presented above, in which a line of source elements of continuously-varying strength was used. It is more obviously used through the use of discrete elementary flow elements, as is the case in panel methods. These have already been introduced for lifting flows in Fig. 2.60. The class or application of panel methods which will be considered engineering-level methods here is restricted to panel methods which do not require panelling of the wake. This essentially restricts the consideration to

- Non-lifting panel methods, such as velocity-potential sink-source methods for bodies,
- Lifting panel methods based in the acceleration-potential formulation, such as the doublet-lattice method (DLM).

The latter is particularly useful in unsteady flows, as has been broadly adopted in aeroelastic analysis codes for wing-like surfaces. An example of its adoption is in the ZONA51 code, which has been implemented in Nastran, and the ZONA7U and other codes within the ZAERO suite of software [79]. Due to its broad implementation, a brief overview of the essence of the method is given here. A full description of the mathematics and key equations of the method is found in [102].

The key in the development of the doublet-lattice method lies in the linearity in terms of ϕ of the potential equation Eq. (2.58) and the use of the linearized pressure equation. The latter is obtained from Eqs. (2.40) and (2.41) as

$$p - p_\infty \approx -\rho_\infty(\phi_t + V_\infty \phi_x)\,, \tag{2.80}$$

where as before, ϕ is the perturbation velocity-potential. As noted by Blair [102], the linearity of Eq. (2.58) in terms of ϕ leads to the equation holding the same form if the velocity-potential ϕ is replaced by the acceleration-potential ψ, which is defined as

$$\psi \equiv \frac{\mathrm{d}\phi}{\mathrm{d}t} = \phi_t + V_\infty \phi_x \approx (p - p_\infty)/\rho_\infty\,. \tag{2.81}$$

Since the same mathematical potential equation holds for both ψ and ϕ, it follows that the elementary flows will have the same mathematical form [102]. This gives rise to the existence of an acceleration-doublet, or through Eq. (2.81) equivalently a pressure-doublet, as the counterpart to the elementary velocity-doublet flow.

The typical procedure of velocity-potential panel methods is to first solve for the velocities (through ϕ and its boundary conditions at the surface). The pressure is the calculated as a consequence of ϕ and its gradients. The DLM circumvents this through directly relating the pressure difference on the lifting surface to its downwash boundary-conditions. To accomplish this, an inverse relation to that of Eq. (2.80) is developed, in which the velocity-potential is expressed as an integral of the pressure-differential. Since an inviscid wake cannot support a force, the pressure-differential across the wake is identically zero. In this way, the DLM removes the necessity of panelling the wake behind an inviscid-lifting wing. The mathematical relation between the downwash at the surface and the pressure distribution over the lifting surface, and the resulting definition of the kernel function, may be cast in different forms. The general form adopted in [79] is quoted below as

$$w(x_0,y_0,z_0) = \frac{\beta}{2E\pi}\iint_{\text{wing}} \Delta C_p(x,y,z)\exp(-\mathrm{i}k\beta\xi)\bar{K}(\xi,\eta,\zeta)\mathrm{d}S\,, \tag{2.82}$$

where ΔC_p is the difference in pressure coefficient between the upper and lower surfaces of the wing, w is the downwash velocity, and $\bar{K}$ is the kernel function, with the rest of the terms defined by

$$\bar{K} = -\int_X^{\xi} \exp(\mathrm{i}k\tau/\beta)\frac{\partial^2 K}{\partial n^2}\,\mathrm{d}\tau\,, \tag{2.83}$$

$$K = \begin{cases} \frac{\exp(-\mathrm{i}\lambda R)}{R}, & \text{for} \quad M_\infty < 1 \\ \frac{\cos(\lambda R)}{R}, & \text{for} \quad M_\infty > 1 \end{cases}, \tag{2.84}$$

$$E = \begin{cases} 4, & \text{for} \quad M_\infty < 1 \\ 2, & \text{for} \quad M_\infty > 1 \end{cases}, \tag{2.85}$$

$$X = \begin{cases} -\infty, & \text{for} \quad M_\infty < 1 \\ \sqrt{\eta^2+\zeta^2}, & \text{for} \quad M_\infty > 1 \end{cases}, \tag{2.86}$$

$$\lambda = \frac{kM_\infty}{\beta}\,, \tag{2.87}$$

$$\beta = \sqrt{|1-M_\infty^2|}\,, \tag{2.88}$$

$$k = \frac{\omega L_{ref}}{V_\infty}\,, \tag{2.89}$$

$$R = \sqrt{\xi^2+\mu\eta^2+\mu\zeta^2}\,, \tag{2.90}$$

$$\xi = \frac{x-x_0}{\beta L_{ref}}\,, \tag{2.91}$$

$$\eta = \frac{y - y_0}{L_{ref}}, \tag{2.92}$$

$$\zeta = \frac{z - z_0}{L_{ref}}, \tag{2.93}$$

$$\mu = \begin{cases} 1, & \text{for} \quad M_\infty < 1 \\ -1, & \text{for} \quad M_\infty > 1 \end{cases}, \tag{2.94}$$

where n denotes the surface-normal direction, and subscript "0" denotes the fixed point which is influenced by the surrounding doublet sheet.

In the numerical solution of the DLM, the wing surface is discretized into panels located on its thickness-plane. An acceleration-potential doublet line is placed along the $0.25c$ of each panel. The influence of these doublet lines is calculated at collocation points, located at the mid-span of each panel at the $0.75c$ chordwise station. As noted by Blair [102], the use of numerical values of $0.25c$ and $0.75c$ is empirical, having no mathematical basis. Further details on the integration of the kernel function and on best practices for panelling may be found in [79, 102]. An example of mixed panelling, with acceleration-potential doublets along the wing surface and velocity-potential sources on body-like surfaces, is shown in Fig. 2.62 from [79].

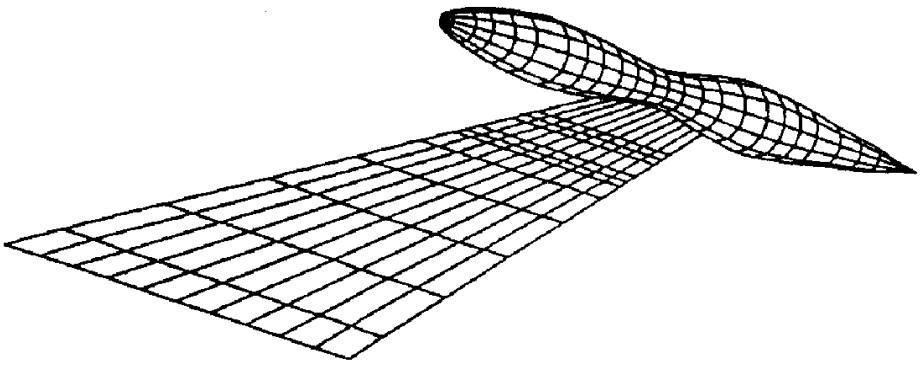

Fig. 2.62 A mixture of DLM panels and velocity-source panels used in modelling a wing with a tip-tank [79].

An advantage of panel methods, including the DLM, is that the 3D flow and the influence of panels on one another is correctly modelled. An inevitable disadvantage of panel methods lies in their basis in linear potential flows. This leads to a degradation in their accuracy at high supersonic and hypersonic speeds. This was partially addressed in the ZONA7U code, in which the influence coefficients from the kernel function were supplemented by nonlinear thickness terms computed from piston theory [79].

Local-Inclination Methods

The surface discretization implemented in panel methods may also be used in a range of engineering-level methods which predict the local surface pressure as a function of the inclination of the surface. An immediate advantage of these methods is their conceptual and mathematical simplicity. The aerodynamic influence coefficient matrix, which describes the influence of panels on one another, is rendered a sparse matrix. For purely local methods such as Newtonian impact theory [27], piston theory [88, 103], and Van Dyke's [104] second-order potential theory for planar flows, the matrix becomes diagonal. This decreases the computational cost of constructing and inverting the matrix, and renders the methods computationally cheaper than panel methods which produce non-sparse influence matrices. Methods such as first-order shock-expansion theory [58] and and Donov's theory [105] require the conditions behind the leading-edge shock to be determined. Thereafter, the methods have a local character. The methods covered here are all based in supersonic flows.

Newtonian impact theory provides surface pressure prediction for hypersonic speeds and is particularly useful for blunt-body flows. A detailed overview of various cases and extensions of the method is given in [27]. Only the simpler formulations, which are local-inclination methods, will be noted here. The method is based in the assumption that fluid particles which impact the body surface lose all momentum normal to the surface, while maintaining their momentum tangential no the surface. The loss in normal momentum is reflected as an increase in the surface pressure. The resulting equation for the pressure coefficient on the surface is given by [27] as

$$C_p = C_{p(max)} \sin^2 \delta \,, \tag{2.95}$$

where δ is the local inclination of the surface to the freestream, and $C_{p(max)}$ takes on different values depending on the formulation of Newtonian theory used, as detailed by

$$C_{p(max)} = \begin{cases} 2, & \text{Newtonian} \\ \frac{2}{\gamma M_\infty^2}\left[\left(\frac{\gamma+1}{2}M_\infty^2\right)^{\frac{\gamma}{\gamma-1}}\left(\frac{\gamma+1}{2\gamma M_\infty^2-\gamma+1}\right)^{\frac{1}{1-\gamma}}-1\right], & \text{Modified Newtonian} \end{cases} \tag{2.96}$$

where so-called Modified Newtonian theory typically defines $C_{p(max)}$ as the pressure coefficient behind a normal shock. Other formulations of Modified Newtonian shock theory developed for cones, ogives, hemispheres, and wings are defined by different expressions for $C_{p(max)}$ and are detailed in [114]. These are empirical relations. Further extensions to Newtonian theory account for the structure of the shock layer and for centrifugal effects due to body curvature [25, 27]. In doing so, the local nature of the method is lost. As noted

by [25], the prediction accuracy of these extensions is often lower than that provided by the simpler empirical relations. Finally, it is noted that the simpler form of Newtonian theory outlined above is for steady flows. The method may be applied to quasi-steady flows, as done in [115], without losing the local character. An extension to unsteady flows, as detailed in [27], increases the complexity of the method and destroys its local character. As noted by [27], the underlying assumptions of Newtonian theory are best approximated in the limit of $M_\infty \to \infty$ for near-zero density flows. Under these conditions, the shock layer lies close to the surface of a blunt body.

Piston theory is another method originally developed for hypersonic flows [88, 103]. In contrast to Newtonian theory, it is intended for slender profiles. A detailed overview of the development of piston theory and its various formulations and extensions is reserved for Chapter 3. The use of piston theory as in reduced-order perturbation modelling was described in Section 2.2.3 and was referred to as local piston theory (LPT). The use of piston theory to calculate the overall loading (without a background solution) is referred to here as classical piston theory (CPT). The mathematical formulation of CPT is essentially similar to that of LPT introduced in Eqs. (2.36) and (2.37). The downwash is given as

$$w = -\mathbf{V}_\infty \cdot \hat{\mathbf{n}} + \mathbf{V_b} \cdot \hat{\mathbf{n}}, \tag{2.97}$$

where $\mathbf{n}$ is the local unit normal vector of the surface. By comparison with Eq. (2.37), it is evident that CPT models perturbations (both steady and unsteady) relative to the freestream, while LPT models perturbations relative to the local mean steady flow. The pressure equation due to Lightill's [88] original formulation of piston theory is given up to third-order as

$$p_u = p_\infty + \gamma p_\infty \left[\left(\frac{w}{a_\infty} \right) + \frac{\gamma+1}{4} \left(\frac{w}{a_\infty} \right)^2 + \frac{\gamma+1}{12} \left(\frac{w}{a_\infty} \right)^3 \right]. \tag{2.98}$$

It is briefly noted here that the first-order term in the pressure equation may also be derived from linear potential flow theory. The differences in theoretical bases that provide a piston-theory-like pressure equation will be discussed in Section 2.2.3 along with the adaptation required to apply piston theory to panels and shells. It is also noted here that CPT due to Lighthill, due to its local nature, does not account for upstream flow history. This renders it an effectively quasi-steady method.

An equation similar to Eq. (2.98) was obtained by Van Dyke, rooted in his second-order potential flow theory for supersonic flows [104]. The essence of the second-order theory is an iteration procedure. The nonlinear potential equation is separated with linear terms on the LHS and nonlinear terms on the RHS. The first-order solution is obtained by setting

the RHS to zero and solving the linearized potential flow equation. The first-order potential function, having been solved for, is then used to define the RHS terms of the second-order potential equation. In this manner, the second-order problem is cast as an equivalent first-order problem with non-zero sources. A number of closed-form solutions were obtained by Van Dyke [104] using the theory. Of particular interest was the solution obtained for plane flow over a smoothly curved wall. The resulting second-order equation for the pressure at the surface of the wall may be cast as

$$p_u = p_\infty + \gamma p_\infty \left[\frac{M_\infty}{m_\infty} \left(\frac{w}{a_\infty} \right) + \frac{(\gamma+1)M_\infty^4 - 4m_\infty^2}{4m_\infty^4} \left(\frac{w}{a_\infty} \right)^2 \right], \tag{2.99}$$

where $m_\infty = \sqrt{M_\infty^2 - 1}$. The downwash w may be defined as in CPT by Eq. (2.97). While Eq. (2.99) was developed for a steady flow, its extension to quasi-steady flows is given through the body-motion term in Eq. (2.97). The results for bodies of revolution, as well as the procedures required to treat bodies with corners, are detailed in [104].

First-order shock-expansion theory assumes that the flow behind the bow shock of a body or airfoil is turned isentropically [27, 58]. The reflection from the bow shock and shear layers of Mach waves generated by the body is neglected. This neglect of interaction renders the method a local-inclination method, with only the conditions behind the bow shock being required in addition to the local inclination. A detailed exposition of the method, its assumptions, and of extensions to second-order shock-expansion theory is given in [27].

Donov's [105] theory for flow past supersonic airfoils with leading-edge shocks may be seen as the final step in the progression of increasingly rigorous developments of local-inclination methods covered thus far. The development utilizes the method of characteristics [25] in solving the Euler equations. In so doing, Donov developed an expression for the pressure distribution on the surface an airfoil with an attached leading-edge shock. The treatment accounted for reflection of Mach waves from the leading-edge shock and for rotationality generated by the curvature of the bow shock. The equation for the pressure distribution is given below as

$$p = p_\infty + q_\infty \left[a_1 \delta(x) + a_2 \delta^2(x) + a_3 \delta^3(x) + a_4 \delta^4(x) \right] + \Delta p_e + \mathscr{O}\left(\delta^5\right), \tag{2.100}$$

where $\delta(x)$ is the local surface inclination at a distance x from the leading-edge, and $q_\infty = \gamma p_\infty M_\infty^2/2$ is the freestream dynamic pressure. The expression up to the term Δp_e models the contribution to pressure due to isentropic effects, while Δp_e is the contribution due to

entropy-effects generated by the leading-edge shock. This latter term is given by

$$\Delta p_e = \; q_\infty \left[a_{1e}\delta^3(0) + a_{2e}\delta^4(0) + a_{3e}\delta^3(0)\delta(x) \right] + \Delta p_{rot}\,, \tag{2.101}$$

$$\Delta p_{rot} = q_\infty \left[a_{4e} x \delta^3(0)\delta_x(0) \right], \tag{2.102}$$

where Δp_{rot} is the component associated with flow rotationality, and δ_x is the rate of change of inclination. The coefficients a_i are given here up to third order as

$$a_1 = 2m_\infty^{-1}\,, \tag{2.103}$$

$$a_2 = m_\infty^{-4}\left(2 - 2M_\infty^2 + \frac{\gamma+1}{2}M_\infty^4\right), \tag{2.104}$$

$$a_3 = m_\infty^{-7}\left[\frac{4}{3} - 2M_\infty^2 + \frac{5}{3}(\gamma+1)M_\infty^4 + \frac{2\gamma^2-7\gamma-5}{6}M_\infty^6 + \frac{\gamma+1}{6}M_\infty^8\right], \tag{2.105}$$

with the reader referred to [105, 116] for higher-order coefficients. The coefficients a_{ie} associated with non-isentropic contributions are described in [105, 116]. Only the coefficient a_{1e}, which is associated with a third-order term, is given here as

$$a_{1e} = \frac{M_\infty^6 m_\infty^{-7}}{2}\left[\frac{\gamma^2-7\gamma+2}{3} + \frac{(\gamma+1)^2}{8}M_\infty^2\right] - \frac{(\gamma+1)}{6}M_\infty^4 m^{-3}\,. \tag{2.106}$$

It is noted that for thin airfoils, the expression remains a local-inclination method up to third-order. The method was developed for steady flows. As the non-isentropic effects only enter from third-order, an extension to quasi-steady flows at second-order follows directly as in the case of Van Dyke's second-order theory.

Viscous-Crossflow Analogy

One significant semi-empirical method which is widely used is the viscous crossflow analogy (also known as the impulsive-flow analogy), originally developed for isolated bodies of revolution by Allen [117] and matured by Allen and Perkins [111]. The method considers the 3D flow around a slender body to be equivalent to an impulsively-started 2D flow in the crossflow plane, with the crossflow plane swept down the body at a speed equal to the axial component of the freestream velocity. The viscous drag experienced by the analogous cross-sectional shape is interpreted as a viscous normal-force in the 3D representation. This viscous component is added to the inviscid normal-force that is generated by axial variation

in the cross-sectional area. The normal force was given as

$$C_N = \frac{S_B}{S_{ref}} \sin 2\alpha \cos\frac{\alpha}{2} + \eta C_{d_c} \frac{S_p}{S_{ref}} \sin^2\alpha\,, \tag{2.107}$$

where S_{ref} is the reference area, S_p is the planform area of the body, S_B is the area of the base, C_{d_c} is the crossflow drag coefficient of the 2D cross-section, and η is the ratio of crossflow drag coefficient of a finite-length cylinder to that of a 2D (infinite-length) cylinder, also known as the crossflow drag proportionality factor. The first term on the right-hand side of the equation is the essentially-linear inviscid contribution, while the second term is the semi-empirical modelling of the nonlinear contribution due to viscosity. The pitching-moment coefficient was given as

$$C_m = \left[\frac{V - S_B\left(L - x_{ref}\right)}{SL_{ref}}\right] \sin 2\alpha \cos\frac{\alpha}{2} + \eta C_{d_c} \frac{S_p}{S_{ref}} \left(\frac{x_{ref} - x_c}{L_{ref}}\right) \sin^2\alpha\,, \tag{2.108}$$

where V is the volume of the body, x_{ref} is the axial location of the moment reference centre, L_{ref} is the reference length, and x_c is axial location of planform-area centroid. Jorgensen extended the method to bodies with non-circular cross-sections [112] and bodies with wings [113], and also provided an adjustment [113] for crossflow Mach number effects on the η. The equations in the extension of Jorgensen remain essentially similar, with the effect of non-circular cross-section accounted for by slender-body theory in the inviscid terms and by Newtonian-impact theory in the viscous terms. It was noted that end-effects on the viscous term become negligible at supersonic-crossflow Mach numbers, with $\eta = 1$.

The viscous crossflow analogy was utilized by Ortell [118] in formulating a semi-empirical model for the normal force of highly-swept wings of low aspect ratios at supersonic speeds. The method utilized a correction factor κ to adjust the predicted normal-force, with κ determined empirically from a large experimental database. The resulting equation for the wing-alone normal-force was given as

$$\frac{C_{N_W}}{\kappa} = C_{N_{\alpha(W)}}\alpha + C_{d_c}\frac{S_W}{S_{ref}}\sin^2\alpha\,, \tag{2.109}$$

in which C_{d_c} is the crossflow drag coefficient for a 2D cylinder, $C_{N_{\alpha(W)}}$ is the linear lift-slope of the wing, and S_W is the wing planform area. The similarity to the viscous crossflow formulation for bodies-alone is obvious. Ortell applied the same formulation (using the same definition of κ) to wing-body combinations, utilizing the slender-body values for wing-body

interference and nose-lift, giving the total normal-force for the wing-body combination as

$$\frac{C_N}{\kappa} = \big(K_{W(B)} + K_{B(W)}\big) C_{N_{\alpha(W)}} \alpha \frac{S_W}{S_{ref}} + 2\alpha \frac{S_N}{S_{ref}} + C_{d_c} \frac{S_W}{S_{ref}} \sin^2 \alpha \,, \tag{2.110}$$

where S_N is maximum cross-sectional area of the nose. The method was found to compare favourably with other semi-empirical methods [119] for wing-alone (with separate models for upper-surface and lower-surface normal force) and wing-body normal-force prediction, as well as to experiment.

Equivalent Angle-of-Attack Method

A range of semi-empirical methods for estimating full-vehicle characteristics and interference factors also exist, as detailed in [30, 46]. The most widely used method is the equivalent angle-of-attack method [46, 47]. The method is considered a semi-empirical method here for two reasons. Firstly, the authors of the method recommend the use of empirical or semi-empirical methods to determine component-alone loads [46]. Secondly, the basis for the method is heuristic, with confidence in the method having been established through its successful application in practice [46]. The method is considered [46] a nonlinear extension of the classical method of Pitts-Nielsen-Kaattari [101], and as such, will receive greater attention. An overview of the method follows, with greater detail available in [46, 47].

The essence of the equivalent angle-of-attack method lies in equating the loads produced by an isolated fin-set to those produced by a fin-set integrated on the vehicle. It is assumed that the aerodynamic interference on the integrated fin-set may be expressed as an equivalent angle-of-attack at which the isolated fin-set produces the same load. The concept is illustrated in Fig. 2.63. This is expressed as

$$C_{N_{W(B)}}(\alpha_c, \phi, \delta) = C_{N_W}\big(\alpha_{eq}\big) \,, \tag{2.111}$$

where α_{eq} is the equivalent angle of attack, α_c is the incidence of the body centerline, ϕ is the roll angle, and δ is the fin deflection. In applying the method, the equivalent angle-of-attack is calculated from known (or estimated) quantities. The overall load on the vehicle-integrated fin-set is then estimated from a model for the wing-alone load curve. The extension to nonlinearity, particularly at high angle-of-attack, is achieved by utilizing a nonlinear load-curve for the wing-alone, such as provided an empirical database [46].

As noted in [46], the wing-loads must be considered separately to body-loads when computing the equivalent angle-of-attack. The component build-up formulation for the

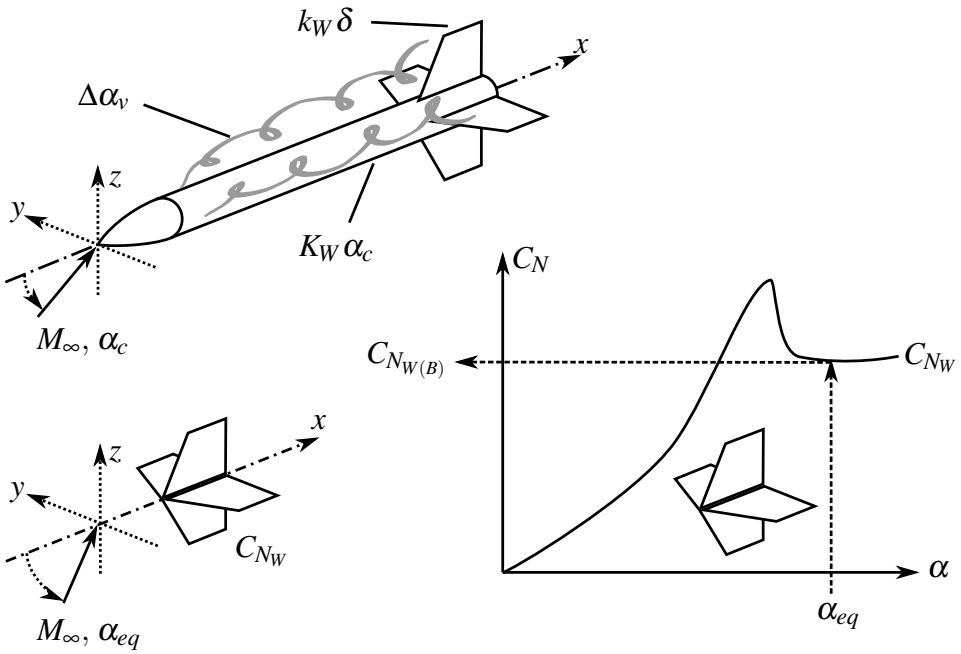

Fig. 2.63 Illustration of the equivalent angle-of-attack concept.

overall normal-force on the vehicle was given in Eq. (2.1), and is repeated here:

$$C_N = C_{N_B} + C_{N_{W(B)}} + C_{N_{B(W)}}\,. \tag{2.112}$$

The linear representation for the wing-load as a function of fin deflection and body influence for zero bank angle is given by [46] as

$$C_{N_{W(B)}} = (K_W\,\alpha_c + k_W\,\delta + \Delta\alpha_v)\frac{\partial C_{N_W}}{\partial\,\alpha}\,, \tag{2.113}$$

where $\Delta\alpha_v$ is the equivalent upwash generated over the fin-set by upstream vorticity, and $k_W = \left[C_{N_{W(B)}}/C_{N_W}\right]_{\alpha_c=0,\,\delta\neq 0}$ is known as the wing-deflection factor. The equivalent angle-of-attack for in the linear representation for zero roll is then

$$\alpha_{eq} = K_W\,\alpha_c + k_W\,\delta + \Delta\alpha_v\,. \tag{2.114}$$

The more general linear formulation accounts for fin-on-fin interference in k_W through the introduction of the control-effectiveness parameter Λ_{ji} and for roll angle ϕ. The nomenclature is elaborated on in [46], with the formulation for a "+" configuration expressed as

$$\alpha_{eq} = \hat{\alpha}_{eq} + \sum_{j=1}^{4}\Lambda_{ji}\delta_j\,, \tag{2.115}$$

$$\hat{\alpha}_{eq} = K_W \alpha_c \cos\phi_i + \frac{2}{AR} K_\phi \alpha_c^2 \sin 2\phi_i + \Delta\alpha_{v(i)}\,, \tag{2.116}$$

where $\hat{\alpha}_{eq}$ is the equivalent angle-of-attack without fin deflection, and K_ϕ is an interference factor accounting for sideslip. The linear representation, in which angles-of-attack are summed, is not recommended [46] for incidences above $\alpha_c > 20°$. At higher incidences, Hemsch [46] recommends summing the induced velocities, giving

$$\tan\hat{\alpha}_{eq} = K_W \tan\alpha_c \cos\phi_i + \frac{2}{AR} K_\phi \tan\alpha_c \sin\alpha_c \sin 2\phi_i + \tan\Delta\alpha_{v(i)}\,. \tag{2.117}$$

It is noted that in the absence of fin-deflection, fin deflection, and upstream vorticity, the above equation gives

$$K_W = \frac{\tan\hat{\alpha}_{eq}\big|_{\phi=\delta=0}}{\tan\alpha_c}\,, \tag{2.118}$$

which is to be used to compute K_W in the equivalent angle-of-attack method. Hemsch [46] notes that a number of methods for determining $\Delta\alpha_v$ may be employed, with the most common being to use strip-theory approximate the equivalent angle-of-attack due to vorticity. That is to say, $\Delta\alpha_{v(i)} \approx \bar{\alpha}_{v(i)}$, where

$$\bar{\alpha}_{v(i)} = \frac{1}{S_F}\int_a^{s_m} \alpha_{v(i)}(r,\phi)\, c(r,\phi)\,\mathrm{d}r\,, \tag{2.119}$$

where c is the chord at station (r,ϕ), S_F is the planform area of fin i, a is the radius of the body, s_m is the radial position of the fin-tip, and $\alpha_{v(i)}$ is the local downwash on the fin. The method was extended [120] to account for variations in the local flowfield, as caused by strong vorticity or an entropy gradient. This was achieved by averaging the variation in the local dynamic pressure and Mach number over the exposed span of the fin. The average dynamic pressure $\bar{q}$ was used to scale the normal-force coefficient obtained from the wing-alone loading-curve for the average Mach number $\bar{M}$:

$$\bar{q} = \frac{1}{s_m - a}\int_a^{s_m} q(r,\phi)\,\mathrm{d}r\,, \tag{2.120}$$

$$\bar{M} = \frac{1}{s_m - a}\int_a^{s_m} M(r,\phi)\,\mathrm{d}r\,, \tag{2.121}$$

$$C_{N_{F(B)}} = \frac{\bar{q}(\phi)}{q_\infty} c_{N_W}\left(\alpha_{eq}, \bar{M}(\phi)\right). \tag{2.122}$$

The relative successes and shortcomings of this method were highlighted in Fig. 2.46b and discussed in Section 2.1.3. In particular, it was noted that good correlation was achieved by the method, although it was unable to account for fin-vortex interactions with the body vortices. The equivalent angle-of-attack method remains widely used as an engineering-level method, and has been implemented in Missile DATCOM [5] and the APC [6] prediction codes.

2.3 Summary

The methods outlined in Sections 2.2.2 to 2.2.4 are representative of the spectrum of methods available for slender body aeroprediction. A high-level summary and comparison of the methods is given in Tables 2.3 and 2.4. The purpose of this summary is to highlight the niche which is filled by reduced-order perturbation modelling methods. The methods in Table 2.3 are listed in a descending order of fidelity. This is accompanied by a decrease in the relative computational cost of obtaining a time history of loading. The progression of cost reduction is not monotonic. It is seen that reduced-order perturbation modelling methods are less expensive than full-potential solvers, despite having higher fidelity. In fact, in certain cases the accuracy of loading prediction by CFD-based LPT has been within 5% of values obtained by full unsteady Euler solutions [14]. This underscores the chief merit of reduced-order perturbation modelling methods: they offer significant cost-reduction while maintaining accurate prediction.

In the case of CFD-based LPT, this accuracy has only been demonstrated for relatively simple geometries without aerodynamically interfering components. This hints at the limitations of LPT. It is seen to stand out in Table 2.3 as the only method in which perturbations are modelled as local, as opposed to influencing the surrounding flowfield. Since the propagation of perturbations is not modelled, they do not persist in time, and the method is effectively quasi-steady. Only the perturbation pressure at the surface (which is related to the perturbation downwash Mach number) is computed. Other fluid properties are not modelled directly. While these approximations are the source of LPT's significant cost reduction, they may be expected to limit the applicability of the method in interference flows. The importance of interference in slender body aerodynamics has been highlighted in Section 2.1.3.

The quasi-steady and local-perturbation limitations of CFD-based LPT may be addressed by modelling perturbations to the mean-steady CFD solution as linear potential flows. This was implemented in the ZAERO suite of software, with panel methods used to model the unsteady perturbations around a mean-steady solution [79]. An additional advantage offered by linear potential perturbations is their applicability in subsonic flows. This is in contrast

to the supersonic domain of LPT. The implementation in [79] was developed as a dynamic linearization of the TSD equations. It may be expected that the method could similarly be extended to higher-order formulations.

The limits dynamic linearization places on the magnitude of unsteady perturbations may be circumvented through a higher-order formulation. Sychev's [4] method and hypersonic SDT [27, 77, 78] allow for accurate modelling of interference and the propagation of perturbations under conditions in which linear potential flows break down. However, this step in modelling fidelity is accompanied by a significant increase in the relative computational cost of obtaining loading histories. This increased cost obstructs the application of the methods in early stages of the design cycle.

On the other hand, the engineering-level methods of Table 2.4 are constrained to preliminary design due to their lower fidelity. With the exception of some methods, such as slender body theory and linear potential flows, engineering-level methods offer little insight into the flowfield structure and physics. The methods are also largely quasi-steady or steady in nature. Semi-empirical methods in particular are limited in modelling perturbations caused by deforming geometry. This has places obvious limitations on the use of these methods in aeroelastic analysis.

In this sense, CFD-based LPT truly is an intermediate-level method. It marries the low computational cost of approximate engineering-level methods with the fidelity of advanced-level methods. In the progression from engineering-level to higher-fidelity methods, it offers the greatest increase in fidelity at the lowest cost increment amongst comparable intermediate-level methods. The affordability it offers allows for high-fidelity aeroelastic analysis earlier in the design cycle.

With the context of piston theory as a valuable reduced-cost aeroprediction method thus established, the attention will be turned to the literature available on the method.

Table 2.3 Summary of intermediate- and advanced-level aeroprediction methods.

Method	Viscous?	Rotation?	Shock capture?	Steady?	Influence?	Predicted quantities	Discret. required	Comp. cost[1]	Mach range	Separation modelled?
Navier-Stokes	Yes	Yes	Yes	No	3D	All	3D field	High	All	Yes
Euler with BL interaction	Yes	Yes	Yes	No	3D	All	3D field	High	All	Yes
Euler	No	Yes	Yes	No	3D	All	3D field	High	All	No
Hypersonic SDT	No	Yes	Yes	No	3D	All	2D field	High	Hypersonic, $\alpha \ll 1$	No
Sychev's method	No	Yes	Yes	No	3D	All	2D field	High	Hypersonic, $M \sin\alpha > 1$	No
CFD-based linear potential perturbations	No[2]	No	No	No	3D	All	3D field / surface	Low / moderate	Subsonic, supersonic	No
CFD-based LPT	No[2]	Yes	No	Quasi	Local	p, M	3D field / surface	Low / moderate	Supersonic, hypersonic	No
Full potential equation	No	No	Yes[3]	No	3D	All	3D field	Moderate	Subsonic, transonic, supersonic	No
Transonic SDT	No	No	Yes[3]	No	3D	All	3D field	Moderate	Transonic	No
Distrib. vort. modelling	No	No	No	Yes	3D	All	Surface	Moderate	Subsonic, supersonic	Yes

[1] Relative cost of computing a time-history of loading.
[2] Perturbations are inviscid.
[3] Energy not conserved.

Table 2.4 Summary of engineering-level aeroprediction methods.

Method	Viscous?	Rotation?	Shock capture?	Steady?	Influence?	Predicted quantities	Discret. required	Comp. cost	Mach range	Separation modelled?
Concentrated vorticity modelling	No	No	No	Yes	3D	All	Axial[2]	Low / moderate	Subsonic, supersonic	Yes
Slender body theory	No	No	No	Quasi	3D	All	Axial[3]	Low	Subsonic, supersonic	No
Linear potential flow panels	No	No	No	No	3D	All	Surface	Low / moderate	Subsonic, supersonic	No
Newtonian theory	No	No	No	Quasi	Local	p	Surface	Low	Hypersonic	No
Classical piston theory	No	No	No	Quasi	Local	p, M	Surface	Low	Supersonic, hypersonic	No
Van Dyke's $\mathcal{O}(\delta^3)$ theory	No	No	No	Quasi	Local	p, M	Surface	Low	Supersonic, hypersonic	No
FOSET	No	Yes	No	Quasi	Local	All	Surface	Low	Supersonic, hypersonic	No
Donov's theory	No	Yes	No	Quasi	Local	p, M	Surface	Low	Supersonic, hypersonic	No
Viscous cross-flow analogy	Yes[1]	Yes[1]	No	Quasi	Locally 2D	Forces	Axial[3]	Low	Transonic	Yes[1]
Equivalent AoA method	Yes[1]	Yes[1]	No	Yes	3D	Forces	Axial[2]	Low	Subsonic, supersonic	Yes[1]

[1] Only as an increment to the integrated forces.
[2] Cross-section distribution and vortex core.
[3] Cross-section distribution.

Chapter 3

Review of Piston Theory

The content of this chapter draws extensively from previous publications of the author [59, 87, 116, 121–123], which have been reproduced and adapted here with permission from the respective copyright holders. Section 3.1 will introduce a generalized formulation for piston theory applicable to airfoils, and includes material from [59, 121]. The conceptual basis and generalized equations are introduced, and a discussion on the validity and accuracy of piston theory is given. Section 3.2 will detail significant milestones in the development of piston theory, and also draws from [59, 121]. The review leads to a discussion on the theoretical validity bounds of the linear potential flow basis for piston theory. This is addressed in [116, 121], but has not been included in the present work for the sake of brevity. Section 3.3 will discuss the significance of higher-order terms in piston theory, and includes material from [122, 123]. Finally, a summary of the material presented on piston theory is given in Section 3.4.

3.1 Introduction

The term "piston theory" has primarily been used to describe a pressure-downwash relationship of a particular form. A variety of methods yield a similar local relationship. As a result, the same term "piston theory" has been applied to methods with differing underlying assumptions. These methods will be introduced in Section 3.2 as historical developments to piston theory. The similarity of the methods will be highlighted by interpreting them in terms of a generalized formulation for piston theory developed by the author [59] and presented here in Section 3.1. The generalized formulation was largely inspired by earlier work on piston theory by Rodden et al [124] and Liu et al [125].

3.1.1 Conceptual Representation

The conceptual basis of piston theory lies in the unsteady analogy, previously introduced in Section 2.2.3. The unsteady analogy, also referred to as the law of plane sections [77], has its roots in Hayes' hypersonic similitude for slender bodies [75]. A graphical representation of the concept is given in Fig. 3.1. Consider a slender body moving at a constant velocity of V_∞ relative to a stationary reference frame. Suppose a laser-sheet is set up in the reference frame in a plane normal to the body velocity. As the body passes through the sheet, it traces its cross-sectional shape in the plane of the sheet. Spatial variation in the body cross-section is perceived as a time-dependent deformation and motion of the cross-section in the plane of the sheet. This is time-dependent velocity of the cross-section is denoted $w(t)$ in Fig. 3.1.

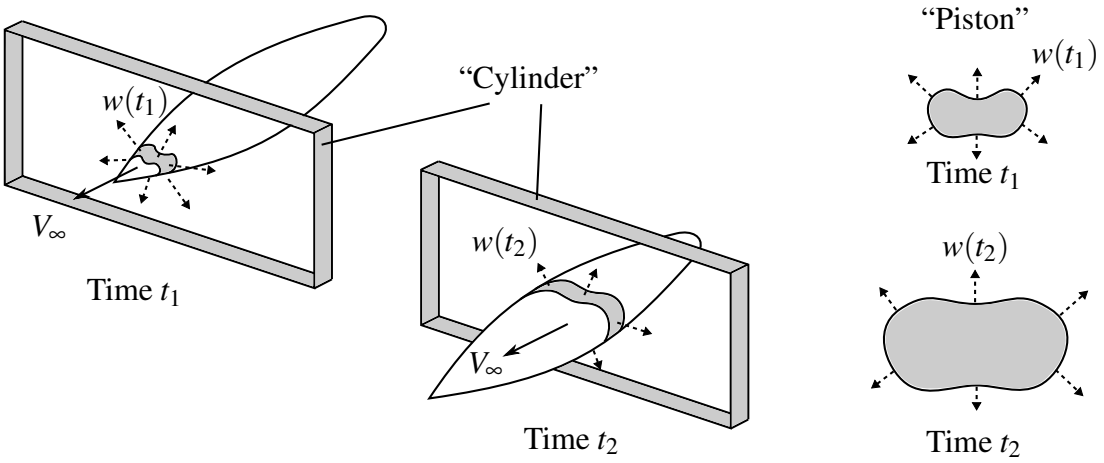

Fig. 3.1 Visual representation of the unsteady analogy and the arising piston / cylinder terminology.

The extension of this physical analogy to fluid flow gives rise to terminology employed in piston theory. In place of the laser sheet, a "fluid slab" (Lighthill [88]) or "plane section" (Il'yushin [77]) of fluid is considered. The motion of the cross-sectional shape is interpreted as a two-dimensional "piston" expanding and contracting in the "cylinder" that is the plane section of fluid.

The thought experiment up to this point captures the essence of the physical intepretation behind the small-parameter approximation methods introduced in Section 2.2.3. In both Sychev's [4] method and hypersonic SDT [27, 77, 78], a three-dimensional fluid flow is reduced to flow in the two-dimensional advected plane. The differences in interpretation are associated with the alignment of the plane. Classically, hypersonic SDT has considered the plane to be advected in the direction of the mean body velocity. Sychev's method considers the plane to be advected down the longest axis of the body.

The above two methods are inherently formulated as two-dimensional field-type problems. This is in contrast to piston theory, which has a local, algebraic formulation. Early developments of piston theory, as due to Lighthill [88], considered flow about a two-dimensional body which was reduced to a one-dimensional piston problem through the unsteady analogy. While this is conceptually equivalent to the interpretation for three-dimensional bodies, the mathematical formulation is different. The distinction between the definitions of the "fluid slab" is depicted in Fig. 3.2. It should be noted that hypersonic SDT and Sychev's method have advection definitions similar to that depicted for slender body theory in Fig. 3.2.

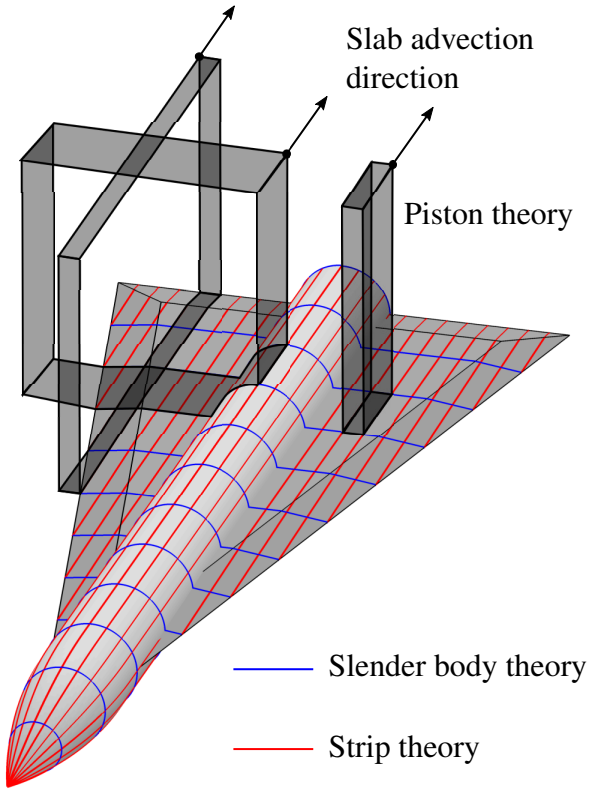

Fig. 3.2 Distinction between fluid slab definition in piston theory, strip theory, and slender-body-type theories. Advection direction is denoted by arrows.

The discussion thus far has been based in a stationary frame with an initially undisturbed plane section of fluid. This is the basis of classical piston theory. Perturbations to the fluid are produced due to the physical shape and motion of the body, and hence the physical interpretation is intuitive. The essence of local piston theory is in modelling perturbations relative to the mean steady flow. Physical interpretation by means of visualization follows less directly in this case. If the mean steady flow is considered, the variation in body shape must cause no effective piston motion. This may be realised through aligning the cylinder

normal to the local body surface at each axial station. Effectively, the inclination of the cylinder changes as the cylinder is advected down the length of the body.

An alternative visualization, which was used in developing the generalized formulation of [59], is achieved by changing from a stationary reference frame to one moving at the mean body velocity V_∞. This is essentially a change from an earth-fixed frame with a moving body (which will also be referred to as the Galilean frame) to a wind-tunnel frame (which will be referred to as the Eulerian frame). Rather than having the body pass through a single slab of fluid initially at rest, separate instantaneous fluid slabs are locally advected at each axial position in the wind-tunnel frame.

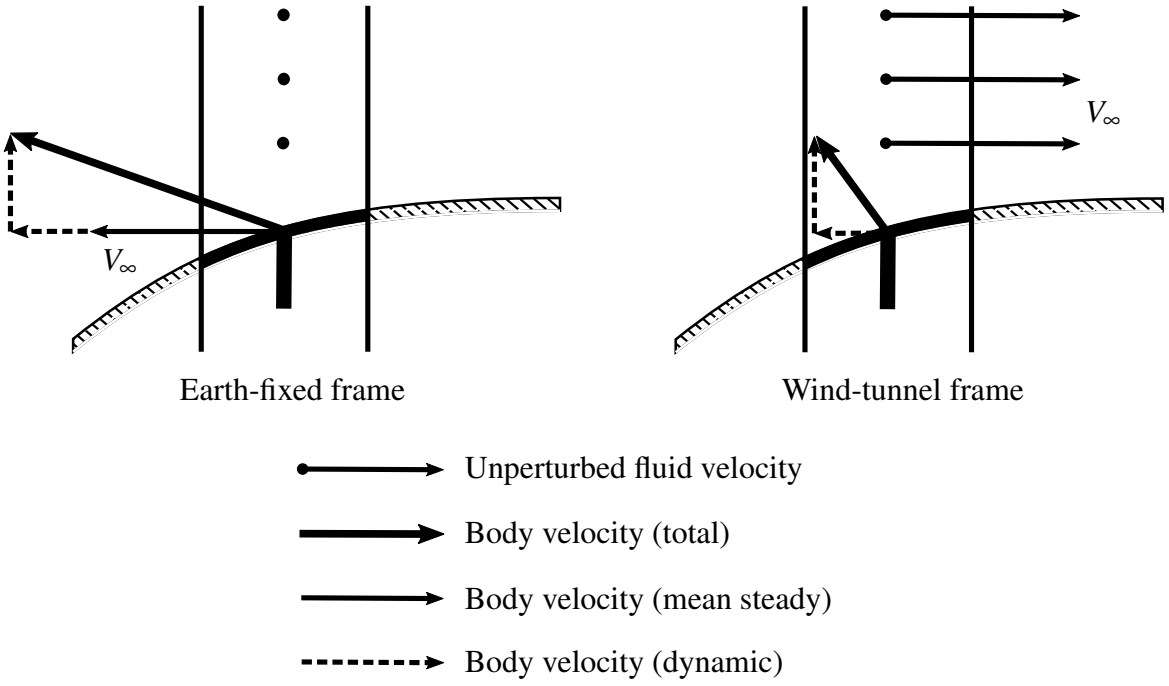

Fig. 3.3 Distinction between the earth-fixed frame and wind-fixed frame visualizations in classical piston theory.

Using the Eulerian frame, the cylinder orientation remains constant (aligned normal to V_∞) at each station in CPT. On the other hand, LPT requires that the cylinder be oriented normal to the local mean-steady body surface. With the conceptual basis of piston theory thus established and the Eulerian visualization defined, the generalized formulation of piston theory for arbitrary cylinder orientation may be introduced.

3.1.2 Generalized Downwash Equation

In the context of the piston-cylinder analogy, downwash will be defined as the relative velocity of the piston face in the direction of the cylinder orientation. The wind-tunnel frame will be used in formulating the generalized downwash equation. This requires the relative motion of the cylinder (as it is advected) to be correctly accounted for. The nomenclature used is defined in Fig. 3.4. Suppose that the body is mounted in a wind-tunnel operating at the equivalent mean-steady velocity of the body. The body is attached to a mount which allows for dynamic motion $\mathbf{V_b}$ of the body. At any instant in time, let the unit normal vector to the body surface at a point of interest be denoted $\hat{\mathbf{n}}$. Let the unit vector normal to the mean steady surface at the same point be denoted $\hat{\mathbf{n}}_\mathbf{m}$. These quantities are independent of the cylinder definition.

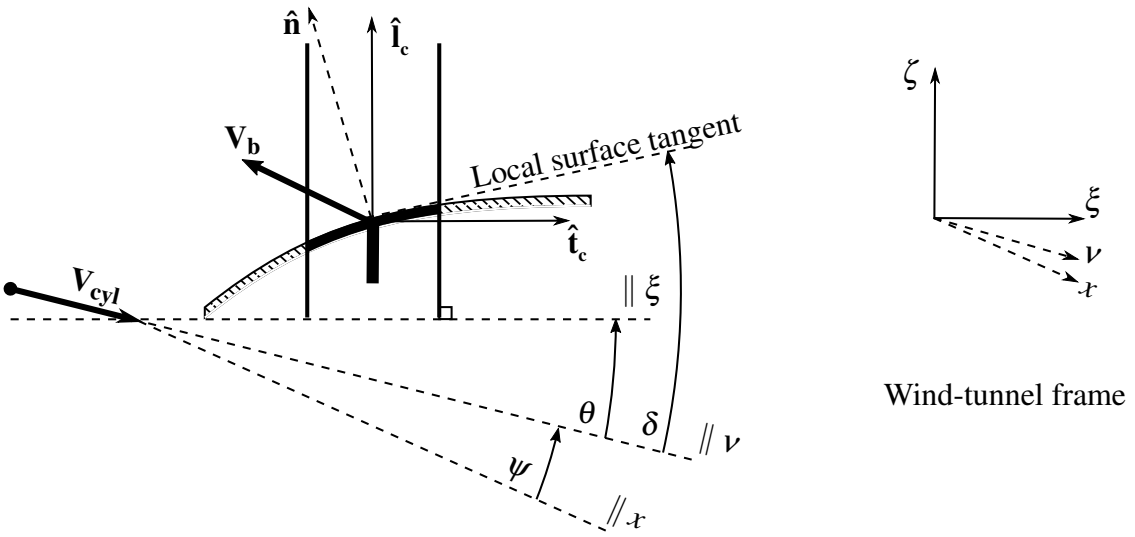

$\mathbf{V_{cyl}}$: Velocity of cylinder advection
$\mathbf{V_b}$: Body velocity (dynamic)
ξ: Cylinder transverse axis
ζ: Cylinder longitudinal axis
ν: Direction of cylinder advection
x: Body axis
$\hat{\mathbf{n}}$: Surface normal after deformation
$\hat{\mathbf{l}}_\mathbf{c}$: Cylinder-longitudinal unit vector
$\hat{\mathbf{t}}_\mathbf{c}$: Cylinder-transverse unit vector
ψ: Advection angle relative to body axis
θ: Cylinder orientation relative to advection
δ: Surface inclination relative to advection

Fig. 3.4 Nomenclature associated with the generalized formulation of piston theory.

Let the cylinder (representing a slab of fluid) be advected at a velocity $\mathbf{V_{cyl}}$ in a direction inclined an angle ψ as measured from the body axis. Suppose that the slab of fluid is not in fact oriented normal its the direction of advection. The angle by which the fluid slab deviates

from being normal to the advection direction is denoted θ, and is termed the "cylinder orientation". The inclination of the instantaneous local surface tangent to the direction of cylinder advection is denoted δ.

The downwash equation is derived here for an arbitrary cylinder orientation θ and advection direction ψ. The cylinder-bound coordinates ξ and ζ, with associated direction vectors $\hat{\mathbf{t}}_\mathbf{c}$ and $\hat{\mathbf{l}}_\mathbf{c}$ will be used. Let the surface of the body be described by $\zeta = \zeta_b(\xi)$. The downwash is then defined by

$$w \equiv \frac{\mathrm{d}\zeta_b}{\mathrm{d}t} = \left(\mathbf{V_b} - \mathbf{V_{cyl}}\right) \cdot \hat{\mathbf{l}}_\mathbf{c} - \left(\mathbf{V_b} - \mathbf{V_{cyl}}\right) \cdot \hat{\mathbf{t}}_\mathbf{c} \tan\left(\delta - \theta\right), \tag{3.1}$$

$$= V_{cyl} \frac{\sin\delta}{\cos\left(\delta - \theta\right)} + \left(\mathbf{V_b} \cdot \hat{\mathbf{l}}_\mathbf{c}\right) - \left(\mathbf{V_b} \cdot \hat{\mathbf{t}}_\mathbf{c}\right) \tan\left(\delta - \theta\right), \tag{3.2}$$

where $V_{cyl}^2 = \mathbf{V_{cyl}} \cdot \mathbf{V_{cyl}}$, the velocity of the piston face relative to a stationary cylinder is given by $\left(\mathbf{V_b} - \mathbf{V_{cyl}}\right)$, and $(\delta - \theta)$ is the deviation of the local surface tangent from being normal to the cylinder. Following the approach in [59], the downwash may be split into two components as

$$w_c \equiv \left(\mathbf{V_b} - \mathbf{V_{cyl}}\right) \cdot \hat{\mathbf{l}}_\mathbf{c}, \tag{3.3}$$

$$w_a \equiv -\left(\mathbf{V_b} - \mathbf{V_{cyl}}\right) \cdot \hat{\mathbf{t}}_\mathbf{c} \tan\left(\delta - \theta\right), \tag{3.4}$$

where w_c is the component due to advection down the length of the cylinder, and w_a is the downwash component arising from cylinder-normal advection. Alternatively, the approach of [122] may be adopted, splitting the downwash into a fluid-velocity term w_f and a body-velocity term w_b as

$$w_f \equiv -\mathbf{V_{cyl}} \cdot \left[\hat{\mathbf{l}}_\mathbf{c} - \hat{\mathbf{t}}_\mathbf{c} \tan\left(\delta - \theta\right)\right], \tag{3.5}$$

$$w_b \equiv \mathbf{V_b} \cdot \left[\hat{\mathbf{l}}_\mathbf{c} - \hat{\mathbf{t}}_\mathbf{c} \tan\left(\delta - \theta\right)\right]. \tag{3.6}$$

For completeness, it is noted here that the following relationship may be shown:

$$\left[\hat{\mathbf{l}}_\mathbf{c} - \hat{\mathbf{t}}_\mathbf{c} \tan\left(\delta - \theta\right)\right] = \frac{\hat{\mathbf{n}}}{\cos\left(\delta - \theta\right)}. \tag{3.7}$$

The use of the nomenclature $\mathbf{V_{cyl}}$ and the term "velocity of cylinder advection" is deliberate. The definition of downwash in piston theory arises purely due to relative motion of the piston down the length of the cylinder. It is directly related to the motion of cylinder frame, rather than to the fluid velocity. As a result, the cylinder-longitudinal component of the actual local fluid velocity will generally differ from the piston-theory-defined downwash. Similarly, the

component of the actual fluid velocity in the cylinder-normal direction will not necessarily be equal to the component of the frame (cylinder) velocity in that direction.

3.1.3 Generalized Pressure Equation

The use of the term "piston theory" to describe a particular downwash-pressure relationship has been noted earlier. Rodden et al [124] proposed a generalized pressure equation in which different theories were distinguished by the coefficients they contribute to the equation. This approach was extended by the author in [59] to include LPT. As has been noted earlier, the underlying difference between CPT and LPT is in the reference conditions which are being perturbed. These will be referred to as "cylinder conditions", with quantities denoted by a subscript "cyl". The generalized pressure equation put forward in [59] is then written up to third-order in downwash Mach number as

$$\frac{p}{p_{cyl}} = 1 + \gamma \left[c_1 \left(\frac{w}{a_{cyl}} \right) + c_2 \left(\frac{w}{a_{cyl}} \right)^2 + c_3 \left(\frac{w}{a_{cyl}} \right)^3 \right], \tag{3.8}$$

where γ is the ratio of specific heats, and the coefficients c_i are defined by the method yielding the pressure relation. It is common to see the equation cast in terms of the pressure coefficient C_p. For the generalized formulation, this is written as

$$C_p = C_{p_{cyl}} + \left(\frac{p_{cyl} M_{cyl}^2}{p_\infty M_\infty^2} \right) \frac{2}{M_{cyl}^2} \left[c_1 \left(\frac{w}{a_{cyl}} \right) + c_2 \left(\frac{w}{a_{cyl}} \right)^2 + c_3 \left(\frac{w}{a_{cyl}} \right)^3 \right], \tag{3.9}$$

where $M_{cyl} = V_{cyl}/a_{cyl}$ is the Mach number of the cylinder frame-advection referenced to the local fluid conditions in the cylinder, and $C_{p_{cyl}}$ is the pressure coefficient of the local cylinder conditions, given by

$$C_{p_{cyl}} = \frac{p_{cyl} - p_\infty}{\frac{1}{2} \gamma p_\infty M_\infty^2}. \tag{3.10}$$

The quantity $C_{p_{cyl}}$ is essentially the coefficient of the gauge-pressure of the cylinder conditions relative to freestream conditions.

The distinctive feature of Eq. (3.8) is that it provides an algebraic relationship between the local surface geometry and the fluid pressure at the surface. The downwash relation of Eq. (3.1) is similarly local and algebraic. This offers substantial reduction in computational cost for aerodynamic (and by extension, aeroelastic) analysis. It may be seen from the equations that acceleration and time do not enter into the formulation. The quasi-steady, local nature of piston theory has the disadvantage of neglecting the following features:

- Propagation (and lag) of upstream perturbations,

- Interaction with surrounding flow features,
- Acceleration-induced pressures.

3.1.4 Considerations of Validity Bounds

Piston theory has thus far been presented on a heuristic level, with appeals to analogies and with a number of implicit assumptions. This raises the question of the validity bounds within which these assumptions and analogies hold, and in which piston theory is an effective aeroprediction method. A rigorous treatment of this topic requires a mathematical basis from which piston theory is derived. The work of Il'yushin [77] and Goldsworthy [126] in defining the error in the assumptions will be introduced in Section 3.2. The work of other authors in quantifying validity bounds on the results of piston theory may be found along with a framework for estimating the validity of the linear potential flow basis in [116, 121]. The purpose of the present section is to introduce the considerations of a validity analysis from a physical perspective.

The basic requirements in deriving piston theory from a higher-order flow model are as follows:

- The spatial dimension of the equations describing the flow must be reduced to one,
- The one-dimensional field problem must have an algebraic, surface-local solution.

The physical interpretation of these requirements is essentially that contributions to the local surface pressure must be dominated by the local inclination or motion of the surface. Within the context of the piston-cylinder analogy, the following assumptions are made:

1. The cylinder (plane section) represents a control mass of fluid,
   (a) The cylinder advection velocity represents the fluid velocity prior to perturbations due to piston motion,
   (b) Piston motion causes an in-plane fluid velocity perturbation at the boundary of the control mass,
2. Plane sections of fluid remain plane,
   (a) The fluid velocity normal to the plane section is constant throughout the plane,
   (b) Piston motion causes no out-of-plane fluid velocity perturbations,
3. The flow in one plane section is independent of flow in other plane sections,

   (a) There is no out-of-plane propagation of perturbations,

4. Perturbations produced by the piston at time t do not interfere (interact with or reflect off of) any previous or subsequent perturbations.

Assumptions 1 through 3 above are also applicable to the unsteady analogy as used in hypersonic SDT [27, 77, 78] and Sychev's [4] method. However, these methods omit assumption 4, which is required to obtain a surface-local algebraic solution to the reduced field problem. Assumption 4 essentially addresses the question of in-plane interference, perturbation propagation, and time-history of the flow.

The sources of error in the piston theory are then essentially related directly to the validity of the assumptions listed above. Potential sources of error include:

- Disagreement between the chosen cylinder orientation and the actual direction of minimum flow gradients,
  - An example of this is the improvement obtained by moving from CPT [88] to LPT [14] and to Bird's [127] formulation when considering wedge flow,
- Significant variation in the out-of-plane velocity down the length of the cylinder. This may be due to
  - Strong body curvature (essentially non-slender portions of the body),
  - Strong shock curvature (which results in an entropy wake),
  - A boundary-layer (although this could be limited to a small region close to the surface),
- Out-of-plane velocity perturbations and pressure gradients being comparable to their in-plane counterparts. This occurs when
  - Low supersonic Mach numbers are approached,
  - The component of the surface normal in the streamwise direction increases (larger deflections),
- Non-negligible interference due to geometry or flow features.

An illustration of how the prediction accuracy of LPT varies with Mach number is given in Figs. 3.5 to 3.10. The figures are concerned with the variation of $\frac{\partial C_p}{\partial \alpha}$ and $\frac{\partial^2 C_p}{\partial \alpha^2}$ over the parameter space of M_∞ and α for flow on the compression surface of a flat plate. The values $\frac{\partial C_p}{\partial \alpha}$ and $\frac{\partial^2 C_p}{\partial \alpha^2}$ represent the linear and quadratic aerodynamic stiffness, respectively. The

exact values are obtained from the oblique shock equations, and are shown in Figs. 3.5 and 3.6. A sharp increase in in the gradient is noted for both the linear and quadratic stiffness terms as shock detachment is approached. The values obtained using LPT are shown in Figs. 3.7 and 3.8. Distinct differences in the topology of the parameter space between the exact solution and LPT prediction are noted. In particular, LPT predicts much more mild gradients in the limit of shock detachment. It also fails to reproduce the more complex topology of $\frac{\partial^2 C_p}{\partial \alpha^2}$ observed at $M_\infty > 3$. The relative error in LPT prediction is shown in Figs. 3.9 and 3.10. It is noted that the linear stiffness may be predicted within 10% over a wide range of the parameter space. In contrast, the quadratic stiffness prediction is accurate only within a small band where the oblique shock is weak. Both stiffness terms are in gross error in the limit of $M_\infty < 2$ and as shock detachment is approached.

The reasons for these inaccuracies may be understood within the context of the assumptions listed above. As the shock detachment angle is approached, the local Mach number at the surface of the flat plate decreases into the low supersonic range, eventually becoming subsonic. The variation of local Mach number has been superimposed over the relative error in linear stiffness prediction in Fig. 3.11. The correlation is clear. The assumption that out-of-plane perturbations are negligible relative to in-plane perturbations becomes increasingly accurate outside of hypersonic flows. It is therefore not surprising that as the local Mach number approaches $M_{cyl} \approx 1.7$, the prediction error from LPT is in the range of $10\% \sim 20\%$. Similarly, Figs. 3.12 and 3.13 show the relative error in linear stiffness with the angle between the shock and the surface and its gradient, respectively. The hypersonic assumptions in the unsteady analogy imply the assumption that the shock lies close to the body. As the shock detachment angle is approached and the local Mach number is lowered, the angle between the body and the shock increases. This correlates with the degradation in LPT accuracy, as seen in Fig. 3.12. The role of the gradient $\frac{\partial(\beta-\alpha)}{\partial \alpha}$, where β is the shock angle and $(\beta - \alpha)$ is the angle between the body and the shock, may be understood as follows. The fluid conditions at the shock are determined by the Rankine-Hugoniot equations, in which β is a key parameter. The surface boundary-condition is essentially driven by α through the non-penetration condition. If the change in the relative angle between the body and the shock for a given perturbation to α is small, the change in the cylinder approximation is minimal, and the pressure perturbation is dominated by the surface boundary condition. The correlation of accurate LPT predictions in the lower-α band with small $\frac{\partial(\beta-\alpha)}{\partial \alpha}$ is shown in Fig. 3.13.

The illustration of LPT inaccuracies for a flat plate is informative, but gives no insight into the role of body or shock curvature on LPT accuracy. A treatment of their roles is not within the scope of the present section.

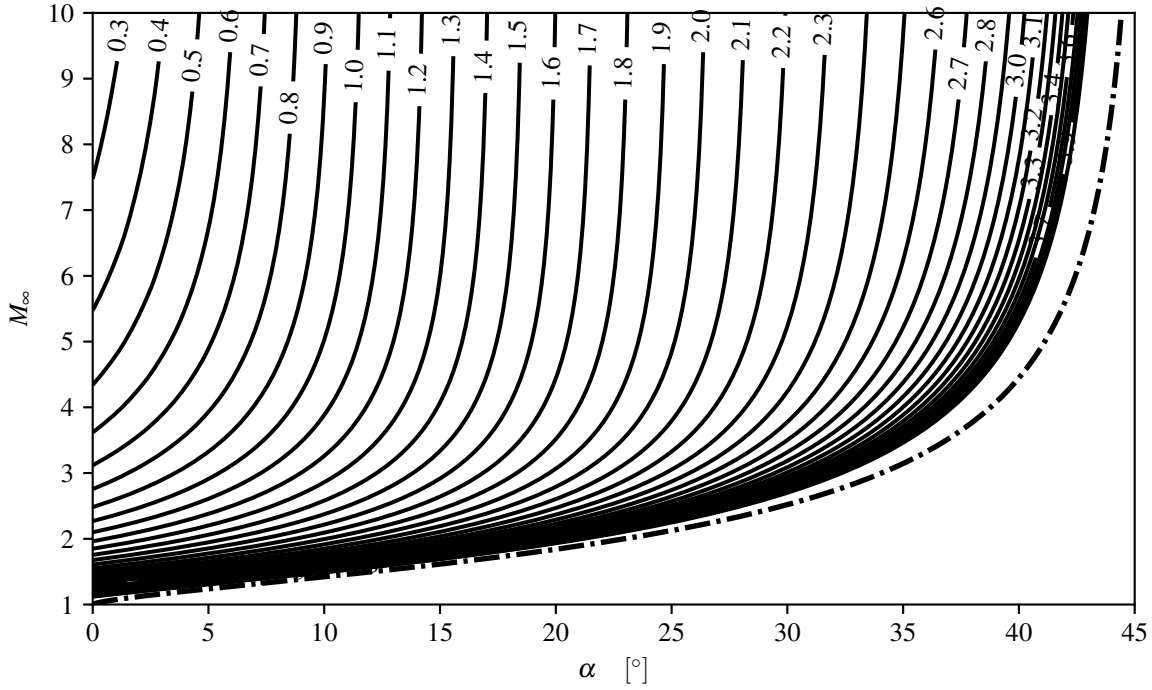

Fig. 3.5 Exact value of $\partial C_p/\partial\alpha$ for the compression surface. Contours of [rad^{-1}].

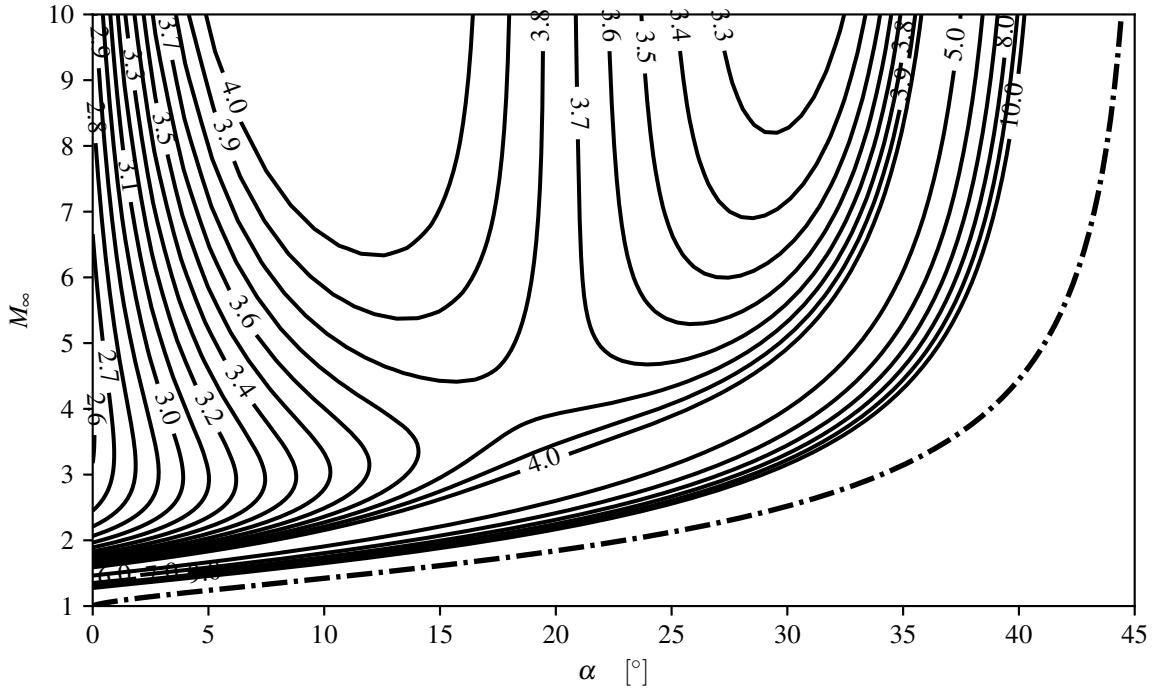

Fig. 3.6 Exact value of $\partial^2 C_p/\partial\alpha^2$ for the compression surface. Contours of [rad^{-2}].

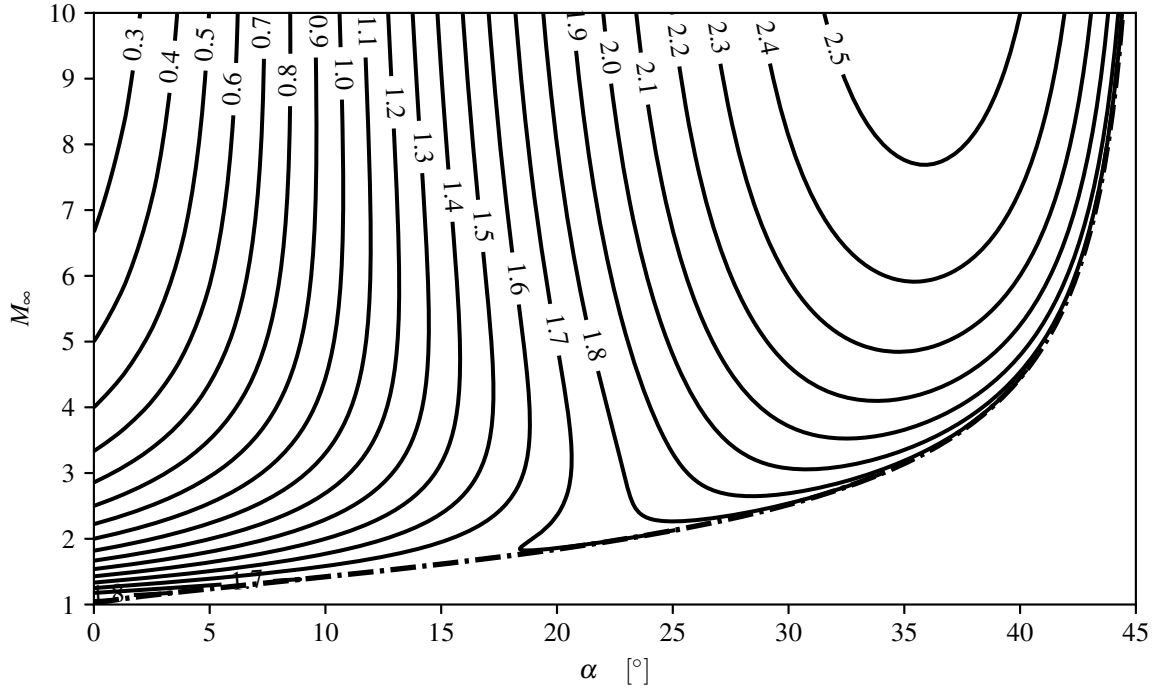

Fig. 3.7 LPT prediction of $\partial C_p/\partial\alpha$ for the compression surface. Contours of [rad^{-1}].

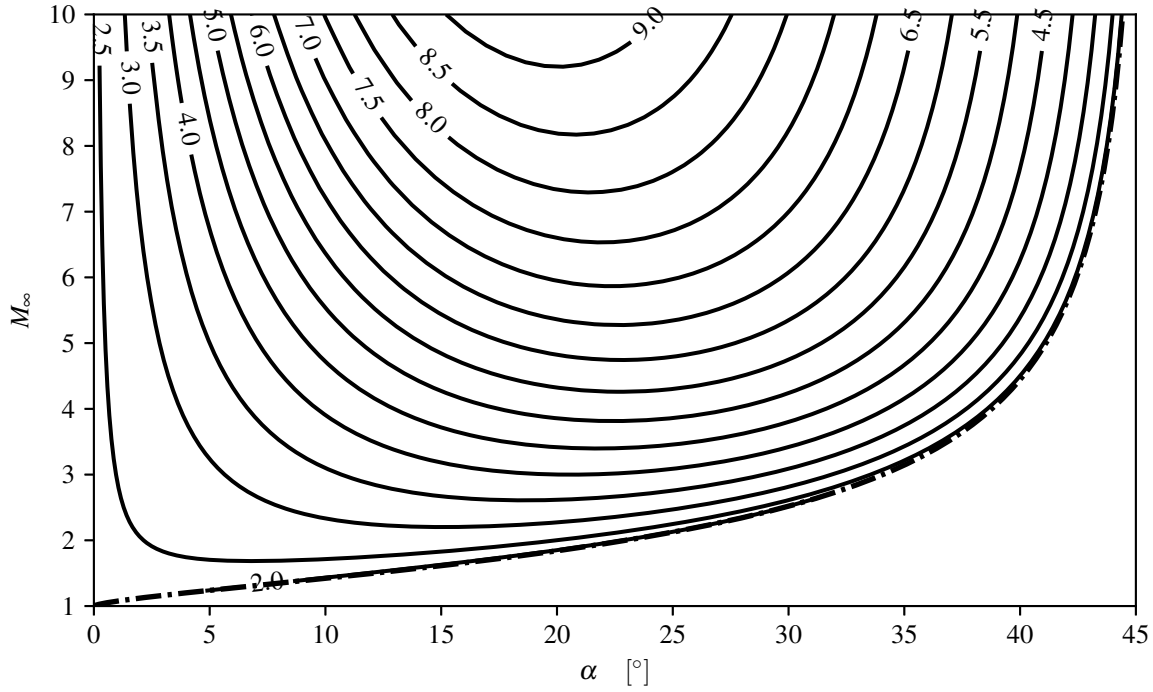

Fig. 3.8 LPT prediction of $\partial^2 C_p/\partial\alpha^2$ for the compression surface. Contours of [rad^{-2}].

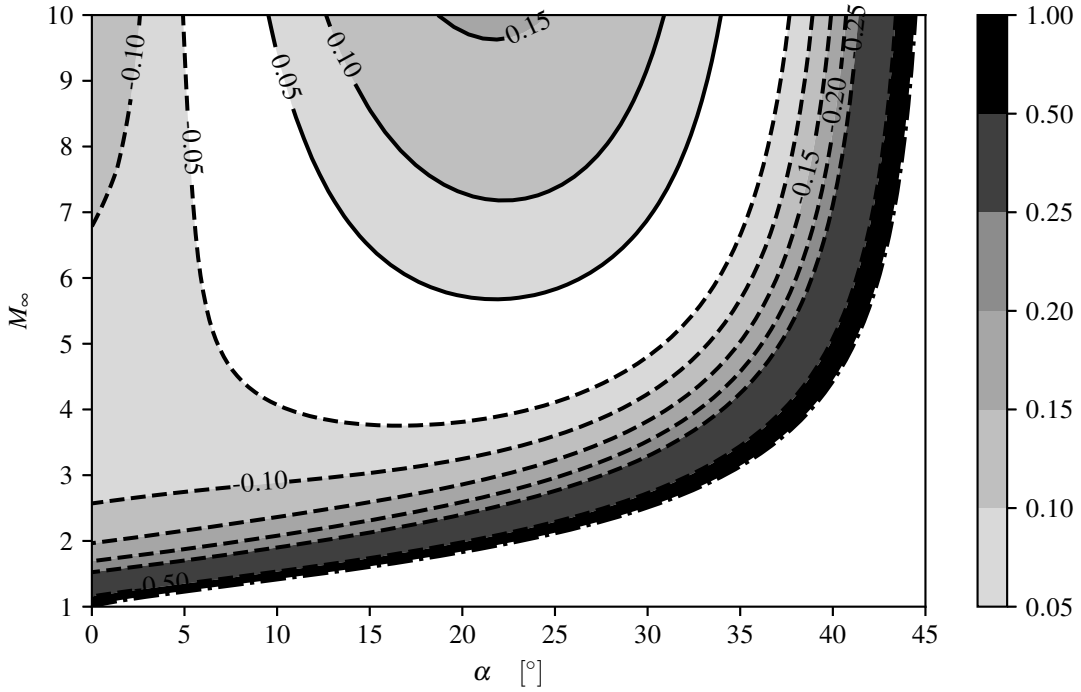

Fig. 3.9 Relative error in LPT prediction of $\partial C_p/\partial\alpha$ for the compression surface.

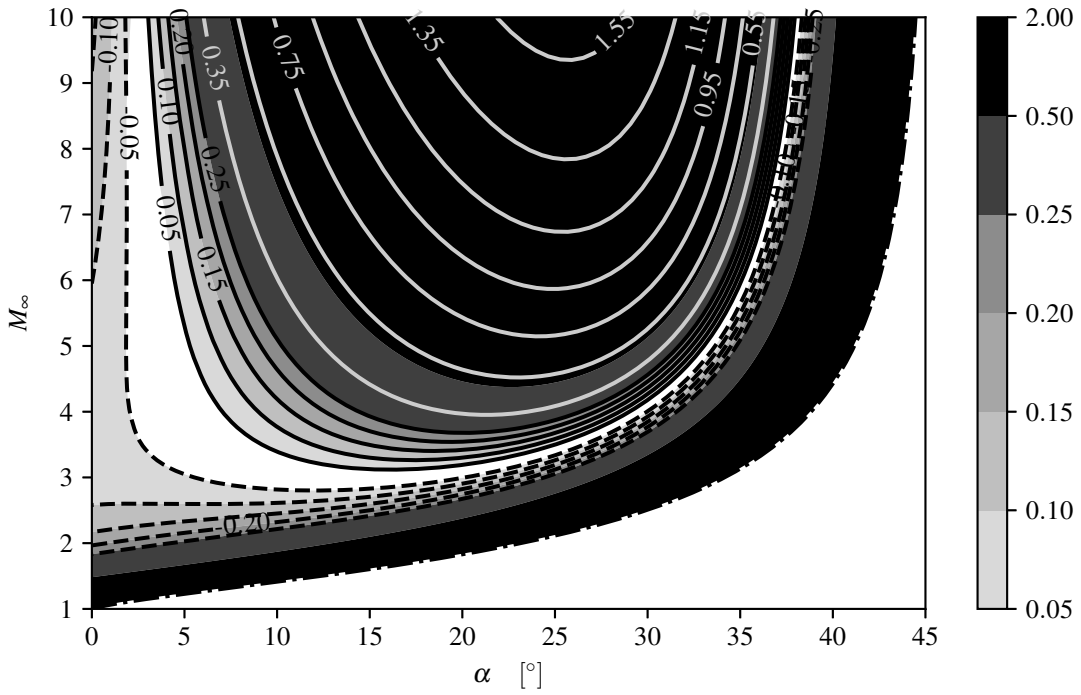

Fig. 3.10 Relative error in LPT prediction of $\partial^2 C_p/\partial\alpha^2$ for the compression surface.

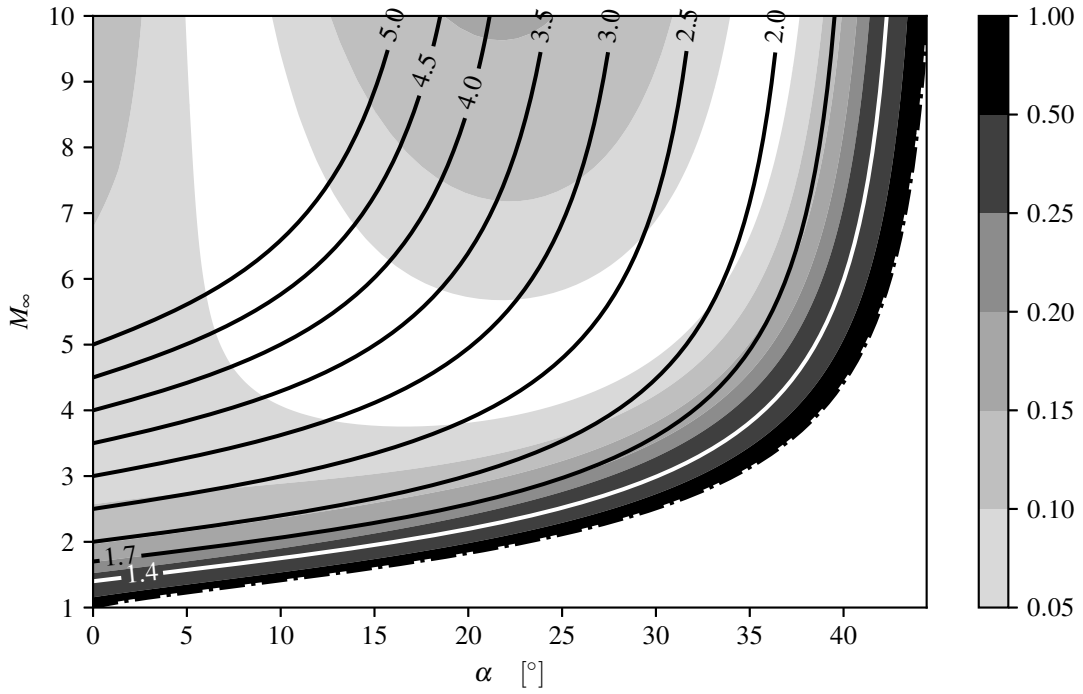

Fig. 3.11 Correlation of error in LPT prediction of $\partial C_p/\partial\alpha$ (filled contours) with the local Mach number M_{cyl} (contour lines) on the compression surface.

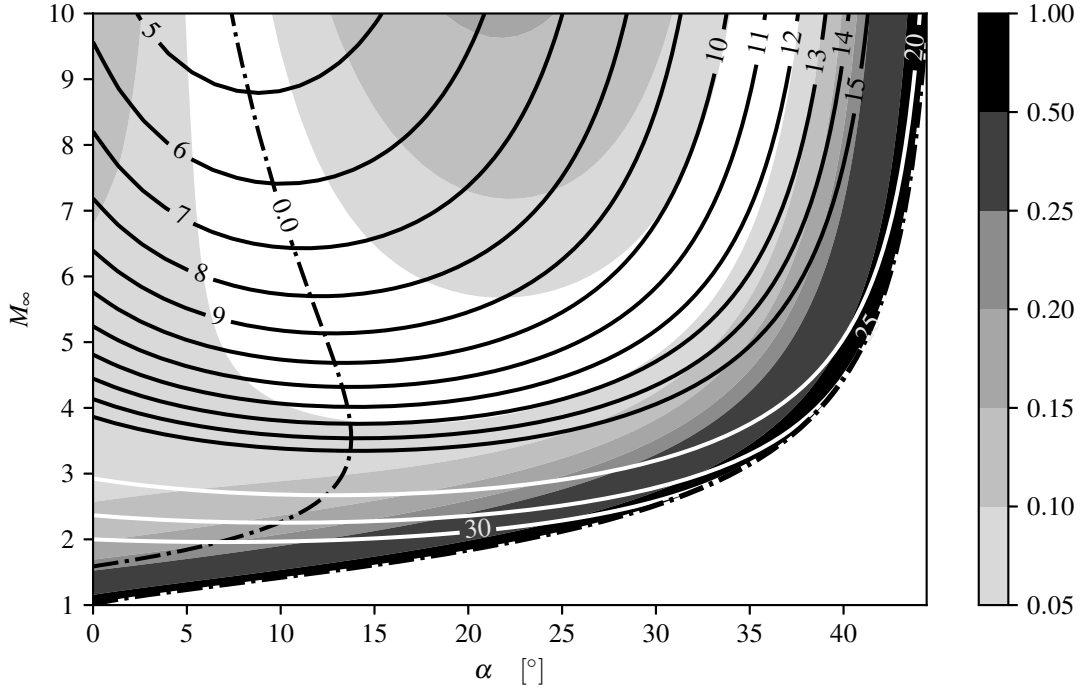

Fig. 3.12 Correlation of error in LPT prediction of $\partial C_p/\partial\alpha$ (filled contours) with the relative angle between the shock and the compression surface $\beta - \alpha$ (contour lines of [°]).

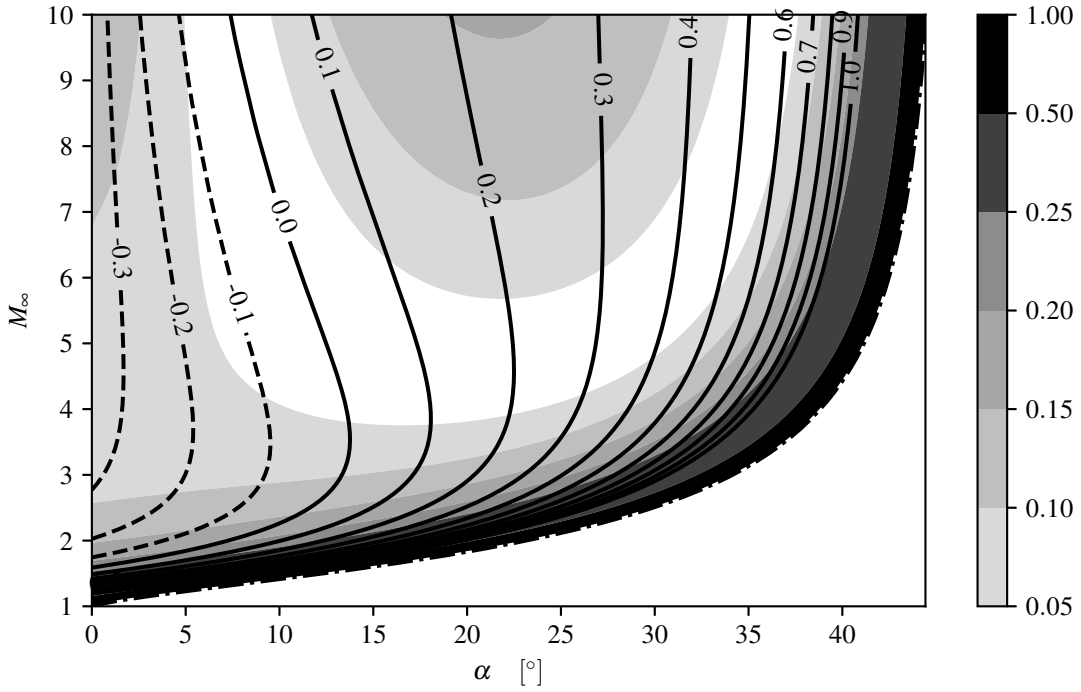

Fig. 3.13 Correlation of error in LPT prediction of $\partial C_p/\partial\alpha$ (filled contours) with the rate of change in the surface-relative shock angle with incidence $\partial(\beta-\alpha)/\partial\alpha$ (contour lines).

3.2 Historical Developments

Piston theory has a long history that is marked by independent developments, varied theoretical bases, and extensions to the basic method. The significant works in the literature on piston theory are summarized here. The generalized formulation of [59] introduced in Section 3.1 will be used to draw attention to differences in their approaches. These works will not be introduced in chronological order. Instead, they will be introduced in the context of their contribution to piston theory. This will cover

- CPT as a heuristic method in planar flows,
- The introduction of a generalized formulation for the pressure equation, thereby including other methods under the label of "piston theory",
- The extension of CPT to supersonic piston downwash,
- The derivation of CPT from three-dimensional flow equations,
- The extension of CPT to include upstream influence and unsteadiness,
- The extension of piston theory to non-planar flows,
- The introduction of LPT as a heuristic method and early applications,
- The recognition of LPT as a special case in hypersonic SDT for flow over a wedge,
- The application of LPT as a perturbation to solutions obtained by CFD.

This will effectively summarize the current body of knowledge related to piston theory.

3.2.1 CPT as a Heuristic Method in Planar Flows

Early publications associated with the establishment of "piston theory" include the seminal works of Lighthill [88] and of Ashley and Zartarian [103]. These are among the most widely-cited works in the literature on piston theory. Piston theory is introduced in these works on the basis of a physical analogy. It is presented as a heuristic method, with greater focus placed on application of the method to practical problems. This trades off a deeper understanding of the limitations of the method and of its origin. In the review of piston theory by Ashley and Zartarian [103], the method is applied to a range of problems, including three-dimensional geometries. No serious consideration is made of the error in applying the method outside its theoretical validity. The heuristic approach to piston theory set forth

in these papers has persisted in the majority of widely-cited works on the method, and has influenced the development and application of LPT. This section will give a brief overview of CPT and its introduction in the literature as a heuristic method for planar flows.

The pressure-downwash relation which is at the core of CPT was introduced by Lighthill [88]. In the context of generalized piston theory, with reference to Fig. 3.4 and Eqs. (3.2) and (3.8), the formulation is characterized by the following definitions:

$$c_1 = 1\,, \tag{3.11}$$

$$c_2 = \frac{\gamma+1}{4}\,, \tag{3.12}$$

$$c_3 = \frac{\gamma+1}{12}\,, \tag{3.13}$$

$$\theta = 0^\circ\,, \tag{3.14}$$

$$\mathbf{V_{cyl}} = \mathbf{V}_\infty\,, \tag{3.15}$$

$$p_{cyl} = p_\infty\,. \tag{3.16}$$

These definitions are common between the publications of Lighthill [88] and of Ashley and Zartarian [103]. Slight differences in their perspective on the limits within which CPT applies arise due to the greater development of the work that had taken place by the time of publication [103]. A more significant difference is that the original development by Lighthill [88] did not suggest the application of the method to three-dimensional problems. The salient points of these two publications will be introduced before moving on to the work of Bird [127].

Lightill [88] based his development on Hayes' [75] development of the unsteady analogy for hypersonic flows. Lighthill reasoned that for $M_\infty \geq 4$, thin airfoils would produce:

- Streamwise velocity perturbations an order of magnitude smaller than transverse velocity perturbations,

- Streamwise flow gradients an order of magnitude smaller than transverse flow gradients,

thereby setting up conditions for which Hayes' unsteady analogy would be accurate. Lighthill noted that a mathematical treatment of the error in the analogy was developed by Goldsworthy [126], citing that the error is of the order $\mathscr{O}\left(1/M_\infty^2\right)$. While Goldsworthy's [126] development assumed that $M_\infty\delta = \mathscr{O}(1)$, Lighthill enforced the assumption that $M_\infty\delta < 1$. This is an important distinction, as it influenced the subsequent definition of the pressure equation, as well as delayed the extension of CPT to supersonic piston downwash. Accounting for the contribution due to steady effects through δ and due to unsteady oscillations through the

reduced frequency k and the nondimensional amplitude of oscillation A, Lighthill expressed the validity limit of CPT as

$$M_\infty \delta + A M_\infty k < 1\,. \tag{3.17}$$

Lighthill [88] remarked that this provided the advantage of allowing the pressure equation for a one-dimensional simple wave driven by a piston to be employed, given as

$$\frac{p}{p_\infty} = \left(1 + \frac{\gamma - 1}{2}\frac{w}{a_\infty}\right)^{\frac{2\gamma}{\gamma-1}}, \tag{3.18}$$

which holds for isentropic flow down the cylinder. Lighthill [88] argued that the advantage of enforcing the subsonic piston downwash condition was that the surface pressure would then depend only on the instantaneous surface velocity. He noted that if the piston produced an initial shock (as occurs at the leading edge), this would enter into the pressure-downwash relation at downstream axial stations. While noting that this could be accounted for using shock-expansion theory, Lighthill argued that this was unnecessary. This was because the relative accuracy of expanding Eq. (3.18) up to third-order in the downwash Mach number was within 6% of the shock-expansion pressure prediction. Regarding the third-order coefficient in the pressure equation, Lightill reasoned that the difference between the isentropic and non-isentropic coefficients was within the error bound of the piston-theory approximation itself, and proceeded to use the isentropic coefficients defined in Eqs. (3.11) to (3.13). Lighthill concluded his presentation of the method with an application to oscillating airfoils. A generalization of Lighthill's application is given in Section 3.3.

The review of applications of CPT by Ashley and Zartarian [103] noted the use of the term "piston theory" to describe the local pressure-downwash relation which is generalized as Eq. (3.8). It was noted that a variety of aeroprediction methods yield this type of relation. The review included mention of methods prior to Lighthill's [88] work as well as subsequent developments such as that by Landahl [128]. This allowed a broader consideration of the validity limits of CPT to be made. Ashley and Zartarian [103] maintained Lighthill's [88] assumption of subsonic piston downwash. They identified the approximate bounds of validity as $M_\infty > 2.5$ with $M_\infty \delta < 1$, while noting usable results from CPT at Mach numbers as low as $M_\infty = 2$. Ashley and Zartarian [103] also cited the validity limits of other developments as requiring one of the following

$$M_\infty^2 \gg 1 \quad kM_\infty^2 \gg 1 \quad k^2 M_\infty^2 \gg 1\,, \tag{3.19}$$

in addition to the subsonic piston downwash limitation of Eq. (3.17). No alteration was made to the cylinder or coefficient definitions given in Eqs. (3.11) to (3.16). With regards to the

condition $k^2 M_\infty^2 \gg 1$, Ashley and Zartarian [103] speculated that CPT might be applied at subsonic Mach numbers provided that the reduced frequency k is very large. This was echoed by Dowell [129], with the further hypothesis that CPT could be used for the prediction of farfield pressures in aeroacoustics.

A significant feature of the publication by Ashley and Zartarian [103] was in its stance on three-dimensional applications. While noting that the approximate errors associated with Landahl's [128] formulation did not apply in three-dimensional flows, Ashley and Zartarian [103] suggested that CPT may be used for such flows regardless. They subsequently showcased the application of CPT to a range of practical problems, including flutter of finite wings and panel flutter. The application to finite wings gave no definition of wing geometry, and no remarks were made on the extent of three-dimensional effects.

The interpretation of CPT due to Bird [127] is marked by a return to the foundations for CPT as laid out by Hayes [75] and Goldsworthy [126]. Bird [127] noted that special cases of planar flow exist in which the two-dimensional steady flow equations may be identically transformed to one-dimensional unsteady equations without approximation. The particular examples that were cited were the case of an oblique shock over a wedge and a Prandtl-Meyer expansion around a sharp corner. Bird noted that for these cases, a flow direction existed in which no velocity gradient was generated throughout the flowfield. In the oblique shock case, this direction was along the shock wave. Bird remarked that the governing equations could then be interpreted as one-dimensional unsteady through considering the "cylinder" to be oriented normal to the direction of zero velocity-gradient, with the piston velocity defined by the surface boundary condition. With reference to Fig. 3.4 and Eq. (3.2), the formulation is characterized by the following definitions:

$$\theta = \beta\,, \tag{3.20}$$

$$\mathbf{V_{cyl}} = \mathbf{V}_\infty\,, \tag{3.21}$$

where β is the shock angle. It was noted that this transform was valid for any supersonic Mach number or deflection, provided that the flowfield remained supersonic throughout. Noting that the angle between the shock and the wedge $\beta - \delta$ could be approximated by the freestream Mach angle μ, Bird went on to show that the piston downwash could be expressed as

$$\frac{w}{a_\infty} \approx M_\infty \frac{\sin\delta}{\cos\mu} \approx \frac{M_\infty^2}{\sqrt{M_\infty^2 - 1}} \sin\delta\,. \tag{3.22}$$

Bird [127] offered this result as an explanation for the improved results obtained by CPT when the downwash definition of Eq. (3.4) as empirically changed as follows:

- For large deflections, $\tan\delta$ is replaced by $\sin\delta$,
- At low supersonic Mach numbers, M_∞ is replaced by $\frac{M_\infty^2}{\sqrt{M_\infty^2-1}}$.

As noted by Bird [127], the latter is a reflection of Van Dyke's [130] unified supersonic-hypersonic similarity law. While establishing that the governing equations reduce to one-dimensional unsteady, Bird [127] offered no suggestion for a closed-form expression for the pressure at the surface. Nonetheless, his result gives valuable physical insight into the approximations inherent in the unsteady analogy and in piston theory. Specifically, it allows for differences in the formulation between CPT and LPT, as well as between the use of $\tan\delta$ and $\sin\delta$ to be critically understood. To this end, the work of Bird [127] largely informed the development of generalized piston theory in [59] in terms of arbitrary cylinder orientation.

3.2.2 Generalized Formulation for Pressure Equations

The fact that a "piston theory" pressure relationship could be obtained from different aeroprediction methods was noted by Ashley and Zartarian [103]. This was also noted by Morgan et al [131], who reviewed a number of aeroprediction methods suitable for flutter prediction at high supersonic Mach numbers. Among the methods reviewed were

- Van Dyke's [104] second-order potential flow theory,
- Landahl's [128] second-order method,
- Lighthill's [88] CPT formulation,
- The tangent-wedge method [48].

Morgan et al [131] noted that under certain circumstances, the methods gave very similar predictions, and were similar in their mathematical formulation. This was elaborated on by Rodden et al [124], who developed a generalized formulation for the CPT pressure equation. The equation was essentially similar to Eq. (3.9). However, the formulation did not account for local cylinder conditions, despite citing the work of Morgan et al [131] which contained this suggestion. Nonetheless, the formulation of Rodden et al [124] is significant in having introduced the idea of different "formulations" of a common piston theory through the coefficients c_1, c_2, and c_3. The work of Rodden et al [124] originally only included coefficients due to Lighthill [88] and Van Dyke [104]. However, an extension of CPT's application to swept wings was made.

The formulation of Rodden et al [124] was expanded on by Liu et al [125] in developing a hybrid method based on CPT / linear theory. Liu et al [125] noted that the generalized

formulation also encapsulated the works of Donov [105], Busemann [132], Linnell [133], Carafoli [134], and Kahane and Lees [135]. The majority of these developments were based in the method of characteristics. Greater detail on the development of Donov is given in [116, 121]. These works were included through appropriate definition of the coefficients c_1, c_2, and c_3. In terms of generalized piston theory, these are all formulations of CPT, with $\theta = 0°$, $\mathbf{V_{cyl}} = \mathbf{V}_\infty$, and $p_{cyl} = p_\infty$. The form of Eq. (3.9) is adapted here to account for the contribution due to the leading-edge shock as

$$C_p = \frac{2}{M_\infty^2}\left[c_1 M_\infty \delta(x) + c_2 M_\infty^2 \delta^2(x) + c_3 M_\infty^3 \delta^3(x) - d_3 M_\infty^3 \delta^3(0)\right], \tag{3.23}$$

where δ is the local flow-turning angle at the airfoil surface, $x = 0$ is the leading edge, the coefficients c_1, c_2, and c_3 fulfil the same role as in Eq. (3.9), and the coefficient d_3 accounts for the contribution of the leading-edge shock. For isentropic flows with no leading-edge shock, $d = 0$. A generalized form of the coefficients c_1, c_2, c_3, and d_3 developed by the various authors is given by

$$c_1 = \frac{M}{m}, \tag{3.24}$$

$$c_2 = \frac{M^4(\gamma+1) - 4m^2}{4m^4}, \tag{3.25}$$

$$c_3 = \frac{1}{12Mm^7}\left(e_8 M^8 + e_6 M^6 + e_4 M^4 + e_2 M^2 + e_0\right), \tag{3.26}$$

$$d_3 = \frac{(\gamma+1)}{96Mm^7}\left(f_8 M^8 + f_6 M^6 + f_4 M^4\right), \tag{3.27}$$

where $m = \sqrt{M_\infty^2 - 1}$. Some disagreement in the correct definition of the terms in the c_3 coefficient arose, largely due to algebraic or typographical errors in various publications. This was discussed by Jones [136], who provided a derivation of the coefficients to correct those given by Busemann [132]. Jones [136] noted that similar corrections had also been made by other authors, including Laitone [137]. The terms as derived by Jones [136] are in agreement with the terms as derived by Donov [105], and are quoted below as

$$e_0 = 8, \tag{3.28}$$

$$e_2 = -12, \tag{3.29}$$

$$e_4 = 10(\gamma+1), \tag{3.30}$$

$$e_6 = 2\gamma^2 - 7\gamma - 5, \tag{3.31}$$

$$e_8 = \gamma + 1, \tag{3.32}$$

$$f_4 = 8\,, \tag{3.33}$$

$$f_6 = 4(\gamma - 3)\,, \tag{3.34}$$

$$f_8 = 5 - 3\gamma. \tag{3.35}$$

The unification of these different methods under a common formulation and terminology of "piston theory" is beneficial from the standpoint of computational implementation. An unfortunate consequence is that this hides the underlying theoretical bases for the various methods, which informs a deeper understanding of the limitations of the methods. This is reflected in the misconception often noted in the literature that piston theory is limited to subsonic piston downwash.

3.2.3 Extension to Supersonic Piston Downwash

The early development of piston theory due to Lighthill [88] was originally based in the assumption of subsonic piston downwash in order that the isentropic pressure relation may be used to a good approximation. While Lighthill [88] noted that a shock-expansion approach could be utilized to account for the leading-edge shock, he deemed it undesirable from the standpoint of the formulation simplicity. The unintended consequence of this was that a misconception developed in the literature that "piston theory" as a whole is inherently limited to subsonic piston downwash. The later recognition that a number of different methods yield a pressure-downwash relationship which may be described as "piston theory" facilitated the extension of CPT to supersonic piston downwash. The extension is associated with a number of different names, which are introduced in this section.

The various treatments of supersonic piston downwash extension may be distilled into two categories:

- Extensions based in the hypersonic, small-angle approximation to the oblique shock equations. The majority of works fall into this category,
- Empirically derived formulations.

The term "strong-shock piston theory" is used by the majority of authors to describe the resulting formulations. The terminology is typically associated with Miles [138]. The development of Miles [138] falls into the first category of treatments. The basis for this category lies in an approximation to the relation between the oblique shock angle β, surface angle δ, and undisturbed Mach number M_∞. An exposition of this approximation is given by Anderson [25] and is not repeated here. The essence lies in assuming that β and δ are small such that trigonometric functions of the angles may be simplified by small angle assumptions.

These assumptions are based on the premise of slender bodies in hypersonic flows, essentially written as $\delta \ll 1$ and $M_\infty^2 \gg 1$. At this point, if it is assumed that $M_\infty^2 \beta^2 \gg 1$, then the shock relations reduce to their hypersonic limit form. If this assumption is not made, then a relationship between β and δ may be derived in terms of the hypersonic similarity parameter $K = M_\infty \delta$. This relationship may be written as

$$\frac{\beta}{\delta} = \frac{\gamma+1}{4} + \sqrt{\left(\frac{\gamma+1}{4}\right)^2 + \frac{1}{K^2}}\,. \tag{3.36}$$

Substitution of the above relation into the equation for the pressure ratio across an oblique shock yields

$$\frac{p}{p_\infty} = 1 + \gamma K^2 \left[\frac{\gamma+1}{4} + \sqrt{\left(\frac{\gamma+1}{4}\right)^2 + \frac{1}{K^2}}\right]. \tag{3.37}$$

The result is an equation describing the surface pressure on a wedge which creates an oblique shock. The pressure is a function purely of the hypersonic similarity parameter based on the surface inclination. The engineering-level aeroprediction method which utilizes this pressure relation is known as the tangent-wedge method [48]. The same equation has also been referred to as "Ghosh's piston theory" [139] in a number of articles on oscillating bodies in hypersonic flows. It has also been dubbed "strong shock piston theory". The extension of the oblique-shock result to a piston-theory formulation is facilitated by the result that

$$\frac{w}{a_\infty} = M_\infty \delta\,, \tag{3.38}$$

within the context of the small-angle approximations which the development is based in. It is remarked here for completeness that the square-root in Eq. (3.37) may be expanded in series form. Truncating the resulting series at third order results in the familiar form of Eq. (3.8). The resulting formulation may be described by generalized piston theory (with reference to Fig. 3.4 and Eqs. (3.2) and (3.8)) using the following definitions:

$$c_1 = 1\,, \tag{3.39}$$

$$c_2 = \frac{\gamma+1}{4}\,, \tag{3.40}$$

$$c_3 = \frac{(\gamma+1)^2}{32}\,, \tag{3.41}$$

$$\theta = 0^\circ\,, \tag{3.42}$$

$$\mathbf{V}_{\mathbf{cyl}} = \mathbf{V}_\infty\,, \tag{3.43}$$

$$p_{cyl} = p_\infty \,. \tag{3.44}$$

The difference between the third-order coefficient of the tangent-wedge formulation in Eq. (3.41) and of Lighthill's isentropic formulation in Eq. (3.13) was noted by Lightill [88]. Lighthill remarked that the difference could be considered negligible. Nevertheless, the basis from which the tangent-wedge formulation of Eq. (3.37) was derived does not assume that $M_\infty \delta < 1$, and thereby gave a basis for applying CPT to supersonic (and indeed hypersonic) piston downwash Mach numbers.

For completeness, a brief note is included on the works of Ghosh [139–141]. With the exception of [140], these were heuristic applications of CPT, with the defining feature being the use of Eq. (3.37) in place of a power-series in w/a_∞. In the downwash equation of Eq. (3.2), the resulting $\tan\delta$ was replaced by $\sin\delta$, as is typical of treatments involving large deflections. In a later development, Ghosh [142] implemented the downwash formulation of Bird [127] for wedges, as described by Eqs. (3.20) and (3.21).

The second category of supersonic piston downwash extensions is defined by the development of Raymond [143]. Raymond cited an empirically determined relationship between the pressure coefficients due to expansion $C_{p(e)}$ and due to compression $C_{p(c)}$ in the form of

$$C_{p(e)} + C_{p(c)} = (\gamma+1)\delta^2 \,. \tag{3.45}$$

The empirical relation was determined for two-dimensional hypersonic flows. The pressure coefficient due to expansion was defined by Raymond [143] to be that given by isentropic expansion. In terms of the pressure, this relation is given in Eq. (3.18). Raymond [143] noted that for $M_\infty > 1.4$, this could be approximated to within 4% by the pressure coefficient at vacuum, and thus adopted

$$C_{p(e)} = -\frac{2}{\gamma M_\infty^2} \,. \tag{3.46}$$

By substituting Eq. (3.46) into the empirical relation of Eq. (3.45), Raymond [143] approximated the pressure coefficient due to compression as

$$C_{p(c)} = \frac{2}{\gamma M_\infty^2} + (\gamma+1)\delta^2 \,, \tag{3.47}$$

or in terms of the pressure,

$$\frac{p_c}{p_\infty} = 2 + \frac{\gamma(\gamma+1)}{2} K^2 \,. \tag{3.48}$$

In terms of generalized piston theory, the formulations differs from that in Eqs. (3.39) to (3.44) by assuming that $M_\infty \delta > 1$ and adopting the following coefficients:

$$c_1 = 0\,, \tag{3.49}$$

$$c_2 = \frac{\gamma+1}{2}\,, \tag{3.50}$$

$$c_3 = 0\,. \tag{3.51}$$

A departure from the generalized piston theory formulation is noted in Eq. (3.48), which predicts a pressure ratio of $p_c/p_\infty = 2$ for the case of $\delta = 0$. However, given the limitation of Eq. (3.48) to flows for which $M_\infty \delta > 1$, this is not a concern. For flows of $M_\infty \delta < 1$, Raymond [143] recommended the isentropic pressure relation of Eq. (3.18), which would be equivalent to Lighthill's [88] piston theory formulation.

3.2.4 Derivation of CPT from Three-Dimensional Flow Equations

The developments presented thus far were rooted in planar flows. The use of the piston-theory pressure relation was motivated heuristically in some works, as in that by Lighthill [88]. In others, such as the work of Donov [105], it was arrived at by mathematical rigour. The unifying basis for these works is the application – whether heuristically or rigorously – of the unsteady analogy. This leads to the reduction of the two-dimensional flow problem to a one-dimensional formulation. The application of the unsteady analogy to three-dimensional flows to arrive at a piston theory formulation is considered here. More specifically, works rooted in a mathematical treatment will be considered. Three key works will be discussed, namely

- Il'yushin's [77] initial development of the law of plane sections for slender bodies at high Mach numbers (the unsteady analogy) and its reduction to piston theory,
- The review of various hypersonic similitudes by Hayes and Probstein [27] and the reduction of these to piston theory,
- The development of a three-dimensional formulation of Dowell and Bliss' [144] "extended piston theory" by Aravinth et al [145]. This work will be discussed in the context of similar work in Section 3.2.5.

The work of Il'yushin [77] is an important early development of piston theory. Unfortunately, it received limited attention in Western literature due in part to its delayed publication, as discussed by Hayes and Probstein [27]. Il'yushin [77] developed the law of plane sections

for slender bodies from an order-of-magnitude analysis. This included an analysis of the order of the error in the method. The application of the method to a range of geometries was demonstrated, which included

- Finite lifting surfaces,
- Cones, ogives, and cylinders,
- General plane profiles (with the special case of a wedge also considered).

The mathematical development of Il'yushin [77] will not be reproduced here. It will be revisited as a special case of the development in Chapter 4. However, some remarks on the key points in the development will be made here. Among the key assumptions in the development was that the inclination of the surface to the freestream, τ, was small such that $\tau \ll 1$. This allowed both slender bodies and thin wings to be considered. This also renders the analysis an essentially small-incidence hypersonic SDT formulation. The fundamental parameter resulting from Il'yushin [77] subsequent analysis was found to be the hypersonic similarity parameter $K = M_\infty \tau$. Il'yushin showed that the error in applying the law of plane sections to reduce a three-dimensional flow to a two-dimensional flow in a plane perpendicular to the freestream was $\mathscr{O}\left(\tau^2 + M_\infty^{-2}\right)$. Il'yushin further demonstrated that the law of plane sections could be applied with an equal degree of accuracy in the spanwise direction as in the axial direction. This required the axial and spanwise rates of change of the surface slopes to be $\mathscr{O}(\tau)$ smaller than the rate of change in the thickness direction. The result was that the three-dimensional flow formulation could be reduced to a one-dimensional piston problem. Il'yushin noted the breakdown of these underlying assumptions in the vicinity of the wing-tips, in which case the two-dimensional crossflow-plane formulation would be required. In essence, Il'yushin [77] thereby demonstrated the conditions for piston theory to be applied in non-planar flows.

Il'yushin [77] offered a physical interpretation of the law of plane sections in terms of a piston and cylinder analogy. This was exploited in adopting a Lagrangian approach in several of the analytical solutions obtained by Il'yushin [77]. The approach in these solutions was to start with the reduced one-dimensional formulation, and to then consider the boundary conditions at both the body and the shock. Closed-form solutions were thus obtained for both the linearized range of $M_\infty \tau \ll 1$ and the hypersonic range of $M_\infty \tau = \mathscr{O}(1)$. Among the solutions recovered were

- First-order piston theory for linearized supersonic flows of $M_\infty \tau \ll 1$,
- The oblique-shock solution of Eq. (3.44) for wedge flows,

- The isentropic solution of Eq. (3.16) for shock-free flows,
- An approximate solution for cones and ogives at zero incidence in the form of

$$\frac{p}{p_\infty} = \frac{\gamma p_\infty}{2} \frac{K^2}{\sqrt{1-K^2}} \ln\left(\frac{1+\sqrt{1-K^2}}{1-\sqrt{1-K^2}}\right) \tag{3.52}$$

- A solution for airfoils with attached shocks including the effect of wave reflections from the shock.

In summary, these results demonstrated the mathematically rigorous application of the law of plane sections (and by extension, formulations of piston theory) to both planar and non-planar flows, with both subsonic and supersonic piston downwash Mach numbers being considered.

Hayes and Probstein [27] provided a review of a range of hypersonic similitudes. The correlation between the similitudes and the limiting processes required for their reduction was discussed, and is depicted in Fig. 3.14. The nomenclature of Hayes and Probstein [27] as been retained for this figure. It should be noted that in the case of flattened bodies (those subjected to $\tau \to 0$), the parameter α is to be interpreted as a yaw angle. The figure also depicts the orientation of independent fluid slabs in each similitude. It may be noted that in similitudes associated with strip theory, fluid slabs are oriented parallel to the freestream velocity. This is consistent with neglecting spanwise derivatives. Similarly, in similitudes associated with classical hypersonic SDT, fluid slabs are perpendicular to the freestream velocity. This is consistent with neglecting streamwise gradients. Finally, the similitude of Sychev [4] is seen to orient the fluid slabs perpendicular to the axis of body slenderness. The differences in the nuances of the similitudes were discussed by Hayes and Probstein [27], and will not be repeated here. However, it is noted here that the development due to Sychev [4] generally permits larger perturbations than the other similitudes.

The "yawed wing" similitude of Fig. 3.14 is elaborated on in Fig. 3.15. The similitudes all apply to the same geometry and its orientation to the flow. It is noted that the reduction to piston theory is accomplished by neglecting derivatives in both the x and y directions. This is equivalent to applying both the strip theory approximation and the hypersonic SDT approximation simultaneously. The only remaining directional derivative in the governing flow equations is that in the thickness direction, and the equations may be interpreted as one-dimensional unsteady. Hayes and Probstein [27] provided a comparison of the error in the methods of Fig. 3.15, which has been reproduced in Table 3.1.

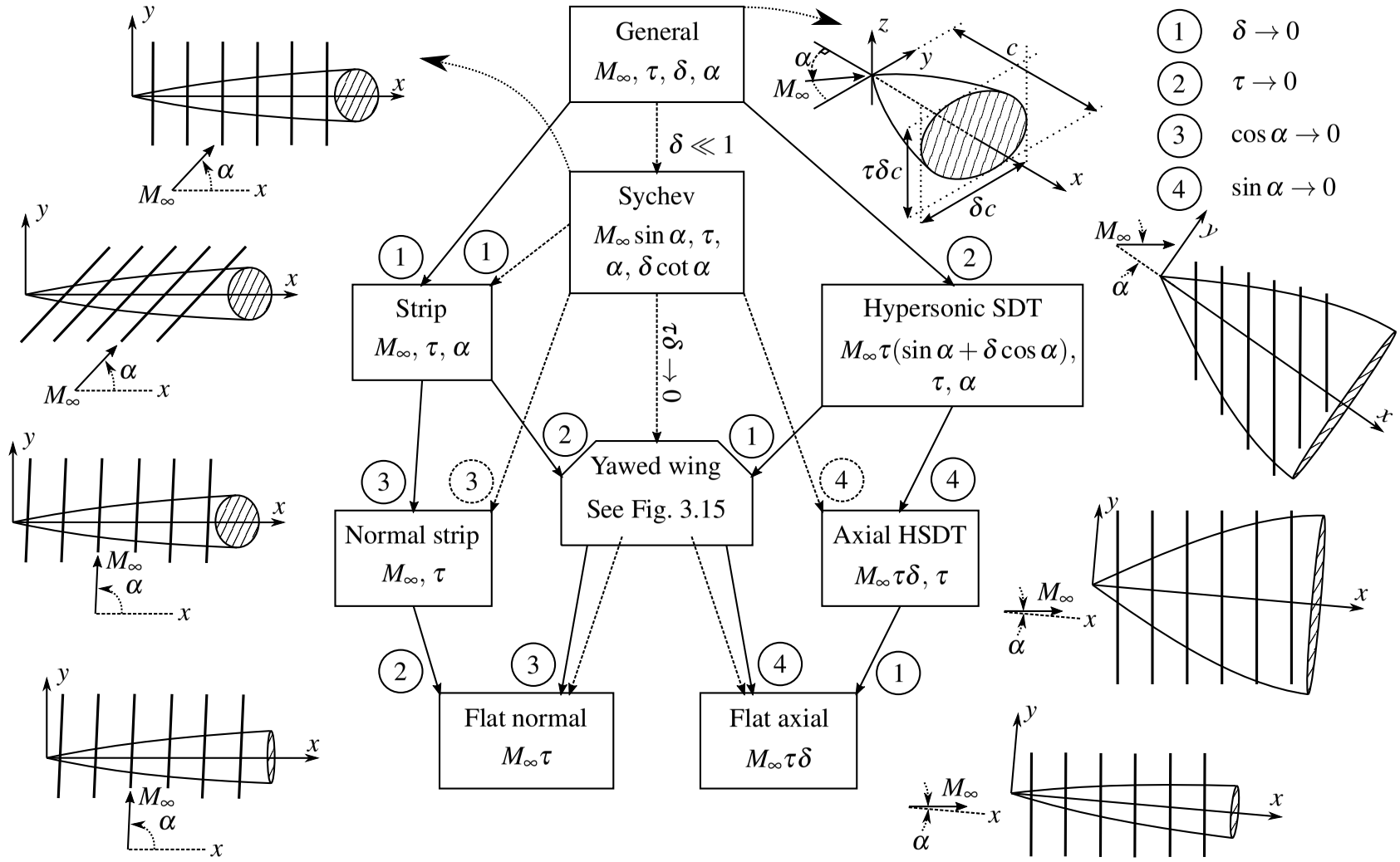

Fig. 3.14 Correlation of hypersonic similitudes with independent fluid slabs. Adapted from Hayes and Probstein [27].

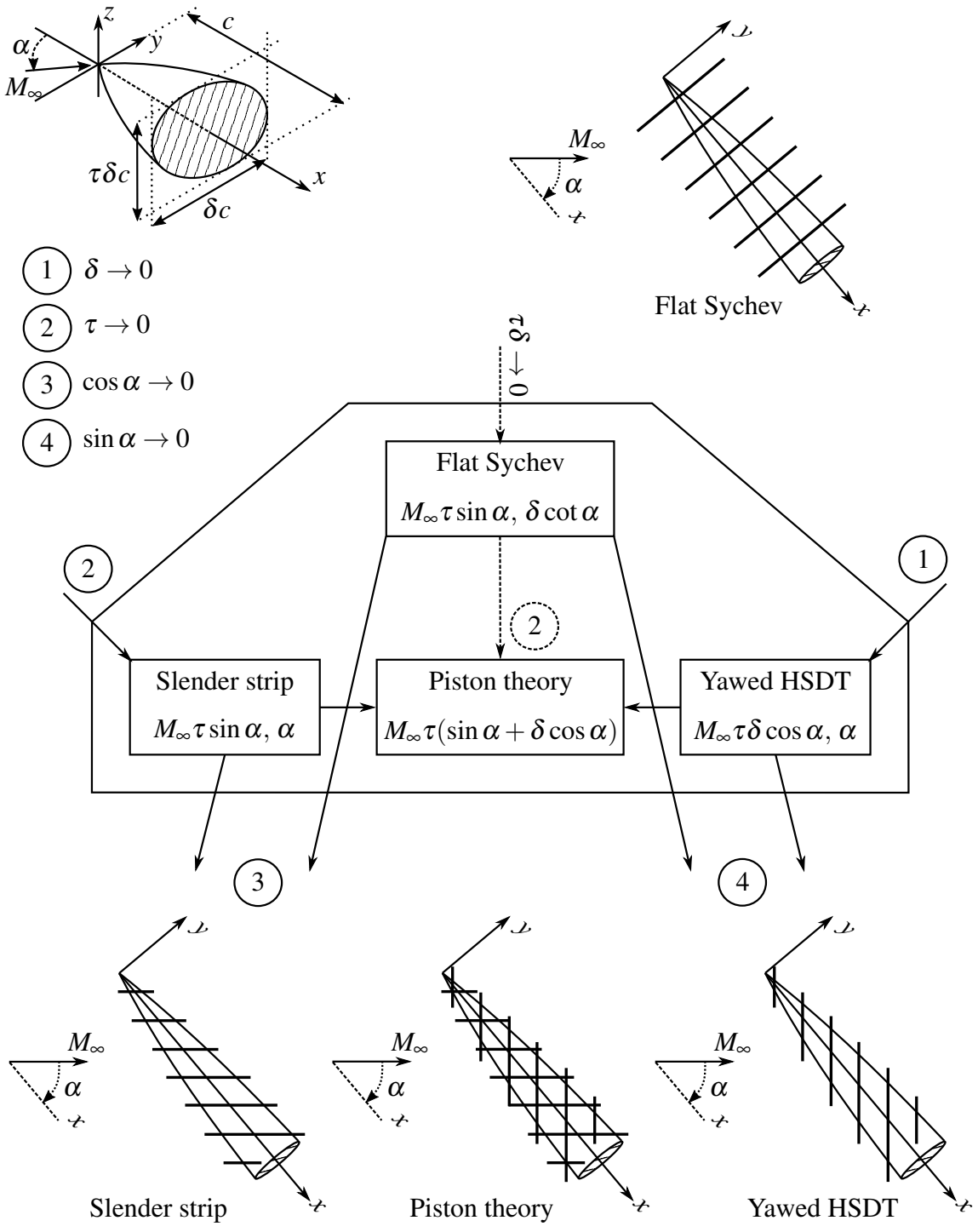

Fig. 3.15 Correlation of hypersonic similitudes for yawed wings with independent fluid slabs. Adapted from Hayes and Probstein [27].

Table 3.1 Comparison of yawed-wing hypersonic similitudes depicted in Fig. 3.15. Adapted from Hayes and Probstein [27].

Approach	Direction of neglected derivative	Error parameter
Sychev	Axial	$\tau^2\delta^2$
Piston theory	Axial, spanwise	τ^2
Hypersonic SDT	Streamwise (M_∞)	$\tau^2\left(\sin^2\alpha+\delta^2\cos^2\alpha\right)$
Strip theory	Binormal to M_∞ and thickness direction	$\tau^2\left(\cos^2\alpha+\delta^2\sin^2\alpha\right)$

Hayes and Probstein [27] also gave a brief, heuristic discussion on the validity of applying the similitudes (including piston theory) to unsteady flows. The scenario generated for the discussion is depicted in Fig. 3.16. It was assumed that unsteady disturbances were generated by the body which varied smoothly both spatially and in time. The parameter λ was introduced as a characteristic length of the spatial distribution of disturbances, and can be associated with a wavelength of this distribution. The unsteadiness of the disturbances was characterized by a frequency f and an associated maximum lateral velocity of the body, v. The unsteady equivalent of the thickness ratio was introduced as the ratio of v to the steady freestream velocity V_∞. This ratio was represented by τ. The space within which the effect of unsteady disturbance propagation was felt was defined as τc, where c is the axial scale of the steady flow.

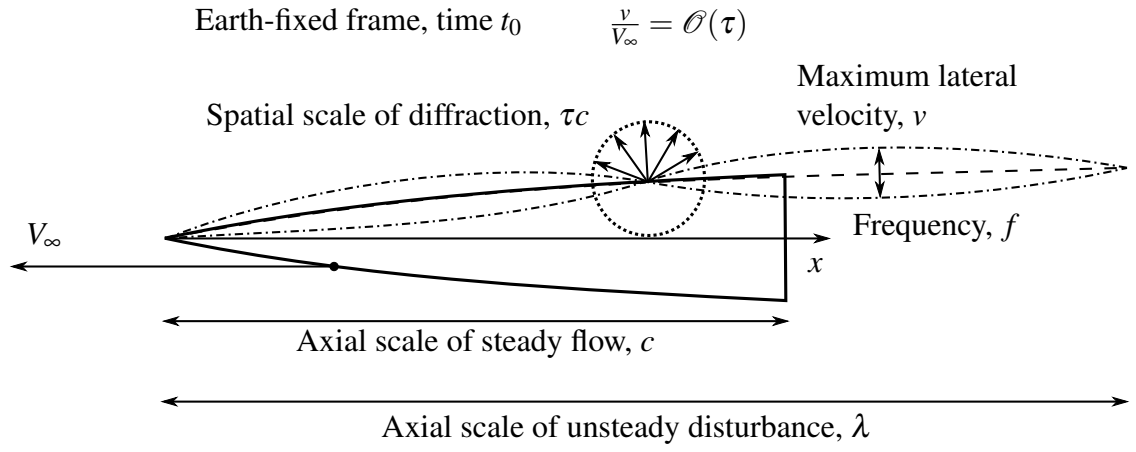

Fig. 3.16 Characterization of unsteady disturbance propagation in the heuristic argument of similitude application in unsteady flows due to Hayes and Probstein [27].

Within this framework, Hayes and Probstein [27] noted that the unsteady disturbances at a point could be viewed as a travelling wave with velocity $f\lambda$. It was then argued that Hayes' [75] hypersonic equivalence (the unsteady analogy) would apply provided that the

local Mach number in the unsteady flow was sufficiently high. This was expressed as

$$|V_\infty - f\lambda| \gg a_\infty, \tag{3.53}$$

where a_∞ is the speed of sound in the freestream. Reasoning that the flow was hypersonic, and hence $M_\infty \tau = \mathcal{O}(1)$, Hayes and Probstein [27] gave the first condition for the unsteady analogy to hold in unsteady flows as

$$\tau \ll \left| 1 - \frac{f\lambda}{V_\infty} \right|, \tag{3.54}$$

which may be viewed as an alternative form of Eq. (3.17). The author notes that the ratio of the propagation wave speed to the freestream velocity in Eq. (3.54), given by $f\lambda/V_\infty$, is essentially similar to the typical definition of the reduced frequency k. In this light, Eq. (3.54) provides a restriction on the effective amplitude of oscillation through τ for a given reduced frequency. It is seen that a higher degree of unsteadiness (whether through a higher temporal frequency of oscillation or a shorter spatial wavelength) places a more stringent requirement on the effective perturbation strength than simply $\tau \ll 1$. This is reflected in the second-order smallness assumption used for the oscillation amplitude in McIntosh's [146] development of oscillating wedges, which is treated in Section 3.2.8.

Hayes and Probstein [27] further argued the flow within the first wavelength of disturbances is primarily a transient one, and that the unsteady analogy was valid for this flow. The second condition for the validity of the unsteady analogy applied to unsteady flows about finite bodies was given as

$$\tau \ll \frac{\lambda}{c}, \tag{3.55}$$

which essentially requires the scale of local transience due to diffraction (τc) to be smaller than the scale of global transience associated with the distribution of disturbances (λ). Hayes and Probstein [27] noted the implicit assumption in the analysis that the axial scale of the steady flow c was of the order of the body length. A brief extension of the argument to the unsteady application of strip theory was also given, and is not repeated here.

The derivation of CPT (in a sense) from the three-dimensional flow equations is also possible without requiring the application of the unsteady analogy and strip theory. This was recently accomplished by Aravinth et al [145]. The resulting pressure formulation contains first-order CPT is a special case. The method is based in linear potential flows, and accounts for upstream influence and unsteadiness. It will be discussed in the context of similar methods in the following section.

3.2.5 Accounting for Upstream Influence and Unsteadiness in CPT

In reviewing the contributions to piston theory according to the categories used in this chapter, a certain amount of overlap is inevitable. In particular,

- Several methods which account for upstream influence and unsteadiness are treated in Section 3.2.8. This is due to the author's emphasis on these methods containing LPT as a special case,
- A number of methods treated in Section 3.2.6 also account for upstream influence and unsteadiness. However, the author chooses to emphasize the contribution of these methods to the application of piston theory to non-planar flows.

With this caveat, the emphasis of the present section will be on works with a potential flow basis which contain CPT as a special case. These methods typically account for upstream influence and the time history of the flow through integral terms. The resulting pressure formulation does not have the strictly self-influenced form typically associated with piston theory. However, the leading terms in the formulation are self-influenced and may be associated with piston theory. This has led to the use of descriptors such as "extended piston theory" being applied to the methods. A final introductory remark is offered that the majority of the methods reviewed here are based in *linearized* potential flows, making them amenable to solution by frequency-domain methods. The majority of the works are associated with panel-flutter problems. The methods reviewed may be loosely grouped as follows:

- Methods based in exact linearized potential flows, such as the work of Chueshov et al [147], the numerous works of Vedeneev [148–158], and that of Garrick and Rubinow [159],
- Methods based in series-expansion approximations to exact formulations, such as Landahl's [128] method and the various formulations of "extended piston theory" associated with Dowell and Bliss [144], Dowell and Ganji [160] and Aravinth et al [145],
- Methods based in an a low-frequency piston-theory approximation to the exact linearized potential flow model, such as the works of Dugundji [161], Dowell and Voss [162], and Fung [163].

The predominant use of potential flow models for aerodynamic modelling in panel flutter studies was discussed by Dowell [164]. Dowell [164] noted the importance of accounting for three-dimensionality and unsteadiness in the flow, and noted that quasi-steady methods (such as piston theory) omit these.

Methods Based in Exact Solutions

The role of the unsteadiness (and upstream influence) in panel flutter was clarifed by Chueshov et al [147], who considered the exact linearized potential theory and its reduction to piston theory. Their treatment is aimed at a mathematically-oriented audience, and will not be reproduced here. Chueshov et al [147] noted that the governing aeroelastic equations for the plate may be written with the aerodynamic terms representing a forcing function to the structural system. These aerodynamic terms consist of "piston-theoretic" self-influenced terms and of a second term-grouping. The piston-theoretic terms are quasi-steady, depending only on the instantaneous dynamics of the structure. The latter term-grouping accounts for the time-history of the flow of upstream perturbations. Chueshov et al [147] posited that a time exists such that the behaviour of the flow may be captured by a delayed aerodynamic forcing. In this light, the second term-grouping was referred to as a delay term. This results in a phase-shift in the aerodynamic loading, which may be interpreted as a change in the effective aerodynamic stiffness (in-phase loads) and damping (out-of-phase loads). Chueshov et al [147] noted that an inverse-proportionality exists between the delay term and the Mach number of the flow for "sufficiently large" supersonic Mach numbers. Thus, in the limit of hypersonic flow, the contribution of the delay term could be neglected and the reduction to quasi-steady piston theory could be achieved. Chueshov et al [147] noted that the "extended piston theory" of Dowell and Bliss [144] could be interpreted as an approximation to the delay term, expressed as an asymptotic expansion in inverse Mach number. Also noted was the widespread use of piston-theory formulation due a low-frequency approximation to the exact linearized potential flow, which will be discussed shortly.

The importance of accounting for unsteadiness and upstream influence in panel flutter is emphasized in the works of Vedeneev [148–158]. The majority of these works utilize exact linearized potential flow solutions. Such a solution in planar flows is given in dimensional form by Garrick and Rubinow [159] as

$$\phi(x,t) = -\frac{1}{m_\infty}\int_0^x w(\xi,t)D_1(\xi,x)\,\mathrm{d}\xi\ , \tag{3.56}$$

$$p = p_\infty - \rho_\infty\left(\frac{\partial\phi}{\partial t} + V_\infty\frac{\partial\phi}{\partial x}\right), \tag{3.57}$$

where $m_\infty = \sqrt{M_\infty^2 - 1}$, w is the downwash, and $D_1(\xi,x)$ represents the effect of delay in propagation (to the point in consideration at x) of disturbances produced at ξ. These are

given for sinusoidal motion $z = \bar{z}\exp(\mathrm{i}\omega t)$ as

$$w(\xi,t) = \frac{\partial z}{\partial t} + V_\infty \frac{\partial z}{\partial \xi} = \left[\mathrm{i}\omega\bar{z}(\xi) + V_\infty \frac{\partial \bar{z}(\xi)}{\partial \xi}\right]\exp(\mathrm{i}\omega t)\,, \tag{3.58}$$

$$D_1(\xi,x) = \exp\left(-\mathrm{i}k_\xi^* M_\infty\right) J_0\left(k_\xi^*\right), \tag{3.59}$$

$$k_\xi^* = \frac{\omega(x-\xi)}{V_\infty}\frac{M_\infty}{m_\infty^2}, \tag{3.60}$$

where J_0 is the Bessel function of the first kind with order 0, and k_ξ^* has been introduced as a shorthand. Vedeneev [151] noted that this may also be written as

$$p(x,t) = p_\infty + \rho_\infty a_\infty \frac{M_\infty}{m_\infty} w(x,t) + \frac{\rho_\infty \omega}{m_\infty^{2/3}} \int_0^x w(\xi,t) D_2(\xi,x)\,\mathrm{d}\xi\,, \tag{3.61}$$

where $w(x,t)$ is the local instantaneous downwash at the point of interest, $w(\xi,t)$ is the downwash at the point ξ at which perturbations were created upstream, and $D_2(\xi,x)$ represents the effect of delayed propagation of these upstream perturbations, and is given by

$$D_2(\xi,x) = \exp\left(-\mathrm{i}k_\xi^* M_\infty\right)\left[\mathrm{i}J_0\left(k_\xi^*\right) + M_\infty J_1\left(k_\xi^*\right)\right], \tag{3.62}$$

where J_1 is the Bessel function of the first kind with order 1, and k_ξ^* has been defined in Eq. (3.60). Vedeneev [151] thus showed the relation between the exact linearized potential flow solution and CPT. Consider the first two terms on the RHS of Eq. (3.61). Comparison of these terms with Eq. (3.8) shows that this is equivalent to a first-order CPT with a coefficient due to Van Dyke, as given in Eq. (3.24). Comparison of Eq. (3.58) and Eqs. (3.3) and (3.4) shows that the downwash definition is unaltered. The integral term on the RHS of Eq. (3.61) has been noted to account for upstream influence and delay, and is the "delay term" referred to by Chueshov et al [147]. Thus it is shown that first-order CPT may be derived from a potential flow basis if the influence of upstream perturbations and unsteadiness is neglected. A similar approach was adopted by Algazin and Kiiko [165], who provided the following alternative formulation:

$$p(x,t) = p_\infty + \rho_\infty a_\infty \frac{M_\infty}{m_\infty} w_A(x,t) - \frac{\rho_\infty M_\infty \omega^2}{m_\infty^5} \int_0^x z(\xi,t) D_3(\xi,x)\,\mathrm{d}\xi\,, \tag{3.63}$$

where the downwash definition has been changed to $w_A(x,t)$ and a new delay function $D_3(\xi,x)$ is introduced. These may be found by manipulation of the formulation of Algazin

and Kiiko [165] as

$$w_A(x,t) = \left(\frac{M_\infty^2 - 2}{M_\infty^2 - 1}\right)\frac{\partial z(x,t)}{\partial t} + V_\infty \frac{\partial z(x,t)}{\partial x}, \tag{3.64}$$

$$D_3(\xi, x) = \exp\left(-\mathrm{i}k_\xi^* M_\infty\right)\left[\frac{M_\infty^2 + 2}{M_\infty} J_0\left(k_\xi^*\right) - 2\mathrm{i}J_1\left(k_\xi^*\right) - \frac{M_\infty}{2} J_2\left(k_\xi^*\right)\right], \tag{3.65}$$

where J_2 is the Bessel function of the first kind of order 2, and k_ξ^* has been defined in Eq. (3.60). The downwash definition provided by Algazin and Kiiko [165] in Eq. (3.64) is associated with the phrase "low-frequency piston theory", and will be treated in the third category of works in Section 3.2.5.

The importance of the physics contained in the delay term is clearly emphasized in the various of works of Vedeneev [148–158]. In particular, Vedeneev [151, 152] compared the linear CPT approximation with the full potential formulation in considering flutter of an infinite-width panel of finite chord. Vedeneev used the classical downwash formulation of Eq. (3.58). Vedeneev then showed that linear CPT in this form can only predict coupled-mode flutter. Using the exact linearized potential flow formulation of Eq. (3.61), Vedeneev showed that single-mode flutter was possible at Mach numbers of $M_\infty < 1.7$. Comparing the results, Vedeneev noted that the single-mode flutter was a "higher-frequency" flutter mode in comparison to the "lower-frequency" coupled-mode flutter predicted by piston theory. Vedeneev [152] noted that the low-frequency downwash formulation of Eq. (3.64) also predicts single-mode instability for Mach numbers of $M_\infty < \sqrt{2}$. However, he remarked that the formulation is overly simplistic, as all modes are modelled as becoming unstable at the same time (once $M_\infty < \sqrt{2}$). A detailed discussion may be found in [151, 152].

For completeness, a brief note is made on some of Vedeneev's subsequent works [153–156]. These methods do not directly treat piston theory, and are rooted in small-disturbance linearizations of the Navier-Stokes equations, as described by Lees and Lin [166]. However, their relation to piston theory may be deduced from the foregoing discussion on the role of unsteadiness, upstream influence, and the law of plane sections. A significant feature of these works of Vedeneev [153–156] is the extension of inviscid panel-flutter analysis to viscous flows. The mathematical details of these works and their formulation of the pressure equation will not be entered into here. It will merely be noted that the pressure equation is cast as the inverse of a sum involving inviscid and viscous contributions. The analysis lends itself to various asymptotic approximations. A number of such simplifications are considered in [154]. The effect of the boundary later on coupled-mode and single-mode panel flutter is explored in [155]. The analysis is extended to larger boundary-layer thicknesses in [156]. Due to these works not directly involving piston theory, they are not treated further in Section 3.2.9.

In essence, the delay of upstream propagations as described by Eqs. (3.60) to (3.62) may significantly change the effective aerodynamic stiffness and damping. The "delay term" in the pressure loading is seen to be a (non-trivial) function of the freestream Mach number M_∞, the frequency of the unsteadiness ω, and of the upstream geometry. The essence of most "extensions" to and various formulations of piston theory lies in developing a simpler, approximate formulation of the delay term. Methods which approach this using series-expansion approximations are covered in the following category, with a number of methods also covered in Section 3.2.6. Methods which forego an attempt to model the delay term and rely on a low-frequency approximation to the exact linear potential solution will briefly be noted in the final category of Section 3.2.5.

Methods Based in Series-Expansion Approximations

An important distinction arises between the methods that will be reviewed in this subsection:

- The "extended piston theory" of Dowell and Bliss [144], as well as its further treatment by Dowell and Ganji [160] and its extension to three-dimensional flows by Aravinth et al [145], is based in the linearized (in terms of thickness) potential flow equation of Eq. (2.58). To emphasize this, the full potential function Φ may be written as an expansion in powers δ, where δ is a measure of the thickness. The linear (in terms of thickness) truncation is then $\Phi = U_\infty x + \phi + \mathscr{O}\left(\delta^2\right)$, where $\phi = \mathscr{O}(\delta)$. This essentially mirrors Eq. (2.42). The method assumes simple harmonic motion,

- The method of Landahl [128] is based in Van Dyke's [104] successive-approximation approach in reducing the full nonlinear potential equation of Eq. (2.43). The full potential may be written as $\Phi = U_\infty x + \varphi + \psi + \mathscr{O}\left(\delta^3\right)$, with $\varphi = \mathscr{O}(\delta)$ and $\psi = \mathscr{O}\left(\delta^2\right)$. As a result, Landahl's [128] method is nonlinear (second-order) in thickness. The method does not assume simple harmonic motion.

Despite this difference, there are underlying similarities between the methods of Dowell and Bliss [144] and of Landahl [128]. The chief similarity is in expanding the potential function as a series in some power in order to yield a solution involving simpler functions than those present in the exact linear potential solution of Eq. (3.56). With these introductory remarks completed, the attention will now be shifted to the particulars of each method. For brevity, two-dimensional forms of the methods will be considered. It is to be noted that Landahl's [128] development was originally for three-dimensional flows, while the development of Dowell and Bliss [144] was initially limited to two-dimensional flows.

As was noted earlier, the method due to Dowell and Bliss [144] is rooted in linear potential flows. Simple harmonic motion is assumed, such that the linear perturbation

potential may be written $\phi(x,z,t) = \bar{\phi}(x,z)\exp(\mathrm{i}\omega t)$ and the downwash may similarly be written $w(x,z,t) = \bar{w}(x,z)\exp(\mathrm{i}\omega t)$. The governing equation for the flow is then

$$\bar{\phi}_{zz} - \left[\left(M_\infty^2 - 1\right)\frac{\partial^2}{\partial x^2} + 2\mathrm{i}\frac{M_\infty \omega}{a_\infty}\frac{\partial}{\partial x} - \frac{\omega^2}{a_\infty^2}\right]\bar{\phi} = 0\,, \tag{3.66}$$

with the boundary condition at the surface written as

$$\left.\frac{\partial \phi}{\partial z}\right|_{z=0} = w \equiv \frac{\partial z}{\partial t} + V_\infty \frac{\partial z}{\partial x}\,. \tag{3.67}$$

Appyling the Laplace transform with respect to the streamwise coordinate x, these may be written in the frequency domain in terms of the Laplace variable s as:

$$\frac{\partial^2}{\partial z^2}\mathscr{L}\{\bar{\phi}\} - \mu^2 \mathscr{L}\{\bar{\phi}\} = 0\,, \tag{3.68}$$

$$\frac{\partial}{\partial z}\mathscr{L}\{\bar{\phi}\} = \mathscr{L}\{\bar{w}\}\,, \tag{3.69}$$

where μ is introduced as a shorthand, and essentially represents the streamwise derivatives of the flow in the Laplace domain. Its definition is

$$\mu^2 \equiv \left(M_\infty^2 - 1\right)s^2 + 2\mathrm{i}\frac{M_\infty \omega}{a_\infty}s - \frac{\omega^2}{a_\infty^2}\,, \tag{3.70}$$

where s is the Laplace variable. As is shown in [167], the solution for the potential function at the surface of the body may be found as

$$\bar{\phi}(x,0) = -\int_0^\infty \bar{w}(\xi)\mathscr{L}^{-1}\left\{\frac{1}{\mu}\right\}\mathrm{d}\xi\,, \tag{3.71}$$

where $\mathscr{L}^{-1}$ represents the inverse Laplace transform. The pressure at the body surface is then given by Eq. (3.57).

As is discussed in [167], analytical inversion of $1/\mu$ in the above equation leads to the exact solution for linear potential flows, which involves Bessel functions. It has already been presented in Eq. (3.56). The various formulations of "extended piston theory" are characterized by their approaches to representing $1/\mu$ as an expansion series. These are detailed in the publication by Dowell and Bliss [144], with further elaboration given by Dowell and Ganji [160]. The philosophy behind the representation of $1/\mu$ as an expansion series is to approximate a single "difficult" computation as a series of "simpler" computations. This is reflected in the resulting cumbersome, yet simple formulations associated with

"extended piston theory". The full forms of the "extended piston theory" formulations will not be given, and the coefficients will not be repeated here. The reader interested in the lengthy algebraic definitions is referred to the publication by Dowell and Ganji [160].

The three expansion approaches presented by Dowell and Bliss [144] and by Dowell and Ganji [160] include expansion in powers of:

- ω^{-1}: as noted by Dowell and Bliss [144], this expansion requires the reduced frequency to be sufficiently large than 1. Expanding

$$\frac{1}{\mu} = \frac{a_\infty}{\mathrm{i}\omega}\left[1 - \frac{2\mathrm{i}M_\infty a_\infty s}{\omega} + \frac{\left(M_\infty^2 - 1\right)}{4M_\infty^2}\left(\frac{2\mathrm{i}M_\infty a_\infty s}{\omega}\right)^2\right]^{-\frac{1}{2}}, \tag{3.72}$$

  the perturbation pressure is obtained from [160] in the form of

$$\bar{p} = \rho_\infty a_\infty\left[\bar{w} - \frac{1}{2}\left(\frac{a_\infty}{\omega}\right)^2\frac{\partial^2\bar{w}}{\partial x^2} - \mathrm{i}M_\infty\left(\frac{a_\infty}{\omega}\right)^3\frac{\partial^3\bar{w}}{\partial x^3} + \ldots\right]. \tag{3.73}$$

  This may be compared to high-frequency CPT in the form of $\bar{p} = \rho_\infty a_\infty \bar{w}$. The additional terms are corrections which account for the deviation from the limit of $\omega \to \infty$. It is seen that the additional terms involve the local downwash. Thus, the high-frequency approximation does not account for upstream influence. However, the presence of terms such as $\frac{\partial^2\bar{w}}{\partial x^2}$ suggests that some acceleration effects due to short wavelengths of periodic vibrations are modelled.

- M_∞^{-2}: also termed an "inverse Rayleigh-Janzen method" by Landahl [128], this involves the expansion of

$$\frac{1}{\mu} = \frac{1}{M_\infty}\left[\left(s + \frac{\mathrm{i}\omega}{V_\infty}\right)^2 - \frac{s^2}{M_\infty^2}\right]^{-\frac{1}{2}}. \tag{3.74}$$

  As demonstrated by Dowell and Ganji [160], for small reduced frequencies such that $k \ll 1$, the perturbation pressure takes the simplified form of

$$\bar{p} = \rho_\infty a_\infty \frac{M_\infty}{m_\infty}\left[\bar{w} - \mathrm{i}\omega\frac{m_\infty}{M_\infty}\left(\frac{1}{M_\infty^2} + \frac{3}{2M_\infty^4} + \ldots\right)\int_0^x \frac{\bar{w}(\xi)}{V_\infty}\mathrm{d}\xi\right], \tag{3.75}$$

  This may be compared to high-Mach CPT in the form of $\bar{p} = \rho_\infty a_\infty \frac{M_\infty}{m_\infty}\bar{w}$. The additional terms are corrections which account for the deviation from the limit of $M_\infty \to \infty$. It is seen that the additional terms account for upstream influence through the integral term. This upstream influence is proportional to M_∞^{-2}, and diminishes in the limit of high Mach numbers. This leads to the locally-influenced form of CPT.

- $\frac{\omega}{sV_\infty}$: essentially an expression for the reduced frequency based on the local distance from the leading-edge, this involves the expansion of

$$\frac{1}{\mu} = \frac{1}{m_\infty s}\left[1 + \frac{M_\infty^2}{m_\infty^2}\left(2\mathrm{i}\varepsilon + \varepsilon^2\right)\right]^{-\frac{1}{2}}, \tag{3.76}$$

where $\varepsilon = \frac{\omega}{sV_\infty}$ becomes the local reduced frequency after inversion to the physical domain. The perturbation pressure is presented in a variety of forms by Dowell and Ganji [160]. It is presented here as

$$\bar{p} = \rho_\infty a_\infty \frac{M_\infty}{m_\infty}\mathscr{L}^{-1}\left\{\left(1 + \mathrm{i}B_1\varepsilon + B_2\varepsilon^2 + \mathrm{i}B_3\varepsilon^3 + \ldots\right)\mathscr{L}(\bar{w})\right\}, \tag{3.77}$$

where the coefficients B_i are functions of Mach number alone, and are defined in the publication by Dowell and Ganji [160]. The inversion of the expression in Eq. (3.77) leads to a lengthy series of terms. These involve correction terms of the form:

  - $\left(\frac{\omega}{V_\infty}\right)^n C_n I_{n-1}$, where I_{n-1} represents $n-1$ successive integrals with respect to the streamwise variable and the coefficients C_n are functions of the Mach number only,
  - $\left(\frac{\omega}{V_\infty}\right)^n B_n x^{n-1}$, where x is the streamwise coordinate as measured from the leading edge.

Nonetheless, it is worth noting that if the expression is truncated such that terms in $\mathscr{O}\left(\varepsilon^2\right)$ are discarded, the remaining expression may be written as

$$\bar{p}(x) = \rho_\infty a_\infty \frac{M_\infty}{m_\infty}\left\{\left[\left(\frac{M_\infty^2 - 2}{M_\infty^2 - 1}\right)\mathrm{i}\omega\bar{z}(x) + V_\infty\frac{\partial\bar{z}(x)}{\partial x}\right] - \left[-\frac{1}{m_\infty^2}\mathrm{i}\omega\bar{z}(0) + V_\infty\bar{z}(0)\delta(x)\right]\right\}, \tag{3.78}$$

where $\delta(x)$ is defined such that $\bar{z}(x)\delta(x)$ represents the maximum inclination of the local surface to the freestream. Comparison of the first bracketed term shows the equivalence of the formulation to the "low-frequency" piston theory formulation of Eq. (3.64). Inspection of the second bracketed term shows that it is concerned with the change in conditions at the leading-edge. This latter consideration is typically neglected in CPT, with the exception being formulations such as that by Fung [163], who accounts for the $-\frac{1}{m_\infty^2}\mathrm{i}\omega\bar{z}(0)$ term.

While the full form of the pressure equation obtained by expansion in powers of reduced frequency is not shown here, the significance of the additional terms relative to "low-frequency" piston theory is evident. The additional terms are corrections

which account for the deviation from the limit of $k \to 0$. As the reduced frequency is increased, higher-order terms in ε are required to improve the approximation to the exact linear solution. These additional terms involve the propagation of upstream perturbations.

The attention is now turned to the nonlinear (in terms of thickness) method of Landahl [128]. As stated earlier, the basis of Landahl's [128] method lies in Van Dyke's [104] second-order theory for supersonic potential flows. A brief overview of key steps in the development will be given to highlight the differences between Landahl's [128] method and other "extended piston theories" such as that of Dowell and Bliss [144].

The perturbation potential function ϕ of in the full nonlinear potential equation of Eq. (2.43) is to be replaced by $\varphi + \psi$. Here, $\varphi = \mathscr{O}(\delta)$ is the first-order (in thickness) perturbation potential, and $\psi = \mathscr{O}\left(\delta^2\right)$ is the second-order (in thickness) perturbation potential. For the sake of clarity, the surface boundary condition of Eq. (2.44) will be elaborated on. Consider an surface defined such that

$$z = \delta h(x,y,t)\,, \tag{3.79}$$

represents the body surface. Within the context of the piston-cylinder analogy, a point on the surface of the body will produce the following apparent downwash in a cylinder oriented along the z-axis:

$$w = \delta(h_t + V_\infty h_x)\,. \tag{3.80}$$

However, the non-permeability condition at the surface yields the following full surface boundary condition:

$$\phi_z(x,y,\delta h,t) = (V_\infty + \phi_x)\delta h_x + \phi_y \delta h_y + \delta h_t\,. \tag{3.81}$$

Following the development due to Landahl [128], if the z-component of fluid velocity at the surface is expressed as a Taylor series about $z = 0$, then the following second-order relation is obtained:

$$\phi_z(x,y,0,t) = \delta w + \delta\left.\left(h_x\phi_x + h_y\phi_y - h_z\phi_{zz}\right)\right|_{z=0}\,. \tag{3.82}$$

The relation for the pressure coefficient C_p may similarly be expressed up to second-order, following Landahl's [128] development, as

$$C_p = -\frac{1}{V_\infty^2}\left[2(\phi_t + V_\infty\phi_x) - M_\infty^2(\phi_t + V_\infty\phi_x)^2 + \left(\phi_x^2 + \phi_y^2\right)\right]_{z=0}$$

$$-\frac{\delta^2}{V_\infty^2}\left[w^2+2h\left(V_\infty\frac{\partial}{\partial x}+\frac{\partial}{\partial t}\right)^2 h\right], \tag{3.83}$$

The full nonlinear governing equation of Eq. (2.43) is not repeated here. At this point, Landahl [128] substituted $\phi=\varphi+\psi$ into Eqs. (2.43), (3.82) and (3.83). Grouping terms in $\mathscr{O}(\delta)$ results in the following first-order (in thickness) problem:

$$\text{Governing:}\quad \left(1-M_\infty^2\right)\varphi_{xx}+\varphi_{yy}+\varphi_{zz}-\frac{2M_\infty}{a_\infty}\varphi_{xt}-\frac{1}{a_\infty^2}\varphi_{tt}=0\,, \tag{3.84}$$

$$\text{Surface BC:}\quad \varphi_z(x,y,0,t)=w\,. \tag{3.85}$$

Thus, the linearized potential equation in terms of φ is recovered at $\mathscr{O}(\delta)$. Grouping terms in $\mathscr{O}\left(\delta^2\right)$ results in the following second-order (in thickness) problem:

$$\begin{aligned}\text{Governing:}\quad &\left(1-M_\infty^2\right)\psi_{xx}+\psi_{yy}+\psi_{zz}-\frac{2M_\infty}{a_\infty}\psi_{xt}-\frac{1}{a_\infty^2}\psi_{tt}=\\ &\frac{(\gamma-1)}{a_\infty^2}(\varphi_t+V_\infty\varphi_x)(\varphi_{xx}+\varphi_{yy}+\varphi_{zz})+\left(\frac{\partial}{\partial t}+V_\infty\frac{\partial}{\partial x}\right)\left(\varphi_x^2+\varphi_y^2+\varphi_z^2\right),\end{aligned} \tag{3.86}$$

$$\text{Surface BC:}\quad \psi_z(x,y,0,t)=\left(h_x\varphi_x+h_y\varphi_y-h\varphi_{zz}\right)_{z=0}. \tag{3.87}$$

This highlights the essense of Van Dyke's [104] second-order theory. The full nonlinear potential equation, at $\mathscr{O}\left(\delta^2\right)$, may be considered as a linear potential equation in terms of the second-order potential ψ, with the RHS of the equation representing additional source terms. These source terms are defined in terms of the first-order potential φ. Thus, solving the first-order (in thickness) problem renders these terms known quantities, and allows for the second-order potential to be solved. Inspection of the surface boundary condition shows that the perturbations to the fluid velocity only begin to contribute from the second-order problem onwards.

The essence of Landahl's [128] method lies in the procedure adopted to solve the first-order and second-order potential problems. The first-order (in thickness) problem is identically a linear problem in φ. The application of Laplace transforms to obtaining the linear potential φ has been reviewed in the proceeding methods. It is reiterated here that the exact Laplace inversion yields the exact solution to the linear potential φ, which involves the Bessel function. Various approximations to the inversion were reviewed in the context of the work by Dowell and Ganji [160]. Landahl's [128] approach to the solution of the first-order (in thickness) potential equation is essentially equivalent to the expansion in powers of M_∞^{-2} treated by Dowell and Ganji [160].

However, the application of Van Dyke's [104] method renders the second-order (in thickness) problem linear (in terms of ψ) as well. With the first-order solution known, this allows the second-order solution to be found using similar Laplace transform approaches. Landahl's [128] approximation to the exact potentials φ and ψ is given by the following expansions:

$$\varphi = \frac{\delta}{M_\infty}\left(\varphi_1 + \frac{\varphi_2}{M_\infty^2} + \frac{\varphi_3}{M_\infty^4}\right) + \ldots, \tag{3.88}$$

$$\psi = \delta^2\left(\psi_1 + \frac{\psi_2}{M_\infty^2}\right) + \ldots, \tag{3.89}$$

which is seen to be an expansion in powers of M_∞^{-2}. Thus, Landahl's [128] method involves two physically different approximations:

- An expansion of the total potential ϕ in powers of thickness δ, yielding $\phi = \delta(\ldots) + \delta^2(\ldots) + \mathscr{O}\left(\delta^3\right)$. This is needed to transform the nonlinear problem into two linear problems,

- An expansion of the first- and second-order (in thickness) potential functions in powers of M_∞^{-2}, as described in Eqs. (3.88) and (3.89). This is allows the solution to be expressed as a sum of simpler computations,

Landahl [128] applied the expansions of Eqs. (3.88) and (3.89) to the pressure coefficient as well, and correlated terms to the solutions obtained for the potential functions φ and ψ. Landahl's [128] nomenclature for the pressure-coefficient expansion is described by

$$C_p = \frac{\delta}{M_\infty}\left(C_{p1}^{(\varphi)} + \frac{C_{p2}^{(\varphi)}}{M_\infty^2} + \frac{C_{p3}^{(\varphi)}}{M_\infty^4}\right) + \delta^2\left(C_{p1}^{(\psi)} + \frac{C_{p2}^{(\psi)}}{M_\infty^2}\right) + \mathscr{O}\left(\frac{\delta}{M_\infty^7} + \frac{\delta^2}{M_\infty^4}\right), \tag{3.90}$$

in which the terms $C_{pn}^{(\varphi)}$ denote the contribution from the first-order thickness problem (hence φ) and from the n-th term in the expansion in powers of M_∞^{-2}. In this sense, $n = 1$ represents the $M_\infty \to \infty$ approximation, with higher n extending the model to lower Mach numbers. Similarly, terms in the form of $C_{pn}^{(\psi)}$ represent the contribution associated with nonlinear thickness. Considering that first-order CPT has been shown to be the limit of the linear potential solution as $M_\infty \to \infty$, it is not surprising that Landahl's [128] method recovers second-order CPT in the same limit. In Landahl's [128] notation,

$$C_{p1}^{(\varphi)} = 2w, \tag{3.91}$$

$$C_{p1}^{(\psi)} = \left(\frac{\gamma+1}{2}\right) w^2 \,, \tag{3.92}$$

which may be compared to Lighthill's coefficients in Eqs. (3.11) and (3.12) with due consideration of the definition of Eq. (3.90). The corresponding terms for $n > 1$ are not repeated here, and may be found in the publication of Landahl [128]. These are integro-differential terms which account for the delay in propagation of upstream disturbances.

In closing, it is remarked that the implementation of Van Dyke's [104] method to render the second-order (in thickness) problem linear could be used to extend the "extended piston theories" of Dowell and Bliss [144] and Aravinth et al [145] to second-order in thickness. Alternatively, the methods of the latter authors could be used to extend Landahl's [128] method to arbitrary reduced frequencies.

Methods Using "Low-Frequency" Piston Theory

Finally, it is noted in closing that the "low-frequency" form of linear CPT derived from a linear potential flow basis has been widely adopted by various authors in panel flutter studies. Variations in the formulation are slight, with the basic formulation (as used by Dugundji [161] and by Dowell and Voss [162], among numerous others) given as

$$p = p_\infty + \rho_\infty a_\infty \frac{M_\infty}{m_\infty} \left\{ \left(\frac{M_\infty^2 - 2}{M_\infty^2 - 1}\right) \frac{\partial}{\partial t} + V_\infty \frac{\partial}{\partial x} \right\} z(x,y,t) \,, \tag{3.93}$$

where z is the thickness-direction displacement of the surface, and $m_\infty = \sqrt{M_\infty^2 - 1}$. This may be compared to Eq. (3.8). It is seen that Eq. (3.93) is equivalent to a first-order CPT pressure formulation with a first-order coefficient c_1 due to Van Dyke, as in Eq. (3.24). This is suggestive of its validity at lower supersonic speeds than a formulation using Lightill's coefficient, as in Eq. (3.11). Further comparison of Eq. (3.93) to Eqs. (3.3) and (3.4) shows that the downwash definition is altered. While the stiffness-related term (Eq. (3.4), or $V_\infty \frac{\partial z}{\partial x}$) is unchanged, the damping-related term has been modified. The form due to Eq. (3.93) may be interpreted as having a reduced effective damping, which is seen to become negative for $M_\infty < \sqrt{2}$.

A slight variation is noted in the formulation of Fung [163], who accounts for the contribution from the leading-edge of the panel through

$$p = p_{inner} + \rho_\infty a_\infty \frac{M_\infty}{m_\infty} \left\{ \left(\frac{1}{M_\infty^2 - 1}\right) \frac{\partial}{\partial t} \right\} z(0,y,t) \,, \tag{3.94}$$

where p_{inner} is the pressure on the inner field of the plate, given by Eq. (3.93), and the second term gives the contribution from the leading-edge boundary of the plate.

3.2.6 Extension to Non-Planar Flows

The extension of piston theory to non-planar geometries and flows was accomplished by a variety of approaches. These range from empirical applications of strip theory, through to more mathematically rigorous developments. The extension of linear CPT to three-dimensional flows as achieved through potential-flow methods by Landahl [128] and by Aravinth et al [145] has been noted in Section 3.2.5. The potential-flow basis has also been used to extend the method to axisymmetric flows, as will be discussed shortly. Non-planar flows are of fundamental interest, as most geometries of engineering interest exhibit regions of non-uniform, non-planar flows. Some of the notable efforts towards extending the application of piston theory to such flows may thus be categorized according to the geometry considered:

- Works concerned with flutter of cylindrical shells and axisymmetric flows, such as those by Leonard and Hedgepeth [168], Krumhaar [169, 170], and Ghosh [140],
- Works concerned with the flutter of finite, flat panels, such as those by Vedeneev [148, 158],
- Works in which upstream influence on finite wings is accounted for rigorously, such as those by Landahl [128], Aravinth et al [145], Liu and Hui [171], and Liu et al [125],
- Works in which upstream influence on finite wings is account for heuristically, such as those by Chen [172] and Wang [173],
- Works in which strip theory is applied to finite wings, such as those by Chen [174], Yang and Song [175], and Ghosh [141].

As was noted in Section 3.2.5, a certain amount of overlap is inevitable in discussing the contributions to piston theory according to the categorizations used in Section 3.2. In particular, a number of works discussed in Sections 3.2.5 and 3.2.8 are rooted in a three-dimensional basis. The focus of the present section, however, will be on the variety of approaches adopted towards extending piston theory to non-planar flows.

Cylindrical Shells and Axisymmetric Flows

A parallel to the treatment of methods with a potential-flow basis in Section 3.2.5 may be drawn here. The exact solution to the linear-potential problem for axisymmetric flow

down the axis of an infinite cylindrical shell was given by Leonard and Hedgepeth [168]. A depiction of a portion of the representative geometry is given in Fig. 3.17. No reduction or correlation to piston theory was made. In determining the exact solution, Leonard and Hedgepeth [168] assumed that the deflection of the shell, which will be denoted $z(x,\theta,t)$, was given in the form of

$$z(x,\theta,t) = \mathrm{Re}\{\bar{z}\exp(-\mathrm{i}N_x x)\exp(\mathrm{i}\omega t)\cos N_\theta\theta\}\,, \tag{3.95}$$

where $\bar{z}$ is the complex amplitude of the shell displacement, ω is the frequency of oscillation, N_x is the longitudinal wave number, and N_θ is the number of full waves around the circumference of the section. It is to be noted that a slightly different nomenclature for $z(x,\theta,t)$ is adopted here than that depicted in Fig. 3.17. Leonard and Hedgepeth [168] gave the corresponding perturbation pressure as

$$p(x,\theta,t) = RN_x^2\,\mathrm{Re}\{\bar{p}\bar{z}\exp[-\mathrm{i}(N_x x-\omega t)]\}\,, \tag{3.96}$$

$$\bar{p} = -\rho_\infty a_\infty^2 F(M_\infty - k, RN_x, N_\theta) + \rho_i a_i^2 F_i(a_\infty k/a_i, RN_x, N_\theta)\,, \tag{3.97}$$

where R is the radius of curvature of the panel in the circumferential direction, and the subscript "i" denotes quantities associated with any fluid contained within the cylindrical shell. The reduced frequency $k = \frac{\omega}{N_x a_\infty}$ may also be interpreted as the Mach number of axial travelling waves. The functions F and F_i are given by Leonard and Hedgepeth [168] as

$$F(\xi,RN_x,n) = \begin{cases} \xi^2\dfrac{K_n(\zeta)}{\zeta K_n'(\zeta)}, & |\xi|<1 \\ \xi^2\dfrac{H_n^{(j)}(z)}{zH_n'^{(j)}(z)}, \quad \text{with} \quad j=\begin{cases}1 & \text{for} \quad RN_x\xi>0\\ 2 & \text{for} \quad RN_x\xi<0\end{cases}, & |\xi|>1 \end{cases} \tag{3.98}$$

$$F_i(\xi,RN_x,n) = \begin{cases} \xi^2\dfrac{I_n(\zeta)}{\zeta I_n'(\zeta)}, & |\xi|<1 \\ \xi^2\dfrac{J_n(z)}{zJ_n'(z)}, & |\xi|>1 \end{cases} \tag{3.99}$$

where $\zeta = |RN_x|\sqrt{1-\xi^2}$, $z = |RN_x|\sqrt{\xi^2-1}$, J_n is the Bessel function of the first kind, $H_n^{(j)}$ is the Hankel function of the first or second kind, and I_n and K_n are modified Bessel functions of the first and second kinds, respectively. The n in the subscript of these functions denotes the order of the Bessel functions, and is equal to N_θ. The primed functions denote the derivative of the function with respect to the entire argument of the function.

$$z(x,\theta,t) = A s_x(x) s_\theta(\theta) \exp(\mathrm{i}\omega t), \qquad \begin{matrix} s_x(x) = \sin(N_x x) & \text{or} & \cos(N_x x) \\ s_\theta(\theta) = \sin(N_\theta \theta) & \text{or} & \cos(N_\theta \theta) \end{matrix}$$

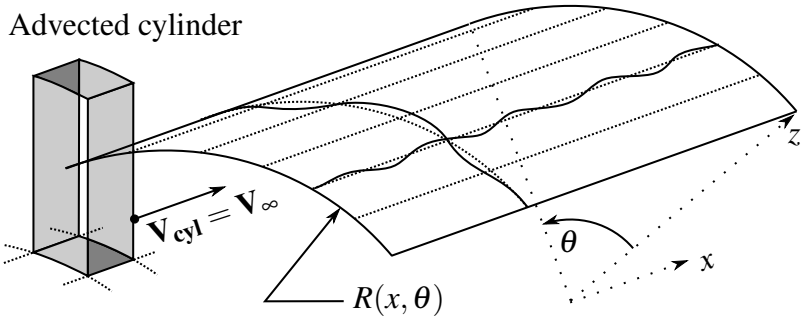

Fig. 3.17 Illustration of the configuration considered in Krumhaar's [169] method, with equivalent piston-theory cylinder shown.

A significant simplification of the exact result of Leonard and Hedgepeth [168] was achieved by Krumhaar [169, 170]. Krumhaar introduced the notation

$$M_1 = M_\infty - \frac{\omega}{N_x a_\infty}, \tag{3.100}$$

$$M_2 = M_\infty + \frac{\omega}{N_x a_\infty}, \tag{3.101}$$

to denote the Mach number of the flow relative to downstream-travelling and upstream-travelling waves due to vibrations in the surface. This may be correlated to ξ in the notation of Eqs. (3.98) and (3.99). Krumhaar [169, 170] used the asymptotic form of the Hankel functions in the limit of $|RN_x|\sqrt{\xi^2-1} \to \infty$ to obtain a series representation of the functions. Special attention was given to the case of $|M_1| > 1$, $|M_2| > 1$, as Krumhaar [169, 170] found that the asymptotic form of the exact solution could be correlated to CPT for this case. In terms of Eq. (3.98), this corresponds to $|\xi| > 1$. The resulting expression for the exact perturbation pressure (in the asymptotic limit) was given as

$$\begin{aligned} p = \rho_\infty a_\infty \left(\frac{\partial z}{\partial t} + V_\infty \frac{\partial z}{\partial x}\right) + \frac{p_\infty a_\infty^2}{2}\left[\sum_{i=0}^{3} \frac{1}{R^i}\left(F_i z + F_i^* \frac{\partial z}{\partial x}\right) - \mathrm{i}N_x(M_2 - M_1)z - (M_1 + M_2)\frac{\partial z}{\partial x}\right] \\ + z\left[\mathscr{O}\left(\frac{1}{N_x^3 R^4}\frac{1}{M_1^3\left(1-M_1^{-2}\right)^{5/2}}\right) + \mathscr{O}\left(\frac{1}{N_x^3 R^4}\frac{1}{M_2^3\left(1-M_2^{-2}\right)^{5/2}}\right)\right] \\ + \frac{\partial z}{\partial x}\left[\mathscr{O}\left(\frac{1}{N_x^4 R^4}\frac{1}{M_1^3\left(1-M_1^{-2}\right)^{5/2}}\right) + \mathscr{O}\left(\frac{1}{N_x^4 R^4}\frac{1}{M_2^3\left(1-M_2^{-2}\right)^{5/2}}\right)\right], \end{aligned} \tag{3.102}$$

in which the first term-grouping is the linear term in CPT. Krumhaar [169, 170] remarked that the second term grouping represented "correction terms" to the linear CPT term. The remaining terms were noted to tend to zero if at least one of the following parameters tended to ∞: $|M_\infty|$, R, ω, or $|N_x|$. The correction terms were defined by

$$F_i = \frac{\mathrm{i}A_i^*}{N_x^{i-1}} B_i \,, \tag{3.103}$$

$$F_i^* = \frac{A_i^*}{N_x^i} B_i^* \,, \tag{3.104}$$

$$B_i = \frac{(-1)^{i-1}}{M_1^{i-1}\left(1-M_1^{-2}\right)^{\frac{i+1}{2}}} + \frac{1}{M_2^{i-1}\left(1-M_2^{-2}\right)^{\frac{i+1}{2}}} \,, \tag{3.105}$$

$$B_i^* = \frac{(-1)^{i}}{M_1^{i-1}\left(1-M_1^{-2}\right)^{\frac{i+1}{2}}} + \frac{1}{M_2^{i-1}\left(1-M_2^{-2}\right)^{\frac{i+1}{2}}} \,, \tag{3.106}$$

$$A_i^* = \begin{cases} 1, & \text{for} \quad i=0 \\ \mathrm{i}/2, & \text{for} \quad i=1 \\ \frac{1}{2}\left(N_\theta^2 - \frac{3}{4}\right), & \text{for} \quad i=2 \\ \mathrm{i}\left(N_\theta^2 - \frac{3}{8}\right), & \text{for} \quad i=3 \end{cases} , \tag{3.107}$$

It is worth noting that the correction terms do not involve integrals, and are effectively corrections to the downwash definition. The lack of integrals stems from the assumption of Leonard and Hedgepeth [168] of an infinitely long cylinder with sinusoidally varying displacement. It is also noted that the circumferential wave number only enters the correction terms through terms of $\mathscr{O}\left(1/R^2\right)$. Krumhaar [169, 170] remarked that for large values of N_θ, with $N_\theta \leq 20$ often considered in shell flutter, these higher-order terms may become important. Krumhaar [169, 170] considered the asymptotic behaviour of the correction terms in various limits. It is repeated here that the limits are considered simultaneously with the conditions

$$|RN_x|\left[\left(M_\infty - \frac{\omega}{N_x a_\infty}\right)^2 - 1\right]^{\frac{1}{2}} \to \infty, \quad |RN_x|\left[\left(M_\infty + \frac{\omega}{N_x a_\infty}\right)^2 - 1\right]^{\frac{1}{2}} \to \infty \to \infty, \tag{3.108}$$

The results have been summarized in Table 3.2. Krumhaar's [169, 170] analysis for cylindrical shells with axial flow showed that:

- Linear CPT is the asymptotic form of the exact linearized potential-flow solution in the limit of one of the following:

Table 3.2 Summary of Krumhaar's [169, 170] asymptotic linear-potential pressure relations for cylindrical shells in axial flows.

Limit	$F_i/R^i \to 0$ for	$F_i^*/R^i \to 0$ for	Asymptotic form of exact linear-potential pressure p:
$\lvert M_\infty\rvert, R \to \infty$, or $R, \omega \to \infty$, or $\lvert N_x\rvert, \lvert M_\infty\rvert, R \to \infty$	$i = 1,2,3$	$i = 1,2,3$	$p \to p_{PT}$ (3.109)
$\lvert M_\infty\rvert \to \infty$, or $\omega \to \infty$, or $\lvert N_x\rvert, \lvert M_\infty\rvert \to \infty$	$i = 0,2,3$	$i = 0,1,2,3$	$p \to p_{PT} - \dfrac{\rho_\infty a_\infty^2}{2R} z$ (3.110)
$\lvert N_x\rvert \to \infty$	$i = 2,3$	$i = 1,2,3$	$p \to p_{PT} + \rho_\infty a_\infty \left[\left(\dfrac{\lvert M_\infty\rvert}{m_\infty} \right) \left(\dfrac{M_\infty^2 - 2}{M_\infty^2 - 1} \right) \dfrac{\partial z}{\partial t} + \left(\dfrac{\lvert M_\infty\rvert}{m_\infty} \right) V_\infty \dfrac{\partial z}{\partial x} - \dfrac{M_\infty^2}{m_\infty^2} \dfrac{a_\infty}{2R} z - \dfrac{p_{PT}}{\rho_\infty a_\infty} \right]$ (3.111)
$R \to \infty$	$i = 1,2,3$	$i = 1,2,3$	$p \to p_{PT} + \dfrac{\rho_\infty a_\infty^2}{2} \left[\mathrm{i} N_x \left(-\dfrac{M_1}{\sqrt{1 - M_1^{-2}}} + \dfrac{M_2}{\sqrt{1 - M_2^{-2}}} + M_1 - M_2 \right) z + \left(\dfrac{M_1}{\sqrt{1 - M_1^{-2}}} + \dfrac{M_2}{\sqrt{1 - M_2^{-2}}} - M_1 - M_2 \right) \dfrac{\partial z}{\partial x} \right]$ (3.112)

  - High Mach number and low cross-stream curvature, with $M_\infty \to \infty$ and $R \to \infty$,
  - High temporal frequency of oscillations and low cross-stream curvature, with $\omega \to \infty$ and $R \to \infty$,

- Linear CPT with an additional damping term, as described in Eq. (3.110), is the asymptotic form of the exact linearized potential-flow solution in the limit of one of the following:

  - High Mach number, with $M_\infty \to \infty$,
  - High temporal frequency of oscillations, with $\omega \to \infty$,

  This form of CPT is often referred to as "piston theory with curvature correction",

- The "low-frequency" form of CPT previously discussed in Section 3.2.5, together with the aforementioned "curvature correction term" is the asymptotic form of the exact linearized potential-flow solution in the limit of large axial wave number, with $N_x \to \infty$. The resulting equation is given in Eq. (3.111). This may be interpreted as a low spatial-frequency, or a large axial wavelength of displacements. It is noted that reduction to Eq. (3.93) is achieved by taking the additional limit of $R \to \infty$,

- Substantial corrections to linear CPT are required if the only limit considered is that of non-axisymmetric flow as $R \to \infty$. This is reflected in the form of Eq. (3.112).

Similarly substantial corrections to linear CPT are required if the relative Mach numbers M_1 or M_2 are subsonic. These scenarios are considered in [170].

Finally, the extension of piston theory to axisymmetric flows about quasi-cones by Ghosh [140] is considered. The application of the law of plane sections to slender quasi-cones at zero incidence and the subsequent derivation of pressure relations by Il'yushin [77] has already been noted in Section 3.2.4. Ghosh [140] essentially extends the analysis to non-slender quasi-cones. Ghosh [140] shows that in a space-fixed coordinate system initially aligned with the body surface at $t = 0$, the 2D unsteady Euler equations may be reduced to 1D unsteady equations along the axis normal to the body surface at $t = 0$. This reduction is accurate to $\mathscr{O}(\varepsilon \tan \delta)$ for axisymmetric flows, where the angle between the shock and the body is $\beta - \delta = \mathscr{O}(\varepsilon)$ with $\varepsilon \ll 1$. Ghosh [140] estimates that these conditions hold provided that the Mach number behind the shock is $M_m \geq 2.5$. In essence, this is an axisymmetric application of the unsteady analogy, with the conico-annular cylinder defined normal to the generating ray of the cone at $t = 0$. This is illustrated in Fig. 3.18. The pressure relation

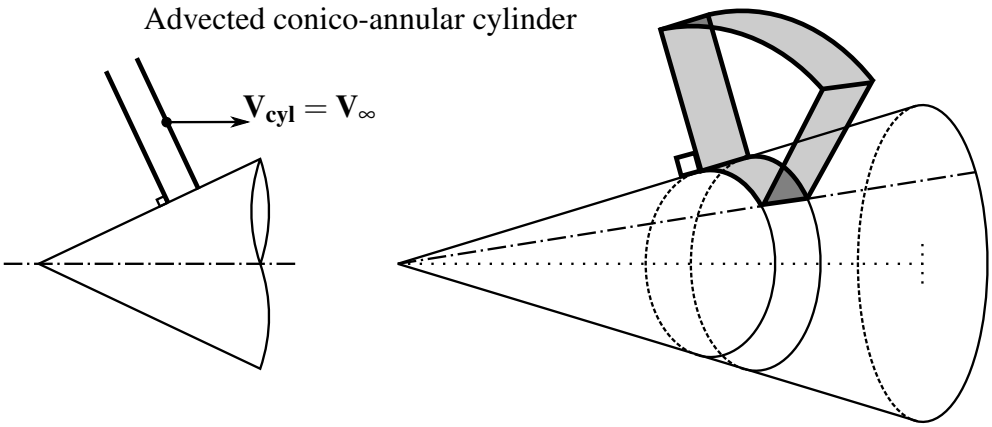

Fig. 3.18 Illustration of the configuration considered in Ghosh's [140] piston theory for cones.

given by Ghosh [140] for axisymmetric flow over the quasi-cone is repeated below as

$$\frac{p}{p_\infty} = 1 + \gamma M_p^2 \left\{ 1 + \frac{1}{4} \left[\frac{2 + (\gamma - 1) M_p^2}{2 + (\gamma + 1) M_p^2} \right] \right\}, \tag{3.113}$$

$$M_p \equiv \frac{w}{a_\infty} = M_\infty \sin \delta \,. \tag{3.114}$$

Flat Plates of Finite Width

A thorough introduction to historical developments in aerodynamic modelling of panel flutter is given by Vedeneev in [158]. Vedeneev noted the shortcomings of piston theory, particularly for $M_\infty < \sqrt{2}$. In particular, the existence of single-mode flutter could not be predicted by CPT. However, Vedeneev [158] also noted that series-expansion approximations to the exact linear-potential solution, such as the "extended piston theory" of Dowell and Bliss [144] and of Ganji and Dowell [176], correctly predicted the single-mode flutter phenomenon. Vedeneev [158] also gave a review of the application of higher-fidelity aerodynamic models. Vedeneev applied the exact 3D linear-potential formulation to finite aspect-ratio rectangular plates and compared the solution to that obtained by CPT. Marked improvement in the linear CPT prediction was obtained at $M_\infty < 4$ through the use of Van Dyke's coefficient as per Eq. (3.24) in place of Lighthill's coefficient of Eq. (3.11). The modified results were accurate down to $M_\infty = 2$ for $AR > 1$. Accurate predictions at lower Mach numbers were obtained only for higher aspect ratios. Nonetheless, the piston theory models could not replicate the single-mode flutter which dominates at $M_\infty < \sqrt{2}$.

In this sense, Vedeneev [158] essentially demonstrated that CPT may be applied to finite plates, provided the Mach number is sufficiently removed from $M_\infty = \sqrt{2}$, and provided the aspect ratio of the plate is sufficiently higher than 1. As these bounds are approached, more exact aerodynamic methods are required. The application of the 3D extended piston theory due to Aravinth et al [145] is expected to correctly predict the occurence of single-mode flutter, and may be viewed as an alternative to exact linear-potential flow formulations (such as that due to Vedeneev [158]).

Finite Wings

A variety of justifications for the application of piston theory (in one form or another) to finite wings may be encountered in the literature. Representative works in this category may be classed as

- Works which rigorously account for three-dimensional influence. "Rigorous" in the present sense means that the account of 3D influence is theoretically consistent or mathematically justified. These works may be further categorized as works in which
  - Piston theory is a special case of higher-fidelity methods in uniform-flow regions. The work of Liu and Hui [171] is representative of this approach,
  - A potential-flow basis is used, with CPT as the leading term in a series accounting for upstream influence. The works of Landahl [128] and of Aravinth et al [145] are representative,
  - Potential-flow computations are supplemented by CPT to provide nonlinear thickness effects. This is the modelling philosophy behind the ZONA7U software developed by Liu et al [125],
- Works in which piston theory computations are heuristically adjusted for 3D effects in the flow. Representative works include the methods of Chen [172] and Wang [173],
- Works in which strip theory is applied to allow the use of two-dimensional methods. The majority of works which apply piston theory to non-planar flows adopt this approach. Representative works include those of Yang and Song [175], Chen [174], and Ghosh [141].

The work of Liu and Hui [171] is a small-disturbance theory for oscillating delta wings with attached shocks. The underlying assumptions in the development are essentially similar to other theories of Hui [177] as presented in Section 3.2.8. In particular, it is assumed that the reduced frequency k and amplitude ε of oscillation are both small, such that $k, \varepsilon \ll 1$. The

resulting formulation is linear both in amplitude and frequency. The mathematical treatment and the closed-form results are lengthy, and are presented in [171]. Here, it will only be noted that separate formulations arise in uniform-flow and in conical-flow regions. Such regions are depicted in Fig. 3.19. Within the uniform-flow regions, Hui's [177, 178] theory for oscillating wedges applies. As is discussed in Section 3.2.8, this contains LPT as a special case when the reflection of acoustic waves from the bow shock is neglected. In this sense, the work of Liu and Hui [171] provides an additional mathematically-based justification for the application of piston theory in uniform-flow regions of finite wings.

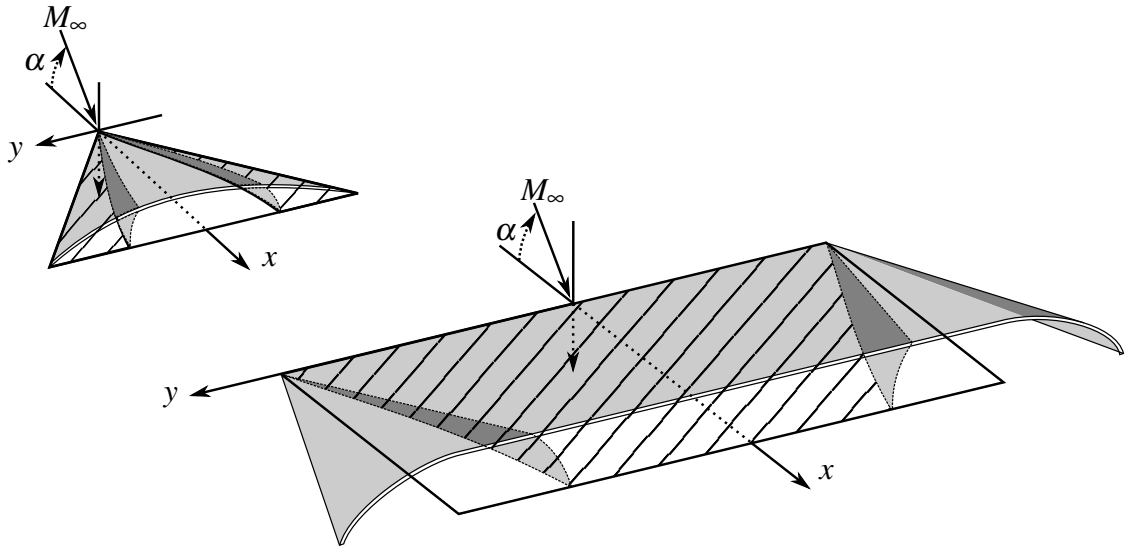

Fig. 3.19 Illustration of uniform-flow regions (hatched areas) and approximate Mach cones on the windward side of finite wings.

The method of Landahl [128] was rooted in a 3D potential flow formulation, and has been discussed in Section 3.2.5. Similarly, the basis for the method of Aravinth et al [145] is a linear-potential flow formulation which is simply a three-dimensional interpretation of the methods of Dowell and Bliss [144] and of Ganji and Dowell [176]. These latter methods have been discussed in Section 3.2.5.

The modelling philosophy of Liu et al [125] in developing ZONA7U is now considered. The linear potential formulation was adopted in modelling 3D upstream influence on the finite wing. The resulting aerodynamic-influence-coefficient matrix is supplemented by an additional matrix accounting for nonlinear thickness effects. In the notation of Liu et al [125], this is written as

$$([\mathbf{D}]+[\mathbf{E}])\{\Delta C_p\} = \{w_b\}, \tag{3.115}$$

where $\{\Delta C_p\}$ is the vector of total lifting pressures between the lower and upper surfaces of the wing, $\{w_b\}$ is the vector of unsteady downwash (essentially equivalent to Eq. (3.6)), [**D**] is the aerodynamic-influence-coefficient (AIC) matrix from linear potential flow, and [**E**] is the AIC matrix accounting for nonlinear thickness effects. As noted by Liu et al [125], the latter matrix may be obtained from a variety of methods. One suggested method is the application of strip theory and of the perturbed Euler characteristic method of Chavez and Liu [179] (itself a numerical implementation of Hui's [177, 178] theory for oscillating wedges). In this case, [**E**] contains strip-wise upstream influence. The practical implementation in ZONA7U uses third-order CPT to generate the supplementary matrix. Because CPT does not account for upstream influence, [**E**] is a diagonal matrix of self-influenced terms in this case. In this sense, the work of Liu et al [125] uses CPT as an extension to nonlinear thickness for an underlying three-dimensional linear potential flow model. While the supplemental application of CPT borders on heuristic, the account of three-dimensionality by the linear potential base-solution is rigorous.

A number of methods adopt a more heuristic approach to modelling 3D influence in the application of piston theory. Chen 1989 [172] used the Hui's [177] 2D theory for oscillating wedges as a base method for computing pressures with an account of stripwise upstream influence. This is applied to rectangular wings of finite span. As expected from Fig. 3.19, good prediction was obtained within the uniform-flow portion of the wing. The three-dimensionality at the wing tips was accounted for by Chen 1989 [172] through a pressure scaling-factor. This may be defined as

$$P_{SF}(x,y) = \frac{P_{3D}(x,y)}{P_{2D}(y)}\,, \tag{3.116}$$

where P_{SF} is the scaling factor, P_{3D} is the pressure predicted by 3D linear supersonic theory, and P_{2D} is the pressure in the uniform-flow region of the wing as predicted by 3D linear supersonic theory. This pressure-scaling factor was used to adjust the pressure predicted by Hui's [177] method (which contains LPT as a special case). This may be written as

$$P_{Chen}(x,y) = P_{SF}(x,y)P_{Hui}(x,y)\,. \tag{3.117}$$

A similar approach was adopted by Wang [173]. Wang's definition of the pressure-scaling factor differed somewhat, and may be written as

$$P_{SF}(x,y) = \frac{P_{3D}(x,y)}{\tilde{P_{3D}}(y)}\,, \tag{3.118}$$

where P_{3D} is the pressure predicted from linear supersonic theory, and $\tilde{P_{3D}}$ is a stripwise weighted-average of the conical flow pressure. The definition of $\tilde{P_{3D}}$ differs for subsonic and supersonic leading-edges, and is given in the original publication by Wang [173]. The pressure prediction from CPT was then adjusted by the pressure-scaling factor to heuristically account from three-dimensionality as

$$P_{Wang}(x,y) = P_{SF}(x,y)P_{CPT}(x,y)\,. \tag{3.119}$$

Finally, as mentioned earlier, in a wide range of works, strip theory is applied in order to apply 2D methods to finite wings. This has been applied to both CPT, as by Ghosh [141], as well as LPT, as by Yang and Song [175] and by Chen [174]. This is not discussed further here.

3.2.7 LPT as a Heuristic Method

The first suggestion to use the local mean-steady fluid state for the definition of cylinder conditions in Eq. (3.8) was made by Morgan et al [131]. This suggestion was made in the context of theoretical considerations of flutter at "extreme" Mach numbers. Morgan et al [131] noted that the "local flow piston theory" presented the possibility of studying mean angle-of-attack effects on the flutter boundary. The theoretical case study considered by Morgan et al [131] was a 4% thickness double-wedge airfoil within the Mach range of $3 \leq M_\infty \leq 10$. The mean-steady solution was obtained using the oblique-shock relations. The difference between "local flow piston theory" and CPT was considered to be small, and no further consideration was given to the method. Furthermore, it is unclear whether the downwash equation was updated to reflect the local cylinder advection speed as in Eq. (3.2). Nevertheless, the work of Morgan et al [131] may be considered the first formulation of LPT based in heuristic reasoning. Morgan et al [131] also considered the possibility of using Newtonian flow to model the blunted leading edges of airfoils, with a transition to CPT over the portion of the airfoil for which the piston downwash was subsonic. This suggestion was similarly based in heuristic reasoning. The use of local cylinder conditions in piston theory, with the conditions determined behind an oblique shock, has also been referred to as the "Miles' [138] strong shock piston theory" by a number of authors. In this sense, it may also be considered a development of LPT as a heuristic method.

In its early history, the spectrum of applications to which LPT was applied was typically amenable to solution using other engineering-level aeroprediction methods. In this context, LPT did not offer significant savings in computational cost, and the method did not find wide application in the literature. A number of examples of its early application may be

noted. LPT was typically used as a perturbation to a mean-steady solution obtained using the first-order shock-expansion method. One examples of this is the work of Yates and Bennett [115].The formulation of Yates and Bennett is significant four respects:

- The cylinder orientation was defined as normal to the local mean-steady surface (referring to Fig. 3.4, $\psi = \psi_m$ and $\delta_m = 0$, where subscript "m" refers to the mean-steady conditions and ψ_m is the inclination of the local mean-steady surface relative to the body axis),
- The downwash velocity as defined in Eq. (3.2) utilized the local mean-steady velocity $\mathbf{V_m}$,
- The perturbation pressure coefficient correctly accounted for dynamic-pressure scaling through the factor q_m/q_∞ in Eq. (3.9),
- The use of $m_m = \sqrt{M_m^2 - 1}$ in place of M_m was investigated and the connection to a local-flow formulation of Van Dyke's [104] second-order theory was made.

The significance of these points is not to be underestimated, as they are evidence of a lucid understanding of LPT. Some later applications of LPT using mean-steady solutions from CFD do not account for the dynamic-pressure scaling in the pressure-coefficient, and simply adopt a blanket replacement of freestream conditions with local mean-steady conditions [13]. Furthermore, Yates and Bennett [115] consider a first-order coefficient other than that due to Lighthill [88] and consider a quasi-steady application of Van Dyke's [104] second-order theory. It was noted by Yates and Bennett [115] that in the limit of shock detachment, LPT based on Lighthill's [88] coefficients predicted substantially different flutter trends compared to LPT based on Van Dyke's [104] first-order coefficient. This was explained by the factor of $1/m_m \to \infty$ in Van Dyke's coefficient, while $1/M_m \to 1$ in Lighthill's coefficient as shock detachment was approached. Finally, Yates and Bennett [115] recognized that while CPT was not valid (under the assumption of subsonic piston downwash) for the case-studies considered, the LPT formulation was.

Chen and Cao [180], following the development of Yates and Bennett [115], developed an essentially similar LPT. The chief difference lies in the definition of the cylinder as normal to the mean-steady chordline in the formulation due to Chen and Cao [180]. However, the method similarly accounts for dynamic pressure scaling and models the downwash as a perturbation to the mean velocity. First-order shock-expansion theory is used for the mean-steady flow. The method is once again compared to CPT due to Lighthill [88] and to Van Dyke's [104] second-order theory. It is also compared to the more exact theory of Hui [181]. Excellent agreement is obtained with Hui's [181] method over the parameter space of M_∞, δ,

and α_0, where δ is the semi-angle of the wedge and α_0 is the mean-steady angle of attack. Poor modelling is obtained immediately prior to shock detachment. Poor modelling is also obtained for $\alpha_0 > 5°$ when $M_\infty < 2$, and for approximately $\alpha_0 > 10$ at $M_\infty > 5$. This may be expected due to the role of wave reflection in these cases, which is not modelled in the LPT due to Chean and Cao [180] but is accounted for in Hui's [181] method. Overall, significant improvement in the prediction by LPT was noted over CPT due to Lighthill [88] and due to Van Dyke [104].

3.2.8 LPT as a Special Case of Hypersonic SDT

Various analyses based in the hypersonic perturbation equations include LPT as a special case. These analyses were typically concerned with the loads on oscillating wedges or quasi-wedges [139, 142, 146, 178, 179, 181–185], cones or quasi-cones [140] or wings and general three-dimensional bodies [86, 141, 171, 177]. Most of these analyses were mathematically rigorous developments. However, as their focus was not on developing piston theory, they are treated in the present section. In these works, LPT is found to be a special case of the more general solutions obtained. This special case considers the limit of negligible reflection of Mach waves from the bow shock produced by the body. The resulting LPT is termed "strong shock piston theory" by a number of authors. A number of differences are noted between the various analyses. These will briefly be discussed in the text that follows. The common ground between the works is that the reference cylinder conditions being perturbed in the LPT formulation are those in the mean-steady flow behind the bow shock. The analyses may be loosely grouped into three categories:

- Analyses based in perturbations relative to the freestream. These typical utilize the classical hypersonic SDT assumptions [27, 83, 83]. The x-axis is aligned with the body axis and perturbations relative to the freestream variables are considered. Examples include the works of [86, 146, 182],

- Analyses based in perturbations relative to the mean-steady flow behind the bow shock for a wedge-like surface. The x-axis is aligned with the mean-surface tangent of the body surface. It is typically assumed that deviations of the body surface from the approximating mean-steady wedge (whether due to deformation of the surface, rigid body motion, or due to the body not being a wedge) are small. Examples include the works of [140, 171, 177–179, 185],

- Analyses based in a heuristic application of LPT on the basis of the above two categories. Examples include the works primarily due to Ghosh [139, 141, 142] an Orlik-Rückemann [183, 184].

Analyses Based in Perturbations Relative to the Freestream

The first developments were due to Appleton [182] and McIntosh [146]. The development of Appleton [182] utilized the hypersonic SDT assumptions (referred to as the "piston theory model" in the development) to apply the unsteady analogy to an oscillating slender wedge in hypersonic flow. The treatment aimed to account for the effect of wave reflection from the bow shock on the pitch stiffness and damping. However, a number of errors arose in the development, as discussed by Orlik-Rückemann [184]. The same problem was treated by McIntosh [146]. The treatment of McIntosh [146] is illustrated in Fig. 3.20. McIntosh [146] also invoked the classical hypersonic SDT assumptions, while allowing for unsteady flow. In particular, the assumptions included that

- The inclination of the bow shock to the freestream was given by $\beta = \mathscr{O}(\tau)$, with $\tau \ll 1$ being a small parameter,
- The inclination of the wedge surface to the freestream was given by $\delta = \mathscr{O}(\tau)$,
- Streamwise perturbations to the freestream velocity were $\mathscr{O}\left(\tau^2\right)$,
- Transverse velocity perturbations v were $\mathscr{O}(\tau)$,
- The amplitude of oscillation A was $\mathscr{O}\left(\tau^2\right)$,
- The reduced frequency of oscillation k was $\mathscr{O}(1)$.

The Euler equations were non-dimensionalized, with the governing equations truncated to terms up of $\mathscr{O}(\tau)$. Harmonic perturbations about the spatially-invariant mean-steady wedge flow were considered. This allowed the time-derivatives of variables to be expressed through the parameter k, with the remaining independent variables being the spatial coordinates. A similar treatment of the boundary conditions at the surface and at the shock was given. Transformation of the variables allowed the equations to be expressed as a wave-type problem with a general solution given by characteristics. The mathematical detail of the solution of the characteristic equation is given in [146], and is not repeated here. The result of the analysis was that the fluid variables at any given point in the flow between the body surface and the bow shock were described by an infinite series. This series summed the contributions due to perturbations along the characteristics passing through the point of interest. It thereby

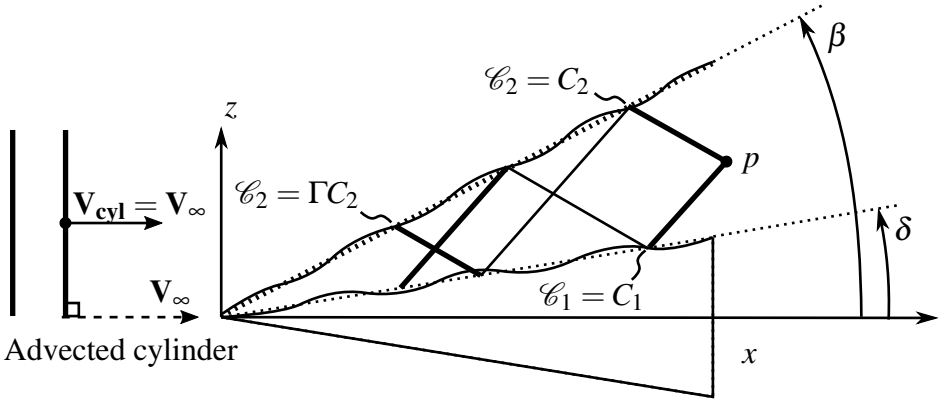

Fig. 3.20 Illustration of the configuration considered in McIntosh's [146] method, with equivalent piston-theory cylinder shown.

accounted for the reflection and attenuation of characteristics from the bow shock (and body surface). This was described in terms of an attenuation factor λ and a reflection coefficient Γ. Adapting McIntosh's [146] expressions to the present nomenclature gives

$$\lambda = \frac{\left(\frac{\rho_m a_m}{\rho_\infty a_\infty}\right)\left(K_\beta^2+1\right) - 2K_\beta^3}{\left(\frac{\rho_m a_m}{\rho_\infty a_\infty}\right)\left(K_\beta^2+1\right) + 2K_\beta^3}, \tag{3.120}$$

$$\Gamma = -\frac{M_\infty(\beta-\delta) - \frac{a_m}{a_\infty}}{M_\infty(\beta-\delta) + \frac{a_m}{a_\infty}}, \tag{3.121}$$

where $K_\beta = M_\infty\beta$ is the hypersonic similarity parameter based on the bow-shock angle, a is the speed of sound, and subscript "m" denotes the mean-steady values behind the bow shock. As noted by McIntosh [146], these parameters are zero in the limit of a Mach wave, and tend to positive values less than 1 in the limit of $K_\beta \to \infty$ for $\gamma = 1.4$. The significance of the zero-limit for weak shocks, in particular $\lambda \to 0$, follows from McIntosh's [146] result for the pressure at a point in the fluid, given in the present nomenclature as:

$$p = p_m - \rho_m a_m V_\infty A \exp\{\mathrm{i}k\tilde{t}\}\left[f_w^*(\mathscr{C}_1) + \sum_{n=1}^{\infty}(-\lambda)^n f_w^*(\Gamma^n\mathscr{C}_1) + \sum_{n=1}^{\infty}(-\lambda)^n f_w^*(\Gamma^n\mathscr{C}_2)\right], \tag{3.122}$$

where the following have been introduced for brevity:

$$\tilde{t} = V_\infty t - x, \tag{3.123}$$

$$\mathscr{C}_1 = -\frac{V_\infty}{a_m}\left[z - \left(\frac{v_m + a_m}{V_\infty}\right)x\right], \tag{3.124}$$

$$\mathscr{C}_2 = \frac{V_\infty}{a_m}\left[z - \left(\frac{v_m - a_m}{V_\infty}\right)x\right], \tag{3.125}$$

$$f_w^*(x) = \exp(\mathrm{i}kx)\mathscr{D}_x f_w(x), \tag{3.126}$$

$$\mathscr{D}_x f_w(x) = \mathrm{i}k f_w(x) + \frac{\partial f_w(x)}{\partial x}, \tag{3.127}$$

where $f_w = \mathscr{O}(1)$ is the non-dimensional function describing the mode-shape of the wedge oscillation or deformation, $\mathscr{C}_1$ is associated with left-running characteristics (which appear to come from the surface), $\mathscr{C}_2$ is associated with right-running characteristics (which appear to come from the shock), and A is the amplitude of oscillation. The first term in the brackets represents the contribution along characteristic lines due to the closest point on the body surface. The second term represents the contribution, along the same characteristic line, from surface points further upstream. These contributions have been reflected off of the shock, and hence involve the attenuation factor λ and the reflection coefficient Γ. The index n in the series corresponds to the number of times the contribution has been reflected off of the shock. The third term represents the contribution along the characteristic line incident from the shock of upstream surface points. It is immediately evident by comparison of Eq. (3.122) and Eq. (2.36) that the LPT is obtained when the reflection of waves off the bow shock is identically zero (through $\lambda = 0$). This allows the pressure to be a function of only the local surface behaviour. However, it is noted that the formulation due to McIntosh [146] defines the downwash as $V_\infty A$, as opposed to $V_m A$ in LPT. From the above, McIntosh [146] gave the differential pressure coefficient for a wedge oscillating about zero incidence as

$$C_{P(L)} - C_{P(L)} = 4\beta A \exp\{\mathrm{i}kV_\infty t\}\left[\frac{2\gamma K_\beta^2 - (\gamma-1)}{2+(\gamma-1)K_\beta^2}\right]^{1/2}\Bigg[\mathscr{D}_x f_w(x) + 2\exp\{-\mathrm{i}kx\}\sum_{n=1}^{\infty}(-\lambda)^n \exp\{\mathrm{i}k\Gamma^n x\}\mathscr{D}_x f_w(\Gamma^n x)\Bigg]. \tag{3.128}$$

It may be shown from the oblique shock relations that

$$\frac{\rho_m a_m}{\rho_\infty a_\infty} = K_\beta\left[\frac{2\gamma K_\beta^2 - (\gamma-1)}{2+(\gamma-1)K_\beta^2}\right]^{1/2}. \tag{3.129}$$

It is noted here that Orlik-Rückemann [184] gave a closed-formed approximation of the above results by developing the method in terms of a power-series in ik and neglecting terms of $\mathscr{O}\left(k^2\right)$. McIntosh [146] proceeded to compare Eq. (3.128) with that predicted by piston theory. The comparison and discussion that followed included CPT, a heuristic extension

to LPT, and the correlation with Miles' [138] strong-shock piston theory. The heuristic extension to LPT by McIntosh [146] was rooted in the reasoning that the mean-steady flow behind the wedge could be regarded as an equivalent freestream. The mean-steady wedge surface could then be treated as a flat plate, and the resulting small perturbations could then be modelled using CPT to perturb the new cylinder conditions. For ease of comparison with Eq. (3.128), the (full isentropic) CPT result was given as

$$C_{P(L)} - C_{P(L)} = \frac{4\beta}{K_\beta} A \exp\{\mathrm{i}kV_\infty t\} \left[1 + \left(\frac{\gamma+1}{2}\right) K_\delta\right] \mathscr{D}_x f_w(x)\,, \tag{3.130}$$

where $K_\delta = M_\infty \delta$ is the hypersonic similarity parameter based on the mean-steady surface slope δ. The extension of LPT due to McIntosh [146] resulted in the following formulation:

$$C_{P(L)} - C_{P(L)} = 4\beta A \exp\{\mathrm{i}kV_\infty t\} \left[\frac{2\gamma K_\beta^2 - (\gamma-1)}{2 + (\gamma-1)K_\beta^2}\right]^{1/2} \mathscr{D}_x f_w(x)\,, \tag{3.131}$$

which was termed "corrected piston theory". McIntosh [146] provided a numerical illustration of prediction differences between CPT, "corrected piston theory", and the full unsteady hypersonic SDT solution. It was shown that LPT provided significant improvements over CPT in the prediction of the normal-force stiffness and damping. However, neither method could capture the phase-shift with K_β in the unsteady loading that was predicted by the full theory. This is a direct consequence of upstream perturbations and lag being disregarded in point-function formulation of piston theory. The error associated with the results due to McIntosh [146] is $\mathscr{O}\left(\beta^2\right)$, where β is the shock angle.

McIntosh's [146] method was used by Bailie and McFeely [186] in a study of the flutter of wedge-mounted panels in hypersonic flow. A number of parameters were studied, including the role of the distance of the panel from the leading edge and the length of the panel. These parameters were particularly important in determining the portion of the panel subjected to the reflection of acoustic waves off of the shock wave. This may be heuristically understood by picturing a panel of fixed length at various axial stations in Fig. 3.20. The conclusion reached by Bailie and McFeely [186] was that for the purposes of panel flutter, the interaction of acoustics waves (as generated by panel vibration) with the bow shock could be neglected. The resulting shock-expansion / LPT approach yielded high accuracy in panel flutter analyses. It is important to note that these conclusions were reached with the caveat of small wave-number and limited panel length.

Analyses Based in Perturbations Relative to the Mean Steady Flow

An extension to thicker wedges and lower Mach numbers was achieved by Hui [177, 178]. Hui [177] developed a hypersonic SDT for oscillating caret wings. The development considered perturbations about the mean-steady design conditions. The x-axis was aligned with the mean-steady surface along the centerline. The adaption of this method to wedges, as in Hui [178], is illustrated in Fig. 3.21. The key assumptions of the development were that

- All perturbations about the mean-steady conditions, as well as the angular amplitude of oscillations, were of order $\mathscr{O}(\varepsilon)$, with $\varepsilon \ll 1$,
- The reduced frequency of oscillation k was small, such a power-series for dependent variables in powers of ik could be truncated after $\mathscr{O}(k)$,
- The caret-wing design was such that at mean-steady conditions, the y- and z-components of velocity were identically zero,
- The bow shock was attached to the leading-edges at the mean-steady conditions.

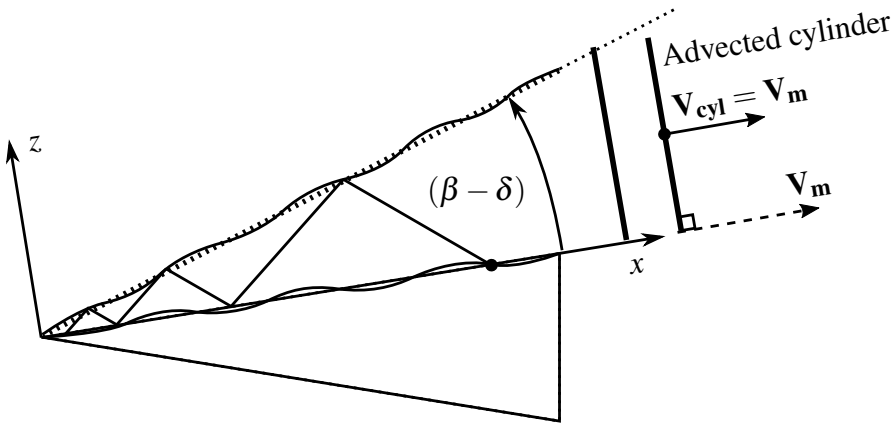

Fig. 3.21 Illustration of the configuration considered in Hui's [178] method, with equivalent piston-theory cylinder shown.

The resulting method was thus first-order in both perturbation smallness ε and reduced frequency k. It is remarked here that the method of Hui [177] was extended to higher powers in ik by Yang and Chen [187]. Yang and Chen [187] found good agreement in the method with CPT and Van Dyke's [104] second-order theory for wedge semi-angles of 5°. The mathematical details of the results of Hui's [177] analysis will not be entered into, as the development did not consider a reduction to LPT. However, three key conclusions from Hui's [177] are repeated here:

- A small, steady perturbation in pitch did not change the two-dimensionality of the flowfield,
- Unsteady perturbations in pitch (i.e., oscillations) produced a three-dimensional effect on the flowfield,
- The resulting development for wedges included the work of McIntosh [146] as a slender-wedge case, and yielded excellent agreement with exact results for wedges of arbitrary thickness (up to shock detachment) for $M_m \geq 2$.

While Hui [177] was not concerned with LPT, these conclusions may be interpreted in the context of LPT. In particular, the consideration of perturbations to the mean steady conditions (as done in LPT), resulted in better prediction and a broader range of application then when considering perturbations to the freestream (as done in CPT). To facilitate this, alignment of the axes with the mean-steady surface is beneficial (this has implications for the cylinder orientation). Finally, it is emphasized that unsteady perturbations produce a three-dimensional effect, which is not modelled by LPT. For completeness, a number of works related to or expanding on Hui's [177] SDT are noted here. Hui [178] examined the unsteady interaction of Mach waves and a strong bow shock for wedge flows. The subsequent analysis utilized a perturbation series in powers of M_m^{-2}, truncated at $\mathcal{O}\left(M_m^{-2}\right)$. The resulting formulation was valid for general reduced frequency k. This may be compared to the original development of Hui [177], which was exact in M_m, but valid up to the first order in $\mathcal{O}(k)$. The work of Hui [178] was later expanded upon by Hui and Hamilton [185]. They extended the perturbation series to higher-order terms in M_m^{-2}. These higher-order terms were shown to improve prediction accuracy when $M_m < 2$. The original method of Hui [177] was applied to oscillating double-wedge airfoils by Hui [181], with a misprint in Hui [177] also being corrected. Chavez and Liu [179] utilized the theory of Hui [177] as the basis for a computational method named the Perturbed Euler Characteristics (PEC) method. Finally, the work of Liu and Hui [171] in applying Hui's [177] theory to oscillating delta wings with attached leading-edge shocks is noted. The conclusions drawn by Liu and Hui [171] may once again be interpreted in the context of LPT. They noted that the method of Hui [177] could be used to account for rotationality produced by the shock provided $A \ll B$, where

- A is the effect of interaction between the unsteady wedge flow and the mean-steady flow. In this context, "wedge flow" refers to the portion of the delta-wing flow upstream of the Mach cone through the wing apex,
- B is the unsteady flow contribution from the wedge flow region alone.

This may be interpreted in the context of LPT as follows. The reduction from a 3D flow to a 2D approximation requires that the unsteady interaction with the mean-steady 3D flow be negligible compared to the unsteadiness in the 2D plane. The further reduction from a 2D representation to a 1D representation with wave reflection off the shock is subject to similar considerations. Finally, reduction to LPT requires these reflections to be neglected. In summary, if the interaction between boundary unsteadiness and the mean-steady flow is not negligible, LPT will not be valid.

Analyses Based in Large-Incidence Methods

Finally, LPT may be considered as a special case of large-incidence hypersonic theory. Such a treatment is found in the work of Voevodenko and Panteleev [86]. They consider the application and validity bounds of Sychev's [4] theory in the context of delta wings of a variety of aspect ratios. They showed that the method yields accurate prediction even for wings of relatively low sweep angles (numerical results were obtained for sweep angles as low as 30°) and moderate aspect ratio ($AR = \mathcal{O}(1)$). As noted by Voevodenko and Panteleev [86], when the method is applied to wings of non-small aspect ratio, it is required that the density ratio between the freestream and the windward flow be assumed a small parameter. This is achieved as a consequence of $\alpha = \mathcal{O}(1)$ or $M_\infty^2 \sin^2\alpha \gg 1$. While Voevodenko and Panteleev [86] did not consider an analytical modelling of wave reflection from the shock, the physics is captured in the numerical solution of Sychev's [4] equations. Voevodenko and Panteleev [86] showed that in the case of steady flow past a wedge, with the x axis aligned with the wedge surface, Sychev's [4] method reduces the flow to the problem of a 1D plane shock. Voevodenko and Panteleev [86] expressed the resulting surface pressure as a power-series in ρ_∞/ρ, which is assumed to be a small parameter $\varepsilon \ll 1$. The expression for the pressure is given as

$$\frac{p}{p_\infty} = \frac{2\gamma}{\gamma+1} M_n^2 (1-\varepsilon)^{-2} - \frac{\gamma-1}{\gamma+1}, \tag{3.132}$$

$$\varepsilon = \frac{\rho_\infty}{\rho} = \frac{\gamma-1}{\gamma+1} + \frac{2}{(\gamma+1)M_n^2}, \tag{3.133}$$

$$M_n = M_\infty \sin\delta \quad (\approx K), \tag{3.134}$$

where δ is the inclination of the wedge surface to the freestream and K is the hypersonic similarity parameter based on δ. This may be compared to the exact oblique shock equation, given as

$$\frac{p}{p_\infty} = \frac{2\gamma}{\gamma+1} M_n^2 \left(\frac{\sin^2\beta}{\sin^2\delta}\right) - \frac{\gamma-1}{\gamma+1}, \tag{3.135}$$

with the same definition for M_n. With Voevodenko and Panteleev [86] having aligned the x-axis with the wedge surface, the similarity of the method to the works of Hui [177] may be seen. The extension to LPT could be achieved by through neglecting wave reflection at the shock, as was noted in the discussion by McIntosh [146]. Voevodenko and Panteleev [86] noted that the error in the high-incidence formulation was $\mathscr{O}\left(\varepsilon^2\right)$, which is essentially similar to $\mathscr{O}\left(1/M_\infty^2 \sin^2\alpha\right)$ or $\mathscr{O}\left(K^{-2}\right)$.

3.2.9 Application of Piston Theory to Viscous Flows

Piston theory has also been used to model unsteady aerodynamics in viscous flows. The majority of approaches rely on interpreting viscous effects as geometric changes to an equivalent inviscid flow. In treating static viscous-inviscid interactions, the boundary-layer displacement thickness δ^* is used to define an "effective shape" for the inviscid flow. In dynamic viscous-inviscid interactions, the dynamic response of the displacement thickness $\frac{\mathrm{d}\delta^*}{\mathrm{d}t}$ is used to modify the effective piston downwash. The present section will give a brief overview of representative works in the application of piston theory to viscous flows, which may be broadly categorized as

- Approaches which model perturbations (whether due to viscous interaction or otherwise) as equivalent wedges embedded in a mean-steady flow, as due to Ericsson [188],
- Approaches which utilize a higher-order inviscid method, of which LPT is a special case, as due to Orlik-Rückemann [183] and Hui and East [189],
- Approaches which use CFD to compute the mean-steady viscous flow, and which neglect dynamic viscous interaction, as due to McNamara et al [13] and Liu et al [18].

Ericsson [188] considered the effects of viscous and elastic perturbations on the unsteady aerodynamics of airfoils. These perturbations were modelled as small wedges embedded in the mean-steady flowfield. The first-order truncation of the tangent-wedge pressure equation (or equivalently, first-order piston theory) was used to model the pressure increment due to the perturbation. Ericsson [188] modelled the surface pressure due to static perturbations as

$$p = p_e\left(1 + \frac{\Delta p_{v(s)}}{p_e}\right), \tag{3.136}$$

$$\frac{\Delta p_{v(s)}}{p_e} = \gamma K_v = \gamma M_e \frac{\mathrm{d}\delta^*}{\mathrm{d}x}, \tag{3.137}$$

where p_e is the pressure at the boundary-layer edge (as computed for inviscid flow), $\Delta p_{v(s)}$ is the increment due to static viscous effects, and K_v is the local hypersonic similarity parameter

based on the equivalent wedge angle due to viscous effects. The comparison of Eqs. (3.136) and (3.137) with the first-order truncation of Eq. (3.8) clearly shows the piston-theory application. A laminar boundary layer was assumed, and the following relationship used in defining the static viscous-inviscid interaction:

$$M_e \frac{\mathrm{d}\delta^*}{\mathrm{d}x} = B\bar{\chi}\,, \tag{3.138}$$

$$\bar{\chi} = M_e^3 \sqrt{\frac{C^*}{Re_x}}\,, \tag{3.139}$$

$$B = B_1 + \frac{B_2}{M_e^2}\,, \tag{3.140}$$

where Re_x is the Reynolds number based on fluid properties at the boundary-layer edge at a distance x from the wedge leading-edge, $\bar{\chi}$ is the viscous-interaction similarity parameter, and the variables B_1, B_2, C^* are defined as functions of γ, the wall temperature T_w, T_e, the Prandtl number Pr, and M_e in the original work of Ericsson [188]. It is noted here that Ericsson gave a closed form expression for M_e as a function of γ and the inviscid pressure ratio p_e/p_∞. The inviscid pressure ratio was computed using the tangent-wedge equation, given in Eq. (3.37), based on the physical wedge shape. This summarizes the methodology of Ericsson [188] in using piston theory to model static viscous interaction. His approach to modelling dynamic viscous interaction was essentially similar. The dynamic perturbation equivalent to Eq. (3.137) was given as

$$\frac{\Delta p_{v(d)}}{p_e} = \gamma M_e \frac{1}{V_e} \frac{\mathrm{d}\delta^*}{\mathrm{d}t}\,, \tag{3.141}$$

where V_e is the fluid velocity at the boundary-layer edge and $\Delta p_{v(d)}$ is the increment due to dynamic viscous effects. The term $\frac{1}{V_e}\frac{\mathrm{d}\delta^*}{\mathrm{d}t}$ essentially represents the angle of the equivalent wedge due to the dynamic response of the boundary-layer displacement thickness to oscillations. It was assumed by Ericsson [188] that this response occurred instantaneously for the reduced frequencies typically associated with structural motions at hypersonic speeds. This led to the further relationship between the boundary-layer response and the surface-normal velocity of the surface $V_\perp$ due to oscillations

$$\frac{\mathrm{d}\delta^*}{\mathrm{d}t} = \frac{\partial \delta^*}{\partial \theta} \frac{\partial}{\partial t}\left(\frac{V_\perp}{V_\infty}\right), \tag{3.142}$$

where θ is the change in inclination of the wedge due to oscillations. Ericsson gave the boundary-layer response to static changes in inclination as

$$\frac{1}{x}\frac{\mathrm{d}\delta^*}{\mathrm{d}\theta} = -\frac{\mathrm{d}C_{p(e)}}{\mathrm{d}\theta}\frac{\Delta p_{v(s)}}{p_e}\left(\frac{p_e}{p_\infty}\right)^{-\frac{3}{2}}\frac{M_\infty^2}{M_e}\left[\left(\frac{3}{4}-\frac{B_2}{BM_e^2}\right)G_1+G_2+\frac{1}{4}\right], \tag{3.143}$$

where $\Delta p_{v(s)}$ is the pressure increment due to static viscous effects, and where G_1 and G_2 are functions of γ, p_e/p_∞, and M_e and are defined in Ericsson's original paper [188]. Ericsson [188] noted that the boundary-layer displacement thickness decreased when subjected to compressive oscillations. He noted that this had a "cushioning effect" which decreased the piston effectiveness. Ericsson [188] successfully used the same principle of embedded equivalent edges to model the pressure increment due to various non-viscous perturbations.

A similar approach was used earlier by Orlik-Rückemann [183]. The inviscid pressure loading on the wedge was computed using McIntosh's [146] piston theory (with wave reflections from the bow shock neglected). The effect of static viscous interaction on the inviscid pressure was computed using a semi-empirical model. This model was based in flat-plate boundary layer theory, with Orlik-Rückemann [183] demonstrating its extension to wedges. The resulting formulation for the surface pressure, including static viscous interaction, may be written as

$$\frac{p}{p_\infty} = \frac{p_{inv}}{p_\infty}\frac{p_{vis}}{p_{inv}}, \tag{3.144}$$

$$p_{inv} = p_m + \rho_m a_m V_\infty \theta_p, \tag{3.145}$$

$$\frac{p_{vis}}{p_{inv}} = E + f_0 G_0 d\bar{\chi}, \tag{3.146}$$

where p_{inv} is the inviscid pressure, p_{vis}/p_{inv} is the pressure scaling due to static viscous interaction, θ_p is the perturbation to the surface inclination due to motion of the wedge, and the variables in Eq. (3.146) are defined in the paper of Orlik-Rückemann [183]. It is noted here that $E \approx 1$, f_0 accounts for scaling of the flat-plate constant G_0, and d accounts for the wall temperature. To account for dynamic viscous interaction, Orlik-Rückemann [183] noted that the effective piston downwash must be adjusted for the boundary-layer response. The resulting formulation for the surface pressure, accounting for both static and dynamic viscous interaction, may be written as

$$p = \frac{p_{vis}}{p_{inv}}\left[p_m + \rho_m a_m\left(V_\infty\theta_p + \frac{\mathrm{d}\delta^*}{\mathrm{d}t}\right)\right]. \tag{3.147}$$

Orlik-Rückemann [183] provided expressions for the boundary-layer response $\frac{d\delta^*}{dt}$ in both the strong interaction and weak interaction regimes. It is noted here that these expressions are a function of $\frac{dK_\theta}{dt}$, where K_θ is the hypersonic similarity parameter based on the inclination of the wedge to the freestream.

The methods developed by Orlik-Rückemann [183] and Ericsson [188] both utilized first-order piston theory in their analysis. However, the approach towards modelling the viscous interaction differed. Nonetheless, neither method accounted for unsteady inviscid reflections from the bow shock or the impact of this on the boundary layer. Orlik-Rückemann [183] proposed that this could be accounted for by including McIntosh's [146] reflection terms in Eq. (3.145). The spirit of this suggestion was realized by Hui and East [189]. Hui and East [189] used a first-order coupling between the inviscid and viscous flows, with the solution procedure as follows:

- The unsteady inviscid flow for an oscillating wedge, including the effect of wave reflections, was computed using Hui's [177, 178] theory,
- The boundary layer corresponding to the unsteady inviscid flow past the physical wedge was calculated. This determined a new, unsteady effective shape,
- First-order coupling was achieved by using the effective shape as the new geometry in an inviscid computation by Hui's [177, 178] theory.

This methodology accounts for the static and dynamic interaction between the inviscid and viscous flows, with wave reflection due to both accounted for. The neglect of wave reflections would reduce the theory to a special case of LPT applied to viscous interaction.

Finally, the recent application of piston theory to mean-steady viscous flows computed by CFD is considered [13, 171]. The methods which will be covered are essentially similar. The differences are chiefly associated with the method used to define the effective shape. McNamara et al [13] consider the application of Euler-based LPT and of CPT to a mean-steady flow computed using the Navier-Stokes equations. The approach is described in Section 3.2.10. They also consider the use of effective shape corrections to the application of CPT. Two methods are considered to compute the effective shape:

- A semi-empirical relation for the laminar displacement-thickness on flat plates,
- Using CPT to correlate the viscous pressure gradient to an effective boundary-layer slope.

McNamara et al [13] note that the two methods yield notably different effective shapes for a double-wedge airfoil at hypersonic speeds. The laminar flat-plate relation provides

only a slight increase in thickness, which is fairly insensitive to the Mach number. The CPT-correlation method predicts an effective shape which is notably thicker on the aft portion of the double-wedge, and is more sensitive to the freestream Mach number. The effect on the flutter boundary differs between the two methods. This led McNamara et al [13] to conclude that the effective-thickness approaches examined were not a reliable means of accounting for viscous interaction. It is reiterated here that no dynamic viscous interaction was modelled.

Liu et al [18] developed an approach for estimating the effective shape from CFD computations. LPT was then applied about this effective shape using local flow conditions along the shape. The defining feature of the work of Liu et al [18] is the method for effective shape determination. Liu et al [18] posited that a effective shape could be determined as the locus of a limiting value of vorticity in the flow. This was based in the reasoning that the boundary layer is a region of high vorticity. Noting that the laminar boundary-layer thickness on a flat-plate in the strong viscous interaction regime had the following proportionality,

$$\delta^* \propto M_\infty^{1/2} Re_1^{-1/4} x^{3/4} . \tag{3.148}$$

Liu et al [18] defined an effective-shape shape coefficient C_{eff} such that the outer inviscid flow was defined by

$$|\xi| < C_{eff} \frac{V_{x\infty}}{M_\infty^{1/2} Re_1^{-1/4} x^{3/4}} , \tag{3.149}$$

where $V_{x\infty}$ is the x-component of the freestream velocity, and Re_1 is the Reynolds number based on a unit length. A given value of C_{eff} essentially determines the effective shape for a given mean-steady Navier-Stokes solution. The effective-shape coefficient C_{eff} was determined as a function of the viscous interaction parameter by minimizing the error between unsteady Navier-Stokes solutions and the LPT solution for a given value of C_{eff}. In this sense, the relationship between C_{eff} and $\bar{\chi}$ is tuned for a given geometry and parameter-space of flow parameters. Liu et al [18] subsequently examined the application of the method to a variety of airfoil thicknesses and flow incidences. The method yielded improved prediction of aerodynamic forces over LPT. The application of the method to slender waveriders was also considered, with similar improvement over LPT noted.

3.2.10 CFD-based LPT as a Heuristic Method

Formulations

As noted in the earlier section on LPT as a heuristic method, the initial problems to which LPT was applied could also be solved by other engineering-level aeroprediction methods. This

meant that LPT did not offer significant savings in computational cost. The value of LPT as a perturbation method for computational cost-reduction in CFD was only recognized towards the 1990s. One of the early examples of CFD-based LPT is the work of Hunter [190, 191]. Hunter used piston theory to model both steady and unsteady perturbations about a mean-steady Euler solution. The local mean-steady conditions were used as the cylinder reference conditions, with the cylinder oriented normal to the local mean-steady surface tangent. This may be described in the context of generalized piston theory as

$$\theta = 0^\circ, \tag{3.150}$$

$$\mathbf{V_{cyl}} = \mathbf{V_m}, \tag{3.151}$$

$$p_{cyl} = p_m. \tag{3.152}$$

The downwash definition used by Hunter was based on the projection of fluid and body velocities onto the surface normal following deformation. This may be written in the nomenclature of Fig. 3.4 as

$$w = (\mathbf{V_b} - \mathbf{V_m}) \cdot \hat{\mathbf{n}}, \tag{3.153}$$

where $\hat{\mathbf{n}}$ is the unit normal vector following a deformation or displacement, $\mathbf{V_b}$ is the velocity vector of the body due to motion, and $\mathbf{V_m}$ is the mean-steady fluid velocity vector at the surface. It may be noted that $\mathbf{V_m} \cdot \hat{\mathbf{n}}_\mathbf{m} = 0$, where $\hat{\mathbf{n}}_\mathbf{m}$ is the unit normal vector to the mean-steady surface. It should also be noted that this downwash definition results in $\tan\delta$ being replaced by $\sin\delta$. Hunter [190, 191] investigated the application of the so-called "piston-perturbation method" to axisymmetric cone flows, deforming panels in the presence of shock interaction, hypersonic glide vehicles, and a vehicle with a conical body and swept wing of moderate aspect ratio. Hunter [190, 191] noted excellent agreement in the results compared with full unsteady Euler computations. It is noted here that Hunter utilized the full-form of the isentropic pressure equation as given in Eq. (3.18).

The formulation of LPT put forward by Zhang et al [14] is fundamentally similar to that due to Hunter [190]. The sole difference is that the pressure relation is given by the first-order truncation of Eq. (3.8). Zhang et al [14] considered the application of LPT to circular-arc airfoils, a NACA 0012 airfoil, and to a trapezoidal-planform fin. Once again, excellent correspondence with full unsteady Euler results was obtained. It is to be noted that a number of publications detailing the development and application of LPT in China in the early 1990s are available in Chinese, including papers on Euler-based LPT [192]. However, it is the publication by Zhang et al [14] that generated significant attention and renewed interest in CFD-based LPT in English-language literature. Since this publication of Zhang et al [14], CFD-based LPT has been widely adopted and applied to a number of engineering

problems. The formulation of LPT has generally remained unchanged, with few exceptions found in the literature. These will be briefly noted here, along with examples of applications.

The suitability of a number of aeroprediction methods for hypersonic aeroelasticity were investigated by McNamara et al [13]. LPT was one of the methods considered, along with a method referred to as "static flow approximation with piston theory correction." The implementation of LPT by McNamara et al [13] utilized the following equations for the downwash and the local pressure coefficient:

$$w = \frac{\partial Z(x,t)}{\partial t} + V_m \frac{\partial Z(x,t)}{\partial x}, \tag{3.154}$$

$$C_p = \frac{2}{M_m^2}\left[c_1\left(\frac{w}{a_m}\right) + c_2\left(\frac{w}{a_m}\right)^2 + c_3\left(\frac{w}{a_m}\right)^3\right], \tag{3.155}$$

where $Z(x,t)$ describes the chordwise distribution of transverse displacement, and Lighthill's coefficients as per Eqs. (3.11) to (3.13) were used for c_1, c_2, and c_3. While the downwash equation is correct for airfoils of negligible thickness thickness, the equation used by McNamara et al [13] for the pressure coefficient is in error. This may be seen by comparison with Eq. (3.9). The formulation of McNamara et al [13] seen in Eq. (3.155) is arrived at by a blanket replacement of freestream quantities with local flow quantities in a CPT formulation. This results in the dynamic pressure scaling and reference pressure offset in Eq. (3.9) being omitted.

The "static flow approximation with piston theory correction" used by McNamara et al [13] is a CPT / CFD hybrid method. The modelling approach replaces the purely advective contribution (through terms involving $\frac{\partial Z}{\partial x}$ with no coupling with $\frac{\partial Z}{\partial t}$) to the CPT pressure equation with the mean-steady pressure computed by CFD. In essence, CPT is used to model damping terms, while steady CFD is used to model stiffness terms. Good correlation between this method, LPT, and full unsteady CFD was noted [13].

Applications

The application of CFD-based LPT in literature generally adopts the formulation due to Zhang et al [14]. A broad range of engineering problems have been studied with the method. Some examples include

- Full vehicle aerodynamic analysis,
  - Shi et al [16] used Euler-based LPT to determine the flutter boundaries of a conical body with a highly-swept, low-wing delta wing, depicted in Fig. 3.22. The geometry represents an interesting application case for LPT, as aerodynamic

interference plays an important role at low incidences for the configuration. The flutter boundary predicted by LPT was in worse agreement with full unsteady Euler results than is typically reported of LPT in the literature. This was particularly true for the tail flutter mode at low incidences. It may be expected that interaction between the leeside flow features and the tail aerodynamics occurs under these conditions, as discussed in Section 2.1.3,

- Yan et al [17] used Euler-based LPT as their unsteady aerodynamic method in a dynamic flight-stability study of hypersonic vehicles. The coupling between rigid and elastic modes was considered. No reference values from full unsteady CFD were reported to assess the accuracy of LPT. The geometry considered is shown in Fig. 3.23. This is also an interesting application case for LPT, as it represents a geometry of practical interest in general flight vehicle design,
- Liu et al [18] used LPT with a correction for the effective shape computed from Navier-Stokes results. The method is discussed in Section 3.2.9. The method was applied to a pair of waveriders. Generally good agreement was obtained with full unsteady Navier-Stokes results, with an improvement noted over Euler-based LPT. The waverider geometries are shown in Fig. 3.24,
- Dreyer et al 2017 [12] used two variants of LPT in their full-vehicle aerodynamic analysis. The first method was a NS-based local-flow implementation of the "static-flow approximation with piston theory correction" method due to McNamara et al [13]. The effective shape was estimated a-priori by the use of an approximate relation for the turbulent boundary-layer height on a flat plate. The second method utilized the same LPT approximation, but used local-flow quantities computed by first-order shock-expansion theory. These LPT implementations were compared to full unsteady NS solutions. It was found that the NS-based LPT implementation gave better agreement with the full solution. The highest error in the LPT implementations was noted in the region of the aft-body fins. Dreyer et al [12] attributed the error to flow interactions in this region, as may be expected from Section 2.1.3. Dreyer et al [12] noted significant savings in computational cost when using the LPT implementations. The computational cost of an unsteady prediction by LPT was estimated at 0.01% of the cost by unsteady CFD.

- Design parameter-space studies,
  - Zhang et al [15] used Euler-based LPT to model the change in aerodynamic characteristics produced by deviations in airfoil shape from a reference NACA

0012 profile. A steady Euler solution was obtained for the reference profile (and wing). Euler-based LPT about this reference solution provided an extremely low-cost aerodynamic method in an airfoil-shape optimization study. Zhang et al [15] compared the computational cost of optimization by LPT versus optimization by Euler solution. It was found that optimization by LPT required 0.01% of the time needed for optimization by Euler solution. The aerodynamics of the optimized shape were re-evaluated using steady Euler CFD. The error between the predicted (by LPT) and Euler force-coefficients for the optimized shape were within 1% for the lift coefficient and within 5% for the pitching-moment coefficient.

- Panel-flutter studies,
  - Yang et al [193] used Euler-based LPT to model the static and dynamic aeroelasticity of curved panels. The pressure formulation used the first-order coefficient c_1 due to Van Dyke [130], as given in Eq. (3.24), in order to extend the analysis to lower supersonic Mach numbers. The definition of c_1 was based on the local mean-steady Mach number, and is given as $c_1 = M_m/m_m$. The downwash formulation was equivalent to that due to Chen and Cao [180], with the cylinder defined normal to the mean-steady chordline.
- Shock-panel interaction studies,
  - Gogulapati et al [194, 195] investigate the modelling of shock-impingement and SBLI in the context of 3D panel flutter. An experimental investigation is also conducted. The computational investigation utilizes NS-based LPT for the aerodynamic modelling. It is not clear from the publication [194] where in the flowfield local quantities are evaluated. No comparison to unsteady CFD is provided, but reasonable agreement is noted between NS-based LPT and experiment,
  - Brouwer and McNamara [19] expanded on the work of Gogulapati et al [194]. Brouwer and McNamara [19] investigated the use of a broad range of computational methods. Their implementation of "CFD enriched piston theory" is a local-flow variant of the "static-flow approximation with piston theory correction" due to McNamara et al [13] applied at an effective thickness computed using the CPT-correlation method of McNamara et al [13]. Both these latter methods have been discussed in Sections 3.2.9 and 3.2.10. The fluid-structure interaction of both a 2D panel and a 3D panel was investigated. Good correspondence with full unsteady Navier-Stokes results was obtained by the NS-based LPT variant

for the steady load component. Similarly good correspondence was obtained with full unsteady Euler results for unsteady load component. Brouwer and McNamara [19] demonstrated the significant savings in computational achievable by piston theory. The time required by the NS-based LPT implementation to compute the necessary time-history of response was 0.03% of that required unsteady CFD in the 2D case. Similarly, 0.14% of the time was needed in the 3D case.

It is remarked here that the trend in recent literature on CFD-based LPT has been towards the application of LPT to increasingly complex engineering problems. The examples of full-vehicle analysis, viscous mean-steady flows, and shock-panel interaction may be considered representative of this trend. However, the application to more complex physics has not been accompanied or informed by a mathematical consideration of the validity of such application. This stands in contrast to earlier investigations, such as those discussed in Sections 3.2.8 and 3.2.9, which are typically more mathematically rigorous and conscious of the limitations of the analysis. This trend motivated the study of the mathematical basis of LPT presented in Chapter 4 of the present work.

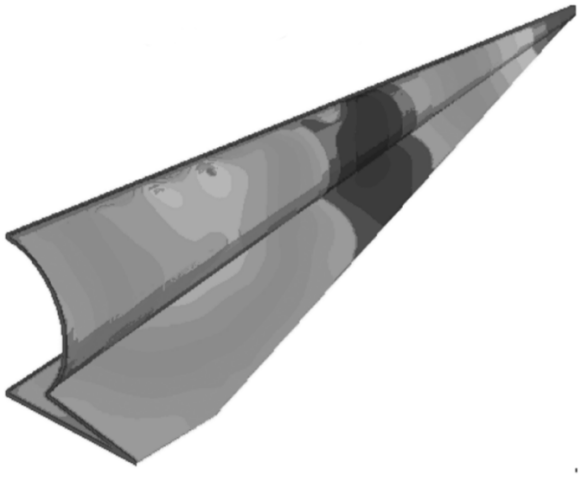

Fig. 3.22 Full vehicle geometry considered by Shi et al [16].

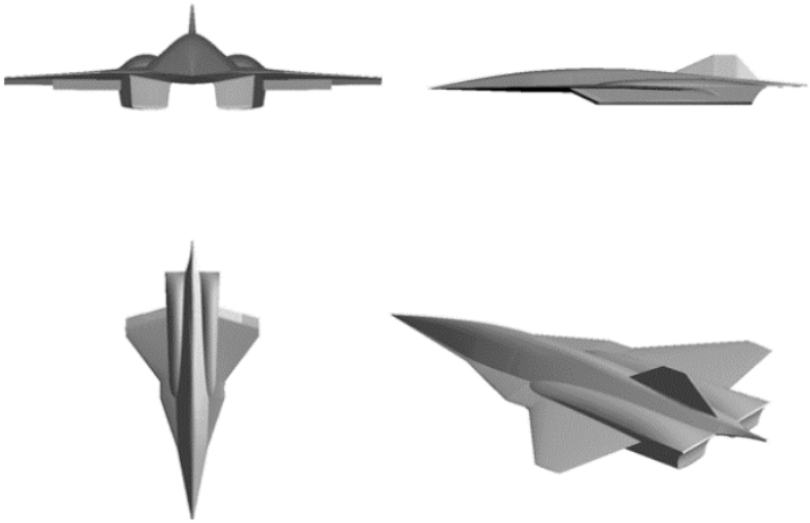

Fig. 3.23 Full vehicle geometry considered by Yan et al [17].

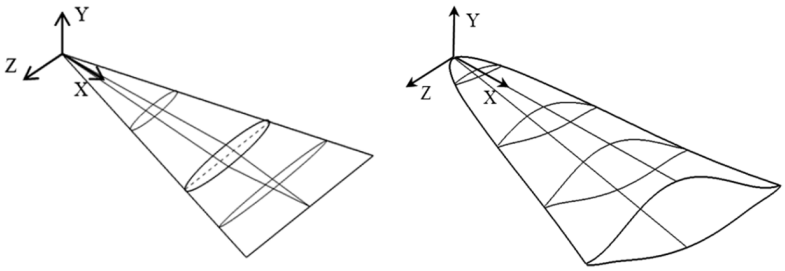

Fig. 3.24 Full vehicle geometry considered by Liu et al [18].

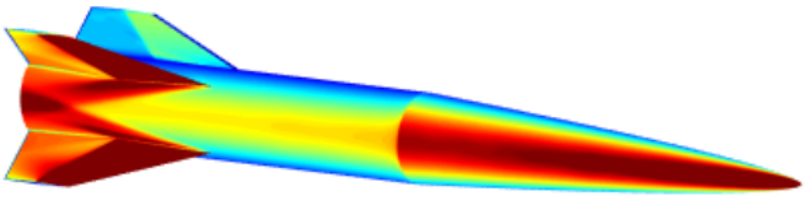

Fig. 3.25 Full vehicle geometry considered by Dreyer et al [12].

3.3 Significance of Higher-Order Formulations

As has been noted in Section 3.2, pressure relations [128, 144] have been developed which extend beyond the frame cast by the generalized piston-theory pressure relation of Eq. (3.8) or Eq. (3.9). In particular, these relations account for upstream influence and unsteadiness, as discussed in Sections 3.2.5 and 3.2.8. Mathematically, these involve non-local downwash terms. These "extended piston theories" may be considered a higher-order formulation than generalized piston theory in the sense of perturbation propagation. They have already been discussed in Section 3.2.5, and will not be discussed further here. Generalized piston theory is essentially zeroth-order in perturbation propagation, while the "extended piston theories" include non-zero propagation terms.

The generalized pressure relation of Eq. (3.8) or Eq. (3.9) is nonlinear in the downwash-Mach number, w/a_{cyl}. In this sense, a piston-theory formulation involving $\left(w/a_{cyl}\right)^2$ or $\left(w/a_{cyl}\right)^3$ may be considered a "higher-order" formulation relative to linear (first-order) piston-theory. These "higher-order" contributions are due to nonlinear local-downwash terms. Thus, the formulations represent an extension to higher-order pressure equation in terms of local effects. They will be discussed in Sections 3.3.1 and 3.3.2.

The content of Sections 3.3.1 and 3.3.2 draws significantly from previous publications of the author (from [122] and [123], respectively), which have been reproduced and adapted here with permission from the respective copyright holders. The physical significance of the contribution from higher-order local downwash terms may be effectively illustrated by two simple case studies. The first (Section 3.3.1) will consider a more general airfoil shape in order to highlight the impact of geometry on pressure modelling in CPT. The second (Section 3.3.2) will consider a flat plate at incidence in order to highlight inherent modelling differences between CPT and LPT.

3.3.1 Higher-Order Local Effects in CPT

Consider a general airfoil, as depicted in Fig. 3.26, with a surface described by the equation $z = z_a(x)$, where x is the coordinate along the chordline. Let the subscripts "U" and "L" be used for the upper and lower airfoil surfaces respectively. Suppose the airfoil thickness has a thickness distribution described by the function $z_t(x)$ and a camber distribution described by $z_c(x)$. The equations for the lower and upper surfaces are then given by

$$z_L = z_c - z_t \,, \tag{3.156}$$

$$z_U = z_c + z_t \,. \tag{3.157}$$

Let the airfoil chordline be inclined at an incidence of α to the freestream. Adopting the CPT formulation of $\theta = 0$, the equivalent $\tan\delta$ to be used in Eq. (3.2) may be found from first principles. Expressing the result in the nomenclature of Eq. (3.5), it is found that for the lower and upper surfaces that

$$w_{f(L)} = V_\infty \left(\frac{\tan\alpha - \frac{\partial z_L}{\partial x}}{1 + \frac{\partial z_L}{\partial x}\tan\alpha} \right), \tag{3.158}$$

$$w_{f(U)} = V_\infty \left(\frac{\frac{\partial z_U}{\partial x} - \tan\alpha}{1 + \frac{\partial z_U}{\partial x}\tan\alpha} \right). \tag{3.159}$$

By introducing the approximations that $\frac{\partial z_L}{\partial x}\tan\alpha \ll 1$ and $\frac{\partial z_U}{\partial x}\tan\alpha \ll 1$, the following linear relationships are obtained:

$$w_{f(L)} = V_\infty \left(\frac{\partial z_t}{\partial x} - \frac{\partial z_c}{\partial x} + \tan\alpha \right), \tag{3.160}$$

$$w_{f(U)} = V_\infty \left(\frac{\partial z_t}{\partial x} + \frac{\partial z_c}{\partial x} - \tan\alpha \right). \tag{3.161}$$

Further introducing the nomenclature

$$w_t = V_\infty \frac{\partial z_t}{\partial x}, \tag{3.162}$$

$$w_c = V_\infty \frac{\partial z_c}{\partial x}. \tag{3.163}$$

$$w_i = V_\infty \tan\alpha, \tag{3.164}$$

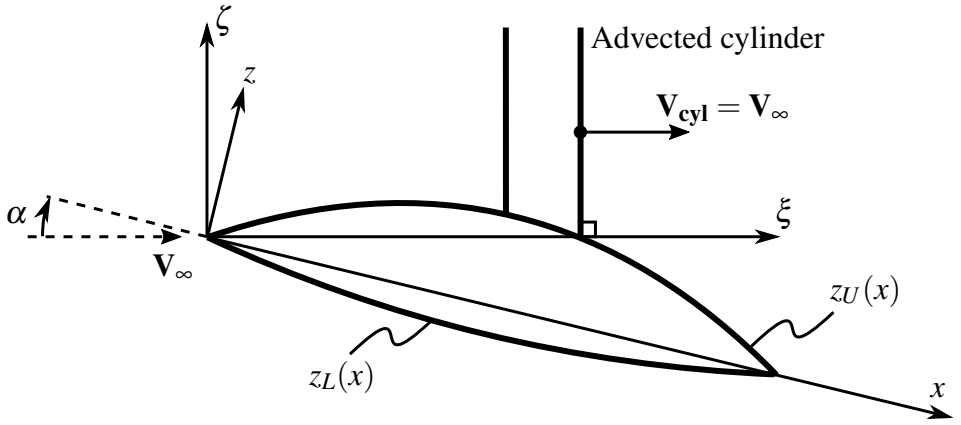

Fig. 3.26 Airfoil considered in the illustration of higher-order local effects in CPT.

as the contributions to downwash due to the thickness distribution, the camber distribution, and incidence, respectively, allows Eqs. (3.160) and (3.161) to be rewritten as

$$w_{f(L)} = w_t - w_c + w_i \,, \tag{3.165}$$

$$w_{f(U)} = w_t + w_c - w_i \,. \tag{3.166}$$

It is clear from the above equations that the downwash term due to thickness, w_t, is symmetrical. "Symmetry" in this context is intended to mean that the term has the same sign for both upper- and lower-surface cases. This is in contrast to the camber- and incidence-related contributions w_c and w_i, which give anti-symmetrical contributions. An expression for the downwash contribution due to body motion, w_b, is not offered here. However, it is noted that w_b in general will not give symmetrical contributions.

Symmetry and anti-symmetry may be exploited in taking the difference between lower- and upper-surface contributions. For compactness in the following equations, the differencing operator Δ_L^U is introduced and defined as follows:

$$\Delta_L^U(XY) \equiv X_L Y_L - X_U Y_U \,. \tag{3.167}$$

In this notation, the following may be shown:

$$\Delta_L^U\left(w_f\right) = 2(-w_c + w_i) \,, \tag{3.168}$$

$$\Delta_L^U\left(w_f^2\right) = 4w_t(-w_c + w_i) \,, \tag{3.169}$$

$$\Delta_L^U\left(w_f^3\right) = 6w_t^2(-w_c + w_i) + 6\left(-w_c w_i^2 + w_i w_c^2\right) + 2\left(-w_c^3 + w_i^3\right) . \tag{3.170}$$

Recalling that the downwash has contributions due to steady flow, w_f, and due to body motion, w_b, the total downwash w may be written as:

$$\Delta_L^U(w) = \Delta_L^U(w_b) + \Delta_L^U\left(w_f\right) , \tag{3.171}$$

$$\Delta_L^U\left(w^2\right) = \Delta_L^U\left(w_b^2\right) + 2\Delta_L^U\left(w_b w_f\right) + \Delta_L^U\left(w_f^2\right) , \tag{3.172}$$

$$\Delta_L^U\left(w^3\right) = \Delta_L^U\left(w_b^3\right) + 3\Delta_L^U\left(w_b^2 w_f\right) + 3\Delta_L^U\left(w_b w_f^2\right) + \Delta_L^U\left(w_f^3\right) . \tag{3.173}$$

These equations will be utilized when considering the difference between upper- and lower-surfaces pressure coefficients. With reference to Eq. (3.9) and Fig. 3.4, the chordwise distribution of normal-force coefficient may be written as

$$\frac{\partial C_N}{\partial x} = \frac{2}{M_\infty^2}\Delta_L^U\left\{\left[c_1\left(\frac{w}{a_\infty}\right) + c_2\left(\frac{w}{a_\infty}\right)^2 + c_3\left(\frac{w}{a_\infty}\right)^3\right]\cos\left(\psi + \delta\right)\right\} . \tag{3.174}$$

To obtain greater insight into the role of the higher-order terms, some simplifying assumptions will now be introduced to the case study. For example, if a symmetrical airfoil is considered, then $w_c = 0$ and $\Delta_L^U[\cos(\psi+\delta)] = 0$. This then leads to the expression

$$\frac{\partial C_N}{\partial x} = \frac{2}{M_\infty^2}\cos(\psi+\delta)\left[\frac{c_1}{a_\infty}\Delta_L^U(w) + \frac{c_2}{a_\infty^2}\Delta_L^U\left(w^2\right) + \frac{c_3}{a_\infty^3}\Delta_L^U\left(w^3\right)\right] \tag{3.175}$$

for which Eqs. (3.168) to (3.173) are available for substitution. The lifting load on the airfoil is then seen to be a function of the downwash contributions due to thickness and incidence (with camber having been assumed to be zero). The following conclusions regarding first- and higher-order terms in CPT applied to steady flows may then be made:

- From Eq. (3.168) it is seen that first-order CPT does not model any thickness effects on the steady lifting load. Only linear contributions from incidence and camber are modelled,
- From Eq. (3.169) it is seen that second-order CPT models a linear scaling due to thickness effects on the contributions from incidence and camber. This is essentially a linear coupling with thickness,
- From Eq. (3.170) it is seen that third-order CPT introduces nonlinear thickness scaling of linear camber and incidence contributions. Cubic contributions from camber and incidence are modelled. Finally, third-order terms are introduced for the nonlinear coupling between incidence and camber effects.

The extension of these considerations to unsteady flows may be carried out through consideration of Eqs. (3.171) to (3.173). Some simplification is possible in the special case of anti-symmetrical contributions due to body motion. That is to say, $w_{b(U)} = -w_{b(L)} = w_d$. As noted from Eqs. (3.6) and (3.7), this case may be realised for a flat plate, such that $\hat{\mathbf{n}}_\mathbf{U} = -\hat{\mathbf{n}}_\mathbf{L}$. In this case, $w_t = 0$. The following conclusions may then be drawn regarding first- and higher-order terms in CPT applied to flows with body motion:

- From Eq. (3.171) it is seen that first-order CPT does not model any coupling between the steady flow and the contribution due to body motion,
- From Eq. (3.172) it is seen that second-order CPT models a linear coupling between the steady flow and the contribution due to body motion. For the special case of anti-symmetric w_b, the linear-coupled term would be a linear scaling of w_d due to thickness effects. However, in order to realize anti-symmetric w_d, it is effectively required that $w_t = 0$. Thus, there is in practice little or no coupling between the steady

and unsteady downwash contributions. The nonlinear contribution due to body motion is effectively zero due to anti-symmetry of w_d. From the point of view of damping, this suggests that second-order CPT offers no substantial contribution over first-order CPT,

- From Eq. (3.173) it is seen that third-order CPT introduces a non-zero, uncoupled contribution from body motion. Coupling between the steady and unsteady contributions is also introduced.

From the discussion thus far, it is evident that first-order piston theory is entirely linear, with no coupling between geometrical (or physical) sources of downwash. The significance of higher-order terms describing local effects in CPT lies in coupling these sources. Second-order CPT offers minimal coupling between thickness effects and incidence or damping-related terms. It is only from third-order and higher that nonlinear coupling and nonlinear uncoupled contributions due to thickness, incidence, and damping-related terms occur.

3.3.2 Higher-Order Local Effects in LPT

Consider a flat plate inclined at an angle of α to the freestream, as shown in Fig. 3.27. Suppose that a mean-steady solution is available at α_m, and that LPT is applied in modelling a perturbation of $\tilde{\alpha}$ relative to α_m. For the purposes of this case study, the following assumptions are made with reference to Eq. (3.2):

- No dynamic effects occur ($\mathbf{V_b} = \mathbf{0}$),
- The cylinder is oriented normal to its advection direction ($\theta = 0^\circ$).

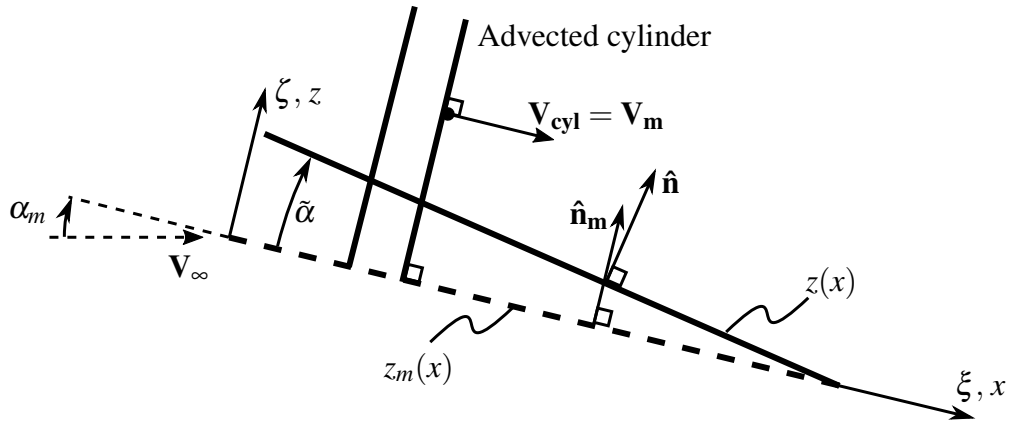

Fig. 3.27 Flat plate considered in the illustration of higher-order local effects in LPT.

The resulting definition of terms in generalized piston theory that will be used in Eqs. (3.2) and (3.9) is given in Table 3.3. Subscripts "U" refer to the upper (expansion) surface,

subscripts "L" refer to the lower (compression) surface, and subscripts "m" refer to the mean-steady solution. In this case study, the mean-steady solution will be obtained using the Prandtl-Meyer and oblique shock relations for expansion and compression, respectively. Results obtained using these relations will be termed the "exact solution". Lighthill's [88] coefficients for piston theory will be used for illustration.

Table 3.3 Definition of generalized piston-theory terms in case-study 2.

Term	LPT	CPT
$\mathbf{V_{cyl}}$	$\mathbf{V_m}$	$\mathbf{V}_\infty$
θ	0°	0°
ψ	$\tilde{\alpha}$	$\alpha_m + \tilde{\alpha}$
δ	$-\psi$	$-\psi$
w_U	$-V_{m(U)} \tan\tilde{\alpha}$	$-V_\infty \tan(\alpha_m + \tilde{\alpha})$
w_L	$V_{m(L)} \tan\tilde{\alpha}$	$V_\infty \tan(\alpha_m + \tilde{\alpha})$
$(p,V,a,M)_{cyl(U)}$	$(p,V,a,M)_{m(U)}$	$(p,V,a,M)_\infty$
$(p,V,a,M)_{cyl(L)}$	$(p,V,a,M)_{m(L)}$	$(p,V,a,M)_\infty$

The physical significance of the second- and higher-order terms in LPT will be illustrated through consideration of the aerodynamic pitch-stiffness of the flat plate. Suppose that the normal-force coefficient of the plate is written as a Taylor series about the mean-steady solution:

$$C_N = C_N(\alpha_m) + \left.\frac{\partial C_N}{\partial \alpha}\right|_{\alpha=\alpha_m} \tilde{\alpha} + \left.\frac{\partial^2 C_N}{\partial \alpha^2}\right|_{\alpha=\alpha_m} \tilde{\alpha}^2 + \ldots . \tag{3.176}$$

The aerodynamic stiffness may then be considered to have a linear component $\frac{\partial C_N}{\partial \alpha}$ and nonlinear stiffness components given by higher-order derivatives. The above equation may also be expressed in terms of the pressure coefficient on the upper and lower surfaces through substitution of the relation $C_N = C_{p(L)} - C_{p(U)}$. Furthermore, it is noted that the expression may be written in terms of derivatives with respect to $\tilde{\alpha}$, seeing that $\alpha = \alpha_m + \tilde{\alpha}$ yields $\frac{\partial \alpha}{\partial \tilde{\alpha}} = 1$. With this in mind, we may write the normal force as predicted by piston theory as

$$C_N = \Delta_L^U(C_p)\Big|_{\tilde{\alpha}=0} + \Delta_L^U\left(\frac{\partial C_p}{\partial \tilde{\alpha}}\right)\Big|_{\tilde{\alpha}=0} \tilde{\alpha} + \Delta_L^U\left(\frac{\partial^2 C_p}{\partial \tilde{\alpha}^2}\right)\Big|_{\tilde{\alpha}=0} \tilde{\alpha}^2 + \ldots \tag{3.177}$$

From the above it is clear that the derivatives of the pressure coefficient predicted by piston theory with respect to changes in incidence will be important. These may be obtained through

differentiation of Eq. (3.9) as

$$\frac{\partial C_p}{\partial \tilde{\alpha}} = \frac{2p_{cyl}}{p_\infty M_\infty^2}\left(\frac{c_1}{a_{cyl}}\frac{\partial w}{\partial \tilde{\alpha}} + \frac{2c_2 w}{a_{cyl}^2}\frac{\partial w}{\partial \tilde{\alpha}} + \frac{3c_3 w^2}{a_{cyl}^3}\frac{\partial w}{\partial \tilde{\alpha}}\right), \tag{3.178}$$

$$\frac{\partial^2 C_p}{\partial \tilde{\alpha}^2} = \frac{2p_{cyl}}{p_\infty M_\infty^2}\left\{\frac{c_1}{a_{cyl}}\frac{\partial^2 w}{\partial \tilde{\alpha}^2} + \frac{2c_2}{a_{cyl}^2}\left[w\frac{\partial^2 w}{\partial \tilde{\alpha}^2} + \left(\frac{\partial w}{\partial \tilde{\alpha}}\right)^2\right] + \frac{3c_3}{a_{cyl}^3}\left[w^2\frac{\partial^2 w}{\partial \tilde{\alpha}^2} + 2w\left(\frac{\partial w}{\partial \tilde{\alpha}}\right)^2\right]\right\}, \tag{3.179}$$

It is noted that when taking the derivative, piston theory assumes the cylinder reference conditions are invariant with piston motion. The terms $(p,V,a,M)_m$ in LPT are assumed to be a function of α_m, but not of $\tilde{\alpha}$. Differentiating the downwash terms as defined in Table 3.3 and substituting into the above gives

$$\frac{\partial C_p}{\partial \tilde{\alpha}} = \frac{2p_{cyl}}{p_\infty M_\infty^2 \cos^2\psi}\left(\mp c_1 M_{cyl} + 2c_2 M_{cyl}^2 \frac{\tan\psi}{\cos^2\psi} \mp 3c_3 M_{cyl}^3 \frac{\tan^2\psi}{\cos^2\psi}\right), \tag{3.180}$$

$$\frac{\partial^2 C_p}{\partial \tilde{\alpha}^2} = \frac{4p_{cyl}}{p_\infty M_\infty^2 \cos^2\psi}\left\{\mp c_1 M_{cyl}\tan\psi + \frac{c_2 M_{cyl}^2}{\cos^2\psi}\left(2\sin^2\psi + 1\right) \mp \frac{3c_3 M_{cyl}^3 \tan\psi}{\cos^2\psi}\left(\sin^2\psi + 1\right)\right\}, \tag{3.181}$$

where the upper sign in $\mp$ is associated with the upper surface, and ψ is defined in Table 3.3. Taking the difference between the lower and upper surfaces and evaluating at $\tilde{\alpha} = 0$, it is found that for CPT:

$$\Delta_L^U(C_p)\Big|_{\tilde{\alpha}=0} = \Delta_L^U\left(C_{p(CPT)}\right), \tag{3.182}$$

$$\Delta_L^U\left(\frac{\partial C_p}{\partial \tilde{\alpha}}\right)\Big|_{\tilde{\alpha}=0} = \frac{4}{M_\infty^2 \cos^2\alpha_m}\left(c_1 M_\infty + 3c_3 M_\infty^3 \frac{\tan^2\alpha_m}{\cos^2\alpha_m}\right), \tag{3.183}$$

$$\Delta_L^U\left(\frac{\partial^2 C_p}{\partial \tilde{\alpha}^2}\right)\Big|_{\tilde{\alpha}=0} = \frac{8}{M_\infty^2 \cos^2\alpha_m}\left\{c_1 M_\infty \tan\alpha_m + \frac{3c_3 M_\infty^3 \tan\alpha_m}{\cos^2\alpha_m}\left(\sin^2\alpha_m + 1\right)\right\}, \tag{3.184}$$

while the results for LPT are given by:

$$\Delta_L^U(C_p)\Big|_{\tilde{\alpha}=0} = \Delta_L^U\left(C_{p(exact)}\right), \tag{3.185}$$

$$\Delta_L^U\left(\frac{\partial C_p}{\partial \tilde{\alpha}}\right)\Big|_{\tilde{\alpha}=0} = \frac{2c_1}{p_\infty M_\infty^2}\left[(pM)_{(exact)L} + (pM)_{(exact)U}\right], \tag{3.186}$$

$$\Delta_L^U \left(\frac{\partial^2 C_p}{\partial \tilde{\alpha}^2} \right) \Bigg|_{\tilde{\alpha}=0} = \frac{4c_2}{p_\infty M_\infty^2} \Delta_L^U \left[\left(pM^2 \right)_{(exact)} \right], \tag{3.187}$$

A comparison of Eqs. (3.182) to (3.184) and of Eqs. (3.185) to (3.187) provides valuable insight into the fundamental modelling differences between CPT and LPT. Firstly, the difference in definition of cylinder conditions, of ψ, and in Eqs. (3.182) and (3.185) highlights the role of piston theory as a perturbation method. From the above, the role of LPT as a perturbation relative to an existing solution is evident. It's successful application at higher incidences (or for blunter airfoils) than CPT, as illustrated in [14], is understood as LPT modelling small perturbations $\tilde{\alpha}$ about a large α_m. For the same incidence, CPT must model a larger perturbation of $\alpha_m + \tilde{\alpha}$.

Moving to the linear aerodynamic stiffness as defined by Eqs. (3.183) and (3.186), further insights are obtained. It is noted that in both CPT and LPT, the second-order term makes no contribution in the flat-plate case. The role of second-order piston theory in introducing thickness-coupling was illustrated in the previous case study. Importantly, it is seen here that CPT has a linear-stiffness contribution from the third-order term. In LPT, only the first-order term affects the linear stiffness. This difference is important, as it shows that poor aeroprediction by linear LPT for vanishingly small perturbations cannot be improved by the application of a higher-order LPT. Another difference is in the dependence of the stiffness term on M_∞ and α_m. In CPT, this dependence is purely a function of the local geometry and M_∞. It is seen that in LPT, the dependence is less explicit. Instead, the local linear-stiffness term is dependent on the local mean-steady solution. In the case of CFD-based LPT, this mean-steady solution will account for the effect of shock waves and three-dimensionality in the steady flow.

The first nonlinear stiffness term introduced is given by Eqs. (3.184) and (3.187), and is essentially a quadratic-stiffness term. Once again, it is noted that the second-order CPT term makes no contribution in the flat-plate case. This is in contrast with the LPT modelling. The quadratic-stiffness term as modelled by LPT receives contributions from only the second-order LPT term. The difference in dependence on M_∞ and α_m is as discussed for the linear-stiffness term. The non-zero contribution from the second-order term is by virtue of the cylinder conditions differing between the upper and lower surfaces at non-zero α_m. This marks a fundamental modelling difference between LPT and CPT: improvement on the first-order result requires an extension to third-order when using CPT, while an improvement is already obtained at second-order when using LPT.

An interpretation of the physical significance of the contribution from the second-order LPT term follows from consideration of Eqs. (3.176) and (3.187). The representation of the normal-force coefficient as a Taylor-series expansion about the mean-steady solution

emphasizes the perturbation nature of LPT. The computational cost associated with the method is concentrated almost entirely in obtaining the mean-steady solution. In performing parameter studies, it is therefore desirable to utilize the same mean-steady solution as much as is allowable. As with any approximation or Taylor-series, the accuracy of the approximation diminishes with distance $\tilde{\alpha}$ from the unperturbed state. The approximation accuracy may be improved by higher-order terms in the Taylor expansion. This is essentially the function or utility of second-order LPT, as noted from Eq. (3.187). It allows LPT to be applied for greater perturbations about the mean-steady solution than first-order LPT.

To illustrate this, the flat-plate case study is examined for a nominal freestream Mach-number of $M_\infty = 3$. The exact mean-steady solutions are obtained using the oblique-shock equations for the lower (compression) surface and using the Prandtl-Meyer relation for the upper (expansion) surface. When applying piston theory to the expansion surface, a lower-limit on pressure was enforced. Pressures lower than vacuum pressures were not permitted. This is the sole source of difference between first-order and second-order CPT in the results which are shown below. A comparison of the prediction of C_N by CPT and by LPT is given in Fig. 3.28. In Fig. 3.28b, LPT has been applied about a nominal mean-steady solution denoted by a solid circle. A comparison of LPT to exact solutions is given for the normal-force coefficient derivatives in Fig. 3.29. Similar comparisons are given for the pressure-coefficient derivatives for the lower- and upper-surfaces in Figs. 3.30 and 3.31, respectively. In assessing the accuracy of LPT, the considerations given in the section on validity bounds at the end of Section 3.1 apply, and are not repeated here.

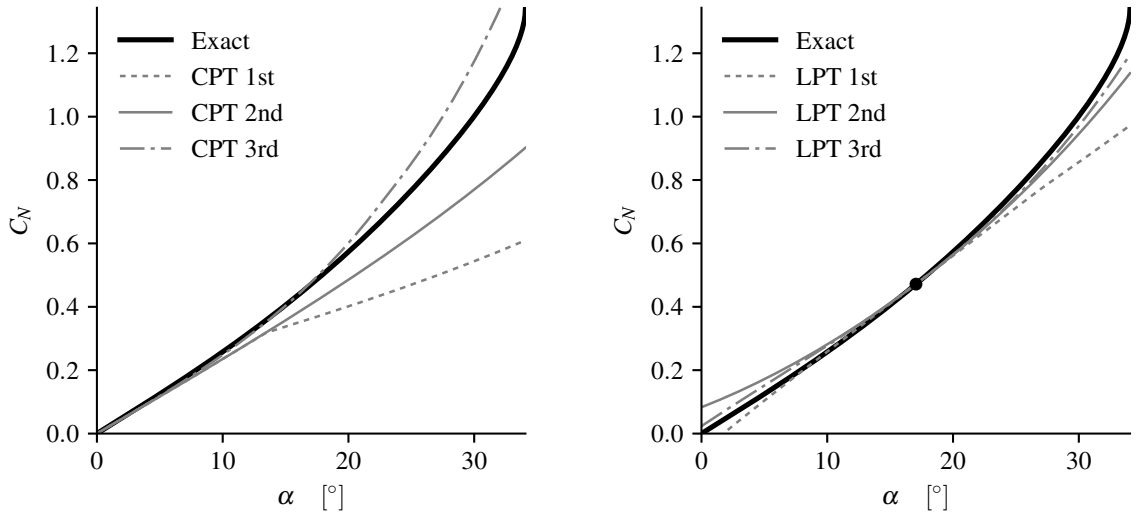

(a) Classical piston theory (b) Local piston theory

Fig. 3.28 Prediction of normal-force coefficient for a flat-plate at $M_\infty = 3$.

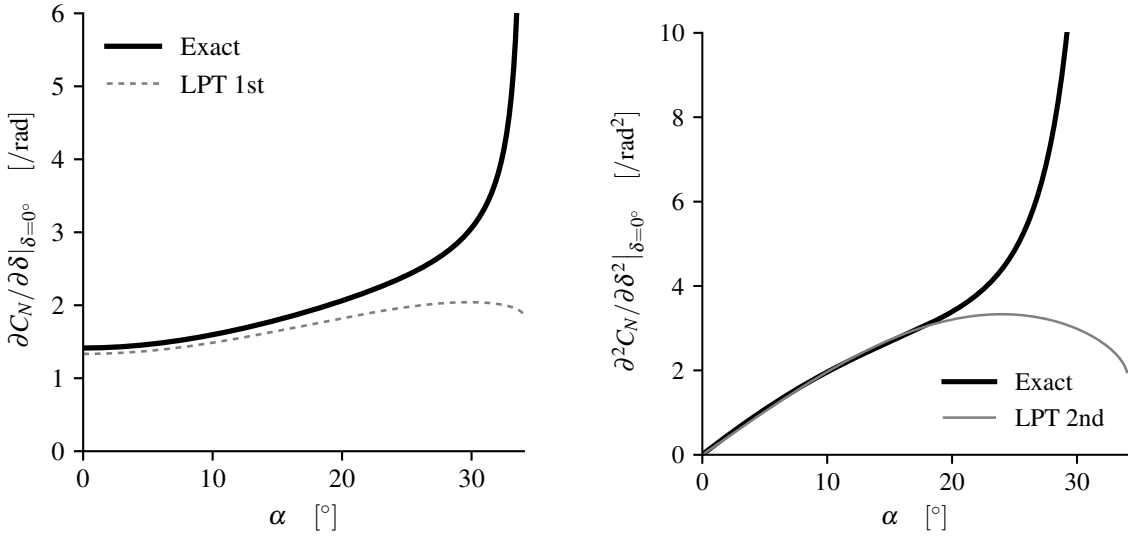

(a) Linear-stiffness term (b) Quadratic-stiffness term

Fig. 3.29 Prediction of normal-force coefficient derivatives by LPT for a flat-plate at $M_\infty = 3$.

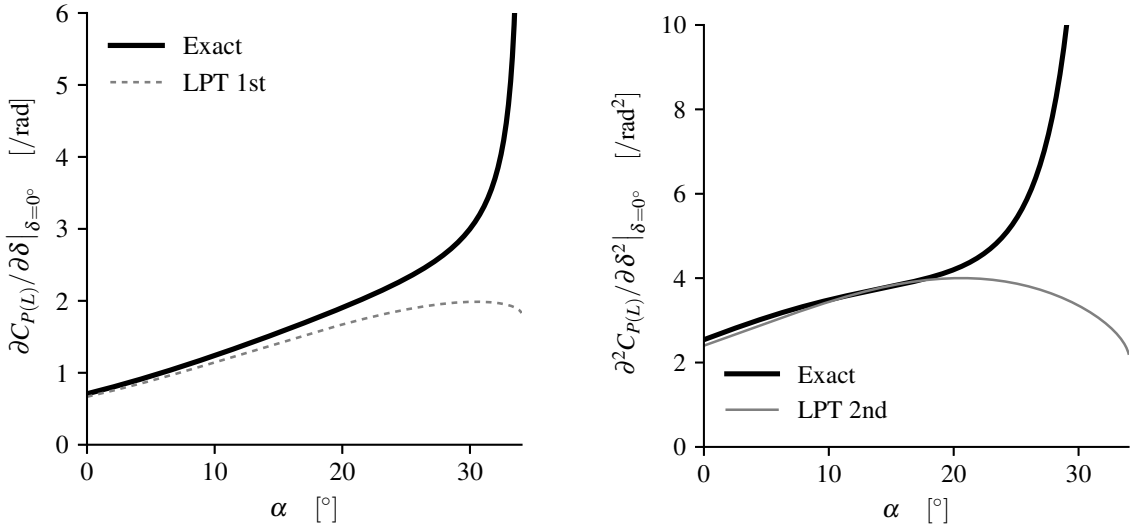

(a) Linear-stiffness term (b) Quadratic-stiffness term

Fig. 3.30 Prediction of pressure-coefficient derivatives by LPT for the compression surface of a flat-plate at $M_\infty = 3$.

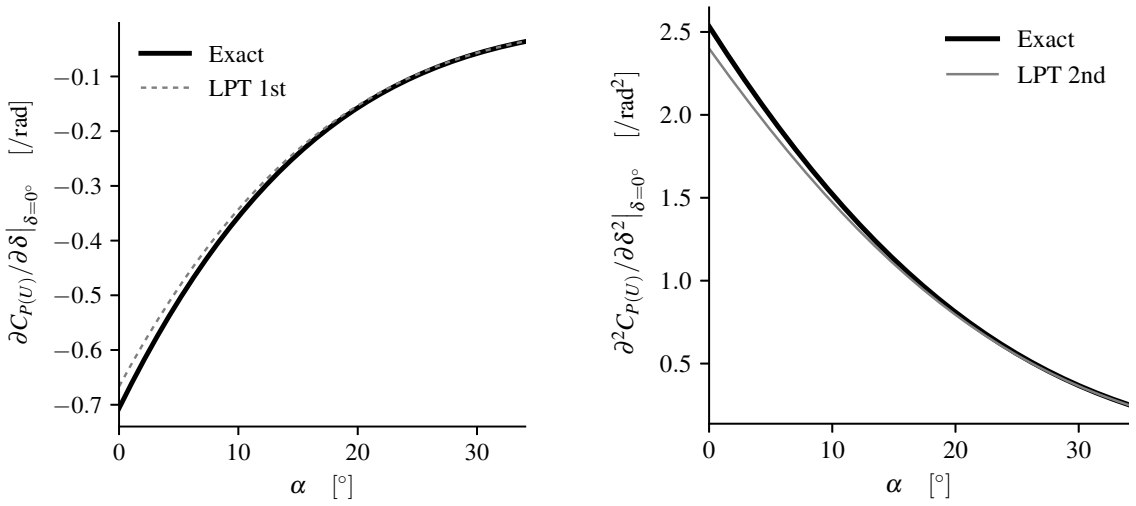

(a) Linear-stiffness term (b) Quadratic-stiffness term

Fig. 3.31 Prediction of pressure-coefficient derivatives by LPT for the expansion surface of a flat-plate at $M_\infty = 3$.

3.4 Summary

The presentation of material in this chapter is intended to give the reader a comprehensive overview of piston theory. A summary of the material may be centred around three topics:

- The variety of theoretical bases and of formulations associated with the term "piston theory",
- The limits of validity of piston theory and of the approximations it is based in,
- Recent trends and gaps in the literature relating to the application or extension of piston theory.

3.4.1 Theoretical Bases and Formulations of Piston Theory

A conceptual introduction to piston theory was given in Section 3.1. From the outset, it was noted that the term "piston theory" was associated with a number of methods yielding an algebraic relationship between the local downwash and the local fluid pressure. The physical analogy – in particular, the unsteady analogy – giving rise to the terminology of "piston" and "cylinder" was introduced in Section 3.1.1. Generalized formulations for the downwash and pressure expressions were introduced in Sections 3.1.2 and 3.1.3, respectively. While these formulations do not encompass all varieties of expressions associated with "piston theory", they do encapsulate the majority of point-local, planar formulations of both CPT and LPT. A more in-depth foray into the extensive literature associated with piston theory was made in Section 3.2. The purpose of Section 3.2 was two-fold:

- To give a high-level overview of historical developments and extensions to the method.

  This serves to showcase the extensive developments that have already been accomplished. It is the author's intention to bring attention to these previous developments in order that they may inform the future application of and developments to piston theory. Further discussion on this point is given in Section 3.4.3.

- To highlight the variety of formulations which are associated with the phrase "piston theory".

  It is the author's intention to bring attention to the broad variety of theoretical bases (with associated limitations and assumptions) which yield a "piston-theory"-type pressure-downwash relationship. An appreciation of these origins of the method serves to simultaneously:

- Remove unnecessary restrictions to the method. One example of a typically employed restriction of this type is in limiting piston theory to subsonic downwash,
- Promote better-informed application of the method. Attention is brought to implicit assumptions in the method which are often disregarded when applying the method. Examples include the assumption of negligible spanwise gradients (through an implicit invocation of strip theory) when applying piston theory to finite wings.

An abridged summary of the formulations introduced in Section 3.2 is given in Tables 3.4 and 3.5. It is to be noted that all methods in the list require upstream influence to be neglected in order to obtain a strictly self-influenced pressure-downwash relation. Retaining upstream influence results in a range of so-called "extended piston theories". The use of δ in Tables 3.4 and 3.5 denotes the nondimensional thickness, β is the angle of the bow shock, and $\varepsilon = \beta - \delta$.

3.4.2 Limits of Validity of Piston Theory

A variety of theoretical bases for piston theory is noted in Tables 3.4 and 3.5. Broadly speaking, the bases may be categorized as those involving:

- The application of the unsteady analogy,
- Various small-disturbance formulations,
- Potential flows,

It may be noted that linear potential flows serve as the basis for a significant number of the formulations which account for upstream influence, unsteadiness, or for the non-planar nature of the flow. In these formulations, the unsteady analogy is not invoked. Thus, the underlying assumptions of these methods differ from those based in hypersonic SDT formulations. The variety of theoretical bases therefore represents a variety of limits of validity of the resulting methods. A detailed treatment of the limits of validity of the broad range of formulations is not within the scope of the present work. However, some summarized remarks relating to the validity of these bases are offered below.

An introductory discussion on the validity limits of formulations employing the unsteady analogy was given in Section 3.1.4. The validity of the law of plane sections essentially hinges on the gradients of fluid properties being significantly smaller in the direction of plane advection than in the remaining directions. This condition typically arises as a consequence of body slenderness. To further reduce the governing equations to one dimension requires the resulting crossflow plane to similarly be dominated by a single direction. This illustrates

Table 3.4 Summary of piston theory formulations reviewed in Section 3.2 – Part 1.

Equation	Page number	Remarks	References	Theoretical basis	Upstream influence?	Bow-shock reflection?	Viscous interaction?
Eq. (3.18)	Page 130	Full isentropic form, $w/a_\infty < 1$	[88, 103]	1D Isentropic, Unsteady analogy	No	No	No
Eq. (3.8)	Page 119	Generalized form, Various bases, Includes models for $w/a_\infty > 1$, Includes LPT	[88, 103], [104, 105], [124, 125], [138, 143], [13, 14]	Unsteady analogy, Potential flow, Characteristics, Oblique shock	No	No	No
Eq. (3.52)	Page 139	Slender axisymmetric quasi-cone, $\mathscr{O}\left(\delta^2 + M_\infty^{-2}\right)$, $M_\infty \delta = \mathscr{O}(1)$	[77]	Unsteady analogy	No	No	No
Eq. (3.114)	Page 162	Axisymmetric quasi-cone, $\mathscr{O}(\varepsilon \tan \delta)$, $M_m > 2.5$	[140]	Unsteady analogy	No	No	No
Eq. (3.93)	Page 155	Low-frequency asymptotic form, $w/a_\infty < 1$, $\mathscr{O}(\delta)$, $\mathscr{O}(k)$, $k \ll 1$	[160, 161], [162, 163]	Linear potential flow	No	No	No
Eq. (3.73)	Page 150	High-frequency series form, $w/a_\infty < 1$, $\mathscr{O}(\delta)$	[144, 160], [145]	Linear potential flow	No	No	No
Eq. (3.77)	Page 151	Low-frequency series form, $w/a_\infty < 1$	[144, 160], [145]	Linear potential flow	Yes (3D)	No	No
Eq. (3.75)	Page 150	High-Mach series form, $w/a_\infty < 1$, $\mathscr{O}(\delta)$	[144, 160], [145]	Linear potential flow	Yes (3D)	No	No
Eq. (3.90)	Page 154	Second-order thickness, $w/a_\infty < 1$, $\mathscr{O}\left(\delta^2\right)$	[128]	Nonlinear potential flow	Yes (3D)	No	No
Eq. (3.110)	Page 160	Shell, high-Mach / high-frequency, $w/a_\infty < 1$, $\mathscr{O}(\delta)$	[169, 170]	Nonlinear potential flow	Yes[1]	No	No
Eq. (3.111)	Page 160	Shell, low spatial-frequency, $w/a_\infty < 1$, $\mathscr{O}(\delta)$	[169, 170]	Nonlinear potential flow	Yes[1]	No	No

[1] Assumes cylinder of infinite length with sinusoidal oscillations.

Table 3.5 Summary of piston theory formulations reviewed in Section 3.2 – Part 2.

Equation	Page number	Remarks	References	Theoretical basis	Upstream influence?	Bow-shock reflection?	Viscous interaction?
Eq. (3.115)	Page 164	Nonlinear thickness correction, $w/a_\infty > 1$ permitted	[125]	Linear potential flow	Yes[1]	No[2]	No
Eq. (3.117) Eq. (3.119)	Page 165 Page 166	Heuristic influence correction, $w/a_\infty < 1$	[172], [173]	Linear potential flow	Yes[3] (3D)	No	No
Eq. (3.122)	Page 170	Slender wedge, $\mathscr{O}(\beta)$, $\beta \ll 1$	[146]	Unsteady analogy, Hypersonic SDT	Yes (2D)	Yes	No
Ref [178]	Page 173	Non-slender wedge, $\mathscr{O}\left(\varepsilon + M_m^{-2}\right)$, $\varepsilon \ll 1$, $M_m > 2$	[178]	Unsteady analogy, Hypersonic SDT	Yes (2D)	Yes	No
Eq. (3.137) Eq. (3.141)	Page 176 Page 177	Viscous embedded wedge, Laminar boundary layer	[188]	Tangent wedge, Laminar BL	No	No	Yes
Eq. (3.146) Eq. (3.147)	Page 178 Page 178	Viscous interaction correction, Strong and weak interactions	[183]	LPT, Semi-empirical BL	No	No	Yes
Ref [189]	Page 179	First-order viscous coupling,	[189]	Hypersonic SDT, BL model	Yes (2D)	Yes	Yes
Eq. (3.8)	Page 181	First-order Euler-based LPT	[14]	Heuristic	Yes[4] (3D)	Yes[4]	No
Eq. (3.8)	Page 180 Page 182	Effective-shape correction, First-order NS-based LPT	[18], [13]	Heuristic	Yes[4] (3D)	Yes[4]	Yes[5]

[1] 3D influence from linear potential flow. Alternatively, 2D influence from perturbed Euler characteristics.
[2] Available if using perturbed Euler characteristics.
[3] Heuristic pressure-scaling factor from linear potential flow analysis.
[4] Mean-steady solution only.
[5] Only through mean-steady effective shape correction.

the failure of piston theory in the proximity of wing-tips and when applied to cylinders with significant crossflow.

The underlying assumptions in the SDT methods were introduced along with the methods themselves in Section 3.2, with emphasis on the methods in Sections 3.2.4 and 3.2.8. The assumptions are largely similar to those governing the application of the law of plane sections. The variety of methods introduced in Section 3.2.8 vary in their assumptions regarding flow unsteadiness and body slenderness. It is typically required that the bow shock lie close to the body (such that the Mach number behind the shock is approximately $M_m > 2.5$). Furthermore, small reduced frequencies and amplitudes of oscillation are typically invoked. The reduction of the formulations to a piston theory form requires the reflection of acoustic waves off of the bow shock to be neglected.

A discussion of the validity of the linear potential flow basis in the steady limit may be found in other works of the author [116, 121]. An extension of the analysis to unsteady flows is outside the scope of the present work. It was shown in [116, 121] that the linear truncation of the pressure equation is valid for approximately $M_\infty \delta < 0.2$. A framework for estimating the significance of nonlinear terms in the full potential equation was also presented in [116, 121].

Finally, the physical significance of second-order and third-order terms in piston theory was discussed in Section 3.3. No previous consideration of higher-order terms in LPT has been noted in the literature. The consideration of these terms in Section 3.3.2 demonstrated the potential for extending the validity of LPT predictions to larger deviations about the mean-steady flow solution.

3.4.3 Trends and Gaps in the Literature

The review of historical developments to piston theory in Section 3.2 was structured by the thematic contributions made, rather than chronologically. Nonetheless, a clear trend emerges when considering the recent renewed interest in CFD-based LPT, as discussed in Section 3.2.10. Following the successes of Euler-based LPT as applied to airfoils and to a wing-alone configuration [14], LPT has been applied to progressively more complex flows and geometries.

Examples include the application of Euler-based LPT to hypersonic vehicles by Shi et al [16] and by Yan et al [17]. The geometries were depicted in Figs. 3.22 and 3.23, respectively. It is clear from the geometries that regions of significant three-dimensionality in the flow will be present. It is thus not surprising that noticeably less accurate aeroprediction was reported by Shi et al [16] than is typical of Euler-based LPT when applied to simpler flows [14].

Recent literature has also shown an increase in the application of LPT relative to a viscous mean-steady solution obtained using the RANS equations (NS-based LPT). The applications have included wing-alone prediction [13, 18], full-vehicle aeroprediction [12, 18], and a variety of SBLI studies on panels [19, 194, 195].

The above applications of LPT have been heuristically justified as valid for "small perturbations". However, no justification has been offered for the application of LPT to three-dimensional flows. Similarly, in the application to viscous mean-steady flows have implicitly assumed that no viscous-inviscid interaction occurs. This reflects an unfortunate consequence of the extent of the body of literature utilizing piston theory: many historical extensions and accomplishments are overlooked. In particular, many of the historical developments to extend piston theory to

- Supersonic downwash,
- Accounting for upstream influence and unsteadiness,
- Non-planar flows,
- Viscous flows,

are overlooked in recent literature. This is reflected in the recent works on NS-based LPT, which do not consider the previous accomplishments of Ericsson [188] and Orlik-Rückemann [183] (with other works noted in Section 3.2.9) towards accounting for viscous-inviscid interaction in piston theory. It is the author's intention in Chapter 3 to bring attention to these often-overlooked works which have served to further piston theory as a method. These works provide valuable insight towards further extending the method.

The review of Section 3.2 has also served to identify a gap in the existing literature on piston theory. The vast majority of applications of CFD-based LPT have been heuristically justified. The identification of first-order LPT as a special case of inviscid hypersonic small-disturbance formulations in Section 3.2.8 serves to move the theoretical basis for LPT from the realm of "heuristic" towards "rigorous". Nonetheless, a general derivation or treatment of LPT (akin to that of CPT in Section 3.2.4) is noticeably absent in the literature. Such a derivation would serve to:

- Inform the application of Euler-based LPT to complex geometries and flows,
- Lay a foundation for the rigorous development of NS-based LPT,
- Inform future extensions to LPT,

Such a derivation from the three-dimensional Euler equations is the topic of Chapter 4.

Chapter 4

Mathematical Basis for Piston Theory

4.1 Introduction

The present chapter focusses predominantly on a unified treatment of the mathematical bases of classical piston theory (CPT) and local piston theory (LPT). It is an extension of the author's work originally presented in [196]. The context for and relevance of this work is presented in Section 4.1.1. An outline of the approach adopted in the development is given in Section 4.1.2. This is followed by the development of the general basis in Sections 4.2 to 4.4, the derivation of CPT in Section 4.5, and the derivation of LPT in Section 4.6. The mathematics is followed by a discussion of the derivations and their implications in Section 4.7. The chapter closes with a summary in Section 4.8.

4.1.1 Context and Relevance

An extensive review of the myriad of mathematical formulations of disparate bases that are referred to as "piston theory" was given in Sections 3.2 and 3.4. A summary of gaps and current trends in the literature surrounding piston theory was similarly given in Section 3.4. One of the significant gaps identified was the absence of mathematical basis for (or development leading to) local piston theory.

Particularly lucid insight into the mathematical basis for CPT may be found in the original development of Il'yushin [77] and in the categorization of CPT by Hayes and Probstein [27]. These treatments deal with the derivation of CPT from a 3D steady Euler formulation. However, these works have been largely overlooked in recent literature, with greater attention given to the engineering application of piston theory and to heuristic extensions of the method. The unfortunate consequences of this have been discussed in Section 3.4. The recent resurgence of interest in piston theory, including in CPT [144, 145, 160], presents an

opportunity to revisit the mathematics behind the method and to gain a deeper understanding into its limitations.

The same opportunity is presented for LPT. However, a significant difference is that no mathematical basis for LPT has been previously been presented in the literature. The generalized formulation of piston theory developed by the author in [59] highlighted the similarities and key differences between CPT and LPT through treatment from a common, generalized basis. This same philosophy is adopted in the present chapter. The derivation of LPT from the Euler equations is intended to provide a deeper understanding of LPT. It is the author's intention that this would serve to guide the application and development of further extensions to LPT. Furthermore, the mathematical basis would shed light on shortcomings in current formulations and applications of LPT [12, 16, 18, 19, 194, 195].

4.1.2 Approach to the Development

As noted in the introduction, the present chapter is an extension of the author's work originally presented in [196]. It also follows the spirit of the author's previous work in [59] in approaching both CPT and LPT from a common, generalized basis. The basic philosophy of the derivation lies in:

1. Presentation of a generalized non-dimensional formulation of the governing equations,
    (a) Identifying the general non-dimensional parameters of the governing equations and boundary conditions,
    (b) Identifying appropriate reference values for the non-dimensionalization as a function of the fluid state and geometry,
2. Case-specific development,
    (a) Specification of un-perturbed and perturbation quantities and reference values,
    (b) Determining the conditions required for reduction from a 3D to a 1D formulation,
    (c) Truncation of the development at a desired order of accuracy.

The roadmap for the development and its presentation is as follows:

- Section 4.2 will be concerned with Step 1 of the derivation philosophy in the context of total-value quantities. (In this context, "total-value" is to be understood as including both the un-perturbed and perturbation values.) The dimensional Euler equations

and the boundary conditions will be introduced in a variety of forms. A general non-dimensionalization will also be introduced,

- Section 4.3 will be concerned with Step 1 of the derivation philosophy in the context of perturbation quantities. The perturbation form of the Euler equations and boundary conditions will be introduced. A general non-dimensionalization for the perturbation form will be developed,
- Section 4.4 will introduce the considerations surrounding appropriate reference values for the non-dimensionalization. A discussion of reference values for flow gradients will be offered. This will conclude Step 1 of the derivation philosophy,
- The derivation of CPT from the non-dimensional perturbation form of the Euler equations will be presented in Section 4.5, which largely follows Step 2 of the derivation philosophy:
  - The specification of the reference values and perturbations will be given in Section 4.5.1. The derivation which will follow is similar to that due to Il'yushin [77], and conceptually follows the interpretation of CPT due to Hayes and Probstein [27],
  - The reduction from a 3D to a 2D formulation will be presented in Section 4.5.2,
  - The further reduction to a 1D formulation will be presented in Section 4.5.3,
  - The development will close in Section 4.5.4 with a discussion on the reduction to an algebraic relation between the surface-pressure and surface geometry.
- The derivation of LPT from the non-dimensional perturbation form of the Euler equations will be presented in Section 4.6. Essentially the same process will be followed as in Section 4.5,

Due to the volume of mathematics that is to be presented, minimal attention will be devoted to introductory remarks regarding the mathematics. The author recommends the works of [63, 64, 66, 197–202] for exposition of the mathematics, notations, and underlying fluid mechanics. Where convenient, Einstein summation notation will be introduced and a tensor form will be used.

4.1.3 Conceptual Introduction

The present section provides an introductory discussion surrounding non-dimensionalization, scaling analysis, and perturbation analysis / asymptotic development.

Non-Dimensionalization and Scaling Analysis

Non-dimensionalization in its essence is a transformation of variables from their physical quantities to purely numerical quantities. This is accomplished through describing the physical quantities as a fraction of some representative reference values. This may be written as

$$X_N = \frac{X}{X_R}, \tag{4.1}$$

where X is the variable described by its physical value, X_R is the reference value for the variable, and X_N is the variable described its non-dimensional value. The aim of the non-dimensionalization is to normalize the ranges of different variables X, such that $X_N = \mathscr{O}(1)$ for all the variables. This is essentially a scaling operation on the variables (and coordinates), and (in the context of asymptotic methods) has been described as "using a mathematical microscope" [201]. The result of non-dimensionalization is a mathematical description of the physics in which all scale-related terms appear in dimensionless parameter-groups that characterize the numerics of the phenomenon. This allows for two activities:

- It facilitates the comparison of physical phenomena with different scales or of different conditions. From a mathematical point of view, two different physical scenarios are equivalent if the dimensionless parameters describing the physics are the same between the scenarios. While the comparison of different physical flows is not of interest in the present work, the dimensionless parameter-groups describing the physics of the flow are,

- It facilitates the comparison of the different mathematical terms describing the physics of a given phenomenon. The aforementioned dimensionless parameter-groups accentuate the numerical (non-dimensional) magnitude of their companion terms (which are $\mathscr{O}(1)$). Comparison of the relative magnitudes of these groups allow for "smaller" mathematical terms to be neglected, as they make a negligible (in relative terms) contribution to the non-dimensional mathematical problem.

The latter of the two activities may be referred to as relative-magnitude analysis or scaling analysis. The non-dimensional parameter-groups that arise from the non-dimensionalization are often governing parameters of the physics, and are associated with non-dimensional numbers such as the Reynolds number, Mach number, reduced frequency, and more.

The use of scaling analysis in developing approximate mathematical models may be associated with the development of the boundary-layer equations, the Euler equations, the transonic small-disturbance form of the potential flow equation, and the linear potential equation. Further examples of scaling analysis with particular emphasis on fluid-structure

interaction may be found in [197–200]. Non-dimensionalization and scaling-analysis form a core component of perturbation analysis or asymptotic development.

Extent of Validity of Non-Dimensionalization

In practice, it is typical that the reference value X_R used for non-dimensionalization is treated as a constant. In the absence of coordinate-scaling, the result is that the non-dimensional variable X_N has the same temporal and spatial variation as the dimensional variable X, albeit scaled by the constant X_R. This emphasizes the difference between $X_N = 1$ and $X_N = \mathcal{O}(1)$. The non-dimensionalization does not eliminate the variation of the variable X_N, and regions of $X_N \ll 1$ may still occur. This raises the question of regions (or extent) of suitability (or validity) of a particular non-dimensionalization.

This is perhaps most intuitive through considering the introduction of coordinate scaling in order to render gradients $\mathcal{O}(1)$. It is known that in viscous flows, large flow gradients exist within a small distance from the surface of the body. Outside of this region, much small gradients are observed. The first region (the boundary layer) requires a different non-dimensionalization to that of the second (the inviscid "outer" flow).

The need for different non-dimensionalizations may arise either from the physics of the flow or from the introduction of small perturbations or parameters into the mathematical description of the flow. Some examples of flow features (or regions) which give rise to the need for a separate non-dimensionalization local to the region are:

- Entropy layers,
- Boundary layers,
- Regions of mixed subsonic / supersonic flows.

A non-dimensionalization which is valid throughout the entire domain of interest is termed "uniformly valid". When regions requiring different non-dimensionalizations exist in the full fluid domain, the "full solution" must be obtained by "stitching together" solutions from the various "domains of validity" in their region of overlap. This is the essence of the method of matched asymptotic expansions [201, 202]. In scenarios where different non-dimensionalizations are required, with complete (spatial) overlap of their domains of validity, the method of multiple scales [201] is used, in which scaled coordinates associated with each scale are introduced.

Perturbations and Asymptotic Developments

The essence of perturbation methods / asymptotic developments is in introducing a (mathematically) small deviation from a known solution or reference state / formulation. The expansion of the total variables into (known) un-perturbed variables and a series of (small) perturbation variables offers the possibility of a simpler mathematical formulation of the physical problem in terms of perturbation variables. This simplicity is typically achieved through truncating the expansion at some order of relative smallness. The neglect of (relatively) smaller terms emphasizes the connection between perturbation analysis, scaling analysis, and non-dimensionalization. An example of the use of perturbation methods to arrive at a mathematically simpler description of the physics is hypersonic SDT [78].

The introduction of the artificially small parameter opens the possibility of disparate scales and non-dimensionalizations being required, as well as the mathematical nature of the problem being altered. An example of the latter is the elimination of all second-order differential terms in the NS equations when viscosity is treated as vanishingly small (resulting in the first-order Euler equations). For non-zero viscosity, different physics (and non-dimensionalizations) act in different domains of the fluid.

4.2 General Equations

The starting point for the development is a general non-dimensionalization of the Euler equations. This will be extended to the body and shock boundary-conditions. The non-dimensionalization will begin with the equations in dimensional form. Following the introduction of reference quantities, additional terms will be introduced to describe non-dimensional groups. The nomenclature associated with the present chapter is expanded on in Section 4.2.1.

4.2.1 Nomenclature

Noting that reference values are also dimensional, the relationship between dimensional, reference, and non-dimensional values of a quantity is given by

$$X = X_R X_N \,, \tag{4.2}$$

where X is the dimensional value of the quantity, X_R is the reference value, and X_N is the non-dimensional value of the quantity. A definition of the nomenclature surrounding terms in the governing equations is given in Tables 4.1 to 4.3.

Where convenient, different reference frames will be used to define or derive various quantities. Broadly speaking, use will be made of the following categories of frames:

- $\mathscr{E}$ – an inertial frame translating at a uniform velocity relative to an earth-fixed frame. This relative velocity is equal to the mean steady translational velocity of the moving body of interest. For a rigid, non-rotating, non-accelerating body, $\mathscr{E}$ appears stationary relative to a body-fixed frame. The frame $\mathscr{E}$ shall be called the Eulerian frame,
- $\mathscr{G}$ – an inertial frame translating at a uniform velocity relative to $\mathscr{E}$. Relative to a body-fixed frame on a rigid, non-rotating, non-accelerating body, $\mathscr{G}$ appears to translate with uniform velocity. The frame $\mathscr{G}$ shall be called the Galilean frame, as it is obtained by performing a Galilean transform on $\mathscr{E}$,
- $\mathscr{A}$ – a locally-defined Cartesian frame adapted to an arbitrary surface. The frame is defined by a triad of orthogonal unit vectors, one of which is coincident with the instantaneous local surface-normal unit vector. The frame definition is thus local both in a spatial and temporal sense,
- $\mathscr{F}$ – a convected frame (material coordinates), attached to a fluid particle moving through space. In particular, a Frenet-Serret frame is defined for the particle.

The reference frames (with the exception of $\mathscr{G}$) are depicted in Fig. 4.1.

Table 4.1 Nomenclature of vectors.

Quantity	Dimensional	Reference	Non-dimensional
Velocity	$\mathbf{V}$	—	—
Unit normal-vector	—	—	$\hat{\mathbf{n}}$

Table 4.2 Nomenclature of scalars and components.

Quantity	Dimensional	Reference	Non-dimensional
Spatial gradients	$\frac{\partial}{\partial x_i}$	$\frac{1}{L_i}, \frac{1}{L_R}$	$\frac{\partial}{\partial \xi_i}$
Temporal gradients	$\frac{\partial}{\partial t}$	$\frac{1}{t_R}$	$\frac{\partial}{\partial t_N}$
Fluid density	ρ	ρ_R	ρ_N
Fluid pressure	p	p_R	p_N
Adiabatic exponent	—	—	γ
Specific enthalpy	h	h_R	h_N
Specific entropy	s	s_R	s_N
Fluid velocity	v_i	U_i, U_R	u_i
Speed of sound	a	a_R	a_N
Normal-velocity of shock	G	—	—
Frame velocity	w_i	—	—
Unit normal-vector	—	—	n_i

Table 4.3 Nomenclature of total-quantity form non-dimensional parameters.

Quantity	Definition	Associated with
k_t	$\frac{L_R}{U_R t_R}$	Time-derivatives
k_{xi} with $i = 1, 2, 3$	$\frac{L_R U_i}{L_i U_R}$	Spatial-derivatives
k_{ui} with $i = 1, 2, 3$	$\frac{U_i}{U_R}$	Mean flow direction
k_{bi} with $i = 1, 2, 3$	$\frac{U_{bi}}{U_R}$	Body translational velocity
k_f	$\frac{p_R}{\rho_R U_R^2}$	Momentum-equation pressure gradient
k_a	$\frac{p_R}{\rho_R a_R^2}$	Energy-equation pressure gradient

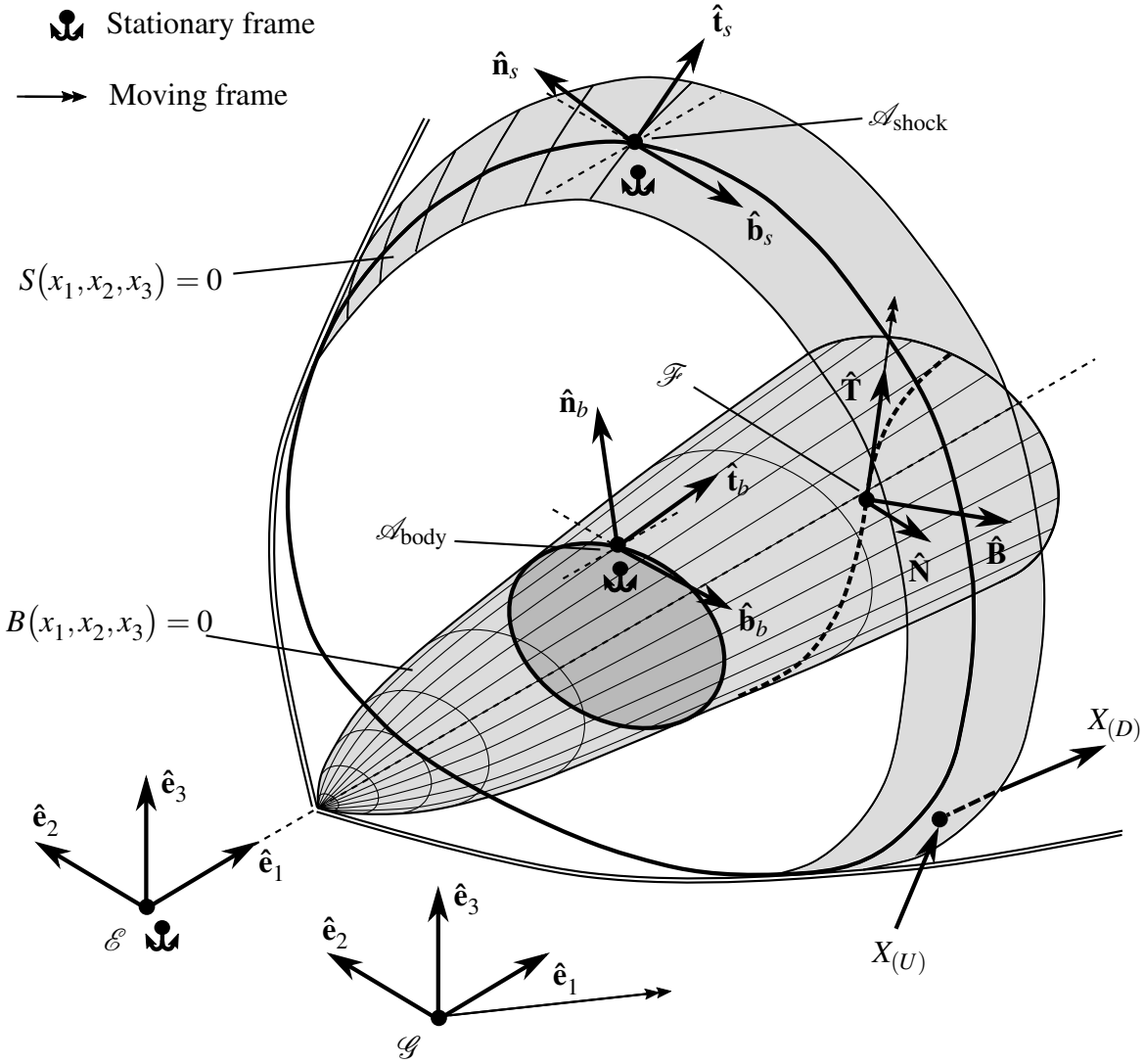

Fig. 4.1 Illustration of reference frames used.

The general definition of the adapted frame $\mathscr{A}$ will be narrowed for the purposes of the present work. In particular, the following specifications will be made regarding orientation of the adapted frame $\mathscr{A}$ and the nomenclature surrounding it:

- Let the basis vectors of the Eulerian frame $\mathscr{E}$ be given as $\hat{\mathbf{e}}_\mathbf{i}$. Attention is drawn to a distinction in nomenclature:
  - Vectors are typeset in boldface, while components are not,
  - $\hat{\mathbf{e}}_\mathbf{i}$ denotes the i-th direction vector in the coordinate basis of the Eulerian frame $\mathscr{E}$,
- The adapted frame $\mathscr{A}$ is defined by the triad of mutually orthogonal unit vectors $\hat{\mathbf{t}}$, $\hat{\mathbf{b}}$, $\hat{\mathbf{n}}$. The use of a subscript "s" or "b" will distinguish (where necessary) between the adapted frame $\mathscr{A}$ on the shock surface and on the body surface, respectively,
- By definition, $\hat{\mathbf{n}}$ is the instantaneous, local unit normal-vector to the surface to which the frame $\mathscr{A}$ is adapted. If the surface is described by a function $\mathbb{A}(x_i,t) = 0$, then

$$\hat{\mathbf{n}} \equiv \sum_{i=1}^{3} n_i \hat{\mathbf{e}}_\mathbf{i}\,, \tag{4.3}$$

$$\hat{\mathbf{n}} \equiv \frac{\nabla \mathbb{A}}{|\nabla \mathbb{A}|}\,, \tag{4.4}$$

  It will be the convention to orient $\hat{\mathbf{n}}$ into the fluid when $\mathscr{A}$ is adapted to the body, and into the pre-shock domain when $\mathscr{A}$ is adapted to the shock,
- To define the orientation of the frame $\mathscr{A}$, $\hat{\mathbf{b}}$ will be defined to lie in the plane normal to $\hat{\mathbf{e}}_\mathbf{1}$. In other words,

$$\hat{\mathbf{b}} \equiv \sum_{i=2}^{3} b_i \hat{\mathbf{e}}_\mathbf{i}\,, \tag{4.5}$$

$$\hat{\mathbf{b}} \cdot \hat{\mathbf{e}}_\mathbf{1} \equiv 0\,, \tag{4.6}$$

- The final orientation of the adapted frame $\mathscr{A}$ will be given by orienting the remaining surface-tangential unit-vector t downstream, such that

$$\hat{\mathbf{t}} \equiv \sum_{i=1}^{3} t_i \hat{\mathbf{e}}_\mathbf{i}\,, \tag{4.7}$$

$$\hat{\mathbf{t}} \cdot \hat{\mathbf{e}}_\mathbf{1} \geq 0\,, \tag{4.8}$$

The following transformation between the oriented adapted-frame $\mathscr{A}$ and the Eulerian frame $\mathscr{E}$ may then be found:

$$\begin{pmatrix} \hat{\mathbf{t}} \\ \hat{\mathbf{n}} \\ \hat{\mathbf{b}} \end{pmatrix} = \begin{bmatrix} \zeta_{23} & -\frac{n_1 n_2}{\zeta_{23}} & -\frac{n_1 n_3}{\zeta_{23}} \\ n_1 & n_2 & n_3 \\ 0 & -\frac{n_3}{\zeta_{23}} & \frac{n_2}{\zeta_{23}} \end{bmatrix} \begin{pmatrix} \hat{\mathbf{e}}_1 \\ \hat{\mathbf{e}}_2 \\ \hat{\mathbf{e}}_3 \end{pmatrix}, \tag{4.9}$$

where

$$\zeta_{23} \equiv \sqrt{n_2^2 + n_3^2} = \sqrt{1 - n_1^2}. \tag{4.10}$$

The transformation matrix between frames, as well as the components of the unit normal-vector $\hat{\mathbf{n}}$, may be more conveniently expressed in terms of two angles:

- The angle between the unit normal-vector $\hat{\mathbf{n}}$ and the positive x_3 axis, which will be defined by the symbol η:

$$\cos\eta \equiv \hat{\mathbf{n}} \cdot \hat{\mathbf{e}}_3, \tag{4.11}$$

  This angle may be loosely interpreted as the "thickness angle" for a wedge with its thickness mid-plane oriented normal to $\hat{\mathbf{e}}_3$. The angle has the range $\eta = [0, \pi]$ in radians.

- The angle between the projection of $\hat{\mathbf{n}}$ onto the x_1x_2-plane and the $-x_1$ axis, which will be defined by the symbol λ:

$$\cos\lambda \equiv -\frac{\mathbf{n}_{12} \cdot \hat{\mathbf{e}}_1}{\left|\mathbf{n}_{12} \cdot \hat{\mathbf{e}}_1\right|}, \tag{4.12}$$

  where $\mathbf{n}_{12} \equiv n_1 \hat{\mathbf{e}}_1 + n_2 \hat{\mathbf{e}}_2$, and the angle is defined as positive for rotations about $\mathbf{e}_3$. This angle may be loosely interpreted as the "sweep angle" for a wedge with its thickness mid-plane oriented normal to $\hat{\mathbf{e}}_3$. The angle has the range $\eta = [-\pi, \pi]$ in radians. The portion of the range $\left[-\frac{\pi}{2}, \frac{\pi}{2}\right]$ is associated with inclination of $\hat{\mathbf{n}}$ along the $-x_1$ axis (upstream).

In terms of these angles, the transformation between the oriented adapted-frame $\mathscr{A}$ and the Eulerian frame $\mathscr{E}$ of Eq. (4.9) is written as

$$\begin{pmatrix} \hat{\mathbf{t}} \\ \hat{\mathbf{n}} \\ \hat{\mathbf{b}} \end{pmatrix} = \begin{bmatrix} \cos\eta\sqrt{1+\chi^2} & -\frac{\chi \sin\eta\cos\lambda}{\sqrt{1+\chi^2}} & +\frac{\sin\eta\cos\lambda}{\sqrt{1+\chi^2}} \\ -\sin\eta\cos\lambda & -\sin\eta\sin\lambda & \cos\eta \\ 0 & -\frac{1}{\sqrt{1+\chi^2}} & -\frac{\chi}{\sqrt{1+\chi^2}} \end{bmatrix} \begin{pmatrix} \hat{\mathbf{e}}_1 \\ \hat{\mathbf{e}}_2 \\ \hat{\mathbf{e}}_3 \end{pmatrix}, \tag{4.13}$$

where $\chi \equiv \tan\eta \sin\lambda$.

4.2.2 Governing Equations

The following key assumptions will be made throughout the course of the development:

1. The fluid is assumed to be inviscid everywhere in the fluid domain,
2. The equation of state of an ideal gas will be assumed,
3. The flow is assumed to be adiabatic,
4. Gravitational and buoyant forces are neglected,
5. The fluid is assumed to be of homogeneous composition, with chemical reactions neglected.

The Euler equations will thus govern the physics of the flow throughout the entire domain. The Euler equations may be presented in a variety of alternative yet equivalent forms and notations. They may also be expressed in a variety of reference frames. Some of these are explored below.

Dimensional Form in the Eulerian Frame

Of particular interest in the present work is the tensor form given by Aris [63] in the Eulerian frame $\mathscr{E}$, which is valid in both Cartesian and curvilinear coordinate frames:

$$\text{Continuity:} \quad \frac{\partial \rho}{\partial t} + v^m \rho_{;m} + \rho v^m{}_{;m} = 0\,, \tag{4.14}$$

$$\text{Momentum:} \quad \frac{\partial v^i}{\partial t} + v^m v^i{}_{;m} + \frac{1}{\rho} g^{im} p_{;m} = 0\,, \tag{4.15}$$

$$\text{Energy:} \quad \frac{\partial p}{\partial t} + v^m p_{;m} + \rho v^m{}_{;m} a^2 = 0\,, \tag{4.16}$$

where Einstein summation notation has been used, indices in the upper position denote components of contravariant vectors, indices in the lower position denote components of covariant vectors, and the ";" notation denotes the covariant derivative. The tensor g^{ij} is the metric tensor of the coordinate basis.

The particular form of the energy equation in Eq. (4.16) was shown in [203] to not require the assumption of an ideal gas. The energy equation in particular has a number of alternative forms, two of which are given below (also is tensor form in the Eulerian frame $\mathscr{E}$):

$$\text{Energy:} \quad \frac{\partial s}{\partial t} + v^m s_{;m} = 0\,, \tag{4.17}$$

$$\text{Energy:} \quad \frac{\partial p}{\partial t} - \rho v_m \frac{\partial v^m}{\partial t} - \rho v_m v^l v^m{}_{;l} + \rho a^2 v^m{}_{;m} = 0\,. \tag{4.18}$$

Dimensional Form in the Galilean Frame

Following Aris' [63] treatment of the convected derivative of tensors in curvilinear space, the following definitions of the time derivative can be written in a frame which is conducted with velocity w^i relative to the Eulerian frame $\mathscr{E}$:

For a scalar f:

$$\frac{\delta f}{\delta t} = \frac{\partial f}{\partial t} + w^m f_{;m}\,. \tag{4.19}$$

For a contravariant vector v^i:

$$\frac{\delta v^i}{\delta t} = \frac{\partial v^i}{\partial t} + w^m v^i{}_{;m} - v^m w^i{}_{;m}\,. \tag{4.20}$$

For a covariant vector u_i:

$$\frac{\delta v_i}{\delta t} = \frac{\partial v_i}{\partial t} + w^m v_{i;m} + v_m w^m{}_{;i}\,. \tag{4.21}$$

where derivatives of the form $\frac{\delta}{\delta t}$ are time-derivatives in the Galilean frame $\mathscr{G}$.

Upon substitution of the above expressions into the Euler equations in the Eulerian frame $\mathscr{E}$, given by Eqs. (4.14) to (4.16), we obtain the Euler equations in the Galilean frame $\mathscr{G}$ as:

$$\text{Continuity:} \quad \frac{\delta \rho}{\delta t} + (v^m - w^m)\rho_{;m} + \rho v^m{}_{;m} = 0\,, \tag{4.22}$$

$$\text{Momentum:} \quad \frac{\delta v^i}{\delta t} + (v^m - w^m)v^i{}_{;m} + \frac{1}{\rho} g^{im} p_{;m} = -v^m w^i{}_{;m}\,, \tag{4.23}$$

$$\text{Energy:} \quad \frac{\delta p}{\delta t} + (v^m - w^m)p_{;m} + \rho a^2 v^m{}_{;m} = 0\,, \tag{4.24}$$

The energy equation may once again be combined with the momentum equation to give the alternative form of the energy equation as

$$\frac{1}{\rho}\frac{\delta p}{\delta t} - (v_l - w_l)\frac{\delta v^l}{\delta t} - (v_l - w_l)(v^m - w^m)v^l{}_{;m} + v^m{}_{;m} a^2 = (v_l - w_l)v^m w^l{}_{;m}\,, \tag{4.25}$$

where the terms appearing on the right-hand-side of the equations, involving $v^m w^i{}_{;m}$, may be interpreted as the directional derivative of the frame-convection vector (w^i) in the direction of the local fluid velocity (v^m).

Non-Dimensional Form in Cartesian Coordinates

The Euler equations are now non-dimensionalized in the Eulerian frame $\mathscr{E}$ in a Cartesian coordinate basis. This is done for the simplicity of illustration and interpretation offered by the Cartesian system. Most notably:

- The metric tensor g_{ij} does not vary throughout the coordinate space,
- No distinction needs to be made between covariant and contravariant components of vectors,
- No distinction needs to be made between partial differentiation and covariant differentiation.

The analysis which follows in the remainder of Chapter 4 may be extended to non-Cartesian coordinate systems. However, this is outside the scope of the present work.

With the preliminaries regarding the selection of coordinate system completed, the attention is turned to the dimensional form of the Euler equations in the Eulerian frame $\mathscr{E}$ in Cartesian coordinates, which may be written in tensor form as

$$\text{Continuity:} \quad \frac{\partial \rho}{\partial t} + v_m \rho_{,m} + \rho v_{m,m} = 0\,, \tag{4.26}$$

$$\text{Momentum:} \quad \frac{\partial v_i}{\partial t} + v_m v_{i,m} + \frac{1}{\rho} p_{,i} = 0\,, \tag{4.27}$$

$$\text{Energy:} \quad \frac{\partial p}{\partial t} + v_m p_{,m} + \rho a^2 v_{m,m} = 0\,, \tag{4.28}$$

where "," notation denotes partial differentiation. It is noted that $v_{m,m}$ denotes the divergence of velocity, while terms of the form $v_m X_{,m}$ denote the advection of the quantity or tensor X.

A final preliminary step will be taken before introducing the non-dimensionalization by writing out the equations in component from with consistent notation for spatial and temporal partial derivatives. Terms will be arranged according to the coordinates w.r.t. which derivatives are taken:

$$\text{Continuity:} \quad \frac{\partial \rho}{\partial t} + v_1 \frac{\partial \rho}{\partial x_1} + \rho \frac{\partial v_1}{\partial x_1} + v_2 \frac{\partial \rho}{\partial x_2} + \rho \frac{\partial v_2}{\partial x_2} + v_3 \frac{\partial \rho}{\partial x_3} + \rho \frac{\partial v_3}{\partial x_3} = 0\,, \tag{4.29}$$

$$\text{Momentum:} \quad \frac{\partial v_i}{\partial t} + v_1 \frac{\partial v_i}{\partial x_1} + v_2 \frac{\partial v_i}{\partial x_2} + v_3 \frac{\partial v_i}{\partial x_3} + \frac{1}{\rho} \frac{\partial p}{\partial x_i} = 0\,, \tag{4.30}$$

$$\text{Energy:} \quad \frac{\partial p}{\partial t} + v_1 \frac{\partial p}{\partial x_1} + \rho a^2 \frac{\partial v_1}{\partial x_1} + v_2 \frac{\partial p}{\partial x_2} + \rho a^2 \frac{\partial v_2}{\partial x_2} + v_3 \frac{\partial p}{\partial x_3} + \rho a^2 \frac{\partial v_3}{\partial x_3} = 0\,. \tag{4.31}$$

The nomenclature of the non-dimensionalization will follow Eq. (4.2) and Table 4.2. In the total-quantity form of the equations, reference values X_R for non-dimensionalization are chosen such that

$$X_N = \frac{X}{X_R} = \mathscr{O}(1)\,, \tag{4.32}$$

with the explicit assumption that gradients are non-dimensionalized using characteristics lengths L_i and a characteristic time t_R such that

$$\frac{\partial}{\partial x_i} = \frac{1}{L_i}\frac{\partial}{\partial \xi_i} \quad \text{with} \quad \frac{\partial}{\partial \xi_i} = \mathscr{O}(1)\,, \tag{4.33}$$

$$\frac{\partial}{\partial t} = \frac{1}{t_R}\frac{\partial}{\partial t_N} \quad \text{with} \quad \frac{\partial}{\partial t_N} = \mathscr{O}(1)\,, \tag{4.34}$$

where some abuse of notation has been committed to relay the idea that non-dimensional gradients are $\mathscr{O}(1)$. The implicit assumption in the above is that the gradients of all variables X may be appropriately non-dimensionalized using the same scale L_t or t_R. The validity of this approach is questionable where variables have different scales of gradients. An example of this would be comparing the variation of v_1 and p in the surface-normal direction in a boundary-layer, or in constant-density flows. The present analysis may readily be extended through the addition of ad-hoc "switching" parameters (in essense similar to the Kronecker delta) to re-scale the non-dimensionalization of particular terms. This is outside the scope of the present development.

With the understanding that reference quantities are chosen such that the *total value* (including the mean and the perturbation) of fluid quantities is non-dimensionalized to $\mathscr{O}(1)$, the following total-quantity form of the generally non-dimensionalized Euler equations is obtained:

Continuity:

$$\left.\begin{aligned} &\left(\frac{\rho_R}{t_R}\right)\frac{\partial \rho_N}{\partial t_N} + \left(\frac{\rho_R U_1}{L_1}\right)u_1\frac{\partial \rho_N}{\partial \xi_1} + \left(\frac{\rho_R U_1}{L_1}\right)\rho_N\frac{\partial u_1}{\partial \xi_1} \\ &\quad + \left(\frac{\rho_R U_2}{L_2}\right)u_2\frac{\partial \rho_N}{\partial \xi_2} + \left(\frac{\rho_R U_2}{L_2}\right)\rho_N\frac{\partial u_2}{\partial \xi_2} \\ &\quad + \left(\frac{\rho_R U_3}{L_3}\right)u_3\frac{\partial \rho_N}{\partial \xi_3} + \left(\frac{\rho_R U_3}{L_3}\right)\rho_N\frac{\partial u_3}{\partial \xi_3} \end{aligned}\right\} = 0\,, \tag{4.35}$$

$$\text{Momentum:}\quad \left.\begin{aligned}&\left(\frac{U_i}{t_R}\right)\frac{\partial u_i}{\partial t_N}+\left(\frac{U_iU_1}{L_1}\right)u_1\frac{\partial u_i}{\partial \xi_1}\\&+\left(\frac{U_iU_2}{L_2}\right)u_2\frac{\partial u_i}{\partial \xi_2}\\&+\left(\frac{U_iU_3}{L_3}\right)u_3\frac{\partial u_i}{\partial \xi_3}\end{aligned}\right\}=-\left(\frac{p_R}{\rho_R L_i}\right)\frac{1}{\rho_N}\frac{\partial p_N}{\partial \xi_i}\,, \tag{4.36}$$

$$\text{Energy:}\quad \left.\begin{aligned}&\left(\frac{p_R}{t_R}\right)\frac{\partial p_N}{\partial t_N}+\left(\frac{p_RU_1}{L_1}\right)u_1\frac{\partial p_N}{\partial \xi_1}+\left(\frac{\rho_Ra_R^2U_1}{L_1}\right)\rho_Na_N^2\frac{\partial u_1}{\partial \xi_1}\\&+\left(\frac{p_RU_2}{L_2}\right)u_2\frac{\partial p_N}{\partial \xi_2}+\left(\frac{\rho_Ra_R^2U_2}{L_2}\right)\rho_Na_N^2\frac{\partial u_2}{\partial \xi_2}\\&+\left(\frac{p_RU_3}{L_3}\right)u_3\frac{\partial p_N}{\partial \xi_3}+\left(\frac{\rho_Ra_R^2U_3}{L_3}\right)\rho_Na_N^2\frac{\partial u_3}{\partial \xi_3}\end{aligned}\right\}=0\,. \tag{4.37}$$

In the above equations, the non-dimensional term-groupings are of $\mathscr{O}(1)$. The relative magnitude of terms comes from the term-groupings in parentheses preceding each group of non-dimensional terms. The above equations may be manipulated to highlight the fundamental non-dimensional groups or characteristic parameters of the equations as below:

$$\text{Continuity:}\quad \left.\begin{aligned}&\left(\frac{L_R}{U_Rt_R}\right)\frac{\partial \rho_N}{\partial t_N}+\left(\frac{L_RU_1}{L_1U_R}\right)u_1\frac{\partial \rho_N}{\partial \xi_1}+\left(\frac{L_RU_1}{L_1U_R}\right)\rho_N\frac{\partial u_1}{\partial \xi_1}\\&+\left(\frac{L_RU_2}{L_2U_R}\right)u_2\frac{\partial \rho_N}{\partial \xi_2}+\left(\frac{L_RU_2}{L_2U_R}\right)\rho_N\frac{\partial u_2}{\partial \xi_2}\\&+\left(\frac{L_RU_3}{L_3U_R}\right)u_3\frac{\partial \rho_N}{\partial \xi_3}+\left(\frac{L_RU_3}{L_3U_R}\right)\rho_N\frac{\partial u_3}{\partial \xi_3}\end{aligned}\right\}=0\,, \tag{4.38}$$

$$\text{Momentum:}\quad \left.\begin{aligned}&\left(\frac{L_R}{U_Rt_R}\right)\frac{\partial u_i}{\partial t_N}+\left(\frac{L_RU_1}{L_1U_R}\right)u_1\frac{\partial u_i}{\partial \xi_1}\\&+\left(\frac{L_RU_2}{L_2U_R}\right)u_2\frac{\partial u_i}{\partial \xi_2}\\&+\left(\frac{L_RU_3}{L_3U_R}\right)u_3\frac{\partial u_i}{\partial \xi_3}\end{aligned}\right\}=-\left(\frac{p_R}{\rho_RU_R^2}\frac{U_R^2}{U_i^2}\frac{L_RU_i}{L_iU_R}\right)\frac{1}{\rho_N}\frac{\partial p_N}{\partial \xi_i}\,, \tag{4.39}$$

$$\text{Energy:}\quad \left.\begin{aligned}&\left(\frac{p_R}{\rho_R a_R^2}\frac{L_R}{U_R t_R}\right)\frac{\partial p_N}{\partial t_N}+\left(\frac{p_R}{\rho_R a_R^2}\frac{L_R U_1}{L_1 U_R}\right)u_1\frac{\partial p_N}{\partial \xi_1}+\left(\frac{L_R U_1}{L_1 U_R}\right)\rho_N a_N^2\frac{\partial u_1}{\partial \xi_1}\\ &+\left(\frac{p_R}{\rho_R a_R^2}\frac{L_R U_2}{L_2 U_R}\right)u_2\frac{\partial p_N}{\partial \xi_2}+\left(\frac{L_R U_2}{L_2 U_R}\right)\rho_N a_N^2\frac{\partial u_2}{\partial \xi_2}\\ &+\left(\frac{p_R}{\rho_R a_R^2}\frac{L_R U_3}{L_3 U_R}\right)u_3\frac{\partial p_N}{\partial \xi_3}+\left(\frac{L_R U_3}{L_3 U_R}\right)\rho_N a_N^2\frac{\partial u_3}{\partial \xi_3}\end{aligned}\right\}=0\,. \tag{4.40}$$

Following the introduction of the non-dimensional parameters defined in Table 4.3, these may be condensed into the following form, with the explicit term descriptions dropped in favour of the k-notation:

$$\text{Continuity:}\quad \left.\begin{aligned}&(k_t)\frac{\partial \rho_N}{\partial t_N}+(k_{x1})\left[u_1\frac{\partial \rho_N}{\partial \xi_1}+\rho_N\frac{\partial u_1}{\partial \xi_1}\right]\\ &+(k_{x2})\left[u_2\frac{\partial \rho_N}{\partial \xi_2}+\rho_N\frac{\partial u_2}{\partial \xi_2}\right]\\ &+(k_{x3})\left[u_3\frac{\partial \rho_N}{\partial \xi_3}+\rho_N\frac{\partial u_3}{\partial \xi_3}\right]\end{aligned}\right\}=0\,, \tag{4.41}$$

$$\text{Momentum:}\quad \left.\begin{aligned}&(k_t)\frac{\partial u_i}{\partial t_N}+(k_{x1})u_1\frac{\partial u_i}{\partial \xi_1}\\ &+(k_{x2})u_2\frac{\partial u_i}{\partial \xi_2}\\ &+(k_{x3})u_3\frac{\partial u_i}{\partial \xi_3}\end{aligned}\right\}=-\left(\frac{k_f k_{xi}}{k_{ui}^2}\right)\frac{1}{\rho_N}\frac{\partial p_N}{\partial \xi_i}\,, \tag{4.42}$$

$$\text{Energy:}\quad \left.\begin{aligned}&(k_a k_t)\frac{\partial p_N}{\partial t_N}+(k_a k_{x1})u_1\frac{\partial p_N}{\partial \xi_1}+(k_{x1})\rho_N a_N^2\frac{\partial u_1}{\partial \xi_1}\\ &+(k_a k_{x2})u_2\frac{\partial p_N}{\partial \xi_2}+(k_{x2})\rho_N a_N^2\frac{\partial u_2}{\partial \xi_2}\\ &+(k_a k_{x3})u_3\frac{\partial p_N}{\partial \xi_3}+(k_{x3})\rho_N a_N^2\frac{\partial u_3}{\partial \xi_3}\end{aligned}\right\}=0\,. \tag{4.43}$$

These may be further condensed through re-introduction of the summation-notation as

$$\text{Continuity:}\quad (k_t)\frac{\partial \rho_N}{\partial t_N}+(k_{xm})\left[u_m\frac{\partial \rho_N}{\partial \xi_m}+\rho_N\frac{\partial u_m}{\partial \xi_m}\right]=0\,, \tag{4.44}$$

$$\text{Momentum:}\quad (k_t)\frac{\partial u_i}{\partial t_N}+(k_{xm})u_m\frac{\partial u_i}{\partial \xi_m}=-\left(\frac{k_f k_{xi}}{k_{ui}^2}\right)\frac{1}{\rho_N}\frac{\partial p_N}{\partial \xi_i}\,,\quad \text{no sum on } i \tag{4.45}$$

$$\text{Energy:} \qquad (k_a k_t)\frac{\partial p_N}{\partial t_N} + (k_a k_{xm})u_m \frac{\partial p_N}{\partial \xi_m} + (k_{xm})\rho_N a_N^2 \frac{\partial u_m}{\partial \xi_m} = 0\,. \tag{4.46}$$

This is the final variation considered of the non-dimensional total-quantity form of the Euler equations in a Cartesian basis in the Eulerian frame $\mathscr{E}$. It is repeated here that for the total-quantity form, the reference values for non-dimensionalization are chosen such that, e.g., $p_N = \frac{p}{p_R} = \mathscr{O}(1)$. Components of velocities and gradients are individually non-dimensionalized by, for example, $u_i = \frac{v_i}{U_i} = \mathscr{O}(1)$, while comparison between components is facilitated by the reference value U_R.

4.2.3 Shock Boundary Conditions

The shock boundary conditions are strictly-speaking compatibility relations for the discontinuity in the fluid. The final "outer boundary" of the fluid domain lies "outside" the shock and has an influence in defining the shock structure and fluid properties behind the shock. An interpretation of boundary conditions and permissible prescription of physical and numerical conditions based on characteristics, as put forward in Chapters 16 and 19 of [66], is challenging when applied to shocks. It is noted that the Mach-number of the flow downstream of the shock boundary, normal to the shock surface, is subsonic. As a consequence, the shock boundary acts as a subsonic inlet of sorts. This places restrictions on the physical boundary conditions which may be prescribed. Without dwelling on this point, it is noted that the equations governing the shock prescribe the necessary relations between the primitive variables (ρ, p, and $\mathbf{V}$) as a function of the upstream fluid state and of the shape and orientation of the shock surface.

The view of the shock relations as compatibility conditions internal to the fluid domain is reinforced by the derivation of the Rankine-Hugoniot equations in Chapter 2 of [64]. It is noted that the discontinuities in fluid gradients (C^1 and higher) exist across the shock, and so the Euler equations can only be satisfied in an integral sense (C^0). This is clearly shown through the transformation from the differential form of the Euler equations in [64] as

$$\frac{\partial \mathbf{U}}{\partial t} + \nabla \cdot \mathbf{F} = 0\,, \tag{4.47}$$

to the integral form of

$$\frac{\partial}{\partial t}\iiint_V \mathbf{U}\,\mathrm{d}V + \iint_S \mathbf{F}\cdot\mathrm{d}\mathbf{S}\,, \tag{4.48}$$

which, for a moving shock surface described by $\Sigma(x_i,t)=0$ may be written (for a vanishingly small control volume) as

$$[\mathbf{F}]^{(S)}\cdot\nabla\Sigma+[\mathbf{U}]^{(S)}\frac{\partial\Sigma}{\partial t}\,, \tag{4.49}$$

In the above, $\mathbf{U}=\{\rho,\rho\mathbf{V},\rho E\}$ is the vector of conservative variables (H being the total internal energy), and $\mathbf{F}=\{\rho\mathbf{V},\rho\mathbf{V}\mathbf{V}+\mathbf{P},\rho\mathbf{V}H\}$ is the flux vector ($\mathbf{P}$ being the stress tensor and H being the total enthalpy). Furthermore,

$$[X]^{(S)}\equiv X_{(D)}-X_{(U)}\,, \tag{4.50}$$

Is the notation for the jump in a quantity X across the shock from its upstream value $X_{(U)}$ to its downstream value $X_{(D)}$. Equation (4.49) is the general form of the Rankine-Hugoniot equations, which describe the relationship between fluid properties downstream and upstream of the shock surface.

It is emphasized that the Rankine-Hugoniot equations provide compatibility conditions for the zeroth-derivative in the fluid variables as a function of the shock orientation (through $\nabla\Sigma$) and of the shock translational velocity (through $\frac{\partial\Sigma}{\partial t}$) in the Eulerian frame $\mathscr{E}$. While further insight may be gained into flow gradients through consideration of the shock shape (curvature) and rotational velocity, a discussion of these points is reserved for Section 4.4. For the present purposes, it is sufficient to note that the Rankine-Hugoniot equations provide compatibility relations for the jump in zeroth-derivatives of fluid variables at the interior of the fluid domain. While it has been stressed that the shock surface is not strictly the exterior boundary of the fluid, it is convenient in the present work to consider it as the "boundary" with associated boundary conditions for the portion of the fluid domain bounded by the body surface and the shock surface.

With these extensive preliminaries aside, the attention may be turned to the shock relations themselves. No derivation of the relations will be offered, as this has been covered extensively in the literature. The relations may be expressed in a variety of forms and notations. The following nomenclature is associated with the shock relations:

- The total-quantity form of the velocity of the fluid relative to the Eulerian frame $\mathscr{E}$ is given by $\mathbf{V_f}$,
- The total-quantity form of the (translational) velocity of the shock surface relative to the Eulerian frame $\mathscr{E}$ is given by $\mathbf{V_s}$,
- The total-quantity form of the fluid velocity relative to the shock surface is then given by

$$\mathbf{V_r}=\mathbf{V_f}-\mathbf{V_s}\,, \tag{4.51}$$

- The unit-vector normal to the instantaneous shock surface is given by $\hat{\mathbf{n}}$. It is repeated here that $\hat{\mathbf{n}}$ is oriented into the pre-shock domain,

- The relative-velocity of the fluid normal to the shock surface is then denoted by w, with

$$w \equiv (\mathbf{V_f} - \mathbf{V_s}) \cdot \hat{\mathbf{n}}. \tag{4.52}$$

  Note that $w < 0$ denotes an inflow into the post-shock domain.

The present work will first introduce the shock relations in a dimensional form used in a number of works on curved shocks [203–205]:

$$[\rho]^{(S)} = \rho_{(U)}\sigma, \tag{4.53}$$

$$[\mathbf{V_f}]^{(S)} = -\frac{\sigma}{1+\sigma} w_{(U)} \hat{\mathbf{n}}, \tag{4.54}$$

$$[p]^{(S)} \quad \frac{\sigma}{1+\sigma} \rho_{(U)} w_{(U)}^2, \tag{4.55}$$

$$\sigma = \frac{2\left(w_{(U)}^2 - a_{(U)}^2\right)}{2a_{(U)}^2 + (\gamma-1)w_{(U)}^2}, \tag{4.56}$$

For the purposes of the present work, it is preferable to express these variables without the shock-jump notation $[X]^{(S)}$. The variables downstream of the shock are then found as

$$\rho_{(D)} = \rho_{(U)}(1+\sigma), \tag{4.57}$$

$$\mathbf{V_{f(D)}} = \mathbf{V_{f(U)}} - \frac{\sigma}{1+\sigma} w_{(U)} \hat{\mathbf{n}}, \tag{4.58}$$

$$p_{(D)} = p_{(U)} + \frac{\sigma}{1+\sigma} \rho_{(U)} w_{(U)}^2, \tag{4.59}$$

The following remarks are made regarding the shock relations and the outlook for their further application:

- As expected, it is evident from Eq. (4.58) that only the shock-normal component of the fluid velocity is changed by the shock, with the tangential components unchanged,

- For a stationary (in the Eulerian frame $\mathscr{E}$) shock surface, $\mathbf{V_s} = 0$ and consequently that $w_{(U)} = \mathbf{V_{f(U)}} \cdot \hat{\mathbf{n}}$.

  The maximum value of $w_{(U)}$ is then $w_{(U)} = \left|\mathbf{V_{f(U)}}\right|$ and is achieved for a normal shock. It follows that $\left|w_{(U)}\right| < \left|\mathbf{V_{f(U)}}\right|$ for oblique shocks.

However, for the shock to exist in the first place, it is required that $\left|w_{(U)}\right| \geq a_{(U)}$, i.e. that the upstream shock-normal Mach-number be greater than or equal to 1.

As a result, the following bound for $\left|w_{(U)}\right|$ exists for a stationary shock:

$$a_{(U)} \leq \left|w_{(U)}\right| \leq \left|\mathbf{V}_{\mathbf{f}(U)}\right|,$$

- The following relations may be shown:

$$1+\sigma = \frac{\gamma+1}{2m_{\perp}^2+(\gamma-1)}, \tag{4.60}$$

$$\frac{\sigma}{1+\sigma} = \frac{2}{\gamma+1}\left(1-m_{\perp}^2\right), \tag{4.61}$$

$$m_{\perp}^2 \equiv \frac{a_{(U)}^2}{w_{(U)}^2}, \tag{4.62}$$

where $m_{\perp}$ may be interpreted as the inverse of the shock-normal relative Mach-number. It may be shown that $m_{\perp} \to 1$ is the limit of the shock becoming a Mach wave (infinitesimal shock), while $m_{\perp} \to 0$ is the hypersonic limit of shock strength. The corresponding limits of σ are found:

$$\text{Mach-wave limit:} \quad m_{\perp} \to 1, \quad \sigma \to 0, \tag{4.63}$$

$$\text{Hypersonic limit:} \quad m_{\perp} \to 0, \quad \sigma \to \frac{2}{\gamma-1}. \tag{4.64}$$

Consequently, it is seen that the expressions in Eqs. (4.60) and (4.61) remain bounded and are $\mathscr{O}(1)$ or at worst $\mathscr{O}\left(\frac{\gamma+1}{\gamma-1}\right)$ in the limit of hypersonic shocks.

- For the purposes of piston theory, the chief domain of interest will be that bounded by the body surface and the shock surface. As the "downstream" quantities $X_{(D)}$ are thus of chief interest, their subscript will be dropped in the development which follows.

The shock relations may then be written in a non-dimensional form by forming ratios of dimensional quantities. It is stressed that the form of the equation presented here is an *inherent* non-dimensionalization, rather than an independent or general non-dimensionalization as has been performed up until this point. The justification for the non-dimensionalization may be found in the above remarks. Equations (4.57) to (4.59) then become:

$$\frac{\rho}{\rho_{(U)}} = (1+\sigma), \tag{4.65}$$

$$\frac{\mathbf{V}}{\left|\mathbf{V}_{(U)}\right|} = \hat{\mathbf{V}}_{(U)} - \frac{\sigma}{1+\sigma}\frac{w_{(U)}}{\left|\mathbf{V}_{(U)}\right|}\hat{\mathbf{n}}\,, \tag{4.66}$$

$$\frac{p}{\rho_{(U)}\left|\mathbf{V}_{(U)}\right|^2} = \frac{1}{\gamma M_{(U)}^2} + \frac{\sigma}{1+\sigma}\frac{w_{(U)}^2}{\left|\mathbf{V}_{(U)}\right|^2}\,, \tag{4.67}$$

4.2.4 Body Boundary Conditions

Within the inviscid framework of the Euler equations, the boundary conditions applied at the body surface are limited to the non-permeability condition. No further a-priori definition of the surface pressure, density, or tangential velocities may be given (in the direct problem). This is explained in detail in Chapters 16 and 19 of [66]. Specifically, the zero normal-velocity specification is associated with a characteristic propagating into the fluid domain. The characteristic originating from the fluid domain effectively determines the remaining primitive variables (ρ, p, and tangential velocity components) at the body surface.

With this in mind, the following definitions apply in outlining the body boundary conditions:

- The total-quantity form of the velocity of the fluid relative to the Eulerian frame $\mathscr{E}$ is given by $\mathbf{V_f}$,
- The total-quantity form of the (translational) velocity of the body surface relative to the Eulerian frame $\mathscr{E}$ is given by $\mathbf{V_b}$,
- The total-quantity form of the fluid velocity relative to the body surface is then given by

$$\mathbf{V_r} = \mathbf{V_f} - \mathbf{V_b}\,, \tag{4.68}$$

- The unit-vector normal to the instantaneous body surface is given by $\hat{\mathbf{n}}$.

With this nomenclature, the non-permeability condition is written

$$\mathbf{V_r}\cdot\hat{\mathbf{n}} = 0\,, \tag{4.69}$$

or in terms of dimensional components,

$$(v_1 - v_{b1})n_1 + (v_2 - v_{b2})n_2 + (v_3 - v_{b3})n_3 = 0\,, \tag{4.70}$$

where the subscript "b" is used to denote body velocities. The introduction of reference values allows the above to be rendered non-dimensional. It is noted that the components of

the unit vector $\hat{\mathbf{n}}$ are already non-dimensional. The non-dimensional total-quantity form of the non-permeability condition at the body surface may then be written compactly using the summation convention and non-dimensional parameters of Table 4.3 as

$$(n_m)[(k_{um})u_m - (k_{bm})u_{bm}] = 0\,. \tag{4.71}$$

4.3 Perturbation Equations

As in Section 4.2, the treatment of the perturbation form of the governing equations will begin with the equations in dimensional form. Following the introduction of reference quantities for non-dimensionalization, additional terms will be introduced to describe non-dimensional groups. The nomenclature associated with the present section is expanded on in Section 4.3.1.

4.3.1 Nomenclature

The previous nomenclature of Section 4.2.1 is carried through to the present development, with some additions to distinguish between un-perturbed and perturbation quantities. As before, the relationship between dimensional, reference, and non-dimensional values of a quantity is given by

$$X = X_R X_N\,, \tag{4.72}$$

The following nomenclature is adopted for perturbations:

$$X = \bar{X} + \tilde{X}\,, \tag{4.73}$$

where X is the total-value of the quantity of interest, $\bar{X}$ is its un-perturbed value, and $\tilde{X}$ is the perturbation-value of quantity. A more detailed description of the non-dimensionalization and its associated nomenclature is given in Tables 4.4 and 4.5.

Table 4.4 Nomenclature of non-dimensionalization of perturbation-form variables.

Quantity	Dimensional	Reference	Non-dimensional
Density: total	$\rho = \bar{\rho} + \tilde{\rho}$	ρ_R	$\rho_N = \mathscr{O}(1)$
Density: un-perturbed	$\bar{\rho}$	$\bar{\rho}_R$	$\bar{\rho}_N = \mathscr{O}(1)$
Density: perturbation	$\tilde{\rho}$	$\tilde{\rho}_R$	$\tilde{\rho}_N = \mathscr{O}(1)$
Pressure: total	$p = \bar{p} + \tilde{p}$	p_R	$p_N = \mathscr{O}(1)$
Pressure: un-perturbed	$\bar{p}$	$\bar{p}_R$	$\bar{p}_N = \mathscr{O}(1)$
Pressure: perturbation	$\tilde{p}$	$\tilde{p}_R$	$\tilde{p}_N = \mathscr{O}(1)$
Velocity: total	$v_i = \bar{v}_i + \tilde{v}_i$	U_i	$u_i = \mathscr{O}(1)$
Velocity: un-perturbed	$\bar{v}_i$	$\bar{U}_i$, $\bar{U}_R$	$\bar{u}_i = \mathscr{O}(1)$
Velocity: perturbation	$\tilde{v}_i$	$\tilde{U}_i$	$\tilde{u}_i = \mathscr{O}(1)$
Speed of sound: total	$a = \bar{a} + \tilde{a}$	a_R	$a_N = \mathscr{O}(1)$
Speed of sound: un-perturbed	$\bar{a}$	$\bar{a}_R$	$\bar{a}_N = \mathscr{O}(1)$
Speed of sound: perturbation	$\tilde{a}_N$	$\tilde{a}_N$	$\tilde{a}_N = \mathscr{O}(1)$

Table 4.5 Nomenclature of perturbation form non-dimensional parameters.

Quantity			Definition	Associated with
$\bar{k}_t$			$\frac{\bar{L}_R}{\bar{U}_R \bar{t}_R}$	Time-derivatives
$\bar{k}_{xi}$	with	$i = 1, 2, 3$	$\frac{\bar{L}_R \bar{U}_i}{\bar{L}_i \bar{U}_R}$	Advection
$\bar{k}_{Li}$	with	$i = 1, 2, 3$	$\frac{\bar{L}_R}{\bar{L}_i}$	Spatial gradients
$\bar{k}_{ui}$	with	$i = 1, 2, 3$	$\frac{\bar{U}_i}{\bar{U}_R}$	Mean un-perturbed flow direction
$\bar{k}_{bi}$	with	$i = 1, 2, 3$	$\frac{\bar{U}_{bi}}{\bar{U}_R}$	Un-perturbed body translation velocity
$\bar{k}_f$			$\frac{\bar{p}_R}{\bar{\rho}_R \bar{U}_R^2}$	Momentum-equation pressure gradient
$\bar{k}_a$			$\frac{\bar{p}_R}{\bar{\rho}_R \bar{a}_R^2}$	Energy-equation pressure gradient
ε_t			$\frac{\tilde{t}_R}{\bar{t}_R}$	Relative magnitude of perturbation time-scale
ε_{Li}	with	$i = 1, 2, 3$	$\frac{\tilde{L}_i}{\bar{L}_R}$	Relative magnitude of perturbation length-scale
ε_{ui}	with	$i = 1, 2, 3$	$\frac{\tilde{U}_i}{\bar{U}_R}$	Relative magnitude of velocity perturbation
ε_{bi}	with	$i = 1, 2, 3$	$\frac{\tilde{U}_{bi}}{\bar{U}_R}$	Relative magnitude of body-velocity perturbation
ε_ρ			$\frac{\tilde{\rho}_R}{\bar{\rho}_R}$	Relative magnitude of density perturbation
ε_p			$\frac{\tilde{p}_R}{\bar{p}_R}$	Relative magnitude of pressure perturbation
ε_a			$\frac{\tilde{a}_R}{\bar{a}_R}$	Relative magnitude of perturbation to a

As a final preliminary, consider the previous relations developed for transformation between the oriented adapted-frame $\mathscr{A}$ and the Eulerian frame $\mathscr{E}$ in Eq. (4.13). These equations will be used with $\bar{\eta}$ and $\bar{\lambda}$ to describe the oriented-frame adapted to the un-perturbed surface $\bar{\mathscr{A}}$. The adapted-frame will be described by the triad of orthogonal unit-vectors $\bar{\hat{\mathbf{t}}}$, $\bar{\hat{\mathbf{n}}}$, $\bar{\hat{\mathbf{b}}}$.

The un-perturbed triad of $\bar{\mathscr{A}}$ is then considered fixed to the surface. The surface is then perturbed. Translation of the point at which the frame $\bar{\mathscr{A}}$ was adapted has no effect on the orientation of the frame $\bar{\mathscr{A}}$ in the global Eulerian-frame $\mathscr{E}$. However, rotation of the surface does. The following definitions are made, with an accompanying illustration in:

- Considered perturbations to the orientation of the surface as arising from a rotation $\tilde{\theta}_r$ about an axis $\hat{\mathbf{r}}$,
- The orientation of the axis of rotation $\hat{\mathbf{r}}$ relative to the global Eulerian-frame $\mathscr{E}$ is described in terms of η_r and λ_r by

$$\hat{\mathbf{r}} = \begin{bmatrix} -\sin\eta_r\cos\lambda_r & -\sin\eta_r\sin\lambda_r & \cos\eta_r \end{bmatrix} \begin{pmatrix} \hat{\mathbf{e}}_1 \\ \hat{\mathbf{e}}_2 \\ \hat{\mathbf{e}}_3 \end{pmatrix}, \tag{4.74}$$

- Rotation of the frame adapted to the un-perturbed surface ($\bar{\mathscr{A}}$) by the rotation vector $\tilde{\theta}_r\hat{\mathbf{r}}$ results in a new triad of orthogonal unit-vectors describing a frame $\mathscr{A}^*$. The new triad is denoted $\hat{\mathbf{t}}^*$, $\hat{\mathbf{n}}^*$, $\hat{\mathbf{b}}^*$,
- It is noted that $\hat{\mathbf{n}}^*$ remains perpendicular to the perturbed surface. However, $\hat{\mathbf{t}}^*$ and $\hat{\mathbf{b}}^*$ do not necessarily meet the orientation conditions of $\hat{\mathbf{b}}^* \cdot \hat{\mathbf{e}}_1 = 0$. The rotated frame $\mathscr{A}^*$ may be further rotated about $\hat{\mathbf{n}}^*$ to meet the orientation conditions set out in Eqs. (4.6) and (4.8). In the present work, however, this is unnecessary,
- The active rotation of the un-perturbed triad $\bar{\hat{\mathbf{t}}}$, $\bar{\hat{\mathbf{n}}}$, $\bar{\hat{\mathbf{b}}}$ is described through Rodrigues' rotation formula, which is written for the unit normal-vector below:

$$\hat{\mathbf{n}}^* = \left(\cos\tilde{\theta}_r\right)\bar{\hat{\mathbf{n}}} + \left(\sin\tilde{\theta}_r\right)\left(\hat{\mathbf{r}} \times \bar{\hat{\mathbf{n}}}\right) + \left(1 - \cos\tilde{\theta}_r\right)\left(\hat{\mathbf{r}} \cdot \bar{\hat{\mathbf{n}}}\right)\hat{\mathbf{r}}, \tag{4.75}$$

  It is noted here that $\hat{\mathbf{r}} \cdot \bar{\hat{\mathbf{n}}} \neq 0$ will result in a "shearing" or "spin" of the surface about its normal. Of greater practical interest in the present application is the group of rotations such that $\hat{\mathbf{r}} \cdot \bar{\hat{\mathbf{n}}} = 0$, which may be interpreted as pure "plate-bending" about $\bar{\hat{\mathbf{b}}}$ and $\bar{\hat{\mathbf{t}}}$.
- The effect of surface-rotation on the triad of the adapted-frame $\bar{\mathscr{A}}$ may be described in terms of perturbation vectors $\tilde{\mathbf{t}}$, $\tilde{\mathbf{n}}$, $\tilde{\mathbf{b}}$. It should be noted that the perturbation vectors

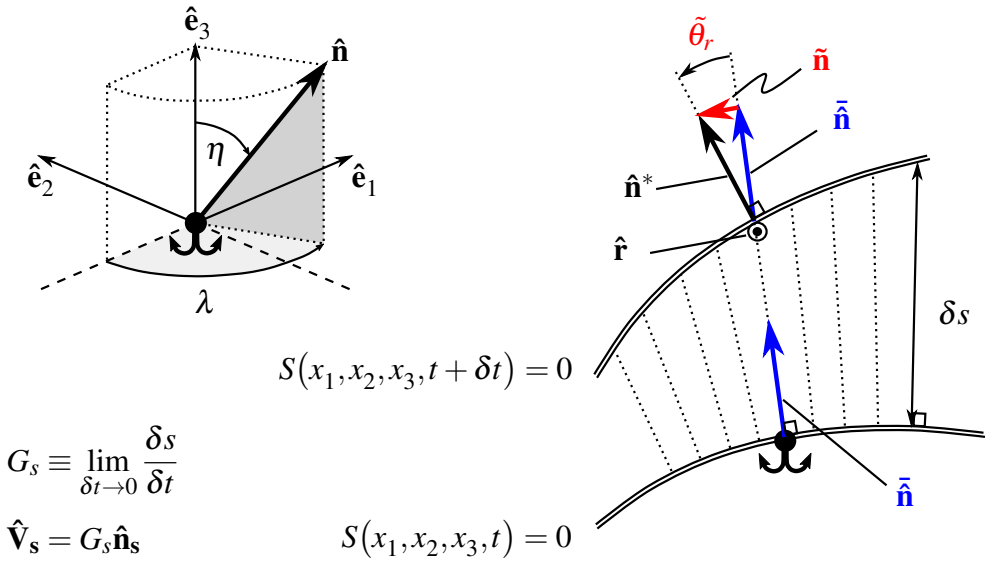

Fig. 4.2 Illustration of the orientation angles for the surface-adapted normal and definition of the frame adapted to the perturbed shock surface.

are not unit-vectors. The following definitions apply for the perturbation vectors:

$$\tilde{\mathbf{t}} = \hat{\mathbf{t}}^* - \bar{\hat{\mathbf{t}}} = \sum_{i=1}^{3} \tilde{t}_i \hat{\mathbf{e}}_\mathbf{i}\,, \tag{4.76}$$

$$\tilde{\mathbf{n}} = \hat{\mathbf{n}}^* - \bar{\hat{\mathbf{n}}} = \sum_{i=1}^{3} \tilde{n}_i \hat{\mathbf{e}}_\mathbf{i}\,, \tag{4.77}$$

$$\tilde{\mathbf{b}} = \hat{\mathbf{b}}^* - \bar{\hat{\mathbf{b}}} = \sum_{i=1}^{3} \tilde{b}_i \hat{\mathbf{e}}_\mathbf{i}\,, \tag{4.78}$$

The use of Rodrigues' rotation formula as in Eq. (4.75) allows the components of perturbation vectors to be written in the form of:

$$\tilde{n}_1 = (r_2\bar{n}_3 - r_3\bar{n}_2)\sin\tilde{\theta}_r - \left(1-\cos\tilde{\theta}_r\right)\left[\bar{n}_1 - \left(\hat{\mathbf{r}}\cdot\bar{\hat{\mathbf{n}}}\right)r_1\right], \tag{4.79}$$

$$\tilde{n}_2 = (r_3\bar{n}_1 - r_1\bar{n}_3)\sin\tilde{\theta}_r - \left(1-\cos\tilde{\theta}_r\right)\left[\bar{n}_2 - \left(\hat{\mathbf{r}}\cdot\bar{\hat{\mathbf{n}}}\right)r_2\right], \tag{4.80}$$

$$\tilde{n}_3 = (r_1\bar{n}_2 - r_2\bar{n}_1)\sin\tilde{\theta}_r - \left(1-\cos\tilde{\theta}_r\right)\left[\bar{n}_3 - \left(\hat{\mathbf{r}}\cdot\bar{\hat{\mathbf{n}}}\right)r_3\right], \tag{4.81}$$

The above considerations and equations allow the similar relationships to be derived for the perturbations to $\bar{\hat{\mathbf{t}}}$ and $\bar{\hat{\mathbf{b}}}$ following a rotation of $\tilde{\theta}_r$ about the axis $\hat{\mathbf{r}}$. However, this is not required for the purposes of the present work.

4.3.2 Governing Equations

Dimensional Form in Cartesian Coordinates

A similar progression may be followed for the perturbation form of the Euler equations in the Eulerian frame $\mathscr{E}$ as was followed in Section 4.2.2. The first step towards the final non-dimensionalized perturbation form is the introduction of the perturbation form into Eqs. (4.29) to (4.31). The use of component-notation will become cumbersome due to the number of terms introduced. Thus, Einstein summation notation will be re-introduced. The corresponding dimensional perturbation form of the Euler equations is given by:

$$\text{Continuity:} \quad \frac{\partial(\bar{\rho}+\tilde{\rho})}{\partial t}+(\bar{v}_m+\tilde{v}_m)\frac{\partial(\bar{\rho}+\tilde{\rho})}{\partial x_m}+(\bar{\rho}+\tilde{\rho})\frac{\partial(\bar{v}_m+\tilde{v}_m)}{\partial x_m}=0\,, \tag{4.82}$$

$$\text{Momentum:} \quad \frac{\partial(\bar{v}_i+\tilde{v}_i)}{\partial t}+(\bar{v}_m+\tilde{v}_m)\frac{\partial(\bar{v}_i+\tilde{v}_i)}{\partial x_m}=-\frac{1}{\bar{\rho}+\tilde{\rho}}\frac{\partial(\bar{p}+\tilde{p})}{\partial x_i}\,, \tag{4.83}$$

$$\text{Energy:} \quad \frac{\partial(\bar{p}+\tilde{p})}{\partial t}+(\bar{v}_m+\tilde{v}_m)\frac{\partial(\bar{p}+\tilde{p})}{\partial x_m}+(\bar{\rho}+\tilde{\rho})(\bar{a}+\tilde{a})^2\frac{\partial(\bar{v}_m+\tilde{v}_m)}{\partial x_m}=0\,. \tag{4.84}$$

If it is assumed that:

- The un-perturbed variables are known a-priori,
- The un-perturbed variables are a solution to the Euler equations,

then the above perturbation form of the equations may be further simplified and the un-perturbed solution may be filtered out. The nonlinear terms in the equations provide coupling between the known un-perturbed solution and the unknown perturbation problem. At present, no assumptions will be made regarding perturbation smallness and no linearization will be performed. Any arrangement of terms is possible, with the following arrangement used to emphasize physical interpretation and to facilitate later non-dimensionalization:

$$\text{Continuity:} \quad \underbrace{\left[\frac{\partial}{\partial t}+\bar{v}_m\frac{\partial}{\partial x_m}\right]\tilde{\rho}}_{\mathrm{C}_1}+\underbrace{\tilde{\rho}\frac{\partial\bar{v}_m}{\partial x_m}}_{\mathrm{C}_2}+\underbrace{\tilde{v}_m\frac{\partial\bar{\rho}}{\partial x_m}+\bar{\rho}\frac{\partial\tilde{v}_m}{\partial x_m}}_{\mathrm{C}_3}+\underbrace{\frac{\partial(\tilde{\rho}\tilde{v}_m)}{\partial x_m}}_{\mathrm{C}_4}=0\,, \tag{4.85}$$

$$\text{Momentum:} \quad \left.\begin{aligned}&\underbrace{(\bar{\rho}+\tilde{\rho})\left[\frac{\partial}{\partial t}+\bar{v}_m\frac{\partial}{\partial x_m}\right]\tilde{v}_i}_{\mathrm{M}_1}+\underbrace{\tilde{\rho}\left[\frac{\partial}{\partial t}+\bar{v}_m\frac{\partial}{\partial x_m}\right]\bar{v}_i}_{\mathrm{M}_2}\\&+\underbrace{(\bar{\rho}+\tilde{\rho})\tilde{v}_m\frac{\partial\tilde{v}_i}{\partial x_m}}_{\mathrm{M}_3}+\underbrace{(\bar{\rho}+\tilde{\rho})\tilde{v}_m\frac{\partial\bar{v}_i}{\partial x_m}}_{\mathrm{M}_4}\end{aligned}\right\}=\underbrace{-\frac{\partial\tilde{p}}{\partial x_i}}_{\mathrm{M}_5}\,, \tag{4.86}$$

$$\text{Energy:} \quad \left.\begin{aligned} &\underbrace{\left[\frac{\partial}{\partial t}+\bar{v}_m\frac{\partial}{\partial x_m}\right]\tilde{p}}_{\mathrm{E}_1}+\underbrace{\tilde{v}_m\frac{\partial \tilde{p}}{\partial x_m}+\tilde{v}_m\frac{\partial \bar{p}}{\partial x_m}}_{\mathrm{E}_2} \\ &\qquad\qquad +\underbrace{(\bar{\rho}+\tilde{\rho})(\bar{a}+\tilde{a})^2\frac{\partial \tilde{v}_m}{\partial x_m}}_{\mathrm{E}_3} \\ &\qquad +\underbrace{(\bar{\rho}+\tilde{\rho})(\bar{a}+\tilde{a})^2\frac{\partial \bar{v}_m}{\partial x_m}-\bar{\rho}\bar{a}^2\frac{\partial \bar{v}_m}{\partial x_m}}_{\mathrm{E}_4} \end{aligned}\right\} = 0\,. \tag{4.87}$$

An interpretation of the labelled groups follows:

- Terms in the continuity equation of Eq. (4.85):
  - C_1 – temporal derivative of perturbation density in a frame advected by the background un-perturbed flow,
  - C_2 – perturbation outflow due to a density perturbation over the un-perturbed velocity field,
  - C_3 – perturbation outflow due to a velocity perturbation over the un-perturbed density field,
  - C_4 – perturbation outflow due to purely perturbation terms,
  - It is noted here that terms C_1 and C_2 together represent (by the Reynolds transport theorem [63]) the net perturbation mass-flux out of a fluid packet advected by the un-perturbed background flow. The remaining terms C_3 and C_4 may then be interpreted as "source" terms which arise due to distortion of the fluid packet by the perturbation velocity. This interpretation arises from the manipulation of Eq. (4.85) by means of the Reynolds transport theorem [63] into the form

$$\frac{\delta}{\delta t}_{\text{mean}} \iiint \tilde{\rho}\,\mathrm{d}V = -\iiint \frac{\partial}{\partial x_m}[(\bar{\rho}+\tilde{\rho})\tilde{v}_m]\mathrm{d}V\,, \tag{4.88}$$

    where $\frac{\delta}{\delta t}_{\text{mean}}$ is the material derivative in the background un-perturbed flow.

- Terms in the momentum equation of Eq. (4.86):
  - M_1 – inertial forces due to the advection by the background un-perturbed flow of velocity perturbations,
  - M_2 – inertial forces due to the advection by the background un-perturbed flow of density perturbations over the background un-perturbed velocity field,

  - M_3 – inertial forces due to the self-advection of velocity perturbations,
  - M_4 – inertial forces due to the advection by the perturbation velocity of the background un-perturbed velocity field,
  - M_5 – perturbation pressure gradient.

- Terms in the energy equation of Eq. (4.87):

  - E_1 – temporal derivative of perturbation pressure in a frame advected by the background un-perturbed flow,
  - E_2 – work done against pressure gradients by the perturbation velocity,
  - E_3 – elastic energy stored in the fluid due to perturbations to the fluid dilation,
  - E_4 – elastic energy stored in the fluid due to perturbations to the thermodynamic state of the fluid over the background un-perturbed dilation.

Two preliminary, forward-looking remarks are offered regarding the definition of the un-perturbed variables:

- If uniform freestream conditions are taken as the un-perturbed solution ($\bar{X} = X_\infty$), then all derivatives of un-perturbed terms will be rendered zero ($\frac{\partial \bar{X}}{\partial t} = \frac{\partial \bar{X}}{\partial x_i} = 0$). This will be encountered in CPT,

- If perturbations are taken about a mean-steady solution $\bar{X} = X_{\text{mean}}(x_i)$, then time-derivatives of the mean-steady terms will be will be rendered zero ($\frac{\partial \bar{X}}{\partial t}$). However, whether spatial derivatives ($\frac{\partial \bar{X}}{\partial x_i}$) will be zero or non-zero depends on the mean-steady solution. This will be encountered in LPT.

Non-Dimensional Form in Cartesian Coordinates

A key difference in the non-dimensionalization of the perturbation form of the equations is that different reference scales must be used for derivatives of un-perturbed and of perturbation quantities. The nomenclature of the non-dimensionalization will follow Table 4.4. The reference values for both un-perturbed and perturbation quantities are chosen such that the non-dimensional variables are $\mathcal{O}(1)$. This is explicitly written as

$$\bar{X}_N = \frac{\bar{X}}{\bar{X}_R} = \mathcal{O}(1) \quad \text{and} \quad \tilde{X}_N = \frac{\tilde{X}}{\tilde{X}_R} = \mathcal{O}(1)\,. \tag{4.89}$$

Similarly, the explicit assumption is made that gradients are non-dimensionalized using characteristics lengths and times such that

$$\frac{\partial \bar{X}}{\partial x_i} = \frac{\bar{X}_R}{\bar{L}_i}\frac{\partial \bar{X}_N}{\partial \xi_i} \quad \text{with} \quad \frac{\partial \bar{X}_N}{\partial \xi_i} = \mathscr{O}(1)\,, \tag{4.90}$$

$$\frac{\partial \tilde{X}}{\partial x_i} = \frac{\tilde{X}_R}{\tilde{L}_i}\frac{\partial \tilde{X}_N}{\partial \xi_i} \quad \text{with} \quad \frac{\partial \tilde{X}_N}{\partial \xi_i} = \mathscr{O}(1)\,, \tag{4.91}$$

$$\frac{\partial \bar{X}}{\partial t} = \frac{\bar{X}_R}{\bar{t}_R}\frac{\partial \bar{X}_N}{\partial t_N} \quad \text{with} \quad \frac{\partial \bar{X}}{\partial t_N} = \mathscr{O}(1)\,, \tag{4.92}$$

$$\frac{\partial \tilde{X}}{\partial t} = \frac{\tilde{X}_R}{\tilde{t}_R}\frac{\partial \tilde{X}_N}{\partial t_N} \quad \text{with} \quad \frac{\partial \tilde{X}}{\partial t_N} = \mathscr{O}(1)\,. \tag{4.93}$$

The previous caveat regarding comparable gradients / scales for all flow variables made on Page 219 applies here as well.

It should be noted in the above that no explicit transformation of coordinates is attempted in the present work. In fact, the same nomenclature of t_N and ξ_i is used to describe "non-dimensional" coordinates when dealing with either un-perturbed or perturbation quantities. This is justified by the requirement that separate reference scales be used such that $\frac{\partial}{\partial t_N} = \mathscr{O}(1)$ and $\frac{\partial}{\partial \xi_i} = \mathscr{O}(1)$ (abuse of notation aside) holds true for both un-perturbed and perturbation quantities. In summary: multiple scales may exist, with distinction between them being made through the reference values, and not through the introduction of new coordinates.

With these preliminaries in mind, the non-dimensional perturbation form of the Euler equations in a Cartesian basis in the Eulerian frame $\mathscr{E}$ is found by the introduction of reference values and non-dimensional variables into Eqs. (4.85) to (4.87). This is done, with the following non-dimensional groups formed:

$$\text{C:} \quad \left.\begin{aligned} &\left(\frac{\tilde{\rho}_R}{\bar{\rho}_R}\right)\left[\left(\frac{\bar{t}_R}{\tilde{t}_R}\frac{\bar{L}_R}{\bar{U}_R\tilde{t}_R}\right)\frac{\partial}{\partial t_N} + \left(\frac{\bar{L}_R}{\tilde{L}_m}\frac{\bar{U}_m}{\bar{U}_R}\right)\bar{u}_m\frac{\partial}{\partial \xi_m}\right]\tilde{\rho}_N \\ &\quad + \left(\frac{\tilde{\rho}_R}{\bar{\rho}_R}\frac{\bar{L}_R\bar{U}_m}{\tilde{L}_m\bar{U}_R}\right)\tilde{\rho}_N\frac{\partial \bar{u}_m}{\partial \xi_m} + \left(\frac{\bar{L}_R}{\tilde{L}_m}\frac{\tilde{U}_m}{\bar{U}_R}\right)\tilde{u}_m\frac{\partial \bar{\rho}_N}{\partial \xi_m} \\ &\quad + \left(\frac{\bar{L}_R}{\tilde{L}_m}\frac{\tilde{U}_m}{\bar{U}_R}\right)\bar{\rho}_N\frac{\partial \tilde{u}_m}{\partial \xi_m} \\ &\quad + \left(\frac{\tilde{\rho}_R}{\bar{\rho}_R}\frac{\bar{L}_R}{\tilde{L}_m}\frac{\tilde{U}_m}{\bar{U}_R}\right)\frac{\partial(\tilde{\rho}_N\tilde{u}_m)}{\partial \xi_m} \end{aligned}\right\} = 0\,, \tag{4.94}$$

$$
\text{M:}\quad
\left.\begin{aligned}
&\left(\frac{\tilde{U}_i}{\bar{U}_R}\right)\left[\bar{\rho}_N+\left(\frac{\tilde{\rho}_R}{\bar{\rho}_R}\right)\tilde{\rho}_N\right]\left[\left(\frac{\bar{t}_R}{\tilde{t}_R}\,\frac{\bar{L}_R}{\bar{U}_R\bar{t}_R}\right)\frac{\partial}{\partial t_N}+\left(\frac{\bar{L}_R}{\tilde{L}_m}\,\frac{\bar{U}_m}{\bar{U}_R}\right)\bar{u}_m\frac{\partial}{\partial\xi_m}\right]\tilde{u}_i\\
&\quad+\left(\frac{\bar{U}_i}{\bar{U}_R}\,\frac{\tilde{\rho}_R}{\bar{\rho}_R}\right)\tilde{\rho}_N\left[\left(\frac{\bar{L}_R}{\bar{U}_R\bar{t}_R}\right)\frac{\partial}{\partial t_N}+\left(\frac{\bar{L}_R\bar{U}_m}{\bar{L}_m\bar{U}_R}\right)\bar{u}_m\frac{\partial}{\partial\xi_m}\right]\bar{u}_i\\
&\quad+\left(\frac{\bar{L}_R}{\tilde{L}_m}\,\frac{\tilde{U}_m}{\bar{U}_R}\,\frac{\tilde{U}_i}{\bar{U}_R}\right)\left[\bar{\rho}_N+\left(\frac{\tilde{\rho}_R}{\bar{\rho}_R}\right)\tilde{\rho}_N\right]\tilde{u}_m\frac{\partial\tilde{u}_i}{\partial\xi_m}\\
&\quad+\left(\frac{\bar{L}_R}{\tilde{L}_m}\,\frac{\tilde{U}_m}{\bar{U}_R}\,\frac{\bar{U}_i}{\bar{U}_R}\right)\left[\bar{\rho}_N+\left(\frac{\tilde{\rho}_R}{\bar{\rho}_R}\right)\tilde{\rho}_N\right]\tilde{u}_m\frac{\partial\bar{u}_i}{\partial\xi_m}\\
&\quad+\left(\frac{\bar{L}_R}{\tilde{L}_i}\,\frac{\tilde{p}_R}{\bar{p}_R}\,\frac{\bar{p}_R}{\bar{\rho}_R\bar{U}_R^2}\right)\frac{\partial\tilde{p}_N}{\partial\xi_i}
\end{aligned}\right\}=0\,,
\tag{4.95}
$$

$$
\text{E:}\quad
\left.\begin{aligned}
&\left(\frac{\tilde{p}_R}{\bar{p}_R}\,\frac{\bar{p}_R}{\bar{\rho}_R\bar{a}_R^2}\right)\left[\left(\frac{\bar{t}_R}{\tilde{t}_R}\,\frac{\bar{L}_R}{\bar{U}_R\bar{t}_R}\right)\frac{\partial}{\partial t_N}+\left(\frac{\bar{L}_R}{\tilde{L}_m}\,\frac{\bar{U}_m}{\bar{U}_R}\right)\bar{u}_m\frac{\partial}{\partial\xi_m}\right]\tilde{p}_N\\
&\quad+\left(\frac{\bar{L}_R}{\tilde{L}_m}\,\frac{\tilde{U}_m}{\bar{U}_R}\,\frac{\tilde{p}_R}{\bar{p}_R}\,\frac{\bar{p}_R}{\bar{\rho}_R\bar{a}_R^2}\right)\tilde{u}_m\frac{\partial\tilde{p}_N}{\partial\xi_m}\\
&\quad-\left(\frac{\bar{L}_R\bar{U}_m}{\bar{L}_m\bar{U}_R}\right)\bar{\rho}_N\bar{a}_N^2\frac{\partial\bar{u}_m}{\partial\xi_m}+\left(\frac{\bar{L}_R}{\tilde{L}_m}\,\frac{\tilde{U}_m}{\bar{U}_R}\,\frac{\bar{p}_R}{\bar{\rho}_R\bar{a}_R^2}\right)\tilde{u}_m\frac{\partial\bar{p}_N}{\partial\xi_m}\\
&\quad+\left(\frac{\bar{L}_R}{\tilde{L}_m}\,\frac{\tilde{U}_m}{\bar{U}_R}\right)\left[\bar{\rho}_N+\left(\frac{\tilde{\rho}_R}{\bar{\rho}_R}\right)\tilde{\rho}_N\right]\left[\bar{a}_N^2+\left(2\frac{\tilde{a}_R}{\bar{a}_R}\right)\bar{a}_N\tilde{a}_N+\left(\frac{\tilde{a}_R^2}{\bar{a}_R^2}\right)\tilde{a}_N^2\right]\frac{\partial\tilde{u}_m}{\partial\xi_m}\\
&\quad+\left(\frac{\bar{L}_R\bar{U}_m}{\bar{L}_m\bar{U}_R}\right)\left[\bar{\rho}_N+\left(\frac{\tilde{\rho}_R}{\bar{\rho}_R}\right)\tilde{\rho}_N\right]\left[\bar{a}_N^2+\left(2\frac{\tilde{a}_R}{\bar{a}_R}\right)\bar{a}_N\tilde{a}_N+\left(\frac{\tilde{a}_R^2}{\bar{a}_R^2}\right)\tilde{a}_N^2\right]\frac{\partial\bar{u}_m}{\partial\xi_m}
\end{aligned}\right\}=0\,.
\tag{4.96}
$$

This cumbersome notation is replaced by k and ε notation as defined in Table 4.5, with some terms rearranged:

$$
\text{C:}\quad
\left.\begin{aligned}
&(\varepsilon_\rho)\left[\left(\frac{\bar{k}_t}{\varepsilon_t}\right)\frac{\partial}{\partial t_N}+\left(\frac{\bar{k}_{um}}{\varepsilon_{Lm}}\right)\bar{u}_m\frac{\partial}{\partial\xi_m}\right]\tilde{\rho}_N\\
&+\left(\frac{\varepsilon_{um}}{\varepsilon_{Lm}}\right)\bar{\rho}_N\frac{\partial\tilde{u}_m}{\partial\xi_m}+\left(\frac{\varepsilon_\rho\varepsilon_{um}}{\varepsilon_{Lm}}\right)\frac{\partial(\tilde{\rho}_N\tilde{u}_m)}{\partial\xi_m}\\
&+(\varepsilon_\rho\bar{k}_{xm})\tilde{\rho}_N\frac{\partial\bar{u}_m}{\partial\xi_m}+(\varepsilon_{um}\bar{k}_{Lm})\tilde{u}_m\frac{\partial\bar{\rho}_N}{\partial\xi_m}
\end{aligned}\right\}=0\,,
\tag{4.97}
$$

$$\text{M:}\quad \left.\begin{aligned}
&(\varepsilon_{ui})\left[\bar{\rho}_N+(\varepsilon_\rho)\tilde{\rho}_N\right]\left[\left(\frac{\bar{k}_t}{\varepsilon_t}\right)\frac{\partial}{\partial t_N}+\left(\frac{\bar{k}_{um}}{\varepsilon_{Lm}}\right)\bar{u}_m\frac{\partial}{\partial\xi_m}\right]\tilde{u}_i\\
&\quad+\left(\frac{\varepsilon_{ui}\varepsilon_{um}}{\varepsilon_{Lm}}\right)\left[\bar{\rho}_N+(\varepsilon_\rho)\tilde{\rho}_N\right]\tilde{u}_m\frac{\partial\tilde{u}_i}{\partial\xi_m}\\
&+(\varepsilon_\rho\bar{k}_{ui})\tilde{\rho}_N\left[(\bar{k}_t)\frac{\partial}{\partial t_N}+(\bar{k}_{xm})\bar{u}_m\frac{\partial}{\partial\xi_m}\right]\bar{u}_i\\
&\quad+(\bar{k}_{Lm}\varepsilon_{um}\bar{k}_{ui})\left[\bar{\rho}_N+(\varepsilon_\rho)\tilde{\rho}_N\right]\tilde{u}_m\frac{\partial\bar{u}_i}{\partial\xi_m}
\end{aligned}\right\}=-\left(\frac{\varepsilon_p\bar{k}_f}{\varepsilon_{Li}}\right)\frac{\partial\tilde{p}_N}{\partial\xi_i}\,, \tag{4.98}$$

$$\text{E:}\quad \left.\begin{aligned}
&(\varepsilon_p\bar{k}_a)\left[\left(\frac{\bar{k}_t}{\varepsilon_t}\right)\frac{\partial}{\partial t_N}+\left(\frac{\bar{k}_{um}}{\varepsilon_{Lm}}\right)\bar{u}_m\frac{\partial}{\partial\xi_m}\right]\tilde{p}_N\\
&\quad+\left(\frac{\varepsilon_{um}\varepsilon_p\bar{k}_a}{\varepsilon_{Lm}}\right)\tilde{u}_m\frac{\partial\tilde{p}_N}{\partial\xi_m}\\
&+\left(\frac{\varepsilon_{um}}{\varepsilon_{Lm}}\right)\left[\bar{\rho}_N+(\varepsilon_\rho)\tilde{\rho}_N\right]\left[\bar{a}_N^2+(2\varepsilon_a)\bar{a}_N\tilde{a}_N+(\varepsilon_a^2)\tilde{a}_N^2\right]\frac{\partial\tilde{u}_m}{\partial\xi_m}\\
&\quad-(\bar{k}_{xm})\bar{\rho}_N\bar{a}_N^2\frac{\partial\bar{u}_m}{\partial\xi_m}+(\bar{k}_{Lm}\varepsilon_{um}\bar{k}_a)\tilde{u}_m\frac{\partial\bar{p}_N}{\partial\xi_m}\\
&+(\bar{k}_{xm})\left[\bar{\rho}_N+(\varepsilon_\rho)\tilde{\rho}_N\right]\left[\bar{a}_N^2+(2\varepsilon_a)\bar{a}_N\tilde{a}_N+(\varepsilon_a^2)\tilde{a}_N^2\right]\frac{\partial\bar{u}_m}{\partial\xi_m}
\end{aligned}\right\}=0\,. \tag{4.99}$$

The above equations are the perturbation form of the non-dimensional Euler equations in the Eulerian frame $\mathscr{E}$ as expressed in a Cartesian basis. The definition of the array of non-dimensional parameters is given in Table 4.5. A short discussion of the perturbation approach and the non-dimensional parameters will now be given in the context of the above equations:

- Regarding perturbations: the initial assumption on Page 232 is repeated here that the un-perturbed variables are known a-priori and are a solution to the Euler equations. The un-perturbed variables will be loosely referred to as the "un-perturbed solution" in the discussion which follows,

- It is noted that the nonlinear terms in the Euler equations lead to coupling between the un-perturbed solution and the perturbation problem. However, the equations describing the perturbation problem are not entirely equivalent to the Euler equations with perturbation-quantities in place of total-quantities. Additional terms are present.

  However, the coupling between the un-perturbed solution and the perturbation problem also results in de-coupling between perturbation variables. This is seen quite clearly in the continuity equation as described in Eq. (4.97). Furthermore, it is noted that the differential-order of the equations is preserved. The coupling between the un-perturbed solution and the perturbation problem thus results in zeroth-order differential terms

in the perturbation quantities appearing. In other words, algebraic (as opposed to differential) terms in the perturbation variables appear.

The above considerations point towards the prospect of significant simplification of the mathematical problem describing perturbation quantities. The possibility (and validity) of this simplification is governed by the relative magnitude of terms in Eqs. (4.97) to (4.99),

- Correct specification of reference values for non-dimensionalization renders all terms in Eqs. (4.97) to (4.99) which are not surrounded in round-parentheses $\mathcal{O}(1)$. This is to say, the magnitude of terms is represented by the non-dimensional groupings in parentheses.

  The individual terms in the dimensionless groupings may be associated with various physical interpretations, some of which are offered below:

  - Generally speaking, terms in ε indicate the magnitude of perturbation quantities relative to their un-perturbed reference values. Typically, $\varepsilon \ll 1$ indicates "small" perturbations.

    An important exception requiring more careful interpretation lies with ε_L and ε_t. These denote the relative magnitude of length- and time-scales. However, the magnitude of gradients is inversely proportional to these scales. This is why the terms appearance as ε_L^{-1} and ε_L^{-1} in the equations. In this sense, a small $\varepsilon_L \ll 1$ implies *large* perturbation gradients compared to the un-perturbed reference gradients,
  - ε_t indicates that the time-derivative of a perturbation quantity is being considered,
  - ε_{Li} indicates that the spatial gradient in the x_i-direction of a perturbation quantity is being considered,
  - If terms in ε may be considered "smallness parameters" for perturbations relative to un-perturbed reference values, then terms in $\bar{k}$ indicate the relative magnitude of different terms in the un-perturbed solution. Comparison of the magnitudes of different $\bar{k}$ allow the relative importance of physical mechanisms in the un-perturbed solution to be assessed,
  - $\bar{k}_t$ indicates the order-of-magnitude of unsteady terms relative to terms involving advection / dilation in a reference-direction (typically the axial or freestream direction) in the un-perturbed solution,
  - $\bar{k}_{xi}$ indicates the order-of-magnitude of advection / dilation in the x_i-direction relative to advection / dilation in a reference-direction in the un-perturbed solution,

  - $\bar{k}_{ui}$ indicates the order-of-magnitude of velocity in the x_i-direction relative to velocity in a reference-direction in the un-perturbed solution. Setting U_R equal to the magnitude of the velocity vector results in $\bar{k}_{ui}$ becoming the direction cosine in the x_i-direction,
  - $\bar{k}_f$ indicates the order-of-magnitude of pressure gradients in the x_i direction relative to inertial terms in a reference-direction in the un-perturbed solution,
  - $\bar{k}_a$ indicates the order-of-magnitude of terms associated with work done against pressure gradients relative to terms associated with energy stored due to dilation.

- The coupling which appears in Eqs. (4.97) to (4.99) between terms in ε and terms in $\bar{k}$ has significant implications for the simplification of the governing equations. Notably, it may arise that small perturbations through $\varepsilon \ll 1$ will not be sufficient to render terms negligible due to the (possible) existence of a coupled $\bar{k} \gg 1$. Conversely, the situation may arise where due to $\bar{k} \ll 1$, a simplification is possible even for relative large perturbations such that $\varepsilon = \mathcal{O}(1)$.

The above discussion points highlight the value of the non-dimensional form of the perturbation-form of the Euler equations. The determination of appropriate reference values for non-dimensionalization – and interpretation of when this non-dimensionalization becomes invalid – is central to the derivation of CPT and LPT from Eqs. (4.97) to (4.99). This is the topic of Section 4.4.

4.3.3 Shock Boundary Conditions

The Rankine-Hugoniot equations of Eqs. (4.57) to (4.59) must apply across the shock surface during and following perturbations to the surface and to the fluid conditions either side of the shock.

Perturbations to flow variables are dictated by the Rankine-Hugoniot equations themselves, rather than by their derivatives. In the general case, perturbations may arise from changes to the shock orientation, changes to the upstream conditions, and from changes to downstream conditions. In the present work, the following simplifying assumptions are made for the purposes of obtaining illustrative results:

- The upstream flow variables are assumed to remain un-perturbed. In the perturbation nomenclature of the present work, this may be expressed as

$$\tilde{X}_{(U)} = 0\,, \tag{4.100}$$

$$X_{(U)} = \bar{X}_{(U)}\,, \tag{4.101}$$

- As a consequence, perturbations to the upstream shock-normal relative-velocity arise solely due to rotation of the shock or due to perturbations to the shock translation velocity in the Eulerian frame $\mathscr{E}$. This results in the following:

$$\mathbf{V}_{\mathbf{r}(U)} = \bar{\mathbf{V}}_{\mathbf{r}(U)} - \tilde{\mathbf{V}}_{\mathbf{s}}\,, \tag{4.102}$$

$$\hat{\mathbf{n}}^* = \bar{\hat{\mathbf{n}}} + \tilde{\mathbf{n}}\,, \tag{4.103}$$

$$w_{(U)} = \mathbf{V}_{\mathbf{r}(U)} \cdot \hat{\mathbf{n}}^*\,. \tag{4.104}$$

  The following perturbation form of the upstream shock-normal velocity is then introduced:

$$w_{(U)} = \bar{w}_{(U)} + \tilde{w}_{(U)}\,, \tag{4.105}$$

$$\bar{w}_{(U)} = \left(\bar{\mathbf{V}}_{\mathbf{f}(U)} - \bar{\mathbf{V}}_{\mathbf{s}}\right) \cdot \bar{\hat{\mathbf{n}}}\,, \tag{4.106}$$

$$\tilde{w}_{(U)} = \left(\bar{\mathbf{V}}_{\mathbf{f}(U)} - \bar{\mathbf{V}}_{\mathbf{s}}\right) \cdot \tilde{\mathbf{n}} - \tilde{\mathbf{V}}_{\mathbf{s}} \cdot \left(\bar{\hat{\mathbf{n}}} + \tilde{\mathbf{n}}\right). \tag{4.107}$$

- The square of the shock-normal relative-velocity appears throughout the Rankine-Hugoniot equations, and will be treated in the following perturbation form:

$$w_{(U)}^2 = \bar{w}_{(U)}^2 + \tilde{\varphi}\,, \tag{4.108}$$

$$\tilde{\varphi} = 2\bar{w}_{(U)}\tilde{w}_{(U)} + \tilde{w}_{(U)}^2\,. \tag{4.109}$$

- In order to relate perturbations in flow variables directly to the causal perturbations, it is assumed that $\left|\tilde{w}_{(U)}\right| \ll \left|\bar{w}_{(U)}\right|$. This allows for expressions of the type $\left[\bar{w}_{(U)} + \tilde{w}_{(U)}\right]^{-1}$ to be expanded as a power series in $\tilde{w}_{(U)}$ and for the series to be truncated after $\mathscr{O}\left(\tilde{w}_{(U)}\right)$.

- A similar assumption is made regarding $\tilde{\varphi}$. Namely, it is assumed that $|\tilde{\varphi}| \ll \left|\bar{w}_{(U)}^2\right|$, to allow for series expansions in $\tilde{\varphi}$. In order to maintain a consistent accuracy between expressions, these series will also be truncated after $\mathscr{O}\left(\tilde{w}_{(U)}\right)$. This results in the following approximation:

$$\tilde{\varphi} = 2\bar{w}_{(U)}\tilde{w}_{(U)} + \mathscr{O}\left(\tilde{w}_{(U)}^2\right). \tag{4.110}$$

These preliminaries may be utilized in deriving the perturbation form of the shock relations of Eqs. (4.57) to (4.59). The perturbation relative-velocities have been defined in Eqs. (4.107) and (4.109), while the perturbation normal-vector $\tilde{\hat{\mathbf{n}}}$ is defined by the relations Eqs. (4.79)

to (4.81). By introducing perturbations into Eqs. (4.57) to (4.59) and discarding terms in $\mathscr{O}\left(\tilde{w}_{(U)}^2\right)$, and following extensive algebraic manipulation, the following equations are obtained:

$$\frac{\tilde{\rho}}{\bar{\rho}} = \left[1 - \left(\frac{\gamma-1}{2}\right)\bar{\sigma}\right]\left(\frac{4}{\gamma+1}\right)\frac{\tilde{w}_{(U)}}{\bar{w}_{(U)}}, \tag{4.111}$$

$$\tilde{\mathbf{V}} = -\left(\frac{\bar{\sigma}}{1+\bar{\sigma}}\right)\bar{w}_{(U)}\tilde{\mathbf{n}} - \left[1 - \left(\frac{\gamma+1}{4}\right)\left(\frac{\bar{\sigma}}{1+\bar{\sigma}}\right)\right]\left(\frac{4}{\gamma+1}\right)\tilde{w}_{(U)}\left(\bar{\hat{\mathbf{n}}} + \tilde{\mathbf{n}}\right), \tag{4.112}$$

$$\frac{\tilde{p}}{\bar{p}} = \left[1 + \left(\frac{\gamma-1}{2}\right)\left(\frac{\bar{\sigma}}{1+\bar{\sigma}}\right)\right]^{-1}\left(\frac{4\gamma}{\gamma+1}\right)\frac{\tilde{w}_{(U)}}{\bar{w}_{(U)}}, \tag{4.113}$$

with the terms clarified in Eqs. (4.56), (4.79) to (4.81), (4.106) and (4.107). It is reiterated that $\bar{\sigma}$ may be interpreted as the small deviation of the shock from the limit ($\bar{\sigma} \to 0$) of a vanishingly weak shock. The above results may be re-written in terms of $\bar{m}_\perp^2$ to describe "small" deviations from the hypersonic limit ($\bar{m}_\perp \to 0$) by use of the relations

$$\bar{\sigma} = \left(\frac{2}{\gamma-1}\right)\left(\frac{1-\bar{m}_\perp^2}{1+\left(\frac{2}{\gamma-1}\right)\bar{m}_\perp^2}\right), \tag{4.114}$$

$$\frac{\bar{\sigma}}{1+\bar{\sigma}} = \left(\frac{2}{\gamma+1}\right)\left(1-\bar{m}_\perp^2\right), \tag{4.115}$$

where $\bar{m}_\perp^2$ is defined by the use of un-perturbed quantities in Eq. (4.62).

4.3.4 Body Boundary Conditions

The non-permeability condition must apply at the body surface during and following perturbations to the surface and to the surface-bound fluid conditions.

It is noted here that derivatives (both temporal and spatial) of the non-permeability condition are valid. These yield terms relating flow gradients to surface curvature and the angular velocity of the surface. A specific example is given in Chapter 19 of [66], in which a relation between the surface-normal pressure-gradient, density, tangential velocity in the surface, and the radius of curvature of the body is obtained. It is noted here that the derivative of the non-permeability condition provides some insight into the origin of gradients in the flow variables, but offers no insight into the perturbation magnitude of the variables.

Perturbations to flow variables are dictated by the non-permeability condition itself, rather than its derivative. In the present work, perturbations to both the flow variables and

to the surface-velocity and -orientation are permitted. The latter two encapsulate surface translation and rotation, respectively. Perturbations to the surface orientation have already been described in terms of perturbation vectors $\tilde{\mathbf{t}}$, $\tilde{\mathbf{n}}$, $\tilde{\mathbf{b}}$ to the un-perturbed oriented adapted-frame $\bar{\mathscr{A}}$ in Section 4.3.1. Perturbations were considered as arising from rotation of the body surface through an angle $\tilde{\theta}_r$ about a rotation axis $\hat{\mathbf{r}}$, with the resulting components of perturbation vectors being of the form of Eqs. (4.79) to (4.81). These relations will be used in the non-permeability condition applied to the body-surface following perturbations to the flow variables and the surface position:

$$\mathbf{V_r} \cdot \hat{\mathbf{n}}^* = 0\,, \tag{4.116}$$

where $\hat{\mathbf{n}}^*$ is the normal to the body surface following perturbations and $\mathbf{V_r}$ is the velocity of the fluid relative to the body (in total-quantity form following perturbations). These vectors may be described in terms of their un-perturbed and perturbation contributions as

$$\mathbf{V_r} = \bar{\mathbf{V}}_\mathbf{r} + \tilde{\mathbf{V}}_\mathbf{r} = \left(\bar{\mathbf{V}}_\mathbf{f} - \bar{\mathbf{V}}_\mathbf{b}\right) + \left(\tilde{\mathbf{V}}_\mathbf{f} - \tilde{\mathbf{V}}_\mathbf{b}\right), \tag{4.117}$$

$$\hat{\mathbf{n}}^* = \bar{\hat{\mathbf{n}}} + \tilde{\mathbf{n}}\,. \tag{4.118}$$

Noting that the un-perturbed solution $\bar{\mathbf{V}}_\mathbf{r} \cdot \bar{\hat{\mathbf{n}}} = 0$ is filtered out, Eq. (4.116) may be in vector form written as

$$\bar{\mathbf{V}}_\mathbf{r} \cdot \tilde{\mathbf{n}} + \tilde{\mathbf{V}}_\mathbf{r} \cdot \left(\bar{\hat{\mathbf{n}}} + \tilde{\mathbf{n}}\right) = 0\,. \tag{4.119}$$

This may be further expressed in component form as

$$(\bar{v}_m - \bar{v}_{bm})\tilde{n}_m + (\tilde{v}_m - \tilde{v}_{bm})(\bar{n}_m + \tilde{n}_m) = 0\,. \tag{4.120}$$

Focusing on the perturbation-velocity of the fluid (as the perturbed orientation of the surface and the surface velocity will generally be prescribed), this may be rearranged to

$$(\bar{n}_m + \tilde{n}_m)\tilde{v}_m = (\bar{n}_m + \tilde{n}_m)\tilde{v}_{bm} - (\bar{v}_m - \bar{v}_{bm})\tilde{n}_m\,. \tag{4.121}$$

At this point, non-dimensionalization may be performed through substitution of the appropriate reference values. It is repeated here that the normal-vector components are non-dimensional. However, it is stressed that while $\bar{\hat{\mathbf{n}}} = \mathscr{O}(1)$, the components may be of disparate orders. They are thus treated in the same manner as reference quantities and are included in the term-groupings describing the relative magnitude of terms. It is thus found that

$$\left(\tilde{U}_m\right)(\bar{n}_m + \tilde{n}_m)\tilde{u}_m = \left(\tilde{U}_{bm}\right)(\bar{n}_m + \tilde{n}_m)\tilde{u}_{bm} - (\tilde{n}_m)[(\bar{U}_m)\bar{u}_m - (\bar{U}_{bm})\bar{u}_{bm}]\,. \tag{4.122}$$

The introduction of the non-dimensional parameters from Table 4.5 allows the equation to be written as

$$(\varepsilon_{um})(\bar{n}_m+\tilde{n}_m)\tilde{u}_m = (\varepsilon_{bm})(\bar{n}_m+\tilde{n}_m)\tilde{u}_{bm} - (\tilde{n}_m)\left[\left(\bar{k}_{um}\right)\bar{u}_m - \left(\bar{k}_{bm}\right)\bar{u}_{bm}\right]. \tag{4.123}$$

4.4 Reference Quantities and Non-Dimensionalization

The present section aims to introduce a framework for selecting appropriate reference values in non-dimensionalizing the governing equations and boundary conditions. The development will open with a discussion on the determination of flow gradients in Section 4.4.1. Section 4.4.2 will define the control parameters used in the non-dimensionalization. The main body of the framework is presented in Appendix A. Section A.1 will focus on parameter definition for the un-perturbed solution. A number of representative cases will be considered in Section A.2. Definition of perturbation parameters will be treated in Section A.3. This will be followed by results of the scaling analysis in Section A.4. This will allow the developments of Sections 4.5 and 4.6 to focus on the reduction of the 3D equations to 1D.

4.4.1 Flow Gradients

The Rankine-Hugoniot equations effectively prescribe the jump in C^0 (zeroth-derivative) quantities across the shock front as a function of

- The local shock orientation,
- The local translational velocity of the shock surface,
- The local pre-shock flow quantities.

Derivatives of the boundary conditions remain valid. The first-derivatives (spatial or temporal) of the Rankine-Hugoniot equations prescribe first-order gradients of post-shock flow quantities as a function of

- The local shock curvature,
- The rotational velocity of the local shock surface,
- Gradients of pre-shock flow quantities.

As will be seen in the subsequent development, scaling analysis of the Rankine-Hugoniot equations results in a number of control variables or parameters which must be known a-priori.

This number increases when considering derivatives of the Rankine-Hugoniot equations. Obtaining closed-form expressions for the post-shock fluid gradients for the general case of curvature and pre-shock quantities, while possible, is an algebraically cumbersome procedure. Varied approaches to the above, and indeed varied results, are noted in the literature [203–210]. A thorough review of the existing literature on unsteady curved shocks and of the inconsistencies therein is outside the scope of the present work.

Similar consideration of the flow-tangency condition at the body surface shows that derivatives of the boundary conditions will enforce a relationship between streamline curvatures at the body surface. No further consideration of this is made in the present work.

No rigorous basis for assumed magnitudes of flow gradients is offered in the present work. However, a number of heuristic considerations may be made. The following points are made regarding flow past a delta wing with its planform in the $\hat{\mathbf{e}}_1\hat{\mathbf{e}}_2$ plane:

- Relative magnitudes of directional gradients arising from infinitesimal perturbations may be estimated from Mach waves in the local flow. For flow directed along the $\hat{\mathbf{e}}_1$ direction, this yields the approximation (for an infinitesimal perturbation at a point) that
$$\frac{\tilde{L}_3}{\tilde{L}_1} = \mathscr{O}\left(\frac{\tilde{L}_2}{\tilde{L}_1}\right) = \mathscr{O}\left(\frac{1}{\sqrt{M^2-1}}\right), \tag{4.124}$$
where M is the local Mach number of the flow,

- A vortex line oriented along the $\hat{\mathbf{e}}_1$ direction would (locally) induce the relative magnitudes of
$$\bar{L}_2 = \mathscr{O}(\bar{L}_3), \tag{4.125}$$

- Planar flow (with spanwise variations being negligble) would be described by
$$\bar{L}_3 \ll \bar{L}_2 \quad \text{and} \quad \bar{L}_1 \ll \bar{L}_2, \tag{4.126}$$

- Finally, it is noted that perturbation gradients may vary substantially from gradients in the un-perturbed flow. Examples of physical scenarios in which this would be encountered include (but are not limited to):
  - Perturbations of short wavelength in comparison to the characteristic length of the steady flow,
  - Perturbations of high temporal frequency or short, violent perturbations.

As no concrete framework is offered in the present for quantifying relative magnitudes of flow gradients, they will be treated as parameters in the subsequent scaling analysis.

4.4.2 Definition of Control Parameters and Coordinates

A large array of non-dimensional parameters is noted in the perturbation equations of Section 4.3. It is the aim of Section 4.4 to define appropriate reference quantities for non-dimensionalization using a minimum number of control parameters which must be known or specified a-priori. The following quantities are assumed known and defined as control parameters:

- It is assumed that all un-perturbed quantities are known a-priori:
  - The orientations and velocities of un-perturbed surfaces are known,
  - The un-perturbed flow quantities are known,
- Perturbations to surface orientations are defined as control parameters:
  - The rotation angle $\tilde{\theta}_r$ and the axis of rotation $\hat{\mathbf{r}}$ are specified for both the body and for the shock,
- Perturbations to surface velocities are defined as control parameters:
  - The perturbation velocity of the body surface $\tilde{\mathbf{V}}_\mathbf{b}$ and the perturbation velocity of the shock surface $\tilde{\mathbf{V}}_\mathbf{s}$ are specified,

Finally, for the purpose of interpretation and discussion, it will be assumed that $\hat{\mathbf{e}}_\mathbf{1}$ is aligned with the body axis or the chordwise direction, and that the planform of lifting surfaces lies in the $\hat{\mathbf{e}}_\mathbf{1}\hat{\mathbf{e}}_\mathbf{2}$ plane.

4.5 Classical Piston Theory

The present section will demonstrate the application of the scaling analysis framework presented in Section 4.4 and Appendix A to deriving CPT from the perturbation form of the Euler equations outlined in Section 4.3. The development to be presented here will utilize the k and ε notation defined in Table 4.5. Justification for the orders of magnitude adopted may be found in Appendix A in the development leading up to Tables A.8 to A.13. These tables may also be used to extend the analysis to other combinations of Mach number, sweep, and incidence.

4.5.1 Specification of Perturbation and Non-Dimensionalization

Definition of Un-Perturbed Solution

The essence of CPT is modelling perturbations relative to the undisturbed freestream. Assuming a uniform, steady freestream, the following un-perturbed solution is defined:

$$\bar{\rho} \to \rho_\infty \,, \tag{4.127}$$

$$\bar{\hat{\mathbf{V}}} \to \hat{\mathbf{V}}_\infty \left[\left(1 - \sin^2\alpha - \sin^2\beta\right)^{\frac{1}{2}} \hat{\mathbf{e}}_\mathbf{1} - \sin\beta\, \hat{\mathbf{e}}_\mathbf{2} + \sin\alpha\, \hat{\mathbf{e}}_\mathbf{3} \right] , \tag{4.128}$$

$$\bar{p} \to p_\infty \,, \tag{4.129}$$

$$\bar{a} \to a_\infty \,, \tag{4.130}$$

where α is the angle of attack and β is the side-slip angle. The above suggest an obvious choice of reference values for the un-perturbed solution. The un-perturbed solution is associated with the absence of a shock wave. This essentially requires the body to be a zero-thickness plane aligned with the freestream, leading to

$$\bar{\hat{\mathbf{n}}}_\mathbf{b} \cdot \hat{\mathbf{V}}_\infty = 0 \tag{4.131}$$

defining the unperturbed unit normal-vector at the body boundary. Similarly, $\bar{\mathbf{V}}_\mathbf{b} = 0$. The absence of a bow shock is equivalent to taking the limit of a Mach wave, leading to

$$\bar{\hat{\mathbf{n}}}_\mathbf{s} \cdot \hat{\mathbf{V}}_\infty = -\frac{1}{M_\infty} \,, \tag{4.132}$$

defining the unperturbed unit normal-vector at the "shock" boundary. Further definitions of shock-related terms in the Mach limit include

$$\bar{\mathbf{V}}_\mathbf{s} = 0 \,, \tag{4.133}$$

$$\frac{\bar{w}_{(U)}}{\left|\bar{\mathbf{V}}_{(U)}\right|} \to -\frac{1}{M_\infty} \,, \tag{4.134}$$

$$\bar{\sigma} \to 0 \,, \quad \bar{m}_\perp^2 = 1 \,, \tag{4.135}$$

The assumption of a uniform and steady freestream leads to the following:

$$\frac{\partial \bar{X}}{\partial x_i} = 0 \,, \tag{4.136}$$

$$\frac{\partial \bar{X}}{\partial t} = 0 \,, \tag{4.137}$$

where $\bar{X}$ is any of the fluid quantities in the freestream. This assumption leads to significant simplification of Eqs. (4.97) to (4.99), (4.111) to (4.113) and (4.123). The simplified Euler equations then become:

$$\text{C:}\quad \left.\begin{aligned}(\varepsilon_\rho)\left[\left(\frac{\bar{k}_t}{\varepsilon_t}\right)\frac{\partial}{\partial t_N}+\left(\frac{\bar{k}_{um}}{\varepsilon_{Lm}}\right)\bar{u}_m\frac{\partial}{\partial \xi_m}\right]\tilde{\rho}_N+\left(\frac{\varepsilon_{um}}{\varepsilon_{Lm}}\right)\bar{\rho}_N\frac{\partial \tilde{u}_m}{\partial \xi_m}\\ +\left(\frac{\varepsilon_\rho\varepsilon_{um}}{\varepsilon_{Lm}}\right)\frac{\partial(\tilde{\rho}_N\tilde{u}_m)}{\partial \xi_m}\end{aligned}\right\}=0\,, \tag{4.138}$$

$$\text{M:}\quad \left.\begin{aligned}(\varepsilon_{ui})\left[\bar{\rho}_N+(\varepsilon_\rho)\tilde{\rho}_N\right]\left[\left(\frac{\bar{k}_t}{\varepsilon_t}\right)\frac{\partial}{\partial t_N}+\left(\frac{\bar{k}_{um}}{\varepsilon_{Lm}}\right)\bar{u}_m\frac{\partial}{\partial \xi_m}\right]\tilde{u}_i\\ +\left(\frac{\varepsilon_{ui}\varepsilon_{um}}{\varepsilon_{Lm}}\right)\left[\bar{\rho}_N+(\varepsilon_\rho)\tilde{\rho}_N\right]\tilde{u}_m\frac{\partial \tilde{u}_i}{\partial \xi_m}\end{aligned}\right\}=-\left(\frac{\varepsilon_p\bar{k}_f}{\varepsilon_{Li}}\right)\frac{\partial \tilde{p}_N}{\partial \xi_i}\,, \tag{4.139}$$

$$\text{E:}\quad \left.\begin{aligned}(\varepsilon_p\bar{k}_a)\left[\left(\frac{\bar{k}_t}{\varepsilon_t}\right)\frac{\partial}{\partial t_N}+\left(\frac{\bar{k}_{um}}{\varepsilon_{Lm}}\right)\bar{u}_m\frac{\partial}{\partial \xi_m}\right]\tilde{p}_N+\left(\frac{\varepsilon_{um}\varepsilon_p\bar{k}_a}{\varepsilon_{Lm}}\right)\tilde{u}_m\frac{\partial \tilde{p}_N}{\partial \xi_m}\\ +\left(\frac{\varepsilon_{um}}{\varepsilon_{Lm}}\right)\left[\bar{\rho}_N+(\varepsilon_\rho)\tilde{\rho}_N\right]\left[\bar{a}_N^2+(2\varepsilon_a)\bar{a}_N\tilde{a}_N+(\varepsilon_a^2)\tilde{a}_N^2\right]\frac{\partial \tilde{u}_m}{\partial \xi_m}\end{aligned}\right\}=0\,. \tag{4.140}$$

The perturbation form of the shock boundary-conditions become:

$$\frac{\tilde{\rho}}{\bar{\rho}}=-\left(\frac{4}{\gamma+1}\right)M_\infty\frac{\tilde{w}_{(U)}}{\left|\bar{\mathbf{V}}_{(U)}\right|}\,, \tag{4.141}$$

$$\frac{\tilde{\mathbf{V}}}{\left|\bar{\mathbf{V}}_{(U)}\right|}=-\left(\frac{4}{\gamma+1}\right)\frac{\tilde{w}_{(U)}}{\left|\bar{\mathbf{V}}_{(U)}\right|}\left(\bar{\hat{\mathbf{n}}}+\tilde{\mathbf{n}}\right), \tag{4.142}$$

$$\frac{\tilde{p}}{\bar{p}}=-\left(\frac{4\gamma}{\gamma+1}\right)M_\infty\frac{\tilde{w}_{(U)}}{\left|\bar{\mathbf{V}}_{(U)}\right|}\,, \tag{4.143}$$

where it is worthwhile noting that

$$\frac{\tilde{p}}{\bar{p}}=\gamma\frac{\tilde{\rho}}{\bar{\rho}}\,, \tag{4.144}$$

which is consistent with a series expansion of the isentropic relation

$$\frac{p}{\bar{p}}=\left(\frac{\rho}{\bar{\rho}}\right)^\gamma \tag{4.145}$$

for small density perturbations. This serves as a reminder that the perturbation form of the shock equations presented in this work were derived with the assumption that $\tilde{w}_{(U)}\ll\bar{w}_{(U)}$. This is clearly not satisfactory for perturbations from a shock-free reference solution in

hypersonic flows (as are typically encountered when applying piston theory). Instead, the total-quantity form of the shock equations as presented in Section 4.2.3 is recommended. The following equations adapted from Eqs. (A.18) and (A.20) to (A.24) may be used, which are essentially similar to Eqs. (4.53) to (4.56):

$$\frac{\tilde{\rho}}{\rho_\infty} = \sigma\,, \tag{4.146}$$

$$\frac{\tilde{v}_1}{V_\infty} = \left(\frac{\sigma}{1+\sigma}\frac{w_{(U)}}{V_\infty}\right)\sin\eta_s\cos\lambda_s\,, \tag{4.147}$$

$$\frac{\tilde{v}_2}{V_\infty} = \left(\frac{\sigma}{1+\sigma}\frac{w_{(U)}}{V_\infty}\right)\sin\eta_s\sin\lambda_s\,, \tag{4.148}$$

$$\frac{\tilde{v}_3}{V_\infty} = \left(\frac{\sigma}{1+\sigma}\frac{w_{(U)}}{V_\infty}\right)\cos\eta_s\,, \tag{4.149}$$

$$\frac{\tilde{p}}{p_\infty} = \left(\frac{\sigma}{1+\sigma}\right)\gamma M_\infty^2\frac{w_{(U)}^2}{V_\infty^2}\,. \tag{4.150}$$

$$\frac{\tilde{a}}{a_\infty} = \left[\frac{1+\tilde{p}/p_\infty}{1+\sigma}\right]^{\frac{1}{2}} - 1\,, \tag{4.151}$$

The body boundary condition becomes:

$$(\varepsilon_{um})(\bar{n}_m+\tilde{n}_m)\tilde{u}_m = (\varepsilon_{bm})(\bar{n}_m+\tilde{n}_m)\tilde{u}_{bm} - (\bar{k}_{um})(\tilde{n}_m)\bar{u}_m\,. \tag{4.152}$$

Scaling Analysis

Scaling analysis on the above simplified equations is facilitated by the tabulated scaling analysis of:

- $\tilde{\mathbf{n}}$ in Table A.5,
- $\bar{\tilde{\mathbf{n}}}+\tilde{\mathbf{n}}$ in Table A.6,
- $\frac{\tilde{w}_{(U)}}{|\tilde{\mathbf{V}}_{(U)}|}$ in Table A.7.

For the shock boundary conditions, the existing results of Appendix A may be adapted for use in the present section as follows:

- The un-perturbed quantities such as $\bar{p}$ in Appendix A are post-shock quantities. Denote these values as X,

- These may be interpreted as total-value quantities for the purposes of the present section,
- The un-perturbed fluid quantities – in the sense of the present section – are the freestream quantities, as described in Eqs. (4.127) to (4.130). Denote these quantities Y,
- Let the perturbation fluid quantities – in the sense of the present section – be denoted Z. These may then be found from the results of Appendix A by

$$Z = X - Y\,. \tag{4.153}$$

  The scaling obtained using the above adjustment will remove the assumption of small $\tilde{w}_{(U)}$.

It is emphasized that Eqs. (4.141) to (4.143) or their nonlinear equivalents in Eqs. (4.146) to (4.151), are intended to provide informed estimates for reference values $\tilde{\rho}_R$, $\tilde{U}_i$, $\tilde{p}_R$, and $\tilde{a}_R$. This in turn leads to estimates for the corresponding ε parameters.

Numerical analysis of Eqs. (4.146) to (4.151) shows that the following scaling applies:

$$\frac{\tilde{\rho}}{\rho_\infty} = \sigma = \mathscr{O}\left(\frac{K_\beta - 1}{K_\beta}\right), \tag{4.154}$$

$$\frac{\sigma}{1+\sigma} = \mathscr{O}(\sigma) = \mathscr{O}\left(\frac{K_\beta - 1}{K_\beta}\right), \tag{4.155}$$

$$\frac{\tilde{p}}{p_\infty} = \left(\frac{2\gamma}{\gamma+1}\right)\left(K_\beta^2 - 1\right) = \mathscr{O}\left(K_\beta^2 - 1\right), \tag{4.156}$$

$$\frac{\tilde{a}}{a_\infty} = \mathscr{O}\left(K_\beta - 1\right), \tag{4.157}$$

$$K_\beta \equiv M_\infty \frac{w_{(U)}}{V_\infty}, \tag{4.158}$$

An example of the application of the above to scaling analysis for a low-sweep delta wing at low incidence is demonstrated in Table 4.6. These set of conditions are associated with earlier developments of classical piston theory such as that due to Lighthill [88] (who assumed 2D flow) and that due to Il'yushin [77]. In Table 4.6, M_∞ and $M_\infty\tau$ (through K_β from Eq. (4.158)) have been left as parameters, although it must be noted that $K_\beta \geq 1$ is required for the existence of a shock wave. This may be interpreted as a minimum required Mach number M_∞ for the assumed shock angles included in $\frac{w_{(U)}}{V_\infty}$, as outlined in Table A.4.

Table 4.6 Scaling analysis non-dimensional parameters for CPT, case code $\lambda 0$-$\alpha 0$-$\eta 0$ with $\hat{\mathbf{r}} = -\hat{\mathbf{e}}_2$, $\tau_\theta = \mathscr{O}(\tau)$.

Quantity X	$\mathscr{O}(X)$ or $\mathscr{O}(X_1)$	$\mathscr{O}(X_2)$	$\mathscr{O}(X_3)$
$\frac{w_{(U)}}{V_\infty}$	$\mathscr{O}(\tau)$		
K_β	$\mathscr{O}(M_\infty \tau)$		
$\bar{k}_t$	$\equiv 0$		
$\bar{k}_{xi}$	$\mathscr{O}\left(\frac{\bar{L}_R}{\bar{L}_1}\right)$	$\mathscr{O}\left(\tau \frac{\bar{L}_R}{\bar{L}_2}\right)$	$\mathscr{O}\left(\tau \frac{\bar{L}_R}{\bar{L}_3}\right)$
$\bar{k}_{Li}$	$\mathscr{O}\left(\frac{\bar{L}_R}{\bar{L}_1}\right)$	$\mathscr{O}\left(\frac{\bar{L}_R}{\bar{L}_2}\right)$	$\mathscr{O}\left(\frac{\bar{L}_R}{\bar{L}_3}\right)$
$\bar{k}_{ui}$	$\mathscr{O}(1)$	$\mathscr{O}(\tau)$	$\mathscr{O}(\tau)$
$\bar{k}_{bi}$	$\equiv 0$	$\equiv 0$	$\equiv 0$
$\bar{k}_f$	$\mathscr{O}\left(\frac{1}{M_\infty^2}\right)$		
$\bar{k}_a$	$\mathscr{O}(1)$		
$\frac{\bar{k}_t}{\varepsilon_t}$	$\mathscr{O}\left(\frac{\bar{L}_R}{V_\infty \tilde{t}_R}\right)$		
ε_{Li}	$\mathscr{O}\left(\frac{\tilde{L}_1}{\bar{L}_R}\right)$	$\mathscr{O}\left(\frac{\tilde{L}_2}{\bar{L}_R}\right)$	$\mathscr{O}\left(\frac{\tilde{L}_3}{\bar{L}_R}\right)$
ε_{ui}	$\mathscr{O}\left(\frac{K_\beta - 1}{K_\beta} \tau^2\right)$	$\mathscr{O}\left(\frac{K_\beta - 1}{K_\beta} \tau^3\right)$	$\mathscr{O}\left(\frac{K_\beta - 1}{K_\beta} \tau\right)$
ε_{bi}	$\mathscr{O}\left(\frac{\tilde{U}_{b1}}{V_\infty}\right)$	$\mathscr{O}\left(\frac{\tilde{U}_{b2}}{V_\infty}\right)$	$\mathscr{O}\left(\frac{\tilde{U}_{b3}}{V_\infty}\right)$
ε_ρ	$\mathscr{O}\left(\frac{K_\beta - 1}{K_\beta}\right)$		
ε_p	$\mathscr{O}\left(K_\beta^2 - 1\right)$		
ε_a	$\mathscr{O}\left(K_\beta - 1\right)$		

Reference values estimated from the above will be valid locally to the point at which they are determined. No attempt is made here to demonstrate the uniform validity of a non-dimensionalization throughout the domain bounded by the bow shock and the body surface. Indeed, a number of scenarios are to be expected in which a non-dimensionalization based on reference values at a given point on the shock surface will *not* be uniformly valid:

- Flows with regions of strong shock curvature or disparate orders of shock inclination,
- Flows in which flow quantities and directions vary significantly between the shock and the body surface. Examples of this include:
  - Flows about finite bodies at very high incidence,
  - Flows with detached shocks.

Finally, it is recalled that CPT is essentially a one-dimensional model of the flow equations. The derivation of CPT from the Euler equations therefore hinges on eliminating two of the three unknown velocities as variables (in the present study, $\tilde{u}_1$ and $\tilde{u}_2$). Advection by means of known, steady velocities in the neglected directions (through $\bar{u}_1 \frac{\partial}{\partial \xi_1}$ and $\bar{u}_2 \frac{\partial}{\partial \xi_2}$) may be interpreted as time-variation in an advected frame, and thus does not affect the physical interpretation of the system as one-dimensional (and unsteady) in the ξ_3 -direction.

As a closing remark, it is noted that different approaches to the neglect of velocity components may be adopted. The approach adopted in the present section will be as follows:

- Equations will be multiplied by a non-dimensional smallness parameter (if required) such that the largest order of any given term grouping in the equation is $\mathscr{O}(1)$,
- Thereafter, the equation will be truncated to terms of a given order of smallness. In the present work, terms which are $\mathscr{O}\left(\tau^2\right)$ with $\tau \ll 1$ will be discarded, resulting in an first-order theory.

4.5.2 Reduction to 2D

3D Equations

For slender bodies, a typical reduction to a 2D is achieved through neglecting $\tilde{u}_1$ relative to the crossflow velocities $\tilde{u}_2$ and $\tilde{u}_3$. Examples of this include classical hypersonic SDT [27] and the high-incidence theory of Sychev [4]. The application of 2D methods to 3D wings is typically facilitated through the invocation of strip theory, in which spanwise variations through $\tilde{u}_2$ are neglected.

In the present work, the reduction from 3D to 2D will be demonstrated through the neglect of $\tilde{u}_1$. This will facilitate comparison with classical hypersonic SDT [27] and Ilyushin's [77] theory. The derivation which follows is demonstrated for case code $\lambda 0$-$\alpha 0$-$\eta 0$ with $\hat{\mathbf{r}} = -\hat{\mathbf{e}}_2$, $\tau_\theta = \mathscr{O}(\tau)$, with the definition of non-dimensional parameters given in Table 4.6. The case is defined by the following physical characteristics:

- A thin wing ($\sin\eta_b = \mathscr{O}(\tau)$ with $\tau \ll 1$),
- Low sweep ($\sin\lambda_b = \mathscr{O}(\tau)$),
- Small incidence ($\sin\alpha = \mathscr{O}(\tau)$),
- A shock inclination of the order of the same order as the body surface or incidence ($\sin\eta_s = \mathscr{O}(\tau)$),
- Perturbations which arise due to a change in incidence or due to pure bending ($\hat{\mathbf{r}} = -\hat{\mathbf{e}}_2$),
- Small perturbations in incidence ($\tau_\theta = \mathscr{O}(\tau)$).

The adaptation of the derivation to different physical scenarios (such as to high incidence, in order to derive Sychev's [4] theory) is achieved by the specification of appropriate case parameters. A framework for this has been provided in Appendix A.

Substituting the non-dimensional parameters from the scaling analysis of Table 4.6 into Eqs. (4.138) to (4.140) and expanding the summation notation to explicit coefficients in the parentheses, the following form of the Euler equations is obtained after some algebraic manipulation:

$$\text{C:}\quad \left.\begin{aligned}&\left[\left(\frac{\tilde{L}_1}{V_\infty \tilde{t}_R}\right)\frac{\partial}{\partial t_N} + \left(1, \tau\frac{\tilde{L}_1}{\tilde{L}_2}, \tau\frac{\tilde{L}_1}{\tilde{L}_3}\right)\bar{u}_m\frac{\partial}{\partial\xi_m}\right]\tilde{\rho}_N \\ &\qquad + \left(\tau^2, \tau^3\frac{\tilde{L}_1}{\tilde{L}_2}, \tau\frac{\tilde{L}_1}{\tilde{L}_3}\right)\bar{\rho}_N\frac{\partial\tilde{u}_m}{\partial\xi_m} \\ &\quad + \left(\frac{K_\beta - 1}{K_\beta}\right)\left(\tau^2, \tau^3\frac{\tilde{L}_1}{\tilde{L}_2}, \tau\frac{\tilde{L}_1}{\tilde{L}_3}\right)\frac{\partial(\tilde{\rho}_N\tilde{u}_m)}{\partial\xi_m}\end{aligned}\right\} = 0\,, \tag{4.159}$$

$$\text{M:}\quad \left.\begin{aligned}&\left[\bar{\rho}_N + \left(\frac{K_\beta - 1}{K_\beta}\right)\tilde{\rho}_N\right]\left[\left(\frac{\tilde{L}_1}{V_\infty \tilde{t}_R}\right)\frac{\partial}{\partial t_N} + \left(1, \tau\frac{\tilde{L}_1}{\tilde{L}_2}, \tau\frac{\tilde{L}_1}{\tilde{L}_3}\right)\bar{u}_m\frac{\partial}{\partial\xi_m}\right]\tilde{u}_i \\ &\quad + \left(\frac{K_\beta - 1}{K_\beta}\right)\left(\tau^2, \tau^3\frac{\tilde{L}_1}{\tilde{L}_2}, \tau\frac{\tilde{L}_1}{\tilde{L}_3}\right)\left[\bar{\rho}_N + \left(\frac{K_\beta - 1}{K_\beta}\right)\tilde{\rho}_N\right]\tilde{u}_m\frac{\partial\tilde{u}_i}{\partial\xi_m} \\ &\qquad + \left(\frac{\tilde{L}_1}{\tilde{L}_i}\frac{V_\infty}{\tilde{U}_i}\frac{K_\beta(K_\beta+1)}{M_\infty^2}\right)\frac{\partial\tilde{p}_N}{\partial\xi_i}\end{aligned}\right\} = 0\,, \tag{4.160}$$

$$\text{E:}\quad \left.\begin{aligned}&\left[\left(\frac{\tilde{L}_1}{V_\infty \tilde{t}_R}\right)\frac{\partial}{\partial t_N}+\left(1,\,\tau\frac{\tilde{L}_1}{\tilde{L}_2},\,\tau\frac{\tilde{L}_1}{\tilde{L}_3}\right)\bar{u}_m\frac{\partial}{\partial \xi_m}\right]\tilde{p}_N\\&+\left(\frac{K_\beta-1}{K_\beta}\right)\left(\tau^2,\,\tau^3\frac{\tilde{L}_1}{\tilde{L}_2},\,\tau\frac{\tilde{L}_1}{\tilde{L}_3}\right)\tilde{u}_m\frac{\partial \tilde{p}_N}{\partial \xi_m}\\&+\left(\frac{1}{K_\beta^2+K_\beta}\right)\left(\tau^2,\,\tau^3\frac{\tilde{L}_1}{\tilde{L}_2},\,\tau\frac{\tilde{L}_1}{\tilde{L}_3}\right)\left[\bar{\rho}_N+(\varepsilon_\rho)\tilde{\rho}_N\right]\left[\bar{a}_N^2+(2\varepsilon_a)\bar{a}_N\tilde{a}_N+(\varepsilon_a^2)\tilde{a}_N^2\right]\frac{\partial \tilde{u}_m}{\partial \xi_m}\end{aligned}\right\}=0\,. \tag{4.161}$$

Similarly, the boundary condition at the body surface becomes

$$\left(\frac{K_\beta-1}{K_\beta}\right)(\tau^2,\,\tau^4,\,1)\tilde{u}_m=\left(\frac{\tilde{U}_{b1}}{V_\infty},\,\tau\frac{\tilde{U}_{b2}}{V_\infty},\,\frac{1}{\tau}\frac{\tilde{U}_{b3}}{V_\infty}\right)\tilde{u}_{bm}-(1,\,0,\,\tau^2)\bar{u}_m\,. \tag{4.162}$$

The perturbation velocity components at the shock boundary are found from Eqs. (4.147) to (4.149) and (4.155) with $\frac{w_{(U)}}{V_\infty}$ estimated from Table A.7:

$$\frac{\tilde{v}_1}{V_\infty}=\mathscr{O}\left(\frac{(K_\beta-1)}{K_\beta}\tau^2\right), \tag{4.163}$$

$$\frac{\tilde{v}_2}{V_\infty}=\mathscr{O}\left(\frac{(K_\beta-1)}{K_\beta}\tau^3\right), \tag{4.164}$$

$$\frac{\tilde{v}_3}{V_\infty}=\mathscr{O}\left(\frac{(K_\beta-1)}{K_\beta}\tau\right). \tag{4.165}$$

The post-shock velocity-component scaling above was used to defined ε_{ui} in Table 4.6.

Requirements for Reduction to 2D

As stated in Section 4.5.1, the approach adopted here in neglecting $\tilde{u}_1$ requires that

- The largest order of any given term grouping in the equation is $\mathscr{O}(1)$,
- Terms in $\tilde{u}_1$ must be of smallness $\mathscr{O}(\tau^2)$ or smaller.

These steps will be applied on a per-equation basis as follows:

- Continuity, through Eq. (4.159):

– The equation as written is normalized with terms involving steady advection in the x_1 direction being $\mathscr{O}(1)$. Specifically, it is assumed that:

$$\bar{u}_1 \frac{\partial \tilde{\rho}_N}{\partial \xi_1} = \mathscr{O}(1) \tag{4.166}$$

and that it has a coefficient of 1. In normalizing terms relative to $\bar{u}_1 \frac{\partial}{\partial \xi_1}$, it has been implicitly assumed that local time variations through $\frac{\partial}{\partial t_N}$ are at most of the same order as steady advection terms through $\bar{u}_1 \frac{\partial}{\partial \xi_1}$. This may be expressed explicitly as:

$$\left(\frac{\tilde{L}_1}{V_\infty \tilde{t}_R} \right) \leq \mathscr{O}(1), \tag{4.167}$$

– Using the normalization above, the following terms involving $\tilde{u}_1$ are found in the continuity equation:

$$(\tau^2) \bar{\rho}_N \frac{\partial \tilde{u}_1}{\partial \xi_1}, \tag{4.168}$$

$$\left(\frac{K_\beta - 1}{K_\beta} \tau^2 \right) \frac{\partial \tilde{\rho}_N \tilde{u}_1}{\partial \xi_1}, \tag{4.169}$$

It is seen that both these terms may be neglected in favour of $\bar{u}_1 \frac{\partial \tilde{\rho}_N}{\partial \xi_1}$ at any K_β without any further assumptions.

• Momentum in the x_2 direction, through Eq. (4.160):

– The equation as written is normalized with terms involving steady advection in the x_1 direction being $\mathscr{O}(1)$. However, due to the smallness of $\tilde{v}_2$, this leads to magnification of the pressure-gradient term. An improved normalization is obtained by normalizing relative to the pressure-gradient term. In particular, it is assumed that

$$\frac{\partial \tilde{p}_N}{\partial \xi_2} = \mathscr{O}(1) \tag{4.170}$$

and that it has a coefficient of 1. This is achieved through multiplying Eq. (4.160) by $\left(\frac{\tilde{L}_2}{\tilde{L}_1} \frac{M_\infty^2}{K_\beta (K_\beta + 1)} \varepsilon_{u2} \right)$ throughout. This results in the following form of the

momentum equation:

$$\left.\begin{aligned}&\left(\frac{K_\beta-1}{K_\beta+1}\right)[\bar{\rho}_N]\left[\left(\tau\frac{\tilde{L}_2}{V_\infty\tilde{t}_R}\right)\frac{\partial}{\partial t_N}+\left(\tau\frac{\tilde{L}_2}{\tilde{L}_1},\tau^2,\tau^2\frac{\tilde{L}_2}{\tilde{L}_3}\right)\bar{u}_m\frac{\partial}{\partial\xi_m}\right]\tilde{u}_i\\&+\left(\frac{(K_\beta-1)^2}{K_\beta(K_\beta+1)}\right)[\tilde{\rho}_N]\left[\left(\tau\frac{\tilde{L}_2}{V_\infty\tilde{t}_R}\right)\frac{\partial}{\partial t_N}+\left(\tau\frac{\tilde{L}_2}{\tilde{L}_1},\tau^2,\tau^2\frac{\tilde{L}_2}{\tilde{L}_3}\right)\bar{u}_m\frac{\partial}{\partial\xi_m}\right]\tilde{u}_i\\&+\left(\frac{(K_\beta-1)^2}{K_\beta(K_\beta+1)}\right)\left(\tau^3\frac{\tilde{L}_2}{\tilde{L}_1},\tau^4,\tau^2\frac{\tilde{L}_2}{\tilde{L}_3}\right)\left[\bar{\rho}_N+\left(\frac{K_\beta-1}{K_\beta}\right)\tilde{\rho}_N\right]\tilde{u}_m\frac{\partial\tilde{u}_i}{\partial\xi_m}\\&+\frac{\partial\tilde{p}_N}{\partial\xi_i}\end{aligned}\right\}=0 \tag{4.171}$$

– Using the normalization above, the following term involving $\tilde{u}_1$ is found in the momentum equation:

$$\left(\frac{(K_\beta-1)^2}{K_\beta(K_\beta+1)}\frac{\tilde{L}_2}{\tilde{L}_1}\tau^3\right)\left[\bar{\rho}_N+\left(\frac{K_\beta-1}{K_\beta}\right)\tilde{\rho}_N\right]\tilde{u}_1\frac{\partial\tilde{u}_2}{\partial\xi_1}\,. \tag{4.172}$$

In order to neglect this term relative to $\frac{\partial\tilde{p}_N}{\partial\xi_2}$, it is required that

$$\left(\frac{(K_\beta-1)^2}{K_\beta(K_\beta+1)}\frac{\tilde{L}_2}{\tilde{L}_1}\tau\right)\leq\mathscr{O}(1)\,, \tag{4.173}$$

which is satisfied at any K_β if $\frac{\tilde{L}_2}{\tilde{L}_1}\leq\mathscr{O}(\tau^{-1})$.

It is of interest to note that if $\frac{\tilde{L}_2}{\tilde{L}_1}=\mathscr{O}(\tau)$ and $\frac{\tilde{L}_2}{\tilde{L}_3}=\mathscr{O}(1)$, the momentum equation would yield

$$\frac{\partial\tilde{p}_N}{\partial\xi_2}=0+\mathscr{O}(\tau^2)\,, \tag{4.174}$$

which immediately suggests that strip-theory will be a suitable approximation for the low-sweep lifting surface considered. Alternatively, for $\frac{\tilde{L}_2}{\tilde{L}_1}=\mathscr{O}(1)$, it is seen that steady advection of the perturbation velocity $\tilde{u}_2$ would remain.

- Momentum in the x_3 direction, through Eq. (4.160):

– The equation as written is normalized with terms involving steady advection in the x_1 direction being $\mathscr{O}(1)$. In particular, it is assumed that

$$\bar{\rho}_N\bar{u}_1\frac{\partial\tilde{u}_3}{\partial\xi_1}=\mathscr{O}(1) \tag{4.175}$$

and that it has a coefficient of 1. This normalization results in the pressure-gradient term appearing as

$$\left(\frac{\tilde{L}_1}{\tilde{L}_3}\,\tau\,\frac{K_\beta+1}{K_\beta-1}\right)\frac{\partial \tilde{p}_N}{\partial \xi_3}\,, \tag{4.176}$$

which will be $\mathscr{O}(1)$ if $\left(K_\beta-1\right)=\mathscr{O}(1)$ and $\frac{\tilde{L}_3}{\tilde{L}_1}=\mathscr{O}(\tau)$, which are typical for hypersonic flow.

– Using the normalization above, the following term involving $\tilde{u}_1$ is found in the momentum equation:

$$\left(\frac{K_\beta-1}{K_\beta}\,\tau^2\right)\left[\bar{\rho}_N+\left(\frac{K_\beta-1}{K_\beta}\right)\tilde{\rho}_N\right]\tilde{u}_1\frac{\partial \tilde{u}_3}{\partial \xi_1}\,. \tag{4.177}$$

It is seen that this term may be neglected relative to $\bar{\rho}_N\bar{u}_1\frac{\partial \tilde{u}_3}{\partial \xi_1}$ at any K_β without any further assumptions.

• Energy, through Eq. (4.161):

– The equation as written is normalized with terms involving steady advection in the x_1 direction being $\mathscr{O}(1)$. In particular, it is assumed that

$$\bar{u}_1\frac{\partial \tilde{p}_N}{\partial \xi_1}=\mathscr{O}(1) \tag{4.178}$$

and that it has a coefficient of 1.

– Using the normalization above, the following terms involving $\tilde{u}_1$ are found in the energy equation:

$$\left(\frac{K_\beta-1}{K_\beta}\,\tau^2\right)\tilde{u}_1\frac{\partial \tilde{p}_N}{\partial \xi_1}\,, \tag{4.179}$$

$$\left(\frac{\tau^2}{K_\beta^2+K_\beta}\right)\left[\bar{\rho}_N+\left(\varepsilon_\rho\right)\tilde{\rho}_N\right]\left[\bar{a}_N^2+(2\varepsilon_a)\bar{a}_N\tilde{a}_N+\left(\varepsilon_a^2\right)\tilde{a}_N^2\right]\frac{\partial \tilde{u}_1}{\partial \xi_1}\,, \tag{4.180}$$

It is seen that both these terms may be neglected in favour of $\bar{u}_1\frac{\partial \tilde{p}_N}{\partial \xi_1}$ at any K_β without any further assumptions.

• Body boundary condition, through Eq. (4.162):

– The equation as written is normalized with the steady un-perturbed velocity in the x_1 direction being $\mathscr{O}(1)$. In particular, it is assumed that

$$\bar{u}_1 = \mathscr{O}(1) \tag{4.181}$$

and that it has a coefficient of 1. Under this normalization, the upper bound of terms in the equation will be $\mathscr{O}(1)$ provided that $\frac{\tilde{U}_{b3}}{V_\infty} \leq \mathscr{O}(\tau)$.

– Using the normalization above, the following term involving $\tilde{u}_1$ is found in the body boundary condition:

$$\left(\frac{K_\beta - 1}{K_\beta}\tau^2\right)\tilde{u}_1\,. \tag{4.182}$$

It is seen that this term may be neglected relative to $\bar{u}_1$ at any K_β without any further assumptions.

Summary

The above process has been summarized in Table 4.7. It may be seen that beyond the inherent assumptions of the case definition given on Page 252 (and the implicit assumption on Mach number of $K_\beta \geq 1$), no further assumptions are required to reduce the 3D formulation to a 2D formulation.

4.5.3 Reduction to 1D

2D Equations

Essentially the same procedure is to be followed as in the reduction from 3D to 2D. The Euler equations have the following form after the reduction from 3D to 2D:

$$\text{C:}\quad \left.\begin{aligned} &\sum_{m=\{1,2,3\}}\left[\left(\frac{\tilde{L}_1}{V_\infty \tilde{t}_R}\right)\frac{\partial}{\partial t_N} + \left(1, \tau\frac{\tilde{L}_1}{\tilde{L}_2}, \tau\frac{\tilde{L}_1}{\tilde{L}_3}\right)\bar{u}_m\frac{\partial}{\partial \xi_m}\right]\tilde{\rho}_N \\ &\qquad + \sum_{m=\{2,3\}}\left(\tau^3\frac{\tilde{L}_1}{\tilde{L}_2}, \tau\frac{\tilde{L}_1}{\tilde{L}_3}\right)\bar{\rho}_N\frac{\partial \tilde{u}_m}{\partial \xi_m} \\ &\quad + \sum_{m=\{2,3\}}\left(\frac{K_\beta - 1}{K_\beta}\right)\left(\tau^3\frac{\tilde{L}_1}{\tilde{L}_2}, \tau\frac{\tilde{L}_1}{\tilde{L}_3}\right)\frac{\partial(\tilde{\rho}_N\tilde{u}_m)}{\partial \xi_m} \end{aligned}\right\} = 0\,, \tag{4.183}$$

Table 4.7 Summary of requirements for 3D to 2D reduction of CPT for case code $\lambda 0$-$\alpha 0$-$\eta 0$ with $\hat{\mathbf{r}} = -\hat{\mathbf{e}}_2$, $\tau_\theta = \mathscr{O}(\tau)$.

Equation	Normalized term	Neglected term(s)	Requirements
Continuity Eq. (4.159)	$\bar{u}_1 \dfrac{\partial \tilde{\rho}_N}{\partial \xi_1}$	$\bar{\rho}_N \dfrac{\partial \tilde{u}_1}{\partial \xi_1}, \dfrac{\partial \tilde{\rho}_N \tilde{u}_1}{\partial \xi_1}$	None
Momentum in x_2 Eq. (4.160)	$\dfrac{\partial \tilde{p}_N}{\partial \xi_2}$	$[\ldots]\tilde{u}_1 \dfrac{\partial \tilde{u}_2}{\partial \xi_1}$	$\dfrac{\tilde{L}_2}{\tilde{L}_1} \leq \mathscr{O}(\tau^{-1})$
Momentum in x_3 Eq. (4.160)	$\bar{\rho}_N \bar{u}_1 \dfrac{\partial \tilde{u}_3}{\partial \xi_1}$	$[\ldots]\tilde{u}_1 \dfrac{\partial \tilde{u}_3}{\partial \xi_1}$	None
Energy Eq. (4.161)	$\bar{u}_1 \dfrac{\partial \tilde{p}_N}{\partial \xi_1}$	$\tilde{u}_1 \dfrac{\partial \tilde{p}_N}{\partial \xi_1}, [\ldots]\dfrac{\partial \tilde{u}_1}{\partial \xi_1}$	None
Body boundary Eq. (4.162)	$\bar{u}_1$	$\tilde{u}_1$	None

$$\text{M:} \quad \left.\begin{aligned} &\sum_{m=\{1,2,3\}} \left[\bar{\rho}_N + \left(\frac{K_\beta - 1}{K_\beta}\right)\tilde{\rho}_N\right]\left[\left(\frac{\tilde{L}_1}{V_\infty \tilde{t}_R}\right)\frac{\partial}{\partial t_N} + \left(1, \tau\frac{\tilde{L}_1}{\tilde{L}_2}, \tau\frac{\tilde{L}_1}{\tilde{L}_3}\right)\bar{u}_m \frac{\partial}{\partial \xi_m}\right]\tilde{u}_i \\ &+ \sum_{m=\{2,3\}} \left(\frac{K_\beta - 1}{K_\beta}\right)\left(\tau^3\frac{\tilde{L}_1}{\tilde{L}_2}, \tau\frac{\tilde{L}_1}{\tilde{L}_3}\right)\left[\bar{\rho}_N + \left(\frac{K_\beta - 1}{K_\beta}\right)\tilde{\rho}_N\right]\tilde{u}_m \frac{\partial \tilde{u}_i}{\partial \xi_m} \\ &+ \left(\frac{\tilde{L}_1}{\tilde{L}_i}\frac{V_\infty}{\tilde{U}_i}\frac{K_\beta(K_\beta + 1)}{M_\infty^2}\right)\frac{\partial \tilde{p}_N}{\partial \xi_i} \end{aligned}\right\} = 0\,, \tag{4.184}$$

$$\text{E:} \quad \left.\begin{aligned} &\sum_{m=\{1,2,3\}} \left[\left(\frac{\tilde{L}_1}{V_\infty \tilde{t}_R}\right)\frac{\partial}{\partial t_N} + \left(1, \tau\frac{\tilde{L}_1}{\tilde{L}_2}, \tau\frac{\tilde{L}_1}{\tilde{L}_3}\right)\bar{u}_m \frac{\partial}{\partial \xi_m}\right]\tilde{p}_N \\ &+ \sum_{m=\{2,3\}} \left(\frac{K_\beta - 1}{K_\beta}\right)\left(\tau^3\frac{\tilde{L}_1}{\tilde{L}_2}, \tau\frac{\tilde{L}_1}{\tilde{L}_3}\right)\tilde{u}_m \frac{\partial \tilde{p}_N}{\partial \xi_m} \\ &+ \sum_{m=\{2,3\}} \left(\frac{1}{K_\beta^2 + K_\beta}\right)\left(\tau^3\frac{\tilde{L}_1}{\tilde{L}_2}, \tau\frac{\tilde{L}_1}{\tilde{L}_3}\right)\left[\bar{\rho}_N + (\varepsilon_\rho)\tilde{\rho}_N\right]\left[\bar{a}_N^2 + (2\varepsilon_a)\bar{a}_N\tilde{a}_N + (\varepsilon_a^2)\tilde{a}_N^2\right]\frac{\partial \tilde{u}_m}{\partial \xi_m} \end{aligned}\right\} = 0\,. \tag{4.185}$$

Similarly, the boundary condition at the body surface becomes

$$\sum_{m=\{2,3\}} \left(\frac{K_\beta - 1}{K_\beta}\right)(\tau^4, 1)\tilde{u}_m = \sum_{m=\{1,2,3\}} \left\{ \left(\frac{\tilde{U}_{b1}}{V_\infty}, \tau\frac{\tilde{U}_{b2}}{V_\infty}, \frac{1}{\tau}\frac{\tilde{U}_{b3}}{V_\infty}\right)\tilde{u}_{bm} - (1, 0, \tau^2)\bar{u}_m \right\}. \tag{4.186}$$

It is stressed that the equations are 2D in terms of the (unknown) perturbation velocities $\tilde{u}_m$ (with $m = \{1,2\}$). The appearance of three (known) un-perturbed velocity components through $\bar{u}_m$ (with $m = \{1,2,3\}$) does not affect the two-dimensionality of the perturbation problem.

Requirements for Reduction to 2D

Essentially the same reduction procedure is adopted. It is now required that

- The largest order of any given term grouping in the equation is $\mathscr{O}(1)$,
- Terms in $\tilde{u}_2$ must be of smallness $\mathscr{O}(\tau^2)$ or smaller.

These steps will again be applied on a per-equation basis. Due to the same normalization being used as in the reduction from 3D to 2D, step 1 is not repeated here.

- Continuity, through Eq. (4.183):
  - Using the normalization relative to $\bar{u}_1 \frac{\partial \tilde{\rho}_N}{\partial \xi_1}$, the following terms involving $\tilde{u}_2$ are found in the continuity equation:

$$\left(\tau^3 \frac{\tilde{L}_1}{\tilde{L}_2}\right)\bar{\rho}_N \frac{\partial \tilde{u}_2}{\partial \xi_2}, \tag{4.187}$$

$$\left(\tau^3 \frac{\tilde{L}_1}{\tilde{L}_2}\frac{K_\beta - 1}{K_\beta}\right)\frac{\partial \tilde{\rho}_N \tilde{u}_2}{\partial \xi_2}, \tag{4.188}$$

    In order to neglect both these terms in favour of $\bar{u}_1 \frac{\partial \tilde{\rho}_N}{\partial \xi_1}$ at any K_β, it is required that

$$\frac{\tilde{L}_2}{\tilde{L}_1} \geq \mathscr{O}(\tau). \tag{4.189}$$

- Momentum in the x_3 direction, through Eq. (4.184):
  - Using the normalization relative to $\bar{\rho}_N \bar{u}_1 \frac{\partial \tilde{u}_3}{\partial \xi_1}$, the following term involving $\tilde{u}_2$ is found in the momentum equation:

$$\left(\tau^3 \frac{\tilde{L}_1}{\tilde{L}_2}\frac{K_\beta - 1}{K_\beta}\right)\left[\bar{\rho}_N + \left(\frac{K_\beta - 1}{K_\beta}\right)\tilde{\rho}_N\right]\tilde{u}_2 \frac{\partial \tilde{u}_3}{\partial \xi_1}. \tag{4.190}$$

In order to neglect this term in favour of $\bar{\rho}_N \bar{u}_1 \frac{\partial \tilde{u}_3}{\partial \xi_1}$ at any K_β , it is required that

$$\frac{\tilde{L}_2}{\tilde{L}_1} \geq \mathscr{O}(\tau)\,. \tag{4.191}$$

- Energy, through Eq. (4.185):
  - Using the normalization relative to $\bar{u}_1 \frac{\partial \tilde{p}_N}{\partial \xi_1}$, the following terms involving $\tilde{u}_2$ are found in the energy equation:

$$\left(\tau^3 \frac{\tilde{L}_1}{\tilde{L}_2} \frac{K_\beta - 1}{K_\beta}\right) \tilde{u}_2 \frac{\partial \tilde{p}_N}{\partial \xi_2}\,, \tag{4.192}$$

$$\left(\frac{\tau^3}{K_\beta^2 + K_\beta} \frac{\tilde{L}_1}{\tilde{L}_2}\right) \left[\bar{\rho}_N + (\varepsilon_\rho)\tilde{\rho}_N\right] \left[\bar{a}_N^2 + (2\varepsilon_a)\bar{a}_N \tilde{a}_N + (\varepsilon_a^2)\tilde{a}_N^2\right] \frac{\partial \tilde{u}_2}{\partial \xi_2}\,, \tag{4.193}$$

    In order to neglect both these terms in favour of $\bar{u}_1 \frac{\partial \tilde{p}_N}{\partial \xi_1}$ at any K_β , it is required that

$$\frac{\tilde{L}_2}{\tilde{L}_1} \geq \mathscr{O}(\tau)\,. \tag{4.194}$$

- Body boundary condition, through Eq. (4.186):
  - Using the normalization relative to $\bar{u}_1$, the following term involving $\tilde{u}_2$ is found in the body boundary condition:

$$\left(\frac{K_\beta - 1}{K_\beta} \tau^4\right) \tilde{u}_2\,. \tag{4.195}$$

    It is seen that this term may be neglected relative to $\bar{u}_1$ at any K_β without any further assumptions.

Summary

The above process has been summarized in Table 4.8. It may be seen that beyond the inherent assumptions of the case definition given on Page 252 (and the implicit assumption on Mach number of $K_\beta \geq 1$), the only further assumption required for reduction from 3D to 1D is

$$\mathscr{O}(\tau) \leq \frac{\tilde{L}_2}{\tilde{L}_1} \leq \mathscr{O}\left(\tau^{-1}\right)\,. \tag{4.196}$$

Table 4.8 Summary of requirements for 2D to 1D reduction of CPT for case code $\lambda 0$-$\alpha 0$-$\eta 0$ with $\hat{\mathbf{r}} = -\hat{\mathbf{e}}_2$, $\tau_\theta = \mathscr{O}(\tau)$.

Equation	Normalized term	Neglected term(s)	Requirements
Continuity Eq. (4.183)	$\bar{u}_1 \frac{\partial \tilde{\rho}_N}{\partial \xi_1}$	$\bar{\rho}_N \frac{\partial \tilde{u}_2}{\partial \xi_2}, \frac{\partial \tilde{\rho}_N \tilde{u}_2}{\partial \xi_2}$	$\frac{\tilde{L}_2}{\tilde{L}_1} \geq \mathscr{O}(\tau)$
Momentum in x_3 Eq. (4.184)	$\bar{\rho}_N \bar{u}_1 \frac{\partial \tilde{u}_3}{\partial \xi_1}$	$[\ldots]\tilde{u}_2 \frac{\partial \tilde{u}_3}{\partial \xi_2}$	$\frac{\tilde{L}_2}{\tilde{L}_1} \geq \mathscr{O}(\tau)$
Energy Eq. (4.185)	$\bar{u}_2 \frac{\partial \tilde{p}_N}{\partial \xi_2}$	$\tilde{u}_2 \frac{\partial \tilde{p}_N}{\partial \xi_2}, [\ldots]\frac{\partial \tilde{u}_2}{\partial \xi_2}$	$\frac{\tilde{L}_2}{\tilde{L}_1} \geq \mathscr{O}(\tau)$
Body boundary Eq. (4.186)	$\bar{u}_1$	$\tilde{u}_2$	None

1D Equations

The final form of the 1D Euler equations resulting from the scaling analysis is:

$$\text{C:} \quad \sum_{m=\{1,2,3\}} \left[\left(\frac{\tilde{L}_1}{V_\infty \tilde{t}_R} \right) \frac{\partial}{\partial t_N} + \left(1, \tau \frac{\tilde{L}_1}{\tilde{L}_2}, \tau \frac{\tilde{L}_1}{\tilde{L}_3} \right) \bar{u}_m \frac{\partial}{\partial \xi_m} \right] \tilde{\rho}_N + \left(\tau \frac{\tilde{L}_1}{\tilde{L}_3} \right) \bar{\rho}_N \frac{\partial \tilde{u}_3}{\partial \xi_3} + \left(\frac{K_\beta - 1}{K_\beta} \right) \left(\tau \frac{\tilde{L}_1}{\tilde{L}_3} \right) \frac{\partial (\tilde{\rho}_N \tilde{u}_3)}{\partial \xi_3} \Bigg\} = 0, \tag{4.197}$$

$$\text{M:} \quad \sum_{m=\{1,2,3\}} \left[\bar{\rho}_N + \left(\frac{K_\beta - 1}{K_\beta} \right) \tilde{\rho}_N \right] \left[\left(\frac{\tilde{L}_1}{V_\infty \tilde{t}_R} \right) \frac{\partial}{\partial t_N} + \left(1, \tau \frac{\tilde{L}_1}{\tilde{L}_2}, \tau \frac{\tilde{L}_1}{\tilde{L}_3} \right) \bar{u}_m \frac{\partial}{\partial \xi_m} \right] \tilde{u}_3 + \left(\frac{K_\beta - 1}{K_\beta} \right) \left(\tau \frac{\tilde{L}_1}{\tilde{L}_3} \right) \left[\bar{\rho}_N + \left(\frac{K_\beta - 1}{K_\beta} \right) \tilde{\rho}_N \right] \tilde{u}_3 \frac{\partial \tilde{u}_3}{\partial \xi_3} + \left(\frac{\tilde{L}_1}{\tilde{L}_3} \tau \frac{K_\beta + 1}{K_\beta - 1} \right) \frac{\partial \tilde{p}_N}{\partial \xi_3} \Bigg\} = 0, \tag{4.198}$$

$$\text{E:}\quad \left.\begin{aligned}&\sum_{m=\{1,2,3\}}\left[\left(\frac{\tilde{L}_1}{V_\infty \tilde{t}_R}\right)\frac{\partial}{\partial t_N}+\left(1,\tau\frac{\tilde{L}_1}{\tilde{L}_2},\tau\frac{\tilde{L}_1}{\tilde{L}_3}\right)\bar{u}_m\frac{\partial}{\partial \xi_m}\right]\tilde{p}_N\\&\qquad+\left(\frac{K_\beta-1}{K_\beta}\right)\left(\tau\frac{\tilde{L}_1}{\tilde{L}_3}\right)\tilde{u}_3\frac{\partial \tilde{p}_N}{\partial \xi_3}\\&+\left(\frac{1}{K_\beta^2+K_\beta}\right)\left(\tau\frac{\tilde{L}_1}{\tilde{L}_3}\right)\left[\bar{p}_N+(\varepsilon_\rho)\tilde{p}_N\right]\left[\bar{a}_N^2+(2\varepsilon_a)\bar{a}_N\tilde{a}_N+(\varepsilon_a^2)\tilde{a}_N^2\right]\frac{\partial \tilde{u}_3}{\partial \xi_3}\end{aligned}\right\}=0\,. \tag{4.199}$$

Similarly, the boundary condition at the body surface becomes

$$\left(\frac{K_\beta-1}{K_\beta}\right)\tilde{u}_3=\sum_{m=\{1,2,3\}}\left\{\left(\frac{\tilde{U}_{b1}}{V_\infty},\tau\frac{\tilde{U}_{b2}}{V_\infty},\frac{1}{\tau}\frac{\tilde{U}_{b3}}{V_\infty}\right)\tilde{u}_{bm}-\left(1,0,\tau^2\right)\bar{u}_m\right\}. \tag{4.200}$$

It is seen that only the x_3 component of the perturbation velocity occurs in the equations through $\tilde{u}_3$. The un-perturbed velocity is seen to only appear together with the time derivative. The equations as written are formulated in the Eulerian frame $\mathscr{E}$. A transformation to a Galilean frame $\mathscr{G}$ advected by the local steady un-perturbed velocity $\bar{\mathbf{V}}$ will result in the time derivative in the Galilean frame being written as

$$\frac{\partial}{\partial t_N^G}=\left(\frac{\tilde{L}_1}{V_\infty \tilde{t}_R}\right)\frac{\partial}{\partial t_N}+\left(1,\tau\frac{\tilde{L}_1}{\tilde{L}_2},\tau\frac{\tilde{L}_1}{\tilde{L}_3}\right)\bar{u}_m\frac{\partial}{\partial \xi_m}\,, \tag{4.201}$$

which is seen to occur in Eqs. (4.197) to (4.199) and emphasize the reduction of the Euler equations from 3D unsteady to 1D unsteady, with the perturbation velocities $\tilde{u}_1$ and $\tilde{u}_2$ being eliminated from consideration.

4.5.4 Reduction to Algebraic Form

The reduction of the Euler equations to a 1D unsteady formulation are the foundation for piston theory. As has been noted in Section 3.2, a number of piston theories are formulated to account for the propagation and persistence of perturbations within the advected 1D "cylinder". This corresponds to a solution for the unsteady 1D field problem formulated by the 1D Euler equations derived above in Section 4.5.3. The most widespread interpretation (or association) of CPT, however, is of the formulation in which an algebraic relationship exists between the surface pressure and the surface velocity or inclination. For ease of reference, the generalized pressure equation for this formulation of piston theory of Eq. (3.8)

is repeated here as:

$$\frac{p}{p_{cyl}} = 1 + \gamma \left[c_1 \left(\frac{w}{a_{cyl}} \right) + c_2 \left(\frac{w}{a_{cyl}} \right)^2 + c_3 \left(\frac{w}{a_{cyl}} \right)^3 \right], \tag{4.202}$$

where w is the downwash as introduced in various forms in Section 3.1.2. As noted previously in Section 3.1.2: *the definition of downwash in piston theory arises purely due to relative motion of the piston down the length of the cylinder. It is directly related to the motion of cylinder frame, rather than to the fluid velocity.* The implications of this distinction for the accuracy of the piston theory analogy were discussed at length in Section 3.1.4. As illustrated in the case study of Section 3.3.1, and indeed as adopted in Section 4.5.1, CPT defines the "cylinder conditions" to be the un-perturbed freestream conditions. In the nomenclature of the present section, Eq. (4.202) may thus be adapted to read

$$\frac{\tilde{p}}{p_\infty} = \gamma \left[c_1 \left(\frac{w}{a_\infty} \right) + c_2 \left(\frac{w}{a_\infty} \right)^2 + c_3 \left(\frac{w}{a_\infty} \right)^3 \right], \tag{4.203}$$

Solutions to the 1D unsteady field problem posed by the Euler equations typically make use of characteristics, as detailed in [146, 184, 211]. The resulting solutions account for the reflection of waves off the bow shock, and thus an account of the time-history of the flow is made. Such solutions do not yield an algebraic, point-local relationship between the pressure and instantaneous surface motion. In order to arrive at a relation similar to Eq. (4.203), it is necessary that the influence of incoming (relative to the body surface) characteristics be neglected (thereby neglecting all influence and interaction with the surrounding fluid). This is perhaps most clearly evident in the results of McIntosh [146], which were discussed in this work in the context of Eq. (3.122). Indeed, this assumption was also made by Il'yushin [77] when demonstrating the application of the law of plane sections to 2D sections of arbitrary shape.

4.6 Local Piston Theory

The present section will illustrate the adaptation of the method of Section 4.5 to deriving the mathematical basis for LPT. The presentation will focus on the general procedure rather than on specific cases of application. The scaling analysis framework of Appendix A may be used for the latter.

4.6.1 Specification of Perturbation and Non-Dimensionalization

Definition of Un-Perturbed Solution

The essence of LPT is modelling perturbations relative to an existing non-trivial solution to the Euler equations. Typically, LPT has been applied to perturbations about a mean-steady reference solution. Furthermore, it is typically assumed that the perturbations about the mean solution are small. In the nomenclature and terminology of the present work:

$$\bar{\rho} = \rho_m \,, \tag{4.204}$$

$$\bar{\hat{\mathbf{V}}} = \hat{\mathbf{V}}_m \,, \tag{4.205}$$

$$\bar{p} = p_m \,, \tag{4.206}$$

$$\bar{a} = a_m \,, \tag{4.207}$$

where the subscript m denotes terms from the mean-steady reference solution to the Euler equations. For non-trivial geometries or flows, the above fluid quantities will vary spatially, while the assumption of a "mean-steady" reference solution renders them time-invariant:

$$\frac{\partial \bar{X}}{\partial x_i} \neq 0 \,, \tag{4.208}$$

$$\frac{\partial \bar{X}}{\partial t} = 0 \,, \tag{4.209}$$

where $\bar{X}$ is any of the fluid quantities from the mean-steady reference solution.

Inspection of the perturbation form of the Euler equations from Eqs. (4.97) to (4.99) shows that Eqs. (4.208) and (4.209) do not offer any inherent simplification of the equations. Time-derivatives of the un-perturbed solution appear alongside other terms un-perturbed terms, which together constitute the Euler equations for the un-perturbed flow. Thus, time-derivatives of the un-perturbed solution "fall out" from the perturbation form of the Euler equations without requiring a "mean-steady reference" assumption that leads to Eq. (4.209). However, the adoption of a mean-steady assumption for the un-perturbed solution means that only spatial variations need to be considered in selecting reference values which would yield uniformly valid non-dimensionalization. For a time-dependent un-perturbed solution, the non-dimensionalization of the un-perturbed fluid quantities may not be uniformly valid in time.

Scaling Analysis

As noted in the introduction, the presentation of Section 4.6 will focus on the general procedure of reducing the Euler equations to a 1D unsteady form. No attempt will be made here to quantify non-dimensional parameters or groups. Nonetheless, the scaling analysis framework of Appendix A may be used to this end for perturbation terms. The scaling an un-perturbed terms and of gradients will depend on the particular application under consideration.

As in the case of CPT, the derivation of LPT from the Euler equations hinges on eliminating two of the three unknown velocities as variables. In the present study, $\tilde{u}_1$ and $\tilde{u}_2$ will be eliminated. A further difference between CPT and LPT arises when considering advection by un-perturbed velocities (through $\bar{u}_1 \frac{\partial}{\partial \xi_1}$ and $\bar{u}_2 \frac{\partial}{\partial \xi_2}$):

- In CPT, the un-perturbed velocities were spatially (and temporally) invariant. Thus, a Galilean transform would be uniformly valid, and the advection by un-perturbed velocities could be interpreted as a time-derivative in the advected frame,

- In LPT, the un-perturbed velocities are generally spatially-variant. Thus, a Galilean transform (and the subsequent interpretation of additional time-variation) would only be locally valid. More generally, the terms associated with un-perturbed advection may be regarded as source terms in a globally-advected frame.

The questions of the range of validity of non-dimensionalizations and of successive local-applications of LPT are not addressed in the present work, and remain open avenues for future investigation.

The approach adopted in the Section 4.5 for neglecting velocity components will be repeated here:

- Equations will be multiplied by a non-dimensional smallness parameter such that the largest order of any given term grouping in the equation is $\mathcal{O}(1)$. The appropriate term for normalization will arise from the particular application. However, the normalized term will be assumed in the present demonstration,

- Thereafter, the equation will be truncated to terms of a given order of smallness. Once again, the present demonstration will only highlight the parameters involved, rather than attempt to quantify them by scaling analysis.

4.6.2 Reduction to 2D

3D Equations

As noted in Section 4.6.1, the specification of reference values in LPT does not lead to any inherent simplification of the Euler equations (or boundary conditions) as in the case of LPT. Thus, the 3D equations of interest are given by Eqs. (4.97) to (4.99), (4.111) to (4.113) and (4.123), which are not repeated here.

Requirements for Reduction to 2D

As stated in Section 4.6.1, the approach adopted here in neglecting $\tilde{u}_1$ requires that

- The largest order of any given term grouping in the equation is $\mathscr{O}(1)$,
- Terms in $\tilde{u}_1$ must be of smallness $\mathscr{O}\left(\tau^2\right)$ or smaller.

These steps will be applied on a per-equation basis as follows:

- Continuity, through Eq. (4.97):
  - It is assumed here that terms involving steady advection in the x_1 direction are $\mathscr{O}(1)$. Specifically, it is assumed that:

$$\bar{u}_1 \frac{\partial \tilde{\rho}_N}{\partial \xi_1} = \mathscr{O}(1) \tag{4.210}$$

    and that it has a coefficient of 1. This normalization may be achieved by multiplying through the equation by a common factor of

$$\frac{\varepsilon_{L1}}{\varepsilon_\rho \bar{k}_{u1}} \qquad \left(= \frac{\bar{\rho}_R}{\tilde{\rho}_R} \frac{\tilde{L}_1}{\bar{L}_R} \frac{\bar{U}_R}{\bar{U}_1} \right), \tag{4.211}$$

  - Using the normalization above, the following terms involving $\tilde{u}_1$ are found in the continuity equation:

$$\left(\frac{\varepsilon_{u1}}{\varepsilon_\rho \bar{k}_{u1}} \right) \bar{\rho}_N \frac{\partial \tilde{u}_1}{\partial \xi_1} \qquad \left[= \left(\frac{\bar{\rho}_R}{\tilde{\rho}_R} \frac{\tilde{U}_1}{\bar{U}_1} \right) \bar{\rho}_N \frac{\partial \tilde{u}_1}{\partial \xi_1} \right], \tag{4.212}$$

$$\left(\frac{\varepsilon_{u1}}{\bar{k}_{u1}} \right) \frac{\partial (\tilde{\rho}_N \tilde{u}_1)}{\partial \xi_1} \qquad \left[= \left(\frac{\tilde{U}_1}{\bar{U}_1} \right) \frac{\partial (\tilde{\rho}_N \tilde{u}_1)}{\partial \xi_1} \right], \tag{4.213}$$

$$\left(\frac{\varepsilon_{u1} \varepsilon_{L1} \bar{k}_{L1}}{\varepsilon_\rho \bar{k}_{u1}} \right) \tilde{u}_1 \frac{\partial \bar{\rho}_N}{\partial \xi_1} \qquad \left[= \left(\frac{\bar{\rho}_R}{\tilde{\rho}_R} \frac{\tilde{L}_1}{\bar{L}_1} \frac{\tilde{U}_1}{\bar{U}_1} \right) \tilde{u}_1 \frac{\partial \bar{\rho}_N}{\partial \xi_1} \right], \tag{4.214}$$

- Momentum in the x_2 direction, through Eq. (4.98):

  - As in Section 4.5, normalization will be done relative to the pressure-gradient term. In particular, it is assumed that

$$\frac{\partial \tilde{p}_N}{\partial \xi_2} = \mathscr{O}(1) \tag{4.215}$$

    and that it has a coefficient of 1. This is achieved through multiplying Eq. (4.98) by a common factor of

$$\left(\frac{\varepsilon_{L2}}{\varepsilon_p \bar{k}_f}\right) \qquad \left(= \frac{\tilde{L}_2}{\bar{L}_R} \frac{\bar{\rho}_R \bar{U}_R^2}{\tilde{p}_R}\right), \tag{4.216}$$

  - Using the normalization above, the following terms involving $\tilde{u}_1$ are found in the momentum equation:

$$\left(\frac{\varepsilon_{L2}\varepsilon_{u1}\varepsilon_{u2}}{\varepsilon_{L1}\varepsilon_p \bar{k}_f}\right)\left[\bar{\rho}_N + (\varepsilon_\rho)\tilde{\rho}_N\right]\tilde{u}_1 \frac{\partial \tilde{u}_2}{\partial \xi_1} \qquad \left\{= \left(\frac{\tilde{L}_2}{\tilde{L}_1} \frac{\bar{\rho}_R \tilde{U}_1 \tilde{U}_2}{\tilde{p}_R}\right)[\ldots]\tilde{u}_1 \frac{\partial \tilde{u}_2}{\partial \xi_1}\right\}, \tag{4.217}$$

$$\left(\frac{\varepsilon_{L2}\bar{k}_{L1}\varepsilon_{u1}\bar{k}_{u2}}{\varepsilon_p \bar{k}_f}\right)\left[\bar{\rho}_N + (\varepsilon_\rho)\tilde{\rho}_N\right]\tilde{u}_1 \frac{\partial \tilde{u}_2}{\partial \xi_1} \qquad \left\{= \left(\frac{\tilde{L}_2}{\tilde{L}_1} \frac{\bar{\rho}_R \tilde{U}_1 \bar{U}_2}{\tilde{p}_R}\right)[\ldots]\tilde{u}_1 \frac{\partial \tilde{u}_2}{\partial \xi_1}\right\}, \tag{4.218}$$

- Momentum in the x_3 direction, through Eq. (4.98):

  - As in Section 4.5, normalization will be done relative to terms involving steady advection in the x_1 direction. In particular, it is assumed that

$$\bar{\rho}_N \bar{u}_1 \frac{\partial \tilde{u}_3}{\partial \xi_1} = \mathscr{O}(1) \tag{4.219}$$

    and that it has a coefficient of 1. This is achieved through multiplying Eq. (4.98) by a common factor of

$$\left(\frac{\varepsilon_{L1}}{\bar{k}_{u1}\varepsilon_{u3}}\right) \qquad \left(= \frac{\tilde{L}_1}{\bar{L}_R} \frac{\bar{U}_R^2}{\bar{U}_1 \tilde{U}_3}\right), \tag{4.220}$$

– Using the normalization above, the following terms involving $\tilde{u}_1$ are found in the momentum equation:

$$\left(\frac{\varepsilon_{u1}}{\bar{k}_{u1}}\right)\left[\bar{p}_N+(\varepsilon_\rho)\tilde{p}_N\right]\tilde{u}_1\frac{\partial\tilde{u}_3}{\partial\xi_1} \qquad \left\{=\left(\frac{\tilde{U}_1}{\bar{U}_1}\right)[\ldots]\tilde{u}_1\frac{\partial\tilde{u}_3}{\partial\xi_1}\right\}, \tag{4.221}$$

$$\left(\frac{\varepsilon_{L1}\bar{k}_{L1}\varepsilon_{u1}\bar{k}_{u3}}{\bar{k}_{u1}\varepsilon_{u3}}\right)\left[\bar{p}_N+(\varepsilon_\rho)\tilde{p}_N\right]\tilde{u}_1\frac{\partial\bar{u}_3}{\partial\xi_1} \qquad \left\{=\left(\frac{\tilde{L}_1}{\bar{L}_1}\frac{\tilde{U}_1}{\bar{U}_1}\frac{\bar{U}_3}{\tilde{U}_3}\right)[\ldots]\tilde{u}_1\frac{\partial\bar{u}_3}{\partial\xi_1}\right\}, \tag{4.222}$$

- Energy, through Eq. (4.99):

  – As in Section 4.5, normalization will be done relative to terms involving steady advection in the x_1 direction. In particular, it is assumed that

$$\bar{u}_1\frac{\partial\tilde{p}_N}{\partial\xi_1}=\mathscr{O}(1) \tag{4.223}$$

  and that it has a coefficient of 1. This is achieved through multiplying Eq. (4.99) by a common factor of

$$\left(\frac{\varepsilon_{L1}}{\bar{k}_{u1}\varepsilon_p\bar{k}_a}\right) \qquad \left(=\frac{\tilde{L}_1}{\bar{L}_R}\frac{\bar{U}_R}{\bar{U}_1}\frac{\bar{\rho}_R\bar{a}_R^2}{\tilde{p}_R}\right), \tag{4.224}$$

  – Using the normalization above, the following terms involving $\tilde{u}_1$ are found in the energy equation:

$$\left(\frac{\varepsilon_{u1}}{\bar{k}_{u1}}\right)\tilde{u}_1\frac{\partial\tilde{p}_N}{\partial\xi_1} \qquad \left\{=\left(\frac{\tilde{U}_1}{\bar{U}_1}\right)\tilde{u}_1\frac{\partial\tilde{p}_N}{\partial\xi_1}\right\}, \tag{4.225}$$

$$\left(\frac{\varepsilon_{u1}}{\bar{k}_{u1}\varepsilon_p\bar{k}_a}\right)\left[\bar{p}_N+(\varepsilon_\rho)\tilde{p}_N\right][\ldots]\frac{\partial\tilde{u}_1}{\partial\xi_1} \qquad \left\{=\left(\frac{\tilde{U}_1}{\bar{U}_1}\frac{\bar{\rho}_R\bar{a}_R^2}{\tilde{p}_R}\right)[\ldots]\frac{\partial\tilde{u}_1}{\partial\xi_1}\right\}, \tag{4.226}$$

$$\left(\frac{\varepsilon_{u1}\varepsilon_{L1}\bar{k}_{L1}}{\bar{k}_{u1}\varepsilon_p}\right)\tilde{u}_1\frac{\partial\bar{p}_N}{\partial\xi_1} \qquad \left\{=\left(\frac{\tilde{L}_1}{\bar{L}_1}\frac{\tilde{U}_1}{\bar{U}_1}\frac{\bar{p}_R}{\tilde{p}_R}\right)\tilde{u}_1\frac{\partial\bar{p}_N}{\partial\xi_1}\right\}, \tag{4.227}$$

- Body boundary condition, through Eq. (4.123):

  – It is assumed that terms involving the dot product $\bar{\mathbf{V}}_{\mathbf{r}\cdot\tilde{\mathbf{n}}}$ are $\mathscr{O}(1)$, and that the remaining terms in the equation are bound by the same order. Under this assumption, no further normalization is required,

– If the above normalization hold, the following term involving $\tilde{u}_1$ is found in the body boundary condition:

$$(\varepsilon_{u1})(\bar{n}_1+\tilde{n}_1)\tilde{u}_1 \qquad \left\{=\left(\frac{\tilde{U}_1}{\bar{U}_R}(\bar{n}_1+\tilde{n}_1)\right)\tilde{u}_1\right\}. \tag{4.228}$$

Summary

The above process has been summarized in Table 4.9. The choice of terms relative to which the equations have been normalized was motivated to facilitate direct comparison of the results to those of Table 4.7 and the derivation of CPT in Section 4.5. Beyond the assumption that the normalized term has the largest coefficient (that being 1) of all the terms in its equation, the results presented in Table 4.9 are entirely general. This is meant in the sense that no assumptions have been made regarding the reference values for non-dimensionalization. By extension, no assumptions have been made regarding the un-perturbed (or perturbation) Mach number, flow angles, and gradients.

It is evident from Table 4.9 that a variety of requirements arise for the reduction from a 3D to a 2D perturbation formulation. However, it is also noted that the ratio $\frac{\tilde{U}_1}{\bar{U}_1}$ appears in the majority of the requirements. The basic requirement of

$$\frac{\tilde{U}_1}{\bar{U}_1} \leq \mathscr{O}\left(\tau^2\right) \tag{4.229}$$

is seen in the requirements for reduction of the continuity equation to a 2D formulation. It is a commonly known approximation in linearized supersonic flows that for a small turning of the flow by $\mathscr{O}(\tau)$, the streamwise velocity perturbation will be of the order $\mathscr{O}\left(\tau^2\right)$, while transverse perturbations will be of the order $\mathscr{O}(\tau)$. Thus, it may be expected that this basic requirement would be satisfied for small perturbations to the surface inclination when applying LPT. An exploration of the scenarios in which the influence of parameters such as impose more stringent requirements for the reduction to a 2D formulation is an open research question. It is expected that this will inform the application of LPT outside of the classical realm of "small perturbations in hypersonic flows". However, such a broad consideration of general cases – while facilitated by the present mathematical framework – is outside the scope of the present work.

Table 4.9 Summary of requirements for 3D to 2D reduction of LPT.

Equation	Normalized term	Neglected term(s)	Requirements
Continuity Eq. (4.97)	$\bar{u}_1 \frac{\partial \tilde{\rho}_N}{\partial \xi_1}$	$\bar{\rho}_N \frac{\partial \tilde{u}_1}{\partial \xi_1}$	$\frac{\bar{\rho}_R}{\tilde{\rho}_R} \frac{\tilde{U}_1}{\bar{U}_1} \leq \mathcal{O}(\tau^2)$
		$\frac{\partial (\tilde{\rho}_N \tilde{u}_1)}{\partial \xi_1}$	$\frac{\tilde{U}_1}{\bar{U}_1} \leq \mathcal{O}(\tau^2)$
		$\tilde{u}_1 \frac{\partial \bar{\rho}_N}{\partial \xi_1}$	$\frac{\bar{\rho}_R}{\tilde{\rho}_R} \frac{\tilde{L}_1}{\bar{L}_1} \frac{\tilde{U}_1}{\bar{U}_1} \leq \mathcal{O}(\tau^2)$
Momentum in x_2 Eq. (4.98)	$\frac{\partial \tilde{p}_N}{\partial \xi_2}$	$[\bar{\rho}_N + (\varepsilon_\rho)\tilde{\rho}_N] \tilde{u}_1 \frac{\partial \tilde{u}_2}{\partial \xi_1}$	$\frac{\tilde{L}_2}{\tilde{L}_1} \frac{\bar{\rho}_R \tilde{U}_1 \tilde{U}_2}{\tilde{p}_R} \leq \mathcal{O}(\tau^2)$
		$[\bar{\rho}_N + (\varepsilon_\rho)\tilde{\rho}_N] \tilde{u}_1 \frac{\partial \bar{u}_2}{\partial \xi_1}$	$\frac{\tilde{L}_2}{\tilde{L}_1} \frac{\bar{\rho}_R \tilde{U}_1 \bar{U}_2}{\tilde{p}_R} \leq \mathcal{O}(\tau^2)$
Momentum in x_3 Eq. (4.98)	$\bar{\rho}_N \bar{u}_1 \frac{\partial \tilde{u}_3}{\partial \xi_1}$	$[\bar{\rho}_N + (\varepsilon_\rho)\tilde{\rho}_N] \tilde{u}_1 \frac{\partial \tilde{u}_3}{\partial \xi_1}$	$\frac{\tilde{U}_1}{\bar{U}_1} \leq \mathcal{O}(\tau^2)$
		$[\bar{\rho}_N + (\varepsilon_\rho)\tilde{\rho}_N] \tilde{u}_1 \frac{\partial \bar{u}_3}{\partial \xi_1}$	$\frac{\tilde{L}_1}{\bar{L}_1} \frac{\tilde{U}_1}{\bar{U}_1} \frac{\bar{U}_3}{\tilde{U}_3} \leq \mathcal{O}(\tau^2)$
Energy Eq. (4.99)	$\bar{u}_1 \frac{\partial \tilde{p}_N}{\partial \xi_1}$	$\tilde{u}_1 \frac{\partial \tilde{p}_N}{\partial \xi_1}$	$\frac{\tilde{U}_1}{\bar{U}_1} \leq \mathcal{O}(\tau^2)$
		$[\bar{\rho}_N + (\varepsilon_\rho)\tilde{\rho}_N][\ldots] \frac{\partial \tilde{u}_1}{\partial \xi_1}$	$\frac{\tilde{U}_1}{\bar{U}_1} \frac{\bar{\rho}_R \bar{a}_R^2}{\tilde{p}_R} \leq \mathcal{O}(\tau^2)$
		$\tilde{u}_1 \frac{\partial \bar{p}_N}{\partial \xi_1}$	$\frac{\tilde{L}_1}{\bar{L}_1} \frac{\tilde{U}_1}{\bar{U}_1} \frac{\bar{p}_R}{\tilde{p}_R} \leq \mathcal{O}(\tau^2)$
Body boundary Eq. (4.123)	$(\tilde{n}_m \bar{k}_{um}) \bar{u}_m$	$(\bar{n}_1 + \tilde{n}_1)\tilde{u}_1$	$\frac{\tilde{U}_1}{\bar{U}_R}(\bar{n}_1 + \tilde{n}_1) \leq \mathcal{O}(\tau^2)$

4.6.3 Reduction to 1D

Requirements for Reduction to 2D

The now-familiar process may be extended to the reduction of the Euler equations to a 1D formulation:

- Continuity, through Eq. (4.97):
  - Using the normalization of Eq. (4.210), the following terms involving $\tilde{u}_2$ are found in the continuity equation:

$$\left(\frac{\varepsilon_{L1}\varepsilon_{u2}}{\varepsilon_\rho \varepsilon_{L2}\bar{k}_{u1}}\right)\bar{\rho}_N\frac{\partial \tilde{u}_2}{\partial \xi_2} \qquad \left[=\left(\frac{\bar{\rho}_R}{\tilde{\rho}_R}\frac{\tilde{L}_1}{\bar{L}_2}\frac{\tilde{U}_2}{\bar{U}_1}\right)\bar{\rho}_N\frac{\partial \tilde{u}_2}{\partial \xi_2}\right], \tag{4.230}$$

$$\left(\frac{\varepsilon_{L1}\varepsilon_{u2}}{\varepsilon_{L2}\bar{k}_{u1}}\right)\frac{\partial(\tilde{\rho}_N\tilde{u}_2)}{\partial \xi_2} \qquad \left[=\left(\frac{\tilde{L}_1}{\bar{L}_2}\frac{\tilde{U}_2}{\bar{U}_1}\right)\frac{\partial(\tilde{\rho}_N\tilde{u}_2)}{\partial \xi_2}\right], \tag{4.231}$$

$$\left(\frac{\varepsilon_{L1}\bar{k}_{L2}\varepsilon_{u2}}{\varepsilon_\rho \bar{k}_{u1}}\right)\tilde{u}_2\frac{\partial \bar{\rho}_N}{\partial \xi_2} \qquad \left[=\left(\frac{\bar{\rho}_R}{\tilde{\rho}_R}\frac{\tilde{L}_1}{\bar{L}_2}\frac{\tilde{U}_2}{\bar{U}_1}\right)\tilde{u}_2\frac{\partial \bar{\rho}_N}{\partial \xi_2}\right], \tag{4.232}$$

- Momentum in the x_3 direction, through Eq. (4.98):
  - Using the normalization relative of Eq. (4.219), the following terms involving $\tilde{u}_2$ are found in the momentum equation:

$$\left(\frac{\varepsilon_{L1}\varepsilon_{u2}}{\varepsilon_{L2}\bar{k}_{u1}}\right)\left[\bar{\rho}_N+(\varepsilon_\rho)\tilde{\rho}_N\right]\tilde{u}_2\frac{\partial \tilde{u}_3}{\partial \xi_2} \qquad \left\{=\left(\frac{\tilde{L}_1}{\bar{L}_2}\frac{\tilde{U}_2}{\bar{U}_1}\right)[\ldots]\tilde{u}_2\frac{\partial \tilde{u}_3}{\partial \xi_2}\right\}, \tag{4.233}$$

$$\left(\frac{\varepsilon_{L1}\bar{k}_{L2}\varepsilon_{u2}\bar{k}_{u3}}{\bar{k}_{u1}\varepsilon_{u3}}\right)\left[\bar{\rho}_N+(\varepsilon_\rho)\tilde{\rho}_N\right]\tilde{u}_2\frac{\partial \bar{u}_3}{\partial \xi_2} \qquad \left\{=\left(\frac{\tilde{L}_1}{\bar{L}_2}\frac{\tilde{U}_2}{\bar{U}_1}\frac{\bar{U}_3}{\tilde{U}_3}\right)[\ldots]\tilde{u}_2\frac{\partial \bar{u}_3}{\partial \xi_2}\right\}, \tag{4.234}$$

- Energy, through Eq. (4.99):
  - Using the normalization relative of Eq. (4.223), the following terms involving $\tilde{u}_2$ are found in the energy equation:

$$\left(\frac{\varepsilon_{L1}\varepsilon_{u2}}{\varepsilon_{L2}\bar{k}_{u1}}\right)\tilde{u}_2\frac{\partial \tilde{p}_N}{\partial \xi_2} \qquad \left\{=\left(\frac{\tilde{L}_1}{\bar{L}_2}\frac{\tilde{U}_2}{\bar{U}_1}\right)\tilde{u}_2\frac{\partial \tilde{p}_N}{\partial \xi_2}\right\}, \tag{4.235}$$

$$\left(\frac{\varepsilon_{L1}\varepsilon_{u2}}{\varepsilon_{L2}\bar{k}_{u1}\varepsilon_p\bar{k}_a}\right)\left[\bar{\rho}_N+(\varepsilon_\rho)\tilde{\rho}_N\right][\ldots]\frac{\partial \tilde{u}_2}{\partial \xi_2} \qquad \left\{=\left(\frac{\tilde{L}_1}{\bar{L}_2}\frac{\tilde{U}_2}{\bar{U}_1}\frac{\bar{\rho}_R\bar{a}_R^2}{\tilde{p}_R}\right)[\ldots]\frac{\partial \tilde{u}_2}{\partial \xi_2}\right\}, \tag{4.236}$$

$$\left(\frac{\varepsilon_{L1}\bar{k}_{L2}\varepsilon_{u2}}{\bar{k}_{u1}\varepsilon_p}\right)\tilde{u}_2\frac{\partial\bar{p}_N}{\partial\xi_2} \qquad \left\{=\left(\frac{\tilde{L}_1}{\bar{L}_2}\frac{\tilde{U}_2}{\bar{U}_1}\frac{\bar{p}_R}{\tilde{p}_R}\right)\tilde{u}_2\frac{\partial\bar{p}_N}{\partial\xi_2}\right\}, \tag{4.237}$$

- Body boundary condition, through Eq. (4.123):
  - Using the normalization relative of Section 4.6.2, the following term involving $\tilde{u}_2$ is found in the body boundary condition:

$$(\varepsilon_{u2})(\bar{n}_2+\tilde{n}_2)\tilde{u}_2 \qquad \left\{=\left(\frac{\tilde{U}_2}{\bar{U}_R}(\bar{n}_2+\tilde{n}_2)\right)\tilde{u}_2\right\}. \tag{4.238}$$

Summary

The above process has been summarized in Table 4.10. The normalization has been conducted using the same terms as in the 3D to 2D reduction process for consistency. This facilitates comparison with Table 4.9. This emphasized in the final column of Table 4.10, which shows the additional requirements for reduction to 1D if the corresponding base requirements (found in Table 4.9) for reduction to 2D have been met.

The additional requirements for reducing the equations to a 1D formulation are seen to consistently require the following relations:

$$\frac{\tilde{L}_1}{\tilde{L}_2}\frac{\tilde{U}_2}{\tilde{U}_1}\leq\mathscr{O}(1) \quad \text{or} \quad \frac{\bar{L}_1}{\bar{L}_2}\frac{\tilde{U}_2}{\tilde{U}_1}\leq\mathscr{O}(1). \tag{4.239}$$

These requirements offer significant insight into the types of perturbations which allow the reduction to a 1D formulation. This will be illustrated through a brief example.

Consider a flat plate, with a point on the plate subjected to a localized out-of-plane deformation. The small deformation is considered such that it produces infinitesimal fluid perturbations which propagate along the Mach cone emanating from the point. Under these circumstances, the typical scaling analysis of perturbation velocities in supersonic flow are $\mathscr{O}(\tilde{U}_2)=\mathscr{O}(\tilde{U}_3)$ and $\mathscr{O}(\tilde{U}_1)=\mathscr{O}(\tau\tilde{U}_2)$. The assumption that the ratio of gradients may be characterized by the Mach angle leads to the scaling $\frac{\tilde{L}_1}{\tilde{L}_2}=\mathscr{O}(\cot\mu)$, with μ being the local Mach angle. Alternatively, this may be written in terms of the local Mach number M as $\frac{\tilde{L}_1}{\tilde{L}_2}=\mathscr{O}\left(\sqrt{M^2-1}\right)$. The result is that for the localized, point-perturbation, the ratio appearing in the reduction requirements has the scaling of

$$\frac{\tilde{L}_1}{\tilde{L}_2}\frac{\tilde{U}_2}{\tilde{U}_1}=\mathscr{O}\left(\tau^{-1}\sqrt{M^2-1}\right). \tag{4.240}$$

While it may appear that this could satisfy the requirement of $\leq \mathscr{O}(1)$ for $\left(M^2-1\right)=\mathscr{O}\left(\tau^2\right)$, for such a transonic Mach number, the assumed scaling of $\mathscr{O}\left(\tilde{U}_1\right)=\mathscr{O}\left(\tau\tilde{U}_2\right)$ would no longer be valid. As a consequence, it is shown that a reduction to a 1D formulation is not mathematically consistent when considering localized deformations. An extension of this line of thought shows that a reduction to a 1D formulation requires that *perturbations in the x_2 direction must vary at least as slowly as perturbation in the x_1 direction if they are of comparable magnitude*. If the velocity perturbations $\tilde{U}_2$ are larger than $\tilde{U}_1$, then the variation $\tilde{L}_2$ needs to be slower (through larger L) than $\tilde{L}_1$ by a proportional amount. This suggests that a reduction to a 1D formulation will be valid (in the context of lifting surfaces) for smooth spanwise-distributed deformations. This would correspond to mode-shapes free of localized bending or twist.

Table 4.10 Summary of additional requirements for 2D to 1D reduction of LPT.

Equation	Normalized term	Neglected term(s)	Additional requirements
Continuity Eq. (4.97)	$\bar{u}_1\frac{\partial\tilde{\rho}_N}{\partial\xi_1}$	$\bar{\rho}_N\frac{\partial\tilde{u}_2}{\partial\xi_2}$	$\frac{\tilde{L}_1}{\tilde{L}_2}\frac{\tilde{U}_2}{\tilde{U}_1}\leq\mathscr{O}(1)$
		$\frac{\partial(\tilde{\rho}_N\tilde{u}_2)}{\partial\xi_2}$	$\frac{\tilde{L}_1}{\tilde{L}_2}\frac{\tilde{U}_2}{\tilde{U}_1}\leq\mathscr{O}(1)$
		$\tilde{u}_2\frac{\partial\bar{\rho}_N}{\partial\xi_2}$	$\frac{\bar{L}_1}{\bar{L}_2}\frac{\tilde{U}_2}{\tilde{U}_1}\leq\mathscr{O}(1)$
Momentum in x_3 Eq. (4.98)	$\bar{\rho}_N\bar{u}_1\frac{\partial\tilde{u}_3}{\partial\xi_1}$	$\left[\bar{\rho}_N+\left(\varepsilon_\rho\right)\tilde{\rho}_N\right]\tilde{u}_2\frac{\partial\tilde{u}_3}{\partial\xi_2}$	$\frac{\tilde{L}_1}{\tilde{L}_2}\frac{\tilde{U}_2}{\tilde{U}_1}\leq\mathscr{O}(1)$
		$\left[\bar{\rho}_N+\left(\varepsilon_\rho\right)\tilde{\rho}_N\right]\tilde{u}_2\frac{\partial\bar{u}_3}{\partial\xi_2}$	$\frac{\bar{L}_1}{\bar{L}_2}\frac{\tilde{U}_2}{\tilde{U}_1}\leq\mathscr{O}(1)$
Energy Eq. (4.99)	$\bar{u}_1\frac{\partial\tilde{p}_N}{\partial\xi_1}$	$\tilde{u}_2\frac{\partial\tilde{p}_N}{\partial\xi_2}$	$\frac{\tilde{L}_1}{\tilde{L}_2}\frac{\tilde{U}_2}{\tilde{U}_1}\leq\mathscr{O}(1)$
		$\left[\bar{\rho}_N+\left(\varepsilon_\rho\right)\tilde{\rho}_N\right][\ldots]\frac{\partial\tilde{u}_2}{\partial\xi_2}$	$\frac{\tilde{L}_1}{\tilde{L}_2}\frac{\tilde{U}_2}{\tilde{U}_1}\leq\mathscr{O}(1)$
		$\tilde{u}_2\frac{\partial\bar{p}_N}{\partial\xi_2}$	$\frac{\bar{L}_1}{\bar{L}_2}\frac{\tilde{U}_2}{\tilde{U}_1}\leq\mathscr{O}(1)$
Body boundary Eq. (4.123)	$\left(\tilde{n}_m\bar{k}_{um}\right)\bar{u}_m$	$(\bar{n}_2+\tilde{n}_2)\tilde{u}_2$	$\frac{\tilde{U}_2}{\tilde{U}_1}\frac{(\bar{n}_2+\tilde{n}_2)}{(\bar{n}_1+\tilde{n}_1)}\leq\mathscr{O}(1)$

1D Equations

The reduction of the 3D unsteady Euler equations of Eqs. (4.97) to (4.99) to 1D unsteady results in the following set of equations:

$$\text{C:}\quad \left.\begin{aligned}(\varepsilon_\rho)\left[\left(\frac{\bar{k}_t}{\varepsilon_t}\right)\frac{\partial}{\partial t_N}+\left(\frac{\bar{k}_{um}}{\varepsilon_{Lm}}\right)\bar{u}_m\frac{\partial}{\partial\xi_m}\right]\tilde{\rho}_N+\left(\frac{\varepsilon_\rho\varepsilon_{u3}}{\varepsilon_{L3}}\right)\tilde{u}_3\frac{\partial(\tilde{\rho}_N)}{\partial\xi_3}\\ +\left(\frac{\varepsilon_{u3}}{\varepsilon_{L3}}\right)\left[\bar{\rho}_N+(\varepsilon_\rho)(\tilde{\rho}_N)\right]\frac{\partial\tilde{u}_3}{\partial\xi_3}\end{aligned}\right\}=-(\varepsilon_\rho\bar{k}_{xm})\tilde{\rho}_N\frac{\partial\bar{u}_m}{\partial\xi_m}-(\varepsilon_{u3}\bar{k}_{L3})\tilde{u}_3\frac{\partial\bar{\rho}_N}{\partial\xi_3}, \tag{4.241}$$

$$\text{M:}\quad \left.\begin{aligned}(\varepsilon_{u3})\left[\bar{\rho}_N+(\varepsilon_\rho)\tilde{\rho}_N\right]\left[\left(\frac{\bar{k}_t}{\varepsilon_t}\right)\frac{\partial}{\partial t_N}+\left(\frac{\bar{k}_{um}}{\varepsilon_{Lm}}\right)\bar{u}_m\frac{\partial}{\partial\xi_m}\right]\tilde{u}_3\\ +\left(\frac{\varepsilon_{u3}\varepsilon_{u3}}{\varepsilon_{L3}}\right)\left[\bar{\rho}_N+(\varepsilon_\rho)\tilde{\rho}_N\right]\tilde{u}_3\frac{\partial\tilde{u}_3}{\partial\xi_3}+\left(\frac{\varepsilon_p\bar{k}_f}{\varepsilon_{L3}}\right)\frac{\partial\tilde{p}_N}{\partial\xi_3}\end{aligned}\right\}=-\left\{\begin{aligned}&(\bar{k}_{L3}\varepsilon_{u3}\bar{k}_{u3})\left[\bar{\rho}_N+(\varepsilon_\rho)\tilde{\rho}_N\right]\tilde{u}_3\frac{\partial\bar{u}_3}{\partial\xi_3}\\ &-\left(\frac{\varepsilon_\rho\bar{k}_f\bar{k}_{x3}}{\bar{k}_{u3}}\right)\frac{\tilde{\rho}_N}{\bar{\rho}_N}\frac{\partial\bar{p}_N}{\partial\xi_3}\end{aligned}\right., \tag{4.242}$$

$$\text{E:}\quad \left.\begin{aligned}(\varepsilon_p\bar{k}_a)\left[\left(\frac{\bar{k}_t}{\varepsilon_t}\right)\frac{\partial}{\partial t_N}+\left(\frac{\bar{k}_{um}}{\varepsilon_{Lm}}\right)\bar{u}_m\frac{\partial}{\partial\xi_m}\right]\tilde{p}_N\\ +\left(\frac{\varepsilon_{u3}\varepsilon_p\bar{k}_a}{\varepsilon_{L3}}\right)\tilde{u}_3\frac{\partial\tilde{p}_N}{\partial\xi_3}\\ +\left(\frac{\varepsilon_{u3}}{\varepsilon_{L3}}\right)\left[\bar{\rho}_N+(\varepsilon_\rho)\tilde{\rho}_N\right]\left[\bar{a}_N^2+(2\varepsilon_a)\bar{a}_N\tilde{a}_N+(\varepsilon_a^2)\tilde{a}_N^2\right]\frac{\partial\tilde{u}_3}{\partial\xi_3}\end{aligned}\right\}=-\left\{\begin{aligned}&(\bar{k}_{L3}\varepsilon_{u3}\bar{k}_a)\tilde{u}_3\frac{\partial\bar{p}_N}{\partial\xi_3}+(\varepsilon_\rho)\tilde{\rho}_N\bar{a}_N^2\frac{\partial\bar{u}_m}{\partial\xi_m}\\ &+(\bar{k}_{xm})\left[\bar{\rho}_N+(\varepsilon_\rho)\tilde{\rho}_N\right]\left[(2\varepsilon_a)\bar{a}_N\tilde{a}_N+(\varepsilon_a^2)\tilde{a}_N^2\right]\frac{\partial\bar{u}_m}{\partial\xi_m}\end{aligned}\right. \tag{4.243}$$

Equations (4.241) to (4.243) have been rearranged such that all terms involving gradients from the un-perturbed (mean-steady) solution appear on the right-hand-side. With this arrangement, the left-hand-sides of the equations have the same form as the total-quantity form or un-perturbed form of the Euler equations, given in Eqs. (4.44) to (4.46). However, here the equations are in terms of perturbation variables, and are limited to variations of these variables in only the x_3 direction. It is noted that in Eqs. (4.241) to (4.243), time-derivatives on the left hand-side appear in the form of

$$\frac{\partial}{\partial t_N^G} = \left[\left(\frac{\bar{k}_t}{\varepsilon_t} \right) \frac{\partial}{\partial t_N} + \left(\frac{\bar{k}_{um}}{\varepsilon_{Lm}} \right) \bar{u}_m \frac{\partial}{\partial \xi_m} \right], \tag{4.244}$$

with an obvious parallel to Eq. (4.201). The derivative above may be interpreted as a time-derivative in a Galilean frame advected by the local un-perturbed velocity through $\bar{u}_m$. Furthermore, it is noted that dilation of the perturbation velocity through $\frac{\partial \tilde{u}_3}{\partial \xi_3}$ is always accompanied by the total-quantity density through $\left[\bar{\rho}_N + \left(\varepsilon_\rho \right) \tilde{\rho}_N \right]$.

The form in which Eqs. (4.241) to (4.243) are emphasizes the differences between CPT and LPT. With CPT modelling perturbations relative to a uniform freestream, the right-hand-sides of the equations become zero. In LPT, the right-hand-side terms do not disappear. Instead, they are interpreted as source terms arising out of the steady gradients of the un-perturbed (mean-steady) solution.

4.6.4 Reduction to Algebraic Form

A comparison of Eqs. (4.241) to (4.243) with Eqs. (4.197) to (4.199) shows that not only has the field-type problem been maintained, but now source terms have been included. As discussed above, these source terms are associated with gradients in the background (un-perturbed) flow. A reduction of this formulation to an algebraic relationship as associated with CFD-based LPT requires (much like in the case of CPT) surface-incident characteristics to be neglected. While many of the same considerations made in Section 4.5.4 apply here, a more in-depth and general discussion of the requirements to derive an algebraic-relation-type LPT is the focus of the following section, and in particular of Section 4.7.4.

4.7 Discussion

The present section will discuss a number of elements that are core to the derivation of both CPT and LPT from the 3D Euler equations, as developed in this chapter. Broadly speaking, the topics discussed may be categorized as being centred on

- Considerations surrounding the mathematical consistency of the assumptions required for the reduction to a 1D algebraic formulation,
- Implications for the practical application of existing Euler-based LPT.

Such a distinction is largely synthetic. This is because the elements which affect the mathematical consistency will be sources of error in the modelling – this will have direct implications for the application of the method. Nevertheless, for the sake of presentation, Section 4.7 will be dedicated to the discussion surround the mathematical considerations. A distillation of this discussion, with emphasis on the implications for practical application of existing Euler-based LPT will be presented in Section 4.8.

The present discussion will be structured around the core elements influencing the reduction of the 3D unsteady field problem to a 1D algebraic relation. These include

- The uniform validity of a chosen non-dimensionalization,
- The role of mean-steady gradients in the flow,
- The role of relative perturbation magnitudes and gradients,
- The neglect of flowfield interaction by means of surface-incident characteristics.

4.7.1 Uniform Validity of Non-Dimensionalizations

An introduction to the discussion surrounding the uniform validity of a given non-dimensionalization was given in Section 4.1.3. Two key assumptions have been made in the development of the mathematical basis in the present chapter. Namely, it has been assumed that:

- Reference values X_R, with their un-perturbed and perturbation equivalents of $\bar{X}_R$ and $\tilde{X}_R$, respectively, have been chosen such that the resulting non-dimensionalization is uniformly valid throughout the flowfield bound by the body and the bow shock,
- Temporal and spatial gradients of *all* fluid variables may be non-dimensionalized using common reference values of t_R and L_R, respectively. The same applies to the un-perturbed and perturbation equivalents.

The first assumption may be loosely rephrased as “the reference values are appropriate everywhere,” while the second may be rephrased as “one gradient-scale fits all variables.” Violation of the first assumption directly leads to a layer-type problem, with common examples being boundary-layer or entropy-layer flows. Violation of the second assumption relates more to the present mathematical development, and necessitates the introduction of a

greater number of distinct reference values L_R associated with particular variables. This has been discussed in the context of the assumption on Page 219. The discussion of Section 4.7.1 will focus primarily on scenarios in which the first assumption is violated, and in which a layer-type problem arises.

A number of layer-type problems may arise. The following are considered here:

- A "globally-embedded" inner layer, such as the boundary-layer on a sharp airfoil, as depicted in Fig. 4.3,
- A "locally-embedded" inner layer, such as the subsonic region of the inviscid flow which exists near the nose of blunted bodies, as depicted in Fig. 4.4.

The use of the terms "global" and "local" in this context refers to the portion of the physical space of interest over which the inner-layer is embedded.

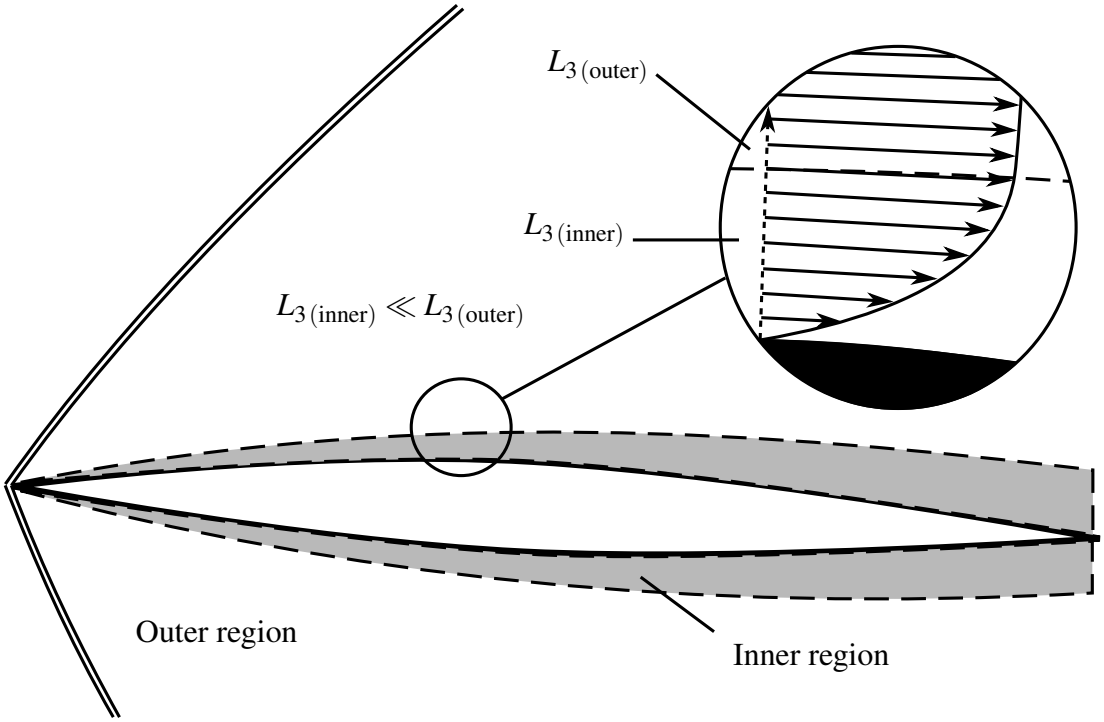

Fig. 4.3 Globally-embedded viscous boundary-layer.

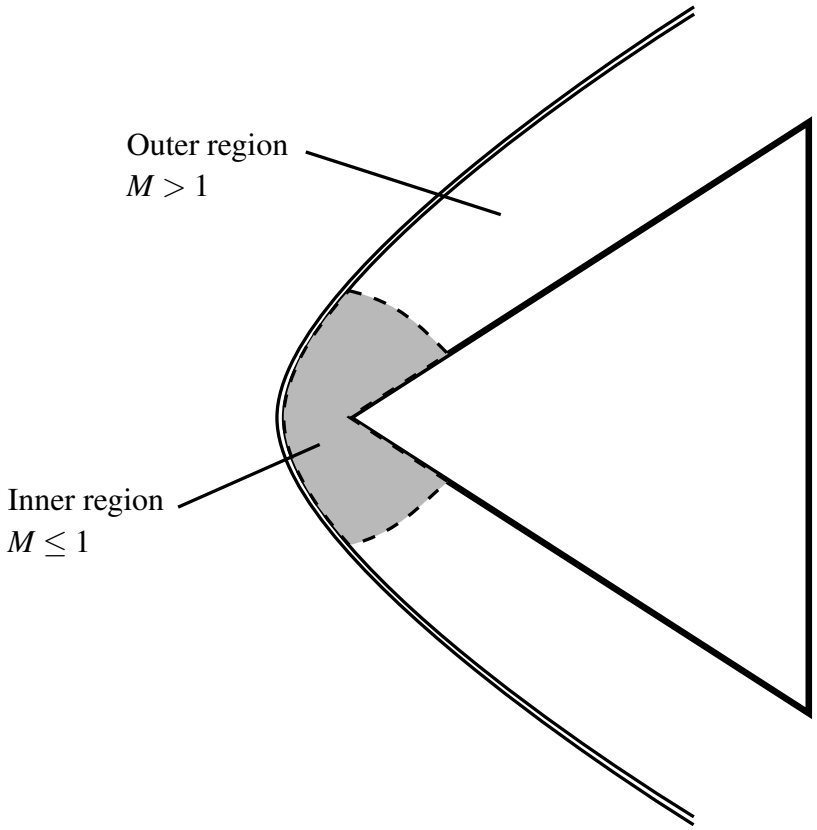

Fig. 4.4 Locally-embedded subsonic inner-layer.

Globally-Embedded Inner Layers

The distinction between layers in the fluid domain typically arises due to the existence of regions of disparate gradient scales – $L_{R\,(\text{inner})}$ and $L_{R\,(\text{outer})}$ – where for a boundary-layer type problem, $L_{R\,(\text{inner})} \ll L_{R\,(\text{outer})}$. This suggests that the existence of

- Localized large second-derivatives of fluid quantities (e.g. due to viscosity), or
- Moderate second-derivatives of fluid quantities acting throughout the fluid domain (e.g. due to large shock- or surface-curvature),

will lead to a layer-type problem. As noted in Section 4.1.3, the solution of layer-type problems is facilitated by the method of matched asymptotic expansions [201, 202]. The solution obtained from the matched asymptotic expansions will introduce a coupling between the mathematics (and physics) of the inner region and of the outer region. However, in the context of LPT, it must be considered that the reduction to a 1D formulation – whether algebraic or not – may not be valid in both the inner and outer regions.

This has been recognized in a number of works relating to hypersonic SDT in the literature, as reviewed in Sections 3.2.6, 3.2.8 and 3.2.9. Particular attention is drawn to

- The work of Liu and Hui [171] on oscillating delta wings. The 2D method for oscillating wedges of Hui [177, 178] is valid within the "outer region" defined by uniform-flow regions on the wing. This is illustrated in Fig. 3.19 for both delta and rectangular wings. The "inner" region is defined by extent of the Mach cone emanating from the delta-wing apex (or the wing-tips of the rectangular wing). Within the "inner" region, the flow is governed by the 3D Euler equations, and the reduction to the simpler 2D method is not valid,

- The work of Hui and East [189] on the stability derivatives of sharp wedges in viscous hypersonic flows. Again, the method of Hui [177, 178] is valid within the inviscid outer region, and is coupled to a viscous model in the inner region of the boundary-layer,

- The work of Orlik-Rückemann [183] and of Ericsson [188] in developing piston-theories with account of inviscid-viscous interaction due to the boundary layer.

For the purposes of the present discussion, particular emphasis will be placed on the inner region of the viscous boundary-layer. As has been illustrated in Section 4.6, the derivation of LPT from the 3D Euler equations requires velocity perturbations in the streamwise and spanwise direction to be neglected. Thereafter, a 1D unsteady field problem is obtained by means of a Galilean transform. The persistence of upstream propagations may be modelled by retaining the field-type formulation. However, as the flow is supersonic, perturbations occurring downstream of the instantaneous fluid slab under consideration have no effect on that slab. This is not the case in the viscous inner region. The flow within the boundary-layer may in fact be subsonic, in which case perturbations occurring downstream of the point in consideration may well propagate upstream. This may be summarized as follows:

- In isolation, the outer inviscid flow allows downstream perturbations to be ignored, which results in a reduction to a 1D unsteady formulation. This may be further simplified to obtain an algebraic relation of LPT,

- When coupled to the viscous inner region, downstream perturbations influence the instantaneous outer solution upstream of those perturbations. Thus, a 2D (or 3D) unsteady formulation is required to determine the boundary conditions of the outer inviscid flow.

Locally-Embedded Inner Layers

The present discussion will consider "locally-embedded inner layers" by virtue of:

- Mach number (subsonic regions embedded in a supersonic outer flow),
- Curvature,
- Concentrated vorticity.

An example of the first of these has been depicted in Fig. 4.4. In the absence of a viscous boundary-layer, embedded subsonic regions in a supersonic freestream as depicted will arise as a consequence of one of the following:

- The freestream Mach number is in the transonic range, and adverse pressure gradients along the body surface result in the formation of a normal shock at the surface. This commonly occurs on airfoils in the transonic range,
- The angle by which the oncoming flow must be turned by the body is sufficiently great that
  - The attached oblique shock approaches detachment, and an embedded subsonic region is formed behind the attached shock,
  - The bow shock detaches from the body, with an embedded subsonic region spanning a portion of the space between the detached shock and the body.

  More generally, this may be attributed to "bluntness."

Classical piston theory is established as method rooted in hypersonic flows around slender profiles. It has historically been applied with the implicit understanding that it is not valid for blunted profiles. The present mathematical basis provides clearer insight into the role of the Mach number (and of bluntness) in influencing the validity (and accuracy) of both CPT and LPT. The momentum and energy equations of Eqs. (4.45) and (4.46) are seen to involve the dimensionless parameters k_f and k_a, respectively. For ease of reference, the definition of these parameters is repeated below:

$$k_f = \frac{p_R}{\rho_R U_R^2}\,, \qquad k_a = \frac{p_R}{\rho_R a_R^2}\,. \tag{4.245}$$

It is recalled here that the selection of the reference values such as p_R is to be guided such that the dimensional quantities (p) are appropriately non-dimensionalized ($p_N = \mathscr{O}(1)$). While the appropriate definition of p_R is dependent on the application (slender-body flows

versus blunt-body flows), it is noted that whether $p_R = p_\infty$ or $p_R = \rho_\infty U_\infty^2$, the square of the freestream Mach number M_∞^2 will appear in either k_f or k_a. The Mach number thus essentially affects the scaling of:

- The pressure-gradient in the momentum equation through k_f,
- The pressure-gradient in the energy equation through k_a.

However, the Mach number has a less visible yet very significant influence on the relative magnitudes of velocities and gradients through terms such as $\frac{\bar{U}_3}{\bar{U}_1}$ and $\frac{\bar{L}_3}{\bar{L}_1}$. The reduction to a 1D formulation required by LPT depends on streamwise gradients (and perturbation velocities) being on order of magnitude smaller than gradients in the thickness direction. However, as the local Mach number decreases into the transonic range, streamwise gradients become increasingly significant, while gradients in the thickness direction become of secondary importance. Similar considerations apply to the perturbation velocities. In the subsonic regime, perturbations propagate in all directions, and the length scales $\bar{L}_i$ may become comparable. It is clear that the above circumstances relating to transonic and embedded subsonic regions will not allow a uniformly valid reduction to 1D to be performed. While it may be possible to obtain a significantly simplified approximate model of the flow in the inner region, it cannot be reasonably expected that LPT (which is valid in the supersonic / hypersonic outer-layer) may be accurately applied in the subsonic / transonic inner-layer.

Locally-embedded inner-layers may also arise due to strong curvature. Particular attention is given at present to curvature in the crossflow plane, as associated with wing-body junctions and wing-tips. This has been illustrated in Fig. 4.5. The inner-layers arising from curvature in the crossflow plane are defined by

- The order of magnitude of relevant reference length-scales $\bar{L}_R$,
- The relative magnitude of crossflow gradients, with $\mathscr{O}(\bar{L}_2) = \mathscr{O}\left(\bar{L}_3\right)$.

The first of the above alludes to the overall higher magnitude of flow gradients which may be observed in the vicinity of the curvature. This may affect the validity (locally) of even a 2D reduction of the 3D Euler equations, as noted in the works of Voevodenko and Panteleev [86]. The second point, namely that $\mathscr{O}(\bar{L}_2) = \mathscr{O}\left(\bar{L}_3\right)$, states that the flow is inherently two-dimensional, and that gradients in one of the crossflow directions may not be neglected in favour of gradients in the other direction. This directly opposes the requirement of neglecting one crossflow direction to arrive at the 1D formulation, as has been shown in Section 4.6.3 and Table 4.10. The failure of CPT in the vicinity of wing-tips by this mechanism has long been understood, having been recognized by Il'yushin [77] in his

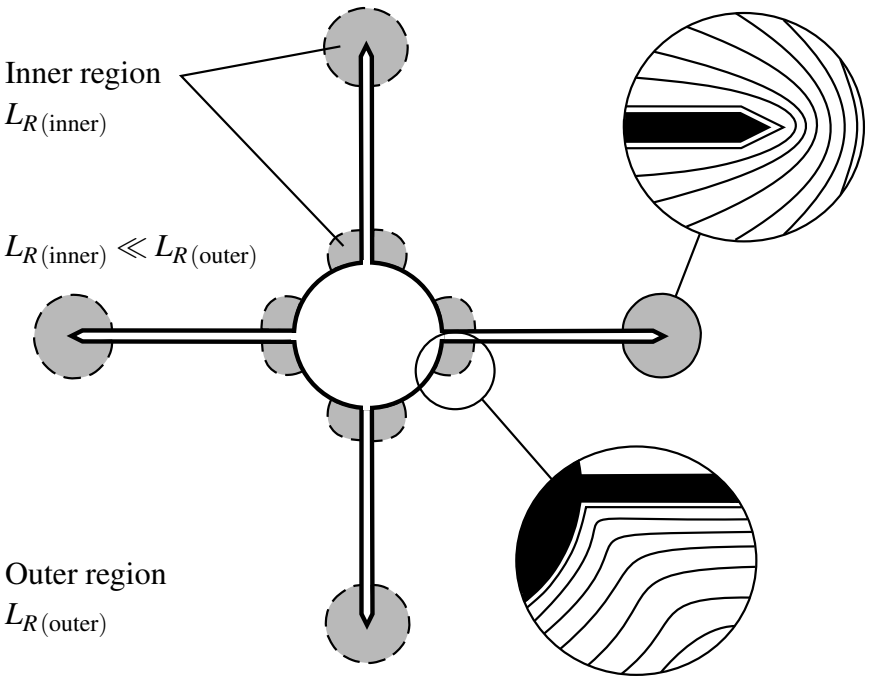

Fig. 4.5 Locally-embedded inner-layers due to curvature.

original development. The extended of this breakdown to LPT is made here. In closing, it is remarked that in a viscous formulation, regions of high curvature will typically be associated with the development (or separation from the surface) of a viscous inner-layer.

This leads to the final type of locally-embedded layer considered in the present discussion. The separation of a viscous boundary-layer – in the context of slender body aerodynamics – is typically associated with the development and shedding of vortices. Regions of strong crossflow curvature are also sources of vortex development. It is thus unsurprising that regions of concentrated vorticity may also be characterized by

- The order of magnitude of relevant reference length-scales $\bar{L}_R$,
- The relative magnitude of crossflow gradients, with $\mathscr{O}(\bar{L}_2) = \mathscr{O}(\bar{L}_3)$.

The interpretation of these regions as locally-embedded inner-layers distinct from the overall crossflow domain is tied to the strength and range of influence of the vortical structure. An example of regions of concentrated vorticity interpreted as locally-embedded inner-layers is illustrated in Fig. 4.6. This is of particular interest in the application of Euler-based LPT to control surfaces on slender bodies. It is possible that the strength of the vortices, together with their proximity to the control surfaces, results in a globally-embedded (in the crossflow

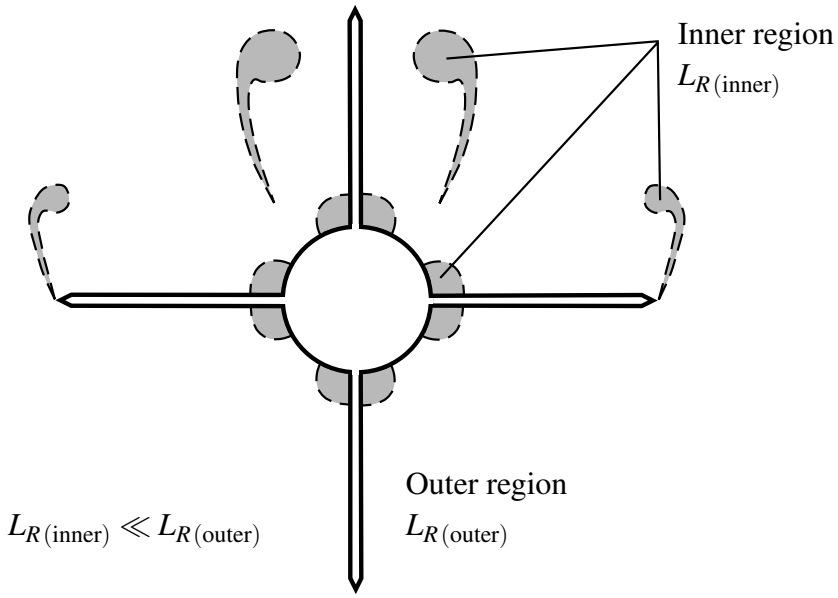

Fig. 4.6 Locally-embedded inner-layers due to concentrated regions of vorticity.

plane) inner-layer in which the reduction to a 1D formulation is not possible. This scenario is of further interest in raising the following questions:

- How do the control-surface perturbations considered (Section 4.7.3) influence the validity of a reduction to a 1D formulation?
- Is the neglect of flowfield interaction (Section 4.7.4) is a valid approximation?

A precursory numerical investigation into these questions is conducted in Chapter 5.

4.7.2 Mean-Steady Gradients

With the role of (a lack of) uniform validity in affecting the reduction from a 3D formulation to a 1D formulation thus addressed, the attention turns to the role of gradients in the unperturbed (mean-steady) flow. Here it will be assumed that the non-dimensionalization is in fact uniformly valid.

The appearance of mean-steady gradients in the 3D Euler equations of Eqs. (4.97) to (4.99) has been interpreted in Section 4.6.3 as additional source-terms in an Euler formulation in terms of perturbation variables. This was clearly shown for the 1D reduced-formulation in

Eqs. (4.241) to (4.243). The reduction to the 1D formulation requires terms of the form

$$\tilde{u}_1 \frac{\partial \bar{\rho}_N}{\partial \xi_1}, \qquad \tilde{u}_2 \frac{\partial \bar{\rho}_N}{\partial \xi_2}, \tag{4.246}$$

$$\tilde{u}_1 \frac{\partial \bar{u}_2}{\partial \xi_1}, \tag{4.247}$$

$$\tilde{u}_1 \frac{\partial \bar{u}_3}{\partial \xi_1}, \qquad \tilde{u}_2 \frac{\partial \bar{u}_3}{\partial \xi_2}, \tag{4.248}$$

$$\tilde{u}_1 \frac{\partial \bar{p}_N}{\partial \xi_1}, \qquad \tilde{u}_2 \frac{\partial \bar{p}_N}{\partial \xi_2}, \tag{4.249}$$

be neglected in favour of the terms listed in Tables 4.9 and 4.10. Above, terms on the left-hand-side (involving $\tilde{u}_1$) are associated with the reduction to a 2D formulation, while those on the right are associated with a further reduction to 1D. It is noted here that the existence of particularly prominent un-perturbed gradients may affect the normalization of the equations in the scaling analysis conducted in Sections 4.6.2 and 4.6.2. Thus, the discussion will not offer direct requirements on terms such as $\frac{\bar{L}_1}{\bar{L}_2}$.

The first scenario considered will be a slender axisymmetric body at incidence to the flow, such as a yawed cylinder. It is assumed that the reduction to a 2D formulation through the neglect of $\tilde{u}_1$ is valid, and that $\bar{L}_1 \; gg 1$. The framework developed in the present work has been presented in a Cartesian coordinate system, but may readily be extended to curvilinear coordinate system, as was done in an earlier development of the framework by the author in [196]. In essence, the elimination of $\tilde{u}_1$ results in the reduction to an unsteady crossflow formulation. Considering an inviscid flow, it is noted that in the vicinity of the body surface, the mean-steady flow gradients in the radial and circumferential directions (or in x_2 and x_3 in the Cartesian formulation) will be of comparable orders of magnitude. This is written in the present notation as $\mathscr{O}(\bar{L}_2) = \mathscr{O}(\bar{L}_3)$. A reduction to a 1D formulation would thus not be possible under these circumstances.

An alternative approach reaching the same conclusion may be taken by considering Eqs. (4.246), (4.248) and (4.249). Under an established crossflow, the mean-steady gradients $\frac{\partial \bar{p}_N}{\partial \xi_2}$, $\frac{\partial \bar{u}_3}{\partial \xi_2}$, and $\frac{\partial \bar{p}_N}{\partial \xi_2}$ are expected to have coefficients which are $\mathscr{O}(1)$. Neglecting terms these terms in $\tilde{u}_2$ in favour of corresponding terms in $\tilde{u}_3$ would require that $\tilde{u}_2 \ll \tilde{u}_3$, which is an unlikely scenario.

Further scenarios in which prominent gradients in the mean-steady flow affect the validity of a reduction to a 1D perturbation problem may be considered. Closely related to the crossflow scenario introduced above is the case of a strong vortex in close proximity to a control surface. As has been discussed before, the vortical flow would be characterized by

$\mathscr{O}(\bar{L}_2) = \mathscr{O}(\bar{L}_3)$. The validity of a reduction to a 1D formulation under deformations of the control surface such that $\tilde{U}_2 \ll \tilde{U}_3$ and $\tilde{L}_2 \gg \tilde{L}_3$ is an open research question of interest.

A final scenario considered is in the application of LPT to a mean-steady solution with a significant mean-steady streamwise-gradient, as would occur in the vicinity of blunted leading-edges or noses. Such a gradient would affect the validity of discarding terms in $\tilde{u}_1$. The limits of validity of applying LPT in blunted regions is another open research question of interest. The mathematical basis for LPT developed in the present work serves as a starting point for future work to address these questions.

4.7.3 Relative Magnitudes of Perturbation Velocities and Gradients

The role of the relative magnitudes of

$$\frac{\tilde{U}_1}{\tilde{U}_2}, \qquad \frac{\tilde{U}_2}{\tilde{U}_3}, \tag{4.250}$$

$$\frac{\tilde{L}_1}{\tilde{L}_2}, \qquad \frac{\tilde{L}_2}{\tilde{L}_3} \tag{4.251}$$

have already been introduced in the preceding discussions. In particular, the role of surface deformations in defining the above relative magnitudes has been noted. The role of these ratios in allowing a reduction to a 2D or a 1D formulation has been emphasized in Tables 4.9 and 4.10.

A discussion of the role of the local Mach number in defining the ratios for localized point-perturbations has been made in the summary of Section 4.6.3 in the context of Table 4.10. The discussion, while relevant to the present discussion, is not repeated in detail here. Only the key conclusions are noted. The first is that

- A reduction to a 1D formulation is *not* permissible if $\mathscr{O}\left(\tilde{L}_2 = \mathscr{O}\left(\tilde{L}_3\right)\right)$ and $\mathscr{O}\left(\tilde{U}_2 = \mathscr{O}\left(\tilde{U}_3\right)\right)$. This is the case for localized point-perturbations.

An extension of the above to more general deformations may be made by the following heuristic:

- The deformation at any point has a streamwise inclination such that it causes an infinitesimal fluid perturbation which propagates along local characteristics. This is used along with the local Mach number to estimate $\frac{\tilde{L}_1}{\tilde{L}_3}$ and $\frac{\tilde{U}_3}{\tilde{U}_1}$,
- The spanwise-gradient of the streamwise inclination ($\frac{\partial n_1}{\partial \xi_2}$ in the present notation) is assumed to be representative of the relationship $\frac{\tilde{L}_1}{\tilde{L}_2}$.

Using the above and the requirements of Table 4.10, the following conclusion may be reached regarding the influence of mode-shapes on the reduction to a 1D formulation:

$$\frac{\partial n_1}{\partial \xi_2}\frac{\tilde{U}_2}{\tilde{U}_1} \leq \mathscr{O}(1)\,. \tag{4.252}$$

This result was stated in Section 4.6.3 as follows: perturbations in the x_2 direction must vary at least as slowly as perturbation in the x_1 direction if they are of comparable magnitude.

4.7.4 Neglect of Flowfield Interaction

The final element to be discussed regarding assumptions required to obtain an algebraic pressure-relation in LPT is the influence of the interior of the fluid domain on perturbation values at its boundary (on the body surface).

The reduction to a 1D unsteady field-type formulation gives rise to the piston-cylinder analogy. The assumption in Il'yushin's [77] development of CPT is that the piston drives a shock into an otherwise uniform, stationary fluid. A physical interpretation of LPT requires some caution. In LPT, any infinitesimally small element of the 1D "slab" of fluid bound between the body and the shock is advected by the local mean-steady (un-perturbed) fluid velocity at that point in space. However, this advection velocity varies throughout the space. This gives rise to the following questions:

- Do plane fluid sections remaining plane as they are advected by the mean-steady background flow?
- What is the spatial extent of validity of a constant advection-velocity approximation?

The variation of other mean-steady fluid also represents a hurdle to a direct physical analogy. Even if the constant advection-velocity approximation is made in order to obtain a plane cylinder with constant orientation to the body, the un-perturbed thermodynamic quantities of the fluid will vary spatially. In the piston-cylinder analogy, this is equivalent to having a non-uniform captive fluid in the cylinder.

In this light, the discussion surrounding the neglect of flowfield interaction will be made from the reference point of the 3D flow, with an approximate association made between the advected-time and the streamwise coordinate tangential to the surface of the body. The term "flowfield interaction" as used in the present work refers collectively to the following:

- The change in the fluid state at a point on the body surface arising from perturbations produced at an upstream point (i.e. upstream influence). The upstream influence will

be considered as arriving along surface-incident characteristics, which may have the following sources:

  - Direct impingement of surface-generated characteristics from other points on the body surface,
  - Impingement by surface-generated characteristics from other points on the body surface that have been reflected off of shocks or vortices (or entropy gradients, in general),
  - Impingement (direct or by reflection) of characteristics associated with perturbations generated at the interior of the fluid or at the shock boundary.

- Mutual interference between established mean-steady flow-structures (with particular emphasis on body-shed vortices) and the deforming body surface.

The discussion will focus on

- Flow scenarios in which flowfield interaction is not negligible,
- The possibilities for accounting for flowfield interaction in LPT.

Flows With Significant Flowfield Interaction

The question of whether flowfield interaction may be neglected is closely related to the previously-discussed influences on the reduction to a 1D formulation. As was noted in Section 4.7.1, the existence of a layer-type problem leads to coupling between the solutions at the interface between the layers. The scenario of a viscous boundary-layer will be used for illustration. In the moderate- or strong-interaction regime, the solution of the inner-layer may significantly influence the adjacent outer-layer. In this case, the neglect of surface-incident characteristics is an unacceptable approximation, as these modify the boundary conditions to the inner-layer and consequently alter the solution of the outer-layer significantly.

The scenario above of the viscous boundary-layer related to globally-embedded inner-layers. The presence of locally-embedded inner layers (such as embedded subsonic regions or regions of concentrated vorticity) may also significantly the validity of neglecting surface-incident characteristics. An important factor in considering their influence is the proximity of these embedded inner-layers to the surface under consideration. If the embedded regions are sufficiently distant from the surface, the surface-generated characteristics that reflect off of the embedded regions may be weak. Furthermore, reflections might not return to the body surface by virtue of a short streamwise-length of the surface of interest. However, if the embedded regions are in close proximity to the surface of interest, the flowfield interaction

may have a significant role in determining the fluid pressure at the surface. In this scenario, surface-incident characteristics may not be negligible (and more generally, a reduction to 1D might also be inappropriate).

These arguments extend to cases in which significant mean-steady gradients exist in the flow. In particular, the existence of a non-negligible entropy-gradient in the mean-steady flow (as arising from shock curvature) or of vortices in the mean-steady flow will result in the reflection of surface-generated characteristics.

In closing, it is recalled that the present definition of "flowfield interaction" includes changes to the fluid pressure at a point on the surface by direct impingement of surface-generated characteristics from other points on the body surface. This is more commonly referred to as "upstream influence", and is important both generally and for geometries with aerodynamically interfering surfaces.

Accounting for Flowfield Interaction

A rigorous account of flowfield interaction in LPT was made for the special case of inviscid flow over a planar wedge by McIntosh [146], Hui [178], and Orlik-Rückemann [184]. The spatially-invariant background (mean-steady) flow between the shock wave and the wedge surface renders the 2D field-type problem amenable to solution by characteristics. The application of characteristics to solving the 1D field-type problem in the context of CPT may be noted in the works of Il'yushin [77] and of Lin et al [211]. Both of these works also deal with scenarios in which (to within a valid approximation) the background (un-perturbed) solution is spatially uniform (having no gradients). The extension of LPT to account for non-negligible gradients in the mean-steady flow and for the associated flowfield interaction is outside the scope of the present work.

The works of Orlik-Rückemann [183] and of Ericsson [188] in accounting for viscous-inviscid interaction may be considered analytical formulations of a "viscous CPT". The extension of these methods to CFD-based LPT holds the potential for improved modelling fidelity over non-interactive effective-shape formulations of RANS-based LPT. This extension is outside the scope of the present work.

Finally, it is noted that the potential-flow-based methods of Landahl [128] and of "extended piston theory" [144, 145, 160] account for the upstream influence and propagation of perturbations within the context of CPT (with a uniform un-perturbed solution). It is posited that an LPT-esque method could be developed from a linearized (for small perturbations) form of the perturbed Euler equation. In this method, the mean-steady (un-perturbed) solution would be obtained from CFD, while perturbations would be solved for using an approximate

method (for example, using a linear potential flow assumption). Such an extension of LPT is outside the scope of the present work.

4.8 Summary

The present chapter demonstrated the derivation of both CPT and LPT from a common, generalized basis rooted in the 3D unsteady Euler equations. As noted in Section 4.1.2, the intention of this was to

- Address the gap in the literature surrounding the mathematical basis for LPT,
- Provide a deeper understanding of LPT with the goal of
  - Better understanding shortcomings of current formulations and applications of LPT [12, 16, 18, 19, 194, 195],
  - Guiding the application and development of further extensions to LPT.

The derivation was based in a scaling analysis of the perturbation form of the Euler equations. The interpretation of CPT as a special case of the 1D steady Euler equations for slender bodies was informed by the original development of piston theory by means of the law of plane sections due to Il'yushin [77]. The motivation for a generalized non-dimensionalization and scaling analysis with no a-priori assumptions on incidence came from Sychev's [4] derivation of high-incidence theory for a 2D application of the law of plane sections. The possibility of extending this to a 1D formulation to achieve piston theory was informed by the categorization of approximate methods by Hayes and Probstein [27]. Finally, the opportunity to develop the mathematical basis for LPT using the above was informed by the recognition of a common generalized formulation for CPT and LPT in the author's previous work [59, 196].

The perturbation form of the Euler equations from which the derivation originates was introduced in Section 4.3. A brief discussion on the selection of appropriate reference quantities for non-dimensionalization was given in Section 4.4, with a framework for this selection being presented in Appendix A. This was followed by a demonstration of this framework through deriving CPT from the perturbation form of the Euler equations for the classical case of a thin wing with low sweep in Section 4.5. The same procedure was followed to illustrate the equivalent derivation of LPT from the 3D Euler equations for the general case in Section 4.6. A discussion surrounding the mathematical requirements to obtain an algebraic LPT relation of the form of Eq. (3.8) was presented in Section 4.7.

To close this chapter, a distillation of the discussion of Section 4.7, with an emphasis on the implications for the practical application of LPT, is presented here. The following key conclusions are drawn:

- LPT is expected to be in significant error when applied to:
  - Transonic flows and flows with embedded subsonic regions,
  - Surfaces immersed in an entropy layer or viscous boundary-layer (in the context of Euler-based LPT), particularly in strong-interaction cases,
  - Surfaces in close proximity to shock-waves, vortices, strong entropy-gradients, or other aerodynamically-interfering surfaces,
  - Surfaces in close proximity to regions of sharp curvature, such as
    - Blunted noses,
    - Wing-tips,
    - Trailing-edges,
    - Subsonic leading-edges,
    - Wing-body junctions.
  - Mode-shapes of deformation involving regions of localized bending or camber, or point-local deformations,
- Extensions to LPT are proposed to be developed with consideration of the mathematical basis developed in Chapter 4 to account for:
  - Non-negligible mean-steady flow gradients through inclusion as an additional source term as outlined in Eqs. (4.241) to (4.243)
  - Flowfield-interaction and upstream-influence by reduction to a reduced-order linear-perturbation method.

A precursory numerical investigation into the application of the Euler-based LPT (without extensions) to a control surface in an aerodynamically-interfering flow with regions of concentrated vorticity, as is typical of slender-body applications, is conducted in Chapter 5. The mathematical basis for LPT developed in the present chapter will inform the interpretation of the results of the numerical study.

Chapter 5

Application of Euler-Based Local Piston Theory to Static Control Deformations

The content of this chapter draws extensively from a previous publication of the author [212], which has been reproduced and adapted here with permission from the copyright holder.

5.1 Introduction

The purpose of the present chapter is to illustrate the application of Euler-based LPT to aeroprediction of slender-body-type vehicles subject to aeroelastic deformations. The physical flow features typical of these geometries have been reviewed in Chapter 2. The utility of Euler-based LPT relative to other aeroprediction methods was discussed in Sections 2.2 and 2.3. Previous examples of the application of Euler-based LPT to full-vehicle geometries were given in Section 3.2.7. It was noted that the justification for the application of Euler-based LPT in these cases of interference flows was heuristic. No prior systematic investigation of the error in LPT in these flows has been noted in the literature. The present chapter aims to address this gap in the literature incrementally. Discussion of the results of the investigation will be informed by the mathematical basis for Euler-based LPT developed in Chapter 4. An outline of the material presented in this chapter follows.

Section 5.1.1 will introduce the slender-body vehicle geometry considered in the present study. Motivation for the geometry definition will be provided. The elastic modes of deformation of the control surfaces will be introduced. Section 5.1.2 will introduce the reference data available for the body-alone case. Section 5.1.3 will define the parameter space considered in the present study. Section 5.1.4 will introduce the numerical solver and methods used. A description will also be given of the LPT implementation and the

coefficients used. Finally, Section 5.1.5 will define the numerical grids used in the mesh-independence studies performed for the body-alone and wing-alone cases. This will conclude the introductory material of Section 5.1.

Section 5.2 will present the results of body-alone case. The mesh-independence study will be described in Section 5.2.1. Section 5.2.2 will introduce the results for the body-alone computations. The purpose of the body-alone case is to verify the `OpenFOAM` solver against `ANSYS Fluent`. In addition, the body-alone case serves to validate the fidelity of the physics modelled by the Euler equations. This is done through comparison of the Euler solutions to reference data from Tuling [30]. The data of Tuling [30] includes both RANS computations and experimental data. A discussion of the results will follow in Section 5.2.2.

The application of Euler-based LPT in predicting the aerodynamic pressure on a statically deformed wing (control surface) is demonstrated in Sections 5.3 and 5.4. These sections share a similar structure. Section 5.3 will introduce the wing-alone case, with the mesh-independence study discussed in Section 5.3.1. The results of the LPT application will be discussed in Sections 5.3.2 and 5.3.3. A general discussion of the wing-alone results will be given in Section 5.3.4. The full-vehicle case will be covered in Section 5.4. The results will be presented in Sections 5.4.1 and 5.4.2. Specific focus on aerodynamic interference is given in Sections 5.4.3 and 5.4.4. A summary discussion of the full-vehicle results will be given in Section 5.4.5.

Finally, a conclusive discussion of the numerical study of this chapter will be presented in Section 5.5.

5.1.1 Geometry and Structural Modes

Aerodynamic interference on bodies of revolution with cruciform aerodynamic controls has been studied extensively. Correspondingly, a large body of literature including experimental data exists for this category of slender-vehicle geometry. This motivated the selection of the geometry for the computational study in the present chapter. The slender-vehicle geometry used is depicted in Fig. 5.1.

The body of the vehicle corresponds directly to that used in a recent computational and experimental study by Tuling [30]. The results of Tuling's [30] study have been used as the reference data for the present work and are presented in Section 5.1.2. The body consists of a 3-calibre ($3D$) tangent-ogive nose followed by a $16D$ cylindrical afterbody. The physical dimensions given in Fig. 5.1 are those of the computational model of Tuling [30]. The experimental model was scaled by 31.25%.

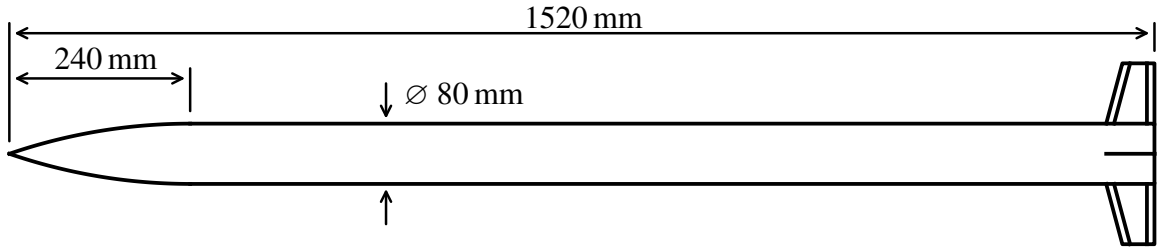

Fig. 5.1 Full-vehicle geometry definition.

The geometry of the control surfaces (which will interchangeably be referred to as wings throughout this chapter) is defined in Fig. 5.2a. The wing geometry definition was governed by two considerations:

- Selection of a low aspect-ratio planform representative of control surfaces typical of this class of slender vehicle,
- Geometry definition which would allow sufficient deformation to exhibit flowfield interaction.

The first consideration dictated the planform specification. The second consideration was a driving factor in the wing thickness specification. A wing thickness of 0.5 mm was used. While this thickness is not useful for practical implementation, it allows thickness effects to be isolated from the computational aerodynamic study. The material specification for the computation of the mode shapes and frequencies is as follows:

- Young's modulus: 73.1 GPa,
- Poisson's ratio: 0.33,
- Density: $2780\,\mathrm{kg\,m^{-3}}$.

The resulting natural modes of the control surfaces are defined in Table 5.1. The mode-shapes are depicted in Figs. 5.2 and 5.3. Modal displacements were defined by the maximum out-of-plane deformation, δ. The red symbols in Figs. 5.2 and 5.3 denote points of maximum (positive and negative) out-of-plane deformation. Displacements in the positive y-direction are denoted by solid lines. The greatest displacement occurs at the wing tip. The modal properties were determined using a clamped boundary condition at the wing root. Mode shapes were computed using quadrilateral finite elements based in Mindlin-Reissner plate theory. Verification against equivalent `QUAD4` elements in `MSC Nastran` was performed. While only static deformations were considered in the subsequent analysis, higher-order

mode-shapes (such as the second-bending mode) were also considered for static aerodynamic prediction, despite typically being associated with dynamic deformations. This was in order to assess the accuracy of LPT when applied to localized deformations.

Table 5.1 Control-surface elastic modes.

			Tip deflection / %		Tip twist / °	
			δ		δ	
Mode	Frequency / Hz	Description	5 mm	10 mm	5 mm	10 mm
1	72.43	First bending	6.0	12	-0.5	-1.0
2	298.4	First torsion	0.45	0.91	-12.3	-23.5
3	403.8	Second bending	-5.6	-11	-1.4	-2.7

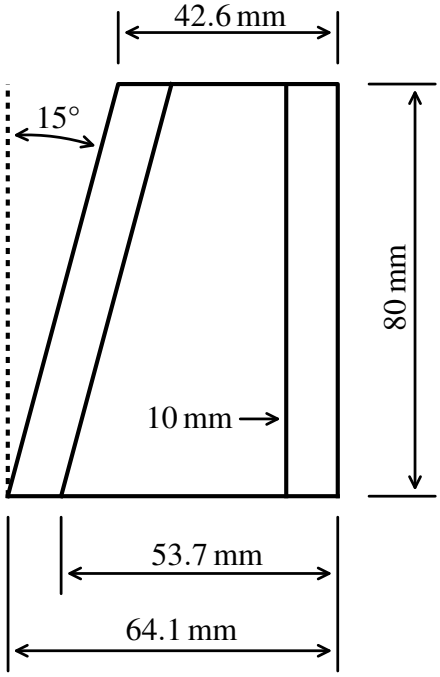

(a) $M_\infty = 0.885$

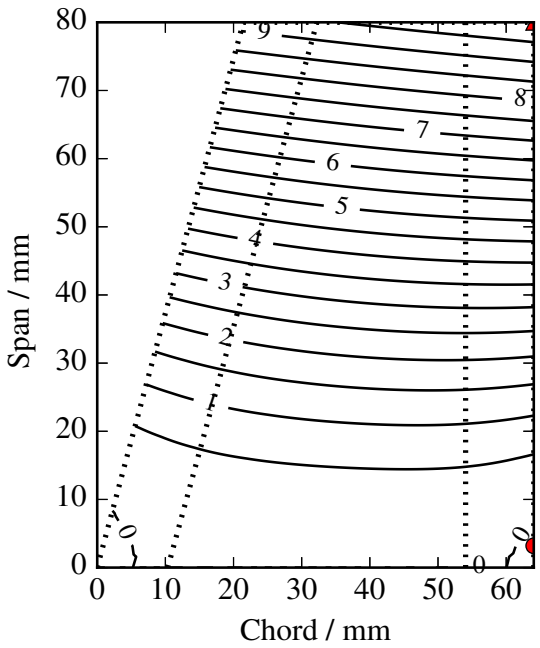

(b) Mode 1: first bending

Fig. 5.2 Control-surface geometry definition and first elastic mode.

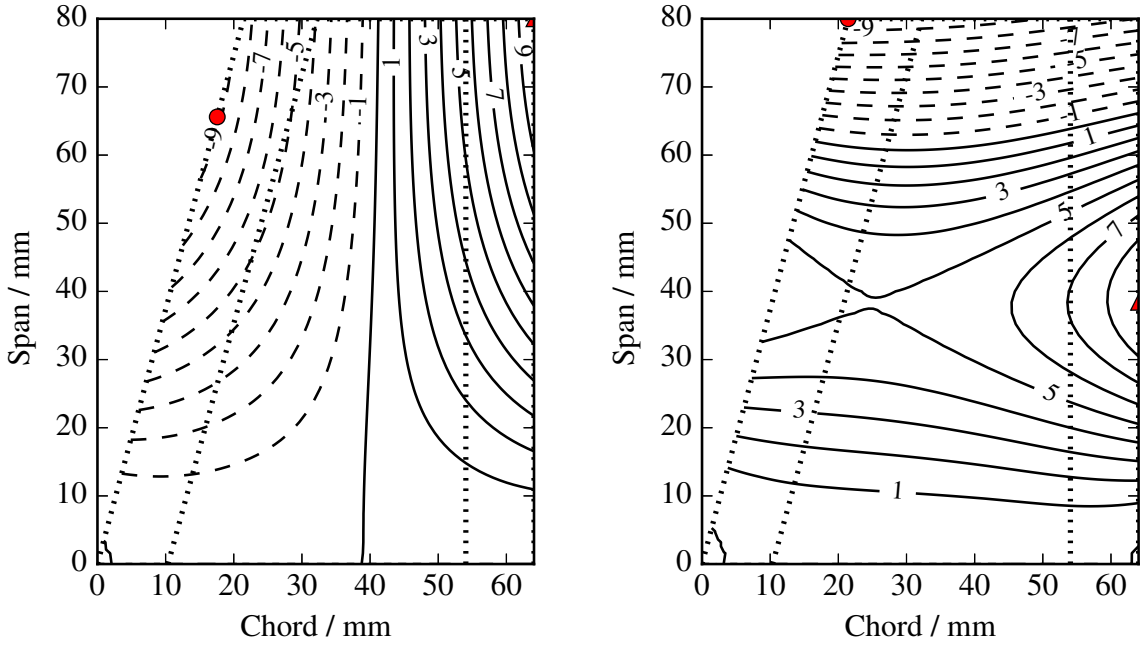

(a) Mode 2: first twist

(b) Mode 3: second bending

Fig. 5.3 Second and third elastic control-surface modes.

5.1.2 Reference Data and Nomenclature

As previously noted, the results of the computational and experimental investigation of Tuling [30] have been chosen as the reference data for the present work. The investigation of Tuling [30] included the aforementioned body-alone geometry of Section 5.1.1, as well as the integration of strakes along the length of the afterbody. Only the body-alone results will be considered here.

The parameter space considered by Tuling [30] spanned the incidence-range of $0° \leq \alpha \leq 25°$, with a freestream Mach set of $M_\infty = [2.0, 2.5, 3.0]$. The difference in freestream conditions used in experiment and used in numerical simulations is noted in Tables 5.2 and 5.3, respectively. Tuling [30] noted that the boundary layer is expected to be turbulent across the parameter space for both experimental and numerical results for the Reynolds numbers used. The uncertainties associated with the experimental results of interest are shown in Table 5.4. The uncertainties are small enough that error bars in subsequent plots of the data are not noticeable, and have hence been omitted. It is noted that mesh- and turbulence-model independence was demonstrated by Tuling [30], and that the RANS results presented were obtained using a Spalart-Allmaras [67–69] model.

Table 5.2 Experimental stagnation and freestream conditions in the study of Tuling [30]

	Pressure / kPa		Temperature / K				
M_∞	p_0	p_∞	T_0	T_∞	V_∞ / m s^{-1}	q_∞ / kPa	Re_D
2.03	180.5	22.02	301.0	167.2	518.4	64.6	5.80×10^5
2.5	293.5	17.18	301.0	133.8	579.5	75.2	7.40×10^5
3.0	490.0	13.34	301.0	107.5	623.4	84.0	9.56×10^5

Table 5.3 Computational stagnation and freestream conditions in the study of Tuling [30]

	Pressure / kPa		Temperature / K				
M_∞	p_0	p_∞	T_0	T_∞	V_∞ / m s^{-1}	q_∞ / kPa	Re_D
2.0	129.0	16.49	288.0	160.0	507.1	46.16	1.33×10^6
2.5	129.0	7.55	288.0	128.0	567.0	33.03	9.11×10^5
3.0	129.0	3.51	288.0	102.9	609.9	22.12	8.20×10^5

Finally, before the reference data is discussed, the nomenclature used to describe forces and moments is introduced in Fig. 5.4. The x-axis is aligned with the body axis. The mid-plane of the undeformed leeside control surface lies within the xz-plane, with $z > 0$. Similarly, the starboard control surface lies within the xy-plane, with $y > 0$. The freestream velocity vector lies in the xz-plane, as no sideslip is assumed. This defines the global coordinate system, in which forces and moments are to be defined. Force-coefficients along the z-axis are denoted C_N, while force-coefficients along the y-axis are denoted C_Y. As axial forces are typically not of importance in aeroelastic studies involving out-of-plane deformations, these have not been considered in the present study. The moment reference centre is located on the body axis at a distance $x_{ref} = 9.5D$ from the nose. Moments about the x-axis are denoted C_l, while moments about the y-axis are denoted C_m. The location of the centre-of-pressure is measured as x_{CP} in calibres from the origin at the nose.

The nomenclature introduced is for forces in the global coordinate system. It should be noted that the use of the phrase "normal-force coefficient" to describe C_N is consistent when considering the body-alone case. However, when considering forces acting on the leeside control surface, it is C_Y which is oriented normal to the control surface. The global nomenclature will not be adapted when considering loads on the control surface.

Table 5.4 Uncertainties in the experimental data in the study of Tuling [30]

	$M_\infty = 2.0$	$M_\infty = 2.5$	$M_\infty = 3.0$
M_∞	9.82×10^{-3}	1.26×10^{-2}	1.69×10^{-2}
α / °	0.163	0.168	0.181
q_∞ / kPa	0.358	0.715	1.179
C_N	5.32×10^{-2}	8.06×10^{-2}	1.26×10^{-1}
C_m	4.84×10^{-2}	7.83×10^{-2}	1.37×10^{-1}

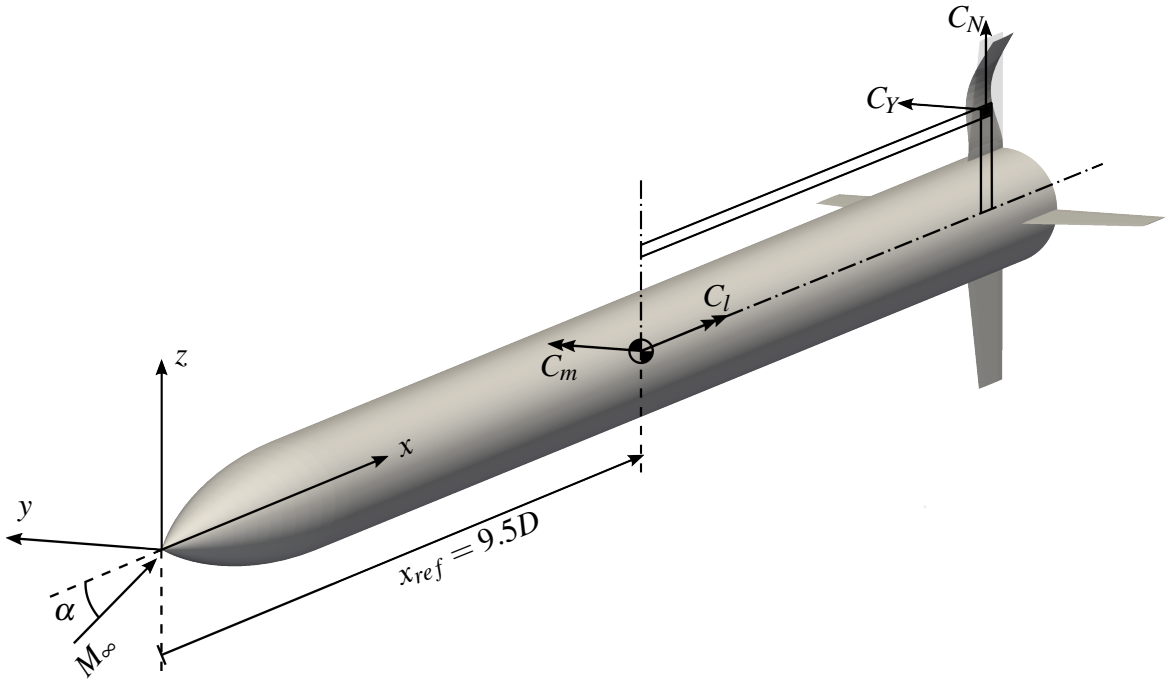

Fig. 5.4 Nomenclature definition for global coordinate system, forces, and moments.

The results of interest to the present work from Tuling's [30] investigation are reproduced in Figs. 5.5 to 5.10. The chief quantities of interest are the normal-force coefficient C_N, the pitching-moment coefficient C_m, and the location of the centre-of-pressure x_{CP}. Figure 5.5 shows these quantities as obtained from experiment for the body-alone case over the M_∞-α parameter space. Figure 5.6 shows the corresponding data obtained from the RANS computations. Inspection of the normal-force coefficient trends in Figs. 5.5a and 5.6a shows no a-typical behaviour, with good correspondence between experimental and computational trends. More interesting features are noted in the pitching-moment trends of Figs. 5.5b and 5.6b and in the centre-of-pressure trends of Figs. 5.5c and 5.6c. The following remarks are made regarding C_m:

- The experimental data in Fig. 5.5b show a Mach-dependence over the parameter space. This includes the linear range of C_m at approximately $\alpha < 8°$. The onset of nonlinearity in the C_m-α curves is associated with the progression of body-shed vortex development. It is noted that when $M_\infty \sin\alpha$ is used as the independent variable, the curves collapse to a single curve for $M_\infty \sin\alpha \leq 0.45$. Thereafter, the data for $M_\infty = 2.0$ follows a similar pattern to that seen in Fig. 5.5b,

- The numerical data in Fig. 5.6b suggest no Mach-dependence in the linear range of the curves (for approximately $\alpha \leq 10°$). This stands in contrast to the experimental observations of Fig. 5.5b. Consequently, if $M_\infty \sin\alpha$ is used as the independent variable, the curves do not collapse to a single curve. This will be discussed shortly in the context of x_{CP},

- Direct comparison of the experimental and RANS results at each Mach number is depicted in Figs. 5.7b, 5.8b and 5.9b. It is seen that despite the aforementioned difference in Mach-dependence modelling, good correspondence in C_m between experiment and computation is obtained at $\alpha \leq 5°$. Significant differences are observed for $\alpha > 10°$, in particular at $M_\infty = 3.0$. This is related to the poorer prediction in C_N noted for this case at $\alpha > 10°$. Tuling [30] posited that this may be related to poorer numerical prediction of the dynamic pressure loss across the bow shock.

The following remarks are made regarding x_{CP}:

- The experimental data in Fig. 5.5c show a non-trivial variation of x_{CP} over the parameter space. This is also noted if $M_\infty \sin\alpha$ is used as the independent variable. Tuling [30] concluded that the notable shifts in x_{CP} observed at $\alpha > 10°$ are associated with changes to the vortex topology. At $\alpha = 15°$, it was observed that the shed vortex-sheet rolled into a single vortex over the length of the body at $M_\infty = 2.0$. However, at

$M_\infty \geq 2.5$, the first vortex was shed from the body, leading to the development of a second vortex-sheet further down the length of the body. This latter structure was observed at all Mach numbers for $\alpha > 20°$,

- The numerical data in Fig. 5.6c show significantly less variability in x_{CP}, with more monotonic trends predicted. Greater Mach- and incidence-dependence is noted at $\alpha > 10°$,

- As before, direct comparison of the experimental and RANS results at each Mach number is depicted in Figs. 5.7c, 5.8c and 5.9c. These figures have been included for completeness. However, greater insight is obtained by plotting the data using $M_\infty \sin\alpha$ as the independent variable. The resulting plots are shown in Fig. 5.10. It is immediately evident that the non-monotonic shifts in x_{CP} observed at $M_\infty = 2.0$ and $M_\infty = 2.5$ occur at $M_\infty \sin\alpha < 0.5$. This is also the parameter space for which the worst agreement between RANS and experiment in x_{CP} is noted. Excellent agreement is typically achieved at $M_\infty \sin\alpha > 0.5$. This is to be expected, as $M_\infty \sin\alpha \approx 0.5$ represents the onset of the crossflow-shock on the body surface. This forcibly sets the boundary-layer separation position. Below this crossflow Mach-number, Reynolds-number effects dominate the cylinder crossflow-drag coefficient and boundary-layer separation. This has been noted in Fig. 2.14. It is noted that the RANS computations of Tuling [30] assumed a fully turbulent boundary-layer. Comparison of the RANS predictions at various Mach numbers in Fig. 5.10d shows that this leads to the curves collapsing to a single function of $M_\infty \sin\alpha$. While the experimental data at $M_\infty = 3.0$, $Re = 9.56 \times 10^{-5}$ support this trend, the data at lower Mach and Reynolds numbers show significant differences at $M_\infty \sin\alpha < 0.5$. It may thus be concluded that the experimental data for $M_\infty = 2.0$ and $M_\infty = 2.5$ at $M_\infty \sin\alpha < 0.5$ are Reynolds-dependent. This may be a factor in the disparate Mach-dependence of C_m at $\alpha \leq 10°$ between experiment and computation.

In the discussion of the reference data thus far, two reoccurring "boundaries" in the parameter space may be noted. The first boundary is noted at $\alpha = 10°$. Associated with this boundary were the observations that:

- The prediction in C_m from RANS suggested Mach-independence at $\alpha \leq 10°$,

- Changes in the shed-vortex topology were observed by Tuling [30] at $\alpha > 10°$.

The second boundary is related to the first, and is at $M_\infty \sin\alpha \approx 0.5$. This boundary is notable in that:

- It marks the onset of the crossflow-shock at the body surface,
- The experimental data exhibit Reynolds-dependence for $M_\infty = 2.0$ and $M_\infty = 2.5$ at crossflow Mach-numbers $M_\infty \sin\alpha \lessapprox 0.5$.

The transition in the shed vortex topology to multiple vortex shedding noted at $\alpha > 10°$ largely motivated the decision to restrict the parameter space of the present study to $\alpha \leq 10°$. It is noted that at $M_\infty = 3.0$, the approximate boundary of $M_\infty \sin\alpha \approx 0.5$ is reach when $\alpha \approx 9.6°$. Thus, when comparing the results of the present study to the experimental data of Tuling [30], it should be considered that the experimental data exhibit Reynolds-dependence. The same dependency does not arise when comparing the results of the present study to the RANS computations of Tuling [30] for $\alpha \leq 10°$.

A discussion of the body-alone vortex-shedding and vortex trajectories is not made here, as it is presented in Tuling's [30] work. Only the approximate positions of the vortex cores at selected parameter points is noted. At $M_\infty = 2.0$, $\alpha = 10°$, the vortex core at $x = 14.5D$ is located at approximately $y \approx 0.3D$, $z \approx 0.8D$. At $M_\infty = 3.0$, $\alpha = 10°$, the vortex core at $x = 14.5D$ is located at approximately $y \approx 0.4D$, $z \approx 0.8D$. The vertical positions correspond to approximately the mid-span of the leeside control-surface. Significant changes in the vertical and lateral positions of the vortex core further down the length of the body were not noted.

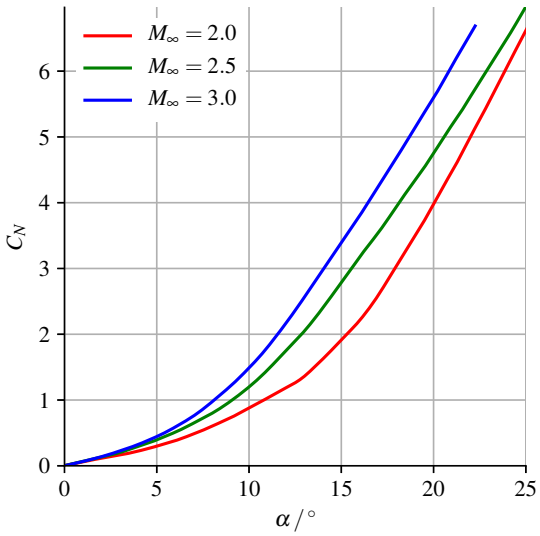

(a) Normal-force coefficient

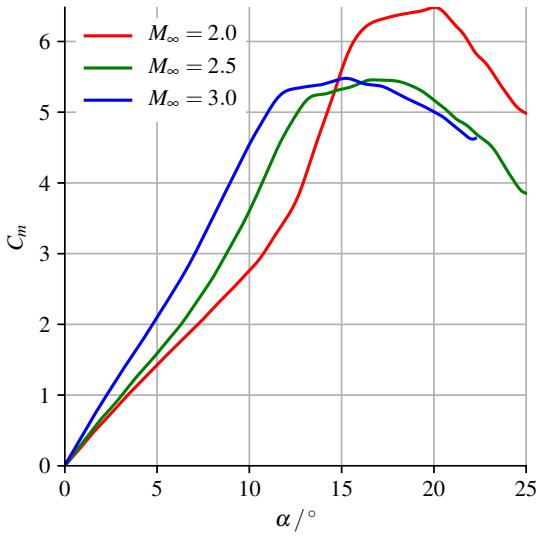

(b) Pitching-moment coefficient

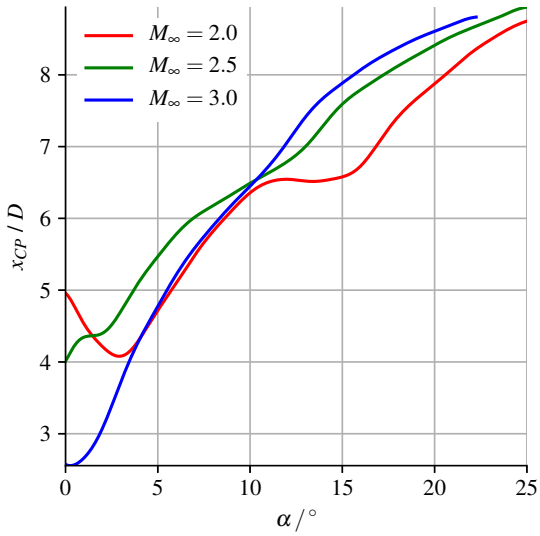

(c) Centre of pressure

Fig. 5.5 Reference data: body-alone experimental results from Tuling [30].

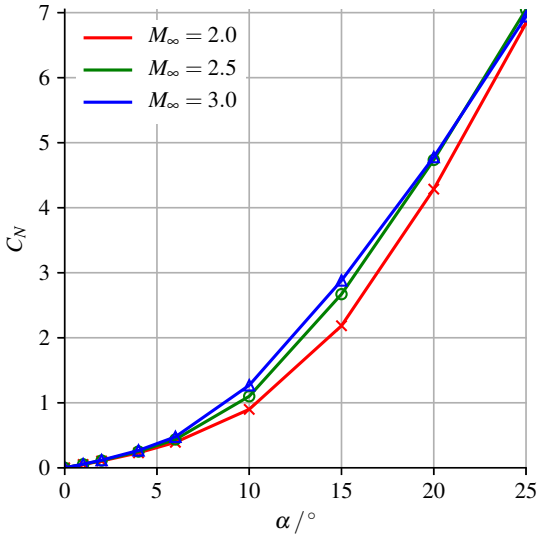

(a) Normal-force coefficient

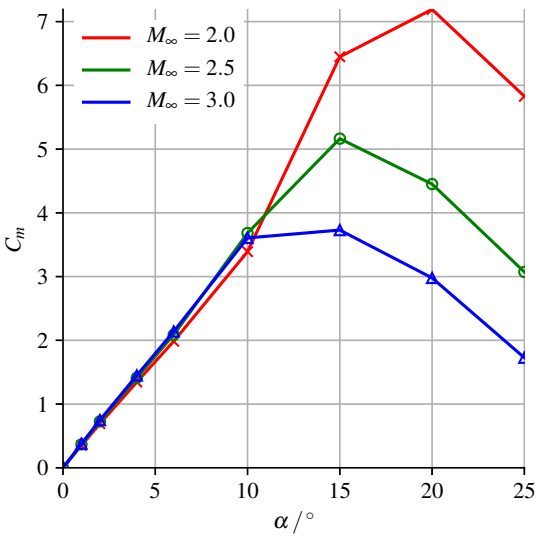

(b) Pitching-moment coefficient

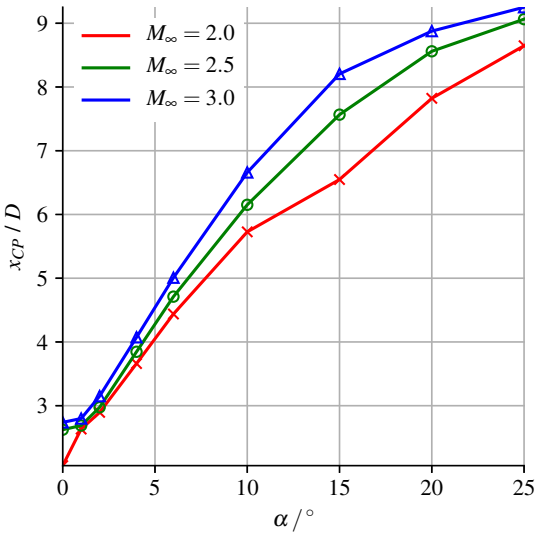

(c) Centre of pressure

Fig. 5.6 Reference data: body-alone computational (RANS) results from Tuling [30].

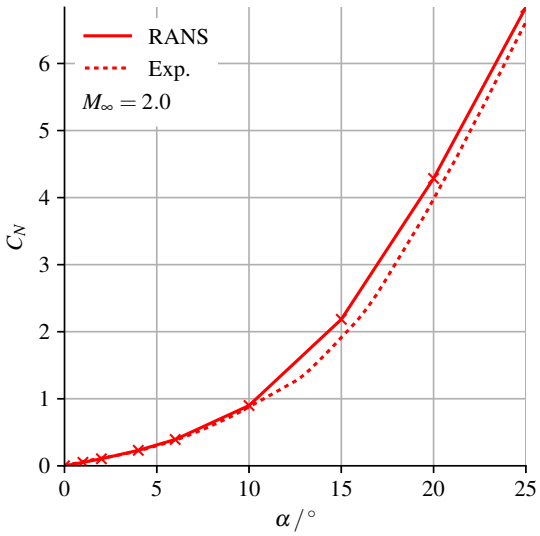

(a) Normal-force coefficient

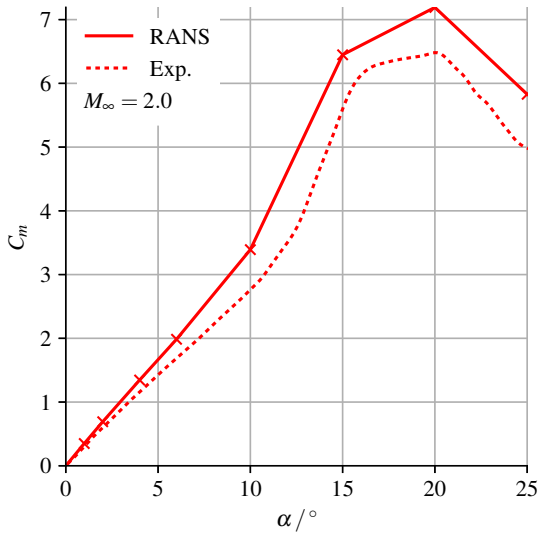

(b) Pitching-moment coefficient

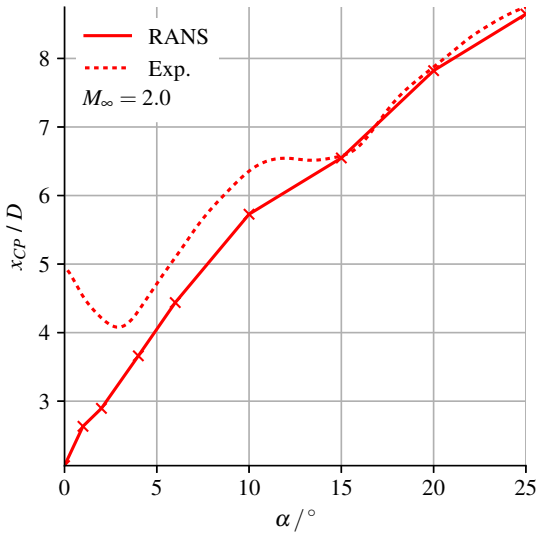

(c) Centre of pressure

Fig. 5.7 Reference data: body-alone results at $M_\infty = 2.0$ from Tuling [30].

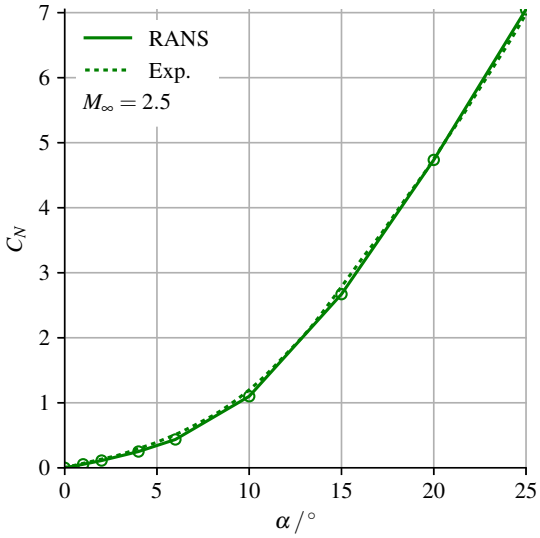

(a) Normal-force coefficient

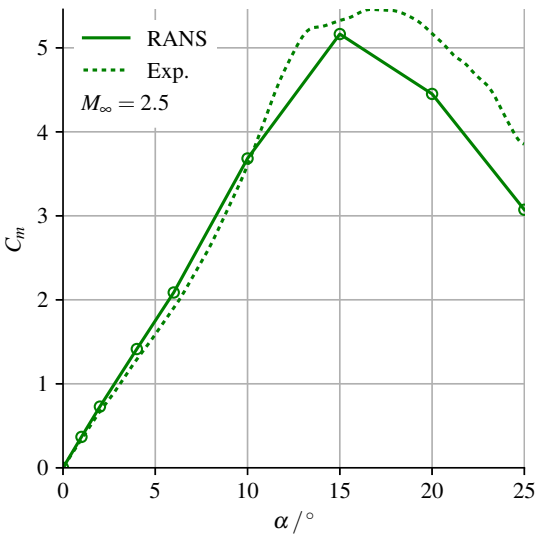

(b) Pitching-moment coefficient

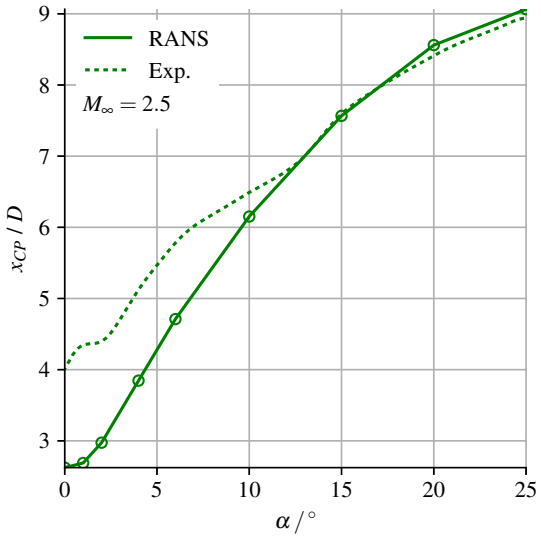

(c) Centre of pressure

Fig. 5.8 Reference data: body-alone results at $M_\infty = 2.5$ from Tuling [30].

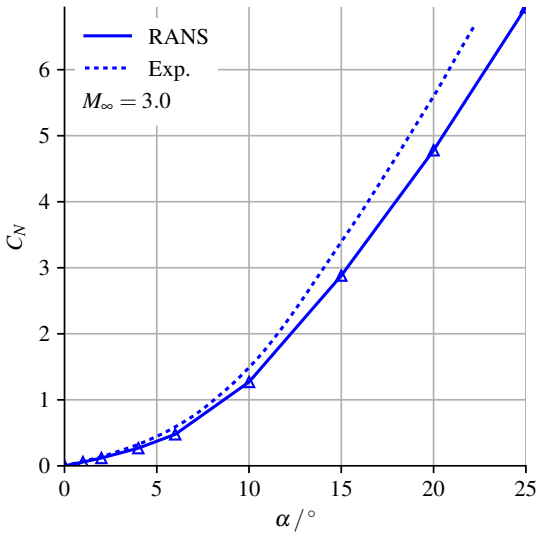

(a) Normal-force coefficient

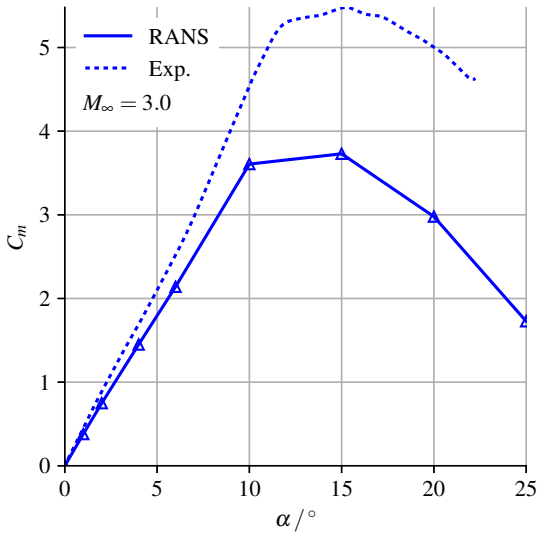

(b) Pitching-moment coefficient

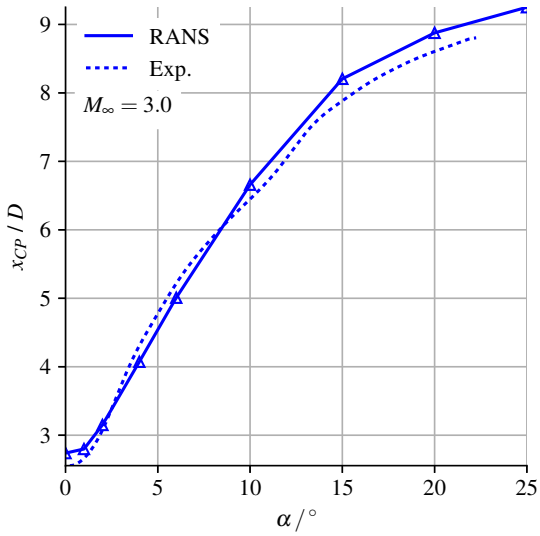

(c) Centre of pressure

Fig. 5.9 Reference data: body-alone results at $M_\infty = 3.0$ from Tuling [30].

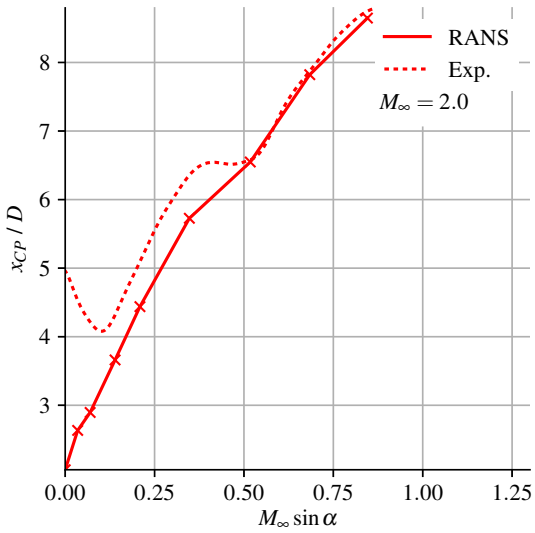

(a) $M_\infty = 2.0$

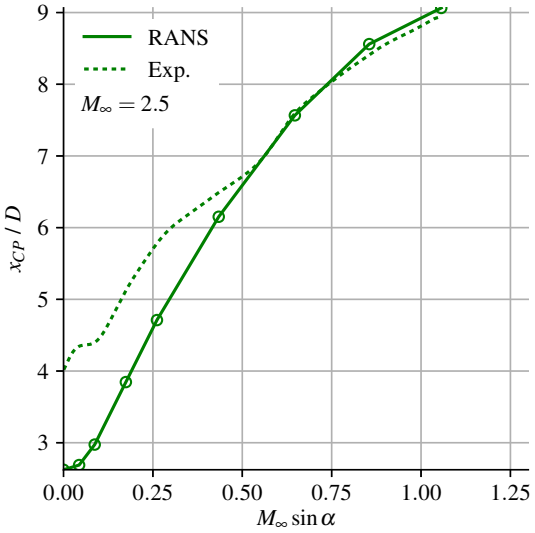

(b) $M_\infty = 2.5$

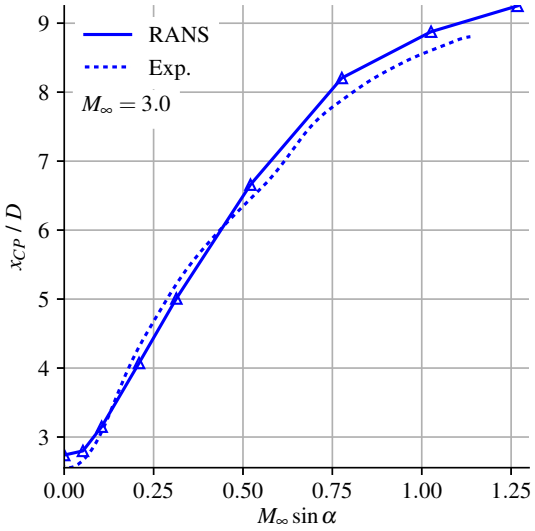

(c) $M_\infty = 3.0$

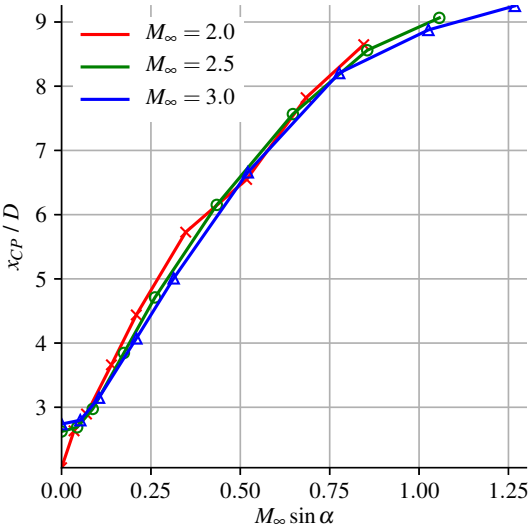

(d) RANS trends

Fig. 5.10 Reference data: body-alone centre-of-pressure results from Tuling [30].

5.1.3 Test Matrix

The parameter space of the present study is defined by four variables. These variables, their ranges, and motivation for the selection of these ranges, are introduced below:

- The freestream Mach number, M_∞:

  $M_\infty = [2.0, 2.5, 3.0]$

  To facilitate comparison with the reference data from Tuling [30], the same set of M_∞ was used in the present study. Moreover, the definition of the freestream conditions of Tuling [30], given in Table 5.3, has been repeated.

- The freestream angle-of-attack, α:

  $\alpha = [0, 2, 4, 6, 8, 10]$

  As discussed in Section 5.1.2, the range of angles-of-attack considered here has been restricted to $0° \leq \alpha \leq 10°$. This was largely to avoid the interaction of multiple body-shed vortices with the control surface. The interval between angles-of-attack of Tuling [30] has been repeated. This is with the exception of $\alpha = 8°$, which was not included in the study by Tuling [30].

- The mode-shape of deformation for the leeside control surface:

  Mode 1: first bending, Mode 2: first torsion, Mode 3: second bending

  Only the first three mode-shapes were considered in the present study. It is the objective of the present study to investigate the application of Euler-based LPT to a control surface subject to an interference flowfield. The simple deformation patterns of the first three modes allows the effect of flowfield-interaction to stand out from effects due purely to changes in geometry.

- The maximum out-of-plane displacement for the given mode-shape, δ.

  $\delta = [0\,\text{mm}, 5\,\text{mm}, 10\,\text{mm}]$

  The values (and increment) used for δ were chosen as nominal values. It was decided to use the same maximum out-of-plane displacement for each mode-shape for the sake of consistency when considering the interaction of control-surface deformation with the interference flowfield. In order to accentuate this interaction, moderate to large deformations were used. The tip displacement (as percentage of the span) and tip twist associated with these values of δ have been introduced in Table 5.1.

Table 5.5 $M_\infty \sin\alpha$ parameter space

α / $^\circ$	$M_\infty = 2.0$	$M_\infty = 2.5$	$M_\infty = 3.0$
0	0	0	0
2	0.07	0.09	0.10
4	0.14	0.17	0.21
6	0.21	0.26	0.31
8	0.28	0.35	0.42
10	0.35	0.43	0.52

Some considerations regarding the angle-of-attack range and the suitability of an Euler formulation in this range follow. In particular, the roles of viscosity and turbulence (which are absent in an Euler formulation) in this range are considered. The mechanism of vortex-shedding from the body is dependent on the crossflow Mach number, $M_c = M\sin\alpha$. The variation of $M_\infty \sin\alpha$ over the parameter space considered is shown in Table 5.5. For sufficiently high freestream crossflow Mach numbers, typically $M_\infty \sin\alpha \geq 0.5$, acceleration of the flow around the body in the crossflow plane leads to local regions of $M_c \geq 1$. This leads to a normal shock forming at the body surface in the crossflow plane. In viscous flows, the driving mechanism of vortex formation is boundary-layer separation at the shock, forced by the adverse pressure gradient of the body-crossflow shock. In inviscid flows, the rotationality introduced by the shock is the driving mechanism of vortex formation. Although the overall structure of the flowfield is similar in either case, the mechanisms for vortex formation differ. The influence of turbulence and viscosity in the high-strain, separated leeside flow is not modelled in an Euler formulation. The formation of secondary vortices and separated regions on the body at $\alpha > 10^\circ$ would also not be modelled in an inviscid formulation.

The suitability of an Euler formulation in the upper half of the truncated α-range in the absence of a body-crossflow shock is not guaranteed. Vortex formation still occurs, but the difference in the flowfield structure between a viscous formulation and an inviscid formulation becomes more pronounced. The driving mechanism of vortex formation in the viscous case is boundary-layer separation due to the adverse pressure gradient in the crossflow plane. In the inviscid case, accumulation of rotationality due to the entropy gradients introduced by the nose-shock leads to vortex formation. The vortices formed in the inviscid case are significantly weaker than their viscous-case counterparts for the same M_∞ and α. The difference in overall structure of the flowfield in the absence of SBLI becomes pronounced.

In summary, an Euler formulation may be expected to be best suited at small incidences at which no separation would occur in a viscous formulation. Under these conditions, whilst the

momentum deficit in the leeside wake would not be modelled, no prominent flow structures would be lacking in the Euler formulation. Good modelling of the flowfield structure may also be expected at higher incidences when vortex formation is driven by the body-crossflow shock. However, this only occurs in the upper M_∞ and α limits of the parameter space considered.

5.1.4 Numerical Methods

Flow Solver

A density-based compressible flow solver named `HiSA` was developed for `OpenFOAM` by Heyns* and Oxtoby† [213] of the Council for Scientific and Industrial Research of South Africa. The decision to utilize this solver was motivated as follows:

- The application of the solver to various scenarios of high-speed flows and its validation was part of a larger project of work at the time,
- The solver and `OpenFOAM` are open source, with no license fees associated with their use.

The Lax-Friedrichs flux-splitting method was used. A cell-limited least-squares interpolation was used for gradient terms. A Van Leer scheme was used for reconstruction. The resulting formulation was second-order. A mesh-motion solver based on cell-centre solid-body rotation stresses was used to obtain the meshes for the deformed control-surface cases. Steady-state analysis was conducted for all cases.

Local Piston Theory Formulation

The steady solution obtained for the undeformed control-surface was used as the mean-steady reference solution to which LPT was applied. The LPT formulation and coefficients used are repeated here for completeness. The pressure on the control surface following deformation was computed as

$$p = p_m + \gamma \left[c_1 \left(\frac{w}{a_m} \right) + c_2 \left(\frac{w}{a_m} \right)^2 + c_3 \left(\frac{w}{a_m} \right)^3 \right], \tag{5.1}$$

*`jheyns@csir.co.za`
†`ooxtoby@csir.co.za`

where the subscript "m" denotes the mean-steady values for the undeformed case. The downwash definition used was

$$w = -\mathbf{V_m} \cdot \hat{\mathbf{n}}, \tag{5.2}$$

where $\mathbf{V_m}$ is the fluid velocity vector obtained from the mean-steady solution for the undeformed case, and $\hat{\mathbf{n}}$ is the unit normal vector following deformation. An investigation of the influence of the order of pressure-equation and of the coefficient definition on the LPT prediction was performed. The former was achieved through truncating Eq. (5.1) to the desired order. The latter involved the use of various definitions for c_1, c_2, and c_3. The various definitions of these coefficients are repeated in Tables 5.6 to 5.8. The coefficients are computed using the local mean-steady Mach number M_m and $m_m = \sqrt{M_m^2 - 1}$. The origin of these definitions and their theoretical bases have been discussed in Chapter 3.

Table 5.6 Local piston theory coefficients used in the present work: first order.

Source	c_1
Lighthill [88]	1
Van Dyke [104]	M/m
Donov [105]	M/m

Table 5.7 Local piston theory coefficients used in the present work: second order.

Source	c_2
Lighthill [88]	$(\gamma+1)/4$
Van Dyke [104]	$[M^4(\gamma+1)-4m^2]/4m^4$
Donov [105]	$[M^4(\gamma+1)-4m^2]/4m^4$

Table 5.8 Local piston theory coefficients used in the present work: third order.

Source	c_3
Lighthill [88]	$(\gamma+1)/12$
Van Dyke [104]	0
Donov [105]	$[8-12M^2+10(\gamma+1)M^4+(2\gamma^2-7\gamma-5)M^6+(\gamma+1)M^8]/12Mm^7$

5.1.5 Mesh

A preliminary mesh configuration study was conducted in order to achieve balance between:

- Solution convergence and stability,
- Resolution of flow features,

subject to the hardware constraints of the workstation used. A structured grid was used. The multi-block definition chosen is defined in Figs. 5.11 to 5.13. The same block definition was used in the body-alone and the full-vehicle cases, with the fin-thickness blocks absent in the body-alone mesh. This was done in order to minimize grid-related differences between the body-alone and full-vehicle cases. Similarly, the axial block-definition from the full-vehicle case was used in the wing-alone mesh. This is seen from Figs. 5.12 and 5.13. The chief difference (aside from geometry) between the full-vehicle and wing-alone grids was in the crossflow-plane meshing strategy. The full-vehicle case utilized cylindrical block definitions to conform with the body-surface. The wing-alone case utilized rectangular blocks to better align the mesh with anticipated flow gradients. These differences are illustrated in Fig. 5.11. The resulting meshes are depicted in Figs. 5.14 and 5.15.

The body-alone and full-vehicle domains span $0.1225L$ upstream of the body, where L is the body length. The outlet is $1.5L$ downstream of the body. The farfield boundary is located $0.75L$ from the wing tips. The cell count for each mesh is listed in Table 5.9. A refinement factor of 2 was used between each level of fineness.

Table 5.9 Mesh cell counts

Fineness	Body-alone	Wing-alone	Full-vehicle
Coarse	62 464	41 040	63 328
Medium	499 712	324 864	503 168
Fine	3 997 696	2 585 088	4 011 520

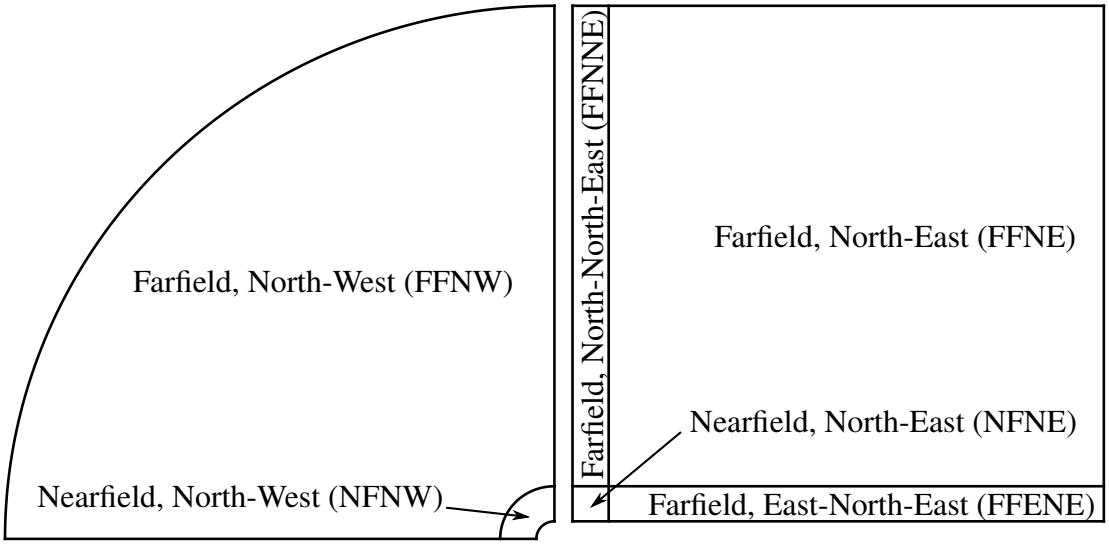

Fig. 5.11 Cross-flow multi-block definition as viewed down the positive x-axis. The body-alone and full-vehicle definitions are shown on the left. The wing-alone block definition is shown on the right.

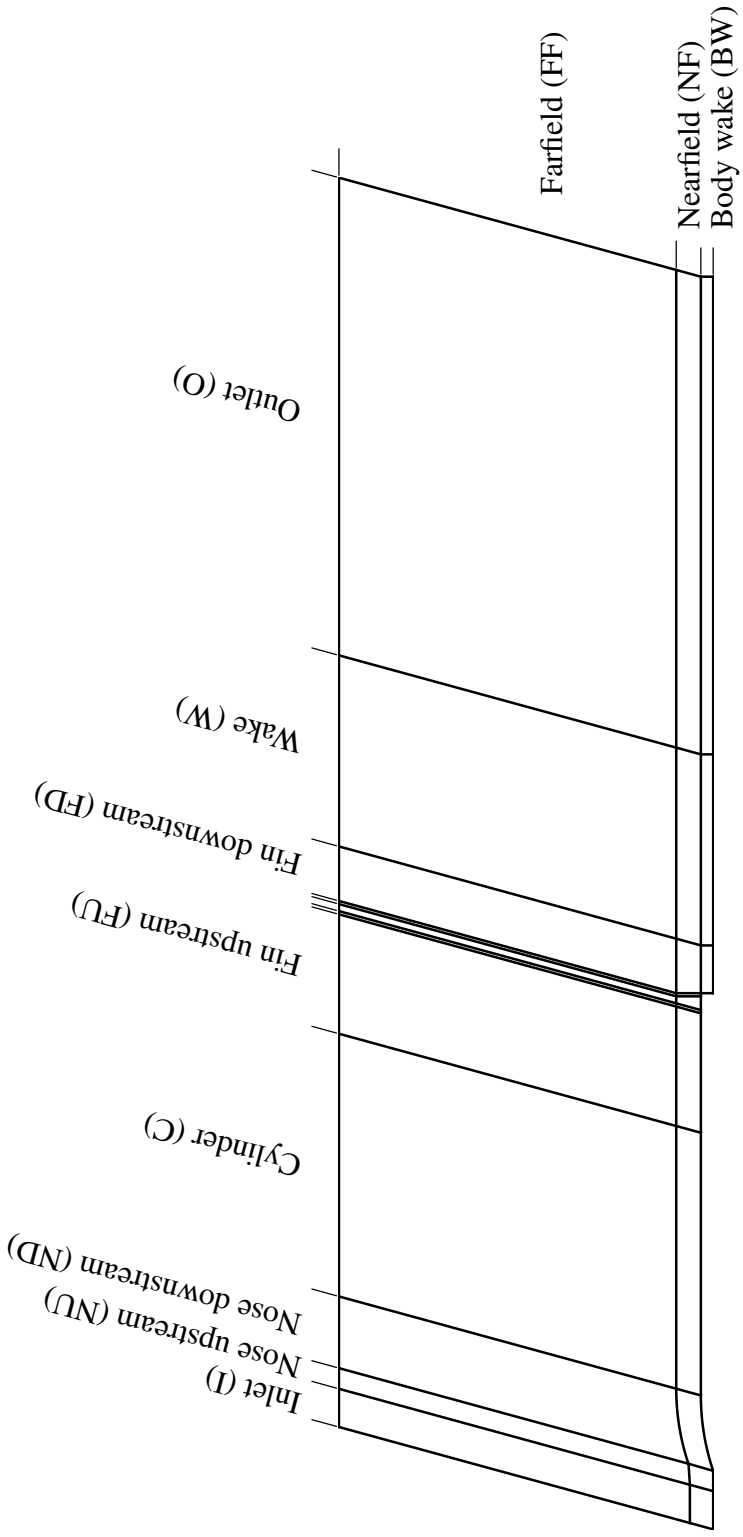

Fig. 5.12 Body-alone and full-vehicle multi-block definition: radial and axial blocks.

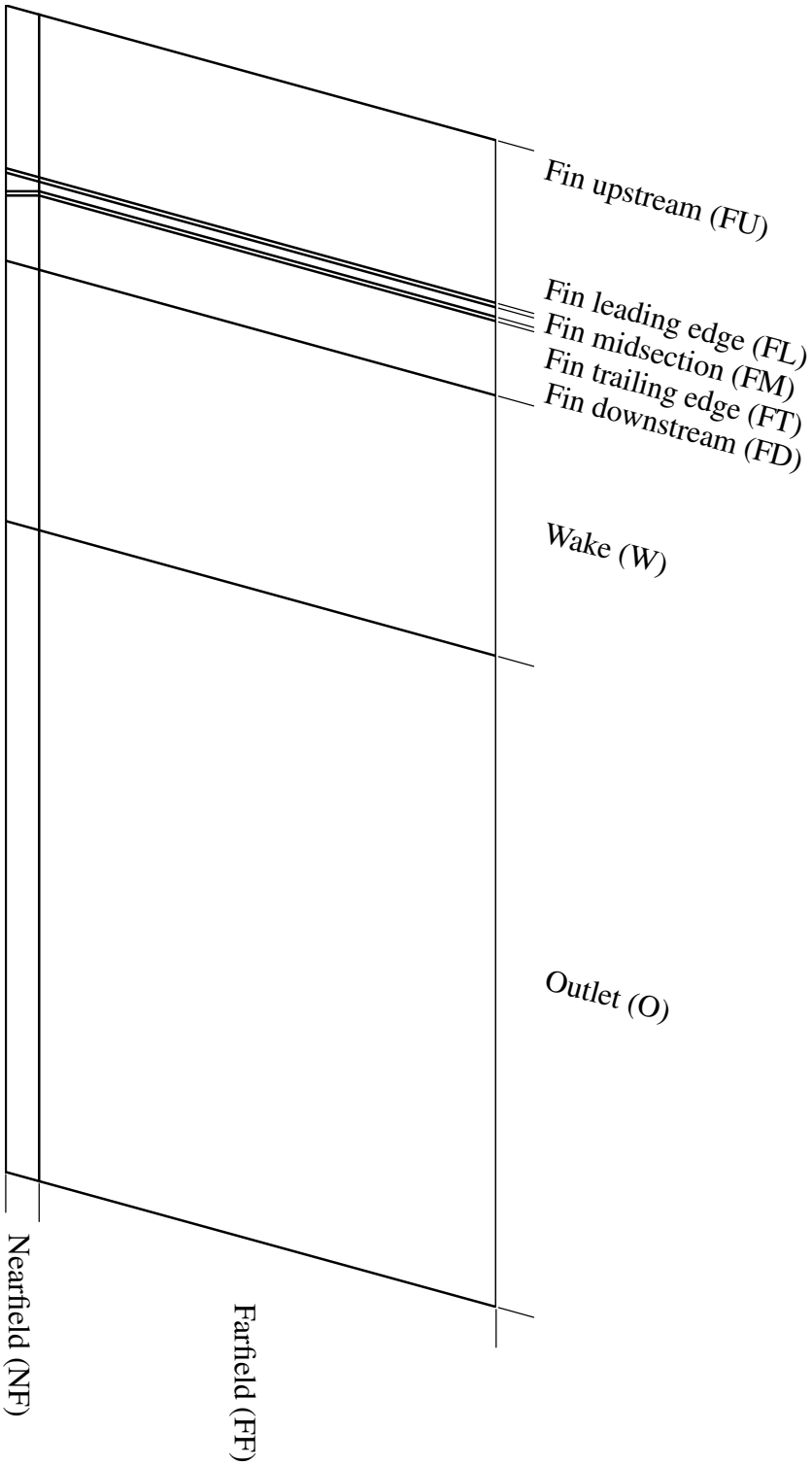

Fig. 5.13 Wing-alone multi-block definition: *xz*- and *xy*-plane block definition.

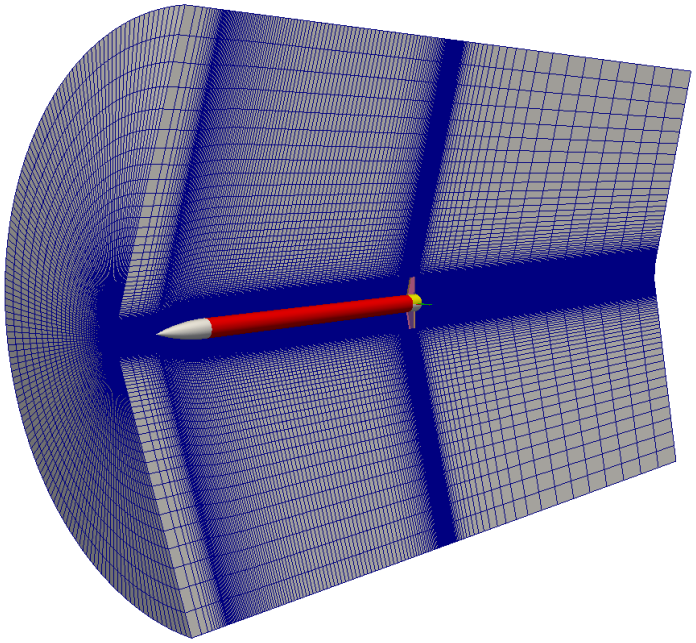

(a) Body-alone and full-vehicle

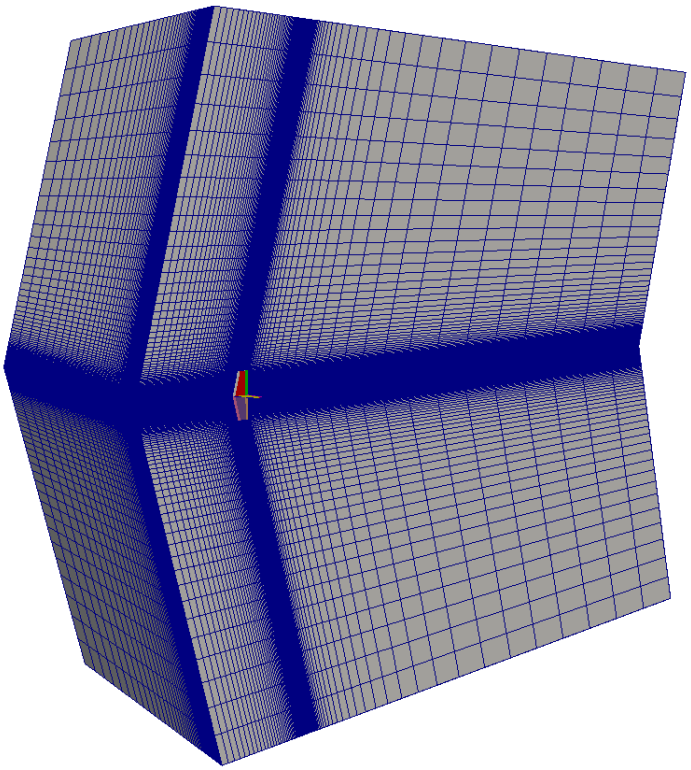

(b) Wing-alone

Fig. 5.14 Volume mesh with $y < 0$ omitted for clarity.

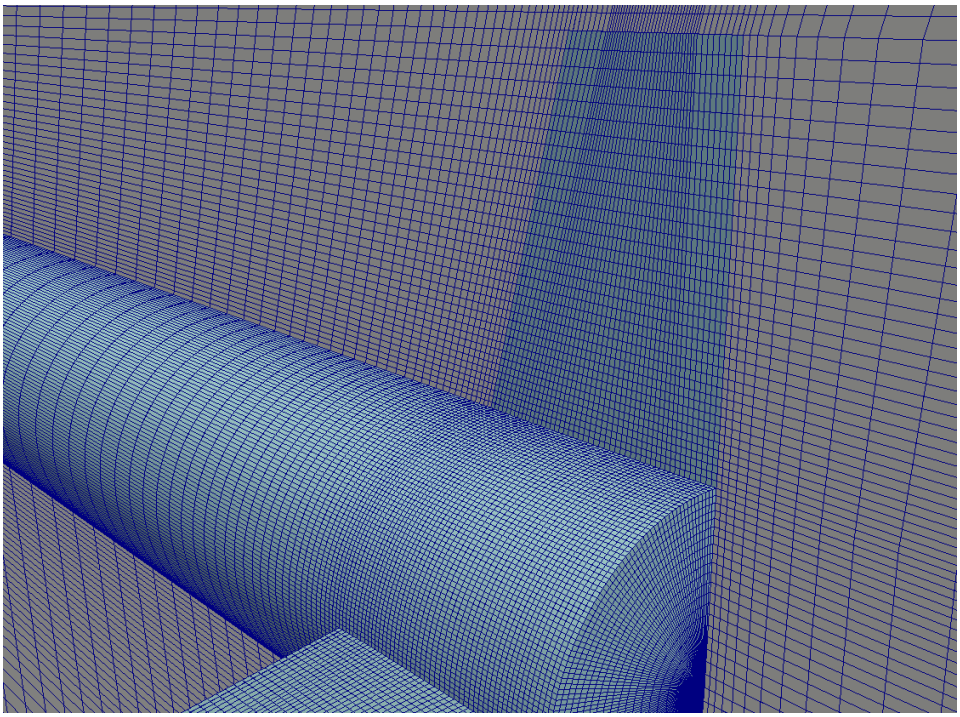

(a) Body-alone and full-vehicle

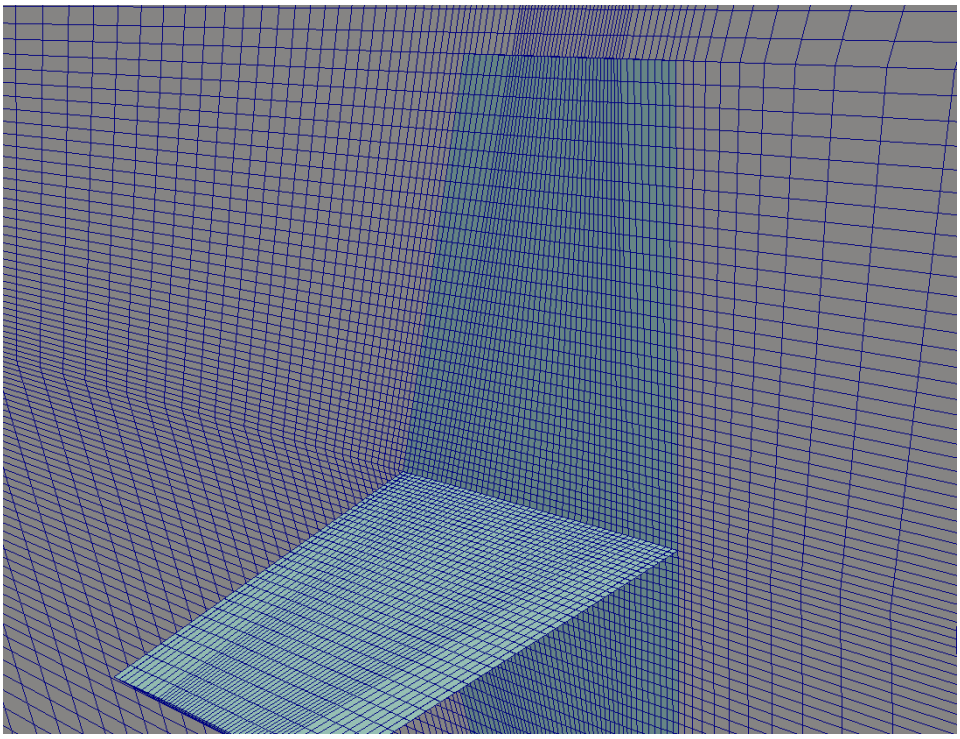

(b) Wing-alone

Fig. 5.15 Surface mesh with focus on the control surface. The volume mesh in the plane $y = 0$ is also shown.

5.2 Body-Alone Aerodynamics

As stated in Section 5.1, the primary purpose of the body-alone case is verification and validation of the modelling. To this end, Section 5.2.1 will introduce the mesh-independence study. The verification of the numerical solver is the topic of the first portion of Section 5.2.2. The second portion of the same section will focus on the physics validation. A discussion of the overall physics and of the verification and validation will be given in Section 5.2.3.

A number of general remarks are offered with regards to the figures to be introduced in Section 5.2:

- Except where explicitly noted otherwise, the results presented were obtained using the `OpenFOAM` solver discussed in Section 5.1.4,
- Results depicting the location of the centre-of-pressure (x_{CP}) will typically not be shown at $\alpha = 0°$. This is because of the inflation of numerical error when a small number (C_m) is divided by a similarly small number (C_N).

5.2.1 Mesh-Independence Study

The details of the body-alone mesh have been provided in Section 5.1.5, with cell counts provided in Table 5.9 and depictions of the mesh provided in Figs. 5.11, 5.12, 5.14 and 5.15. It is to be noted that the body-alone and full-vehicle meshes are nearly identical. The only differences arise through the insertion of thickness blocks for the wings in the latter case. The mesh-independence study for the body-alone case therefore also applies to the body-related physics and flow features of the full-vehicle case.

The variation with mesh fineness of the normal-force coefficient (C_N), the pitching-moment coefficient (C_m), and the axial location of the centre-of-pressure (x_{CP}) is depicted in Figs. 5.16 to 5.18, respectively. These figures are discussed below:

- Figure 5.16: C_N – a significant difference between results on the coarse and medium meshes is noted. This is particularly prominent at $M_\infty = 2.0$ and at higher incidences. The difference between the coarse and medium results reduces with increasing Mach number, but remains noticeable at $M_\infty = 3.0$. The coarse mesh over-predicts C_N and leads to a higher nonlinear (with α) component. This is likely due to the numerical viscosity of the mesh. Fairly close agreement is noted between the medium and fine meshes. This agreement similarly improves with increasing Mach number,
- Figure 5.17: C_m – once again, noticeable differences between the coarse and medium results are observed. Here, C_m is somewhat under-predicted by the coarse mesh. This

suggests that the centre of pressure is closer to the midpoint of the body. This is supported by the results of Figure 5.18. Largely the same trends are noted as were observed in relation to C_N,

- Figure 5.18: x_{CP} – prominent differences in x_{CP} are noted between the meshes. Most significantly, the difference between the medium and fine meshes is noticeable. This latter difference is typically of the order of $0.5D$. On the coarse mesh, x_{CP} is typically $1.5D$ greater than on its value on the fine mesh. It is of interest to note that on the fine mesh, x_{CP} is predicted to be approximately at the centre of the nose (before the onset of crossflow shocks on the cylindrical body). This is consistent with an inviscid physics formulation, in which normal force is only created through unsteadiness or changes in the cross-sectional diameter. The sharp rearward shift in x_{CP} noted at the upper end of the α range at $M_\infty \geq 2.5$ is due to the formation of crossflow shocks further aft on the body.

These results have been quantified in terms of the grid convergence index (GCI) of Roache [214]. The maximum error observed over the M_∞-α parameter space is given in terms of the GCI for each load in Table 5.10 below.

Table 5.10 Grid convergence index for body-alone loads

Fineness	GCI (C_N)	GCI (C_m)	GCI ($x_{CP}\,/\,D$)
Medium	10%	6%	50%
Fine	4%	3%	25%

It is remarked here that significant improvement in the GCI (such that values of $\approx 1\%$ were achieved for all loads) was observed following the onset of the crossflow shocks at $M_\infty = 3$ with $\alpha \geq 8°$. This emphasizes that shock-dominated physics were effectively mesh-independent. However, the (secondary) effects of flow rotationality due to weak curvature of the bow shock exhibited a degree of mesh dependence.

In conclusion, in light of the close agreement between the medium and fine mesh results, the medium mesh was used in the full-vehicle case. While some improvement in the resolution of the body-shed vorticity would be achieved through use of the fine mesh, the medium mesh modelled these flow features at significantly lower computational cost. The medium mesh has slightly higher numerical viscosity (as evidenced by the higher C_N and more rearward x_{CP}) and thus results in less-sharp flow gradients.

All remaining figures in this chapter are for results obtained on the medium mesh.

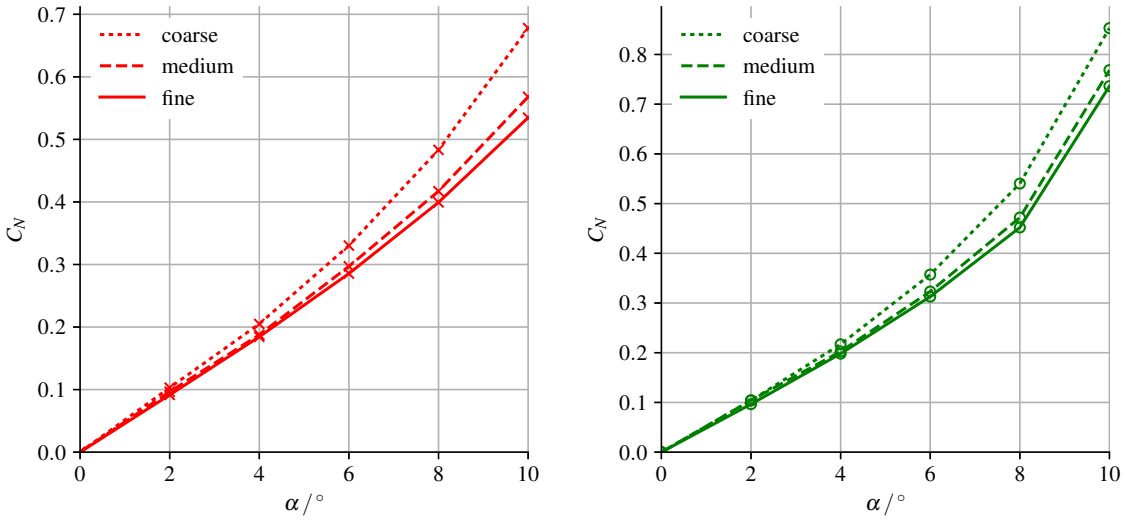

(a) $M_\infty = 2.0$

(b) $M_\infty = 2.5$

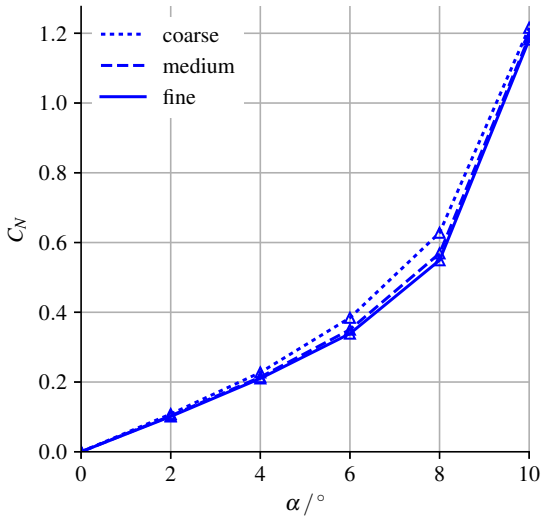

(c) $M_\infty = 3.0$

Fig. 5.16 Body-alone mesh-independence results: normal-force coefficient C_N.

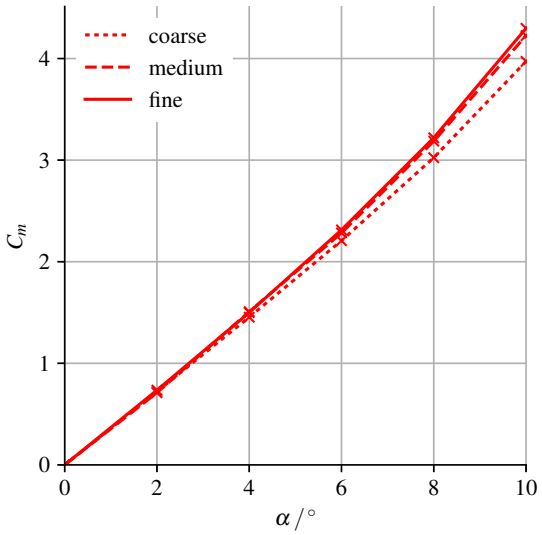

(a) $M_\infty = 2.0$

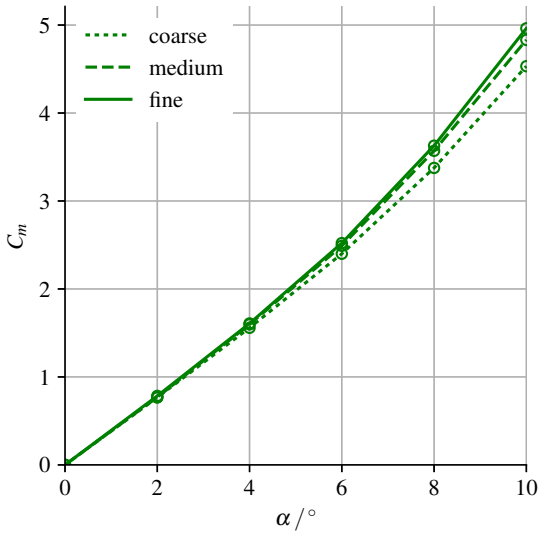

(b) $M_\infty = 2.5$

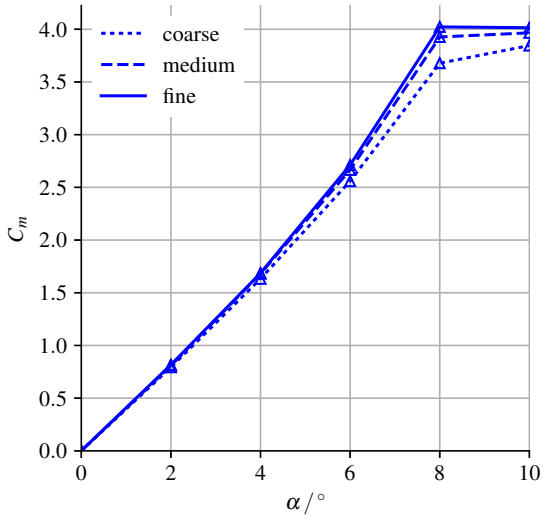

(c) $M_\infty = 3.0$

Fig. 5.17 Body-alone mesh-independence results: pitching-moment coefficient C_m.

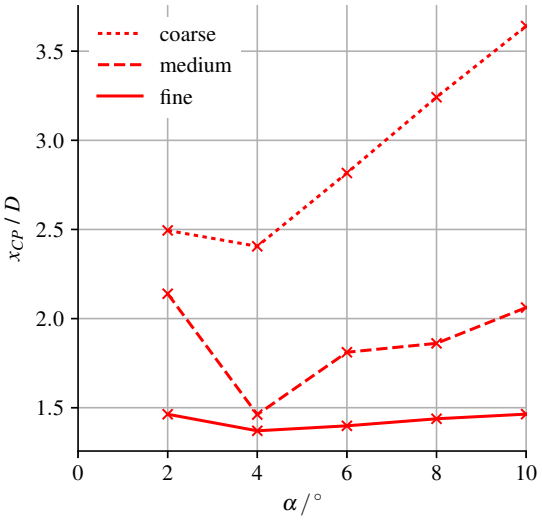

(a) $M_\infty = 2.0$

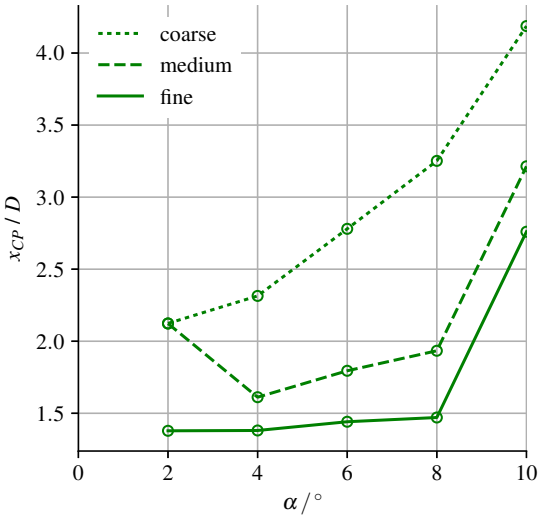

(b) $M_\infty = 2.5$

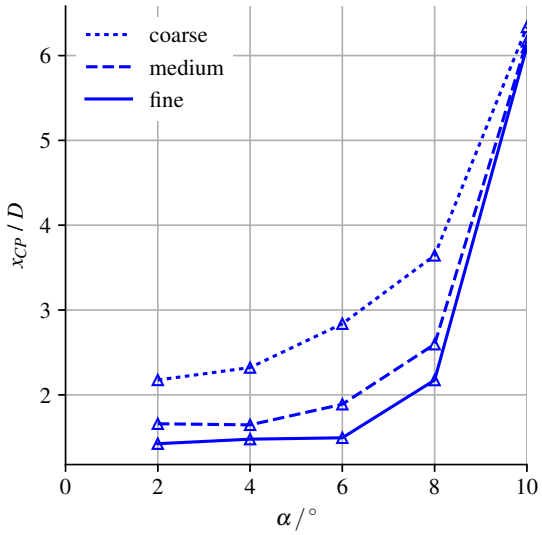

(c) $M_\infty = 3.0$

Fig. 5.18 Body-alone mesh-independence results: centre-of-pressure location x_{CP}.

5.2.2 Results and Validation

Solver Verification

Verification of the numerical solver implemented in `OpenFOAM` was performed through comparison of results obtained by the solver with those obtained in `Fluent` on the same mesh. Where translatable, the same numerical settings (read: discretization schemes and relaxation factors) were used. The results are compared in Figs. 5.19 to 5.21. The following remarks are made:

- Figure 5.19: C_N – good agreement between the solvers is noted. Differences are most noticeable at $\alpha = 10°$ at the lower Mach numbers. Comparison to Fig. 5.16 shows that the Fluent results on the medium mesh are closer to the `OpenFOAM` results obtained on the fine mesh. It is known that `OpenFOAM` offers greater control over the solution parameters, while `Fluent` maintains closed-source code aimed at solution stability and accelerated convergence. The relatively minor differences in the results may be attributed to these factors,

- Figure 5.20: C_m – broadly the same observations may repeated here as were made relating to Fig. 5.19. It is noted that the best agreement in C_m is obtained at $M_\infty = 2.0$. Differences in prediction are noted at the higher end of the α range at $M_\infty \geq 2.5$, and may be related to the onset of crossflow shocks. It is observed that the `OpenFOAM` predictions are slightly lower, suggesting a more rearward x_{CP}. This is seen in Fig. 5.21. Once again, comparison to Fig. 5.17 shows that the `Fluent` results are closer to the fine-mesh `OpenFOAM` results,

- Figure 5.21: x_{CP} – the `Fluent` results are typically within $0.5D$ more forward than the `OpenFOAM` results on the medium mesh. This once again suggests that the `Fluent` results for the medium mesh are comparable to the `OpenFOAM` results on the fine mesh.

It may thus be concluded that while minor differences between the `OpenFOAM` and `Fluent` results are noted, the `OpenFOAM` solver may essentially be considered to be verified against the Fluent solution for the purposes of this study. The same physical trends were noted, with the differences pointing towards a less-forgiving solver in `OpenFOAM`.

Physics Validation

Validation of the physics modelled by the Euler formulation was performed through comparison of the inviscid results obtained (on the medium mesh) in `OpenFOAM` with reference

data from RANS solutions and experiment from Tuling [30]. The results are compared in Figs. 5.22 to 5.24. The figures are discussed below:

- Figure 5.22: C_N – generally good agreement between RANS and experiment is noted. Slight over-prediction by RANS is noted at $M_\infty = 2.0$, with this trend being reversed at higher Mach numbers. This under-prediction of normal-force at higher Mach numbers may be attributed to a number of possible sources including shortcoming in:
  - boundary-layer and separation modelling,
  - SBLI modelling,
  - modelling of the separated vortical flow.

  Regardless, the trends suggest that RANS provides an accurate model of the underlying physics and general flow features.

  This is not mirrored in the results from the Euler formulation. Here, good agreement in the load-slope is obtained only for $\alpha \leq 2°$. Thereafter, the inviscid prediction increasingly under-predicts the normal force. The "missing" load is associated with nonlinear (with α) vortex-induced loading. This shows the impact of "missing physics" (viscosity) in the inviscid model. The result is inaccurate modelling of the physical mechanism for vortex development. This is reflected in the difference between Euler, RANS, and experimental results at $\alpha \geq 8°$ at $M_\infty = 3.0$. Here, while good agreement is achieved in the load slope, a notable offset is observed. This may be attributed to an under-prediction of the strength of the vortices. This is largely due to incorrect modelling of the mechanism by which they are produced.

- Figure 5.23: C_m – similar remarks apply here. The onset of the crossflow shocks in the Euler formulation is more obvious. Consideration of $\alpha > 6°$ at $M_\infty = 3.0$ reflects the fact that the crossflow shocks initially develop just aft of the nose, resulting in an increase in the slope of the pitching moment. As the incidence increases, the crossflow shock extends further aft along the cylindrical body, until it occupies the majority of the body length at $\alpha = 10°$. This is seen as an apparent reduction in the load slope relative to that exhibited at the initial onset of the forward-positioned crossflow shocks at $\alpha \approx 8°$.

  Similar sharp changes in the load slope are not observed for the RANS and experimental results. The more monotonic trends reflect the difference in the vortex-development mechanism. In particular, the boundary-layer separation and later SBLI results in a smoother progression of the load slope.

Finally, larger differences between RANS and experiment are noted than in the C_N prediction. Once again, this may be attributed to shortcomings in boundary-layer and separated-flow modelling. Nonetheless, RANS captures the key features of the underlying physics.

- Figure 5.24: x_{CP} – modelling deficiencies are shown quite well in this figure. Good agreement in the trends is obtained between RANS and experiment, particularly at $M_\infty = 3.0$ and at $\alpha \geq 4^\circ$ in general. At the lower Mach numbers, the offset of approximately $0.5D$ to $1D$ in x_{CP} reflects shortcomings in the mathematical modelling of the physical features. Nevertheless, the agreement in trends shows that these features are accounted for. The starkly different trends predicted by the Euler model shows that key components of the flow physics are not modelled. Nonetheless, improvement in the prediction is obtained at the upper limit of the $M_\infty \sin\alpha$ range considered. This is due to the onset of crossflow shocks around $M_\infty \sin\alpha \approx 0.5$, which effectively fix the separation point.

Overall, the physics validation yields the expected conclusions that for the parameter space considered of $M_\infty \sin\alpha < 0.5$, an inviscid (Euler) formulation has fundamental shortcomings in its physical modelling. This is manifested in a lack of boundary-layer separation and associated vortex lift at $M_\infty \sin\alpha < 0.5$. However, fairly good prediction is obtained at $\alpha \leq 2^\circ$, before significant vortex-development occurs or before a significant viscous wake develops.

The use of an Euler formulation is clearly not preferable for the purposes of accurate physics modelling and prediction over the parameter space considered in this study. Nevertheless, the mathematical basis for Euler-based LPT has been developed, as discussed in Chapter 4. For the purposes of evaluating Euler-based LPT as a valid reduction of the Euler equations, the modelling deficiencies of an Euler formulation relative to RANS are inconsequential. However, they do highlight fundamental physical features which must be accounted for in a RANS-based LPT formulation.

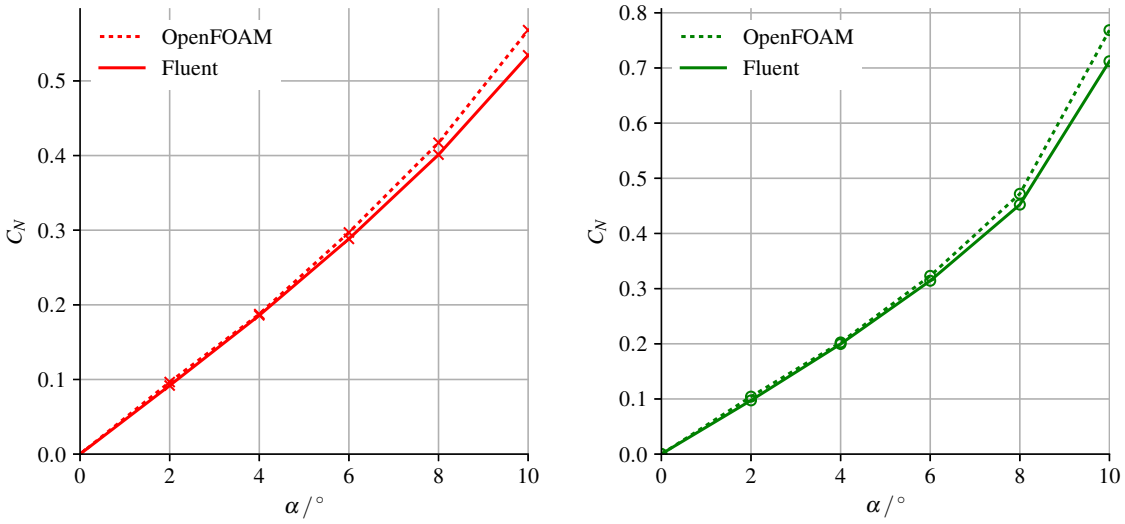

(a) $M_\infty = 2.0$ (b) $M_\infty = 2.5$

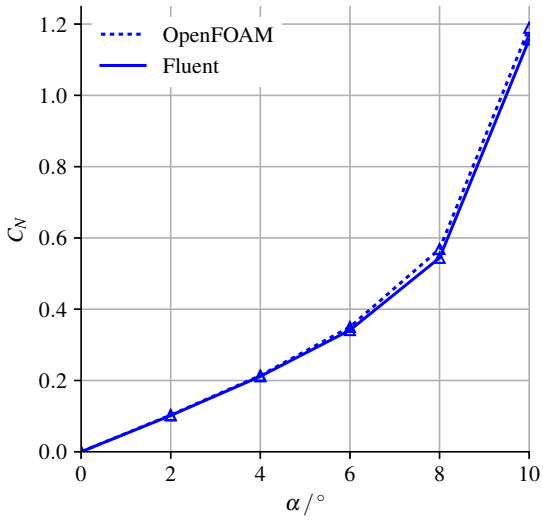

(c) $M_\infty = 3.0$

Fig. 5.19 Solver validation: normal-force coefficient C_N.

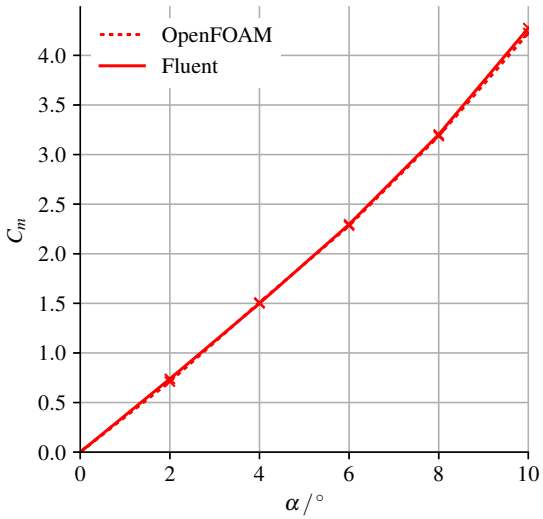

(a) $M_\infty = 2.0$

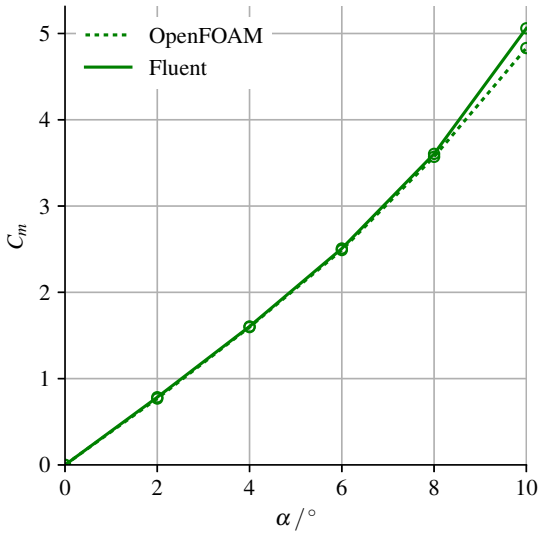

(b) $M_\infty = 2.5$

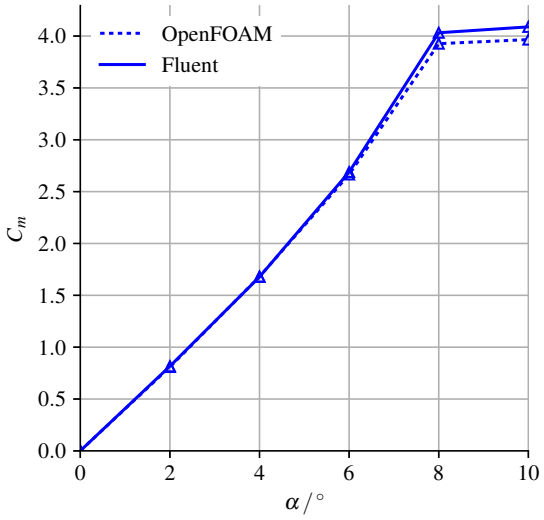

(c) $M_\infty = 3.0$

Fig. 5.20 Solver validation: pitching-moment coefficient C_m.

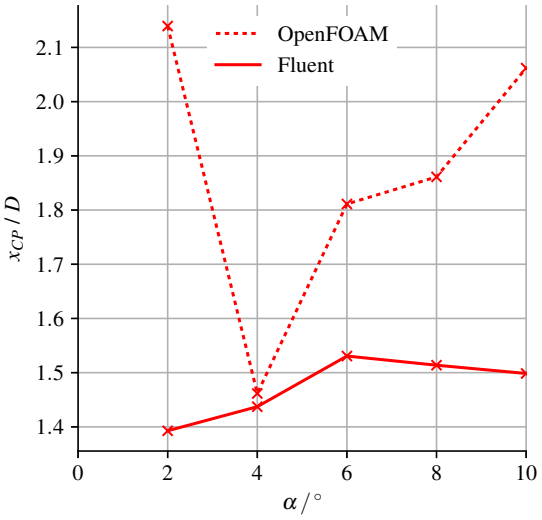

(a) $M_\infty = 2.0$

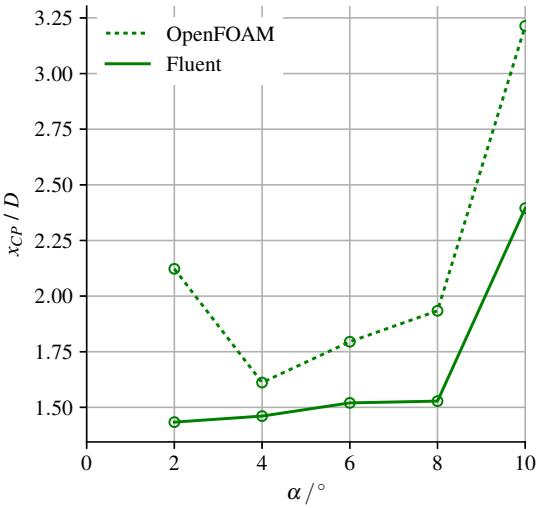

(b) $M_\infty = 2.5$

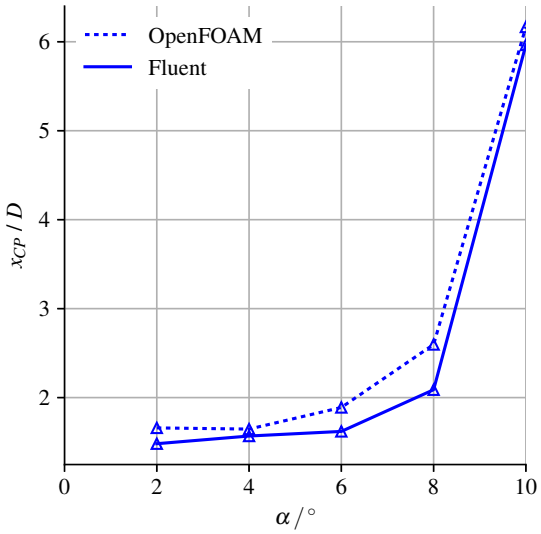

(c) $M_\infty = 3.0$

Fig. 5.21 Solver validation: centre-of-pressure location x_{CP}.

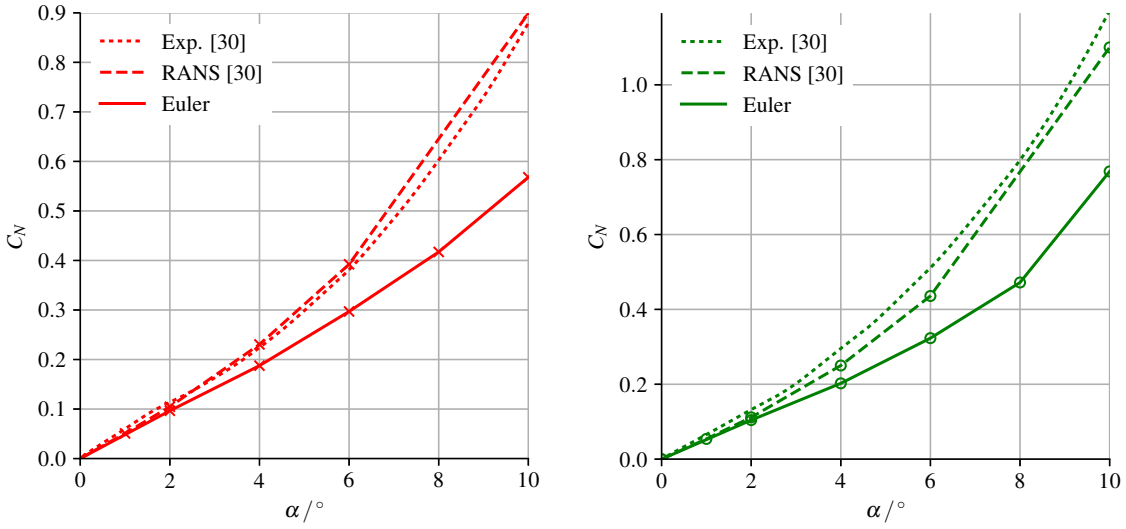

(a) $M_\infty = 2.0$ (b) $M_\infty = 2.5$

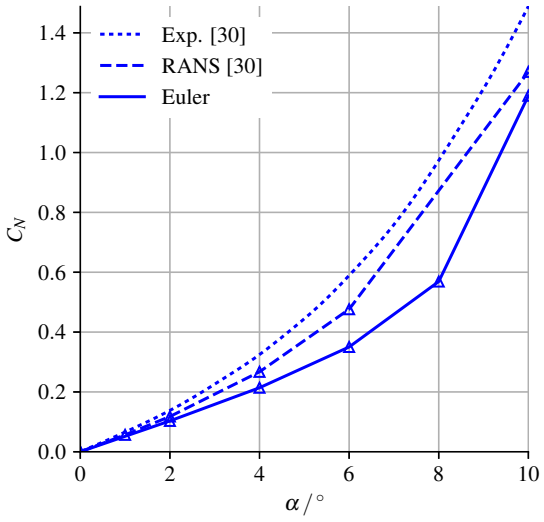

(c) $M_\infty = 3.0$

Fig. 5.22 Body-alone results validation: normal-force coefficient C_N.

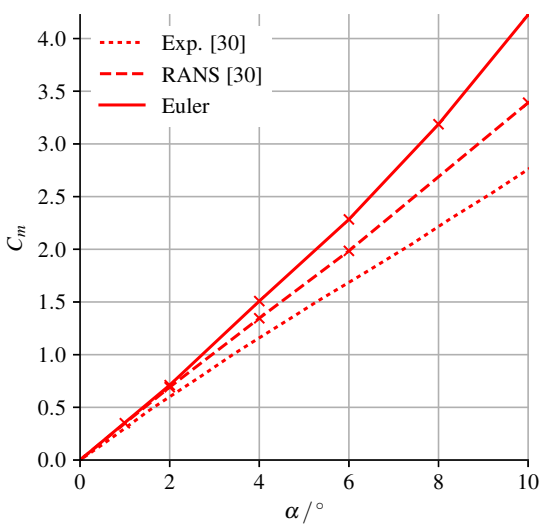

(a) $M_\infty = 2.0$

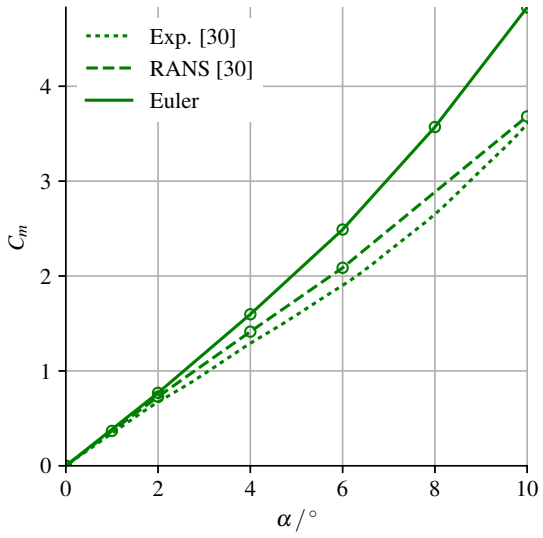

(b) $M_\infty = 2.5$

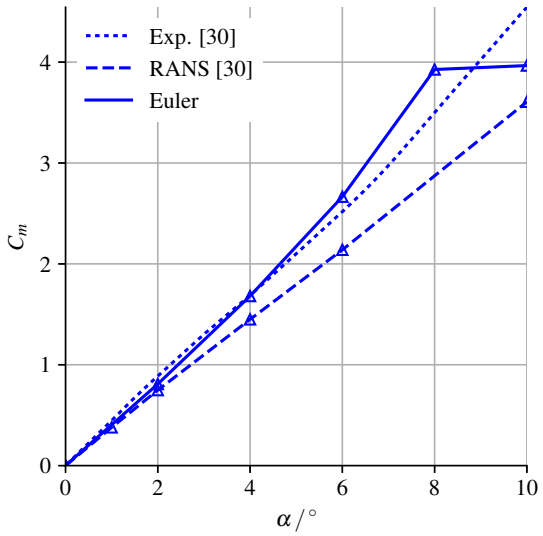

(c) $M_\infty = 3.0$

Fig. 5.23 Body-alone results validation: pitching-moment coefficient C_m.

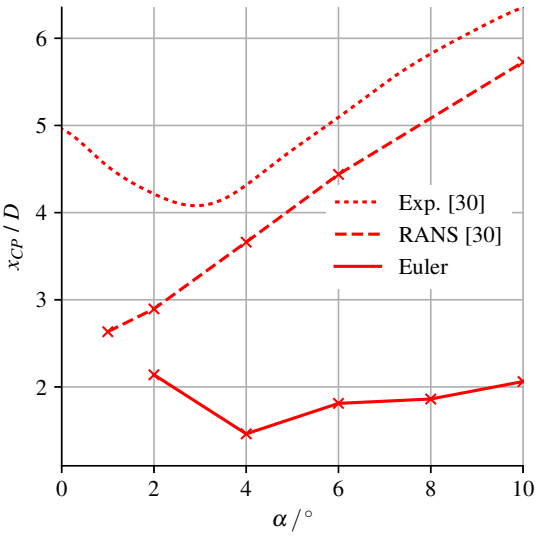

(a) $M_\infty = 2.0$

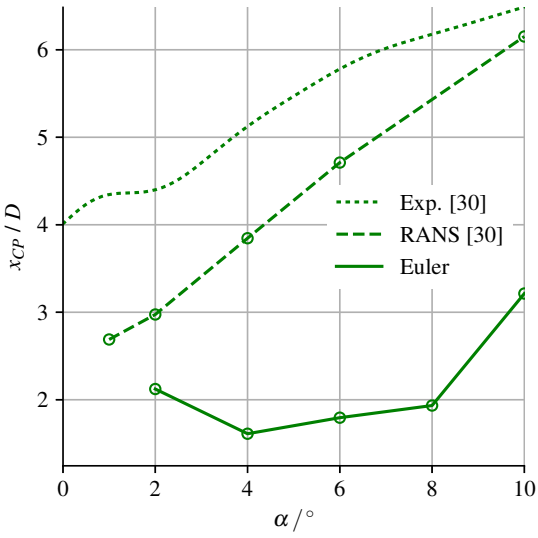

(b) $M_\infty = 2.5$

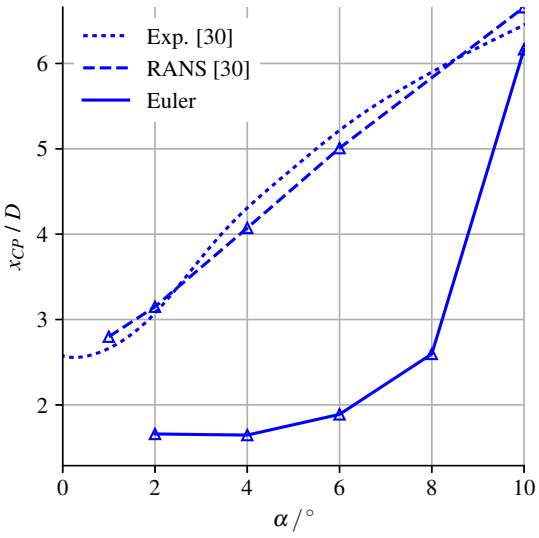

(c) $M_\infty = 3.0$

Fig. 5.24 Body-alone results validation: centre-of-pressure location x_{CP}.

5.2.3 Discussion

In conclusion, the following discussion points are made regarding the results of the body-alone case:

- It is posited that the results converged to the asymptotic mesh-independent values on the fine mesh. This is supported by the minor differences in loads between the medium and fine meshes, which have a refinement factor of 2 between them. The medium mesh was used for all further body-related computations (in particular, for the full-vehicle configuration) with the understanding that it exhibits slightly greater numerical viscosity than the fine mesh. The results may thus be expected to have slightly coarser resolution of vortical features and of other flow gradients,

- As discussed in Section 5.1.4, the use of the numerical solver in `OpenFOAM` was motivated by its lack of licensing fees and by the context of other ongoing work. The comparison in Section 5.2.2 of the results obtained with the solver with those obtained in `Fluent` verifies the use of the `HiSA` solver in `OpenFOAM`. The minor differences that were noted point towards finer solver tuning in `Fluent` than was employed in the present study,

- The comparison of results from the Euler-based `HiSA` solver to RANS and experimental results in Section 5.2.2 shows that the Euler formulation has fundamental shortcomings in physics modelling. Good agreement is achieved at $\alpha \leq 2°$. Trends suggest that fair agreement would also be achieved for $M_\infty \sin\alpha > 0.5$. These observations are in agreement with trends in the literature,

- Weak vortex development is observed at $M_\infty \sin\alpha > 0.4$ in the Euler formulation. Reference to Table 5.5 shows that this corresponds to $\alpha \geq 10°$ at $M_\infty = 2.5$ and to $\alpha \geq 8°$ at $M_\infty = 3.0$. It is essentially only at these angles that significant interference flow structures are generated by the Euler formulation. These conditions are therefore of principal interest for the purposes of evaluating the application of Euler-based LPT to slender bodies.

5.3 Wing-Alone Aerodynamics

In the wing-alone case, the control-surfaces are exposed directly to the freestream. As the surfaces are considered "in isolation" from the body, the leeside control-surface is subjected to minimal aerodynamic interference. The only interference arising for the given geometry and flight speeds is due to the action of the horizontal surfaces. At incidence, these create an expansion from freestream conditions at the root of the leeside surface.

The purpose of the wing-alone case is thus essentially to provide an interference-free reference for the loading on the leeside control surface when subjected to deformation. This will be used for comparison in assessing the aerodynamic interference in the full-vehicle configuration.

This chapter opens with the present introduction, which will include clarifying remarks surrounding the mode-shapes of deformation. This will be followed by Section 5.3.1, which covers the mesh-independence study for the wing-alone configuration. The results for the deforming leeside control-surface will be presented in Sections 5.3.2 and 5.3.3. This will be followed by a general discussion of the results for the wing-alone case in Section 5.3.4.

A number of introductory remarks regarding the results are made below:

- The wing-alone values for C_l and z_{CP} have been adjusted to facilitate direct comparison to the wing-body results. The moments (and centre-of-pressure) have been calculated for the wing-alone configuration occupying the same space as the wings do in the wing-body configuration (shifted one body-radius from the moment-axis),

- Mode 1 (first bending) results in minimal twist along the span of the wing. The mode-shape was depicted in Fig. 5.2b. The maximum out-of-plane deflection occurs at the wing tip, with deflections of 6% and 12% of the wing span being measured for $\delta = 5\,\text{mm}$ and $\delta = 10\,\text{mm}$, respectively. The corresponding twist at the wing tip is 0.5° and 1.0° about the positive z-axis. The deflection induces slight camber.

  The resulting turning of the unit normal-vector of the wing surface into the flow direction (predominantly the x-direction) is minimal. This translates to low subsonic downwash-Mach numbers being recorded for this mode.

- Mode 2 (first twist) is predominantly a torsion mode, with essentially no out-of-plane deflection along the mid-chord of the wing. The mode-shape was depicted in Fig. 5.3a. The maximum out-of-plane deflection occurs at the wing tip, with deflections of 0.45% and 0.91% of the wing span being measured for $\delta = 5\,\text{mm}$ and $\delta = 10\,\text{mm}$, respectively. The corresponding twist at the wing tip is 12.3° and 23.5° about the positive z-axis.

The nominal deformations of $\delta = 5\,\text{mm}$ and $\delta = 10\,\text{mm}$ result in large perturbations in an aerodynamic sense. The maximum flow-turning angles for attached oblique shocks at the freestream Mach numbers $M_\infty = [2.0, 2.5, 3.0]$ are approximately $[23.0°, 29.8°, 34.1°]$, respectively. As a consequence, notable nonlinearity in the load variation with modal deformation is expected. Shock detachment is expected to occur in the vicinity of the wing-tip at $M_\infty = 2.0$ for $\delta = 10\,\text{mm}$.

The resulting turning of the unit normal-vector of the wing surface into the flow direction (predominantly the x-direction) is substantial. This translates to high subsonic to low supersonic downwash-Mach numbers being recorded for this mode,

- Mode 3 (second bending) results in slight twist at the wing-tip and moderate camber at the mid-span position. The mode-shape was depicted in Fig. 5.3b. The maximum out-of-plane deflection occurs at the wing tip, with deflections of -5.6% and -11% of the wing span being measured for $\delta = 5\,\text{mm}$ and $\delta = 10\,\text{mm}$, respectively. The corresponding twist at the wing tip is $1.4°$ and $2.7°$ about the positive z-axis.

  It is to be noted that the secondary point of maximum out-of-plane deflection is at the trailing-edge of the mid-span, with a deflection 90% of that at the wing-tip. This is expected to result in interaction with the body-shed vortices. These are typically located at approximately the mid-span of the wings, and approximately one body-radius from the plane of the un-deformed wing.

  The resulting turning of the unit normal-vector of the wing surface into the flow direction (predominantly the x-direction) is minimal. This translates to low subsonic downwash-Mach numbers being recorded for this mode.

5.3.1 Mesh-Independence Study

An essentially similar presentation to that in Section 5.2.1 is given here for the mesh-independence study of the wing-alone case. The details of the wing-alone mesh have been provided in Section 5.1.5, with cell counts provided in Table 5.9 and depictions of the mesh provided in Figs. 5.11 and 5.13 to 5.15. It is to be noted that the wing-alone and full-vehicle meshes are identical with regards to axial discretization. The differences arise in the radial and circumferential discretization. The nature of the wing-alone geometry lends itself to a rectangular block definition, in contrast to the polar definition used for the full-vehicle case. However, leading from the essential similarity of the meshes, it is posited that the mesh-independence study for the wing-alone case also applies to the wing-related physics and flow features of the full-vehicle case.

The variation with mesh fineness of the normal-force coefficient (C_N), the pitching-moment coefficient (C_m), and the axial location of the centre-of-pressure (x_{CP}) is depicted in Figs. 5.25 to 5.27, respectively. These figures are discussed below:

- Figure 5.25: C_N – excellent agreement is obtained between the medium and fine meshes, with marginal differences noted in the coarse mesh. Moreover, it is noted that the load-slope of the wing-alone configuration is essentially linear over the incidence range $0° \leq \alpha \leq 10°$ at the Mach numbers considered.
- Figure 5.26: C_m – similarly marginal differences are noted for the coarse mesh, with excellent agreement achieved between the medium and fine meshes.
- Figure 5.27: x_{CP} – the scale of the figures accentuates the differences between the meshes. However, it is noted that the differences between the medium and fine meshes is of the order of $0.01D$. This is a nominal difference. It is also seen that there is essentially no shift in x_{CP} with α.

These results have been quantified in terms of the grid convergence index (GCI) of Roache [214]. The maximum error observed over the M_∞-α parameter space is given in terms of the GCI for each load in Table 5.11 below.

Table 5.11 Grid convergence index for wing-alone loads

Fineness	GCI (C_N)	GCI (C_m)	GCI ($x_{CP}\,/\,D$)
Medium	1.50%	1.60%	0.12%
Fine	0.50%	0.50%	0.03%

In conclusion, the close agreement between the medium and fine meshes justifies the use of the medium mesh in the full-vehicle case. The resolution of wing-related physics may thus be considered to be mesh-independent. It is also noted that the wing-alone case exhibits essentially linear (in α) aerodynamics over the range $0° \leq \alpha \leq 10°$.

All remaining figures in this chapter are for results obtained on the medium mesh.

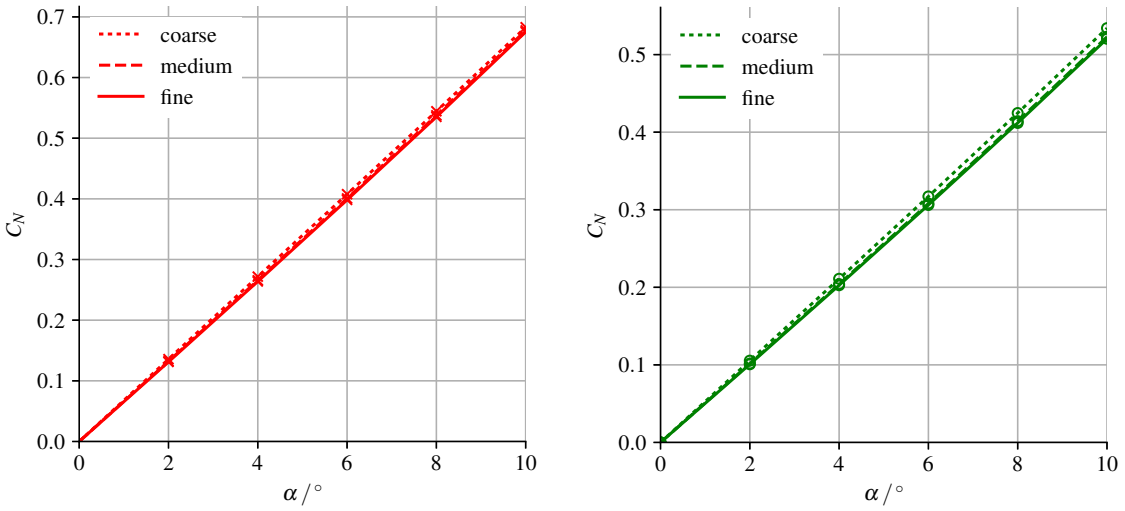

(a) $M_\infty = 2.0$

(b) $M_\infty = 2.5$

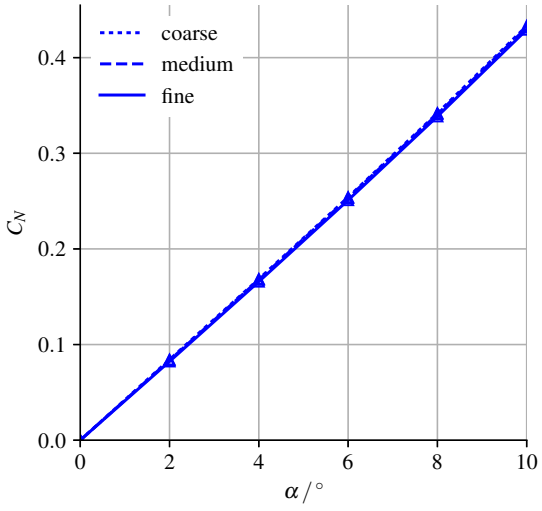

(c) $M_\infty = 3.0$

Fig. 5.25 Wing-alone mesh-independence results: normal-force coefficient C_N.

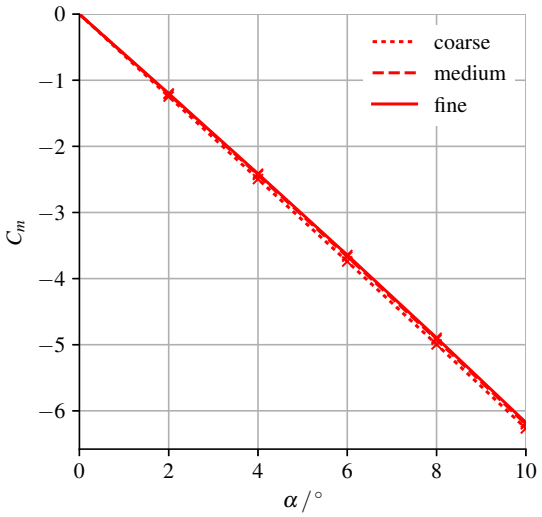

(a) $M_\infty = 2.0$

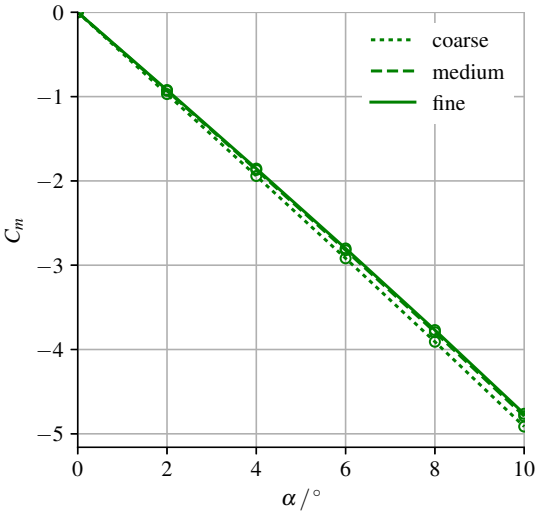

(b) $M_\infty = 2.5$

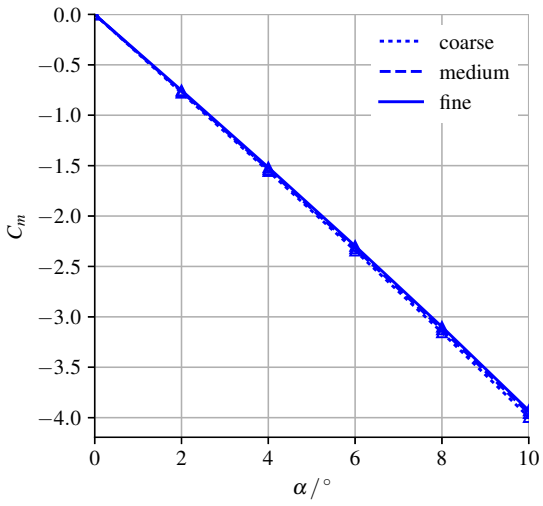

(c) $M_\infty = 3.0$

Fig. 5.26 Wing-alone mesh-independence results: pitching-moment coefficient C_m.

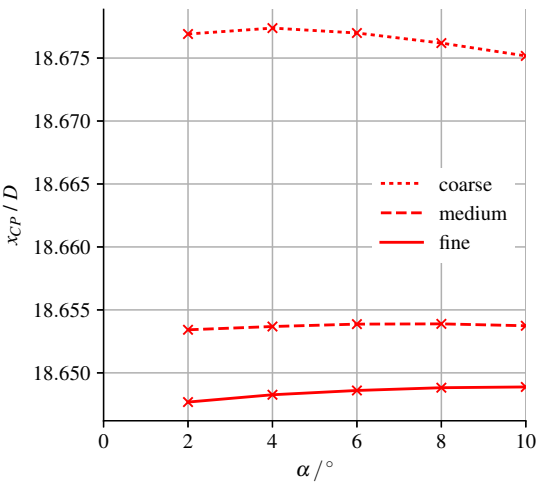

(a) $M_\infty = 2.0$

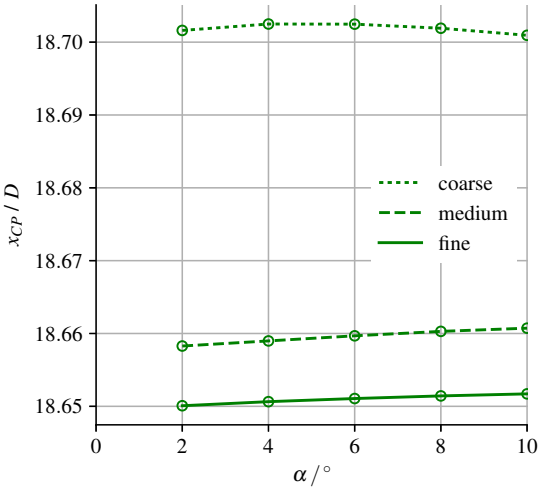

(b) $M_\infty = 2.5$

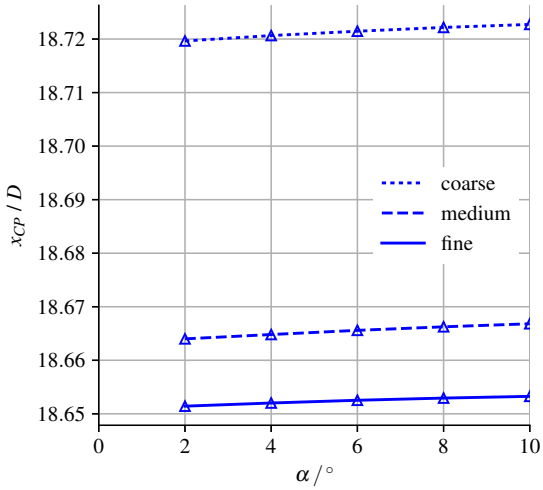

(c) $M_\infty = 3.0$

Fig. 5.27 Wing-alone mesh-independence results: centre-of-pressure location x_{CP}.

5.3.2 Results: Influence of Piston Theory Coefficients

The first set of results to be presented for the wing-alone case investigates the influence of the piston-theory coefficients chosen for the LPT model. The three different theoretical bases, with associated coefficients, which have been utilized in this study were defined in Tables 5.6 to 5.8. Where appropriate, the aerodynamic pressure on expansion surfaces as predicted by LPT was limited to vacuum pressure. The occurrence of this pressure-limiting will be manifested in the results as a visible difference between 1st-order and 2nd-order results of a given formulation (e.g., Lighthill [88]). The results depicting the influence of the choice of piston-theory coefficients are shown in Figs. 5.28 to 5.36, and will be discussed below on a per-mode-shape basis.

Mode 1: First Bending

The side-force (C_Y) and rolling-moment (C_l) coefficients for Mode 1 are shown for the Mach set $M_\infty = [2.0, 2.5, 3.0]$ in Figs. 5.28 to 5.30, respectively. The reader is reminded that in the global coordinate system defined in Fig. 5.4, the side-force acts normal to the leeside control-surface. The following discussion points are made regarding the figures:

- As was noted in the introduction, Mode 1 (first bending) exhibits predominantly bending, with minimal turning of the surface unit-normal vector into the mean steady flow. As a consequence, deformation causes low-subsonic downwash. This is reflected in how the 2nd- and 3rd-order LPT formulations are indistinguishable from the 1st-order formulation. The reader is referred to Eq. (5.1) with $w/a_m \ll 1$ for substantiation,

- This also provides insight into the role of the theoretical source for the coefficients. While no difference is noted between higher-order variations within a theoretical basis (e.g., Lighthill's [88] coefficients or Van Dyke's coefficients), differences are noted between theoretical bases. This is to be expected, as Van Dyke's [104] and Donov's [105] coefficients are Mach-dependent and serve to extend the theories to lower supersonic Mach numbers than are assumed in Lighthill's [88] formulation. However, comparison to the Euler solution shows that better prediction is obtained (at both deflections) by Lighthill's [88] formulation. This is noted for all three freestream Mach numbers considered. Minor differences in the load-slope with α are noted between formulations. The variety of formulations essentially serve to provide an estimation band which, for Mode 1, includes the Euler solution. This band is seen to become narrower as M_∞ increases. This is consistent with the differences between Lighthill's [88] formulation and Van Dyke's [104] formulation being greatest at lower supersonic Mach numbers.

Mode 2: First Twist

The side-force and rolling-moment coefficients for Mode 2 are shown for the Mach set $M_\infty = [2.0, 2.5, 3.0]$ in Figs. 5.31 to 5.33, respectively. The following discussion points are made regarding the figures:

- Mode 2 (first twist) exhibits predominantly torsion, with substantial turning of the surface unit-normal vector into the mean steady flow. As a consequence, deformation causes high-subsonic to supersonic downwash. This is reflected in how the 2^{nd}- and 3^{rd}-order LPT formulations are distinct from one another, particularly at the higher deflection of $\delta = 10\,\text{mm}$. Moreover, the 2^{nd}-order results are distinct from the 1^{st}-order results at $\delta = 10\,\text{mm}$. Since the reference mean-steady solution is equal on both surfaces of the wing, it may be concluded that this difference arises from "pressure limiting" on the expansion surface. This was noted in the introduction. The occurrence of "pressure limiting" points to the large downwash-Mach numbers encountered for this mode-shape at $\delta = 10\,\text{mm}$,

- The previous observations regarding the role of the LPT coefficients also broadly apply to Mode 2. The interpretation of LPT variants providing an estimation band at a given order of LPT is particularly clear in Fig. 5.33. Here, the 1^{st}-order band at $\delta = 10\,\text{mm}$ is seen to under-predict the Euler solution. The 2^{nd}-order band captures the Euler solution. Finally, the 3^{rd}-order bands over-predict the Euler solution. This observation may be informed through consideration of the behaviour of higher-order PT formulations with increasing Mach number. It is known that the 3^{rd}-order formulation becomes unbounded as the downwash-Mach number increases, while the 2^{nd} order formulation adheres to the Mach independence principle. This was discussed in **??**, with particular emphasis given to **??**. Once again, it is of interest that the Lighthill [88] coefficients provide better agreement with the Euler solution over the parameter space considered.

Mode 3: Second Bending

The side-force and rolling-moment coefficients for Mode 3 are shown for the Mach set $M_\infty = [2.0, 2.5, 3.0]$ in Figs. 5.34 to 5.36, respectively. The following discussion points are made regarding the figures:

- Mode 3 (second bending) exhibits predominantly bending, with moderate camber at the trailing-edge of the mid-span. As a consequence, deformation causes predominantly low-subsonic downwash, with localized high-subsonic downwash at the mid-span trailing-edge. This is reflected in how the 2^{nd}- and 3^{rd}-order LPT formulations are

distinct from one another, particularly at the higher deflection of $\delta = 10\,\text{mm}$. The fact that the 2nd-order results are essentially indistinguishable from the 1st-order results shows that vacuum pressure is not reached,

- The observations regarding the role of the LPT coefficients made for Mode 1 also broadly apply to Mode 3. Once again, the 2nd-order Lighthill formulation provides the best agreement with the Euler solution. Here, it is observed that the estimation band narrows with both increasing M_∞ and increasing α. The large overlap between the 2nd- and 3rd-order estimation bands points to the low-subsonic downwash-Mach numbers encountered over the majority of the wing.

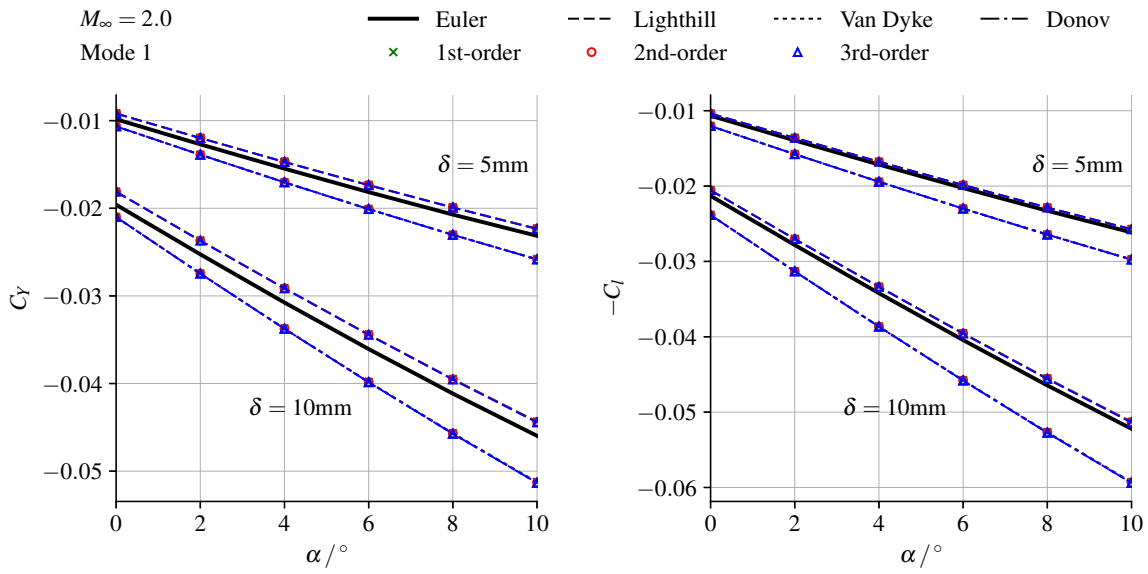

Fig. 5.28 Influence of piston theory coefficients on the prediction of side-force C_Y and rolling-moment C_l coefficients. Mode 1 at $M_\infty = 2.0$.

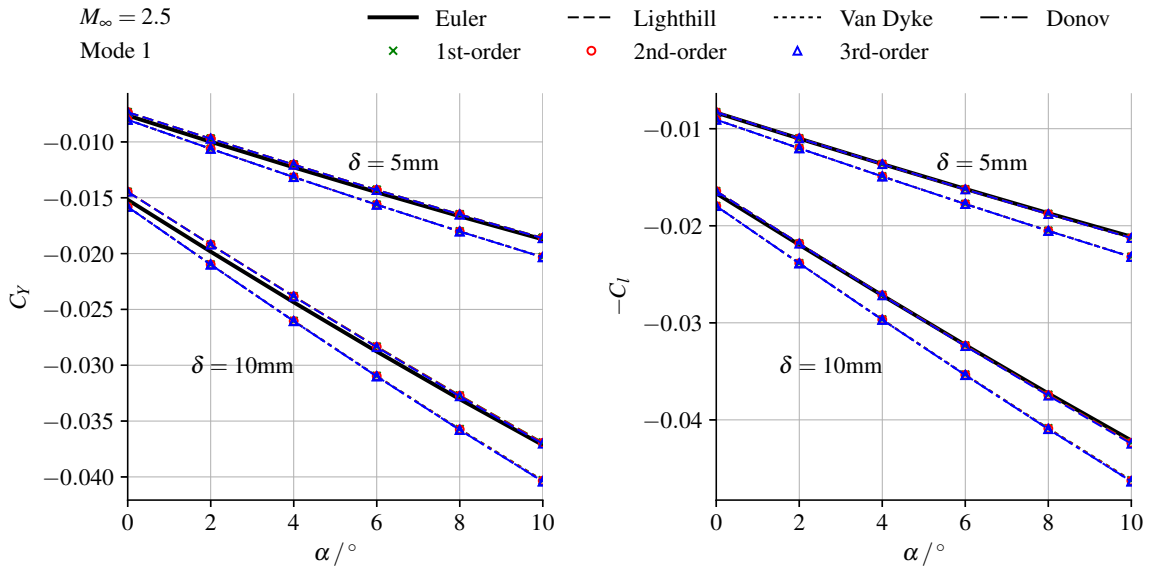

Fig. 5.29 Influence of piston theory coefficients on the prediction of side-force C_Y and rolling-moment C_l coefficients. Mode 1 at $M_\infty = 2.5$.

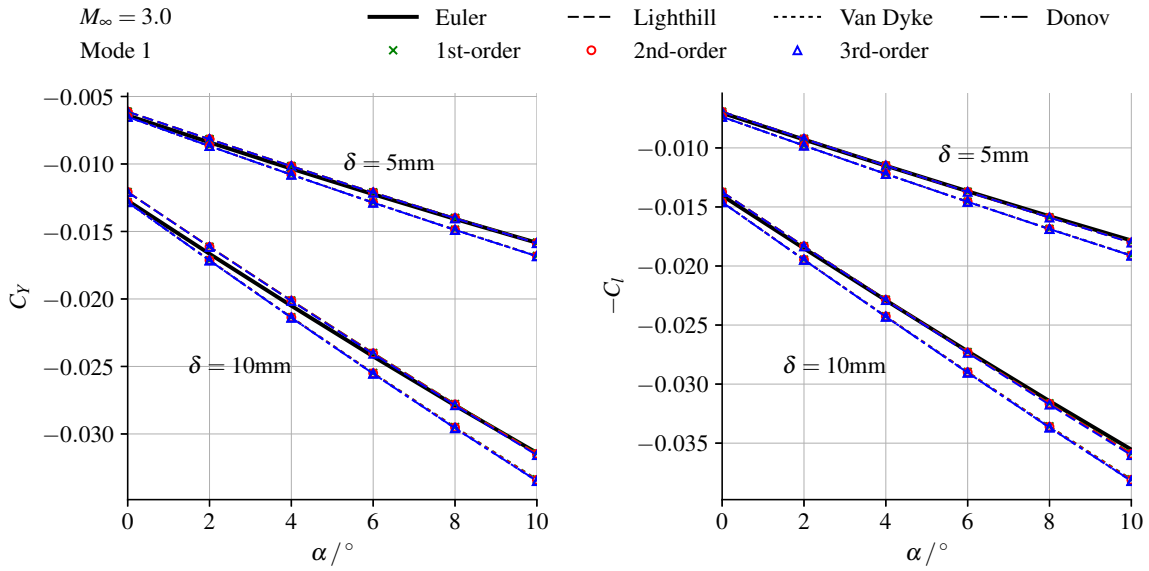

Fig. 5.30 Influence of piston theory coefficients on the prediction of side-force C_Y and rolling-moment C_l coefficients. Mode 1 at $M_\infty = 3.0$.

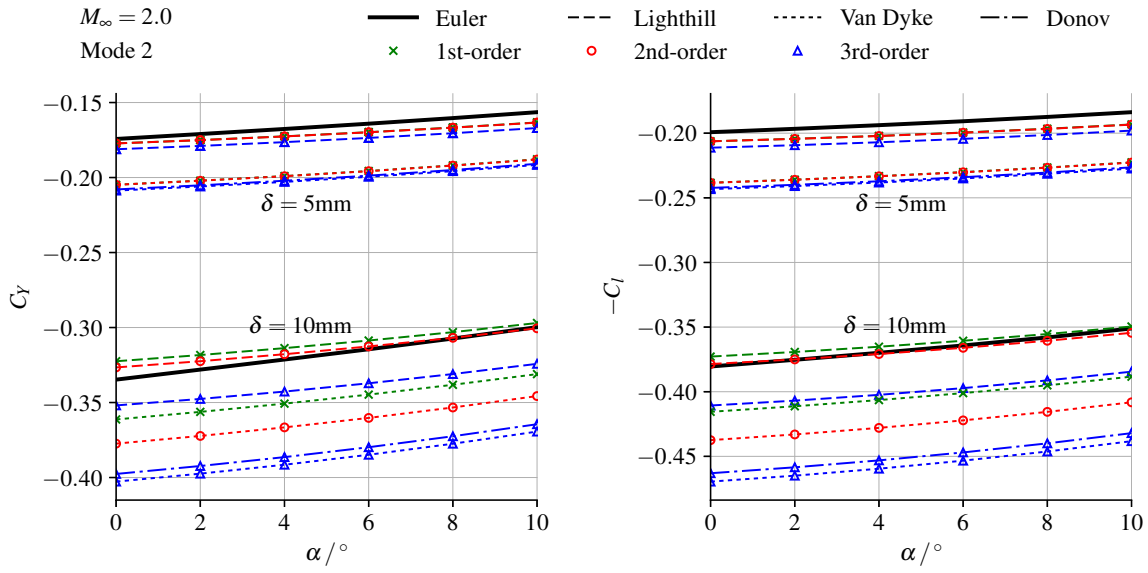

Fig. 5.31 Influence of piston theory coefficients on the prediction of side-force C_Y and rolling-moment C_l coefficients. Mode 2 at $M_\infty = 2.0$.

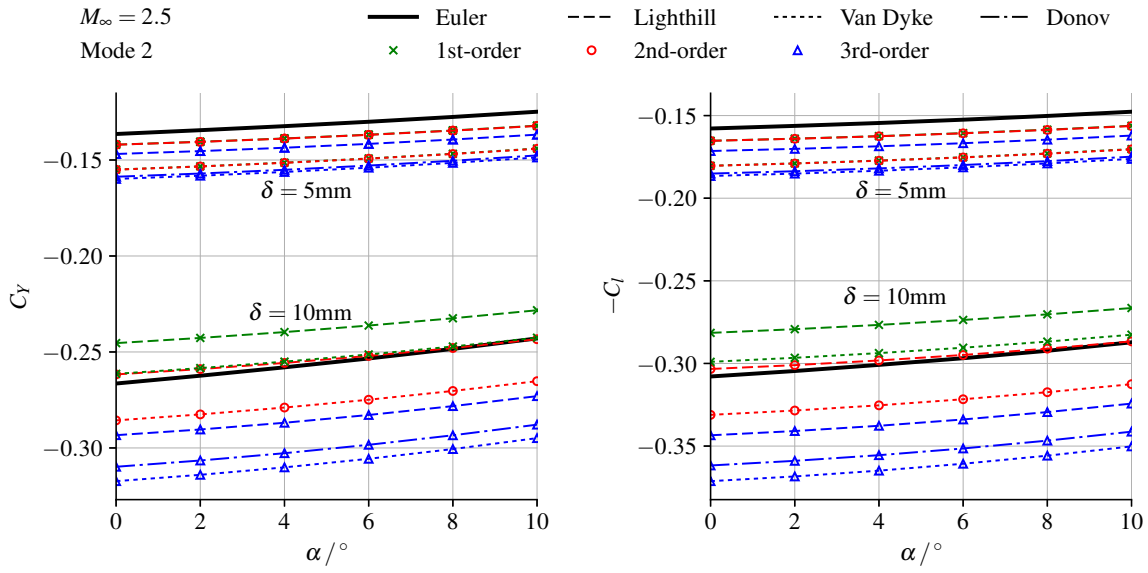

Fig. 5.32 Influence of piston theory coefficients on the prediction of side-force C_Y and rolling-moment C_l coefficients. Mode 2 at $M_\infty = 2.5$.

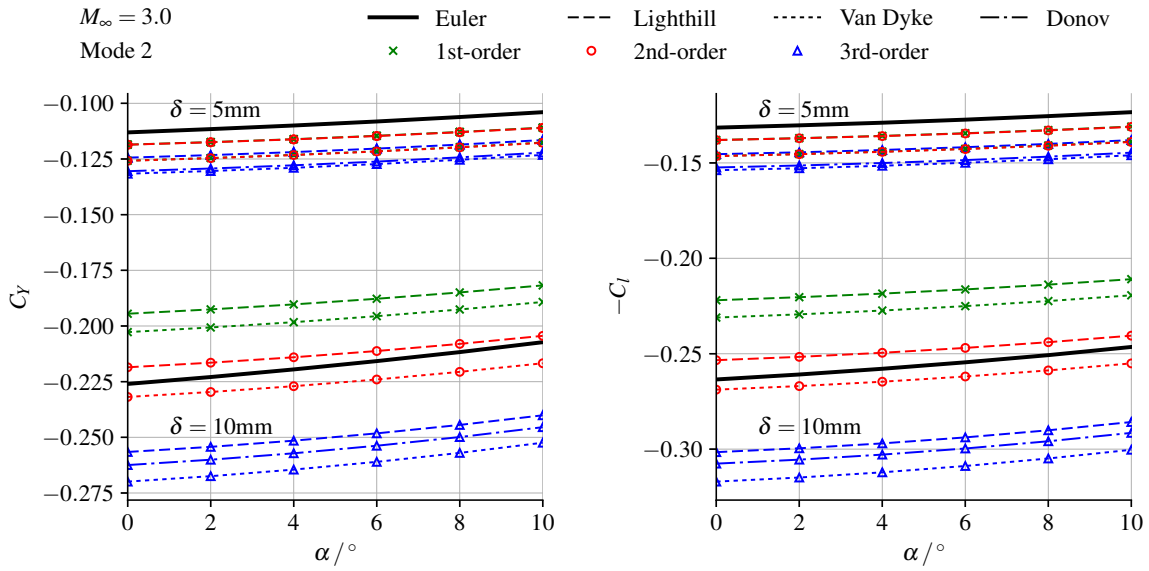

Fig. 5.33 Influence of piston theory coefficients on the prediction of side-force C_Y and rolling-moment C_l coefficients. Mode 2 at $M_\infty = 3.0$.

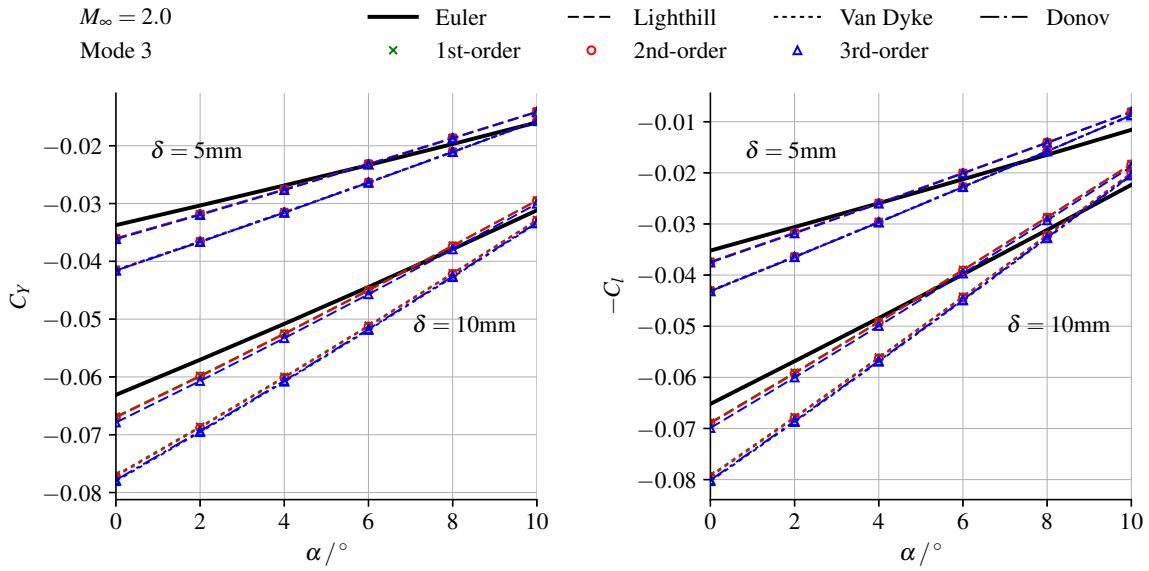

Fig. 5.34 Influence of piston theory coefficients on the prediction of side-force C_Y and rolling-moment C_l coefficients. Mode 3 at $M_\infty = 2.0$.

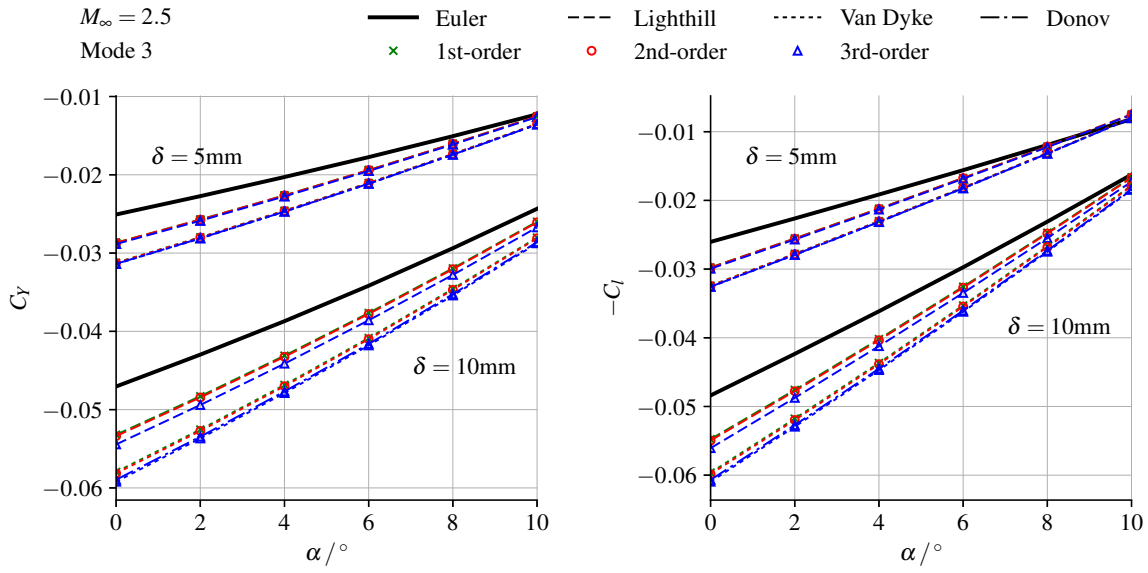

Fig. 5.35 Influence of piston theory coefficients on the prediction of side-force C_Y and rolling-moment C_l coefficients. Mode 3 at $M_\infty = 2.5$.

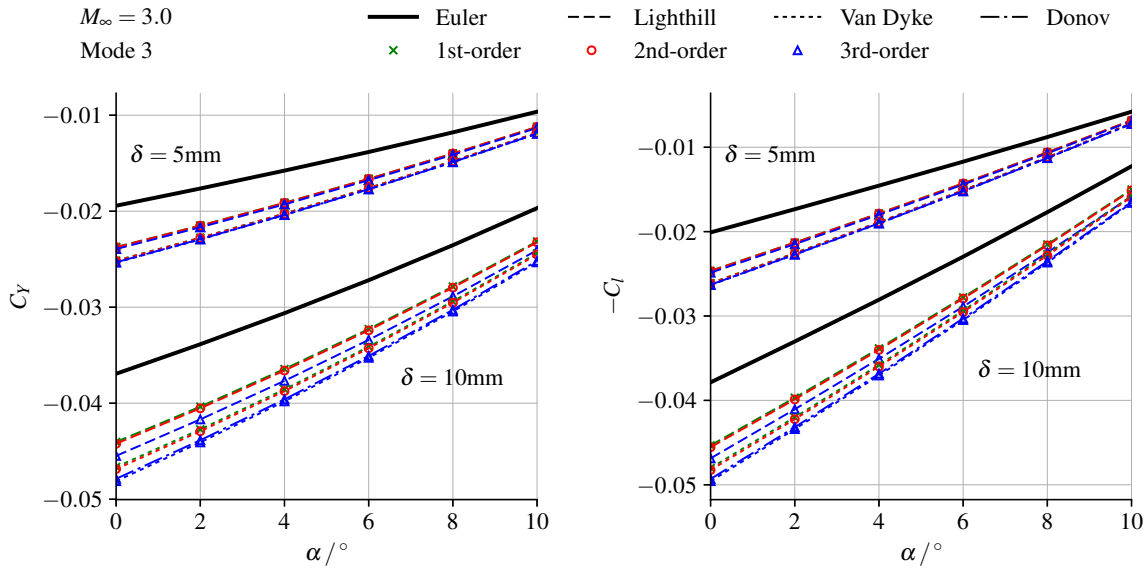

Fig. 5.36 Influence of piston theory coefficients on the prediction of side-force C_Y and rolling-moment C_l coefficients. Mode 3 at $M_\infty = 3.0$.

5.3.3 Results: Influence of Freestream Mach Number

The second set of results to be presented for the wing-alone case investigates the influence of M_∞ on the accuracy of LPT prediction. Following the results of Section 5.3.2, the 2$^{\text{nd}}$-order LPT formulation based on Lighthill's [88] coefficients was chosen for comparison to the "exact" result of the Euler solution. Where of interest, any trends in the variation with α of the load prediction will be noted. The results depicting the influence of M_∞ are shown in Figs. 5.37 to 5.42, and will be discussed below on a per-mode-shape basis.

Mode 1: First Bending

The influence of M_∞ on prediction accuracy for Mode 1 is shown for the deflection set $\delta = [5\,\text{mm}, 10\,\text{mm}]$ in Figs. 5.37 and 5.38, respectively. The following discussion points are made regarding the figures:

- It is seen that prediction accuracy improves with increasing M_∞. Generally, excellent agreement in the side-force and rolling-moment coefficients is obtained. This is noted for both deflection amplitudes.

- Good agreement in the α-dependence is obtained at all Mach numbers. Both C_Y and C_l are noted to predominantly linear in α, with nonlinearity being barely noticeable. The exception to this trend lies in the prediction of z_{CP}. However, the prediction error is within $0.05D$, and is thus considered to be nominal. The variation with M_∞ of x_{CP} is similarly negligible.

Mode 2: First Twist

The influence of M_∞ on prediction accuracy for Mode 2 is shown for the deflection set $\delta = [5\,\text{mm}, 10\,\text{mm}]$ in Figs. 5.39 and 5.40, respectively. The following discussion points are made regarding the figures:

- It is noted that prediction accuracy is relatively insensitive to M_∞ for $\delta = 5\,\text{mm}$, while a nominally greater offset is observed for the $M_\infty = 3.0$ results at $\delta = 10\,\text{mm}$. This offset appears to be insensitive to M_∞ over the Mach range considered. The loads are over-predicted at M_∞ for $\delta = 5\,\text{mm}$, while they are under-predicted at M_∞ for $\delta = 10\,\text{mm}$.

- Good agreement in the α-dependence is obtained at all Mach numbers. Similar to Mode 1, the C_Y and C_l loading of Mode 2 is predominantly linear with α. The

differences observed in the prediction and exact values of x_{CP} and z_{CP} are nominally small.

Mode 3: Second Bending

The influence of M_∞ on prediction accuracy for Mode 3 is shown for the deflection set $\delta = [5\,\text{mm}, 10\,\text{mm}]$ in Figs. 5.41 and 5.42, respectively. The following discussion points are made regarding the figures:

- Few generalized statements may be made regarding the trends in Mode 3. The prediction accuracy and α-dependence at $M_\infty = 3.0$ is seen to be insensitive to the deflection amplitude. However, this is not observed at $M_\infty = 2.0$. It is clear that the load-slopes exhibit a degree of dependence on both M_∞ and $delta$. It is posited that this is due to the more complex mode-shape of deformation (see Fig. 5.3b) leading to greater three-dimensionality in the aerodynamics due to the localized camber at the trailing-edge of the mid-span. This is supported by the comparatively large shift with α noted in z_{CP}.
- Improved agreement in the α-dependence is noted with increasing M_∞. However, this appears to be accompanied by a greater error in the load prediction. Fairly good agreement is observed in the x_{CP} and z_{CP} prediction. Differences in x_{CP} are nominal. However, the differences in z_{CP} and in its Mach-dependence are more notable. In the absence of an interference flowfield, it is posited that these differences point to greater three-dimensionality in the wing-alone aerodynamics due to the localized camber of Mode 3.

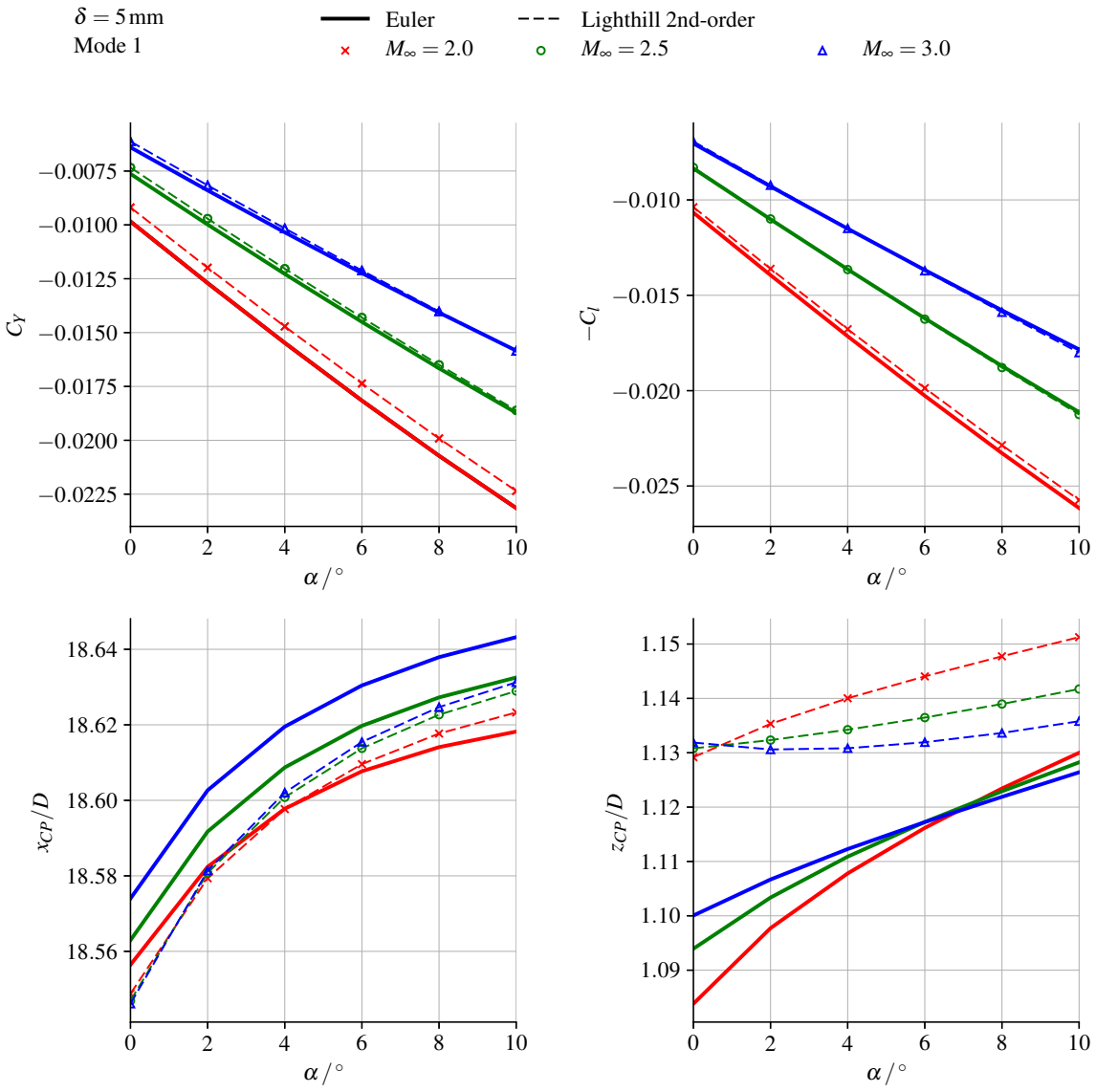

Fig. 5.37 Influence of freestream Mach number on the prediction of the side-force coefficient C_Y, rolling-moment coefficient C_l, axial centre-of-pressure location x_{CP}/D, and vertical centre-of-pressure location z_{CP}/D. Mode 1 with $\delta = 5\,\text{mm}$.

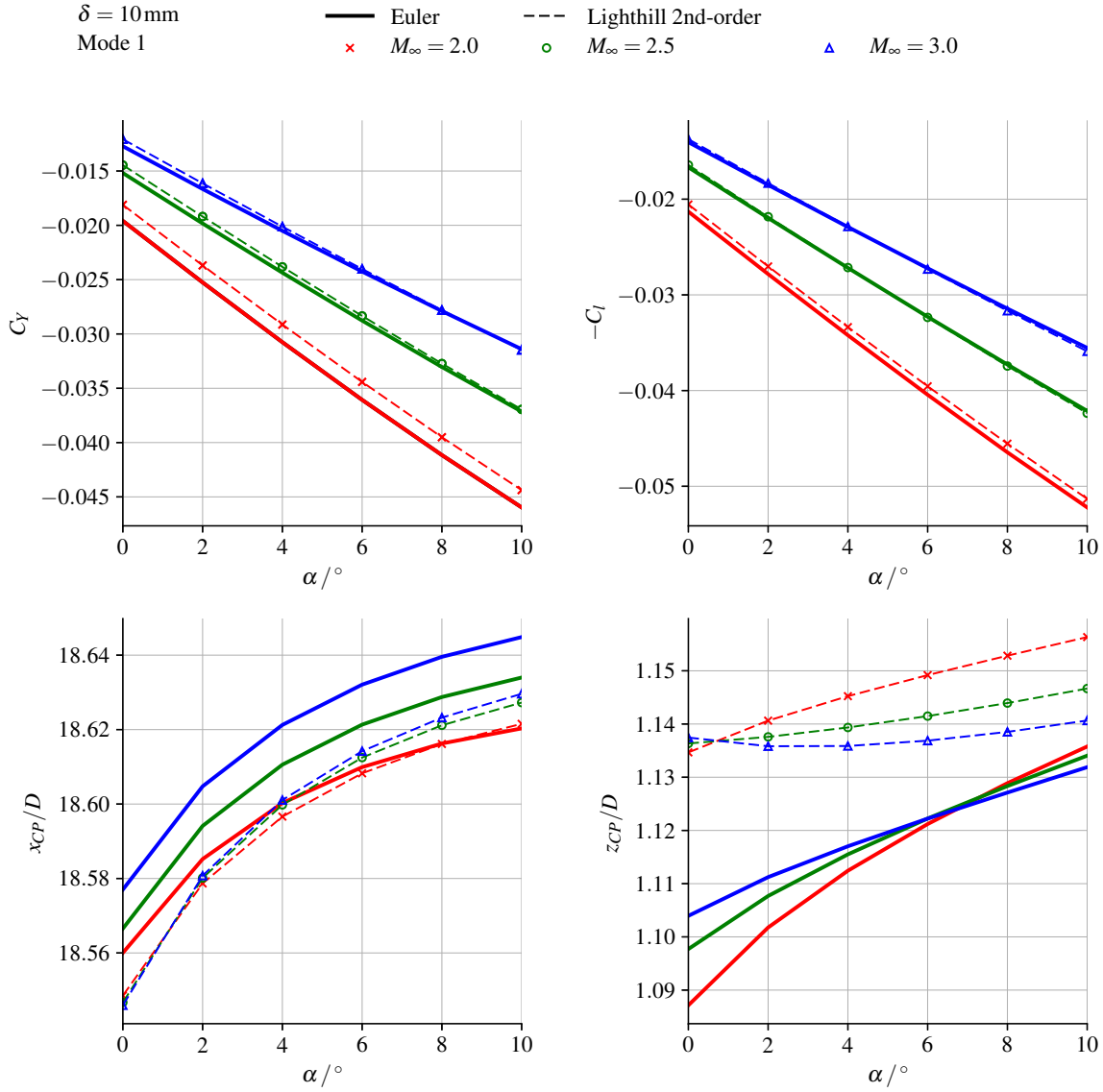

Fig. 5.38 Influence of freestream Mach number on the prediction of the side-force coefficient C_Y, rolling-moment coefficient C_l, axial centre-of-pressure location x_{CP}/D, and vertical centre-of-pressure location z_{CP}/D. Mode 1 with $\delta = 10\,\text{mm}$.

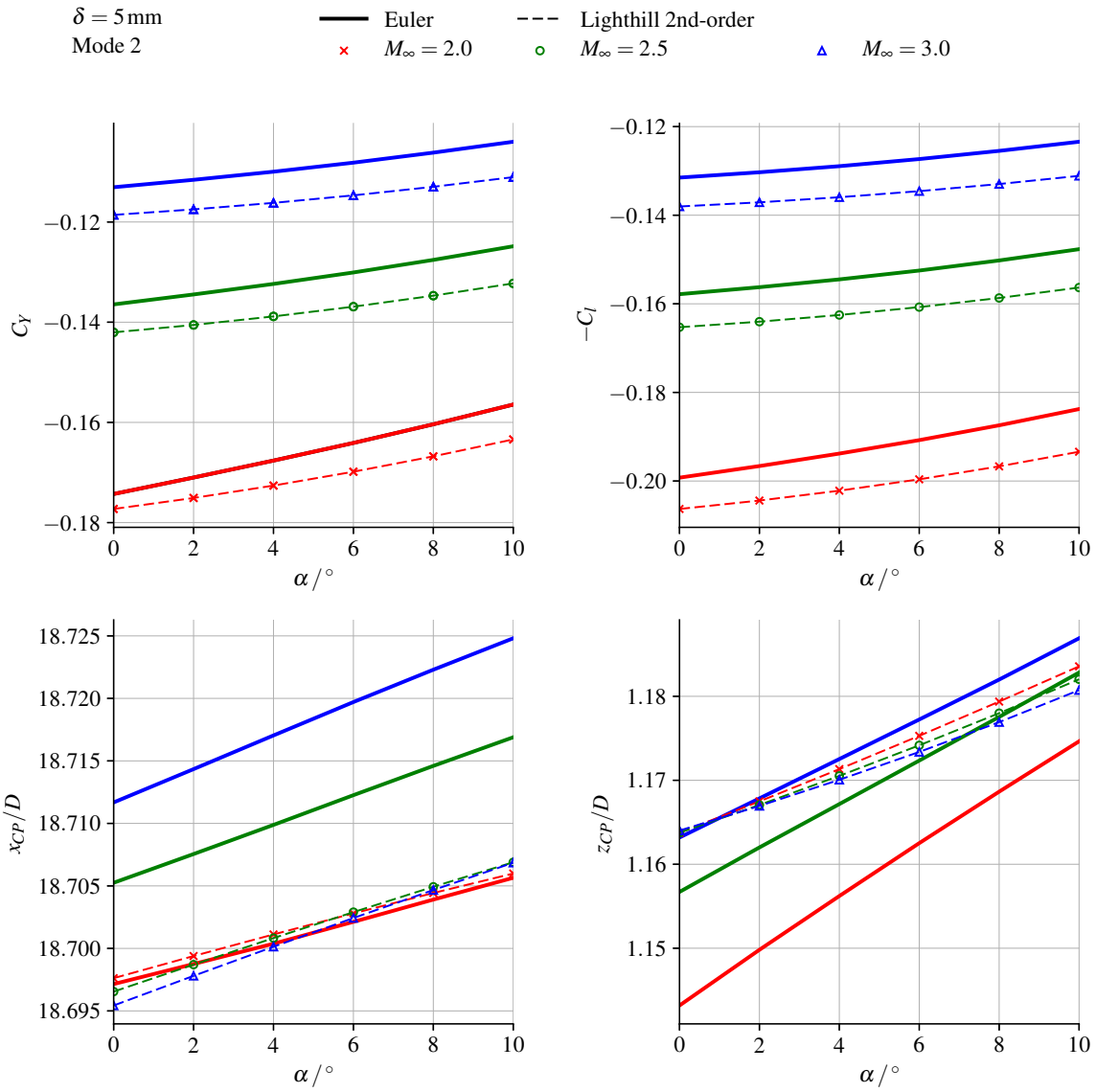

Fig. 5.39 Influence of freestream Mach number on the prediction of the side-force coefficient C_Y, rolling-moment coefficient C_l, axial centre-of-pressure location x_{CP}/D, and vertical centre-of-pressure location z_{CP}/D. Mode 2 with $\delta = 5\,\text{mm}$.

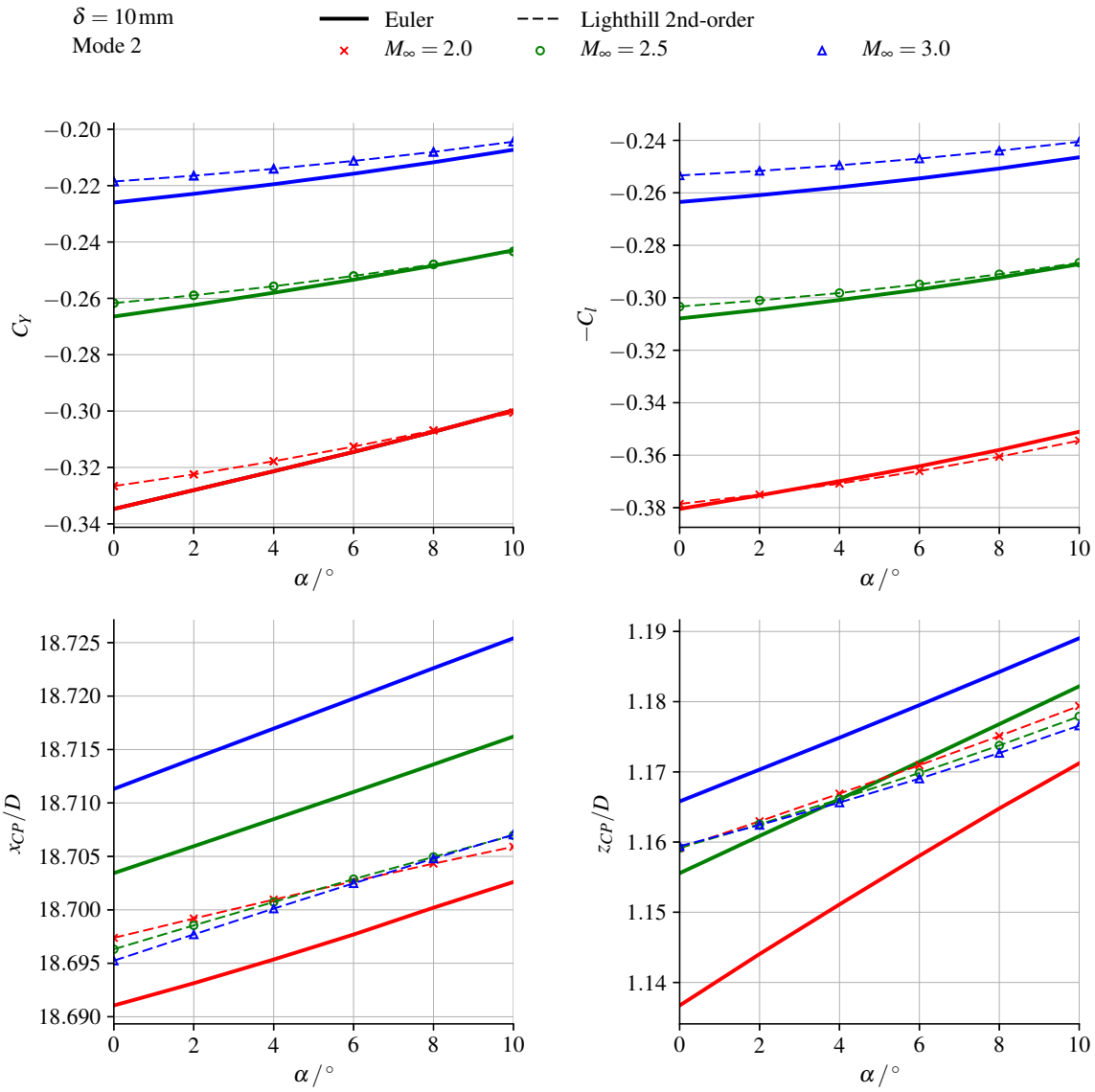

Fig. 5.40 Influence of freestream Mach number on the prediction of the side-force coefficient C_Y, rolling-moment coefficient C_l, axial centre-of-pressure location x_{CP}/D, and vertical centre-of-pressure location z_{CP}/D. Mode 2 with $\delta = 10\,\text{mm}$.

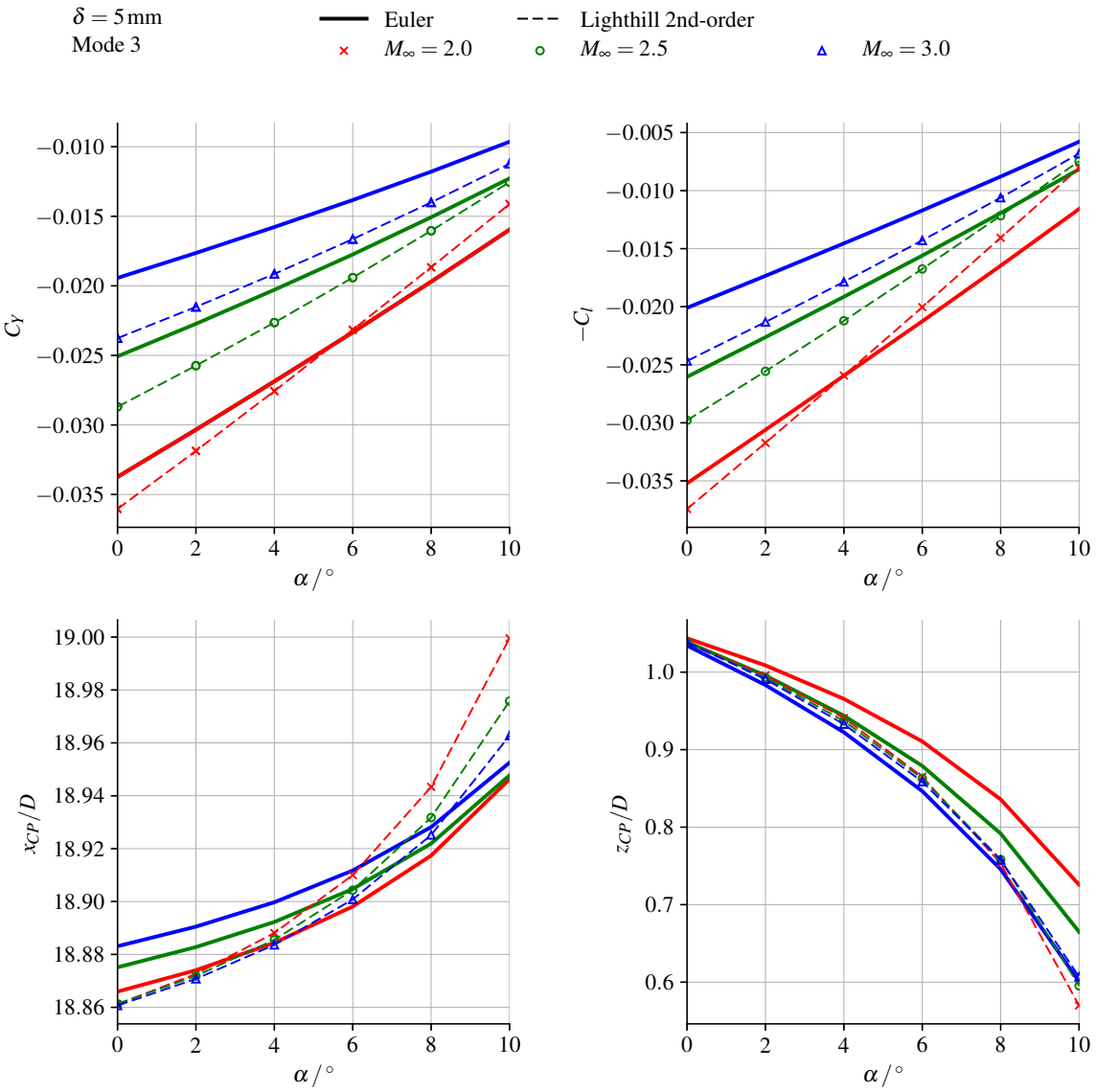

Fig. 5.41 Influence of freestream Mach number on the prediction of the side-force coefficient C_Y, rolling-moment coefficient C_l, axial centre-of-pressure location x_{CP}/D, and vertical centre-of-pressure location z_{CP}/D. Mode 3 with $\delta = 5\,\text{mm}$.

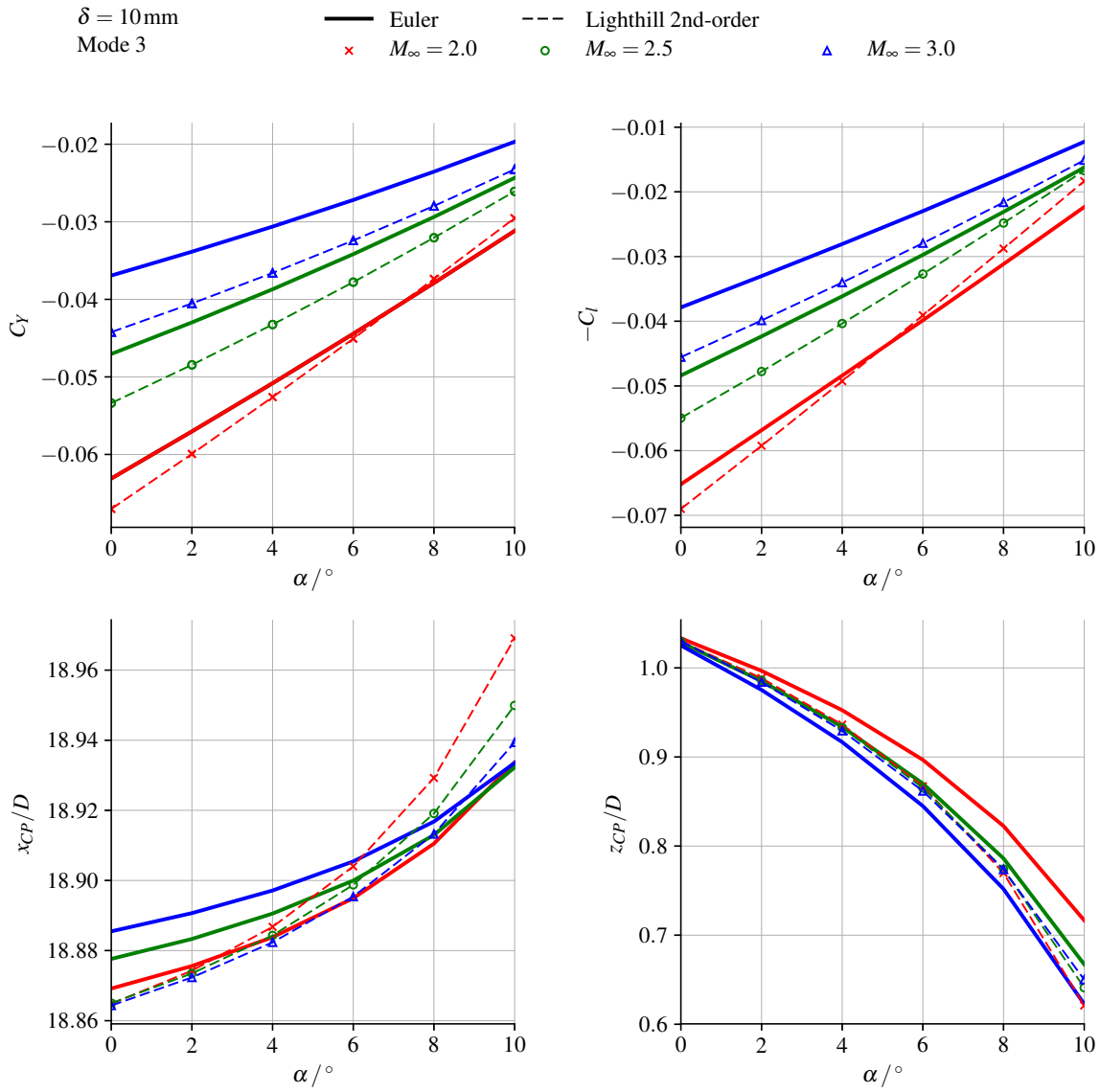

Fig. 5.42 Influence of freestream Mach number on the prediction of the side-force coefficient C_Y, rolling-moment coefficient C_l, axial centre-of-pressure location x_{CP}/D, and vertical centre-of-pressure location z_{CP}/D. Mode 3 with $\delta = 10\,\text{mm}$.

5.3.4 Discussion

Preliminary Remarks

The wing-alone case gives insight into the geometry- and deformation-driven aerodynamics of the leeside control-surface in the absence of an interference flowfield. This allows important insight to be obtained regarding inherent shortcomings of LPT, prior to the introduction of further complications such as interaction with an interference flowfield.

Shortcomings identified in the wing-alone results point towards inaccuracies that stem from the underlying assumptions of LPT. These assumptions have been discussed at length in Sections 3.1.1 and 3.1.4 and Chapter 4 and will not be repeated in depth here. Fundamentally, these assumptions reduce to requirements on the relative order-of-magnitude of flow gradients. This has been detailed in Chapter 4. In the context of application to the leeside control surface:

- Gradients in the chordwise (x) direction must be negligible compared to gradients in the thickness (y) direction,
- Gradients in the spanwise (z) direction must be negligible compared to gradients in the thickness (y) direction.

In order to apply LPT in its current (state of the art) form, it is further required that the above assumptions regarding gradients are valid in the entire region bounded by the vehicle surface and the bow shock. In the absence of an interference flowfield, it is reasonable (and common practice in analytical methods of this class) to assume that if the gradient-restriction are satisfied at the body boundary and at the shock boundary, then they are satisfied in the flowfield between these boundaries. However, in the presence of an interference flowfield, this assumption is no longer implicitly reasonable.

Given the uniformity of flow between the wing bow-shocks and the body in the wing-alone case (due to the absence of an interference flowfield), shortcomings in LPT will point towards the underlying gradient-assumptions being violated in the vicinity of the body boundary. In other words, the assumptions breakdown in the face of non-negligible three-dimensionality of the flow.

Discussion Points

The following are the key conclusions drawn from the wing-alone results presented and discussed in Sections 5.3.1 to 5.3.3:

- The shortcomings of LPT in predicting the C_Y and C_l trends for Mode 3 (second bending) at both deflection amplitudes, as best seen in Figs. 5.41 and 5.42, are attributed to the above-discussed failure of the underlying LPT assumptions due to

three-dimensionality of the flow. Inspection of Fig. 5.3b shows that significant localized camber (second-derivatives of deflection in the x-direction) and localized bending (second-derivatives in the z-direction) are noted at the trailing-edge of the mid-span. The surface curvature results in increased spanwise gradients, and destroys the validity of a strip-theory approach to neglecting spanwise influence.

Further supporting evidence for attributing the observed shortcomings in LPT prediction to flow three-dimensionality include the Mach-dependence, α-dependence, and δ-dependence observed in the prediction error for Mode 3 in Figs. 5.41 and 5.42. These trends stand in contrast to the trends observed for Mode 1 (first bending) and Mode 2 (first twist). Despite having the same nominal out-of-plane deflections as Mode 3, these modes exhibit significantly lower curvatures. The agreement between LPT predictions and Euler results for Mode 1 and Mode 2 is notably better. Regarding the Mach-dependence of the Mode 3 prediction accuracy, it is seen that the worst agreement in α-dependence is obtained at $M_\infty = 2.0$. The sensitivity of the prediction accuracy to flow parameters is noted to reduce as the Mach number is increased to $M_\infty = 3.0$. This that the underlying assumptions of LPT become more accurate at higher Mach numbers for Mode 3. This would be consistent with theory.

- Generally excellent prediction in C_Y and C_l is achieved by LPT for Mode 1 (first bending) and Mode 2 (first twist) over the parameter space considered. A greater degree of δ-dependence in the prediction accuracy is noted for Mode 2. This is not surprising, as Mode 2 results in large aerodynamic twist and correspondingly large perturbations. Regardless, it is noted that for simple mode-shapes with low curvatures, accurate prediction trends may be obtained at both low-subsonic downwash-Mach numbers (Mode 1, small perturbations) and low-supersonic downwash-Mach numbers (Mode 2, large perturbations).

- The investigation of Section 5.3.2 showed that for the near-zero thickness, symmetrical airfoil considered (with static deformations), the order of LPT used did not have any observable effect on the α-dependence of the predicted C_Y and C_l. However, for mode-shapes which yielded larger downwash-Mach numbers ($w/a_m \gtrsim 0.5$), the order of the LPT formulation was noted to influence the offset in the load prediction. This is consistent with the general knowledge surrounding piston theory, with particular reference made to Eq. (5.1),

- The investigation of Section 5.3.2 also yielded much more interesting insight into the influence of the piston-theory coefficients used. It was noted that across the spectrum

of low-subsonic to low-supersonic downwash-Mach numbers, an offset between predictions using different coefficients existed. The predictions using Lighthill's [88], Van Dyke's [104], and Donov's [105] formulations effectively produce a prediction band for a given order of LPT. A general trend is noted in Section 5.3.2 that for a given modal deformation amplitude, the width of the prediction band decreases as M_∞ increases. This is consistent with the Mach-dependence of Van Dyke's [104] and Donov's [105] coefficients diminishing with increasing M_∞ and tending towards Mach-independent coefficients as modelled by Lighthill [88]. To the author's knowledge, this investigation into the influence of LPT coefficients is the first of its kind in the literature. Interestingly, for Modes 2 and 3, consistently better prediction was noted using Lighthill's [88] coefficients. Mode 1 was best replicated using Mach-dependent, low-supersonic extensions as offered by Van Dyke's [104] or Donov's [105] coefficients. However, further investigation would be required to support a generalized recommendation on the selection of LPT coefficients. The present study utilized a 2^{nd}-order LPT formulation based on Lighthill's [88] coefficients for the majority of the figures. This was motivated by the improved agreement obtained using Lighthill's [88] coefficients, while the 2^{nd}-order formulation adhered to the Mach-independence principle.

In conclusion, it is deduced that the application of LPT to the cruciform wing-alone configuration is well supported by numerical investigation. The absence of an interference flowfield and any significant surface-to-surface interference yields conditions which are in good agreement with the theoretical basis and assumptions in LPT as detailed in Sections 3.1.1 and 3.1.4 and Chapter 4. The comparatively worse agreement with the Euler solution for Mode 3 points towards the shortcomings of LPT in the face of curvature-inducing deformations and flow three-dimensionality. A novel study of the influence of the selection of coefficients in piston-theory showed that they serve to provide a prediction-band which typically encompasses the exact (Euler) solution. However, they do not appear to exhibit underlying difference in trend-prediction. The use of higher-order formulations of LPT similarly did not change the prediction of α-dependence of the loads in the present test case.

5.4 Wing-Body Aerodynamics

The phrase "full-vehicle configuration" which has thus far been used refers to the present wing-body case. The defining characteristic of the wing-body configuration is the aerodynamic interference between the body-related flowfield and the wing-related flowfield. The wings (or control surfaces) are embedded in an interference flowfield which may be characterized by:

- Non-uniform radial and circumferential distributions of fluid properties. One particular fluid property of importance is the dynamic pressure, as discussed in Section 2.1.3. These non-uniform distributions may be sharply defined,
- Flow structures originating from upstream, such as vortices and shock wave,

The wing-body case represents a simple geometry of practical engineering interest. It is the purpose of the present study to investigate the application of Euler-based LPT to statically deforming control surfaces on the geometry. This represents a controlled, incremental investigation into the suitability of LPT in interference flows. The suitability of LPT will be assessed by considering:

- The accuracy in load prediction (C_Y, C_l),
- The correctness of the loading trends predicted ($\frac{\partial C_Y}{\partial \alpha}$, etc.),

through comparison of the wing-body case with the interference-free wing-alone case.

This chapter opens with the present introduction. The reader seeking clarifying remarks surrounding the mode-shapes of deformation is referred to the introduction of Section 5.3. This introduction will be followed by Sections 5.4.1 and 5.4.2, in which the results of the wing-body case are presented. This will be followed by Sections 5.4.3 and 5.4.4, in which the comparison between the wing-alone and wing-body case will be made and the interference assessed. The chapter will close with a general discussion of the results for the wing-body case in Section 5.4.5.

5.4.1 Results: Influence of Piston Theory Coefficients

As was done in Section 5.3.2, the first set of results investigates the influence of the piston-theory coefficients chosen. The three different theoretical bases, with associated coefficients, which have been utilized in this study were defined in Tables 5.6 to 5.8. Where appropriate, the aerodynamic pressure on expansion surfaces as predicted by LPT was limited to vacuum pressure. The results depicting the influence of the choice of piston-theory coefficients are shown in Figs. 5.43 to 5.51, and will be discussed below on a per-mode-shape basis.

Mode 1: First Bending

The side-force (C_Y) and rolling-moment (C_l) coefficients for Mode 1 are shown for the Mach set $M_\infty = [2.0, 2.5, 3.0]$ in Figs. 5.43 to 5.45, respectively. The reader is reminded that in the global coordinate system defined in Fig. 5.4, the side-force acts normal to the leeside control-surface. The following discussion points are made regarding the figures:

- As was noted in the introduction of Section 5.3, Mode 1 (first bending) exhibits predominantly bending, with minimal turning of the surface unit-normal vector into the mean steady flow. As a consequence, deformation causes low-subsonic downwash. This is reflected in how the 2$^{\text{nd}}$ and 3$^{\text{rd}}$ order LPT formulations are indistinguishable from the 1$^{\text{st}}$ order formulation,

- Some observations on the trends of the Euler solution are warranted. A distinct shift in the load-slopes (with α) is noted at all Mach numbers considered for $\alpha > 8°$. At $M_\infty = 2.0$ (see Fig. 5.43), the change is fairly benign, with a similarly gradual change noted between $6° < \alpha 8°$ at $M_\infty = 3.0$ in Fig. 5.45. This is associated with the development (through weak crossflow-shocks) or accumulation (from the weakly curved bow shock) of rotationality at the rear of the body at these angles-of-attack. The sharper changes noted at $M_\infty > 8°$ for $M_\infty = 2.5$ and $M_\infty = 3.0$ are associated with the onset of stronger, more distinct vortical structures due to the presence of more extensive crossflow-shocks along the length of the body. It is noted, with reference to Table 5.5 that these trends develop at $M_\infty \sin\alpha > 0.4$,

- Comparison to the Euler solution shows that better prediction is obtained (at both deflections) by the Van Dyke formulation rather than by the Lighthill formulation over the Mach range considered. This is in contrast with the observations made for the wing-alone case in Section 5.3 regarding Figs. 5.43 to 5.45. The different LPT coefficients provide an estimation band as before. As in the wing-alone case, this band is seen to become narrower as M_∞ increases. However, worse agreement of the estimation band with the Euler solution is noted. Fair agreement is noted at $\alpha \leq 4°$ over the Mach range considered. The agreement (both in loads and in their α-dependence) quickly deteriorates as the incidence is increased above $\alpha = 4°$. Particularly poor agreement in the α-dependence is noted immediately prior to and immediately following the onset of the aforementioned vortical structures.

Mode 2: First Twist

The side-force and rolling-moment coefficients for Mode 2 are shown for the Mach set $M_\infty = [2.0, 2.5, 3.0]$ in Figs. 5.46 to 5.48, respectively. The following discussion points are made regarding the figures:

- Many of the same observations apply to the present case as were made in the wing-alone configuration in Section 5.3.2. Mode 2 (first twist) exhibits predominantly torsion, which yields high-subsonic to supersonic downwash. This is reflected in how the 2^{nd} and 3^{rd} order LPT formulations are distinct from one another, particularly at the higher deflection of $\delta = 10\,\text{mm}$. The vacuum-related "pressure-limiting" noted previously is again evident in the difference between the 1^{st} and 2^{nd} order solutions,

- The observations previously made in Section 5.3.2 regarding the role of the LPT coefficients also broadly apply here. The interpretation of LPT variants providing an estimation band at a given order of LPT is particularly clear in Fig. 5.48. The same observations regarding under-prediction and over-prediction by the 1^{st}- and 3^{rd}-order bands again apply. Once again, it is of interest that the Lighthill coefficients provide better agreement with the Euler solution over the parameter space considered.

Mode 3: Second Bending

The side-force and rolling-moment coefficients for Mode 3 are shown for the Mach set $M_\infty = [2.0, 2.5, 3.0]$ in Figs. 5.49 to 5.51, respectively. The following discussion points are made regarding the figures:

- Mode 3 (second bending) exhibits predominantly bending, with moderate camber at the trailing-edge of the mid-span. As a consequence, deformation causes predominantly low-subsonic downwash, with localized high-subsonic downwash at the mid-span trailing-edge. This is reflected in how the 2^{nd} and 3^{rd} order LPT formulations are distinct from one another, particularly at the higher deflection of $\delta = 10\,\text{mm}$. The fact that the 2^{nd} order results are essentially indistinguishable from the 1^{st} order results shows that vacuum pressure is not reached,

- The observations regarding the role of the LPT coefficients made for Mode 1 also broadly apply to Mode 3. Once again, the 2^{nd} order Lighthill formulation provides the best agreement with the Euler solution. Here, it is observed that the estimation band narrows with both increasing M_∞ and increasing α. The large overlap between the 2^{nd} and 3^{rd} order estimation bands points to the low-subsonic downwash-Mach numbers encountered over the majority of the wing.

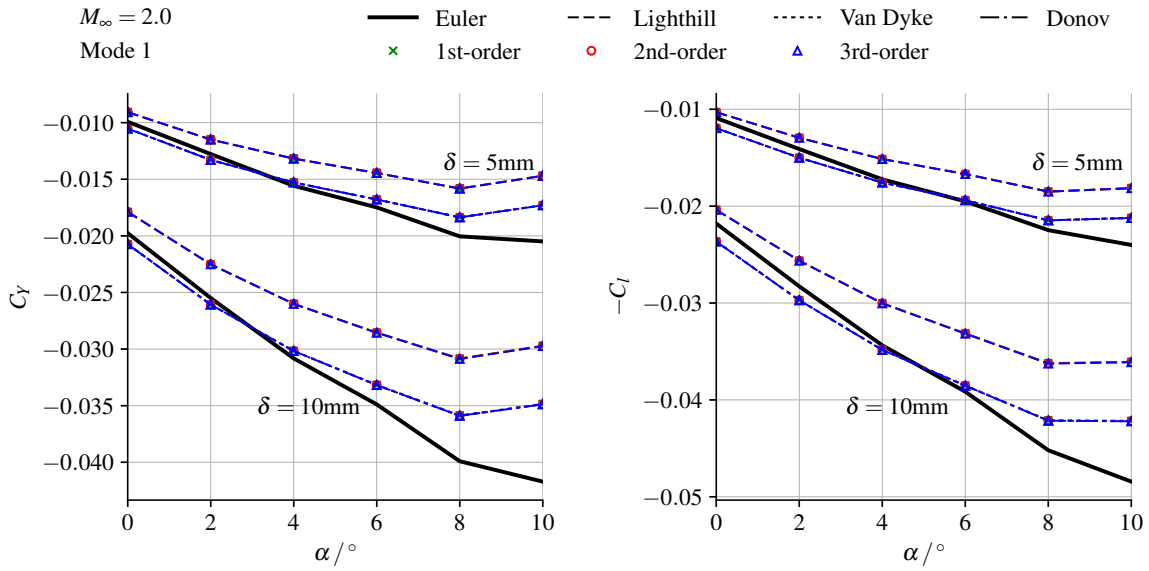

Fig. 5.43 Influence of piston theory coefficients on the prediction of side-force C_Y and rolling-moment C_l coefficients. Mode 1 at $M_\infty = 2.0$.

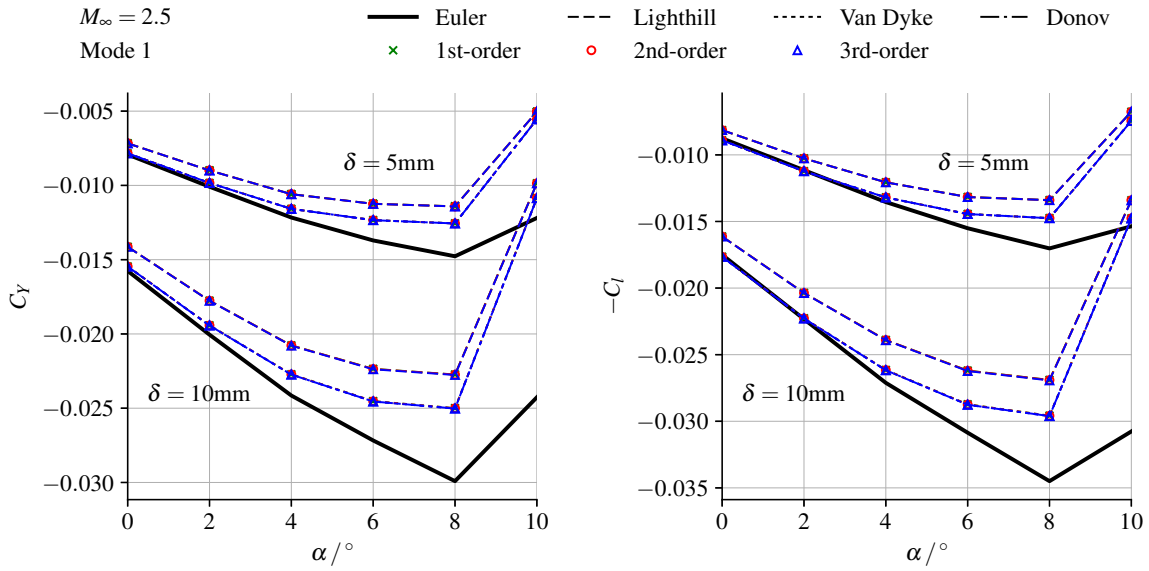

Fig. 5.44 Influence of piston theory coefficients on the prediction of side-force C_Y and rolling-moment C_l coefficients. Mode 1 at $M_\infty = 2.5$.

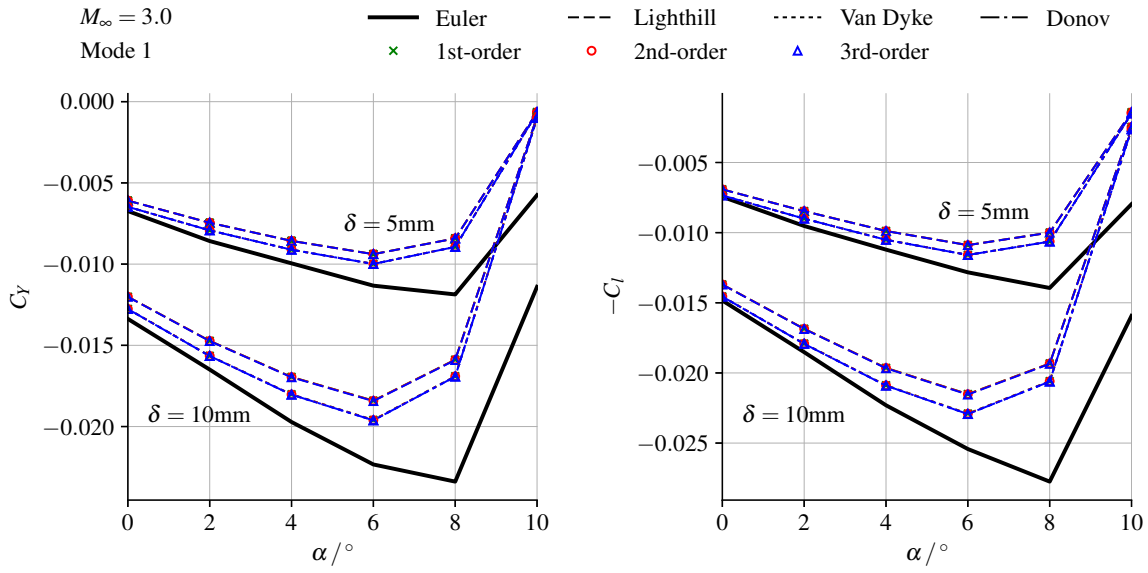

Fig. 5.45 Influence of piston theory coefficients on the prediction of side-force C_Y and rolling-moment C_l coefficients. Mode 1 at $M_\infty = 3.0$.

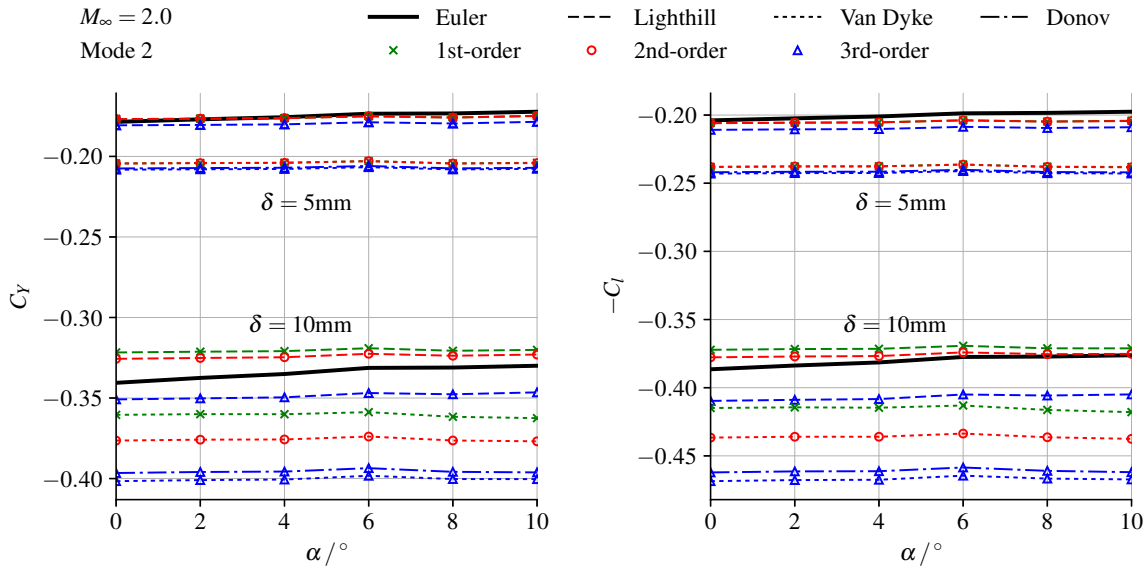

Fig. 5.46 Influence of piston theory coefficients on the prediction of side-force C_Y and rolling-moment C_l coefficients. Mode 2 at $M_\infty = 2.0$.

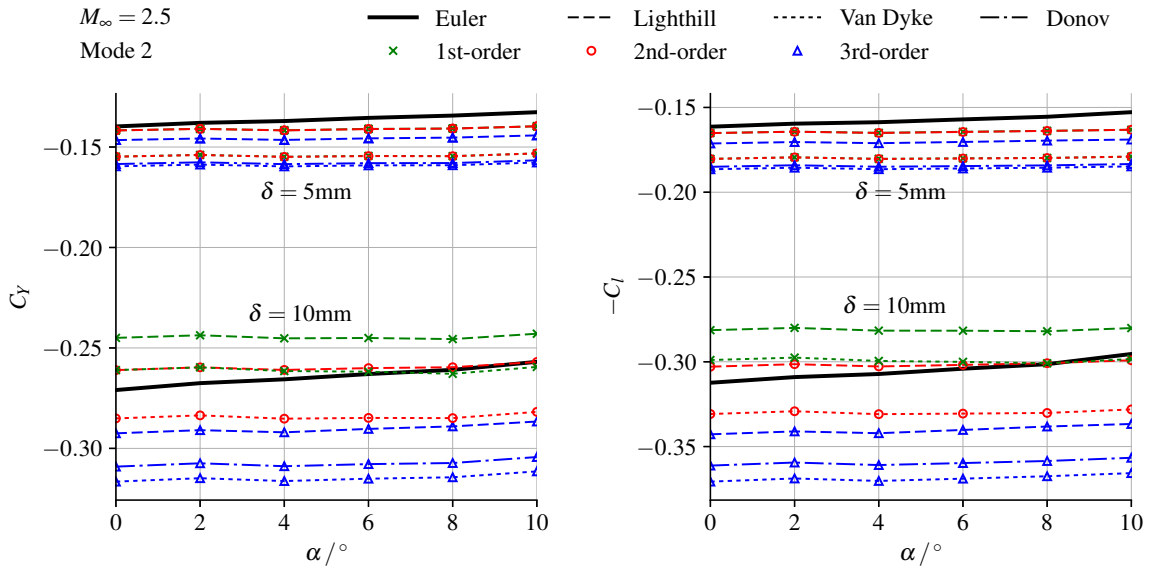

Fig. 5.47 Influence of piston theory coefficients on the prediction of side-force C_Y and rolling-moment C_l coefficients. Mode 2 at $M_\infty = 2.5$.

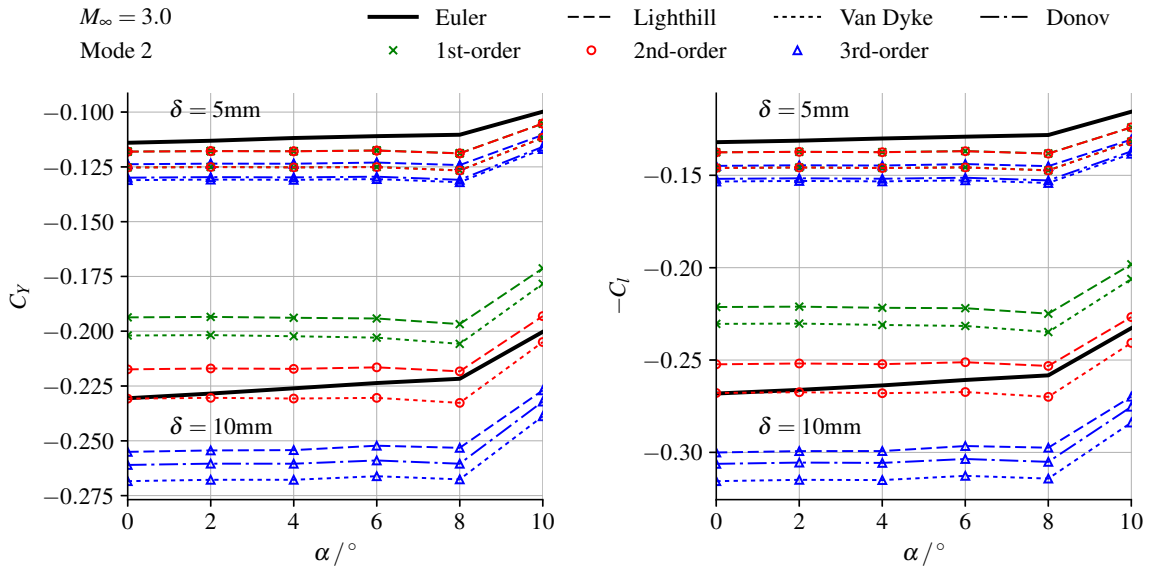

Fig. 5.48 Influence of piston theory coefficients on the prediction of side-force C_Y and rolling-moment C_l coefficients. Mode 2 at $M_\infty = 3.0$.

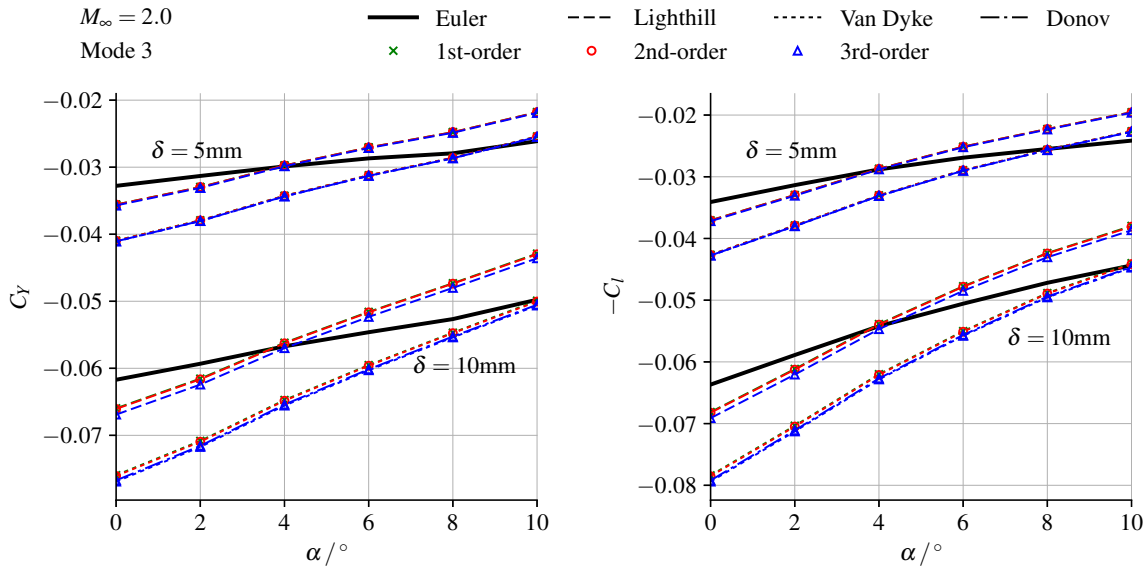

Fig. 5.49 Influence of piston theory coefficients on the prediction of side-force C_Y and rolling-moment C_l coefficients. Mode 3 at $M_\infty = 2.0$.

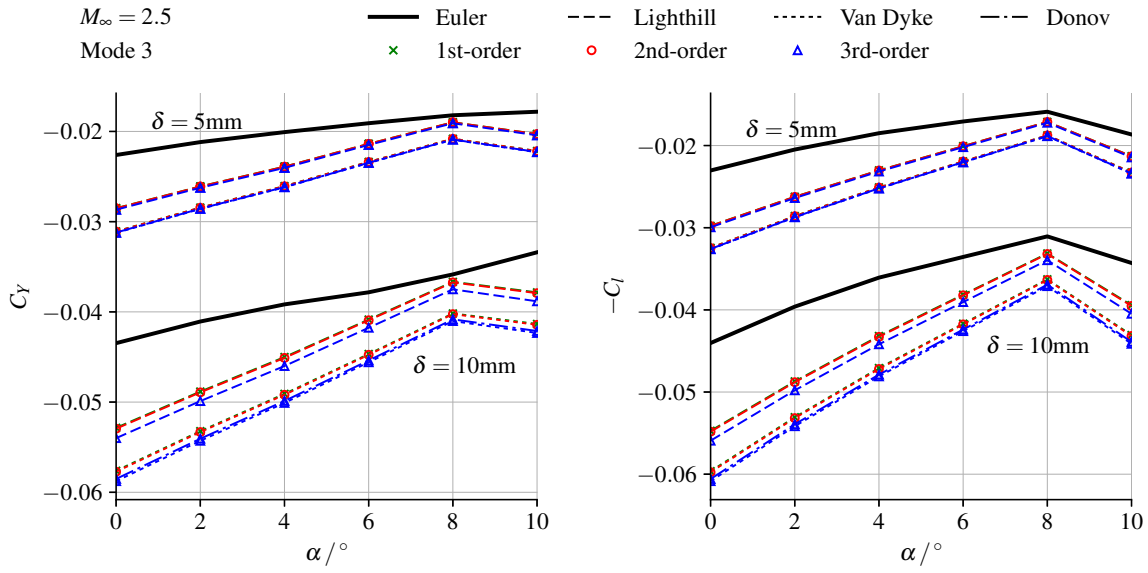

Fig. 5.50 Influence of piston theory coefficients on the prediction of side-force C_Y and rolling-moment C_l coefficients. Mode 3 at $M_\infty = 2.5$.

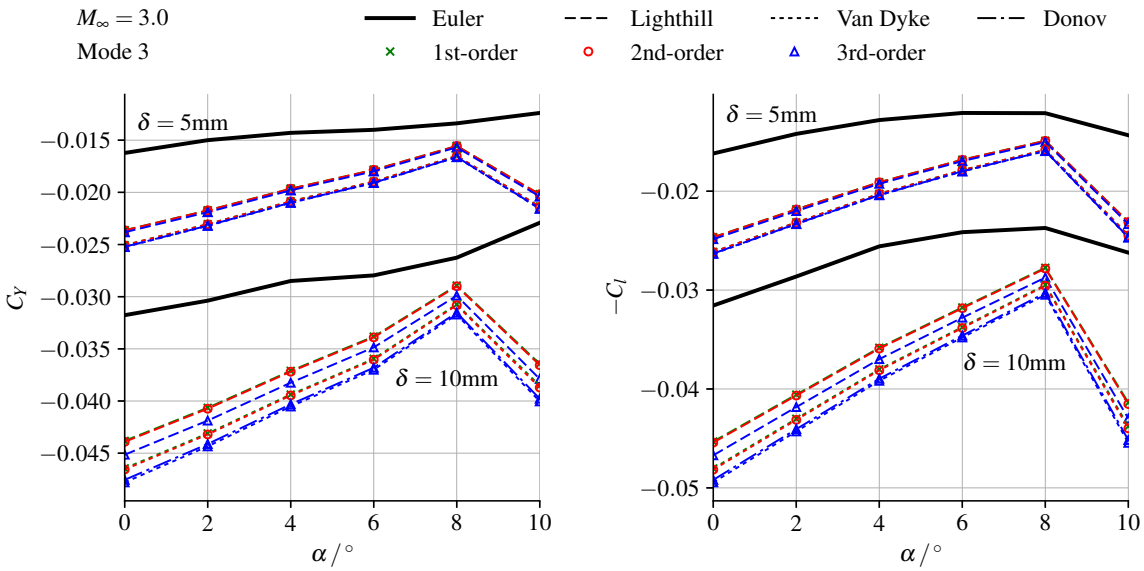

Fig. 5.51 Influence of piston theory coefficients on the prediction of side-force C_Y and rolling-moment C_l coefficients. Mode 3 at $M_\infty = 3.0$.

5.4.2 Results: Influence of Freestream Mach Number

As was done in Section 5.3.3, the second set of results to be presented investigates the influence of M_∞ on the accuracy of LPT prediction. Once again, the 2$^{\text{nd}}$-order LPT formulation based on Lighthill's [88] coefficients is shown. The results depicting the influence of M_∞ are shown in Figs. 5.52 to 5.57, and will be discussed below on a per-mode-shape basis.

Mode 1: First Bending

The influence of M_∞ on prediction accuracy for Mode 1 is shown for the deflection set $\delta = [5\,\text{mm}, 10\,\text{mm}]$ in Figs. 5.52 and 5.53, respectively. The following discussion points are made regarding the figures:

- A weak trend of improvement in prediction accuracy with increasing M_∞ is noted. The offset between LPT and Euler prediction is noted to scale linearly with deflection. Prediction accuracy is noted to degrade with increasing α, particularly as the body-vortex development starts around $\alpha \approx 8°$. Particularly poor prediction in the centre-of-pressure location is noted for $M_\infty = 2.5$ and $M_\infty = 3.0$ at $\alpha = 10°$. However, it must be noted that this is due to the mathematical definition of x_{CP} and z_{CP} becoming poorly defined as $C_Y \to 0$,

- The progression in vortex development with increasing M_∞ at a given α is evident in the Euler results. This is manifested as the changes in the load-slopes (with α) from $\alpha \gtrsim 8°$. Furthermore, this is reflected in the tip-wards progression of z_{CP}. These trends are evidence of the body-shed interference flowfield. Further investigation of the aerodynamic interference is reserved for Sections 5.4.3 and 5.4.4,

- Fair agreement in the α-dependence is obtained consistently only for $\alpha \leq 6°$. It is evident that the accuracy of the load-slope predictions is both M_∞- and α-dependent. Significant errors in the load-slope prediction may be are observed immediately prior to the onset of stronger crossflow-shocks at $M_\infty \sin\alpha \approx 0.45$.

  This is exemplified by the slope predicted between $6° < \alpha < 8°$ at $M_\infty = 3.0$ and between $8° < \alpha < 10°$ at $M_\infty = 2.0$. In these instances, the load-slope predicted by Euler-LPT is of opposite sign to that found in the Euler solution. The trends in the load-slopes point towards LPT predicting an earlier and more benign reversal in sign with increasing α. This has direct implications for the prediction accuracy of flight-dynamical and aeroelastic analyses.

Mode 2: First Twist

The influence of M_∞ on prediction accuracy for Mode 2 is shown for the deflection set $\delta = [5\,\text{mm}, 10\,\text{mm}]$ in Figs. 5.54 and 5.55, respectively. The following discussion points are made regarding the figures:

- The prediction accuracy is noted to have a clear dependence on M_∞, α, and δ. At $\delta = 5\,\text{mm}$, it is observed that a degradation in prediction accuracy is obtained with increasing M_∞. However, at $\delta = 10\,\text{mm}$, the prediction accuracy is comparatively Mach-insensitive. Comparison of Figs. 5.54 and 5.55 shows that the α-trends of the predicted (LPT) loads are essentially similar, with the loads themselves being scaled by δ. The alternate under-prediction and over-prediction of loads at the two values of δ points towards a difference in the δ-stiffness of the predicted and the actual loads,

- The agreement in the α-dependence is at best fair. Differences in the slopes are not obvious in Figs. 5.54 and 5.55 due to the scale required to compare loads over the Mach range considered. The differences in load-slopes and poorer agreement will be more clearly shown in Figs. 5.63 to 5.65 and will be discussed in Section 5.4.3.

  In contrast to Mode 1, it is seen that a notable change in the Euler load-slope (with α) is only observed for $M_\infty = 3.0$ between $8° < \alpha < 10°$. Comparison of the magnitude of the predicted loads for Mode 1 and Mode 2 further suggests that interference from body-shed vorticity plays a secondary role in determining the loads for Mode 2. In light of the mode-shape of Mode 2 – first twist – this is not surprising,

- Inspection of the predicted centre-of-pressure locations shows that Euler-based LPT does not reproduce the shift in x_{CP} and z_{CP} with M_∞. Furthermore, the α-dependence of z_{CP} is incorrectly predicted. However, it must be noted that the variations in x_{CP} and z_{CP} are nominal, and are of secondary concern to the prediction accuracy of C_Y and C_l in the present case.

Mode 3: Second Bending

The influence of M_∞ on prediction accuracy for Mode 3 is shown for the deflection set $\delta = [5\,\text{mm}, 10\,\text{mm}]$ in Figs. 5.56 and 5.57, respectively. The following discussion points are made regarding the figures:

- Generally poor agreement is seen, both in the load prediction and in the trend prediction. Comparison of Figs. 5.56 and 5.57 shows no significant δ-dependence is observed in the overall prediction trends,

- Significant modelling differences in the α-dependence of both C_Y and C_l are with the onset of body-shed vorticity. Inspection of the Euler trends in $\frac{\partial C_Y}{\partial \alpha}$ for $M_\infty = 2.5$ and $M_\infty = 3.0$ shows no sharp changes. On the other hand, the LPT predictions show a sharp sign-reversal between $8° < \alpha < 10°$.

  The Euler trends in $\frac{\partial C_l}{\partial \alpha}$ for $M_\infty = 2.5$ and $M_\infty = 3.0$ show a more gradual influence of the onset of body-shed vorticity. This is not reproduced by the LPT predictions, which again feature a sharp sign reversal between $8° < \alpha < 10°$.

  Interestingly, despite the outright incorrect prediction of trends in $\frac{\partial C_Y}{\partial \alpha}$ at $M_\infty = 2.0$ and $M_\infty = 2.5$, the overall trend in $\frac{\partial z_{CP}}{\partial \alpha}$ is correct. This is contrasted with the incorrect trends being predicted for $\frac{\partial x_{CP}}{\partial \alpha}$. The shift in x_{CP}, however, is nominally small.

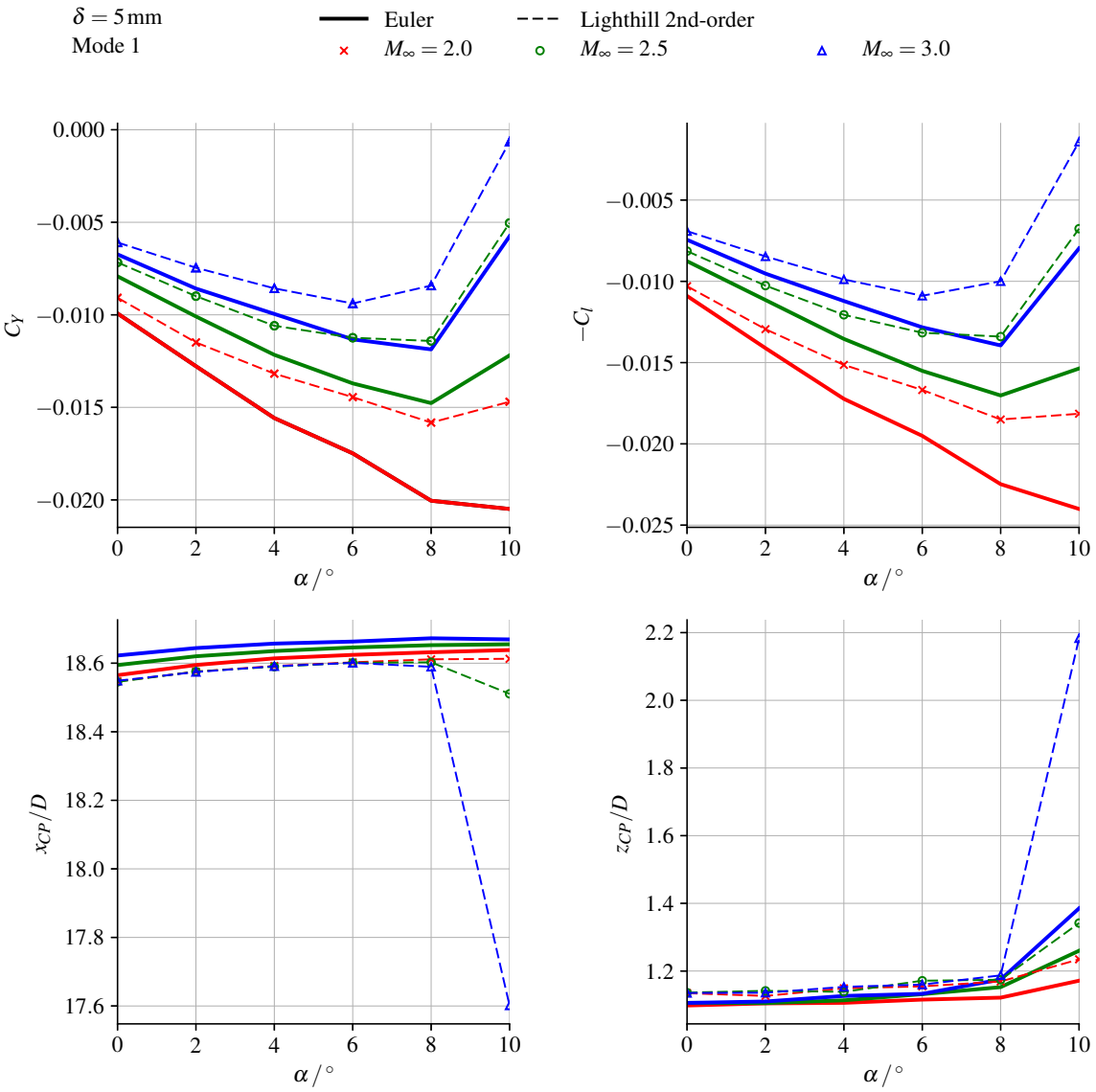

Fig. 5.52 Influence of freestream Mach number on the prediction of the side-force coefficient C_Y, rolling-moment coefficient C_l, axial centre-of-pressure location x_{CP}/D, and vertical centre-of-pressure location z_{CP}/D. Mode 1 with $\delta = 5\,\text{mm}$.

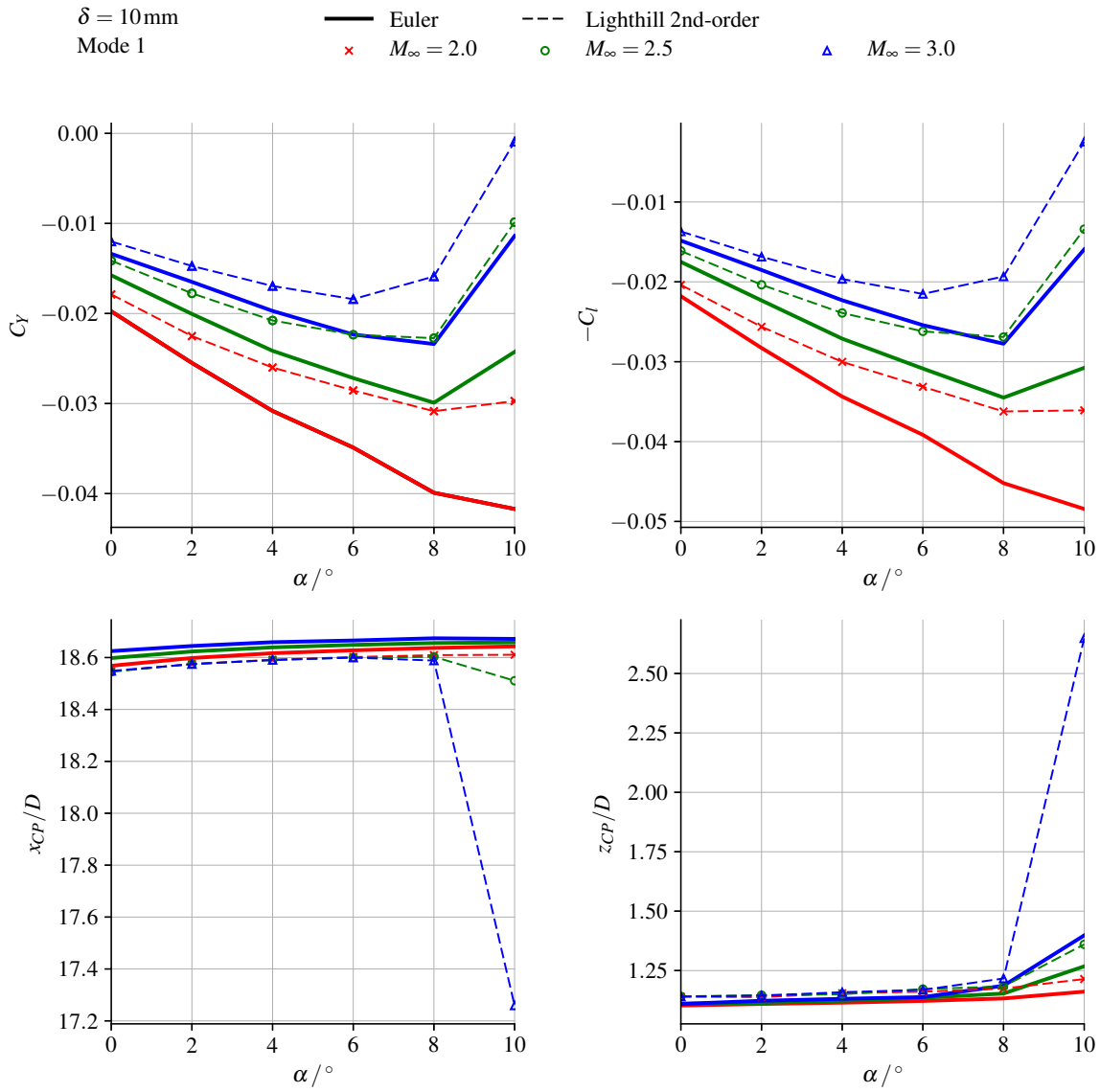

Fig. 5.53 Influence of freestream Mach number on the prediction of the side-force coefficient C_Y, rolling-moment coefficient C_l, axial centre-of-pressure location x_{CP}/D, and vertical centre-of-pressure location z_{CP}/D. Mode 1 with $\delta = 10\,\text{mm}$.

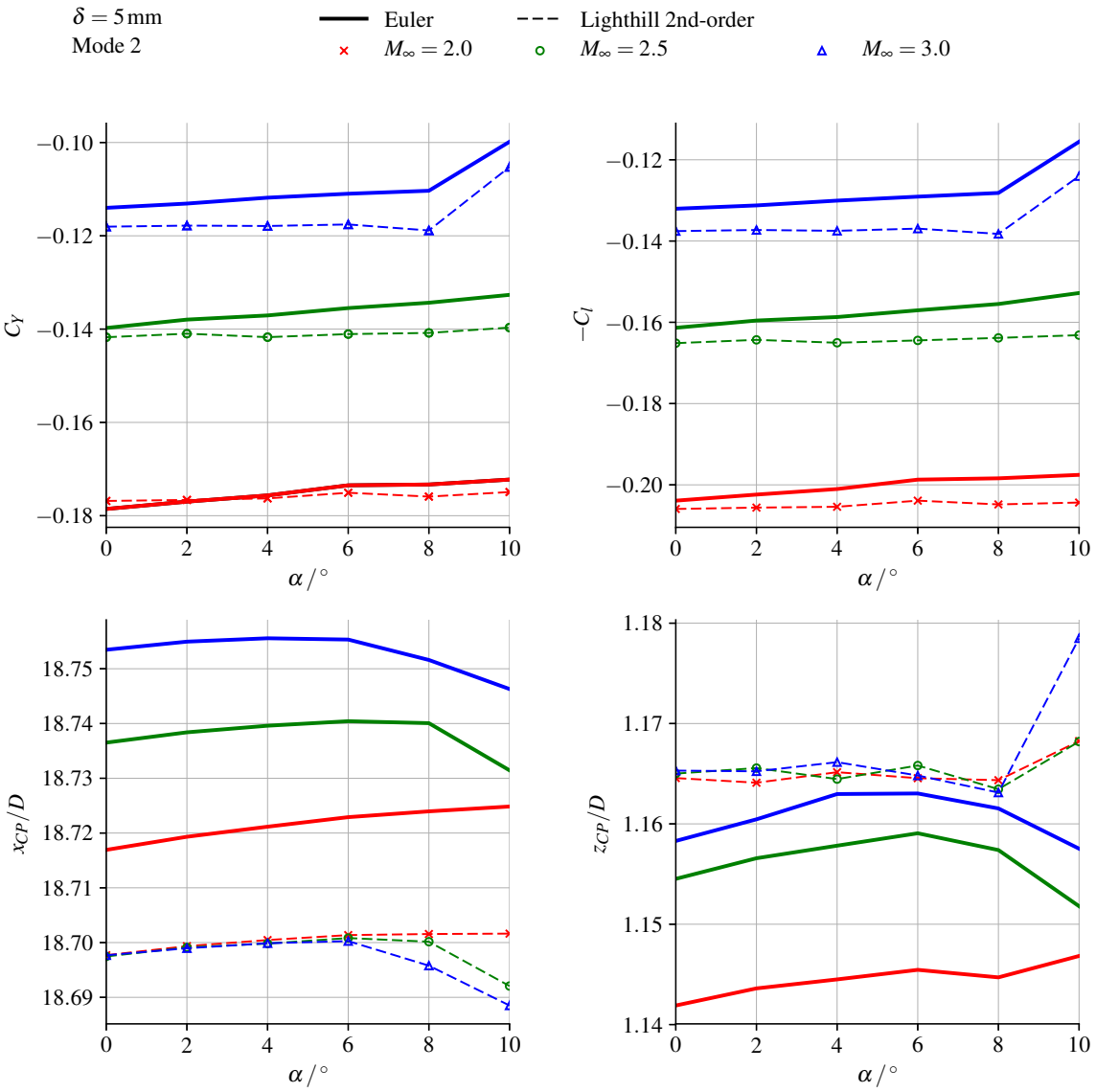

Fig. 5.54 Influence of freestream Mach number on the prediction of the side-force coefficient C_Y, rolling-moment coefficient C_l, axial centre-of-pressure location x_{CP}/D, and vertical centre-of-pressure location z_{CP}/D. Mode 2 with $\delta = 5\,\text{mm}$.

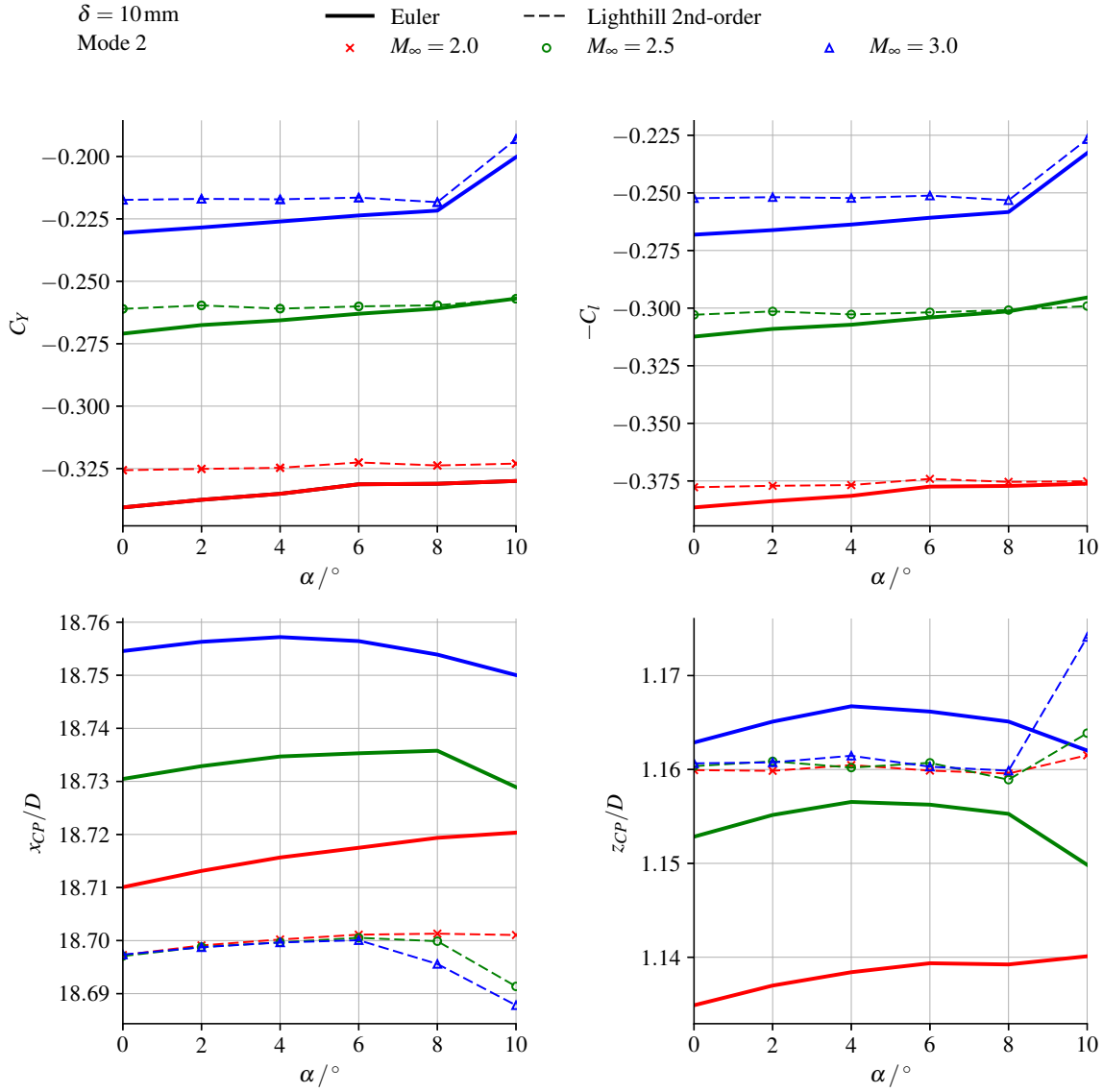

Fig. 5.55 Influence of freestream Mach number on the prediction of the side-force coefficient C_Y, rolling-moment coefficient C_l, axial centre-of-pressure location x_{CP}/D, and vertical centre-of-pressure location z_{CP}/D. Mode 2 with $\delta = 10\,\text{mm}$.

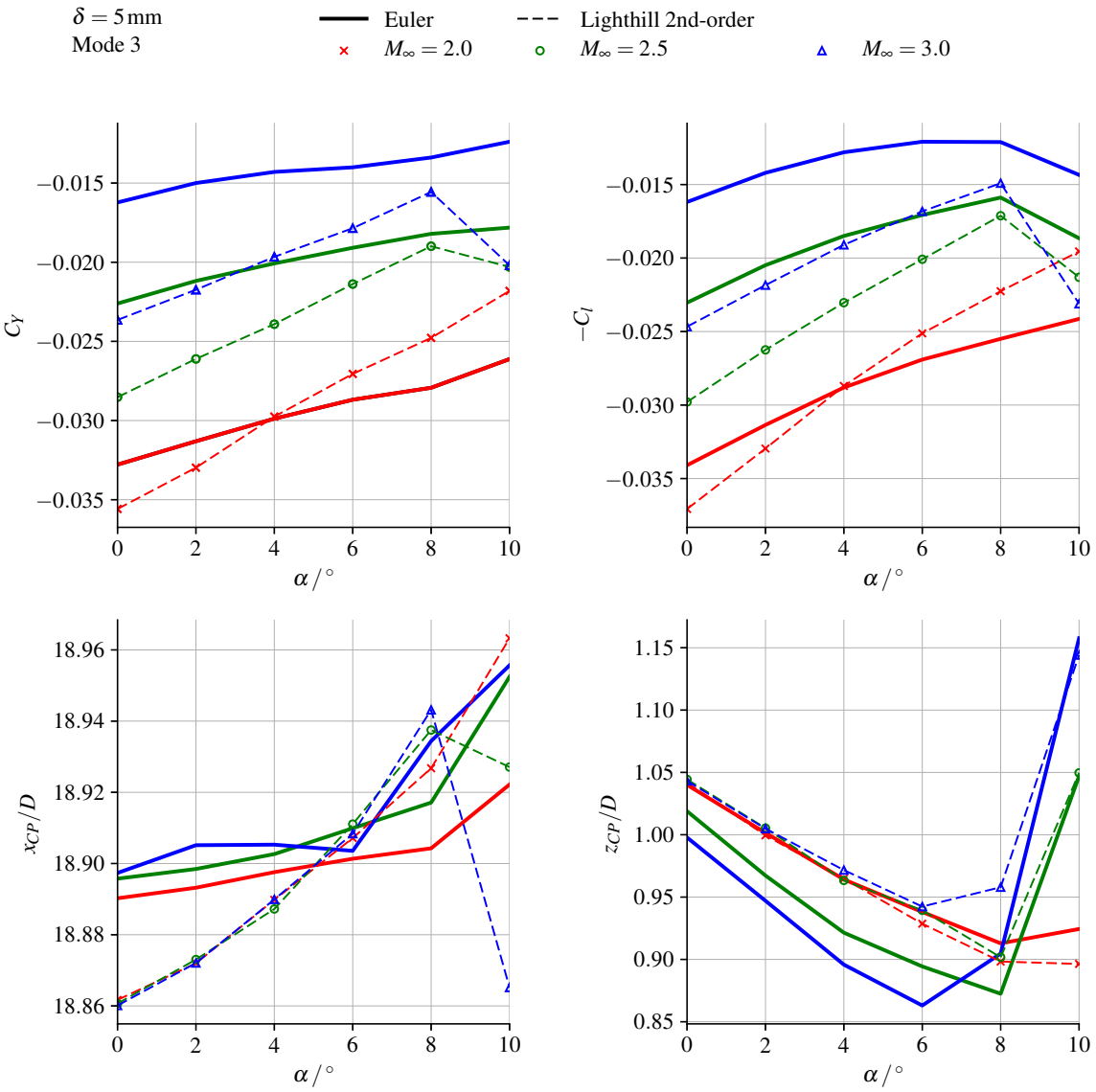

Fig. 5.56 Influence of freestream Mach number on the prediction of the side-force coefficient C_Y, rolling-moment coefficient C_l, axial centre-of-pressure location x_{CP}/D, and vertical centre-of-pressure location z_{CP}/D. Mode 3 with $\delta = 5\,\text{mm}$.

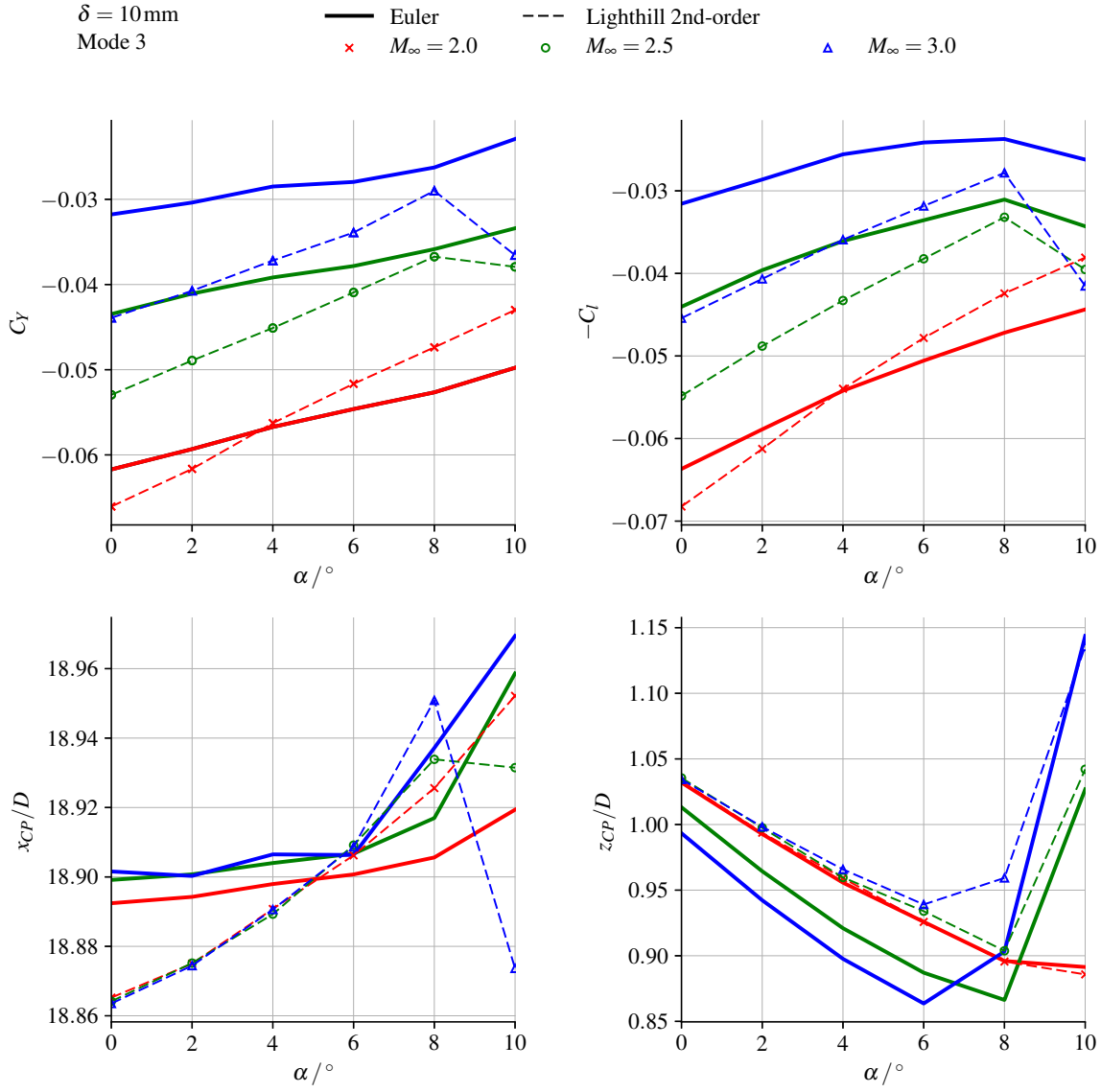

Fig. 5.57 Influence of freestream Mach number on the prediction of the side-force coefficient C_Y, rolling-moment coefficient C_l, axial centre-of-pressure location x_{CP}/D, and vertical centre-of-pressure location z_{CP}/D. Mode 3 with $\delta = 10\,\text{mm}$.

5.4.3 Interference Results: Direct Comparison of Loads

The present set of results will illustrate the aerodynamic interference in the full-vehicle configuration through direct comparison of the wing-alone (W) and the wing-body (B+W) loads. The Euler-based LPT predictions that will be shown refer to the second-order LPT formulation using Lighthill's [88] coefficients. Due to the weak dependence of the results on δ, the figures will be limited to results for $\delta = 10\,\text{mm}$ for the sake of brevity. The direct comparison of loads is shown in Figs. 5.58 to 5.69, with the figures discussed below on a per-mode-shape basis.

Mode 1: First Bending

The comparison of wing-alone and wing-body loads for Mode 1 over the Mach range considered is shown for $\delta = 10\,\text{mm}$ in Fig. 5.58. Due to the density of information depicted, the comparison will also be shown for each Mach number in the set $M_\infty = [2.0, 2.5, 3.0]$ in Figs. 5.59 to 5.61, respectively. The following discussion points are made regarding the Euler solutions:

- The general trend is noted of increasing difference between the loads of the wing-alone case and of the body-alone case as M_∞ increases. This is particularly evident at $\alpha > 8°$, with smaller differences occurring at lower incidences. This is clear evidence of the aerodynamic interference due to body-shed vortices,
- Minor differences between the wing-alone and body-alone loads are noted at $\alpha \leq 4°$. This is accompanied by increased differences in the load-slopes around $\alpha = 0°$. It may be noted that the wing-alone and wing-body loads are very close to each other at $\alpha = 0°$. This points to negligible interaction (following deformation) with the interference flowfield due to the body bow-shock and the associated non-uniform dynamic-pressure distribution. This interaction will be referred to as "integration effects" in the discussion below.

The following discussion points are made regarding the Euler-based LPT predictions:

- As was noted in Section 5.3.3, the wing-alone results show improved accuracy with increasing M_∞. Furthermore, good agreement with the Euler solution is obtained throughout the α-range, both in the loads and in the load-slopes. A predominantly linear loading with α is observed,
- These observations do not apply to the wing-body case. Here, any improvement in prediction accuracy with M_∞ is comparatively nominal. Generally worse prediction

accuracy is obtained, both in the loads and the load-slopes. The prediction error rapidly increases with α. The loading is clearly nonlinear with α,

- It is of interest to note that the predicted loading at $\alpha = 0°$ is essentially identical between the wing-alone and the wing-body cases. This trend will be noted throughout for each mode-shape. A brief discussion of the observation is made here, and will be repeated in Section 5.4.5.

  Differences between the wing-alone and body-alone LPT-predicted loads at $\alpha = 0°$ have a particular origin. In both cases, LPT uses the Euler solution at $\delta = 0\,\text{mm}$ as the mean-steady reference solution being perturbed. The mode-shape (and by extension, turning of the normal-vector) is the same between the wing-alone and the wing-body cases. Thus, the only source for differences in prediction lies in the reference solution.

  The near-negligible prediction difference at $\alpha = 0°$ seen throughout the present study points to the weak effect that the body bow-shock has in changing the steady flow about the un-deformed control-surface. Since LPT does not model interaction with the surrounding flowfield, but is purely a perturbation to the surface solution, no significant difference between the wing-alone and wing-body predictions are to be expected at $\alpha = 0$.

- It is of interest to note that while LPT does not model interaction with the surrounding flowfield, the predicted wing-body loading is clearly nonlinear and shares a similar overall trend with the Euler solution. This warrants further discussion. As remarked above, LPT models perturbations to the surface solution. It does not have any "knowledge" of the surrounding flowfield, and does not mathematically account for it. The source of the nonlinearity in the predicted load is the mean-steady reference solution at $\delta = 0\,\text{mm}$. Specifically, it is the solution at the surface of the wing. Since LPT cannot model interaction with the flowfield, differences between LPT and an Euler solution may to *some* extent be attributed to this interaction.

  It is inaccurate to attribute the entirety of the Euler / LPT difference to interaction with the flowfield. The variety of sources of inaccuracy in LPT prediction have been discussed at length in Sections 3.1.1 and 3.1.4 and Chapter 4. However, considering the excellent agreement obtained for Mode 1 in the wing-alone results, it may be argued that disagreement in the wing-body cases may largely be attributed to flowfield interaction.

  This interpretation allows some insight to be gained into the shortcomings of Euler-based LPT applied to full-vehicle geometries (or generally, in interference flows). It

may be deduced that a (potentially) significant component of the "full-vehicle trends" is captured by the mean-steady solution at the surface of the un-deformed wing. In other words, an LPT prediction may provide fair overall trends if the mean-steady reference solution captured the surface-effects of the interference flowfield.

However, the accuracy (beyond overall trends) of the LPT prediction is thereafter dictated by a variety of factors (Sections 3.1.1 and 3.1.4 and Chapter 4). Interaction (both static and dynamic) with the surrounding flow as the geometry deforms may be expected to be a significant factor. This is reflected in the notably worse prediction accuracy obtained by LPT in the wing-body case than was obtained in the wing-alone case for Mode 1.

Mode 2: First Twist

The comparison of wing-alone and wing-body loads for Mode 2 over the Mach range considered is shown for $\delta = 10\,\text{mm}$ in Fig. 5.62. In order to better resolve differences between data, the comparison will also be shown for each Mach number in the set $M_\infty = [2.0, 2.5, 3.0]$ in Figs. 5.63 to 5.65, respectively. The following discussion points are made regarding the Euler solutions:

- The general trend is noted of diminishing difference between the loads of the wing-alone case and of the body-alone case as M_∞ increases. The differences are inherently larger at the upper portion of the α range. This is also where the effect of M_∞ is most noticeable. Prominent changes to the load-slope following the onset of body-shed vortices are only noted at $\alpha > 8°$ for M_∞,

- Fairly similar load-slopes are noted at $\alpha < 2°$ at $M_infty \geq 2.5$, with greater similarity observed as M_∞ increases. Larger differences between the wing-alone and body-alone loads are noted at $\alpha = 0°$ than were observed for Mode 1. This points to a greater amount of interaction (following deformation) with the interference flowfield due to the body bow-shock than was noted for Mode 1. This is due to differences in the mode-shape of deformation. The smallness of the wing-integration effects at $\alpha = 0°$ relative to the overall load points towards the load being dominated by the surface inclination of the wing. The differences between the wing-alone and wing-body loads (and load-slopes) at higher incidences are a clear sign of aerodynamic interference.

The following discussion points are made regarding the Euler-based LPT predictions:

- It is clear that an error in the prediction of the wing-alone load-slopes exists. This error is seen to decrease with increasing M_∞. Following the discussion on sources of error

in LPT from Mode 1, it may be argued that the prediction error (in both the load and load-slope) is attributable to inherent shortcomings in LPT. The reader is reminded that Mode 2 results in large twist at the wing tip (of the order of 23.5° at $\delta = 10\,\text{mm}$). This represents a large perturbation from the un-deformed reference solution. Furthermore, it is known that aerodynamic loading becomes increasingly nonlinear (with deflection) as shock detachment is approached. The combination of these factors are likely the primary source of error in the wing-alone predictions for Mode 2,

- The above-discussed error in the wing-alone loads is independent of the interference flowfield. Therefore, a proportionate error is to be expected in the wing-body predictions. Inspection of the wing-body results shows that a greater prediction error is obtained. This points to further sources of error being introduced with the interference flowfield.

  One such additional source of error is the interaction (following deformation) with the non-uniform interference flowfield surrounding the initially un-deformed wing. This is evidenced, as before, by the offset between the wing-alone and wing-body Euler loads at $\alpha = 0°$, which is clearly not accounted for by Euler-based LPT,

- As discussed for Mode 1, it is significant to note that a portion of the underlying effect of the interference flowfield is accounted for by LPT. Notably, the LPT predictions replicate the general α trends of the Euler solution. This is clearly shown in the sharp changes in load noted at $\alpha > 8°$ at $M_\infty = 3.0$. However, the offset between the predicted loads and the actual computed loads is seen to be a function of α at each M_∞ examined. This again points towards underlying flowfield interactions being neglected by LPT.

Mode 3: Second Bending

The comparison of wing-alone and wing-body loads for Mode 3 over the Mach range considered is shown for $\delta = 10\,\text{mm}$ in Fig. 5.66. Due to the density of information depicted, the comparison will also be shown for each Mach number in the set $M_\infty = [2.0, 2.5, 3.0]$ in Figs. 5.67 to 5.69, respectively. The following discussion points are made regarding the Euler solutions:

- As with Mode 2, the general trend is noted of diminishing difference between the loads of the wing-alone case and of the body-alone case as M_∞ increases. These differences are related to differences in the load-slopes (with α). Greater similarity in wing-alone and wing-body load-slopes is noted with increasing M_∞. No prominent changes to C_Y

are noted following the onset of body-shed vortices. However, vortex-related changes are noted in C_l,

- The difference between the wing-alone and body-alone loads at $\alpha = 0°$ is noted to increase with increasing M_∞. At $M_\infty = 3.0$, the difference is comparable to that noted for Mode 2. This suggests that the mode-shape of Mode 3 results in prominent flowfield interaction.

  This is further supported by the difference in trends between C_Y and C_l for Mode 3. For Modes 1 and 2, the trends in α-dependence of C_Y and C_l were essentially equivalent. In Mode 3, it is noted that the body-shed vortices clearly influence C_l, with the previously-observed reversal in $\frac{\partial C_l}{\partial \alpha}$. It is notable that this reversal is comparatively benign in comparison to the sharp changes noted in Modes 1 and 2. However, inspection of the C_Y trends for Mode 3 shows that obvious influence of the body-shed vortices. This difference in C_Y and C_l trends points to a more complex interaction between the mode-shape of deformation and the surrounding interference flowfield. This is to be expected as a result of:

  – The higher complexity of the mode-shape itself,

  – The proximity of the mid-span deformation pattern (and point of secondary maximum-deflection) to the body-shed vortices.

The following discussion points are made regarding the Euler-based LPT predictions:

- It is clear that an error in the prediction of the wing-alone load-slopes exists. This error as an underlying shortcoming of LPT has been discussed in Section 5.3.4. As noted for Mode 2 above, it may therefore be expected that a proportionate error in the load-slope be present in the wing-body results,

- Inspection of the wing-body results shows that a greater prediction error is obtained. As for Mode 2, this points to further sources of error being introduced with the interference flowfield.

  The previously-discussed interaction with the non-uniform interference flowfield at $\alpha = 0°$ is noted again. The error is seen to be particularly significant at $M_\infty = 3.0$,

- The most significant error in prediction relates to the general trends in C_Y. For Modes 1 and 2, it was noted that the LPT predictions replicated the general α trends of the Euler solution. This is not the case for Mode 3. Fair replication of the C_l trends are noted, with relatively poor prediction of the behaviour of $\frac{\partial C_l}{\partial \alpha}$ noted at $M_\infty = 3.0$ and $\alpha > 6°$.

However, the prediction of $\frac{\partial C_Y}{\partial \alpha}$ for $M_\infty \geq 2.5$, $\alpha > 8°$ is fundamentally incorrect. It is seen that LPT predicts a sign-reversal which is not present in the Euler solution.

In the discussion of the previous modes, it was remarked that the replication of the general trends pointed to *some* extent of the interference flowfield being accounted for purely by the mean-steady surface solution. The results of Mode 3 show that the LPT-neglected interaction (following deformation) with the interference flowfield may not be negligible. The sign-reversal noted in the LPT predictions stems from the mean-steady surface solution. However, this is clearly countered by flowfield-interaction in the Euler solution. Mode 3 may thus be considered an example of an engineering problem of practical interest and minimal complexity in which LPT fails to capture crucial flow physics.

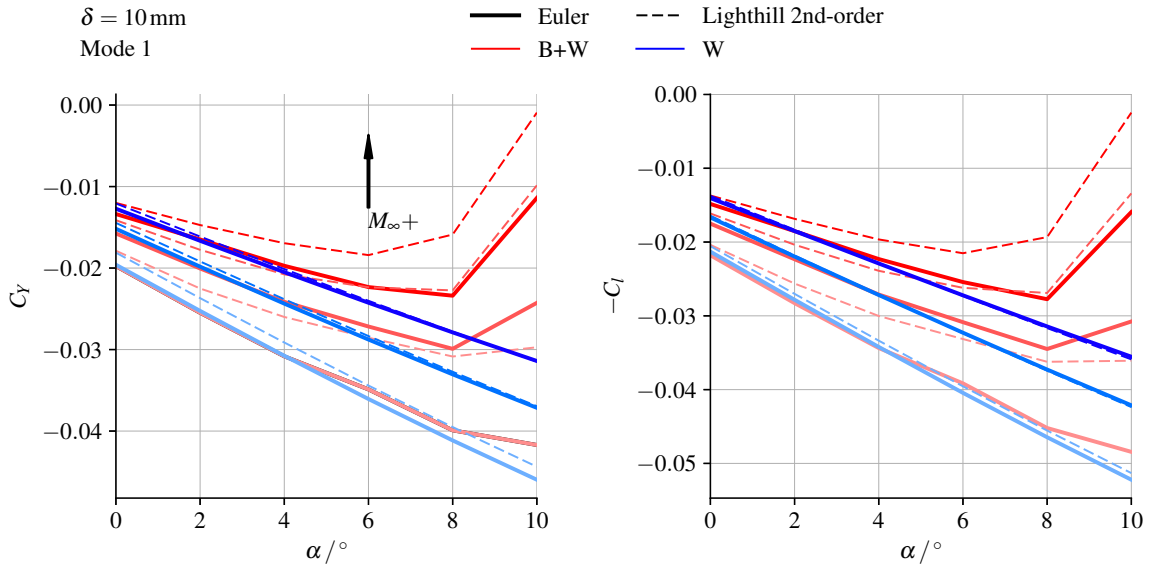

Fig. 5.58 Comparison of the wing-alone and wing-body predictions of the side-force coefficient C_Y and rolling-moment coefficient C_l. Mode 1 with $\delta = 10\,\mathrm{mm}$.

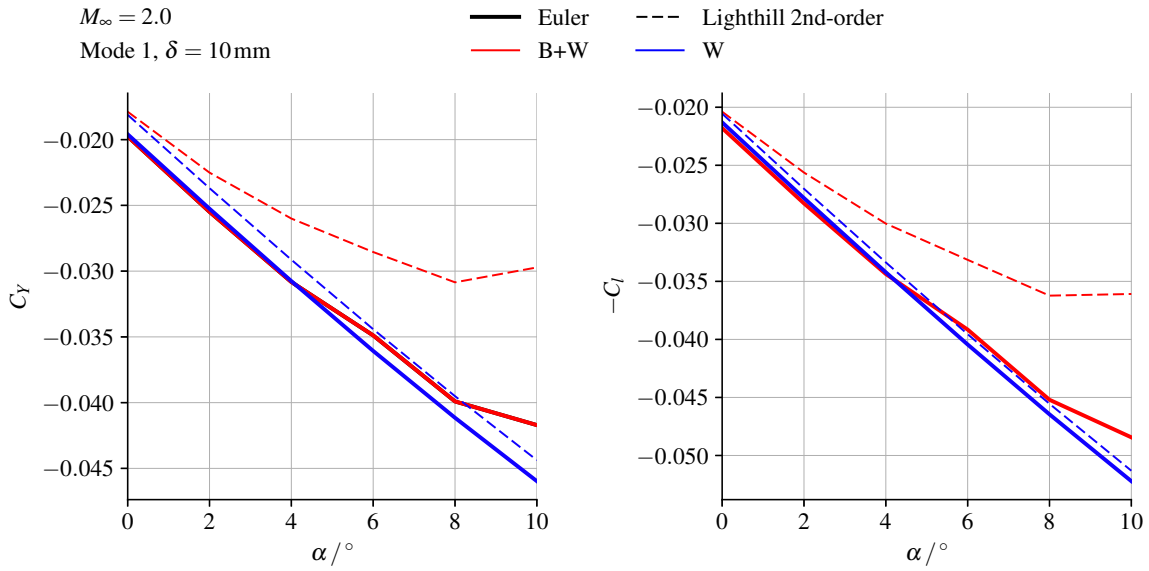

Fig. 5.59 Comparison of the wing-alone and wing-body predictions of the side-force coefficient C_Y and rolling-moment coefficient C_l. Mode 1 with $\delta = 10\,\mathrm{mm}$. $M_\infty = 2.0$.

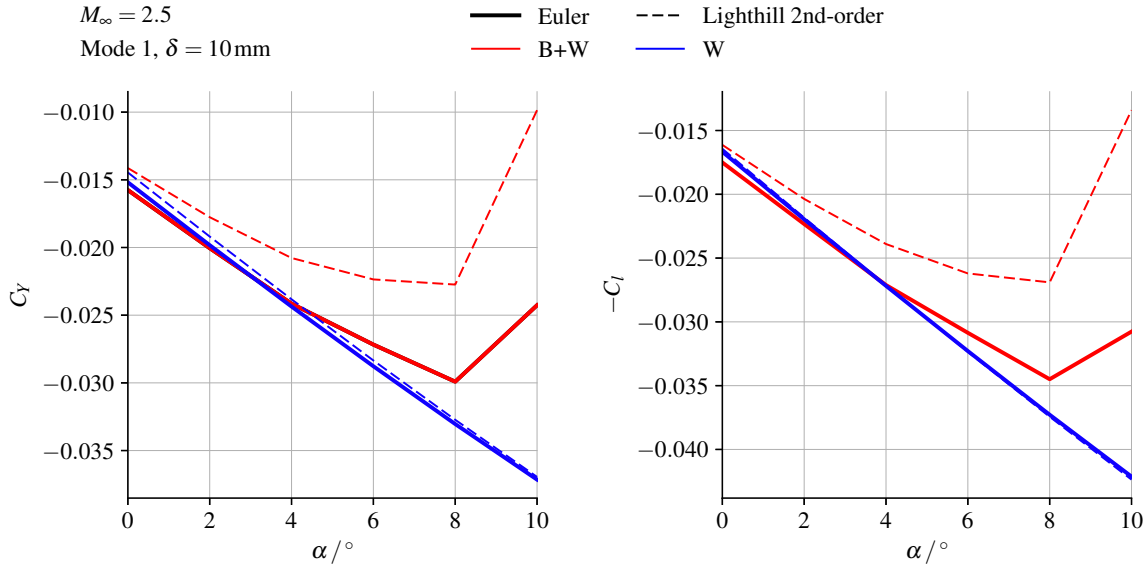

Fig. 5.60 Comparison of the wing-alone and wing-body predictions of the side-force coefficient C_Y and rolling-moment coefficient C_l. Mode 1 with $\delta = 10\,\mathrm{mm}$. $M_\infty = 2.5$.

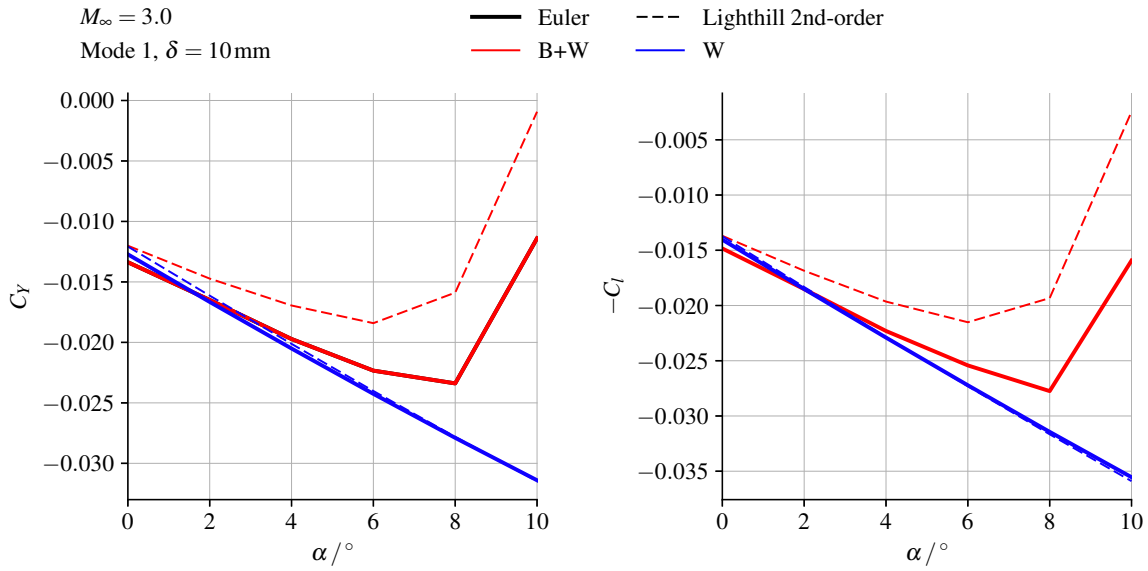

Fig. 5.61 Comparison of the wing-alone and wing-body predictions of the side-force coefficient C_Y and rolling-moment coefficient C_l. Mode 1 with $\delta = 10\,\mathrm{mm}$. $M_\infty = 3.0$.

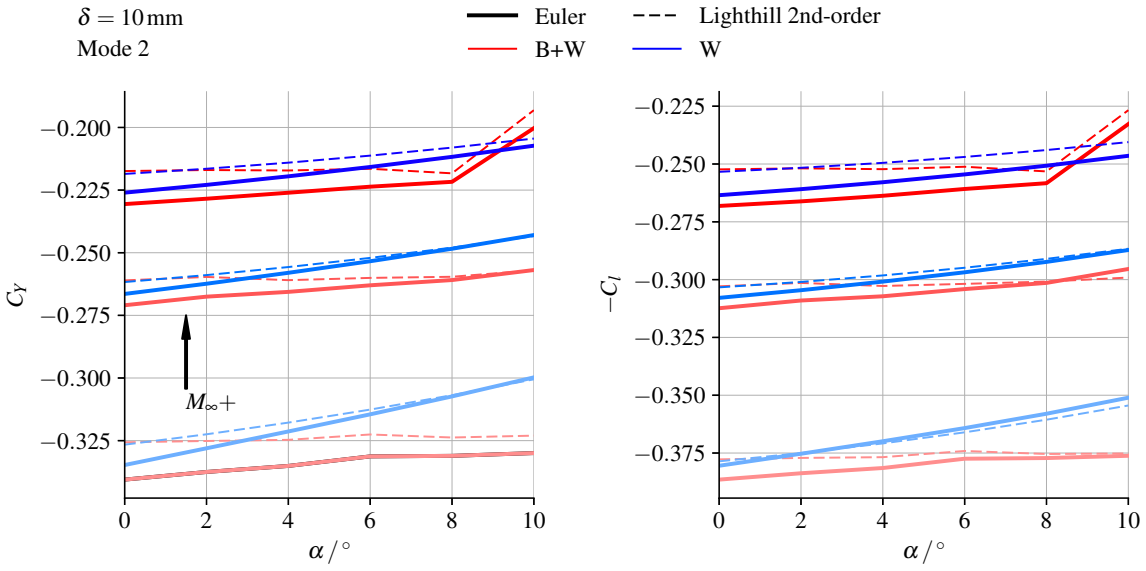

Fig. 5.62 Comparison of the wing-alone and wing-body predictions of the side-force coefficient C_Y and rolling-moment coefficient C_l. Mode 2 with $\delta = 10\,\mathrm{mm}$.

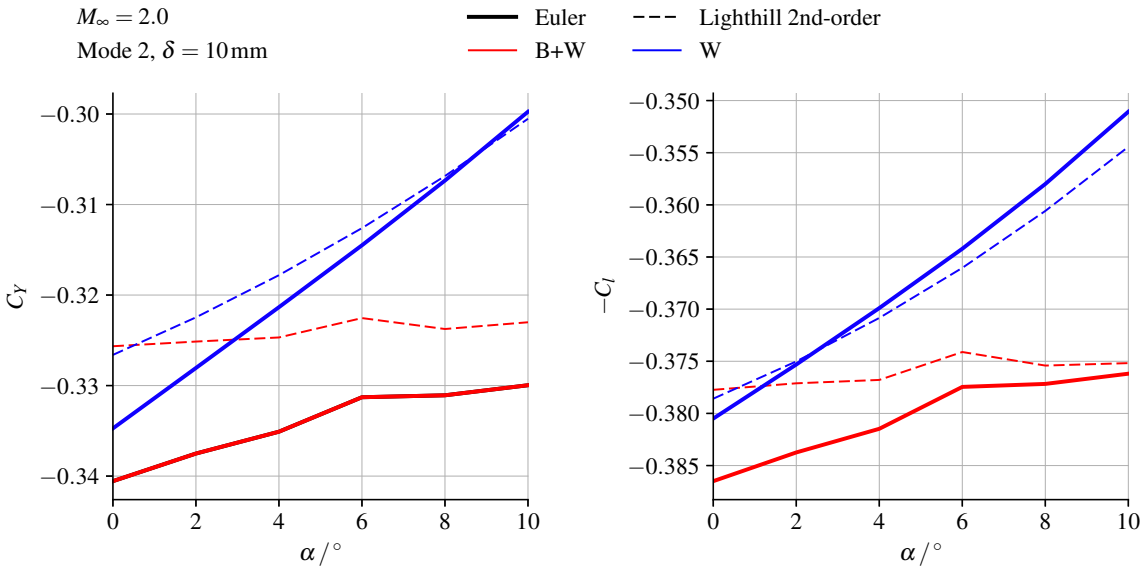

Fig. 5.63 Comparison of the wing-alone and wing-body predictions of the side-force coefficient C_Y and rolling-moment coefficient C_l. Mode 2 with $\delta = 10\,\mathrm{mm}$. $M_\infty = 2.0$.

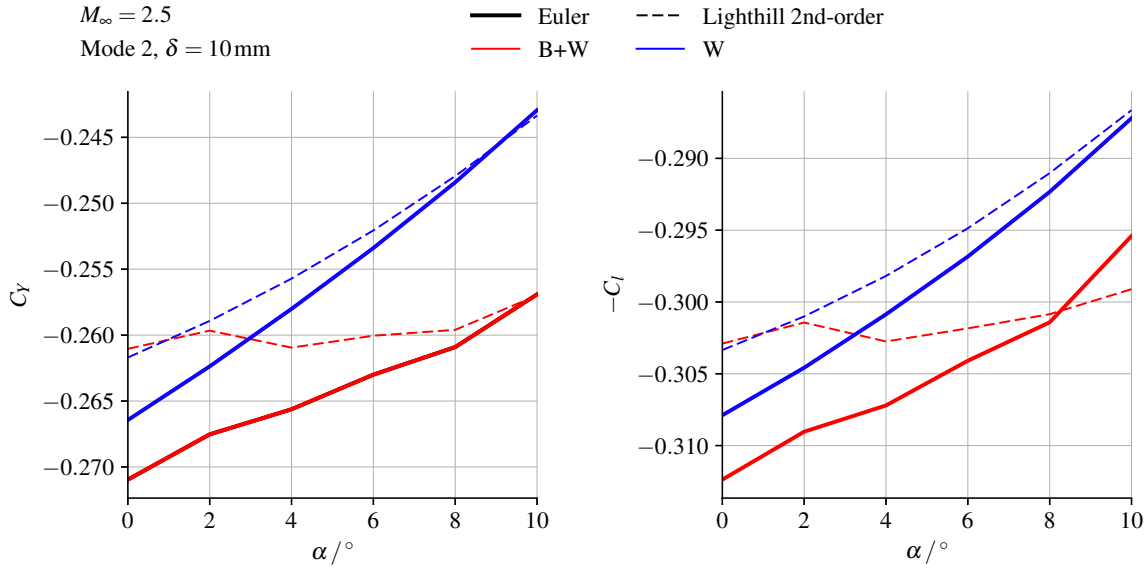

Fig. 5.64 Comparison of the wing-alone and wing-body predictions of the side-force coefficient C_Y and rolling-moment coefficient C_l. Mode 2 with $\delta = 10\,\text{mm}$. $M_\infty = 2.5$.

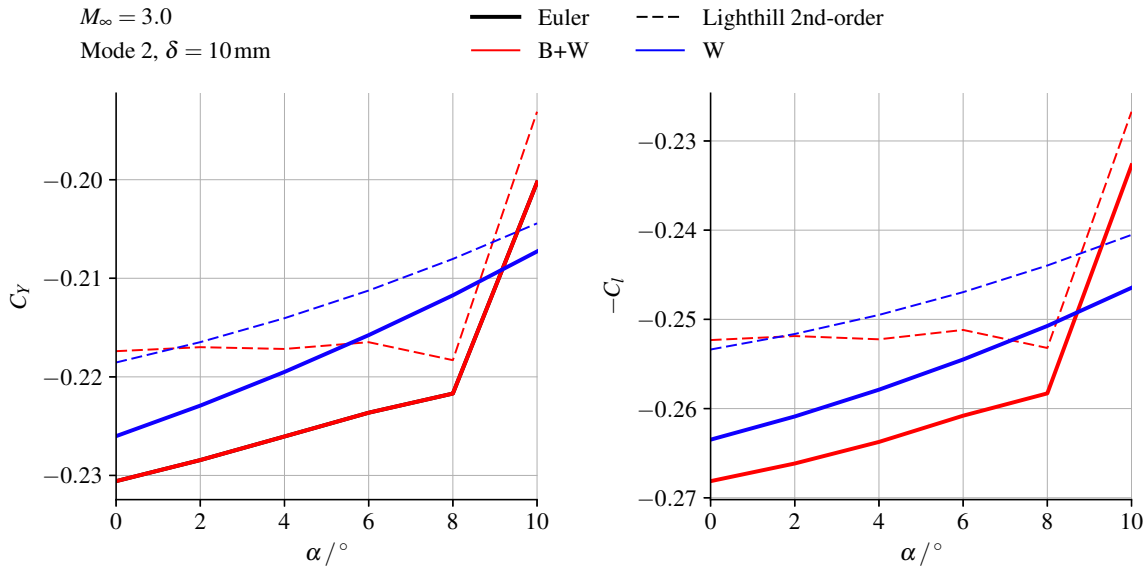

Fig. 5.65 Comparison of the wing-alone and wing-body predictions of the side-force coefficient C_Y and rolling-moment coefficient C_l. Mode 2 with $\delta = 10\,\text{mm}$. $M_\infty = 3.0$.

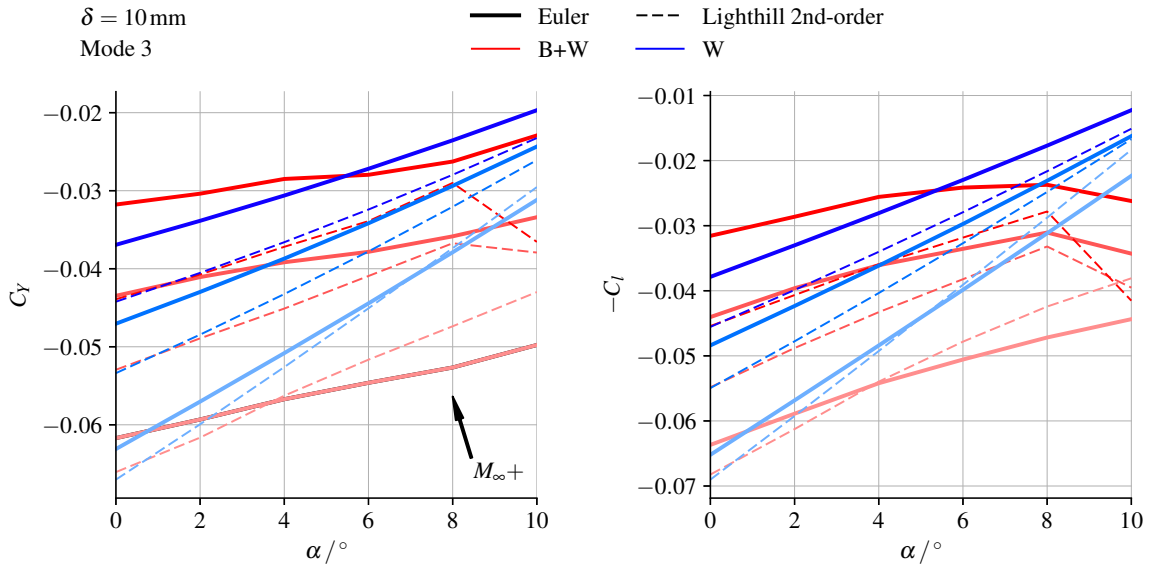

Fig. 5.66 Comparison of the wing-alone and wing-body predictions of the side-force coefficient C_Y and rolling-moment coefficient C_l. Mode 3 with $\delta = 10\,\text{mm}$.

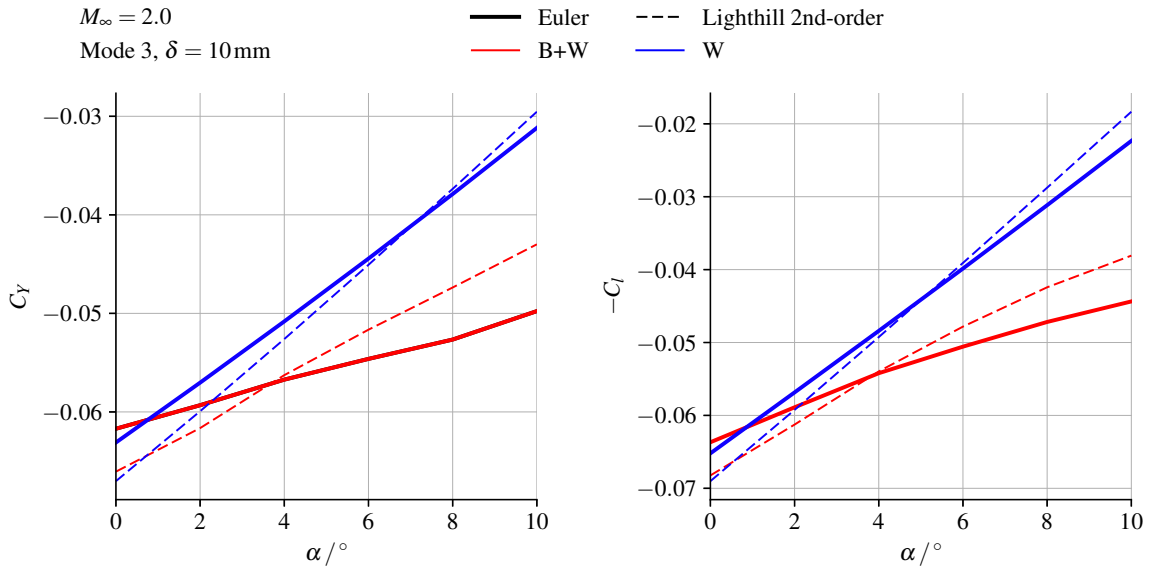

Fig. 5.67 Comparison of the wing-alone and wing-body predictions of the side-force coefficient C_Y and rolling-moment coefficient C_l. Mode 3 with $\delta = 10\,\text{mm}$. $M_\infty = 2.0$.

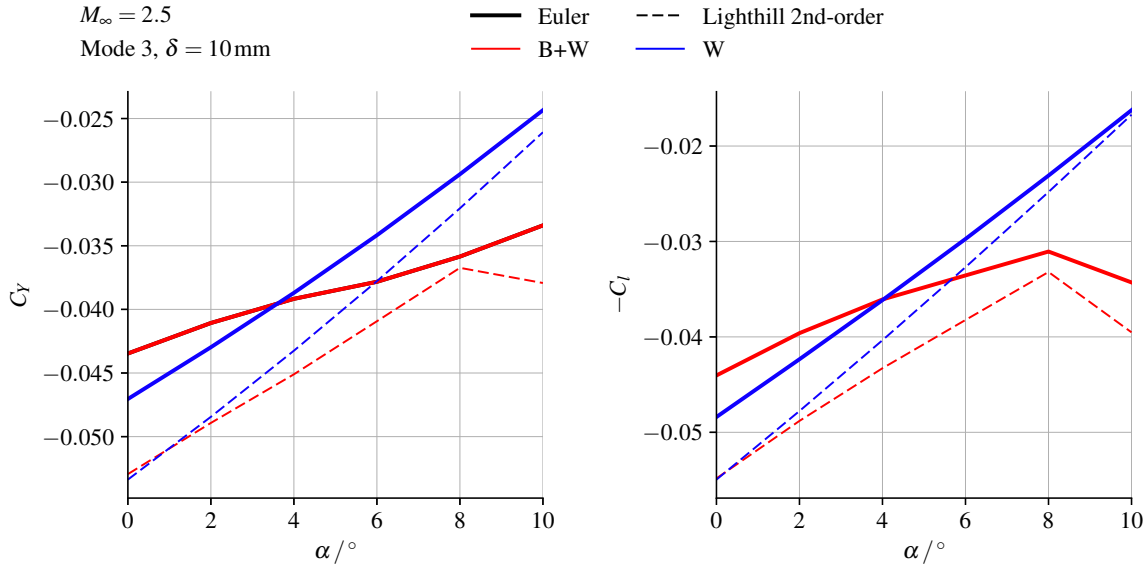

Fig. 5.68 Comparison of the wing-alone and wing-body predictions of the side-force coefficient C_Y and rolling-moment coefficient C_l. Mode 3 with $\delta = 10\,\text{mm}$. $M_\infty = 2.5$.

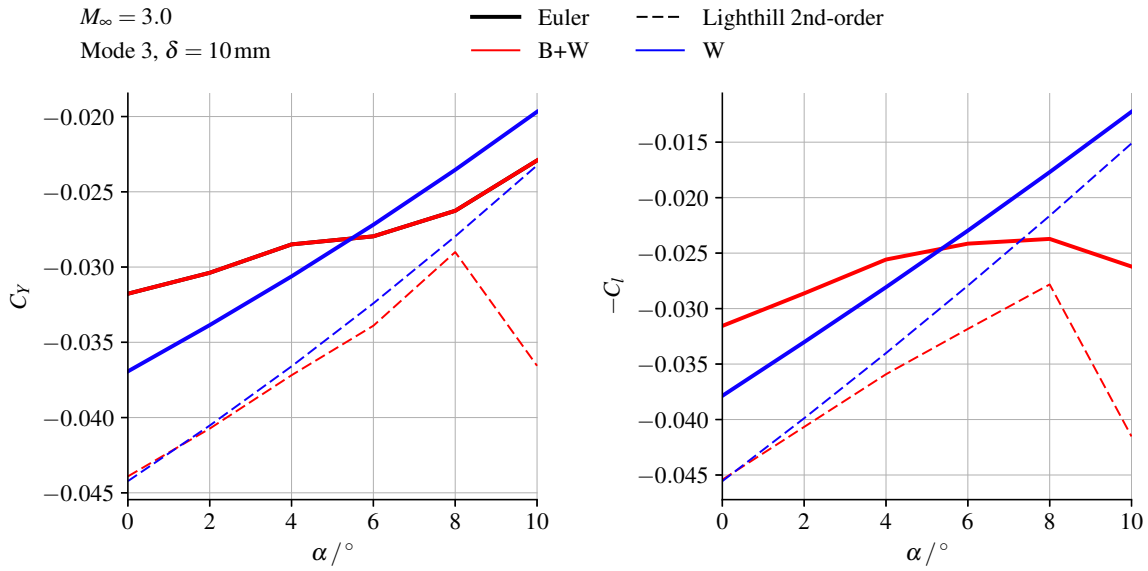

Fig. 5.69 Comparison of the wing-alone and wing-body predictions of the side-force coefficient C_Y and rolling-moment coefficient C_l. Mode 3 with $\delta = 10\,\text{mm}$. $M_\infty = 3.0$.

5.4.4 Interference Results: Interference Factors

The present set of results will illustrate the aerodynamic interference in the full-vehicle configuration through the use of wing carryover-factors. These are presented as

$$\frac{C_{Y(W(B))}}{C_{Y(W)}} \quad \text{and} \quad \frac{C_{l(W(B))}}{C_{l(W)}} \tag{5.3}$$

for the side-force and rolling-moment coefficients, respectively. Comparison to the definition of K_W in Eq. (2.78) motivates the use of the phrase "carryover factor" to describe these ratios. The symbol K_W will be used interchangeably in the discussion below to refer to the quantities in Eq. (5.3). For clarity, it is repeated here that $C_{Y(W(B))}$ refers to the side-force coefficient acting on the leeside wing in the presence of the body (full-vehicle configuration). The side-force on the leeside wing in the wing-alone configuration is given by $C_{Y(W)}$. A carryover factor greater than 1 denotes an increase in the control effectiveness due to interference effects.

The Euler-based LPT predictions that will be shown refer to the second-order LPT formulation using Lighthill's [88] coefficients. The results depicting the wing carryover-factors are shown in Figs. 5.70 to 5.75, with the figures discussed below on a per-mode-shape basis.

Mode 1: First Bending

The influence of M_∞ on the prediction of the wing carryover-factors for Mode 1 is shown for the deflection set $\delta = [5\,\text{mm}, 10\,\text{mm}]$ in Figs. 5.70 and 5.71, respectively. The following discussion points are made regarding the figures:

- Inspection of the Euler results shows equivalent trends between C_Y and C_l. It is seen that aerodynamic interference increases with increasing M_∞ and with increasing α. The onset and influence of body-shed vorticity from $\alpha > 8°$ is evident in the sharp changes in gradient. A minor amount of flowfield interaction is noted at $\alpha = 0°$. No significant changes are noted with δ,

- As was noted in Section 5.4.3, the inability of LPT to model flowfield interaction is accentuated in the results of Figs. 5.70 to 5.75. In particular, this is shown by the consistent prediction of $K_W = 1.0$ at $\alpha = 0°$ regardless of the value of M_∞, δ, or the mode-shape considered. The significance of the deviation of the LPT prediction from the Euler result at $\alpha = 0°$ will be discussed on a per-mod-basis. For Mode 1, as seen in Figs. 5.70 and 5.71, the prediction error is minor, being of the order of 5%,

- The overall trends are replicated by LPT (notably, increasing interference with increasing M_∞ and α, and the influence of body-shed vorticity). However, the prediction error is noted to increase with α. Prediction errors of the order of 10% are noted for $\alpha = 2°$, with errors of 20% noted by $\alpha = 6°$. Following the influence of the body-shed vorticity, these errors rapidly increase to the order of 80% at $M_\infty = 3.0$ and $\alpha = 10°$.

Mode 2: First Twist

The influence of M_∞ on the prediction of the wing carryover-factors for Mode 2 is shown for the deflection set $\delta = [5\,\text{mm}, 10\,\text{mm}]$ in Figs. 5.72 and 5.73, respectively. The following discussion points are made regarding the figures:

- Inspection of the Euler results shows equivalent trends between C_Y and C_l. It is seen that aerodynamic interference increases with with increasing α. A Mach-dependence, most significant at $\alpha = 10°$, is also noted. The onset and influence of body-shed vorticity is only evident as a sharp change in the gradients for $M_\infty = 3.0$ at $\alpha > 8°$. A minor amount ($\approx 2\%$) of flowfield interaction is noted at $\alpha = 0°$. Minor changes are noted with δ, with the interference at $M_\infty = 3.0$ becoming more similar (prior to the onset of body-shed vortices) to the interference factors of $M_\infty = 2.0$ and $M_\infty = 2.5$,

- For Mode 2, the inability of LPT to model flowfield interaction at $\alpha = 0°$ is seen to be inconsequential. The loading is clearly dominated by the local surface inclination, as may be expected for the first-twist mode-shape. This is reflected in the generally good agreement obtained for this mode. An error in the prediction of $\frac{\partial K_W}{\partial \alpha}$ is noted at $M_\infty \geq 2.5$. However, the carryover factor is predicted to within 2% over the parameter space considered. Within this context, LPT may be considered useful and accurate for engineering purposes.

Mode 3: Second Bending

The influence of M_∞ on the prediction of the wing carryover-factors for Mode 3 is shown for the deflection set $\delta = [5\,\text{mm}, 10\,\text{mm}]$ in Figs. 5.74 and 5.75, respectively. The following discussion points are made regarding the figures:

- Inspection of the Euler results shows equivalent trends between C_Y and C_l. A strong dependence of K_W on α and on M_∞ is noted. Significantly, a substantial amount ($\approx 15\%$) of flowfield interaction is noted at $\alpha = 0°$. This interaction exhibits a clear Mach-dependence. The influence of the onset of body-shed vorticity is subtle, and is

arguably best seen in the increased slope for the C_l carryover-factor at $M_\infty = 3.0$ and $\alpha > 8°$. Minor changes are noted with δ, predominantly for $M_\infty = 3.0$ at $\alpha = 10°$,

- For Mode 3, the inability of LPT to model flowfield interaction at $\alpha = 0°$ is seen to be significant. This is in contrast to the observations made for Modes 1 and 2. LPT is seen to poorly predict the Mach-dependence of the interference factors for Mode 3. Most significantly, it is seen that particularly poor prediction is obtained following the onset of body-shed vortices at $\alpha > 8°$ for $M_\infty \geq 2.5$. Prediction errors of up to $\approx 40\%$ are obtained at $\alpha = 10°$. The shortcomings of LPT in predicted the loading of Mode 3 are clear evidence of "missing physics" in the mathematical formulation of LPT. From a viewpoint of application, it is seen that incorrect trends are predicted in an interference flow with flowfield interaction.

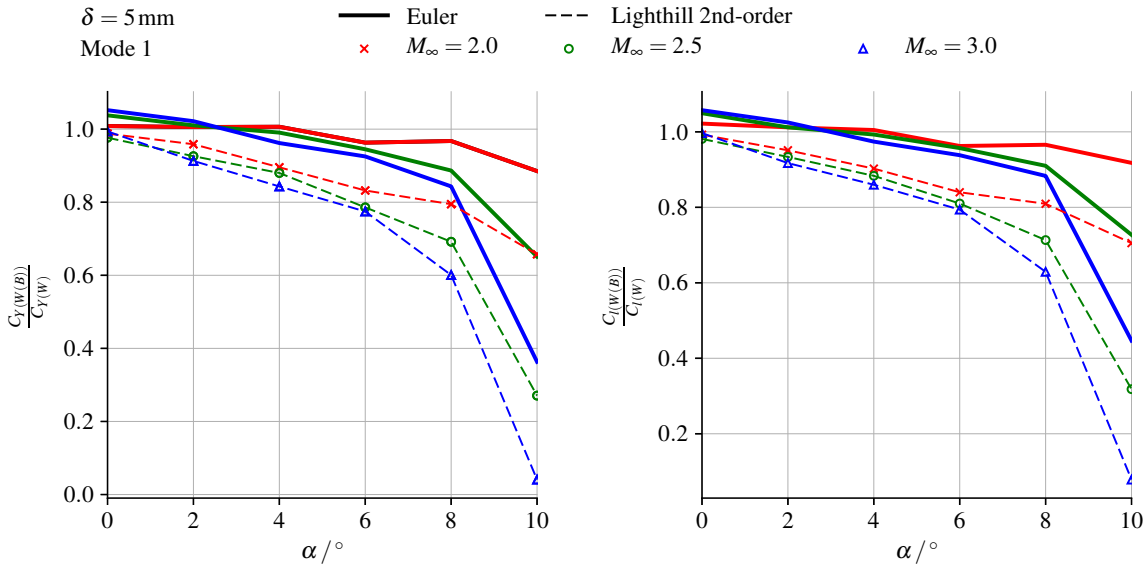

Fig. 5.70 Influence of freestream Mach number on the prediction of the side-force coefficient C_Y, rolling-moment coefficient C_l interference factors. Mode 1 with $\delta = 5\,\text{mm}$.

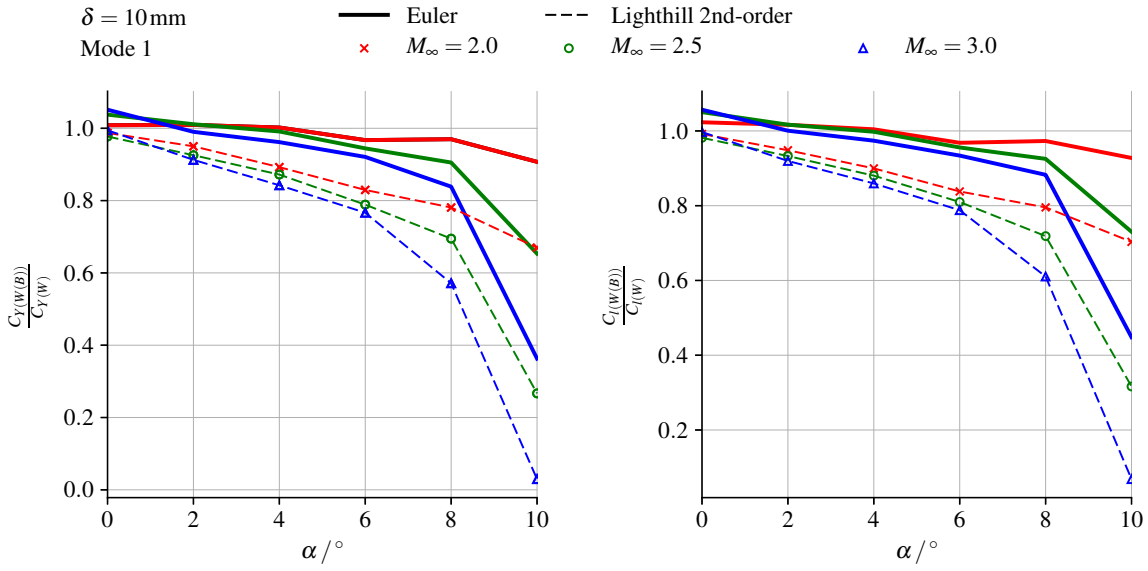

Fig. 5.71 Influence of freestream Mach number on the prediction of the side-force coefficient C_Y, rolling-moment coefficient C_l interference factors. Mode 1 with $\delta = 10\,\text{mm}$.

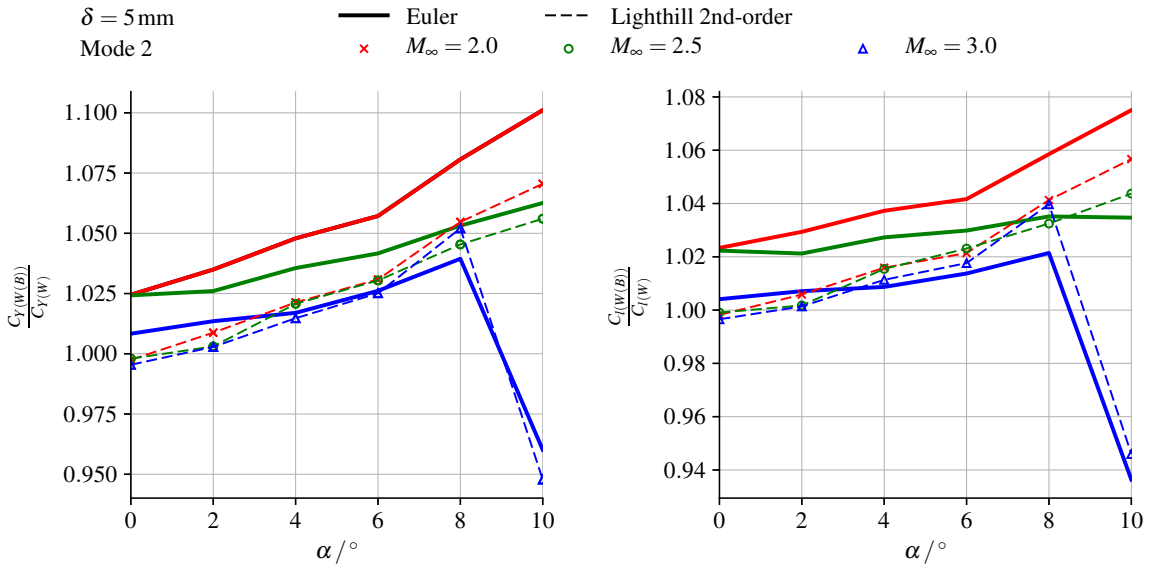

Fig. 5.72 Influence of freestream Mach number on the prediction of the side-force coefficient C_Y, rolling-moment coefficient C_l interference factors. Mode 2 with $\delta = 5\,\text{mm}$.

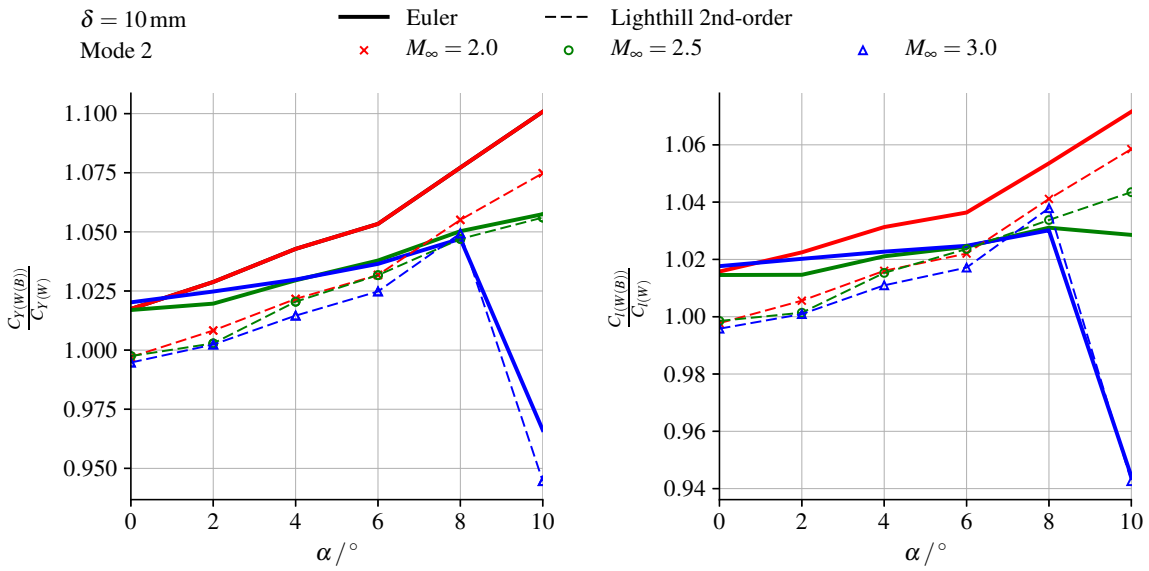

Fig. 5.73 Influence of freestream Mach number on the prediction of the side-force coefficient C_Y, rolling-moment coefficient C_l interference factors. Mode 2 with $\delta = 10\,\text{mm}$.

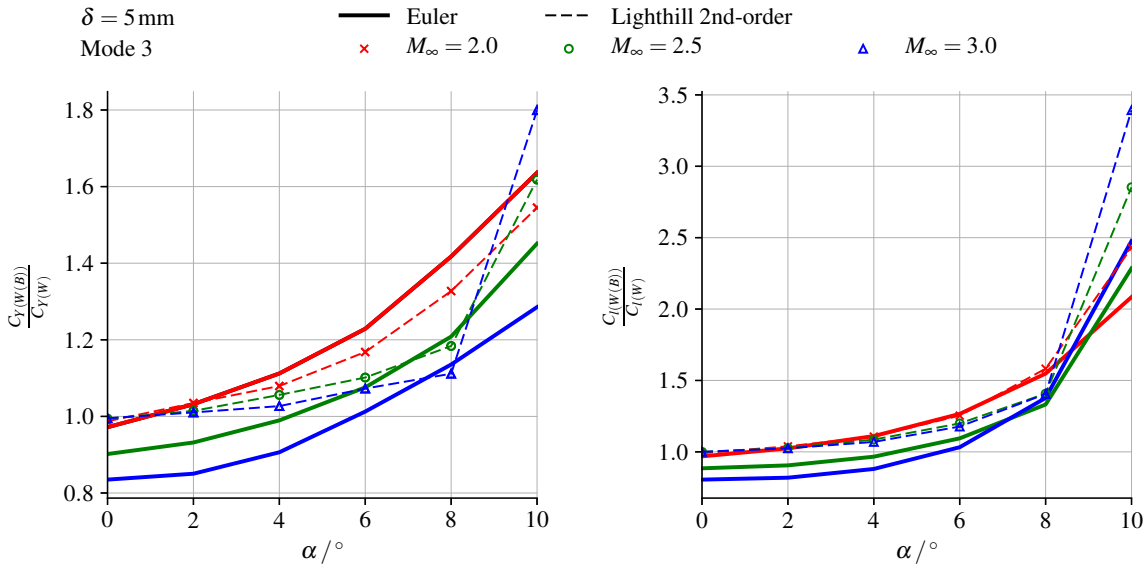

Fig. 5.74 Influence of freestream Mach number on the prediction of the side-force coefficient C_Y, rolling-moment coefficient C_l interference factors. Mode 3 with $\delta = 5\,\text{mm}$.

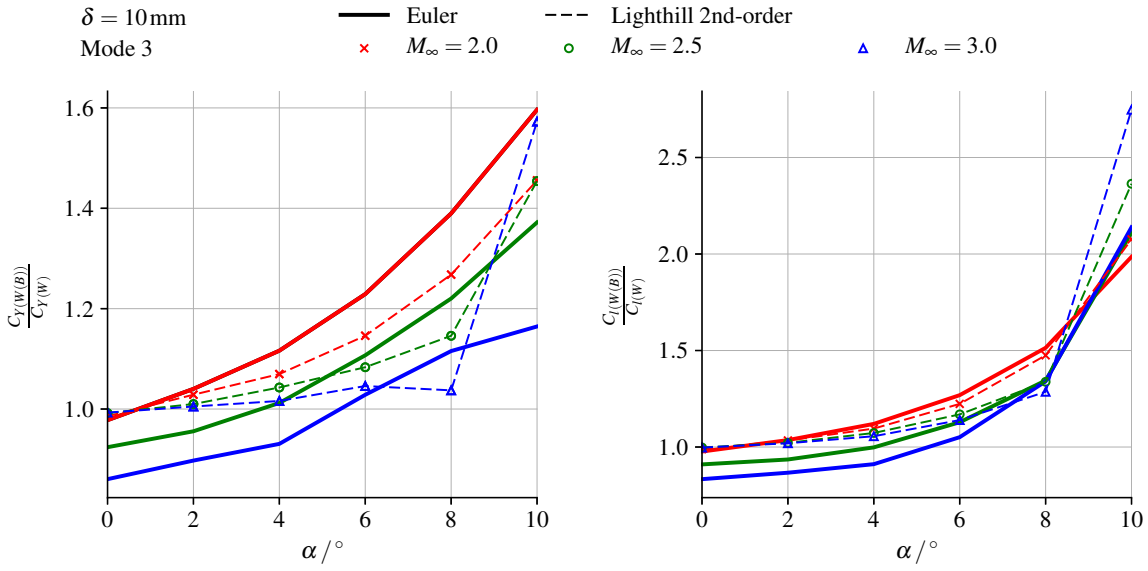

Fig. 5.75 Influence of freestream Mach number on the prediction of the side-force coefficient C_Y, rolling-moment coefficient C_l interference factors. Mode 3 with $\delta = 10\,\text{mm}$.

5.4.5 Discussion

Preliminary Remarks

The wing-body case represents an investigation into aerodynamics of the leeside control-surface in the presence of an interference flowfield. Comparison to the wing-alone case gives insight into additional shortcomings of LPT which arise due to interaction with the non-uniform interference flowfield.

The underlying assumptions of LPT have been discussed at length in Sections 3.1.1 and 3.1.4 and Chapter 4. These form the basis for the shortcomings of LPT in interference flows. Here, the focus will be on the particular assumptions surrounding

- Relative magnitudes of directional gradients and the reduction of the perturbation flow to a one-dimensional formulation,
- Interaction between the captive fluid in the "cylinder" and the "piston" (surface).

The presence of an established, non-uniform interference flow has implications for assumptions relating to both of the above topics:

- For the wing-alone case, the gradients (and flow structure) developed by the mean-steady flow are (broadly speaking) a function of the wing geometry and $M_\infty \sin\alpha$, as outlined in Section 2.1.2. The review of the variations of "piston theory" in Section 3.2 showed an overwhelming majority of applications to 2D geometries, or applications to uniform-flow portions of 3D wings. The typical scenario would involve a uniform flowfield between the body (wing) and the bow-shock. Where a variation in this flowfield was permitted, it was explicitly assumed that the variation was sufficiently small that the unsteady analogy / law of plane sections was not violated. In essence, the variations of piston theory developed thus far have either implicitly or explicitly assumed that the gradients in the mean-steady flowfield facilitate a valid reduction to a 1D formulation.

  Such a reduction is typically not attempted when considering flows around bodies of revolution at incidence. This is because the flow is inherently two-dimensional in the crossflow plane (see Section 2.1.1). The neglect of gradients in one of the crossflow-directions would reduce the problem to an essentially planar formulation, which would be an incorrect representation of the physical flow.

  The immersion of a wing in an interference flow, such as that generated by a body of revolution at incidence, then raises the question of the validity of neglecting directional gradients in order to achieve a 1D formulation. It may be expected that the validity of

the approximation is largely dictated by the relative strength of the interference-flow gradients and of the gradients generated by the wing itself. This will be a chief point of discussion when comparing the accuracy of LPT when applied to Modes 1 and 3 versus its application to Mode 2,

- The review of historical developments to LPT in Section 3.2 included a number of formulations which accounted for the propagation of perturbations throughout the captive fluid in the "cylinder". It was noted that these "piston theories" achieved this at the expense of a strictly point-local relation between surface deflection and surface pressure. Typical assumptions included a wedge geometry and sinusoidal perturbations to the surface and bow shock. Also assumed was a uniform mean-steady flow behind the bow shock. Within this context, these formulations did account for interaction between the captive fluid and the piston. The primary caveat is that the mean-steady flow in the "cylinder" is uniform. This allows the 1D mathematical field problem to be solved using characteristics.

  In the context of bodies of revolution, similar solutions (and by extension, "piston theories") have only been obtained at zero-incidence. The resulting axisymmetric formulation allows similar mathematical treatment to the planar problem.

  The presence of non-uniformities in the crossflow plane (whether due to incidence of the body of revolution or otherwise) significantly complicates the solution of the 2D field problem for the flow bounded by the body and the bow shock. Once again, the question arises of the relative magnitude of the asymmetry and non-uniformity. Regardless, no "piston theories" have been developed to account for the interaction of the non-uniform captive fluid in the crossflow plane and the body surface. The most significant approximations which account for this interaction are hypersonic small-disturbance theory [78, 83] or Sychev's [4] method, which have been covered in Section 2.2.3. The interaction of the leeside wing with the non-uniform interference flow generated by the body will be a second source of prediction error discussed in the present study.

Discussion Points

The following are the key conclusions drawn from the wing-body results presented and discussed in Sections 5.4.1 to 5.4.4:

- No significant conclusions regarding the role of the piston-theory coefficients were reached in the investigation of Section 5.4.1 that were not already uncovered in Sec-

tion 5.3.2. As a consequence, largely the same discussion follows in relation to Section 5.4.1 as was given in Section 5.3.4. Namely,

- The order of LPT used did not have any observable effect on the α-dependence of the predicted C_Y and C_l,
- The use of different piston-theory coefficients for a given order of LPT provides a prediction band. This band narrows with increasing M_∞.

A greater offset between the prediction bands and the Euler solutions was noted for the wing-body case. However, this is unrelated to the choice of coefficients, and is rather a symptom of underlying deficiencies in piston-theory modelling. The conclusion is reached that the choice of LPT coefficients does not fundamentally alter the predicted loading trends. Hence, it has no direct influence on the fundamental applicability of LPT in interference flows.

- The results of Section 5.4.2 show that the overall loading trends are typically replicated by LPT. This is a point of interest which has been discussed at length in the context of Mode 1 in Section 5.4.3. Essentially, it shows that a component (which may be potentially significant) of the interference loading trends is contained in the mean-steady solution at the surface of the wing,

- Comparison of the wing-alone and the wing-body loads as in Section 5.4.3 immediately underscores the shortcomings of LPT when applied in interference flows. Again, a detailed discussion with supporting arguments is given throughout Section 5.4.3. A more quantitative assessment of the relative importance of the prediction error introduced in Section 5.4.3 is given in terms of the wing carryover-factor in Section 5.4.4. The following key conclusions are reached from the study:

  - The numerical results clearly illustrate the inability of LPT to model interaction of the deforming surface with the surrounding interference flowfield. This is evidenced through the essential equivalence of the LPT-predicted wing-alone and body-alone loads at $\alpha = 0°$. In terms of a wing carryover factor, $K_W = 1$ at $\alpha = 0°$,
  - Despite this shortcoming, LPT is a useful prediction method in interference flows provided the loading is dominated by local-inclination effects. This is evidenced through the generally good agreement obtained in the wing carryover-factor predicted for Mode 2 (first twist),

– When applied to mode-shapes for which loading is not dominated by local-inclination effects (Modes 1 and 3, bending modes), LPT may yield significant prediction errors.

  It was found that for simple mode-shapes, such as Mode 1 (first bending), the majority of the prediction error could be attributed to interaction of the deforming surface with the surrounding flowfield. While significant errors in the predicted loading were obtained, the overall trends were replicated.

  The more complex mode-shape of Mode 3 (second bending) was found to induce three-dimensionality in the perturbed flow. This was manifested as notably worse agreement between the LPT predictions and the Euler solutions. Significantly, the prediction error was found to be a function of multiple parameters (M_∞ and α). Most significantly, it was shown that LPT did not replicate the overall loading trends following the onset of body-shed vorticity,

– Prediction errors attributable to surface / flowfield interaction were noted over the full spectrum of α investigated. This is significant in showing that the LPT shortcomings in interference flows are not limited to flows involving crossflow shocks and body-shed vortices.

In conclusion, it is deduced that the application of LPT to a simple wing-body configuration is not well supported by numerical investigation. Useful prediction may be obtained, provided that loading is dominated by local-inclination effects (such as for a first-twist mode). More generally, interaction of the deforming surface with the surround interference flowfield may be a significant source of error in LPT load prediction. It was found that general loading trends may well be captured by LPT if the mean-steady solution accounts for interference at the un-deformed surface. However, incorrect trend prediction has been shown following the onset of body-shed vortices.

The shortcomings of LPT in interference flows may be understood in light of the theoretical and mathematical basis for LPT presented in Sections 3.1.1 and 3.1.4 and Chapter 4. Significant prediction error in LPT may be obtained when perturbations cause spanwise or axial gradients that invalidate the law of plane sections (i.e., which cause appreciable three-dimensionality of the flow). Similarly, LPT is in error when interaction occurs between the surrounding fluid and perturbations from the deforming surface. A novel study of the influence of the selection of coefficients in LPT showed that they serve to provide a prediction-band which narrows with increasing M_∞. However, coefficient selection has no fundamental influence on the validity of LPT in interference flows. The use of higher-order formulations of LPT similarly had no influence on its validity.

5.5 Discussion and Summary

The present discussion offers a high-level summary of key discussion points made throughout Sections 5.3 and 5.4. The supporting arguments are not repeated here for the sake of clarity and brevity.

Chapter 5 demonstrated the application of Euler-based LPT to a slender body subject to aeroelastic effects. The purpose of the numerical investigation was to determine the suitability of Euler-based LPT as an aeroprediction method in interference flows. The review of the literature on LPT in Section 3.2 found that no controlled, incremental investigation had previously been performed to assess the validity of Euler-based LPT in interference flows (as are generated by full-vehicle configurations). The same applies to RANS-based LPT.

This largely motivated the selection of the simple slender-body geometry used in the present study. An extensive body of literature and knowledge exists on aerodynamic interference in this class of geometry. The component build-up approach towards interference (namely considering body-alone, wing-alone, and wing-body loads) typically adopted for this geometry was applied in the present numerical study. The combination of simple geometry and the component build-up approach facilitated a controlled investigation into wing-body interference.

Aeroelastic effects were introduced through prescribing static deformations of the leeside wing (control surface). The decision to prescribe static deformations was similarly motivated by considerations of a controlled, incremental investigation into the validity of Euler-based LPT. In particular, static deformations eliminated flow unsteadiness and dynamic effects as a source of error. In this sense, the present study does not directly draw conclusions regarding the use of Euler-based LPT for the prediction of aerodynamic damping. However, the same principles govern the validity of reduction from a 3D to a 1D formulation, whether the application is static or dynamic perturbations. Furthermore, inherent shortcomings in the mathematical formulation of piston theory will persist regardless of the time-dependence of the boundary conditions. Similar considerations motivated the use of an Euler basis for LPT despite the higher modelling fidelity of RANS.

The discussion of the outcomes of the numerical investigation will centre of three core themes, namely:

- The insights gained into Euler-based LPT,
- The applicability of Euler-based LPT in interference flows,
- The implications of the study for future LPT extensions.

5.5.1 Insights Gained

The present work addressed two gaps in the literature on LPT regarding:

- The extension of LPT to 2nd- and 3rd-order and the implications for modelling capabilities,
- The influence of the coefficients used in LPT.

The first gap was addressed by a mathematical investigation in Section 3.3. The non-zero contribution of 2nd order LPT to the wing-normal force coefficients is not demonstrated by the numerical results. This is due to the use of a symmetrical flowfield (about the un-deformed wing) being used as the mean-steady reference solution in the present study. This is equivalent to having $\alpha_m = 0°$ with $(pM)_{(exact)L} = (pM)_{(exact)U}$ in Eq. (3.187). Comparison of Eq. (3.187) and Eq. (3.184) show that under these particular conditions, 2nd-order LPT makes a zero-contribution to the normal-force derivatives, as is the case in CPT. Differences between the 1st- and 2nd-order LPT results in the present study occur only when local surface pressures are limited to vacuum pressure. Differences noted between the 2nd- and 3rd-order LPT predictions were related to the magnitude of C_Y and C_l. In other words, the extension to higher-order LPT offered no inherently different prediction trends with α, and the modelling of the underlying aerodynamic interference was unchanged. It is reiterated that this is due to the use of a symmetrical (about the un-deformed wing) mean-steady Euler solution.

The second gap was addressed by the present numerical investigation. It was shown the choice of LPT coefficients had no fundamental impact on the modelling of aerodynamic interference. Nominal differences in predicted loading trends were noted. However, these differences diminished with increasing M_∞, which is consistent with the Mach-dependent coefficients of Van Dyke [104] and Donov [105] tending to Mach-independent values as in the case of Lighthill's [88] coefficients. The variety of coefficients available to the engineer essentially provide a prediction band for the loading. This allows a rough estimate to be made of the error inherent in the LPT formulation.

It was numerically demonstrated that LPT does not model the interaction between the deforming surface and the surrounding interference flowfield. This was manifested through an equivalence in wing-alone and wing-body predicted loads at $\alpha = 0°$. However, it was also shown that the general character of loading trends was replicated by Euler-based LPT. This occurred despite flowfield interaction not being modelled. This is significant in highlighting the role of the mean-steady surface solution in determining the interference loading in the wing-body case.

A final outcome of the component build-up approach was the ability to identify sources of error in the wing-body predicted load.The inaccuracy in the predicted loading may be largely attributed to a combination of

- Underlying shortcomings of LPT in modelling perturbations which produce three-dimensionality in the flow (as produced by mode-shapes with localized camber and bending). These are manifested as prediction errors in the wing-alone case,
- The inability of LPT to model interaction between the deforming surface and the surrounding interference flowfield. This is manifested as the remaining prediction error once the wing-alone error is corrected for.

5.5.2 Applicability of Euler-Based LPT in Interference Flows

The numerical study highlighted a number of successes and a number of shortcomings in the application of Euler-based LPT.

Successes

Generally excellent prediction was demonstrated by LPT when applied to the wing-alone case in an interference-free flow. This was most notable for the small perturbations produced by Mode 1 (first-bending). Significantly, good prediction accuracy was also achieved when applied to Mode 2 (first twist), which created large perturbations (up to low supersonic piston downwash).

The large perturbations caused by the turning of the surface unit-normal vector into the flow in Mode 2 dominated the loading definition in the wing-body case. It was thus demonstrated that in spite of the interference flowfield and flowfield-interaction, LPT may provide useful aeroprediction. This is with the significant caveat that the pressure loading was be dominated by surface-inclination, with flowfield-interaction being entirely a secondary effect.

Shortcomings

More significantly, it was shown that LPT may not generally be expected to be accurate in interference flows. This was evidenced by the significant prediction errors obtained in the wing-body case for Mode 1 (first bending) and Mode 3 (second bending).

The excellent agreement obtained in the wing-alone case for Mode 1 allowed the prediction error to be clearly attributed to flowfield-interaction. A significant outcome of the

numerical investigation was the flowfield-interaction was noted to affect the prediction accuracy at all α considered. This is significant, as it demonstrates the shortcomings of the current state-of-the-art of LPT in the simplest of interference flows – no impinging shocks and no body-shed vortices were required for the prediction accuracy to suffer.

While the prediction error for Mode 1 in the interference flow was significant, the general character of the loading trends with α was replicated. This was not the case for Mode 3. Following the onset of body-shed vortices at $M_\infty = 3.0$ and $\alpha > 8°$, Euler-based LPT predicted a sharp reversal in the sign of $\frac{\partial C_Y}{\partial \alpha}$. However, the Euler trend of $\frac{\partial C_Y}{\partial \alpha}$ was largely unchanged. This represents another significant shortcoming of Euler-based LPT in interference flows. It demonstrates that the general character of loading trends may be incorrectly predicted by LPT when interaction between the surface and the interference flowfield occurs.

The prediction error in the wing-body case is not solely attributable to flowfield interaction. A similar (but less significant) error was observed in the wing-alone case. This prediction error was attributed to the three-dimensionality induced by the localized camber and bending of Mode 3. This serves as a reminder that even in the absence of an interference flowfield, Euler-based LPT has inherent shortcomings in its 1D formulation.

5.5.3 Implications for LPT Extensions

The demonstration of underlying shortcomings in Euler-based LPT in interference flows in the present work provides valuable information for the further development and extension of LPT. Key sources of error were identified as

- Perturbations which induce significant three-dimensionality in the flow, violating the 1D point-local character of LPT,
- Interaction between the deforming surface and the surrounding flowfield.

These errors are associated with the fundamental assumptions required to arrive at the mathematical formulation of LPT. A detailed development of the mathematical derivation was provided in Chapter 4. The prediction errors and shortcomings of Euler-based LPT were demonstrated in the present investigation for a geometry and flow characterized by

- Steady flow and static deformations,
- An inviscid fluid,
- A near-zero thickness wing of moderate aspect ratio ($AR = 1.5$) and low sweep ($\Lambda_{LE} = 15°$).

The combination of these factors represents the simplest case study for a geometry of practical interest. Prediction errors encountered at this level of simplification will persist throughout incremental addition of complexity through

- Unsteady flow or dynamic deformations,
- Viscosity,
- Geometry which results in more complex three-dimensional aerodynamics.

In light of the above, a discussion is offered surrounding the implications of the present study for

- Requirements for extension of Euler-based LPT to interference flows,
- Requirements for extension of LPT to a RANS basis.
- The suitability of existing "extended / enhanced piston theories" in interference flows,

The crux of the arguments offered centres on the need for accurate mathematical modelling of underlying physics.

Requirements for Extension to Interference Flows

Flowfield interaction as a source of prediction error in LPT was clearly illustrated by the results of Mode 1 (first bending) in Figs. 5.58 to 5.61. The excellent agreement in the wing-alone loads allows the error in the wing-body loads to be largely attributed to flowfield interaction.

The prediction error in LPT when applied to the wing-alone case for Modes 2 and 3 was naturally also present in the wing-body results for Modes 2 and 3. To further illustrate the role of flowfield interaction, the load-predictions for a select number of parameters have been corrected and illustrated in Figs. 5.76 to 5.79. The "uncorrected" loads represent the basic load prediction by Euler-based LPT. To obtain the "corrected loads", the wing-alone and wing-body LPT predictions were adjusted as follows:

$$C_{Y\,(corrected)} = C_{Y\,(uncorrected)} + \Delta C_Y \,, \tag{5.4}$$

$$\Delta C_Y = C_{Y(W)\,Euler} - C_{Y(W)\,LPT} \,, \tag{5.5}$$

The same correction was applied to C_l. The essence of the correction is to "subtract" the wing-alone error from the wing-body error. While this is a primitive correction, it allows a

precursory interpretation of the prediction error. Moreover, it is not entirely dissimilar to the "correction factor" class of engineering-level methods used to extend simple methods.

It is evident from Figs. 5.76 to 5.79 that while an improvement in the nominal agreement is obtained through the correction, the fundamental loading trends are not significantly different. Most notably, the prediction error is seen to remain a function of the parameter space, notably of α. This highlights the fact that the source of the prediction error lies within the interference flowfield. As has been repeated before, this is attributed to interaction of the deforming surface with the surrounding flowfield.

This interaction is a fundamental component of aerodynamic interference. This interaction is not modelled at a mathematical level in LPT due to the following core assumptions typically invoked:

- The mean-steady flowfield is taken to remain constant as the surface deforms. That is to say, the cylinder reference conditions are constant for the duration of the perturbation,
- The propagation of perturbations and the flow time-history within the "cylinder" are neglected. This is required to reach a point-local formulation in piston theory. Moreover, analytical formulations which do account for the above have assumed a uniform reference flow along the length of the cylinder (essentially an interference-free flowfield),

It may be concluded that for any extension of LPT to faithfully reproduce loading trends in interference flows, the underlying physics of flowfield interaction must be modelled mathematically. It is seen in Figs. 5.76 to 5.79 that a "correction factor" approach is unlikely to be suitable outside a semi-empirical framework, and that a mathematical extension to LPT is required.

Similar arguments may be made surrounding the shortcomings of LPT in the prediction of Mode 3 (second bending) loading trends. An extension of LPT aimed at improved prediction accuracy would need to address the underlying physics (mathematically) of deformation producing 3D perturbations.

Requirements for Extension to Viscous Flows

The application of LPT to viscous flows should similarly be informed by the underlying physics. Applications of CFD-based LPT to viscous flows [12, 13, 18, 19, 194, 195] have not modified formulation of piston theory. Instead, these applications have applied the inviscid method about an effective shape determined by a variety of methods from the mean-steady RANS solution. The implicit assumption in this approach is that the effective shape remains

unchanged following perturbations. This also implicitly assumes that no interaction between the deforming surface and the surrounding flowfield occurs.

The present study serves to inform the improvement in prediction obtained over Euler-based LPT in the majority of these RANS-based LPT studies [12, 13, 18, 19, 194, 195]. It was previously discussed that Euler-based LPT generally replicated the overall interference loading trends, despite not modelling flowfield interaction. This is due to a component of the interference loading being defined by the mean-steady surface solution. This conclusion may be extended to the application of LPT to a RANS reference solution instead of an Euler reference solution. The mean-steady fluid state predicted by the RANS solution influences the unsteady RANS results as well as the RANS-based LPT prediction. An Euler reference solution would provide worse agreement in the mean-steady solution, and subsequently worse prediction of the unsteady loading when compared to the unsteady RANS results.

However, the present study and discussion of the error in LPT when applied to interference flows also highlights the fundamental shortcoming in these works. As no modification is made to the fundamental mathematical formulation of piston theory, these RANS-based LPT applications do not mathematically account for interaction with the boundary layer or the surrounding flow. This may be a significant source of error in the strong-interaction regime often found in hypersonic applications. An improved extension or application of LPT to viscous flows would need to have additional mathematical terms to account for this interaction.

Such additional terms accounting for boundary-layer interaction have already been developed in the context of CPT. Particular attention is drawn to the works of Orlik-Rückemann [183], Ericsson [188], and of Hui and East [189] discussed in Section 3.2.9. It is the opinion of the author that the extension of LPT to include the developments from the above work will yield greater dividends than contemporary efforts into improved definitions of the effective shape.

Suitability of Existing Formulations

The above discussions surrounding the extension of LPT to interference flows and to viscous flows, along with the previous discussions on sources of error in LPT, inform the present assessment of existing methods. The reader is referred to Sections 3.2 and 3.4 and particularly to Tables 3.4 and 3.5 for a review of existing piston theory formulations. The assessment of existing formulations follows the categorization of Tables 3.4 and 3.5:

- Classical point-function formulations of piston theory, in which no upstream influence is accounted for, are unsuitable for interference flows. This encompasses the first six

entries in Table 3.4. In these methods, all interaction with the upstream or surrounding flow is disregarded. This is not strictly the case in LPT, as upstream influence is accounted for the mean-steady solution, albeit not in the propagation of subsequent perturbations,

- The following three entries in Table 3.4 comprise of the "extended / enhanced" piston theories [144, 145, 160] – in particular, in their low-frequency or high-Mach series forms –and of Landahl's [128] method. These methods account for the 3D propagation of upstream perturbations. A significant difference between the methods is that the "extended / enhanced" piston theories are based in linear potential flows, while Landahl's [128] method is based in nonlinear potential flows. The current formulation of the methods does not account for non-uniform flows upstream of the wing, and would require extension to account for interference flowfields. However, these methods do account for sinusoidally-varying 3D perturbations and their propagation downstream,

- The final two entries in Table 3.4 relate to piston theories for shells. These methods were developed for axisymmetric geometries (and flows) of essentially infinite length. The introduction of a crossflow velocity or of wings would destroy the axisymmetric formulation. The methods in their present forms are thus not suitable for application in interference flows,

- The implementation of the hybrid linearized panel / CPT method of [79, 125] and its potential for use as a perturbation relative to a mean-steady reference solution renders the first entry in Table 3.5 the most viable method for application in interference flows at present,

- The following entry in Table 3.5 refers to the heuristic influence-corrections to CPT of Hui [181] and Wang [173]. While these do not model interaction with the flowfield, they provide an approximate account of flow three-dimensionality in the mean-steady solution. In this sense, it is possible that these methods will provide an (at best) approximate replication of the interference loading trends as was noted for LPT, though not of the same fidelity as achieved by LPT,

- The following two entries in Table 3.5 are the hypersonic SDTs developed for oscillating wedges. These methods are significant in being the only methods (together with the higher-order method of Hui and East [189]) that account for reflection of perturbations off of the bow shock. While the methods account for upstream influence and interaction with the surrounding flow, in their present form they are not suitable for application in interference flows. This is due to their solution being obtained for

the uniform reference flow between the (rectilinear) bow shock and the wedge surface. This flowfield uniformity is not characteristic of interference flows, even within a 2D formulation. However, the development of the governing equations prior to their solution is sufficiently general to be accurate for (2D) interference flows (in the absense of impinging shocks and secondary bodies),

- The next two entries in Table 3.5 are the viscous piston-theories of Ericsson [188] and of Orlik-Rückemann [183]. While these are not suitable for interference flows, they were developed specifically to account for boundary-layer interaction in viscous flows, and are suitable for this latter application,

- The next entry in Table 3.5 is the intermediate-level method of Hui and East[189]. It may be considered an extension to viscous-coupling of Hui's [177, 178] inviscid method for wedges. Due to its account of flowfield (particularly boundary-layer) interaction and its iterative nature, it may be argued that it could be applied to 2D interference flows. However, this remains to be substantiated. Due to the complexity of the method, it is unlikely to be implemented as an extension to LPT,

- The final two entries in Table 3.5 are Euler-based and RANS-based LPT. The present numerical investigation has shown that the former does not account for flowfield interaction. The present discussion has also highlighted this shortcoming in present formulations of RANS-based LPT.

The conclusion is reached that in their present form, existing piston theories, including the "extended / enhanced piston theories" of [144, 145, 160], are not well-suited to application in interference flowfields.

It is posited that these methods may be extended to account for vortex-interaction within a potential-flow framework. It would similarly be of value to extend the (essentially linearized) methods to a perturbation form about a mean-steady solution, as is done in LPT. Further avenues of extension of existing methods to account for flowfield interaction may be speculated on. The investigation of these possibilities outside the scope of the present work, but is of prime interest in future work.

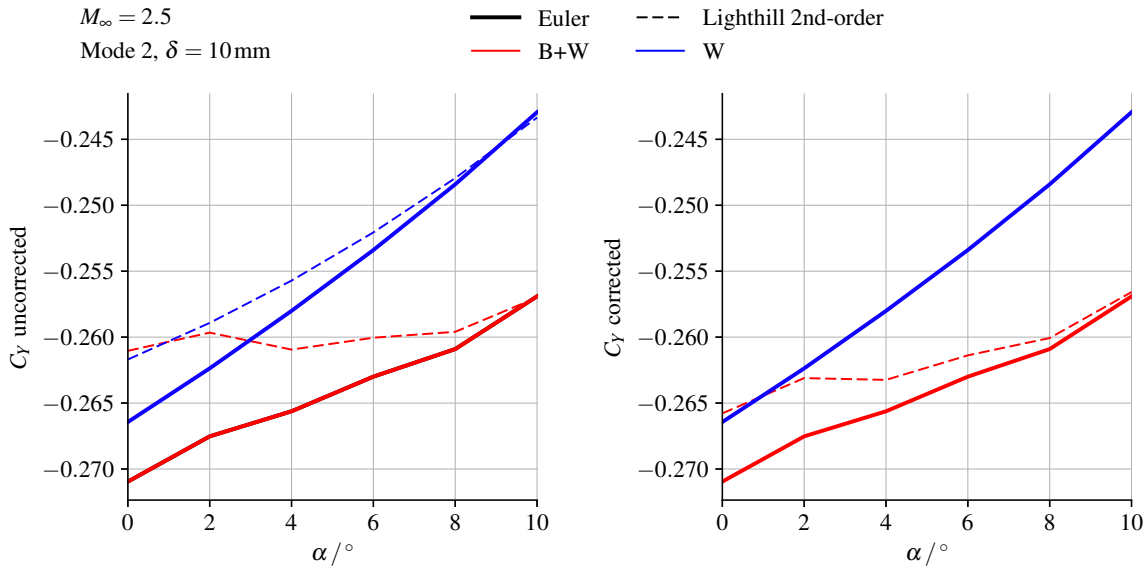

Fig. 5.76 Comparison of the uncorrected and corrected predictions of the side-force coefficient C_Y. Mode 2 with $\delta = 10\,\text{mm}$. $M_\infty = 2.5$.

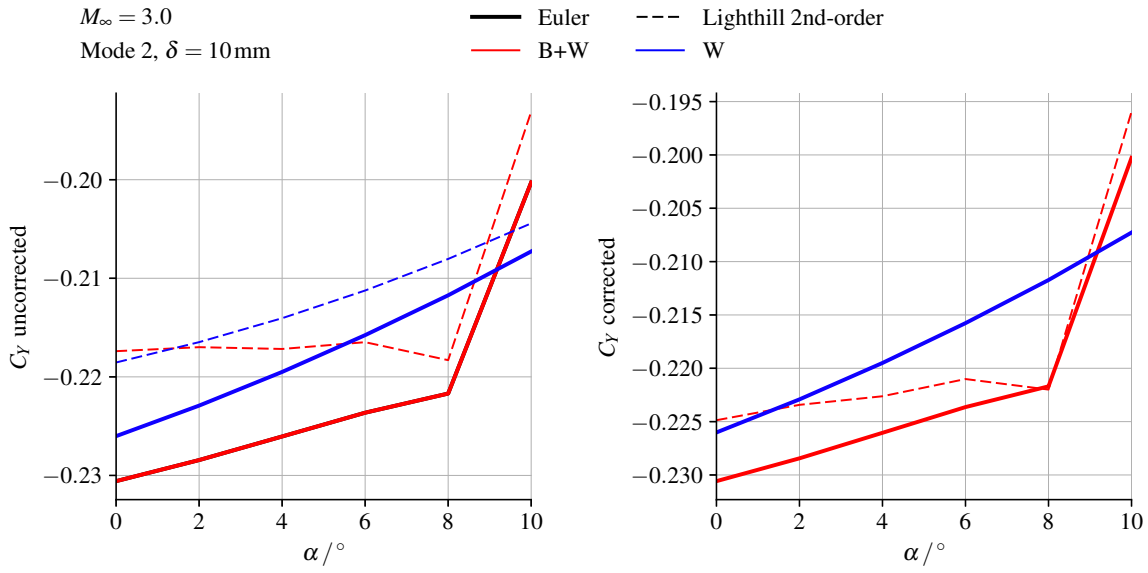

Fig. 5.77 Comparison of the uncorrected and corrected predictions of the side-force coefficient C_Y. Mode 2 with $\delta = 10\,\text{mm}$. $M_\infty = 3.0$.

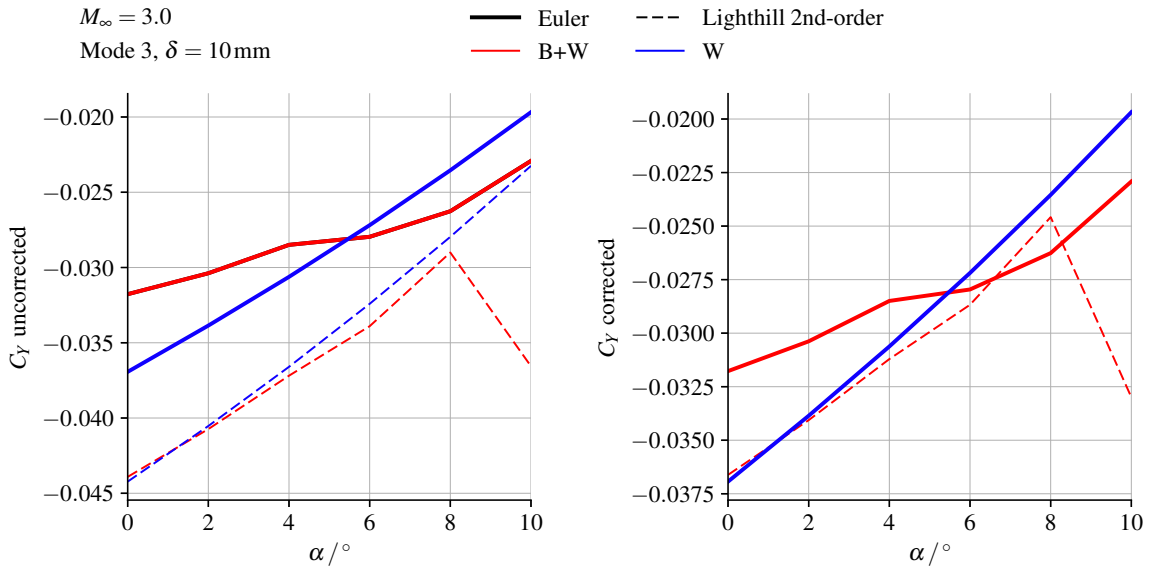

Fig. 5.78 Comparison of the uncorrected and corrected predictions of the side-force coefficient C_Y. Mode 3 with $\delta = 10\,\text{mm}$. $M_\infty = 3.0$.

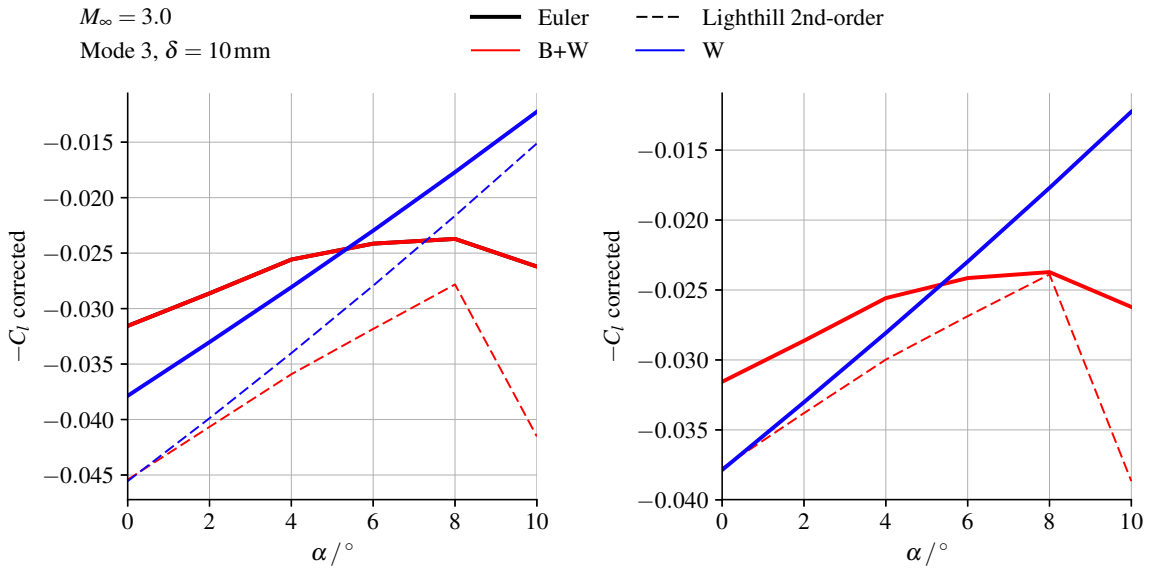

Fig. 5.79 Comparison of the uncorrected and corrected predictions of the rolling-moment coefficient C_l. Mode 3 with $\delta = 10\,\text{mm}$. $M_\infty = 3.0$.

Chapter 6

Conclusions and Recommendations for Future Work

6.1 Conclusions

The present work is concluded with an abridged summary of each chapter in Section 6.1.1. These key points raised in Section 6.1.1 are further reduced to the key conclusions relating to the thesis put forward in Section 1.1. The contributions made to the field by the present work are summarized in Chapter 7, while recommendations for future work are made in Section 6.2.

6.1.1 Summary

The key conclusions of each chapter in the body of the present work are outlined below:

Chapter 2

- The review of the physics associated with flows around slender bodies in Section 2.1 emphasized the importance of
  - Shock waves,
  - The viscous boundary-layer,
  - Vortices,
  - Interaction between the aforementioned flow-structures, as well as between the flowfield and deforming control surfaces.

- The review of broadly-used aeroprediction methods for slender bodies in Sections 2.2 and 2.3 served to
  - Introduce the broad spectrum of methods used, with an emphasis on the physics modelled by the methods,
  - Emphasize the trade-off between modelling fidelity and computational cost,
  - Contextualize classical piston theory (CPT) and CFD-based local piston theory (LPT) in the broader spectrum of methods,
  - Highlight the significance of CFD-based LPT as a low-cost / high-fidelity prediction method.

The chapter served to establish the relative merits of CFD-based LPT as a aeroprediction method for slender bodies with aeroelastic effects.

Chapter 3

- The introduction to generalized piston theory in Section 3.1 emphasized the following core ideas:
  - Piston theory as the extension (or reduction) to 1D of the unsteady analogy (also known as the law of plane sections),
  - The usage of the term "piston theory" as the label for any point-local, algebraic relationship between fluid pressure and surface motion,
  - Sources of error in piston theory as identifiable with neglected physical phenomena or processes.
- The categorization and review of significant historical developments relating to piston theory in Sections 3.2 and 3.4 emphasized
  - The broad spectrum of differing theoretical bases of varying fidelity which lead to methods identified as "piston theory",
  - The extensive work historically completed towards accounting for
    - Upstream influence and flowfield interaction,
    - Viscous interaction,

    in hypersonic small-disturbance theories and CPT,
  - How this work relates to LPT,

  - How this work has been overlooked in the development and application of CFD-based LPT,
  - The trend of application to CFD-based LPT to increasingly complex flows and geometries,
  - The lack of a mathematical basis for LPT from which to justify these applications.

- The review of the theoretical validity of the linear potential flow basis for CPT conducted in [116, 121] provided a framework for assessing
  - The validity of recent renewed-interest in so-called "extended" piston theories based in linear potential flows,
  - The need for a nonlinear potential flow basis, as utilized in Landahl's [128] method,
  - The validity of possible future extensions of LPT to a linear potential-flow basis.

- The review of the significance of second-order and higher-order terms in piston theory in Section 3.3 yielded the following novel conclusions:
  - A fundamental difference in modelling capability between CPT and LPT is observed at second-order in steady flows. Specifically, a non-zero quadratic-stiffness term is introduced at second-order in local piston theory,
  - The extension of LPT to second-order offers the possibility of extending the utility of a given mean-steady CFD solution to larger perturbations.

The chapter served to emphasize the rich body of knowledge pertaining to piston theory (both classical and local). This simultaneously led to the following gaps being identified in the literature:

- No mathematical basis exists for LPT,
- No controlled study into the application of LPT in aerodynamically interfering flows as associated with slender-body geometries has been conducted,
- No investigation into the extension of the pressure-equation of LPT to higher-order has been conducted.

The literature review also motivated the need for this gap to be addressed: current trends in the application of LPT to increasingly complex flows are accompanied with increasing prediction error. There is no mathematical (or indeed semi-empirical) basis justifying or informing the application to these flows.

Chapter 4

- The approach to the mathematical development was introduced in Section 4.1, along with introductory remarks regarding non-dimensionalization and perturbation- and scaling-analysis,
- The perturbation form of the Euler equations and related boundary conditions, non-dimensionalized using un-specified (general) reference values, were presented as the starting point of the development in Section 4.3,
- An introduction to the selection of appropriate reference values was given in Section 4.4, with a framework for quantifying relative orders of magnitude presented in Appendix A,
- The derivation of CPT from the 3D unsteady Euler equations was presented in Section 4.5, with the classical results associated with Il'yushin's [77] development recovered,
- Application of the same process to derive LPT using a different set of reference values was demonstrated in Section 4.6,
- This was followed by a discussion of the mathematical requirements placed on the flow to facilitate this derivation in Section 4.7. The key conclusions will be repeated in Section 6.1.2.

The chapter served to develop the mathematical basis for deriving LPT from the 3D unsteady Euler equations. Interpretation of this mathematical requirements provided significant insight into the shortcomings of recent applications of CFD-based LPT. The mathematical basis also serves to inform future extensions to CFD-based LPT.

Chapter 5

- An introduction was provided in Section 5.1 into
  - The motivation for the geometry selected for the study,
  - The computational and experimental reference data,
  - The methodology of the numerical study.
- The results of the body-alone case were presented in Section 5.2. The body-alone case served to
  - Verify the use of the `HiSA` [213] solver in `OpenFOAM` against `ANSYS Fluent`,

  - Demonstrate the inherent shortcomings of an Euler-based model over the parameter space considered,
  - Establish the interference flowfield in which control surfaces would be immersed. The development of body-shed vortices at $M_\infty \sin\alpha \approx 0.45$ was driven by crossflow-shocks in the inviscid formulation.

- The results of the wing-alone case were presented in Section 5.2. The wing-alone case served to investigate the accuracy of Euler-based LPT when applied to a cruciform control-surface set in the "+"configuration in the absence of an interference flowfield. Furthermore, the influence of the following factors on the accuracy of LPT under these circumstances was investigated:

  - Mode-shapes of deformation and their amplitude,
  - The selection of piston-theory coefficients and the order of the pressure equation,
  - The freestream Mach number.

  The key conclusions from this study will be repeated in Section 6.1.2.

- The results of the wing-body (full vehicle) case were presented in Section 5.4. The influence of the same factors as in the wing-alone case on the accuracy of LPT was investigated. The results also led to a discussion surrounding the prediction errors and suitability of LPT for application in aerodynamically interfering flows typical of slender bodies with aeroelastic effects in Section 5.5. The key conclusions from this study will be repeated in Section 6.1.2.

This chapter yielded

- A controlled investigation into the accuracy of LPT in aerodynamically interfering flows,
- Insight into the underlying shortcomings in the physical modelling of LPT,
- Prediction errors in scenarios which were anticipated by the mathematical basis of Chapter 4,

and thus serves as supporting evidence for the mathematical basis developed in Chapter 4, as well as a valuable first controlled investigation into applying piston theory in interference flows.

6.1.2 Key Conclusions

The key conclusions relating to the thesis are listed below:

Justification by a Theoretical or Mathematical Basis

- A mathematical basis for Euler-based LPT rooted in the 3D unsteady Euler equations was developed. The basis requires that:
  - A uniformly-valid non-dimensionalization is possible,
  - Term groupings involving velocity perturbations in the streamwise direction should be $\mathcal{O}(\tau^2)$ relative to the largest-order term grouping in the relevant equation. The latter will typically involve the mean-steady velocity in the streamwise direction. This facilitates the reduction to a 2D formulation in the crossflow plane,
  - Gradients in the crossflow directions of perturbations to the flow must not be comparable. This prohibits one of the crossflow direction from being neglected in favour of the other, which is necessary for a reduction to a 1D formulation,
  - If velocity perturbations in one of the crossflow directions are comparable in magnitude to velocity perturbations in the streamwise direction, then one of the requirements for a reduction to 1D is the following: perturbation gradients in that crossflow direction must be at least as small as perturbation gradients in the streamwise direction,
  - In order to obtain an algebraic pressure-downwash relationship, the role of surface-incident characteristics must be neglected.
- These requirements from the mathematical basis are violated to varying degrees (both in terms of the magnitude and the spatial extent of the violation) when the following occur:
  - The mean-steady flow is transonic, or if embedded subsonic regions exist,
  - A layer-type problem arises, as associated with
    - Entropy layers,
    - Viscous boundary-layers,
  - The surface to which LPT is applied is in close proximity to
    - Shock-waves,

        - Vortices,
        - Strong entropy-gradients,
        - Other aerodynamically-interfering surfaces,
    - The surface to which LPT is applied is in close proximity to regions of sharp curvature, such as
        - Blunted noses,
        - Wing-tips,
        - Trailing-edges,
        - Subsonic leading-edges,
        - Wing-body junctions,
    - Mode-shapes of deformation involving regions of localized bending or camber or point-local deformations.

- It is noted that many of the above circumstances arise – at least within some spatial extent of the surface of interest – in flows around the geometries of interest to the thesis. It is thus concluded that Euler-based LPT in its present form is *not* mathematically justified in the regions in which the above violations occur, and caution should be exercised in applying the method.

Suitability of Euler-Based LPT in its Present Form

A numerical investigation into the application of Euler-based LPT to the geometry of interest to the thesis was conducted. The key conclusions regarding the suitability of Euler-based LPT in its present form were that

- Useful aeroprediction may be obtained in interference flows for mode-shapes involving strong twist. More specifically, useful prediction is obtained if
    - The pressure-loading is dominated by surface-inclination,
    - Flowfield-interaction is of secondary importance.

  Under these circumstances, useful prediction is obtained even at supersonic downwash Mach numbers.

- The possibility for the general character of load-trends to be predicted in interference-flows purely from the mean-steady interference at the surface was identified. However, it is stressed that categorically incorrect trends were predicted following the onset

of body-shed vortices when considering the second-bending mode (which involved localized bending and camber),

- Significant prediction errors arose when considering bending-dominated mode-shapes:
  - In the case of the first-bending mode, the general loading trend was replicated, and the error was attributed to flowfield-interaction in the absence of body-shed vortices,
  - In the case of the second-bending mode, the prediction error were a non-trivial function of the parameter space. The incorrect prediction of loading trends following the onset of body-shed vorticity has already been noted. It was argued that the prediction errors could not be solely attributed to flowfield interaction, as similar errors were noted for this mode in the wing-alone case. Thus, a portion of the prediction error was attributed to three-dimensionality of the perturbations associated with the localized bending and camber.
- The selection of piston-theory coefficients in the LPT pressure equation had no significant effect on the loading-trend prediction, but served to provide a prediction-band for the load,
- Similarly, the use of second-order and third-order pressure equations in LPT did not change the prediction of loading-trends when the mean-steady solution is symmetrical about the “windward” and ”leeside” surfaces of the deforming control-surface. However, a offset in the load prediction was noted, with second-order LPT generally providing the best agreement with the Euler results,
- The final assessment recommends that results obtained from Euler-based LPT in interference flows be interpreted with caution. It cannot be stated that Euler-based LPT is generally suitable in its present form, as the role of flowfield-interaction may be significant. However, some useful results may still be obtained from the method, and thus it cannot be categorically ruled “invalid”. In order to improve the suitability and reliability of the CFD-based LPT, the author recommends that further work be conducted towards extending LPT in a mathematically consistent way, with the development informed by the mathematical basis presented in Chapter 4.

6.2 Recommendations for Future Work

The following recommendations are made for future work:

- The development of a "flowfield-interactive" LPT which accounts for the persistence and reflection of perturbations generated by the deforming control-surface is of great interest. The author recommends that the development of such a method be initiated by considering linearized perturbations in the equations presented in Section 4.3,
- The scaling analysis presented in Section 4.6 may be adapted for the higher spatial-gradients of perturbations that may arise in problems dealing with panel-flutter. It is expected that this may yield insight into the application of Euler-based LPT to problems of this class,
- The interpretation of strong gradients in the mean-steady flow as additional source terms in a LPT formulation, put forward in Section 4.6, has implications for existing numerical studies on shock-impingement on flexible panels [19, 194, 195]. It is possible that a revised formulation of LPT to account for the shock gradients may be developed using the method of Chapter 4,
- The extension of the mathematical basis to perturbations in a Navier-Stokes framework is recommended. This may provide insight into conditions under which a RANS-based LPT as noted in recent literature [18] with effective-shape corrections may be valid,
- Investigation of the possibility to adapt existing RANS-based LPT to account for viscous-inviscid interaction using the methods of Orlik-Rückemann and Ericsson [188] is recommended,
- Investigation of the possibility to extend the "extended piston theories" of [144, 145, 160] to second-order in thickness using Van Dyke's [104] second-order theory as applied by Landahl [128] is recommended,
- The extension of the numerical investigation conducted in Chapter 5 to include a study of the role of leading-edge sweep, subsonic leading-edges, and unsteady effects is recommended.

Chapter 7

Contributions to the Field

The following novel contributions were made to the field:

- An extensive review and categorization of historical developments relating to both classical and local piston theory, conducted in Chapter 3, with elements from it published as [59, 116, 121]
- The development of the mathematical basis for Euler-based LPT, conducted in Chapter 4 and published in an early form as [196]
- A controlled numerical investigation into the application and suitability of Euler-based LPT to slender-bodies with aerodynamically-interfering control surfaces, conducted in Chapter 5 and published as [212]
- An investigation into the role of higher-order terms in the pressure-equation of LPT and the identification of a non-zero second-order contribution to aerodynamic stiffness, presented in Section 3.3 and published as [123],
- An investigation into the role of selected piston-theory coefficients and higher-order pressure terms in load-trend prediction in LPT, which was conducted in the context of numerical investigation of Chapter 5 and was part of the associated publication of [212].

7.1 Publications from the Work

The following is a list of publications arising from the work conducted towards the completion of the thesis, in chronological order of publication:

- M.-C. Meijer and L. Dala, "On the validity range of piston theory," in 16$^{\text{th}}$ International Forum on Aeroelasticity and Structural Dynamics, (St. Petersburg, Russia), 28 June–2 July 2015. IFASD-2015-004.
- M.-C. Meijer and L. Dala, "Generalized formulation and review of piston theory for airfoils," *AIAA Journal*, vol. 54, no. 1, pp. 17–27, 2016. DOI: 10.2514/1.J054090
- M.-C. Meijer, "Piston theory applied to wing-body configurations: A review of the mathematical basis," in *Research and Education in Aircraft Design 2016*, (Warsaw, Poland), 12–14 Sept. 2016.
- M.-C. Meijer and L. Dala, "Quantifying non-linearity in planar supersonic potential flows," *The Aeronautical Journal*, vol. 121, no. 1237, pp. 372–394, 2017. DOI: 10.1017/aer.2016.141
- M.-C. Meijer and L. Dala, "Local piston theory as an alternative to mesh deformation: slender wing/body configurations," *Journal of Aircraft*, vol. 55, no. 4, pp. 1709–1719, 2018. DOI: 10.2514/1.C034697
- M.-C. Meijer and L. Dala, "On the role of higher-order terms in local piston theory," *Journal of Aircraft*, 2018. Published Online 13 Sept 2018. DOI: 10.2514/1.C034920

References

[1] A. Jameson, "Re-engineering the design process through computation," *Journal of Aircraft*, vol. 36, no. 1, pp. 36–50, 1999.

[2] M. J. Hemsch and J. N. Nielsen, *Tactical Missile Aerodynamics*. New York: American Institute of Aeronautics and Astronautics, Inc., 1986.

[3] J. N. Nielsen, *Missile Aerodynamics*. New York: McGraw-Hill, 1960.

[4] V. V. Sychev, "Three-dimensional hypersonic gas flow past slender bodies at high angles of attack," *Journal of Applied Mathematics and Mechanics*, vol. 24, no. 2, pp. 296–306, 1960. [Online]. Available: http://dx.doi.org/10.1016/0021-8928(60)90033-2

[5] C. Rosema, J. Doyle, and W. B. Blake, "Missile data compendum (datcom): User's manual – 2014 revision," Air Force Research Laboratory, WPAFB, OH, AFRL-RQ-WP-TR-2014-0281, 2014.

[6] F. G. Moore and L. Y. Moore, "The 2009 version of the Aeroprediction Code: The AP09," Defense Technical Information Center, Alexandria, VA, Aeroprediction Report No. 3, 2008.

[7] E. L. Fleeman, *Missile Design and System Engineering*, ser. Education Series. Washington, DC: American Institute of Aeronautics and Astronautics, Inc., 2013. [Online]. Available: http://dx.doi.org/10.2514/4.869082

[8] E. L. Fleeman, *Tactical Missile Design*, 2nd ed. Reston, VA.: American Institute of Aeronautics and Astronautics, Inc., 2006.

[9] J. P. Thomas, E. H. Dowell, and K. C. Hall, "Three-dimensional transonic aeroelasticity using proper orthogonal decomposition-based reduced-order models," *Journal of Aircraft*, vol. 40, no. 3, pp. 544–551, 2003. [Online]. Available: http://dx.doi.org/10.2514/2.3128

[10] A. R. Crowell, J. J. McNamara, and B. A. Miller, "Hypersonic aerothermoelastic response prediction of skin panels using computational fluid dynamic surrogates," *Journal of Aeroelasticity and Structural Dynamics*, vol. 2, no. 2, pp. 3–30, 2011. [Online]. Available: http://dx.doi.org/10.3293/asdj.2011.11

[11] V. Statnikov, M. Meinke, and W. Schröder, "Reduced-order analysis of buffet flow of space launchers," *Journal of Fluid Mechanics*, vol. 815, pp. 1–25, 2017. [Online]. Available: http://dx.doi.org/10.1017/jfm.2017.46

[12] E. R. Dreyer, R. J. Klock, B. J. Grier, J. J. McNamara, and C. E. S. Cesnik, "Multi-discipline modeling of complete hypersonic vehicles using CFD surrogates," in 58^{th} *AIAA/ASCE/AHS/ASC Structures, Structural Dynamics, and Materials Conference, AIAA SciTech Forum*, Kissimmee, FL, 9–13 Jan. 2017, AIAA 2017-0182. [Online]. Available: http://dx.doi.org/10.2514/6.2017-0182

[13] J. J. McNamara, A. R. Crowell, P. P. Friedmann, B. Glaz, and A. Gogulapati, "Approximate modeling of unsteady aerodynamics for hypersonic aeroelasticity," *Journal of Aircraft*, vol. 47, no. 6, pp. 1932–1945, 2010. [Online]. Available: http://dx.doi.org/10.2514/1.C000190

[14] W. W. Zhang, Z. Y. Ye, C. A. Zhang, and F. Liu, "Supersonic flutter analysis based on a local piston theory," *AIAA Journal*, vol. 47, no. 10, pp. 2321–2328, 2009. [Online]. Available: http://dx.doi.org/10.2514/1.37750

[15] Q. Zhang, K. Ye, Z. Y. Ye, and W. W. Zhang, "Aerodynamic optimization for hypersonic wing design based on local piston theory," *Journal of Aircraft*, vol. 53, no. 4, pp. 1065–1072, 2016. [Online]. Available: http://dx.doi.org/10.2514/1.C033381

[16] X. Shi, G. Tang, B. Yang, and H. Li, "Supersonic flutter analysis of vehicles at incidence based on local piston theory," *Journal of Aircraft*, vol. 49, no. 1, pp. 333–337, 2012. [Online]. Available: http://dx.doi.org/10.2514/1.C031465

[17] Y. Yan, C. Xie, J. He, and C. Jiang, "Rigid and elastic coupling stability analysis of hypersonic vehicles," in 17^{th} *International Forum on Aeroelasticity and Structural Dynamics*, Como, Italy, 25–28 Jun. 2017, IFASD-2017-225.

[18] W. Liu, C. A. Zhang, H. Q. Han, and F. M. Wang, "Local piston theory with viscous correction and its application," *AIAA Journal*, vol. 55, no. 3, pp. 942–954, 2017. [Online]. Available: http://dx.doi.org/10.2514/1.J055207

[19] K. R. Brouwer and J. J. McNamara, "Rapid modeling of aeroelastic loads in the presence of shock impingements," in 2018 *AIAA/ASCE/AHS/ASC Structures, Structural Dynamics, and Materials Conference, AIAA SciTech Forum*, Kissimmee, FL, 8–12 Jan. 2018, AIAA 2018-1448. [Online]. Available: http://dx.doi.org/10.2514/6.2018-1448

[20] M. D. Van Dyke, *An Album of Fluid Motion*. Stanford, CA: The Parabolic Press, 1982.

[21] G. F. Glotov, *Aerothermodynamics of Flying Vehicles in Photographs*. Zhukovsky: TsAGI, 2003.

[22] M. J. Hemsch, Ed., *Tactical Missile Aerodynamics: General Topics*, ser. Progress in Astronautics and Aeronautics, Volume 141. Washington, DC: American Institute of Aeronautics and Astronautics, Inc., 1991.

[23] R. J. Krieger and S. R. Vukelich, "Tactical missile drag," in *Tactical Missile Aerodynamics: Prediction Methodology*, ser. Progress in Astronautics and Aeronautics, Volume 142, M. R. Mendenhall, Ed. Washington, DC: American Institute of Aeronautics and Astronautics, Inc., 1991, ch. 1, pp. 225–285.

[24] M. R. Mendenhall, S. C. Perkins, and D. J. Lesieutre, "Vortex cloud model for body vortex shedding and tracking," in *Tactical Missile Aerodynamics: Prediction Methodology*, ser. Progress in Astronautics and Aeronautics, Volume 142, M. R. Mendenhall, Ed. Washington, DC: American Institute of Aeronautics and Astronautics, Inc., 1991, ch. 6, pp. 225–285.

[25] J. D. Anderson, *Hypersonic and high temperature gas dynamics*, 2nd ed. London: American Institute of Aeronautics and Astronautics, 2006.

[26] J. R. Hayes and R. D. Neumann, "Introduction to aerodynamic heating analysis of supersonic missiles," in *Tactical Missile Aerodynamics: Prediction Methodology*, ser. Progress in Astronautics and Aeronautics, Volume 142, M. R. Mendenhall, Ed. Washington, DC: American Institute of Aeronautics and Astronautics, Inc., 1991, ch. 3, pp. 63–114.

[27] W. D. Hayes and R. F. Probstein, *Hypersonic Inviscid Flow*. Dover Publications, 1972.

[28] J. J. Bertin, *Hypersonic Aerothermodynamics*. New York: American Institute of Aeronautics and Astronautics, Inc., 1994.

[29] L. E. Ericsson, "Unsteady flows," in *Tactical Missile Aerodynamics: General Topics*, ser. Progress in Astronautics and Aeronautics, Volume 141, M. J. Hemsch, Ed. Washington, DC: American Institute of Aeronautics and Astronautics, Inc., 1991, ch. 11, pp. 453–503.

[30] S. Tuling, "An engineering method for modeling the interaction of circular bodies and very low aspect ratio cruciform wings at supersonic speeds," Ph.D. dissertation, University of the West of England, Bristol, Faculty of Environment and Technology, 2013.

[31] L. E. Ericsson and J. P. Reding, "Asymmetric flow separation and vortex shedding on bodies of revolution," in *Tactical Missile Aerodynamics: General Topics*, ser. Progress in Astronautics and Aeronautics, Volume 141, M. J. Hemsch, Ed. Washington, DC: American Institute of Aeronautics and Astronautics, Inc., 1991, ch. 10, pp. 391–452.

[32] E. R. Keener, "Oil separation patterns on an ogive forebody," *AIAA Journal*, vol. 21, no. 4, pp. 550–556, 1983. [Online]. Available: http://dx.doi.org/10.2514/3.8112

[33] R. C. Nelson and G. N. Malcolm, "Visualization of high-angle-of-attack flow phenomena," in *Tactical Missile Aerodynamics: General Topics*, ser. Progress in Astronautics and Aeronautics, Volume 141, M. J. Hemsch, Ed. Washington, DC: American Institute of Aeronautics and Astronautics, Inc., 1991, ch. 5, pp. 195–250.

[34] E. R. Keener and G. T. Chapman, "Similarity in vortex asymmetries over slender bodies and wings," *AIAA Journal*, vol. 15, no. 9, pp. 1370–1372, 1977. [Online]. Available: http://dx.doi.org/10.2514/3.60795

[35] J. L. Thomas and P. M. Hartwich, "Navier-stokes analyses of flows over slender airframes," in *Tactical Missile Aerodynamics: Prediction Methodology*, ser. Progress in Astronautics and Aeronautics, Volume 142, M. R. Mendenhall, Ed. Washington,

DC: American Institute of Aeronautics and Astronautics, Inc., 1991, ch. 12, pp. 561–648.

[36] A. J. Smits and T. T. Lim, *Flow Visualization: Techniques and Examples*. London: Imperial College Press, 2000.

[37] L. E. Ericsson and I. M. Scholnik, "Effect of nose bluntness on hypersonic unsteady aerodynamics," *Journal of Spacecraft and Rockets*, vol. 6, no. 3, pp. 321–324, 1969. [Online]. Available: http://dx.doi.org/10.2514/3.29594

[38] J. D. Cole, "Acceleration of slender bodies of revolution through sonic velocity," *Journal of Applied Physics*, vol. 26, no. 3, pp. 322–327, 1955. [Online]. Available: http://dx.doi.org/10.1063/1.1721986

[39] C. M. Jackson and W. M. Sawyer, "Bodies with noncircular cross sections and bank-to-turn missiles," in *Tactical Missile Aerodynamics: General Topics*, ser. Progress in Astronautics and Aeronautics, Volume 141, M. J. Hemsch, Ed. Washington, DC: American Institute of Aeronautics and Astronautics, Inc., 1991, ch. 9, pp. 365–389.

[40] M. Samimy, K. S. Breuer, L. G. Leal, and P. H. Steen, *A Gallery of Fluid Motion*. Cambridge: Cambridge University Press, 2003.

[41] R. L. Stallings, "Low aspect ratio wings at high angles of attack," in *Tactical Missile Aerodynamics: General Topics*, ser. Progress in Astronautics and Aeronautics, Volume 141, M. J. Hemsch, Ed. Washington, DC: American Institute of Aeronautics and Astronautics, Inc., 1991, ch. 6, pp. 251–286.

[42] J. Delery, *Separation in three-dimensional steady flow, Part 3: Topology of some remarkable three-dimensional flows*. Onera, 2011.

[43] A. M. Thu, Y. H. Byun, and J. W. Lee, "Dye visualization of vortical flow structure over a double-delta wing," *Journal of Aerospace Engineering*, vol. 25, no. 4, pp. 541–546, 2012. [Online]. Available: http://dx.doi.org/10.1061/(ASCE)AS.1943-5525.0000195

[44] O. O. Bendiksen, "Review of unsteady transonic aerodynamics: Theory and applications," *Progress in Aerospace Sciences*, vol. 47, pp. 135–165, 2011. [Online]. Available: http://dx.doi.org/10.1016/j.paerosci.2010.07.001

[45] A. B. Wardlaw, F. P. Baltakis, F. J. Priolo, and J. M. Solomon, "Space marching euler solvers," in *Tactical Missile Aerodynamics: Prediction Methodology*, ser. Progress in Astronautics and Aeronautics, Volume 142, M. R. Mendenhall, Ed. Washington, DC: American Institute of Aeronautics and Astronautics, Inc., 1991, ch. 9, pp. 379–444.

[46] M. J. Hemsch, "Component build-up method for engineering analysis at low-to-high angles of attack," in *Tactical Missile Aerodynamics: Prediction Methodology*, ser. Progress in Astronautics and Aeronautics, Volume 142, M. R. Mendenhall, Ed. Washington, DC: American Institute of Aeronautics and Astronautics, Inc., 1991, ch. 4, pp. 115–169.

[47] M. J. Hemsch and J. N. Nielsen, "Equivalent angle-of-attack method for estimating nonlinear aerodynamics of missile fins," *Journal of Spacecraft and Rockets*, vol. 20, no. 4, pp. 356–362, 1983. [Online]. Available: http://dx.doi.org/10.2514/3.25606

[48] A. E. Gentry, D. N. Smith, and W. R. Oliver, "The mark iv supersonic–hypersonic arbitrary-body program: Vol. I – user's manual," Air Force Flight Dynamics Laboratory, WPAFB, OH, AFFDL-TR-73-159, 1973.

[49] L. L. Cronvich, "Aerodynamic considerations for autopilot design," in *Tactical Missile Aerodynamics: General Topics*, ser. Progress in Astronautics and Aeronautics, Volume 141, M. J. Hemsch, Ed. Washington, DC: American Institute of Aeronautics and Astronautics, Inc., 1991, ch. 2, pp. 29–67.

[50] F. G. Moore, "State-of-the-art engineering aeroprediction methods with emphasis on new semiempirical techniques for predicting nonlinear aerodynamics on complete missile configurations," Naval Surface Warfare Center Dahlgren Division, Dahlgren, VA, TR-93/551, 1993.

[51] M. F. E. Dillenius, D. J. Lesieutre, M. C. Hegedus, S. C. Perkins, J. F. Love, and T. O. Lesieutre, "Engineering-, intermediate-, and high-level aerodynamic prediction methods and applications," *Journal of Spacecraft and Rockets*, vol. 36, no. 5, pp. 609–620, 1999. [Online]. Available: http://dx.doi.org/10.2514/2.3479

[52] W. B. Baker, "Use of semiempirical aerodynamic methods for preliminary design," in *NEAR Conference on Missile Aerodynamics*, Monterey, CA, 31 Oct.–2 Nov. 1988.

[53] A. S. Dunn, "Aeropredictive methods for missile analysis," Master's thesis, Naval Postgraduate School, 1989.

[54] F. G. Blottner, "Significance of the thin-layer Navier-Stokes approximation," in *Numerical and Physical Aspects of Aerodynamic Flows III*, T. Cebeci, Ed. New York: Springer-Verlag, Inc., 1986, pp. 184–197.

[55] O. O. Bendiksen, "Improved similarity rules for transonic flutter," in 40^{th} *AIAA/ASME/ASCE/AHS/ASCE SDM conference*, St. Louis, MO, 12–15 Apr. 1999, AIAA 99-1350. [Online]. Available: http://dx.doi.org/10.2514/6.1999-1350

[56] J. C. Tannehill, D. A. Anderson, and R. H. Pletcher, "Numerical methods for the parabolized Navier-Stokes equations," in *Computational Fluid Mechanics and Heat Transfer*, 2nd ed., ser. Series in Computational and Physical Processes in Mechanics and Thermal Sciences. CRC Press, 1997, ch. 8, pp. 537–620.

[57] P. C. Chen and S. Bhasin, "ZONA6 versus the doublet-lattice method for unsteady aerodynamics on lifting surfaces," *Journal of Aircraft*, vol. 49, no. 3, pp. 966–968, 2012. [Online]. Available: http://dx.doi.org/10.2514/1.C031648

[58] L. M. Sheppard and K. D. Thomson, *A shock-expansion theory applicable to wings with attached shock waves*. London, United Kingdom: Aeronautical Research Council CP-392, 1958.

[59] M.-C. Meijer and L. Dala, "Generalized formulation and review of piston theory for airfoils," *AIAA Journal*, vol. 54, no. 1, pp. 17–27, 2016. [Online]. Available: http://dx.doi.org/10.2514/1.J054090

[60] Y. Zhiyin, "Large-eddy simulation: Past, present, and the future," *Chinese Journal of Aeronautics*, vol. 28, no. 1, pp. 11–24, 2015. [Online]. Available: http://dx.doi.org/10.1016/j.cja.2014.12.007

[61] P. Sagaut, "Turbulence, direct numerical simulation, and large-eddy simulation," in *Encyclopedia of Computational Mechanics*, E. Stein, R. de Borst, and T. J. R. Hughes, Eds. John Wiley & Sons, Ltd., 2004, vol. 3, ch. 9, pp. 269–299.

[62] Y. Deng, F. S. Lien, and E. Yee, "The lattice Boltzmann method for compressible flows at high Mach number," in 23^{rd} *Annual Conference of Computational Fluid Dynamics Society of Canada*, Waterloo, Ontario, 7–10 Jun. 2015.

[63] R. Aris, *Vectors, Tensors, and the Basic Equations of Fluid Mechanics*. New York: Dover Publications, Inc., 1989.

[64] C. Hirsch, *Numerical Computation of Internal and External Flows*. New York: John Wiley & Sons, Ltd., 1988.

[65] T. Cebeci, "Three-dimensional boundary layers on missiles," in *Tactical Missile Aerodynamics: Prediction Methodology*, ser. Progress in Astronautics and Aeronautics, Volume 142, M. R. Mendenhall, Ed. Washington, DC: American Institute of Aeronautics and Astronautics, Inc., 1991, ch. 11, pp. 509–560.

[66] C. Hirsch, *Numerical Computation of Internal and External Flows*. New York: John Wiley & Sons, Ltd., 1988.

[67] P. R. Spalart and S. R. Allmaras, "A one-equation turbulence model for aerodynamic flows," in 30^{th} *Aerospace Sciences Meeting and Exhibit*, Reno, NV, 1992, AIAA 92-0439. [Online]. Available: http://dx.doi.org/10.2514/6.1992-439

[68] S. R. Allmaras, F. T. Johnson, and P. R. Spalart, "Modifications and clarifications for the implementation of the Spalart-Allmaras turbulence model," in 7^{th} *International Conference on Computational Fluid Dynamics*, Big Island, HI, 9–13 Jul. 2012, ICCFD7-1902. [Online]. Available: http://dx.doi.org/10.2514/6.1992-439

[69] S. Catris and B. Aupoix, "Density corrections for turbulence models," *Aerospace Science and Technology*, vol. 4, no. 1, pp. 1–11, 2000. [Online]. Available: http://dx.doi.org/10.1016/S1270-9638(00)00112-7

[70] K. Y. Chien, "Predictions of channel and boundary-layer flows with a low-Reynolds-number turbulence model," *AIAA Journal*, vol. 20, no. 1, pp. 33–38, 1982. [Online]. Available: http://dx.doi.org/10.2514/3.51043

[71] F. R. Menter, "Two-equation eddy-viscosity turbulence models for engineering applications," *AIAA Journal*, vol. 32, no. 8, pp. 1598–1605, 1994. [Online]. Available: http://dx.doi.org/10.2514/3.12149

[72] D. C. Wilcox, "Formulation of the k-ω turbulence model revisited," *AIAA Journal*, vol. 46, no. 11, pp. 2823–2838, 2008. [Online]. Available: http://dx.doi.org/10.2514/1.36541

[73] R. Mokhtarpoor, S. Heinz, and M. Stoellinger, "LES and hybrid RANS-LES of high Reynolds number separated flows," in 55^{th} *Aerospace Sciences Meeting and Exhibit*, Grapevine, TX, 9–13 Jan. 2017, AIAA 2017-0994. [Online]. Available: http://dx.doi.org/10.2514/6.2017-0994

[74] L. E. Lijewski, L. B. Simpson, and D. M. Belk, "Time-asymptotic Euler, Navier-Stokes methods for subsonic/transonic flows," in *Tactical Missile Aerodynamics: Prediction Methodology*, ser. Progress in Astronautics and Aeronautics, Volume 142, M. R. Mendenhall, Ed. Washington, DC: American Institute of Aeronautics and Astronautics, Inc., 1991, ch. 10, pp. 445–508.

[75] W. D. Hayes, "On hypersonic similitude," *Quarterly of Applied Mathematics*, vol. 5, no. 1, pp. 102–106, 1947.

[76] F. M. Hamaker, S. E. Neice, and T. J. Wong, *The similarity law for hypersonic flow and requirements for dynamic similarity of related bodies in free flight*. Washington, D.C.: NACA Report 1147, 1953.

[77] A. A. Il'yushin, "The law of plane sections in the aerodynamics of high supersonic speeds," *Applied Mathematics and Mechanics*, vol. 20, no. 6, pp. 733–755, 1956.

[78] M. D. Van Dyke, *A study of hypersonic small-disturbance theory*. Washington, D.C.: NACA Report 1194, 1954.

[79] *ZAERO Version 8.5 Theoretical Manual*, ZONA Technology Inc., Scottsdale, AZ, 2011.

[80] J. P. Thomas, E. H. Dowell, and K. C. Hall, "Nonlinear inviscid aerodynamic effects on transonic divergence, flutter, and limit-cycle oscillations," *AIAA Journal*, vol. 40, no. 4, pp. 638–646, 2002. [Online]. Available: http://dx.doi.org/10.2514/2.1720

[81] J. K. Pittman, "Supersonic full-potential methods for missile body analysis," in *Tactical Missile Aerodynamics: Prediction Methodology*, ser. Progress in Astronautics and Aeronautics, Volume 142, M. R. Mendenhall, Ed. Washington, DC: American Institute of Aeronautics and Astronautics, Inc., 1991, ch. 8, pp. 339–378.

[82] T. Sarpkaya, "Computational methods with vortices – the 1988 Freeman scholar lecture," *Journal of Fluids Engineering*, vol. 111, no. 1, pp. 5–52, 1989. [Online]. Available: http://dx.doi.org/10.1115/1.3243601

[83] M. D. Van Dyke, "Applications of hypersonic small-disturbance theory," *Journal of Aeronautical Sciences*, vol. 21, no. 2, pp. 179–186, 1954. [Online]. Available: http://dx.doi.org/10.2514/8.2955

[84] R. W. Barnwell, "Extension of hypersonic, high-incidence, slender-body similarity," *AIAA Journal*, vol. 25, no. 11, pp. 1519–1522, 1987. [Online]. Available: http://dx.doi.org/10.2514/3.9816

[85] M. J. Hemsch, "Engineering analysis of slender-body aerodynamics using Sychev similarity parameters," *Journal of Aircraft*, vol. 25, no. 7, pp. 625–631, 1988. [Online]. Available: http://dx.doi.org/10.2514/3.45633

[86] N. V. Voevodenko and I. M. Panteleev, "Numerical modeling of supersonic flows over wings with varying aspect ratio on a broad range of angles of attack using the law of plane sections," *Fluid Dynamics*, vol. 27, no. 2, pp. 639–244, 1992. [Online]. Available: http://dx.doi.org/10.1007/BF01052091

[87] M.-C. Meijer and L. Dala, "Zeroth-order flutter prediction for cantilevered plates in supersonic flow," *Journal of Fluids and Structures*, vol. 57, pp. 196–205, 2015. [Online]. Available: http://dx.doi.org/10.1016/j.jfluidstructs.2015.06.018

[88] M. J. Lighthill, "Oscillating airfoils at high Mach numbers," *Journal of the Aeronautical Sciences*, vol. 20, no. 6, pp. 402–406, 1953. [Online]. Available: http://dx.doi.org/10.2514/8.2657

[89] D. D. Liu, Y. F. Kao, and K. Y. Fung, "An efficient method for computing unsteady transonic aerodynamics of swept wings with control surfaces," *Journal of Aircraft*, vol. 25, no. 1, pp. 25–31, 1988. [Online]. Available: http://dx.doi.org/10.2514/3.45536

[90] G. S. Bisnovatyi-Kogan and S. G. Moiseenko, "Isentropic "shock waves" in numerical simulations of astrophysical problems," *Astrophysics*, vol. 59, no. 1, pp. 1–10, 2016. [Online]. Available: http://dx.doi.org/10.1007/s10511-016-9410-4

[91] A. V. Balakrishnan, "Transonic small disturbance potential equation," *AIAA Journal*, vol. 42, no. 6, pp. 1081–1088, 2004. [Online]. Available: http://dx.doi.org/10.2514/1.5101

[92] R. W. Clark, *Non-conical flow past slender wings with leading edge vortex sheets*. London, United Kingdom: Aeronautical Research Council R&M-3814, 1976.

[93] H. Jorgensen, *Calculation of two-dimensional vortex-surface interference using panel methods*. Washington, D.C.: NASA Contractor Report 159334, 1980.

[94] D. Almosnino, "High angle-of-attack calculations of the subsonic vortex flow on slender bodies," *AIAA Journal*, vol. 23, no. 8, pp. 1150–1156, 1985. [Online]. Available: http://dx.doi.org/10.2514/3.9057

[95] M. G. Nagati, J. D. Iversent, and J. M. Vogel, "Vortex sheet modeling with curved higher-order panels," *Journal of Aircraft*, vol. 24, no. 11, pp. 776–782, 1987. [Online]. Available: http://dx.doi.org/10.2514/3.45520

[96] M. R. Mendenhall and D. J. Lesieutre, *Prediction of subsonic vortex shedding from forebodies with chines*. Washington, D.C.: NASA Contractor Report 4323, 1980.

[97] C. E. Brown and W. H. Michael, *On slender delta wings with leading edge separation*. Washington, D.C.: NACA Technical Note 3430, 1955.

[98] A. E. Bryson, "Symmetric vortex separation on circular cylinders and cones," *Journal of Applied Mechanics*, vol. 26, pp. 643–648, 1959.

[99] M. J. Hemsch, J. N. Nielsen, C. A. Smith, and S. C. Perkins, "Component aerodynamic characteristics of banked cruciform missiles with arbitrary control deflections," in 4^{th} *AIAA Atmospheric Flight Mechanics Conference*, Hollywood, FL, 8–10 Aug. 1977, AIAA 77-1153. [Online]. Available: http://dx.doi.org/10.2514/6.1977-1153

[100] H. Ashley and M. Landahl, *Aerodynamics of Wings and Bodies*. New York: Dover Publications, 1965.

[101] W. C. Pitts, J. N. Nielsen, and G. E. Kaattari, *Lift and center of pressure of wing-body-tail combinations at subsonic, transonic, and supersonic speeds*. Washington, D.C.: NACA Report 1307, 1957.

[102] M. Blair, "A compilation of the mathematics leading to th doublet lattice method," Air Force Wright Laboratory, WPAFB, OH, WL-TR-92-3028, 1992.

[103] H. Ashley and G. Zartarian, "Piston theory – a new aerodynamic tool for the aeroelastician," *Journal of the Aeronautical Sciences*, vol. 23, no. 12, pp. 1109–1118, 1956. [Online]. Available: http://dx.doi.org/10.2514/8.3740

[104] M. D. Van Dyke, *A study of second-order supersonic flow theory*. Washington, D.C.: NACA Report 1081, 1952.

[105] A. E. Donov, *A flat wing with sharp edges in a supersonic stream*. Washington, D.C.: NACA TM-1394, 1956.

[106] "Lift-curve slope of wing-body combinations," ESDU, ESDU 91007D, 1995.

[107] "Computer program for the calculation of normal force and pitching moment of forebody-cylinder combinations at angles of attack up to 90 degrees and Mach numbers up to 5, including the effects of conical boat-tailing," ESDU, ESDU 90034C, 2004.

[108] D. J. Lesieutre, J. F. Love, M. F. E. Dillenius, and A. B. Blair, "Recent applications and improvements to the engineering-level aerodynamic prediction software MISL3," in 40^{th} *AIAA Aerospace Sciences Meeting & Exhibit*, Reno, NV, 14–17 Jan. 2002, AIAA 2002-0275. [Online]. Available: http://dx.doi.org/10.2514/6.2002-275

[109] D. J. Lesieutre, J. F. Love, and M. F. E. Dillenius, "Prediction of the nonlinear aerodynamic characteristics of tandem-control and rolling-tail missiles," in *AIAA Atmospheric Flight Conference*, Monterey, CA, 5–8 Aug. 2002, AIAA 2002-4511. [Online]. Available: http://dx.doi.org/10.2514/6.2002-4511

[110] P. Denis, "Le code de prevision aerodynamique de l'ONERA: MISSILE," in *RTO AVT Symposium on "Missile Aerodynamics"*, Sorrento, Italy, 11–14 May 1998.

[111] H. J. Allen and E. W. Perkins, *Characteristics of flow over inclined bodies of revolution*. Washington, D.C.: NACA Research Memorandum A50L07, 1951.

[112] H. Jorgensen, *Prediction of static aerodynamic characteristics for space-shuttle-like and other bodies at angles of attack from* 0° *to* 180°. Washington, D.C.: NASA Technical Note D-6996, 1973.

[113] H. Jorgensen, *Prediction of static aerodynamic characteristics for slender bodies alone and with lifting surfaces to very high angles of attack*. Washington, D.C.: NASA Technical Report R-474, 1977.

[114] A. K. Sreekanth, *Aeropredictive Methods and Their Validation in Hypersonic Flows*. Dehli, India: Defense Research and Development Organization, Ministry of Defense of India, 2003.

[115] E. C. Yates and R. M. Bennett, "Analysis of supersonic-hypersonic flutter of lifting surfaces at angle of attack," *Journal of Aircraft*, vol. 9, no. 7, pp. 481–489, 1972. [Online]. Available: http://dx.doi.org/10.2514/3.59019

[116] M.-C. Meijer and L. Dala, "Quantifying non-linearity in planar supersonic potential flows," *The Aeronautical Journal*, vol. 121, no. 1237, pp. 372–394, 2017. [Online]. Available: http://dx.doi.org/10.1017/aer.2016.141

[117] H. J. Allen, *Estimation of the forces and moments acting on an inclined body of revolution of high fineness ratio*. Washington, D.C.: NACA Research Memorandum A9I26, 1949.

[118] A. R. Ortell, "Supersonic and hypersonic lift of highly swept wings and wing-body combinations," *Journal of Aircraft*, vol. 4, no. 1, pp. 78–79, 1967. [Online]. Available: http://dx.doi.org/10.2514/3.43800

[119] K. A. Fellows and E. C. Carter, *Results and analysis of pressure measurements on two isolated slender wings and slender wing-body combinations at supersonic speeds: Part 1 – analysis*. London, United Kingdom: Aeronautical Research Council CP-1131, 1970.

[120] M. J. Hemsch and J. N. Nielsen, "Extension of equivalent angle-of-attack method for nonlinear flowfields," *Journal of Spacecraft and Rockets*, vol. 22, no. 3, pp. 304–308, 1985. [Online]. Available: http://dx.doi.org/10.2514/3.25748

[121] M.-C. Meijer and L. Dala, "On the validity range of piston theory," in 16^{th} *International Forum on Aeroelasticity and Structural Dynamics*, St. Petersburg, Russia, 28 Jun.–2 Jul. 2015, IFASD-2015-004.

[122] M.-C. Meijer, "Aeroelastic prediction methods in supersonic flows for missile design," Master's thesis, University of the Witwatersrand, Johannesburg, South Africa, 2014.

[123] M.-C. Meijer and L. Dala, "On the role of higher-order terms in local piston theory," *Journal of Aircraft*, 2018, published Online 13 Sept 2018. [Online]. Available: http://dx.doi.org/10.2514/1.C034920

[124] W. P. Rodden, E. F. Farkas, H. Malcom, and A. M. Kliszewski, "Aerodynamic influence coefficients from piston theory: Analytical development and computational procedure," Aerospace Corp., El Segundo, CA, TDR-169 (3230-11) TN-2, 1962.

[125] D. D. Liu, Z. X. Yao, D. Sarhaddi, and F. Chavez, "From piston theory to a unified hypersonic-supersonic lifting surface method," *Journal of Aircraft*, vol. 34, no. 3, pp. 304–312, 1997. [Online]. Available: http://dx.doi.org/10.2514/2.2199

[126] F. A. Goldsworthy, "Two-dimensional rotational flow at high mach numbers past thin aerofoils," *Quarterly Journal of Mechanics and Applied Mathematics*, vol. 5, no. 1, pp. 54–63, 1952. [Online]. Available: http://dx.doi.org/10.1093/qjmam/5.1.54

[127] G. A. Bird, "Some remarks on the foundations of piston theory and supersonic-hypersonic similarity," *Journal of the Aerospace Sciences*, vol. 25, no. 2, pp. 138–139, 1958. [Online]. Available: http://dx.doi.org/10.2514/8.7538

[128] M. T. Landahl, "Unsteady flow around thin wings at high mach numbers," *Journal of the Aeronautical Sciences*, vol. 24, no. 1, pp. 33–38, 1957. [Online]. Available: http://dx.doi.org/10.2514/8.3761

[129] E. H. Dowell, "Far-field predicted by piston theory," *AIAA Journal*, vol. 54, no. 1, pp. 364–366, 2016. [Online]. Available: http://dx.doi.org/10.2514/1.J054460

[130] M. D. Van Dyke, "The combined supersonic-hypersonic similarity rule," *Journal of the Aeronautical Sciences*, vol. 18, no. 7, pp. 499–500, 1951. [Online]. Available: http://dx.doi.org/10.2514/8.2012

[131] H. G. Morgan, H. L. Runyan, and V. Huckel, "Theoretical considerations of flutter at high Mach numbers," *Journal of the Aerospace Sciences*, vol. 25, no. 6, pp. 371–381, 1958. [Online]. Available: http://dx.doi.org/10.2514/8.7688

[132] A. Busemann, "Aerodynamischer auftrieb bei überschallgeschwindigkeit," *Luftfahrt-forschung*, vol. 12, p. 210, 1935.

[133] R. D. Linnell, "Two-dimensional airfoils in hypersonic flow," *Journal of the Aeronautical Sciences*, vol. 16, no. 1, pp. 22–30, 1949. [Online]. Available: http://dx.doi.org/10.2514/8.11718

[134] E. Carafoli, *High-Speed Aerodynamics*. Bucharest, Romania: Editura Technica, 1968.

[135] A. Kahane and L. Lees, "The flow at the rear of a two-dimensional supersonic airfoil," *Journal of the Aeronautical Sciences*, vol. 15, no. 3, pp. 167–170, 1948. [Online]. Available: http://dx.doi.org/10.2514/8.11535

[136] W. P. Jones, *The influence of thickness / chord ratio on supersonic derivatives for oscillating aerofoils*. London, United Kingdom: Aeronautical Research Council R. & M. 2679, 1954.

[137] E. V. Laitone, "Exact and approximate solutions of two-dimensional oblique shock flow," *Journal of the Aeronautical Sciences*, vol. 14, no. 1, pp. 25–41, 1947. [Online]. Available: http://dx.doi.org/10.2514/8.1250

[138] J. W. Miles, "Unsteady flow at hypersonic speeds," in *Hypersonic Flow*, A. R. Collar and J. Tinkler, Eds. London, United Kingdom: Butterworths, 1960, pp. 185–197.

[139] K. Ghosh and B. K. Mistry, "Large incidence hypersonic similitude and oscillating nonplanar wedges," *AIAA Journal*, vol. 18, no. 8, pp. 1004–1006, 1980. [Online]. Available: http://dx.doi.org/10.2514/3.7702

[140] K. Ghosh, "Hypersonic large-deflection similitude for quasi-wedges and quasi-cones," *The Aeronautical Journal*, vol. 88, no. 873, pp. 70–76, 1984. [Online]. Available: http://dx.doi.org/10.1017/S0001924000020236

[141] K. Ghosh, "Hypersonic large-deflection similitude for oscillating delta wings," *The Aeronautical Journal*, vol. 88, no. 878, pp. 357–361, 1984. [Online]. Available: http://dx.doi.org/10.1017/S0001924000020868

[142] K. Ghosh, "Unified supersonic/hypersonic similitude for oscillating wedges and plane ogives," *AIAA Journal*, vol. 24, no. 7, pp. 1205–1207, 1986. [Online]. Available: http://dx.doi.org/10.2514/3.9419

[143] J. L. Raymond, "Piston theory applied to strong shocks and unsteady flow," *Journal of Fluid Mechanics*, vol. 8, no. 4, pp. 509–513, 1960. [Online]. Available: http://dx.doi.org/10.1017/S0022112060000761

[144] E. H. Dowell and D. B. Bliss, "New look at unsteady supersonic potential flow aerodynamics and piston theory," *AIAA Journal*, vol. 51, no. 9, pp. 2278–2281, 2013. [Online]. Available: http://dx.doi.org/10.2514/1.J052088

[145] D. Aravinth, P. Shinde, A. Misra, M. M. Sucheendran, and H. F. Ganji, "Dynamic aeroelasticity of a trapezoidal wing using enhanced piston theory," in 2018 *AIAA/ASCE/AHS/ASC Structures, Structural Dynamics, and Materials Conference, AIAA SciTech Forum*, Kissimmee, FL, 8–12 Jan. 2018, AIAA 2018-1443. [Online]. Available: http://dx.doi.org/10.2514/6.2018-1443

[146] S. C. McIntosh, "Hypersonic flow over an oscillating wedge," *AIAA Journal*, vol. 3, no. 3, pp. 433–440, 1965. [Online]. Available: http://dx.doi.org/10.2514/3.2883

[147] I. Chueshov, E. H. Dowell, I. Lasiecka, and J. T. Webster, "Mathematical aeroelasticity: a survey," *Mathematics in Engineering, Science, and Aerospace*, vol. 7, no. 1, pp. 5–29, 2015. [Online]. Available: https://arxiv.org/pdf/1512.07292

[148] V. V. Vedeneev, "Flutter of a wide strip plate in a supersonic flow," *Fluid Dynamics*, vol. 40, no. 5, pp. 805–817, 2005. [Online]. Available: http://dx.doi.org/10.1007/s10697-005-0118-0

[149] V. V. Vedeneev, "High frequency plate flutter," *Fluid Dynamics*, vol. 41, no. 2, pp. 313–321, 2006. [Online]. Available: http://dx.doi.org/10.1007/s10697-006-0046-7

[150] V. V. Vedeneev, "High frequency flutter of a rectangular plate," *Fluid Dynamics*, vol. 41, no. 4, pp. 641–648, 2006. [Online]. Available: http://dx.doi.org/10.1007/s10697-006-0083-2

[151] V. V. Vedeneev, "Numerical investigation of supersonic plate flutter using the exact aerodynamic theory," *Fluid Dynamics*, vol. 44, no. 2, pp. 314–321, 2009. [Online]. Available: http://dx.doi.org/10.1134/S001546280902015X

[152] V. V. Vedeneev, "Panel flutter at low supersonic speeds," *Journal of Fluids and Structures*, vol. 29, pp. 79–96, 2012. [Online]. Available: http://dx.doi.org/10.1016/j.jfluidstructs.2011.12.011

[153] V. V. Vedeneev, "Single-mode plate flutter taking the boundary layer into account," *Fluid Dynamics*, vol. 47, no. 3, pp. 417–429, 2012. [Online]. Available: http://dx.doi.org/10.1134/S0015462812030167

[154] V. V. Vedeneev, "Coupled-mode flutter of an elastic plate in a gas flow with a boundary layer," *Proceedings of the Steklov Institute of Mathematics*, vol. 281, no. 1, pp. 140–152, 2013. [Online]. Available: http://dx.doi.org/10.1134/S0081543813040123

[155] V. V. Vedeneev, "Coupled-mode flutter of an elastic plate in a gas flow with a boundary layer," *Journal of Fluid Mechanics*, vol. 736, no. 1, pp. 216–249, 2013. [Online]. Available: http://dx.doi.org/10.1017/jfm.2013.522

[156] V. O. Bondarev and V. V. Vedeneec, "Influence of the boundary layer on flutter of elastic plate in supersonic gas flow," in 16^{th} *International Forum on Aeroelasticity and Structural Dynamics*, St. Petersburg, Russia, 28 Jun.–2 Jul. 2015, IFASD-2015-168.

[157] V. V. Vedeneev, "On the application of the asymptotic method of global instability in aeroelasticity problems," *Proceedings of the Steklov Institute of Mathematics*, vol. 295, no. 1, pp. 274–301, 2016. [Online]. Available: http://dx.doi.org/10.1134/S0081543816080174

[158] S. Shitov and V. V. Vedeneev, "Flutter of rectangular simply supported plates at low supersonic speeds," *Journal of Fluids and Structures*, vol. 69, pp. 154–173, 2017. [Online]. Available: http://dx.doi.org/10.1016/j.jfluidstructs.2016.11.014

[159] I. E. Garrick and S. I. Rubinow, *Flutter and oscillating air-force calculations for an airfoil in a two-dimensional supersonic flow*. Washington, D.C.: NACA Report 1158, 1946.

[160] E. H. Dowell and H. F. Ganji, "Investigation of higher order effects in linear piston theory," *Mathematics in Engineering, Science, and Aerospace*, vol. 7, no. 1, pp. 1–12, 2015. [Online]. Available: https://www.researchgate.net/publication/301200993

[161] J. Dugundji, "Theoretical considerations of panel flutter at high supersonic Mach numbers," *AIAA Journal*, vol. 4, no. 7, pp. 1257–1266, 1966. [Online]. Available: http://dx.doi.org/10.2514/3.3657

[162] E. H. Dowell and H. M. Voss, "Theoretical and experimental panel flutter studies in the Mach number range 1.0 to 5.0," *AIAA Journal*, vol. 3, no. 12, pp. 2292–2304, 1965. [Online]. Available: http://dx.doi.org/10.2514/3.3359

[163] Y. C. Fung, "On two-dimensional panel flutter," *Journal of the Aeronautical Sciences*, vol. 25, no. 3, pp. 145–160, 1958. [Online]. Available: http://dx.doi.org/10.2514/8.7557

[164] E. H. Dowell, "Panel flutter – a review of the aeroelastic stability of plates and shells," *AIAA Journal*, vol. 8, no. 3, pp. 385–399, 1970. [Online]. Available: http://dx.doi.org/10.2514/3.5680

[165] S. D. Algazin and I. A. Kiiko, *Flutter of plates and shells*. Moscow, Russia: Nauka, 2006, [In Russian].

[166] L. Lees and C. C. Lin, *Investigation of the stability of the laminar boundary layer in a compressible fluid*. Washington, D.C.: NACA Report 1115, 1946.

[167] R. Clark, D. Cox, H. C. Curtiss, J. W. Edwards, K. C. Hall, D. A. Peters, R. Scanlan, E. Simiu, F. Sisto, and T. W. Strganac, *Investigation of the stability of the laminar boundary layer in a compressible fluid*, 4th ed., E. H. Dowell, Ed. New York, N.Y.: Kluwer Academic Publishers, 2004.

[168] R. W. Leonard and J. M. Hedgepeth, *On panel flutter and divergence of infinitely long unstiffened and ring-stiffened thin-walled circular cylinders*. Washington, D.C.: NACA Report 1302, 1957.

[169] H. Krumhaar, "The accuracy of linear piston theory when applied to cylindrical shells," *AIAA Journal*, vol. 1, no. 6, pp. 1448–1449, 1963. [Online]. Available: http://dx.doi.org/10.2514/3.1832

[170] H. Krumhaar, "The accuracy of applying linear piston theory to cylindrical shells," GALCIT, Pasadena, CA, SM 62-50, 1963.

[171] D. D. Liu and W. H. Hui, "Oscillating delta wings with attached shock waves," *AIAA Journal*, vol. 15, no. 6, pp. 804–812, 1977. [Online]. Available: http://dx.doi.org/10.2514/3.7371

[172] J. S. Chen, "The application of the two dimensional unsteady Euler equations perturbation solutions on the supersonic rectangular wings," *Acta Aerodynamica Sinica*, vol. 7, no. 1, pp. 102–107, 1989, [In Chinese].

[173] X. X. Wang, "A new method for calculating supersonic unsteady aerodynamic forces and its application," *Acta Aeronautica et Astronautica Sinica*, vol. 4, no. 3, pp. 9–18, 1983, [In Chinese]. [Online]. Available: http://hkxb.buaa.edu.cn/EN/Y1983/V4/I3/9

[174] J. S. Chen, "Pitching derivatives of wing in supersonic and hypersonic stream — method for local flow piston theory," *Acta Aerodynamica Sinica*, vol. 9, no. 4, pp. 469–476, 1991, [In Chinese].

[175] B. Y. Yang and W. L. Song, "Supersonic flutter calculation of a wing with attack angle by local flow piston theory," *Journal of Vibration and Shock*, vol. 14, no. 2, pp. 60–63, 1995, [In Chinese]. [Online]. Available: http://dx.doi.org/10.13465/j.cnki.jvs.1995.02.013

[176] H. F. Ganji and E. H. Dowell, "Investigation of higher order effects in linear piston theory," *Mathematics in Engineering, Science and Aerospace*, vol. 7, no. 1, pp. 1–2, 2016.

[177] W. H. Hui, "Stability of oscillating wedges and caret wings in hypersonic and supersonic flows," *AIAA Journal*, vol. 7, no. 8, pp. 1524–1530, 1969. [Online]. Available: http://dx.doi.org/10.2514/3.5426

[178] W. H. Hui, "Interaction of a strong shock with mach waves in unsteady flow," *AIAA Journal*, vol. 7, no. 8, pp. 1605–1607, 1969. [Online]. Available: http://dx.doi.org/10.2514/3.5441

[179] F. R. Chavez and D. D. Liu, "Unsteady unified hypersonic / supersonic method for aeroelastic applications including wave / shock interaction," *AIAA Journal*, vol. 33, no. 6, pp. 1090–1097, 1995. [Online]. Available: http://dx.doi.org/10.2514/3.1237

[180] J. S. Chen and J. Cao, "An approximate calculating method of supersonic / hypersonic unsteady aerodynamic forces of airfoils," *Acta Aerodynamica Sinica*, vol. 8, no. 3, pp. 339–344, 1990, [In Chinese].

[181] W. H. Hui, "Unified unsteady supersonic / hypersonic theory of flow past double wedge airfoils," *Journal of Applied Mathematics and Physics*, vol. 34, no. 4, pp. 458–488, 1983. [Online]. Available: http://dx.doi.org/10.1007/BF00944709

[182] J. P. Appleton, "Aerodynamic pitching derivatives of a wedge in hypersonic flow," *AIAA Journal*, vol. 2, no. 11, pp. 2034–2036, 1964. [Online]. Available: http://dx.doi.org/10.2514/3.2729

[183] K. J. Orlik-Rückemann, "Stability derivatives of sharp wedges in viscous hypersonic flow," *AIAA Journal*, vol. 4, no. 6, pp. 1001–1007, 1966. [Online]. Available: http://dx.doi.org/10.2514/3.3594

[184] K. J. Orlik-Rückemann, "Effect of wave reflections on the unsteady hypersonic flow over a wedge," *AIAA Journal*, vol. 4, no. 10, pp. 1884–1886, 1966. [Online]. Available: http://dx.doi.org/10.2514/3.3813

[185] W. H. Hui and J. Hamilton, "Higher-order solutions for unsteady hypersonic and supersonic flow," *The Aeronautical Quarterly*, vol. 25, no. 1, pp. 59–68, 1974. [Online]. Available: http://dx.doi.org/10.1017/S0001925900006806

[186] J. A. Bailie and J. E. McFeely, "Panel flutter in hypersonic flow," *AIAA Journal*, vol. 6, no. 2, pp. 332–337, 1968. [Online]. Available: http://dx.doi.org/10.2514/3.4498

[187] H. M. Yang and J. S. Chen, "Pitching oscillating derivatives of wedges in supersonic and hypersonic," *Acta Aerodynamica Sinica*, vol. 4, no. 4, pp. 440–444, 1986, [In Chinese].

[188] L. E. Ericsson, "Viscous and elastic perturbation effects on hypersonic unsteady airfoil aerodynamics," *AIAA Journal*, vol. 15, no. 10, pp. 1481–1490, 1977. [Online]. Available: http://dx.doi.org/10.2514/3.60814

[189] W. H. Hui and R. A. East, "Stability derivatives of sharp wedges in viscous hypersonic flow," *The Aeronautical Quarterly*, vol. 22, no. 2, pp. 127–145, 1971. [Online]. Available: http://dx.doi.org/10.1017/S0001925900005710

[190] J. P. Hunter, "An efficient method for time-marching supersonic flutter predictions using cfd," Master's thesis, Oklahoma State University, Stillwater, OK, 1994.

[191] J. P. Hunter and A. S. Arena, "An efficient method for time-marching supersonic flutter predictions using CFD," in 35^{th} *AIAA Aerospace Sciences Meeting and Exhibit*, Reno, NV, 6–9 Jan. 2018, AIAA 1997-0733. [Online]. Available: http://dx.doi.org/10.2514/6.1997-733

[192] W. W. Zhang and Z. Y. Ye, "Numerical method of aeroelasticity based on local flow piston theory," *Chinese Journal of Theoretical and Applied Mechanics*, vol. 37, no. 5, pp. 632–639, 2005, [In Chinese].

[193] Z. Yang, J. Zhou, and Y. Gu, "Integrated analysis on static / dynamic aeroelasticity of curved panels based on a modified local piston theory," *Journal of Sound and Vibration*, vol. 333, no. 22, pp. 5885–5897, 2014. [Online]. Available: http://dx.doi.org/10.1016/j.jsv.2014.06.035

[194] A. Gogulapati, R. Deshmukh, A. R. Crowell, J. J. McNamara, V. Vyas, X. Q. Wang, M. Mignolet, T. Beberniss, S. M. Spottswood, and T. G. Eason, "Response of a panel to shock impingement: Modeling and comparison with experiments," in 55^{th} *AIAA/ASME/ASCE/AHS/ASC Structures, Structural Dynamics, and Materials Conference, AIAA SciTech Forum*, National Harbor, ML, 13–17 Jan. 2014, AIAA 2014-0148. [Online]. Available: http://dx.doi.org/10.2514/6.2014-0148

[195] A. Gogulapati, R. Deshmukh, J. J. McNamara, V. Vyas, X. Q. Wang, M. Mignolet, T. Beberniss, S. M. Spottswood, and T. G. Eason, "Response of a panel to shock impingement: Modeling and comparison with experiments – part 2," in 56^{th} *AIAA/ASCE/AHS/ASC Structures, Structural Dynamics, and Materials Conference, AIAA SciTech Forum*, Kissimmee, FL, 5–9 Jan. 2015, AIAA 2015-0685. [Online]. Available: http://dx.doi.org/10.2514/6.2015-0685

[196] M.-C. Meijer, "Piston theory applied to wing-body configurations: A review of the mathematical basis," in *Research and Education in Aircraft Design* 2016, Warsaw, Poland, 12–14 Sep. 2016.

[197] C. C. Lin, E. Reissner, and H. S. Tsien, "On two-dimensional non-steady motion of a slender body in a compressible flow," *Journal of Mathematics and Physics*, vol. 27, no. 4, pp. 220–231, 1948. [Online]. Available: http://dx.doi.org/10.1002/sapm1948271220

[198] E. H. Dowell, "Transonic unsteady potential flow: scaling analysis of linear and nonlinear dynamics," *AIAA Journal*, vol. 48, no. 5, pp. 1017–1019, 2010. [Online]. Available: http://dx.doi.org/10.2514/1.40426

[199] E. H. Dowell and J. W. Jaworski, "Tutorial on scaling analysis of Navier-Stokes equations: linear and non-linear dynamics of fluid-structure-interaction," *ASD Journal*, vol. 2, no. 2, pp. 79–84, 2011. [Online]. Available: http://dx.doi.org/10.3293/asdj.2011.15

[200] J. W. Jaworski and E. H. Dowell, "Scaling analysis for aeroelastic phenomena using the Navier-Stokes fluid model," *AIAA Journal*, vol. 50, no. 11, pp. 2622–2626, 2012. [Online]. Available: http://dx.doi.org/10.2514/1.J051727

[201] M. D. Van Dyke, "Growing up with asymptotics," in *Asymptotic Modelling in Fluid Mechanics*, ser. Lecture Notes in Physics, vol. 422, P. A. Bois, E. Dériat, R. Gatignol, and A. Rigolot, Eds. Paris, France: Springer, 20–22 Apr. 1994.

[202] P. A. Lagerstrom and R. G. Casten, "Basic concepts underlying singular perturbation techniques," *SIAM Review*, vol. 14, no. 1, pp. 63–120, 1972. [Online]. Available: http://dx.doi.org/10.1137/1014002

[203] R. Ram and R. S. Mishra, "Determination of vorticity, gradients of flow parameters and curvature of streamlines behind unsteady curved shock waves," *Rendiconti del Circolo Matematico di Palermo*, vol. 15, no. 3, pp. 365–379, 1966. [Online]. Available: http://dx.doi.org/10.1007/BF02844112

[204] R. P. Kanwal, "Determination of vorticity and the gradients of flow parameters behind a three-dimensional unsteady curved shock wave," *Archive for Rational Mechanics and Analysis*, vol. 1, no. 1, pp. 225–232, 1957. [Online]. Available: http://dx.doi.org/10.1007/BF00298006

[205] J. C. Pant, "Some aspects of unsteady curved shock waves," *International Journal of Engineering Science*, vol. 7, no. 2, pp. 235–245, 1969. [Online]. Available: http://dx.doi.org/10.1016/0020-7225(69)90059-7

[206] T. Y. Thomas, "Extended compatibility conditions for the study of surfaces of discontinuity in continuum mechanics," *Journal of Mathematics and Mechanics*, vol. 6, no. 3, pp. 311–322, 1957. [Online]. Available: https://www.jstor.org/stable/24900467

[207] T. W. Ting, "Note on the normal deformation of a surface," *The American Mathematical Monthly*, vol. 67, no. 10, pp. 994–997, 1960. [Online]. Available: http://dx.doi.org/10.2307/2309229

[208] A. H. Taub, "Determination of flows behind stationary and pseudo-stationary shocks," *Annals of Mathematics*, vol. 62, no. 2, pp. 300–325, 1955. [Online]. Available: http://dx.doi.org/10.2307/1969684

[209] S. Mölder, "Curved shock theory," *Shock Waves*, vol. 26, no. 4, pp. 337–353, 2016. [Online]. Available: http://dx.doi.org/10.1007/s00193-015-0589-9

[210] W. D. Hayes, "The vorticity jump across a gas dynamic discontinuity," *Journal of Fluid Mechanics*, vol. 2, no. 6, pp. 595–600, 1957. [Online]. Available: http://dx.doi.org/10.1017/S0022112057000403

[211] G. Lin, C. H. Su, and G. E. Karniadakis, "The stochastic piston problem," *Proceedings of the National Academy of Sciences*, vol. 101, no. 45, pp. 15 840–15 845, 2004. [Online]. Available: http://dx.doi.org/10.1073/pnas.0405889101

[212] M.-C. Meijer and L. Dala, "Local piston theory as an alternative to mesh deformation: slender wing/body configurations," *Journal of Aircraft*, vol. 55, no. 4, pp. 1709–1719, 2018. [Online]. Available: http://dx.doi.org/10.2514/1.C034697

[213] J. A. Heyns and O. F. Oxtoby, "Modelling external high-speed aerodynamics," in *5th OpenFOAM User Conference*, Weisbaden, Germany, 17–19 Oct. 2017.

[214] P. J. Roache, "Perspective: a method for uniform reporting of grid refinement studies," *Journal of Fluids Engineering*, vol. 116, no. 3, pp. 405–413, 1994. [Online]. Available: http://dx.doi.org/10.1115/1.2910291

Appendix A

Scaling Analysis of the Perturbed Euler and Rankine-Hugoniot Equations

A.1 Un-Perturbed Solution

It is assumed that all un-perturbed quantities are known a-priori. In particular:

- The orientations and velocities of un-perturbed surfaces are known,
- The un-perturbed flow quantities are known.

The purpose of the present section is to parametrically quantify un-perturbed terms appearing in the governing equations and boundary conditions. The final purpose of this is to quantify the terms listed in Table 4.5.

Inspection of:

- The Euler equations in Eqs. (4.97) to (4.99),
- The shock boundary conditions in Eqs. (4.111) to (4.113),
- The body boundary conditions in Eq. (4.123),

shows that the only surface-associated direction vector of consequence in the equations of interest is the surface-normal vector $\bar{\hat{\mathbf{n}}}$. The other chief direction vector of interest is that of the flow velocity $\bar{\hat{\mathbf{V}}}$. These vectors and their projection onto each other $\bar{\hat{\mathbf{V}}} \cdot \bar{\hat{\mathbf{n}}}$ are important quantities of interest. Other flow quantities are grouped below according to region:

- Pre-shock fluid state and velocity:
  - $\bar{\rho}_{(U)}$, $\bar{p}_{(U)}$, $\bar{a}_{(U)}$, and $\bar{\mathbf{V}}_{(U)}$,

- Shock-related quantities:
  - $\bar{\mathbf{V}}_{\mathbf{s}}$ and $\bar{w}_{(U)}$ (with associated $\bar{m}_{\perp}$ and $\bar{\sigma}$),
- Post-shock fluid state and velocity:
  - $\bar{\rho}$, $\bar{p}$, $\bar{a}$, and $\bar{\mathbf{V}}$,
- Surface-related quantities:
  - $\bar{\mathbf{V}}_{\mathbf{b}}$.

It is repeated here that the post-shock fluid state and velocity are only prescribed at the shock surface. The quantities further downstream must be determined by solution of the governing equations. The non-permeability condition at the body surface effectively reduces the number of free variables associated with the fluid velocity vector $\mathbf{V}$ from three ($|\mathbf{V}|$, α_v, and β_v) to two (by prescribing a relationship between α_v and β_v).

The development in the present section is grouped into terms relating to

- Geometric parameters and direction vectors,
- Post-shock quantities at the shock boundary,
- Velocity relations at the body surface.

A.1.1 Geometric Parameters and Direction Vectors

The unit normal-vector to the unperturbed surface has been defined in terms of angles in a spherical coordinate system with $\hat{\mathbf{e}}_{\mathbf{3}}$ acting as the zenith and $-\hat{\mathbf{e}}_{\mathbf{1}}$ acting as the reference direction for the azimuth. The equation for the un-perturbed normal vector is given as

$$\bar{\hat{\mathbf{n}}} = -\sin\bar{\eta}\cos\bar{\lambda}\,\hat{\mathbf{e}}_{\mathbf{1}} - \sin\bar{\eta}\sin\bar{\lambda}\,\hat{\mathbf{e}}_{\mathbf{2}} + \cos\bar{\eta}\,\hat{\mathbf{e}}_{\mathbf{3}}\,. \tag{A.1}$$

The following interpretations are offered:

- The polar angle η has been defined in Eq. (4.11). It may be interpreted as the "thickness angle" in the direction of steepest ascent in the planform plane. For a flat plate, $\eta = 0$. For swept wedge or a chamfered leading-edge of a wing, η is the wedge / chamfer angle normal to the leading-edge.

  The angle η is dimensionless (radians), and has the range $\eta = [0, \pi]$,

- The azimuthal angle λ has been defined in Eq. (4.12). It may be interpreted as the "sweep angle" of a wedge of thickness η. Inclination of the surface upstream is defined by $-\frac{\pi}{2} < \lambda < \frac{\pi}{2}$,

  The angle λ is dimensionless (radians), and has the range $\lambda = [-\pi, \pi]$,

- The component of the unit-normal vector in the $\hat{\mathbf{e}}_\mathbf{1}$ direction will typically be interpreted as "bluntness". From Eq. (A.1) it is seen that

$$\bar{n}_1 = -\sin\bar{\eta}\cos\bar{\lambda}\,. \tag{A.2}$$

  While η typically characterizes "thickness", the sweep of that thickness away from the chordwise direction by means of λ may result in a geometry which is locally "thin" to flow directed along $\hat{\mathbf{e}}_\mathbf{1}$.

  The vector component $\bar{n}_1$ is dimensionless, and has the range $\bar{n}_1 = [-1, 1]$,

- The component of the unit-normal vector in the $\hat{\mathbf{e}}_\mathbf{2}$ direction will typically be interpreted as a measure of "roll". From Eq. (A.1) it is seen that

$$\bar{n}_2 = -\sin\bar{\eta}\sin\bar{\lambda}\,. \tag{A.3}$$

  For a given sweep angle through λ, the magnitude of $\bar{n}_2$ will be determined by the "roll" through η.

  The vector component $\bar{n}_2$ is dimensionless, and has the range $\bar{n}_2 = [-1, 1]$,

- The component of the unit-normal vector in the $\hat{\mathbf{e}}_\mathbf{3}$ direction will typically be interpreted as a measure of "flatness". From Eq. (A.1) it is seen that

$$\bar{n}_3 = \cos\bar{\eta}\,. \tag{A.4}$$

  For a lifting surface with a planform in the $\hat{\mathbf{e}}_\mathbf{1}\hat{\mathbf{e}}_\mathbf{2}$ plane, a deviation from $\bar{n}_3 = 1$ represents some deviation from the planform plane.

  The vector component $\bar{n}_3$ is dimensionless, and has the range $\bar{n}_3 = [-1, 1]$.

A variety of useful formulations for the un-perturbed fluid-velocity vector may be adopted. Its most general form is

$$\bar{\mathbf{V}} = \left|\bar{\mathbf{V}}\right|\hat{\bar{\mathbf{V}}}\,, \tag{A.5}$$

where $\bar{\hat{\mathbf{V}}}$ is the direction vector of the un-perturbed velocity vector:

$$\bar{\hat{\mathbf{V}}} = \frac{\bar{v}_1}{|\bar{\mathbf{V}}|}\hat{\mathbf{e}}_\mathbf{1} + \frac{\bar{v}_2}{|\bar{\mathbf{V}}|}\hat{\mathbf{e}}_\mathbf{2} + \frac{\bar{v}_3}{|\bar{\mathbf{V}}|}\hat{\mathbf{e}}_\mathbf{3}\,. \tag{A.6}$$

The following definitions of the angle of attack α_v and the angle of side-slip β_v are introduced:

$$\sin\alpha_v \equiv \frac{v_3}{|\mathbf{V}|}\,, \tag{A.7}$$

$$\sin\beta_v \equiv -\frac{v_2}{|\mathbf{V}|}\,. \tag{A.8}$$

In terms of α_v and β_v, the direction vector for velocity may then be written as

$$\bar{\hat{\mathbf{V}}} = \left(1-\sin^2\bar{\alpha}_v - \sin^2\bar{\beta}_v\right)^{\frac{1}{2}}\hat{\mathbf{e}}_\mathbf{1} - \sin\bar{\beta}_v\,\hat{\mathbf{e}}_\mathbf{2} + \sin\bar{\alpha}_v\,\hat{\mathbf{e}}_\mathbf{3}\,. \tag{A.9}$$

The following interpretations are offered:

- The un-perturbed angle of attack $\bar{\alpha}_v$ has been defined as the angle by which the un-perturbed velocity vector $\bar{\mathbf{V}}$ deviates from the $\hat{\mathbf{e}}_\mathbf{1}\hat{\mathbf{e}}_\mathbf{2}$ plane.

  The angle $\bar{\alpha}_v$ is dimensionless (radians), and has the range $\bar{\alpha}_v = \left[-\frac{\pi}{2}, \frac{\pi}{2}\right]$,

- The un-perturbed angle of side-slip $\bar{\beta}_v$ has been defined as the angle by which the un-perturbed velocity vector $\bar{\mathbf{V}}$ deviates from the $\hat{\mathbf{e}}_\mathbf{1}\hat{\mathbf{e}}_\mathbf{3}$ plane for positive $\hat{\mathbf{e}}_\mathbf{1}$.

  The angle $\bar{\beta}_v$ is dimensionless (radians), and has the range $\bar{\beta}_v = [-\pi, \pi]$.

- The advantage of defining angles using resultant velocity, as above, as opposed to using v_1, is that the components of the velocity direction vector $\bar{\mathbf{V}}$ have the range $[-1, 1]$. In the case where they are defined using v_1, the components become unbounded in the limit of large angles.

The surface-normal velocity projection $\hat{\mathbf{V}}\cdot\hat{\mathbf{n}}$ is an important quantity in the shock relations and the body non-permeability condition. In its most general form, it may be written

$$\hat{\mathbf{V}}\cdot\hat{\mathbf{n}} = n_1\left(1-\sin^2\alpha_v - \sin^2\beta_v\right)^{\frac{1}{2}} - n_2\sin\beta_v + n_3\sin\alpha_v\,, \tag{A.10}$$

which may be adapted using Eqs. (A.2) to (A.4) and (A.9) to give

$$\bar{\hat{\mathbf{V}}}\cdot\bar{\hat{\mathbf{n}}} = -\sin\bar{\eta}\cos\bar{\lambda}\left(1-\sin^2\bar{\alpha}_v - \sin^2\bar{\beta}_v\right)^{\frac{1}{2}} + \sin\bar{\eta}\sin\bar{\lambda}\sin\bar{\beta}_v + \cos\bar{\eta}\sin\bar{\alpha}_v\,. \tag{A.11}$$

It is noted that $\bar{\hat{\mathbf{V}}}\cdot\bar{\hat{\mathbf{n}}}$ is dimensionless and has the range $[-1, 1]$.

Finally, it is remarked that the translational velocities of the shock $\bar{\mathbf{V}}_{\mathbf{s}}$ and of the body $\bar{\mathbf{V}}_{\mathbf{b}}$ only appear in the equations of interest through their projections onto their relevant surface normals. These velocities may therefore be described in terms of speeds along the surface normals:

$$\bar{G}_s = \bar{\mathbf{V}}_{\mathbf{s}} \cdot \bar{\hat{\mathbf{n}}}_{\mathbf{s}}\,, \tag{A.12}$$

$$\bar{G}_b = \bar{\mathbf{V}}_{\mathbf{b}} \cdot \bar{\hat{\mathbf{n}}}_{\mathbf{b}}\,. \tag{A.13}$$

A.1.2 Post-Shock Quantities at the Shock Boundary

The above relations allow $\bar{w}_{(U)}$ and the associated $\bar{m}_\perp$ and $\bar{\sigma}$ to be defined. These are important in defining the post-shock fluid quantities $\bar{\rho}$, $\bar{p}$, $\bar{a}$, and $\bar{\mathbf{V}}$. From Eqs. (A.11), (A.12) and (4.106) it follows immediately that

$$\bar{w}_{(U)} = \left|\bar{\mathbf{V}}_{(U)}\right| \left\{ \begin{array}{l} -\sin\bar{\eta}_s \cos\bar{\lambda}_s \left(1-\sin^2\bar{\alpha}_{v(U)} - \sin^2\bar{\beta}_{v(U)}\right)^{\frac{1}{2}} \\ +\sin\bar{\eta}_s \sin\bar{\lambda}_s \sin\bar{\beta}_{v(U)} + \cos\bar{\eta}_s \sin\bar{\alpha}_{v(U)} \end{array} \right\} - \bar{G}_s\,, \tag{A.14}$$

Substituting the above into Eq. (4.62) yields

$$\bar{m}_\perp^2 = \left[\bar{M}_{(U)} \left\{ \begin{array}{l} -\sin\bar{\eta}_s \cos\bar{\lambda}_s \left(1-\sin^2\bar{\alpha}_{v(U)} - \sin^2\bar{\beta}_{v(U)}\right)^{\frac{1}{2}} \\ +\sin\bar{\eta}_s \sin\bar{\lambda}_s \sin\bar{\beta}_{v(U)} + \cos\bar{\eta}_s \sin\bar{\alpha}_{v(U)} \end{array} \right\} - \frac{\bar{G}_s}{\bar{a}_{(U)}} \right]^{-2}, \tag{A.15}$$

which may be substituted into Eqs. (4.60) and (4.61), which are repeated below as

$$1+\bar{\sigma} = \frac{\gamma+1}{2\bar{m}_\perp^2 + (\gamma-1)}\,, \tag{A.16}$$

$$\frac{\bar{\sigma}}{1+\bar{\sigma}} = \frac{2}{\gamma+1}\left(1-\bar{m}_\perp^2\right). \tag{A.17}$$

The above may then be substituted into Eqs. (4.65) to (4.67) to give the post-shock fluid quantities at the shock boundary as

$$\frac{\bar{\rho}}{\bar{\rho}_{(U)}} = (1+\bar{\sigma})\,, \tag{A.18}$$

$$\frac{\bar{\mathbf{V}}}{\left|\bar{\mathbf{V}}_{(U)}\right|} = \bar{\hat{\mathbf{V}}}_{(U)} - \frac{\bar{\sigma}}{1+\bar{\sigma}} \frac{\bar{w}_{(U)}}{\left|\bar{\mathbf{V}}_{(U)}\right|} \bar{\hat{\mathbf{n}}}\,, \tag{A.19}$$

$$\frac{\bar{p}}{\bar{\rho}_{(U)}\left|\bar{\mathbf{V}}_{(U)}\right|^2} = \frac{1}{\gamma \bar{M}^2_{(U)}} + \frac{\bar{\sigma}}{1+\bar{\sigma}} \frac{\bar{w}^2_{(U)}}{\left|\bar{\mathbf{V}}_{(U)}\right|^2}. \tag{A.20}$$

It is noted the velocity vector may be expressed in terms of its components as

$$\frac{\bar{v}_1}{\left|\bar{\mathbf{V}}_{(U)}\right|} = \left(1 - \sin^2 \bar{\alpha}_{v(U)} - \sin^2 \bar{\beta}_{v(U)}\right)^{\frac{1}{2}} + \left(\frac{\bar{\sigma}}{1+\bar{\sigma}} \frac{\bar{w}_{(U)}}{\left|\bar{\mathbf{V}}_{(U)}\right|}\right) \sin \bar{\eta}_s \cos \bar{\lambda}_s, \tag{A.21}$$

$$\frac{\bar{v}_2}{\left|\bar{\mathbf{V}}_{(U)}\right|} = -\sin \bar{\beta}_{v(U)} + \left(\frac{\bar{\sigma}}{1+\bar{\sigma}} \frac{\bar{w}_{(U)}}{\left|\bar{\mathbf{V}}_{(U)}\right|}\right) \sin \bar{\eta}_s \sin \bar{\lambda}_s, \tag{A.22}$$

$$\frac{\bar{v}_3}{\left|\bar{\mathbf{V}}_{(U)}\right|} = \sin \bar{\alpha}_{v(U)} - \left(\frac{\bar{\sigma}}{1+\bar{\sigma}} \frac{\bar{w}_{(U)}}{\left|\bar{\mathbf{V}}_{(U)}\right|}\right) \cos \bar{\eta}_s. \tag{A.23}$$

Finally, it is noted that using the ideal gas equation of state, Eqs. (A.18) and (A.20) may be manipulated to give

$$\frac{\bar{a}^2}{\bar{w}^2_{(U)}} = \left[\frac{2\gamma}{\gamma+1} - \left(\frac{\gamma-1}{\gamma+1}\right)\bar{m}^2_{\perp}\right](1+\bar{\sigma})^{-1}, \tag{A.24}$$

where $\frac{\bar{a}^2}{\bar{w}^2_{(U)}}$ is dimensionless and has the range $\left[1, \frac{2\gamma(\gamma-1)}{(\gamma+1)^2}\right]$ corresponding to the Mach-wave and hypersonic limits, respectively.

A.1.3 Velocity Relations at the Body Surface

The non-permeability condition at the body surface forces the fluid-velocity vector to be tangent to the surface. The fluid-velocity vector could thus be expressed in terms a rotation of the unit surface-tangent vectors $\bar{\hat{\mathbf{t}}}$ and $\bar{\hat{\mathbf{b}}}$ about $\bar{\hat{\mathbf{n}}}$ (see Eq. (4.9)). However, the introduction of further parameters will be avoided here. Instead, it is merely noted that the body boundary condition of Eq. (4.69) prescribes a relationship between allowable combinations of the angles α_v and β_v in terms of which the fluid-velocity vector has already been described. Recalling the relations in Eqs. (A.11) and (A.13), the following velocity relations are prescribed at the body surface:

$$-\sin \bar{\eta} \cos \bar{\lambda} \left(1 - \sin^2 \bar{\alpha}_v - \sin^2 \bar{\beta}_v\right)^{\frac{1}{2}} + \sin \bar{\eta} \sin \bar{\lambda} \sin \bar{\beta}_v + \cos \bar{\eta} \sin \bar{\alpha}_v = \frac{\bar{G}_b}{\left|\bar{\mathbf{V}}\right|} \tag{A.25}$$

A.2 Representative Cases

A.2.1 Vectors

As noted in Section 4.4.2, it will be assumed that $\hat{\mathbf{e}}_1$ is aligned with the body axis or the chordwise direction, and that the planform of lifting surfaces lies in the $\hat{\mathbf{e}}_1\hat{\mathbf{e}}_2$ plane.

Representative values for the body-surface may be obtained by considering a flat plate (zero thickness) and by considering a swept wedge (which may represent a chamfered leading-edge):

- For a flat plate: $\bar{\eta} = 0$, leading to $\bar{\hat{\mathbf{n}}} = \hat{\mathbf{e}}_3$,
- For a wedge with a leading-edge normal thickness angle of $\bar{\eta}$ and a sweepback angle of $\bar{\lambda}$: $\bar{\hat{\mathbf{n}}}$ is given by Eq. (A.1).

Representative values for the shock-surface will be described for an un-swept ($\lambda = 0$) wedge with thickness angle δ, with the freestream directed along $\hat{\mathbf{e}}_1$. The extension to a swept shock surface is accomplished through the introduction of $\lambda \neq 0$:

- In the limit of a vanishingly weak shock (a Mach wave): $\delta = 0$ and the wave angle is given by the Mach angle μ, where $\mu = \sin^{-1}\left(\frac{1}{M_\infty}\right)$. This leads to $\bar{\eta} = \mu$, with $\sin\bar{\eta} = \frac{1}{M_\infty}$ and $\cos\bar{\eta} = \frac{\sqrt{M_\infty^2-1}}{M_\infty}$, or in terms of components:

$$\bar{n}_1 = -\frac{1}{M_\infty}\,, \tag{A.26}$$

$$\bar{n}_2 = 0\,, \tag{A.27}$$

$$\bar{n}_3 = \frac{\sqrt{M_\infty^2-1}}{M_\infty}\,, \tag{A.28}$$

- If the inclination of the wedge such that $\delta \neq 0$ and a shock angle of β is produced, then the orientation of the shock would be given by the use of $\bar{\eta} = \beta$ in Eq. (A.1) with $\bar{\lambda} = 0$ for the un-swept shock.

  Alternatively, if the shock angle β is expressed as $\beta = \mu + \bar{\theta}$, then the components of the unit normal-vector to the shock un-swept shock surface could be written as

$$\bar{n}_1 = -\frac{1}{M_\infty}\cos\bar{\theta} - \frac{\sqrt{M_\infty^2-1}}{M_\infty}\sin\bar{\theta}\,, \tag{A.29}$$

$$\bar{n}_2 = 0\,, \tag{A.30}$$

$$\bar{n}_3 = \frac{\sqrt{M_\infty^2 - 1}}{M_\infty} \cos\bar{\theta} - \frac{1}{M_\infty} \sin\bar{\theta}\,, \tag{A.31}$$

This formulation is particularly useful, as for $M_\infty > 2.0$, the value of $\frac{\partial(\beta-\delta)}{\partial\delta}$ is small for a wide range of δ. This has been shown in Figs. 3.12 and 3.13. This has the implication that $\tilde{\beta} \approx \tilde{\delta}$, or at the very least, $\tilde{\beta} = \mathscr{O}\left(\tilde{\delta}\right)$.

Representative values of the direction vector of the fluid-velocity vector $\hat{\mathbf{V}}$ will be described using the definitions of angle-of-attack α_v and side-slip β_v adopted in Eqs. (A.7) and (A.8):

- It is noted that the ranges of allowable combinations of α_v and β_v are governed by the restriction that

$$0 \leq \sin^2\alpha_v + \sin^2\beta_v \leq 1\,, \tag{A.32}$$

$$\text{or} \quad \sin^2\beta_v \leq \cos^2\alpha_v\,. \tag{A.33}$$

This shows that while simultaneously small angles $\sin\alpha_v \approx \sin\beta_v = \mathscr{O}(\tau)$ with $\tau \ll 1$ are allowed, restrictions are placed on the manner in which the angles are allowed to grow large,

- In the limit of small incidence, such that $\sin\alpha_v \approx \sin\beta_v = \mathscr{O}(\tau)$, the following components are obtained:

$$\frac{v_1}{|\mathbf{V}|} = \sqrt{1 - \sin^2\alpha_v - \sin^2\beta_v} = \mathscr{O}\left(1 - \tau^2\right), \tag{A.34}$$

$$\frac{v_2}{|\mathbf{V}|} = \mathscr{O}(\tau)\,, \tag{A.35}$$

$$\frac{v_3}{|\mathbf{V}|} = \mathscr{O}(\tau)\,, \tag{A.36}$$

The following ratios are also noted:

$$\frac{v_2}{v_1} = \mathscr{O}\left(\tau + \tau^3\right), \tag{A.37}$$

$$\frac{v_3}{v_1} = \mathscr{O}\left(\tau + \tau^3\right), \tag{A.38}$$

- In the scenario in which one of the angles (say α_v) becomes large while the other remains small, various order of magnitude may be considered:

– If α_v is large such that $\cos^2\alpha_v = \mathscr{O}(\tau)$, then it is required that $\sin\beta_v \leq \mathscr{O}\left(\tau^{1/2}\right)$, and the following components are obtained:

$$\frac{v_1}{|\mathbf{V}|} = \sqrt{\cos^2\alpha_v - \sin^2\beta_v} \leq \mathscr{O}\left(\tau^{1/2}\right), \tag{A.39}$$

$$\frac{v_2}{|\mathbf{V}|} = \mathscr{O}\left(\tau^{1/2}\right), \tag{A.40}$$

$$\frac{v_3}{|\mathbf{V}|} = \mathscr{O}(1-\tau), \tag{A.41}$$

The following ratios are also noted:

$$\frac{v_1}{v_3} \leq \mathscr{O}\left(\tau^{1/2} + \tau^{3/2}\right), \tag{A.42}$$

$$\frac{v_2}{v_3} \leq \mathscr{O}\left(\tau^{1/2} + \tau^{3/2}\right), \tag{A.43}$$

– If α_v is larger such that $\cos\alpha_v = \mathscr{O}(\tau)$, then it is required that $\sin\beta_v \leq \mathscr{O}(\tau)$, and the following components are obtained:

$$\frac{v_1}{|\mathbf{V}|} = \sqrt{\cos^2\alpha_v - \sin^2\beta_v} \leq \mathscr{O}(\tau), \tag{A.44}$$

$$\frac{v_2}{|\mathbf{V}|} = \mathscr{O}(\tau), \tag{A.45}$$

$$\frac{v_3}{|\mathbf{V}|} = \mathscr{O}\left(1-\tau^2\right), \tag{A.46}$$

The following ratios are also noted:

$$\frac{v_1}{v_3} \leq \mathscr{O}\left(\tau + \tau^3\right), \tag{A.47}$$

$$\frac{v_2}{v_3} \leq \mathscr{O}\left(\tau + \tau^3\right), \tag{A.48}$$

A.2.2 Post-Shock Quantities

To provide representative values of post-shock quantities, a number of parameters must be accounted for (in particular, all of the vectors considered above). A critical parameter will be $\bar{w}_{(U)}$, which results from a combination of the above vectors. It has been noted that the existence of a shock wave requires that $\bar{w}_{(U)} > \bar{a}_{(U)}$. In the discussion which follows, the windward surface of a parametrically-defined delta wing will be considered. The discussion will be informed by the experimental observations described in Fig. 2.29. This points to the importance of two further parameters:

- The Mach-number normal to the leading-edge of the incident (pre-shock) flow, M_N,
- The inclination of the incident flow in the leading-edge-normal plane relative to the thickness plane, α_N.

These parameters may be described in terms of existing parameters as

$$\bar{M}_N = \bar{M}_{(U)} \left\{ \begin{array}{l} \cos^2\bar{\lambda}_s \cos^2\bar{\beta}_{v(U)} + \sin^2\bar{\lambda}_s \sin^2\bar{\beta}_{v(U)} + \sin^2\bar{\alpha}_{v(U)} \sin^2\bar{\lambda}_s \\ -2\sin\bar{\lambda}_s \cos\bar{\lambda}_s \sin\bar{\beta}_{v(U)} \sqrt{\cos^2\bar{\beta}_{v(U)} - \sin^2\bar{\alpha}_{v(U)}} \end{array} \right\}^{\frac{1}{2}}, \tag{A.49}$$

$$\sin\bar{\alpha}_N = \frac{\bar{M}_{(U)} \sin\bar{\alpha}_{v(U)}}{\bar{M}_N}. \tag{A.50}$$

From Fig. 2.29 it may be seen that the structure of the corssflow flowfield is defined by M_N and α_N. Three regimes are observed in Fig. 2.29b:

- Region C, in which the bow-shock is attached to the leading-edge. This gives $\bar{\lambda}_s = \bar{\lambda}_b$ at the leading-edge, with lesser values of $\bar{\lambda}_s$ occuring towards the centerline of the wing. This regime is defined by $M_N \geq 1$, with α_N smaller than the value required for detachment of an oblique shock over an equivalent wedge. In this regime, no communication occurs between the windward and leeward surfaces,
- Region B, in which the bow-shock is detached from the leading-edge. It is noted that this regime may occur for a supersonic leading-edge ($M_N \geq 1$) at sufficiently high α_N. The detachment of the shock from the leading-edge implies $\bar{\lambda}_s < \bar{\lambda}_b$ at the maximum value of $\bar{\lambda}_s$. Region B is further defined by supersonic expansion about the leading-edges. This essentially leads to one-way propagation of disturbances from the windward surface to the leeward surface,
- Region A, in which the bow-shock is detached from the leading-edge and the post-shock crossflow plane is entirely subsonic. This regime occurs for a subsonic leading-edge ($M_N < 1$) and may occur for a supersonic leading-edge at sufficiently high α_N. The detachment of the shock from the leading-edge again implies $\bar{\lambda}_s < \bar{\lambda}_b$, with the further possibility of the shock being detached from the apex of the delta wing.

It is to be noted that in all of the above scenarios, the inclination of the bow shock will everywhere be such that $\bar{\eta}_s \geq \bar{\eta}_b$. Consideration of the relationship between $\bar{\lambda}_s$ and $\bar{\lambda}_b$ above suggests that $\bar{\lambda}_s = \mathcal{O}(\bar{\lambda}_b)$ is an appropriate characterization. However, significantly larger values of $\bar{\eta}_s$ than $\bar{\eta}_b$ may be encountered. These restrictions allow the following parameter exploration to be conducted:

- Thin wings will be considered such that $\sin\bar{\eta}_b = \mathscr{O}(\tau)$, where $\tau \ll 1$ is a small parameter,
- The following wing sweeps will be considered:
  - Low sweep, such that $\sin\bar{\lambda}_b = \mathscr{O}(\tau)$,
  - Moderate sweep, such that $\sin\bar{\lambda}_b = \mathscr{O}\left(\cos\bar{\lambda}_b\right) = \mathscr{O}(1)$,
  - High sweep, such that $\cos\bar{\lambda}_b = \mathscr{O}(\tau)$,
- Low side-wash will be considered, such that $\sin\bar{\beta}_{v(U)} = \mathscr{O}(\tau)$,
- The following angles of attack will be considered:
  - Low incidence, such that $\sin\bar{\alpha}_{v(U)} = \mathscr{O}(\tau)$,
  - Moderate incidence, such that $\sin\bar{\alpha}_{v(U)} = \mathscr{O}\left(\cos\bar{\alpha}_{v(U)}\right) = \mathscr{O}(1)$,
  - High sweep, such that $\cos\bar{\alpha}_{v(U)} = \mathscr{O}(\tau)$,
- As motivated by the above discussion, it will be assumed that $\bar{\lambda}_s = \mathscr{O}\left(\bar{\lambda}_b\right)$,
- The shock inclination $\bar{\eta}_s$ will be varied using similar definitions of "low", "moderate", and "high" incidence, with the lower limit being defined by $\bar{\eta}_s = \mathscr{O}\left(\bar{\alpha}_{v(U)}\right)$.

A.3 Perturbation Terms

A.3.1 Geometric Parameters and Direction Vectors

The unit-vector describing the axis of rotation, $\hat{\mathbf{r}}$, is a control parameter. It has been defined in Eq. (4.74) using an essentially equivalent definition of polar (η_r) and azimuthal (λ_r) angles as was used for the normal vector $\bar{\hat{\mathbf{n}}}$. Equation (4.74) is repeated below as

$$\hat{\mathbf{r}} = -\sin\eta_r\cos\lambda_r\hat{\mathbf{e}}_\mathbf{1} - \sin\eta_r\sin\lambda_r\hat{\mathbf{e}}_\mathbf{2} + \cos\eta_r\hat{\mathbf{e}}_\mathbf{3}\,. \tag{A.51}$$

The following interpretations are offered:

- In considering lifting surfaces, rotations of practical interest will arise from bending or twist (or both) of the planform. Bending may be associated with rotations about $\hat{\mathbf{e}}_\mathbf{1}$, while twist is associated with rotations about $\hat{\mathbf{e}}_\mathbf{2}$. Rotations about $\hat{\mathbf{e}}_\mathbf{3}$ may be interpreted as a shearing rotation of the planform, and are not of practical interest,

- As a consequence, η_r may be interpreted as a measure of the shearing action, and will typically be $\eta_r \approx \frac{\pi}{2}$. However, it has the formal range of $\eta_r = [0, \pi]$,

- By extension, λ_r may be interpreted as a mixing ratio between pure bending ($\lambda_r =$ 0 or $\pm\pi$) and pure twist ($\lambda_r = \pm\frac{\pi}{2}$). It has the range $\lambda_r = [-\pi, \pi]$,

- Each component r_i has the range $r_i = [-1, 1]$ with the constraint of $|\hat{\mathbf{r}}| = 1$.

The perturbation vector to the normal vector, $\tilde{\mathbf{n}}$ is given below in vector form as

$$\tilde{\mathbf{n}} = \left(\sin\tilde{\theta}_r\right)\left(\hat{\mathbf{r}} \times \bar{\hat{\mathbf{n}}}\right) - \left(1 - \cos\tilde{\theta}_r\right)\left[\bar{\hat{\mathbf{n}}} - \left(\hat{\mathbf{r}} \cdot \bar{\hat{\mathbf{n}}}\right)\hat{\mathbf{r}}\right]. \tag{A.52}$$

The following interpretations are offered:

- The angle $\tilde{\theta}_r$ through which the surface is rotated as a perturbation of its orientation is a control parameter.

  The angle $\tilde{\theta}_r$ is dimensionless (radians) and has the range $\tilde{\theta}_r = [0, 2\pi]$.

- The component of the perturbation vector $\tilde{\mathbf{n}}$ in the $\hat{\mathbf{e}}_\mathbf{1}$ direction will be interpreted as "turning into the flow". It is given below as

$$\tilde{n}_1 = (r_2\bar{n}_3 - r_3\bar{n}_2)\sin\tilde{\theta}_r - \left(1 - \cos\tilde{\theta}_r\right)\left[\bar{n}_1 - \left(\hat{\mathbf{r}} \cdot \bar{\hat{\mathbf{n}}}\right)r_1\right], \tag{A.53}$$

  The vector component $\tilde{n}_1$ is dimensionless, and has the range $\tilde{n}_1 = [-1, 1]$,

- The component of the perturbation vector $\tilde{\mathbf{n}}$ in the $\hat{\mathbf{e}}_\mathbf{2}$ direction will be interpreted as "spanwise turning". It is given below as

$$\tilde{n}_2 = (r_3\bar{n}_1 - r_1\bar{n}_3)\sin\tilde{\theta}_r - \left(1 - \cos\tilde{\theta}_r\right)\left[\bar{n}_2 - \left(\hat{\mathbf{r}} \cdot \bar{\hat{\mathbf{n}}}\right)r_2\right], \tag{A.54}$$

  The vector component $\tilde{n}_2$ is dimensionless, and has the range $\tilde{n}_2 = [-1, 1]$,

- The component of the perturbation vector $\tilde{\mathbf{n}}$ in the $\hat{\mathbf{e}}_\mathbf{3}$ direction will be interpreted as and adjustment to maintain the unit magnitude of $\tilde{\mathbf{n}}$. It is given below as

$$\tilde{n}_3 = (r_1\bar{n}_2 - r_2\bar{n}_1)\sin\tilde{\theta}_r - \left(1 - \cos\tilde{\theta}_r\right)\left[\bar{n}_3 - \left(\hat{\mathbf{r}} \cdot \bar{\hat{\mathbf{n}}}\right)r_3\right], \tag{A.55}$$

  The vector component $\tilde{n}_3$ is dimensionless, and has the range $\tilde{n}_3 = [-1, 1]$,

- The general case of mixed torsion-bending with $\hat{\mathbf{r}} \cdot \hat{\mathbf{e}}_3 = 0$ results in perturbation components given by:

$$\tilde{n}_1 = r_2 \left[\bar{n}_3 \sin\tilde{\theta}_r - \left(1 - \cos\tilde{\theta}_r\right)\left(\bar{n}_1 r_2 - \bar{n}_2 r_1\right) \right], \tag{A.56}$$

$$\tilde{n}_2 = -r_1 \left[\bar{n}_3 \sin\tilde{\theta}_r - \left(1 - \cos\tilde{\theta}_r\right)\left(\bar{n}_1 r_2 - \bar{n}_2 r_1\right) \right], \tag{A.57}$$

$$\tilde{n}_3 = -\left[\left(\bar{n}_1 r_2 - \bar{n}_2 r_1\right)\sin\tilde{\theta}_r + \left(1 - \cos\tilde{\theta}_r\right)\bar{n}_3 \right], \tag{A.58}$$

- For pure bending through an angle of $\tilde{\theta}_r$ about $\hat{\mathbf{r}} = -\hat{\mathbf{e}}_1$, the perturbation vector $\tilde{\mathbf{n}}$ simplifies to:

$$\tilde{n}_1 = 0, \tag{A.59}$$

$$\tilde{n}_2 = \bar{n}_3 \sin\tilde{\theta}_r - \left(1 - \cos\tilde{\theta}_r\right)\bar{n}_2, \tag{A.60}$$

$$\tilde{n}_3 = -\left[\bar{n}_2 \sin\tilde{\theta}_r + \left(1 - \cos\tilde{\theta}_r\right)\bar{n}_3 \right], \tag{A.61}$$

- For pure twist through an angle of $\tilde{\theta}_r$ about $\hat{\mathbf{r}} = -\hat{\mathbf{e}}_2$, the perturbation vector $\tilde{\mathbf{n}}$ simplifies to:

$$\tilde{n}_1 = -\left[\bar{n}_3 \sin\tilde{\theta}_r + \left(1 - \cos\tilde{\theta}_r\right)\bar{n}_1 \right], \tag{A.62}$$

$$\tilde{n}_2 = 0, \tag{A.63}$$

$$\tilde{n}_3 = \bar{n}_1 \sin\tilde{\theta}_r - \left(1 - \cos\tilde{\theta}_r\right)\bar{n}_3, \tag{A.64}$$

It is noted here that the perturbation to the velocity vector, $\tilde{\mathbf{V}}$, is not a control parameter, as the velocity perturbations are determined by the boundary conditions and governing equations of the flow.

The direction-vectors associated with body- and shock-velocity vectors $\tilde{\mathbf{V}}_\mathbf{b}$ and $\tilde{\mathbf{V}}_\mathbf{s}$ (and their un-perturbed counter-parts) may be described using the η-λ formulation adopted for the unit-normal vector in Eq. (A.1) and for the axis of rotation in Eq. (A.51).

A.3.2 Post-Shock Quantities at the Shock Boundary

The above relations allow $\tilde{w}_{(U)}$ to be defined from Eq. (4.107). In the present development, it will be assumed for simplicity's sake that $\tilde{w}_{(U)}$ is dominated by the turning of the un-perturbed velocity vector by the perturbation to the surface normal. This is expressed as follows:

$$\tilde{w}_{(U)} \approx \bar{\mathbf{V}}_{(U)} \cdot \tilde{\mathbf{n}}, \tag{A.65}$$

The perturbations to post-shock fluid quantities $\tilde{\rho}$, $\tilde{\mathbf{V}}$, and $\tilde{p}$. These are adapted from Eqs. (4.111) to (4.113) as

$$\frac{\tilde{\rho}}{\bar{\rho}_R} = \left[1 - \left(\frac{\gamma-1}{2}\right)\bar{\sigma}\right]\left(\frac{4}{\gamma+1}\right)\left(\frac{\bar{\rho}}{\bar{\rho}_R}\frac{\left|\bar{\mathbf{V}}_{(U)}\right|}{\bar{w}_{(U)}}\right)\frac{\tilde{w}_{(U)}}{\left|\bar{\mathbf{V}}_{(U)}\right|}, \tag{A.66}$$

$$\frac{\tilde{\mathbf{V}}}{\left|\bar{\mathbf{V}}_{(U)}\right|} = -\left(\frac{\bar{\sigma}}{1+\bar{\sigma}}\right)\frac{\bar{w}_{(U)}}{\left|\bar{\mathbf{V}}_{(U)}\right|}\tilde{\mathbf{n}} - \left[1 - \left(\frac{\gamma+1}{4}\right)\left(\frac{\bar{\sigma}}{1+\bar{\sigma}}\right)\right]\left(\frac{4}{\gamma+1}\right)\frac{\tilde{w}_{(U)}}{\left|\bar{\mathbf{V}}_{(U)}\right|}\left(\bar{\hat{\mathbf{n}}} + \tilde{\mathbf{n}}\right), \tag{A.67}$$

$$\frac{\tilde{p}}{\bar{p}_R} = \left[1 + \left(\frac{\gamma-1}{2}\right)\left(\frac{\bar{\sigma}}{1+\bar{\sigma}}\right)\right]^{-1}\left(\frac{4\gamma}{\gamma+1}\right)\left(\frac{\bar{p}}{\bar{p}_R}\frac{\left|\bar{\mathbf{V}}_{(U)}\right|}{\bar{w}_{(U)}}\right)\frac{\tilde{w}_{(U)}}{\left|\bar{\mathbf{V}}_{(U)}\right|}, \tag{A.68}$$

A.3.3 Velocity Relations at the Body Surface

While the Rankine-Hugoniot equations effectively prescribe the perturbation velocities at the shock surface, the non-permeability condition does not fully determine the perturbation velocities at the body surface. As in the un-perturbed case, it only enforces flow tangency in the body surface, with the flow direction and velocity magnitude determined by the governing equations in the interior of the fluid domain. Thus, no attempt is made here to perform a scaling analysis of the perturbation to fluid properties at the body surface.

A.4 Scaling Analysis for Delta Wings

The present section showcases some results of the application of the scaling-analysis framework covered in this appendix. In particular, a series of delta wings are considered, parametrically defined by their leading-edge sweep through $\bar{\lambda}_b$. A variety of shock orientations are considered through $\bar{\lambda}_s$ and $\bar{\eta}_b$. The pre-shock Mach number $\bar{M}_{(U)}$ is also treated as a parameter. A range of pre-shock flow incidences are considered through $\bar{\alpha}_{v(U)}$.

The scaling analysis introduces the following small parameters:

- $\tau \ll 1$,
- κ as an intermediate or moderate parameter. In particular, the definition of κ arises from trigonometric functions. For an angle X, κ defines the scenario where

$$\sin X = \mathscr{O}(\cos X) = \mathscr{O}(\kappa), \tag{A.69}$$

which by extension yields the result that

$$\mathscr{O}\left(1-\kappa^2\right)=\mathscr{O}\left(\kappa^2\right). \tag{A.70}$$

The following relative smallness definition will be enforced

$$\tau \ll \kappa, \tag{A.71}$$

while the relative scaling of the following type of expression has not been prescribed:

$$1-\kappa^n \qquad \text{with } n \neq 2, \tag{A.72}$$

$$\kappa^n-\tau \qquad \text{with } n \geq 2. \tag{A.73}$$

In terms of these parameters, the scaling analysis is limited to thin wings such that $\sin\bar{\eta}_b = \mathscr{O}(\tau)$. Similarly, the pre-shock sideslip angle is maintained at a small value such that $\sin\bar{\beta}_{v(U)} = \mathscr{O}(\tau)$.

The geometric parameters pertaining to the body and shock result in the case definition and nomenclature shown in Table A.1. This nomenclature is used as a shorthand throughout, with its adaptations for the velocity and normal vectors shown in Table A.2. Also shown is the quantification of pre-shock vector components.

The final column of Table A.1 provides an estimate of the expected relationship between gradients in the thickness and spanwise directions. This is informed by Eqs. (A.49) and (A.50) and Fig. 2.29. These quantities, along with surface-normal pre-shock velocities, are quantified in Table A.3.

The minimum Mach-number required for a physical shock to exist for the orientations defined in the aforementioned tables is given in Table A.4. The associated shock-strength (or the absence of a shock) is also given.

The components of perturbations to the normal vector for pure bending ($\hat{\mathbf{r}} = -\hat{\mathbf{e}}_1$) and for pure twist ($\hat{\mathbf{r}} = -\hat{\mathbf{e}}_2$) are given in Table A.5. The components of the perturbed normal vector are given in Table A.6. A comparison of the associated un-perturbed and perturbation shock-normal pre-shock velocities is given in Table A.7.

The above tables are used with Eqs. (A.19) and (A.67) to derive the scaling analysis for un-perturbed and perturbation post-shock velocities at a variety of Mach numbers and for pure twist and bending in Tables A.8 to A.13.

The analysis may be extended to the post-shock fluid density, pressure, and speed of sound. However, this is not required in order to eliminate directional-dependence in the governing equations.

Table A.1 Angle- and case-definition for scaling analysis of boundary-related terms.

$\bar{\lambda}_b$	$\bar{\alpha}_{v(U)}$	$\bar{\eta}_s$	Case Code	$\bar{L}_2$ and $\bar{L}_3$
		$\sin\bar{\eta}_s = \mathscr{O}(\tau)$	$\lambda 0$-$\alpha 0$-$\eta 0$	
	$\sin\bar{\alpha}_{v(U)} = \mathscr{O}(\tau)$	$\sin\bar{\eta}_s = \mathscr{O}(\kappa)$	$\lambda 0$-$\alpha 0$-$\eta\kappa$	$\bar{L}_3 = \mathscr{O}(\tau\bar{L}_2)$
		$\cos\bar{\eta}_s = \mathscr{O}(\tau)$	$\lambda 0$-$\alpha 0$-$\eta 1$	
$\sin\bar{\lambda}_b = \mathscr{O}(\tau)$,		$\sin\bar{\eta}_s = \mathscr{O}(\tau)$	$\lambda 0$-$\alpha\kappa$-$\eta 0$	$\bar{L}_3 = \mathscr{O}(\tau\bar{L}_2)$
$\sin\bar{\lambda}_s = \mathscr{O}(\tau)$,	$\sin\bar{\alpha}_{v(U)} = \mathscr{O}(\kappa)$	$\sin\bar{\eta}_s = \mathscr{O}(\kappa)$	$\lambda 0$-$\alpha\kappa$-$\eta\kappa$	or
$\sin\bar{\beta}_{v(U)} = \mathscr{O}(\tau)$		$\cos\bar{\eta}_s = \mathscr{O}(\tau)$	$\lambda 0$-$\alpha\kappa$-$\eta 1$	$\bar{L}_3 = \mathscr{O}(\bar{L}_2)$
		$\sin\bar{\eta}_s = \mathscr{O}(\tau)$	$\lambda 0$-$\alpha 1$-$\eta 0$	
	$\cos\bar{\alpha}_{v(U)} = \mathscr{O}(\tau)$	$\sin\bar{\eta}_s = \mathscr{O}(\kappa)$	$\lambda 0$-$\alpha 1$-$\eta\kappa$	$\bar{L}_3 = \mathscr{O}(\bar{L}_2)$
		$\cos\bar{\eta}_s = \mathscr{O}(\tau)$	$\lambda 0$-$\alpha 1$-$\eta 1$	
		$\sin\bar{\eta}_s = \mathscr{O}(\tau)$	$\lambda\kappa$-$\alpha 0$-$\eta 0$	$\bar{L}_3 = \mathscr{O}(\tau\bar{L}_2)$
	$\sin\bar{\alpha}_{v(U)} = \mathscr{O}(\tau)$	$\sin\bar{\eta}_s = \mathscr{O}(\kappa)$	$\lambda\kappa$-$\alpha 0$-$\eta\kappa$	or
		$\cos\bar{\eta}_s = \mathscr{O}(\tau)$	$\lambda\kappa$-$\alpha 0$-$\eta 1$	$\bar{L}_3 = \mathscr{O}(\bar{L}_2)$
$\sin\bar{\lambda}_b = \mathscr{O}(\kappa)$		$\sin\bar{\eta}_s = \mathscr{O}(\tau)$	$\lambda\kappa$-$\alpha\kappa$-$\eta 0$	
$\sin\bar{\lambda}_s = \mathscr{O}(\kappa)$	$\sin\bar{\alpha}_{v(U)} = \mathscr{O}(\kappa)$	$\sin\bar{\eta}_s = \mathscr{O}(\kappa)$	$\lambda\kappa$-$\alpha\kappa$-$\eta\kappa$	$\bar{L}_3 = \mathscr{O}(\bar{L}_2)$
$\sin\bar{\beta}_{v(U)} = \mathscr{O}(\tau)$		$\cos\bar{\eta}_s = \mathscr{O}(\tau)$	$\lambda\kappa$-$\alpha\kappa$-$\eta 1$	
		$\sin\bar{\eta}_s = \mathscr{O}(\tau)$	$\lambda\kappa$-$\alpha 1$-$\eta 0$	
	$\cos\bar{\alpha}_{v(U)} = \mathscr{O}(\tau)$	$\sin\bar{\eta}_s = \mathscr{O}(\kappa)$	$\lambda\kappa$-$\alpha 1$-$\eta\kappa$	$\bar{L}_3 = \mathscr{O}(\bar{L}_2)$
		$\cos\bar{\eta}_s = \mathscr{O}(\tau)$	$\lambda\kappa$-$\alpha 1$-$\eta 1$	
		$\sin\bar{\eta}_s = \mathscr{O}(\tau)$	$\lambda 1$-$\alpha 0$-$\eta 0$	
	$\sin\bar{\alpha}_{v(U)} = \mathscr{O}(\tau)$	$\sin\bar{\eta}_s = \mathscr{O}(\kappa)$	$\lambda 1$-$\alpha 0$-$\eta\kappa$	$\bar{L}_3 = \mathscr{O}(\bar{L}_2)$
		$\cos\bar{\eta}_s = \mathscr{O}(\tau)$	$\lambda 1$-$\alpha 0$-$\eta 1$	
$\cos\bar{\lambda}_b = \mathscr{O}(\tau)$		$\sin\bar{\eta}_s = \mathscr{O}(\tau)$	$\lambda 1$-$\alpha\kappa$-$\eta 0$	
$\cos\bar{\lambda}_s = \mathscr{O}(\tau)$	$\sin\bar{\alpha}_{v(U)} = \mathscr{O}(\kappa)$	$\sin\bar{\eta}_s = \mathscr{O}(\kappa)$	$\lambda 1$-$\alpha\kappa$-$\eta\kappa$	$\bar{L}_3 = \mathscr{O}(\bar{L}_2)$
$\sin\bar{\beta}_{v(U)} = \mathscr{O}(\tau)$		$\cos\bar{\eta}_s = \mathscr{O}(\tau)$	$\lambda 1$-$\alpha\kappa$-$\eta 1$	
		$\sin\bar{\eta}_s = \mathscr{O}(\tau)$	$\lambda 1$-$\alpha 1$-$\eta 0$	
	$\cos\bar{\alpha}_{v(U)} = \mathscr{O}(\tau)$	$\sin\bar{\eta}_s = \mathscr{O}(\kappa)$	$\lambda 1$-$\alpha 1$-$\eta\kappa$	$\bar{L}_3 = \mathscr{O}(\bar{L}_2)$
		$\cos\bar{\eta}_s = \mathscr{O}(\tau)$	$\lambda 1$-$\alpha 1$-$\eta 1$	

Table A.2 Scaling analysis of un-perturbed pre-shock vectors with $\sin\bar{\beta}_{\nu(U)} = \mathscr{O}(\tau)$.

Vector $\bar{\mathbf{X}}$	Case Code	$\bar{X}_1$	$\bar{X}_2$	$\bar{X}_3$
$\bar{\hat{\mathbf{n}}}_{\mathbf{s}}$	$\lambda 0$-$\eta 0$	$\mathscr{O}\left(\tau\left[1-\tau^2\right]\right)$	$\mathscr{O}\left(\tau^2\right)$	$\mathscr{O}\left(1-\tau^2\right)$
	$\lambda 0$-$\eta\kappa$	$\mathscr{O}\left(\kappa\left[1-\tau^2\right]\right)$	$\mathscr{O}(\tau\kappa)$	$\mathscr{O}(\kappa)$
	$\lambda 0$-$\eta 1$	$\mathscr{O}\left(1-\tau^2\right)$	$\mathscr{O}\left(\tau\left[1-\tau^2\right]\right)$	$\mathscr{O}(\tau)$
	$\lambda\kappa$-$\eta 0$	$\mathscr{O}(\tau\kappa)$	$\mathscr{O}(\tau\kappa)$	$\mathscr{O}\left(1-\tau^2\right)$
	$\lambda\kappa$-$\eta\kappa$	$\mathscr{O}\left(\kappa^2\right)$	$\mathscr{O}\left(\kappa^2\right)$	$\mathscr{O}(\kappa)$
	$\lambda\kappa$-$\eta 1$	$\mathscr{O}\left(\kappa\left[1-\tau^2\right]\right)$	$\mathscr{O}\left(\kappa\left[1-\tau^2\right]\right)$	$\mathscr{O}(\tau)$
	$\lambda 1$-$\eta 0$	$\mathscr{O}\left(\tau^2\right)$	$\mathscr{O}\left(\tau\left[1-\tau^2\right]\right)$	$\mathscr{O}\left(1-\tau^2\right)$
	$\lambda 1$-$\eta\kappa$	$\mathscr{O}(\tau\kappa)$	$\mathscr{O}\left(\kappa\left[1-\tau^2\right]\right)$	$\mathscr{O}(\kappa)$
	$\lambda 1$-$\eta 1$	$\mathscr{O}\left(\tau\left[1-\tau^2\right]\right)$	$\mathscr{O}\left(1-\tau^2\right)$	$\mathscr{O}(\tau)$
$\bar{\hat{\mathbf{V}}}$	$\alpha 0$	$\mathscr{O}\left(1-\tau^2\right)$	$\mathscr{O}(\tau)$	$\mathscr{O}(\tau)$
	$\alpha\kappa$	$\mathscr{O}\left(\kappa\left[1-\tau^2\right]\right)$	$\mathscr{O}(\tau)$	$\mathscr{O}(\kappa)$
	$\alpha 1$	$\mathscr{O}\left(\tau^2\right)$	$\mathscr{O}(\tau)$	$\mathscr{O}\left(1-\tau^2\right)$

Table A.3 Scaling analysis of boundary-related dot-products.

Case Code	$\bar{M}_N \,/\, \bar{M}_{(U)}$	$\sin\bar{\alpha}_N$	$\bar{\hat{\mathbf{V}}}_{(U)} \cdot \bar{\hat{\mathbf{n}}}_{\mathbf{b}}$	$\bar{w}_{(U)} \,/\, \lvert\bar{\mathbf{V}}_{(U)}\rvert$
$\lambda 0$-$\alpha 0$-$\eta 0$				$\mathscr{O}\left(\tau\left[1-\tau^2\right]\right)$
$\lambda 0$-$\alpha 0$-$\eta\kappa$	$\mathscr{O}\left(1-\tau^2\right)$	$\mathscr{O}\left(\tau\left[1+\tau^2\right]\right)$	$\mathscr{O}\left(\tau\left[1-\tau^2\right]\right)$	$\mathscr{O}(\kappa[1+\tau])$
$\lambda 0$-$\alpha 0$-$\eta 1$				$\mathscr{O}\left(1-\tau^2\right)$
$\lambda 0$-$\alpha\kappa$-$\eta 0$				$\mathscr{O}(\kappa[1+\tau])$
$\lambda 0$-$\alpha\kappa$-$\eta\kappa$	$\mathscr{O}\left(1-\tau^2\right)$	$\mathscr{O}\left(\kappa\left[1+\tau^2\right]\right)$	$\mathscr{O}(\kappa[1+\tau])$	$\mathscr{O}\left(\kappa^2\left[1-\tau^2\right]\right)$
$\lambda 0$-$\alpha\kappa$-$\eta 1$				$\mathscr{O}(\kappa[1+\tau])$
$\lambda 0$-$\alpha 1$-$\eta 0$				$\mathscr{O}\left(1-\tau^2\right)$
$\lambda 0$-$\alpha 1$-$\eta\kappa$	$\mathscr{O}\left(1-\tau^2\right)$	$\mathscr{O}\left(1-\tau^2\right)$	$\mathscr{O}\left(1-\tau^2\right)$	$\mathscr{O}\left(\kappa\left[1-\tau^2\right]\right)$
$\lambda 0$-$\alpha 1$-$\eta 1$				$\mathscr{O}\left(\tau\left[1-\tau^2\right]\right)$
$\lambda\kappa$-$\alpha 0$-$\eta 0$				$\mathscr{O}(\tau[1+\kappa-\tau])$
$\lambda\kappa$-$\alpha 0$-$\eta\kappa$	$\mathscr{O}(\kappa[1-\tau])$	$\mathscr{O}\left(\tau\kappa^{-1}[1+\tau]\right)$	$\mathscr{O}(\tau[1+\kappa-\tau])$	$\mathscr{O}\left(\kappa^2\left[1+\tau\left(\kappa^{-1}-1\right)\right]\right)$
$\lambda\kappa$-$\alpha 0$-$\eta 1$				$\mathscr{O}(\kappa[1-\tau])$
$\lambda\kappa$-$\alpha\kappa$-$\eta 0$				$\mathscr{O}(\kappa[1+\tau\kappa])$
$\lambda\kappa$-$\alpha\kappa$-$\eta\kappa$	$\mathscr{O}(\kappa[1-\kappa\tau])$	$\mathscr{O}\left(\kappa^2\left[1+\tau\kappa^{-1}\right]\right)$	$\mathscr{O}(\kappa[1+\tau\kappa])$	$\mathscr{O}\left(\kappa^2[1+\kappa-\tau]\right)$
$\lambda\kappa$-$\alpha\kappa$-$\eta 1$				$\mathscr{O}\left(\kappa^2\left[1-\tau^2\right]\right)$
$\lambda\kappa$-$\alpha 1$-$\eta 0$				$\mathscr{O}\left(1-\tau^2\right)$
$\lambda\kappa$-$\alpha 1$-$\eta\kappa$	$\mathscr{O}\left(1-\tau^2\right)$	$\mathscr{O}\left(1-\tau^2\right)$	$\mathscr{O}\left(1-\tau^2\right)$	$\mathscr{O}(\kappa[1-\tau\kappa])$
$\lambda\kappa$-$\alpha 1$-$\eta 1$				$\mathscr{O}\left(\tau\left[1-\kappa-\tau^2\right]\right)$
$\lambda 1$-$\alpha 0$-$\eta 0$				$\mathscr{O}\left(\tau\left[1-\tau^2\right]\right)$
$\lambda 1$-$\alpha 0$-$\eta\kappa$	$\mathscr{O}\left(\tau\left[1-\tau^2\right]\right)$	$\mathscr{O}\left(1-\tau^2\right)$	$\mathscr{O}\left(\tau\left[1-\tau^2\right]\right)$	$\mathscr{O}\left(\tau\kappa\left[1-\tau^2\right]\right)$
$\lambda 1$-$\alpha 0$-$\eta 1$				$\mathscr{O}\left(\tau^2[1-\tau]\right)$
$\lambda 1$-$\alpha\kappa$-$\eta 0$				$\mathscr{O}\left(\kappa\left[1-\tau^2\right]\right)$
$\lambda 1$-$\alpha\kappa$-$\eta\kappa$	$\mathscr{O}\left(\kappa\left[1-\tau^2\right]\right)$	$\mathscr{O}\left(1-\tau^2\right)$	$\mathscr{O}\left(\kappa\left[1-\tau^2\right]\right)$	$\mathscr{O}\left(\kappa^2\left[1-\tau\left(\kappa^{-1}-1\right)\right]\right)$
$\lambda 1$-$\alpha\kappa$-$\eta 1$				$\mathscr{O}\left(\tau\left[1-\tau^2\right]\right)$
$\lambda 1$-$\alpha 1$-$\eta 0$				$\mathscr{O}\left(1-\tau^2\right)$
$\lambda 1$-$\alpha 1$-$\eta\kappa$	$\mathscr{O}\left(1-\tau^2\right)$	$\mathscr{O}\left(1-\tau^2\right)$	$\mathscr{O}\left(1-\tau^2\right)$	$\mathscr{O}(\kappa[1-\tau])$
$\lambda 1$-$\alpha 1$-$\eta 1$				$\mathscr{O}\left(\tau^2[1-\tau]\right)$

Table A.4 Scaling analysis of shock-strength as a function of $\bar{M}_{(U)}$.

Case Code	$\bar{M}_{(U)} \geq \ldots$	$\bar{\sigma}\,/\,(1+\bar{\sigma})$,		
		$\bar{M}_{(U)} = \mathscr{O}(1)$	$\bar{M}_{(U)} = \mathscr{O}(\kappa^{-2})$	$\bar{M}_{(U)} = \mathscr{O}(\tau^{-1})$
$\lambda 0$-$\alpha 0$-$\eta 0$	$\mathscr{O}(\tau^{-1})$	no shock	no shock	$\mathscr{O}(\tau^2)$
$\lambda 0$-$\alpha 0$-$\eta\kappa$	$\mathscr{O}(\kappa^{-1})$	no shock	$\mathscr{O}(\kappa^2[1+\tau])$	$\mathscr{O}(1-\tau^2)$
$\lambda 0$-$\alpha 0$-$\eta 1$	$\mathscr{O}(1)$	$\mathscr{O}(\tau^2)$	$\mathscr{O}(1-\kappa^4[1+\tau^2])$	$\mathscr{O}(1-\tau^2)$
$\lambda 0$-$\alpha\kappa$-$\eta 0$	$\mathscr{O}(\kappa^{-1})$	no shock	$\mathscr{O}(\kappa^2[1+\tau])$	$\mathscr{O}(1-\tau^2)$
$\lambda 0$-$\alpha\kappa$-$\eta\kappa$	$\mathscr{O}(\kappa^{-2})$	no shock	$\mathscr{O}(\tau^2)$	$\mathscr{O}(1-\tau^2)$
$\lambda 0$-$\alpha\kappa$-$\eta 1$	$\mathscr{O}(\kappa^{-1})$	no shock	$\mathscr{O}(\kappa^2[1+\tau])$	$\mathscr{O}(1-\tau^2)$
$\lambda 0$-$\alpha 1$-$\eta 0$	$\mathscr{O}(1)$	$\mathscr{O}(\tau^2)$	$\mathscr{O}(1-\kappa^4[1+\tau^2])$	$\mathscr{O}(1-\tau^2)$
$\lambda 0$-$\alpha 1$-$\eta\kappa$	$\mathscr{O}(\kappa^{-1})$	no shock	$\mathscr{O}(\kappa^2[1-\tau^2])$	$\mathscr{O}(1-\tau^2)$
$\lambda 0$-$\alpha 1$-$\eta 1$	$\mathscr{O}(\tau^{-1})$	no shock	no shock	$\mathscr{O}(\tau^2)$
$\lambda\kappa$-$\alpha 0$-$\eta 0$	$\mathscr{O}(\tau^{-1})$	no shock	no shock	$\mathscr{O}(\kappa-\tau)$
$\lambda\kappa$-$\alpha 0$-$\eta\kappa$	$\mathscr{O}(\kappa^{-2})$	no shock	$\mathscr{O}(\tau(\kappa^{-1}-1))$	$\mathscr{O}(1-\tau^2)$
$\lambda\kappa$-$\alpha 0$-$\eta 1$	$\mathscr{O}(\kappa^{-1})$	no shock	$\mathscr{O}(\kappa^2[1-\tau])$	$\mathscr{O}(1-\tau^2)$
$\lambda\kappa$-$\alpha\kappa$-$\eta 0$	$\mathscr{O}(\kappa^{-1})$	no shock	$\mathscr{O}(\kappa^2[1+\tau\kappa])$	$\mathscr{O}(1-\tau^2)$
$\lambda\kappa$-$\alpha\kappa$-$\eta\kappa$	$\mathscr{O}(\kappa^{-2})$	no shock	$\mathscr{O}(\kappa-\tau)$	$\mathscr{O}(1-\tau^2)$
$\lambda\kappa$-$\alpha\kappa$-$\eta 1$	$\mathscr{O}(\kappa^{-2})$	no shock	$\mathscr{O}(\tau^2)$	$\mathscr{O}(1-\tau^2)$
$\lambda\kappa$-$\alpha 1$-$\eta 0$	$\mathscr{O}(1)$	$\mathscr{O}(\tau^2)$	$\mathscr{O}(1-\kappa^4[1+\tau^2])$	$\mathscr{O}(1-\tau^2)$
$\lambda\kappa$-$\alpha 1$-$\eta\kappa$	$\mathscr{O}(\kappa^{-1})$	no shock	$\mathscr{O}(\kappa^2[1-\tau\kappa])$	$\mathscr{O}(1-\tau^2)$
$\lambda\kappa$-$\alpha 1$-$\eta 1$	$\mathscr{O}(\tau^{-1})$	no shock	no shock	$\mathscr{O}(\kappa+\tau^2)$
$\lambda 1$-$\alpha 0$-$\eta 0$	$\mathscr{O}(\tau^{-1})$	no shock	no shock	$\mathscr{O}(\tau^2)$
$\lambda 1$-$\alpha 0$-$\eta\kappa$	$\mathscr{O}(\tau^{-1}\kappa^{-1})$	no shock	no shock	$\mathscr{O}(1-\tau^2)$
$\lambda 1$-$\alpha 0$-$\eta 1$	$\mathscr{O}(\tau^{-2})$	no shock	no shock	no shock
$\lambda 1$-$\alpha\kappa$-$\eta 0$	$\mathscr{O}(\kappa^{-1})$	no shock	$\mathscr{O}(\kappa^2[1-\tau^2])$	$\mathscr{O}(1-\tau^2)$
$\lambda 1$-$\alpha\kappa$-$\eta\kappa$	$\mathscr{O}(\kappa^{-2})$	no shock	$\mathscr{O}(\tau(\kappa^{-1}-1))$	$\mathscr{O}(1-\tau^2\kappa^{-4})$
$\lambda 1$-$\alpha\kappa$-$\eta 1$	$\mathscr{O}(\tau^{-1})$	no shock	no shock	$\mathscr{O}(\tau^2)$
$\lambda 1$-$\alpha 1$-$\eta 0$	$\mathscr{O}(1)$	$\mathscr{O}(\tau^2)$	$\mathscr{O}(1-\kappa^4[1-\tau^2])$	$\mathscr{O}(1-\tau^2)$
$\lambda 1$-$\alpha 1$-$\eta\kappa$	$\mathscr{O}(\kappa^{-1})$	no shock	$\mathscr{O}(\kappa^2[1-\tau])$	$\mathscr{O}(\tau^2)$
$\lambda 1$-$\alpha 1$-$\eta 1$	$\mathscr{O}(\tau^{-2})$	no shock	no shock	no shock

Table A.5 Scaling analysis of the perturbation to the shock normal-vector for $\sin\tilde{\theta}_r = \mathscr{O}(\tau_\theta)$.

Rotation Axis	Case Code	$\tilde{n}_1$	$\tilde{n}_2$	$\tilde{n}_3$
$\hat{\mathbf{r}} = -\hat{\mathbf{e}}_1$	$\lambda 0$-$\eta 0$	0	$\mathscr{O}\left(\tau_\theta\left[1-\tau^2\right]-\tau_\theta^2\tau^2\right)$	$\mathscr{O}\left(\tau_\theta\tau^2+\tau_\theta^2\left[1-\tau^2\right]\right)$
	$\lambda 0$-$\eta\kappa$	0	$\mathscr{O}\left(\tau_\theta\kappa-\tau_\theta^2\tau\kappa\right)$	$\mathscr{O}\left(\tau_\theta\kappa\tau+\tau_\theta^2\kappa\right)$
	$\lambda 0$-$\eta 1$	0	$\mathscr{O}\left(\tau_\theta\tau-\tau_\theta^2\tau\left[1-\tau^2\right]\right)$	$\mathscr{O}\left(\tau_\theta\tau\left[1-\tau^2\right]+\tau_\theta^2\tau\right)$
	$\lambda\kappa$-$\eta 0$	0	$\mathscr{O}\left(\tau_\theta\left[1-\tau^2\right]-\tau_\theta^2\tau\kappa\right)$	$\mathscr{O}\left(\tau_\theta\kappa\tau+\tau_\theta^2\left[1-\tau^2\right]\right)$
	$\lambda\kappa$-$\eta\kappa$	0	$\mathscr{O}\left(\tau_\theta\kappa-\tau_\theta^2\kappa^2\right)$	$\mathscr{O}\left(\tau_\theta\kappa^2+\tau_\theta^2\kappa\right)$
	$\lambda\kappa$-$\eta 1$	0	$\mathscr{O}\left(\tau_\theta\tau-\tau_\theta^2\kappa\left[1-\tau^2\right]\right)$	$\mathscr{O}\left(\tau_\theta\kappa\left[1-\tau^2\right]+\tau_\theta^2\tau\right)$
	$\lambda 1$-$\eta 0$	0	$\mathscr{O}\left(\tau_\theta\left[1-\tau^2\right]-\tau_\theta^2\tau\left[1-\tau^2\right]\right)$	$\mathscr{O}\left(\tau_\theta\tau\left[1-\tau^2\right]+\tau_\theta^2\left[1-\tau^2\right]\right)$
	$\lambda 1$-$\eta\kappa$	0	$\mathscr{O}\left(\tau_\theta\kappa-\tau_\theta^2\kappa\left[1-\tau^2\right]\right)$	$\mathscr{O}\left(\tau_\theta\kappa\left[1-\tau^2\right]+\tau_\theta^2\kappa\right)$
	$\lambda 1$-$\eta 1$	0	$\mathscr{O}\left(\tau_\theta\tau-\tau_\theta^2\left[1-\tau^2\right]\right)$	$\mathscr{O}\left(\tau_\theta\left[1-\tau^2\right]+\tau_\theta^2\tau\right)$
$\hat{\mathbf{r}} = -\hat{\mathbf{e}}_2$	$\lambda 0$-$\eta 0$	$\mathscr{O}\left(\tau_\theta\left[1-\tau^2\right]+\tau_\theta^2\tau\left[1-\tau^2\right]\right)$	0	$\mathscr{O}\left(\tau_\theta\tau\left[1-\tau^2\right]-\tau_\theta^2\left[1-\tau^2\right]\right)$
	$\lambda 0$-$\eta\kappa$	$\mathscr{O}\left(\tau_\theta\kappa+\tau_\theta^2\kappa\left[1-\tau^2\right]\right)$	0	$\mathscr{O}\left(\tau_\theta\kappa\left[1-\tau^2\right]-\tau_\theta^2\kappa\right)$
	$\lambda 0$-$\eta 1$	$\mathscr{O}\left(\tau_\theta\tau+\tau_\theta^2\left[1-\tau^2\right]\right)$	0	$\mathscr{O}\left(\tau_\theta\left[1-\tau^2\right]-\tau_\theta^2\tau\right)$
	$\lambda\kappa$-$\eta 0$	$\mathscr{O}\left(\tau_\theta\left[1-\tau^2\right]+\tau_\theta^2\tau\kappa\right)$	0	$\mathscr{O}\left(\tau_\theta\tau\kappa-\tau_\theta^2\left[1-\tau^2\right]\right)$
	$\lambda\kappa$-$\eta\kappa$	$\mathscr{O}\left(\tau_\theta\kappa+\tau_\theta^2\kappa^2\right)$	0	$\mathscr{O}\left(\tau_\theta\kappa^2\left[1-\tau^2\right]-\tau_\theta^2\kappa\right)$
	$\lambda\kappa$-$\eta 1$	$\mathscr{O}\left(\tau_\theta\tau+\tau_\theta^2\kappa\left[1-\tau^2\right]\right)$	0	$\mathscr{O}\left(\tau_\theta\kappa\left[1-\tau^2\right]-\tau_\theta^2\tau\right)$
	$\lambda 1$-$\eta 0$	$\mathscr{O}\left(\tau_\theta\left[1-\tau^2\right]+\tau_\theta^2\tau^2\right)$	0	$\mathscr{O}\left(\tau_\theta\tau^2-\tau_\theta^2\left[1-\tau^2\right]\right)$
	$\lambda 1$-$\eta\kappa$	$\mathscr{O}\left(\tau_\theta\kappa+\tau_\theta^2\kappa\tau\right)$	0	$\mathscr{O}\left(\tau_\theta\tau\kappa\left[1-\tau^2\right]-\tau_\theta^2\kappa\right)$
	$\lambda 1$-$\eta 1$	$\mathscr{O}\left(\tau_\theta\tau+\tau_\theta^2\tau\left[1-\tau^2\right]\right)$	0	$\mathscr{O}\left(\tau_\theta\tau\left[1-\tau^2\right]-\tau_\theta^2\tau\right)$

Table A.6 Scaling analysis of the unit normal-vector to the perturbed shock for $\sin\tilde{\theta}_r = \mathscr{O}(\tau_\theta)$.

Rotation Axis	Case Code	$\bar{n}_1 + \tilde{n}_1$	$\bar{n}_2 + \tilde{n}_2$	$\bar{n}_3 + \tilde{n}_3$
$\hat{\mathbf{r}} = -\hat{\mathbf{e}}_1$	$\lambda 0$-$\eta 0$	$\mathscr{O}\left(\tau\left[1-\tau^2\right]\right)$	$\mathscr{O}\left(\tau_\theta\left[1-\tau^2\right]+\tau^2\left[1-\tau_\theta^2\right]\right)$	$\mathscr{O}\left(\tau_\theta\tau^2-\left[1-\tau_\theta^2\right]\left[1-\tau^2\right]\right)$
	$\lambda 0$-$\eta\kappa$	$\mathscr{O}\left(\kappa\left[1-\tau^2\right]\right)$	$\mathscr{O}\left(\tau_\theta\kappa+\tau\kappa\left[1-\tau_\theta^2\right]\right)$	$\mathscr{O}\left(\tau_\theta\kappa\tau-\kappa\left[1-\tau_\theta^2\right]\right)$
	$\lambda 0$-$\eta 1$	$\mathscr{O}\left(1-\tau^2\right)$	$\mathscr{O}\left(\tau_\theta\tau+\tau\left[1-\tau_\theta^2\right]\left[1-\tau^2\right]\right)$	$\mathscr{O}\left(\tau_\theta\tau\left[1-\tau^2\right]-\tau\left[1-\tau_\theta^2\right]\right)$
	$\lambda\kappa$-$\eta 0$	$\mathscr{O}\left(\tau\kappa\right)$	$\mathscr{O}\left(\tau_\theta\left[1-\tau^2\right]+\tau\kappa\left[1-\tau_\theta^2\right]\right)$	$\mathscr{O}\left(\tau_\theta\kappa\tau-\left[1-\tau_\theta^2\right]\left[1-\tau^2\right]\right)$
	$\lambda\kappa$-$\eta\kappa$	$\mathscr{O}\left(\kappa^2\right)$	$\mathscr{O}\left(\tau_\theta\kappa+\kappa^2\left[1-\tau_\theta^2\right]\right)$	$\mathscr{O}\left(\tau_\theta\kappa^2-\kappa\left[1-\tau_\theta^2\right]\right)$
	$\lambda\kappa$-$\eta 1$	$\mathscr{O}\left(\kappa\left[1-\tau^2\right]\right)$	$\mathscr{O}\left(\tau_\theta\tau+\kappa\left[1-\tau_\theta^2\right]\left[1-\tau^2\right]\right)$	$\mathscr{O}\left(\tau_\theta\kappa\left[1-\tau^2\right]-\tau\left[1-\tau_\theta^2\right]\right)$
	$\lambda 1$-$\eta 0$	$\mathscr{O}\left(\tau^2\right)$	$\mathscr{O}\left(\tau_\theta\left[1-\tau^2\right]+\tau\left[1-\tau_\theta^2\right]\left[1-\tau^2\right]\right)$	$\mathscr{O}\left(\tau_\theta\tau\left[1-\tau^2\right]-\left[1-\tau_\theta^2\right]\left[1-\tau^2\right]\right)$
	$\lambda 1$-$\eta\kappa$	$\mathscr{O}\left(\tau\kappa\right)$	$\mathscr{O}\left(\tau_\theta\kappa+\kappa\left[1-\tau_\theta^2\right]\left[1-\tau^2\right]\right)$	$\mathscr{O}\left(\tau_\theta\kappa\left[1-\tau^2\right]-\kappa\left[1-\tau_\theta^2\right]\right)$
	$\lambda 1$-$\eta 1$	$\mathscr{O}\left(\tau\left[1-\tau^2\right]\right)$	$\mathscr{O}\left(\tau_\theta\tau+\left[1-\tau_\theta^2\right]\left[1-\tau^2\right]\right)$	$\mathscr{O}\left(\tau_\theta\left[1-\tau^2\right]-\tau\left[1-\tau_\theta^2\right]\right)$
$\hat{\mathbf{r}} = -\hat{\mathbf{e}}_2$	$\lambda 0$-$\eta 0$	$\mathscr{O}\left(\tau_\theta\left[1-\tau^2\right]-\tau\left[1-\tau_\theta^2\right]\left[1-\tau^2\right]\right)$	$\mathscr{O}\left(\tau^2\right)$	$\mathscr{O}\left(\tau_\theta\tau\left[1-\tau^2\right]+\left[1-\tau_\theta^2\right]\left[1-\tau^2\right]\right)$
	$\lambda 0$-$\eta\kappa$	$\mathscr{O}\left(\tau_\theta\kappa-\kappa\left[1-\tau_\theta^2\right]\left[1-\tau^2\right]\right)$	$\mathscr{O}\left(\tau\kappa\right)$	$\mathscr{O}\left(\tau_\theta\kappa\left[1-\tau^2\right]+\kappa\left[1-\tau_\theta^2\right]\right)$
	$\lambda 0$-$\eta 1$	$\mathscr{O}\left(\tau_\theta\tau-\left[1-\tau_\theta^2\right]\left[1-\tau^2\right]\right)$	$\mathscr{O}\left(\tau\left[1-\tau^2\right]\right)$	$\mathscr{O}\left(\tau_\theta\left[1-\tau^2\right]+\tau\left[1-\tau_\theta^2\right]\right)$
	$\lambda\kappa$-$\eta 0$	$\mathscr{O}\left(\tau_\theta\left[1-\tau^2\right]-\tau\kappa\left[1-\tau_\theta^2\right]\right)$	$\mathscr{O}\left(\tau\kappa\right)$	$\mathscr{O}\left(\tau_\theta\tau\kappa+\left[1-\tau_\theta^2\right]\left[1-\tau^2\right]\right)$
	$\lambda\kappa$-$\eta\kappa$	$\mathscr{O}\left(\tau_\theta\kappa-\kappa^2\left[1-\tau_\theta^2\right]\right)$	$\mathscr{O}\left(\kappa^2\right)$	$\mathscr{O}\left(\tau_\theta\kappa^2\left[1-\tau^2\right]+\kappa\left[1-\tau_\theta^2\right]\right)$
	$\lambda\kappa$-$\eta 1$	$\mathscr{O}\left(\tau_\theta\tau-\kappa\left[1-\tau_\theta^2\right]\left[1-\tau^2\right]\right)$	$\mathscr{O}\left(\kappa\left[1-\tau^2\right]\right)$	$\mathscr{O}\left(\tau_\theta\kappa\left[1-\tau^2\right]+\tau\left[1-\tau_\theta^2\right]\right)$
	$\lambda 1$-$\eta 0$	$\mathscr{O}\left(\tau_\theta\left[1-\tau^2\right]-\tau^2\left[1-\tau_\theta^2\right]\right)$	$\mathscr{O}\left(\tau\left[1-\tau^2\right]\right)$	$\mathscr{O}\left(\tau_\theta\tau^2+\left[1-\tau_\theta^2\right]\left[1-\tau^2\right]\right)$
	$\lambda 1$-$\eta\kappa$	$\mathscr{O}\left(\tau_\theta\kappa-\kappa\tau\left[1-\tau_\theta^2\right]\right)$	$\mathscr{O}\left(\kappa\left[1-\tau^2\right]\right)$	$\mathscr{O}\left(\tau_\theta\tau\kappa\left[1-\tau^2\right]+\kappa\left[1-\tau_\theta^2\right]\right)$
	$\lambda 1$-$\eta 1$	$\mathscr{O}\left(\tau_\theta\tau-\tau\left[1-\tau_\theta^2\right]\left[1-\tau^2\right]\right)$	$\mathscr{O}\left(1-\tau^2\right)$	$\mathscr{O}\left(\tau_\theta\tau\left[1-\tau^2\right]+\tau\left[1-\tau_\theta^2\right]\right)$

Table A.7 Scaling analysis of un-perturbed and perturbation shock-normal velocities.

Case Code	$\bar{w}_{(U)} / \lvert\bar{\mathbf{V}}_{(U)}\rvert$	$\tilde{w}_{(U)} / \lvert\bar{\mathbf{V}}_{(U)}\rvert$, $\hat{\mathbf{r}} = -\hat{\mathbf{e}}_1$, $\tau_\theta = \mathscr{O}(\tau)$	$\tilde{w}_{(U)} / \lvert\bar{\mathbf{V}}_{(U)}\rvert$, $\hat{\mathbf{r}} = -\hat{\mathbf{e}}_2$, $\tau_\theta = \mathscr{O}(\tau)$
$\lambda 0$-$\alpha 0$-$\eta 0$	$\mathscr{O}(\tau[1-\tau^2])$	$\mathscr{O}(\tau^2[1-\tau^2])$	$\mathscr{O}(\tau[1-\tau^2])$
$\lambda 0$-$\alpha 0$-$\eta\kappa$	$\mathscr{O}(\kappa[1+\tau])$	$\mathscr{O}(\tau^2\kappa[1+\tau])$	$\mathscr{O}(\tau\kappa[1-\tau^2])$
$\lambda 0$-$\alpha 0$-$\eta 1$	$\mathscr{O}(1-\tau^2)$	$\mathscr{O}(\tau^3[1+\tau])$	$\mathscr{O}(\tau^2[1-\tau^2])$
$\lambda 0$-$\alpha\kappa$-$\eta 0$	$\mathscr{O}(\kappa[1+\tau])$	$\mathscr{O}(\tau^2[1-\tau])$	$\mathscr{O}(\tau\kappa[1-\tau^2])$
$\lambda 0$-$\alpha\kappa$-$\eta\kappa$	$\mathscr{O}(\kappa^2[1-\tau^2])$	$\mathscr{O}(\tau^2[1-\tau^2])$	$\mathscr{O}(\tau^2\kappa^2[1-\tau^2])$
$\lambda 0$-$\alpha\kappa$-$\eta 1$	$\mathscr{O}(\kappa[1+\tau])$	$\mathscr{O}(\tau^2\kappa[1+\tau])$	$\mathscr{O}(\tau\kappa[1-\tau])$
$\lambda 0$-$\alpha 1$-$\eta 0$	$\mathscr{O}(1-\tau^2)$	$\mathscr{O}(\tau^2[1-\tau])$	$\mathscr{O}(\tau^2[1+\tau])$
$\lambda 0$-$\alpha 1$-$\eta\kappa$	$\mathscr{O}(\kappa[1-\tau^2])$	$\mathscr{O}(\tau^2[1-\tau^2])$	$\mathscr{O}(\tau^2\kappa[1-\tau])$
$\lambda 0$-$\alpha 1$-$\eta 1$	$\mathscr{O}(\tau[1-\tau^2])$	$\mathscr{O}(\tau^2[1+\tau])$	$\mathscr{O}(\tau[1-\tau^2])$
$\lambda\kappa$-$\alpha 0$-$\eta 0$	$\mathscr{O}(\tau[1+\kappa-\tau])$	$\mathscr{O}(\tau^2[1+\tau])$	$\mathscr{O}(\tau[1-\tau^2])$
$\lambda\kappa$-$\alpha 0$-$\eta\kappa$	$\mathscr{O}(\kappa^2[1+\tau(\kappa^{-1}-1)])$	$\mathscr{O}(\tau^2\kappa[1+\tau(1-\kappa)])$	$\mathscr{O}(\tau\kappa[1+\tau^2])$
$\lambda\kappa$-$\alpha 0$-$\eta 1$	$\mathscr{O}(\kappa[1-\tau])$	$\mathscr{O}(\tau^2\kappa[1+\tau(\kappa^{-1}-1)])$	$\mathscr{O}(\tau^2[1-\tau^2])$
$\lambda\kappa$-$\alpha\kappa$-$\eta 0$	$\mathscr{O}(\kappa[1+\tau\kappa])$	$\mathscr{O}(\tau^2[1-\tau^2])$	$\mathscr{O}(\tau\kappa[1+\tau(1-\kappa)])$
$\lambda\kappa$-$\alpha\kappa$-$\eta\kappa$	$\mathscr{O}(\kappa^2[1+\kappa-\tau])$	$\mathscr{O}(\tau\kappa^3[1+\tau\kappa^{-2}])$	$\mathscr{O}(\tau\kappa^2[1-\kappa+\tau])$
$\lambda\kappa$-$\alpha\kappa$-$\eta 1$	$\mathscr{O}(\kappa^2[1-\tau^2])$	$\mathscr{O}(\tau\kappa^2[1+\tau^2])$	$\mathscr{O}(\tau\kappa^2[1-\tau])$
$\lambda\kappa$-$\alpha 1$-$\eta 0$	$\mathscr{O}(1-\tau^2)$	$\mathscr{O}(\tau^2[1-\tau^2])$	$\mathscr{O}(\tau^2[1-\kappa+\tau])$
$\lambda\kappa$-$\alpha 1$-$\eta\kappa$	$\mathscr{O}(\kappa[1-\tau\kappa])$	$\mathscr{O}(\tau\kappa^2[1+\tau\kappa^{-1}])$	$\mathscr{O}(\tau\kappa^2[1-\tau\kappa^{-1}])$
$\lambda\kappa$-$\alpha 1$-$\eta 1$	$\mathscr{O}(\tau[1-\kappa-\tau^2])$	$\mathscr{O}(\tau\kappa[1+\tau^2\kappa^{-1}])$	$\mathscr{O}(\tau\kappa[1-\tau^2\kappa^{-1}])$
$\lambda 1$-$\alpha 0$-$\eta 0$	$\mathscr{O}(\tau[1-\tau^2])$	$\mathscr{O}(\tau^2[1+\tau])$	$\mathscr{O}(\tau[1-\tau^2])$
$\lambda 1$-$\alpha 0$-$\eta\kappa$	$\mathscr{O}(\tau\kappa[1-\tau^2])$	$\mathscr{O}(\tau^2[1-\tau^2])$	$\mathscr{O}(\tau\kappa[1-\tau^2])$
$\lambda 1$-$\alpha 0$-$\eta 1$	$\mathscr{O}(\tau^2[1-\tau])$	$\mathscr{O}(\tau^2[1-\tau^2])$	$\mathscr{O}(\tau^2[1-\tau^2])$
$\lambda 1$-$\alpha\kappa$-$\eta 0$	$\mathscr{O}(\kappa[1-\tau^2])$	$\mathscr{O}(\tau^2[1-\tau^2])$	$\mathscr{O}(\tau\kappa[1+\tau])$
$\lambda 1$-$\alpha\kappa$-$\eta\kappa$	$\mathscr{O}(\kappa^2[1-\tau(\kappa^{-1}-1)])$	$\mathscr{O}(\tau\kappa^2[1+\tau\kappa^{-1}])$	$\mathscr{O}(\tau\kappa^2[1-\tau^2])$
$\lambda 1$-$\alpha\kappa$-$\eta 1$	$\mathscr{O}(\tau[1-\tau^2])$	$\mathscr{O}(\tau\kappa[1+\tau^2\kappa^{-1}])$	$\mathscr{O}(\tau^3\kappa[1-\tau^2])$
$\lambda 1$-$\alpha 1$-$\eta 0$	$\mathscr{O}(1-\tau^2)$	$\mathscr{O}(\tau^2[1-\tau^2])$	$\mathscr{O}(\tau^2[1-\tau^2])$
$\lambda 1$-$\alpha 1$-$\eta\kappa$	$\mathscr{O}(\kappa[1-\tau])$	$\mathscr{O}(\tau\kappa[1+\tau])$	$\mathscr{O}(\tau^3\kappa[1+\tau])$
$\lambda 1$-$\alpha 1$-$\eta 1$	$\mathscr{O}(\tau^2[1-\tau])$	$\mathscr{O}(\tau[1-\tau^2])$	$\mathscr{O}(\tau^2[1-\tau^2])$

Table A.8 Scaling analysis of post-shock velocity components for $\bar{M}_{(U)} = \mathscr{O}(1)$, $\hat{\mathbf{r}} = -\hat{\mathbf{e}}_1$, $\tau_\theta = \mathscr{O}(\tau)$. Only the dominant terms are shown. $i_n \equiv (1-\kappa^n)$.

Case Code	$\frac{\bar{v}_1}{\lvert\bar{\mathbf{V}}_{(U)}\rvert}$	$\frac{\bar{v}_2}{\lvert\bar{\mathbf{V}}_{(U)}\rvert}$	$\frac{\bar{v}_3}{\lvert\bar{\mathbf{V}}_{(U)}\rvert}$	$\frac{\tilde{v}_1}{\lvert\bar{\mathbf{V}}_{(U)}\rvert}$	$\frac{\tilde{v}_2}{\lvert\bar{\mathbf{V}}_{(U)}\rvert}$	$\frac{\tilde{v}_3}{\lvert\bar{\mathbf{V}}_{(U)}\rvert}$
$\lambda 0$-$\alpha 0$-$\eta 0$	no shock	no shock	no shock	no shock	no shock	no shock
$\lambda 0$-$\alpha 0$-$\eta\kappa$	no shock	no shock	no shock	no shock	no shock	no shock
$\lambda 0$-$\alpha 0$-$\eta 1$	$\mathscr{O}(1)$	$\mathscr{O}(\tau)$	$\mathscr{O}(\tau)$	$\mathscr{O}(\tau^2)$	$\mathscr{O}(\tau^3)$	$\mathscr{O}(\tau^3)$
$\lambda 0$-$\alpha\kappa$-$\eta 0$	no shock	no shock	no shock	no shock	no shock	no shock
$\lambda 0$-$\alpha\kappa$-$\eta\kappa$	no shock	no shock	no shock	no shock	no shock	no shock
$\lambda 0$-$\alpha\kappa$-$\eta 1$	no shock	no shock	no shock	no shock	no shock	no shock
$\lambda 0$-$\alpha 1$-$\eta 0$	$\mathscr{O}(\tau^2)$	$\mathscr{O}(\tau)$	$\mathscr{O}(1)$	$\mathscr{O}(\tau^3)$	$\mathscr{O}(\tau^4)$	$\mathscr{O}(\tau^2)$
$\lambda 0$-$\alpha 1$-$\eta\kappa$	no shock	no shock	no shock	no shock	no shock	no shock
$\lambda 0$-$\alpha 1$-$\eta 1$	no shock	no shock	no shock	no shock	no shock	no shock
$\lambda\kappa$-$\alpha 0$-$\eta 0$	no shock	no shock	no shock	no shock	no shock	no shock
$\lambda\kappa$-$\alpha 0$-$\eta\kappa$	no shock	no shock	no shock	no shock	no shock	no shock
$\lambda\kappa$-$\alpha 0$-$\eta 1$	no shock	no shock	no shock	no shock	no shock	no shock
$\lambda\kappa$-$\alpha\kappa$-$\eta 0$	no shock	no shock	no shock	no shock	no shock	no shock
$\lambda\kappa$-$\alpha\kappa$-$\eta\kappa$	no shock	no shock	no shock	no shock	no shock	no shock
$\lambda\kappa$-$\alpha\kappa$-$\eta 1$	no shock	no shock	no shock	no shock	no shock	no shock
$\lambda\kappa$-$\alpha 1$-$\eta 0$	$\mathscr{O}(\tau^2)$	$\mathscr{O}(\tau)$	$\mathscr{O}(1)$	$\mathscr{O}(\tau^3)$	$\mathscr{O}(\tau^3)$	$\mathscr{O}(\tau^2 i_1)$
$\lambda\kappa$-$\alpha 1$-$\eta\kappa$	no shock	no shock	no shock	no shock	no shock	no shock
$\lambda\kappa$-$\alpha 1$-$\eta 1$	no shock	no shock	no shock	no shock	no shock	no shock
$\lambda 1$-$\alpha 0$-$\eta 0$	no shock	no shock	no shock	no shock	no shock	no shock
$\lambda 1$-$\alpha 0$-$\eta\kappa$	no shock	no shock	no shock	no shock	no shock	no shock
$\lambda 1$-$\alpha 0$-$\eta 1$	no shock	no shock	no shock	no shock	no shock	no shock
$\lambda 1$-$\alpha\kappa$-$\eta 0$	no shock	no shock	no shock	no shock	no shock	no shock
$\lambda 1$-$\alpha\kappa$-$\eta\kappa$	no shock	no shock	no shock	no shock	no shock	no shock
$\lambda 1$-$\alpha\kappa$-$\eta 1$	no shock	no shock	no shock	no shock	no shock	no shock
$\lambda 1$-$\alpha 1$-$\eta 0$	$\mathscr{O}(\tau^2)$	$\mathscr{O}(\tau)$	$\mathscr{O}(1)$	$\mathscr{O}(\tau^3)$	$\mathscr{O}(\tau^3)$	$\mathscr{O}(\tau^2)$
$\lambda 1$-$\alpha 1$-$\eta\kappa$	no shock	no shock	no shock	no shock	no shock	no shock
$\lambda 1$-$\alpha 1$-$\eta 1$	no shock	no shock	no shock	no shock	no shock	no shock

Table A.9 Scaling analysis of post-shock velocity components for $\bar{M}_{(U)} = \mathscr{O}\left(\kappa^{-2}\right)$, $\hat{\mathbf{r}} = -\hat{\mathbf{e}}_1$, $\tau_\theta = \mathscr{O}(\tau)$. Only the dominant terms are shown. $i_n \equiv (1-\kappa^n)$, $j_n \equiv (\kappa^n - \tau)$.

Case Code	$\frac{\bar{v}_1}{\lvert\bar{\mathbf{V}}_{(U)}\rvert}$	$\frac{\bar{v}_2}{\lvert\bar{\mathbf{V}}_{(U)}\rvert}$	$\frac{\bar{v}_3}{\lvert\bar{\mathbf{V}}_{(U)}\rvert}$	$\frac{\tilde{v}_1}{\lvert\bar{\mathbf{V}}_{(U)}\rvert}$	$\frac{\tilde{v}_2}{\lvert\bar{\mathbf{V}}_{(U)}\rvert}$	$\frac{\tilde{v}_3}{\lvert\bar{\mathbf{V}}_{(U)}\rvert}$
$\lambda 0$-$\alpha 0$-$\eta 0$	no shock	no shock	no shock	no shock	no shock	no shock
$\lambda 0$-$\alpha 0$-$\eta\kappa$	$\mathscr{O}(i_4)$	$\mathscr{O}(\tau i_4)$	$\mathscr{O}(j_4)$	$\mathscr{O}(\tau\kappa^4)$	$\mathscr{O}(\tau^2\kappa^4)$	$\mathscr{O}(\kappa^4)$
$\lambda 0$-$\alpha 0$-$\eta 1$	$\mathscr{O}(\kappa^4)$	$\mathscr{O}(\tau\kappa^4)$	$\mathscr{O}(\tau\kappa^4)$	$\mathscr{O}(\tau^2 i_4)$	$\mathscr{O}(\tau^3\kappa^4)$	$\mathscr{O}(\tau i_4)$
$\lambda 0$-$\alpha\kappa$-$\eta 0$	$\mathscr{O}(\kappa)$	$\mathscr{O}(\tau)$	$\mathscr{O}(\kappa^3)$	$\mathscr{O}(\tau\kappa^3)$	$\mathscr{O}(\tau^3\kappa^3)$	$\mathscr{O}(\tau\kappa^3)$
$\lambda 0$-$\alpha\kappa$-$\eta\kappa$	$\mathscr{O}(\kappa)$	$\mathscr{O}(\tau)$	$\mathscr{O}(\kappa)$	$\mathscr{O}(\tau^2\kappa^3)$	$\mathscr{O}(\tau^3\kappa^3)$	$\mathscr{O}(\tau^2\kappa^3)$
$\lambda 0$-$\alpha\kappa$-$\eta 1$	$\mathscr{O}(\kappa^3)$	$\mathscr{O}(\tau i_3)$	$\mathscr{O}(\kappa)$	$\mathscr{O}(\tau\kappa^3)$	$\mathscr{O}(\tau^2\kappa^3)$	$\mathscr{O}(\tau\kappa^3)$
$\lambda 0$-$\alpha 1$-$\eta 0$	$\mathscr{O}(\tau i_4)$	$\mathscr{O}(\tau)$	$\mathscr{O}(\kappa^4)$	$\mathscr{O}(\tau i_4)$	$\mathscr{O}(\tau^4\kappa^4)$	$\mathscr{O}(\tau^2 i_4)$
$\lambda 0$-$\alpha 1$-$\eta\kappa$	$\mathscr{O}(\kappa^4)$	$\mathscr{O}(\tau i_4)$	$\mathscr{O}(i_4)$	$\mathscr{O}(\tau^2\kappa^3)$	$\mathscr{O}(\tau^3\kappa^3)$	$\mathscr{O}(\tau\kappa^3)$
$\lambda 0$-$\alpha 1$-$\eta 1$	no shock	no shock	no shock	no shock	no shock	no shock
$\lambda\kappa$-$\alpha 0$-$\eta 0$	no shock	no shock	no shock	no shock	no shock	no shock
$\lambda\kappa$-$\alpha 0$-$\eta\kappa$	$\mathscr{O}(1)$	$\mathscr{O}(\tau i_4)$	$\mathscr{O}(\tau\kappa^2)$	$\mathscr{O}(\tau\kappa^3)$	$\mathscr{O}(\tau\kappa^3)$	$\mathscr{O}(\tau\kappa^2)$
$\lambda\kappa$-$\alpha 0$-$\eta 1$	$\mathscr{O}(i_4)$	$\mathscr{O}(j_4)$	$\mathscr{O}(\tau i_3)$	$\mathscr{O}(\tau^2\kappa^3)$	$\mathscr{O}(\tau^2\kappa^3)$	$\mathscr{O}(\tau\kappa^4)$
$\lambda\kappa$-$\alpha\kappa$-$\eta 0$	$\mathscr{O}(\kappa)$	$\mathscr{O}(\tau i_4)$	$\mathscr{O}(\kappa^3)$	$\mathscr{O}(\tau\kappa^3)$	$\mathscr{O}(\tau^2\kappa^4)$	$\mathscr{O}(\tau\kappa^3)$
$\lambda\kappa$-$\alpha\kappa$-$\eta\kappa$	$\mathscr{O}(\kappa i_4)$	$\mathscr{O}(\kappa^5 - \tau)$	$\mathscr{O}(\kappa i_4)$	$\mathscr{O}(\tau\kappa^4)$	$\mathscr{O}(\tau\kappa^4 i_1)$	$\mathscr{O}(\tau\kappa^3 i_1)$
$\lambda\kappa$-$\alpha\kappa$-$\eta 1$	$\mathscr{O}(\kappa)$	$\mathscr{O}(\tau)$	$\mathscr{O}(\kappa)$	$\mathscr{O}(\tau\kappa^3)$	$\mathscr{O}(\tau\kappa^3)$	$\mathscr{O}(\tau^2\kappa^2)$
$\lambda\kappa$-$\alpha 1$-$\eta 0$	$\mathscr{O}(\tau\kappa i_4)$	$\mathscr{O}(\tau[1-\kappa i_4])$	$\mathscr{O}(\kappa^4)$	$\mathscr{O}(\tau i_4)$	$\mathscr{O}(\tau^3\kappa^5 i_1)$	$\mathscr{O}(\tau^2 i_4)$
$\lambda\kappa$-$\alpha 1$-$\eta\kappa$	$\mathscr{O}(\kappa^5)$	$\mathscr{O}(j_5)$	$\mathscr{O}(i_4)$	$\mathscr{O}(\tau\kappa^4)$	$\mathscr{O}(\tau\kappa^6)$	$\mathscr{O}(\tau\kappa^5)$
$\lambda\kappa$-$\alpha 1$-$\eta 1$	no shock	no shock	no shock	no shock	no shock	no shock
$\lambda 1$-$\alpha 0$-$\eta 0$	no shock	no shock	no shock	no shock	no shock	no shock
$\lambda 1$-$\alpha 0$-$\eta\kappa$	no shock	no shock	no shock	no shock	no shock	no shock
$\lambda 1$-$\alpha 0$-$\eta 1$	no shock	no shock	no shock	no shock	no shock	no shock
$\lambda 1$-$\alpha\kappa$-$\eta 0$	$\mathscr{O}(\kappa)$	$\mathscr{O}(\tau i_1)$	$\mathscr{O}(\kappa^3)$	$\mathscr{O}(\tau\kappa^3)$	$\mathscr{O}(\tau^2\kappa^3)$	$\mathscr{O}(\tau\kappa^3)$
$\lambda 1$-$\alpha\kappa$-$\eta\kappa$	$\mathscr{O}(\kappa)$	$\mathscr{O}(\tau\kappa^2)$	$\mathscr{O}(\kappa)$	$\mathscr{O}(\tau^2\kappa^2 i_1)$	$\mathscr{O}(\tau\kappa^3)$	$\mathscr{O}(\tau\kappa^3)$
$\lambda 1$-$\alpha\kappa$-$\eta 1$	no shock	no shock	no shock	no shock	no shock	no shock
$\lambda 1$-$\alpha 1$-$\eta 0$	$\mathscr{O}(\tau^2\kappa^4)$	$\mathscr{O}(\tau\kappa^4)$	$\mathscr{O}(\kappa^4)$	$\mathscr{O}(\tau)$	$\mathscr{O}(\tau^3)$	$\mathscr{O}(\tau^2)$
$\lambda 1$-$\alpha 1$-$\eta\kappa$	$\mathscr{O}(\tau j_4)$	$\mathscr{O}(j_4)$	$\mathscr{O}(i_4)$	$\mathscr{O}(\tau\kappa^4)$	$\mathscr{O}(\tau^3\kappa^4)$	$\mathscr{O}(\tau^2\kappa^4)$
$\lambda 1$-$\alpha 1$-$\eta 1$	no shock	no shock	no shock	no shock	no shock	no shock

Table A.10 Scaling analysis of post-shock velocity components for $\bar{M}_{(U)} = \mathscr{O}\left(\tau^{-1}\right)$, $\hat{\mathbf{r}} = -\hat{\mathbf{e}}_1$, $\tau_\theta = \mathscr{O}(\tau)$. Only the dominant terms are shown. $i_n \equiv (1-\kappa^n)$, $j_n \equiv (\kappa^n - \tau)$.

Case Code	$\frac{\bar{v}_1}{\lvert\bar{\mathbf{V}}_{(U)}\rvert}$	$\frac{\bar{v}_2}{\lvert\bar{\mathbf{V}}_{(U)}\rvert}$	$\frac{\bar{v}_3}{\lvert\bar{\mathbf{V}}_{(U)}\rvert}$	$\frac{\tilde{v}_1}{\lvert\bar{\mathbf{V}}_{(U)}\rvert}$	$\frac{\tilde{v}_2}{\lvert\bar{\mathbf{V}}_{(U)}\rvert}$	$\frac{\tilde{v}_3}{\lvert\bar{\mathbf{V}}_{(U)}\rvert}$
$\lambda 0$-$\alpha 0$-$\eta 0$	$\mathscr{O}(1)$	$\mathscr{O}(\tau)$	$\mathscr{O}(\tau)$	$\mathscr{O}(\tau^2)$	$\mathscr{O}(\tau^3)$	$\mathscr{O}(\tau)$
$\lambda 0$-$\alpha 0$-$\eta\kappa$	$\mathscr{O}(\kappa^2)$	$\mathscr{O}(\tau\kappa^2)$	$\mathscr{O}(j_2)$	$\mathscr{O}(\tau\kappa^2)$	$\mathscr{O}(\tau^4\kappa^2)$	$\mathscr{O}(\tau\kappa^2)$
$\lambda 0$-$\alpha 0$-$\eta 1$	$\mathscr{O}(1)$	$\mathscr{O}(\tau)$	$\mathscr{O}(\tau)$	$\mathscr{O}(\tau^2)$	$\mathscr{O}(\tau^3)$	$\mathscr{O}(\tau)$
$\lambda 0$-$\alpha\kappa$-$\eta 0$	$\mathscr{O}(\kappa)$	$\mathscr{O}(\tau)$	$\mathscr{O}(\kappa)$	$\mathscr{O}(\tau\kappa)$	$\mathscr{O}(\tau^5\kappa^3)$	$\mathscr{O}(\tau^2\kappa)$
$\lambda 0$-$\alpha\kappa$-$\eta\kappa$	$\mathscr{O}(\kappa^3)$	$\mathscr{O}(\tau i_3)$	$\mathscr{O}(\kappa^3)$	$\mathscr{O}(\tau\kappa^3)$	$\mathscr{O}(\tau^5\kappa^3)$	$\mathscr{O}(\tau\kappa^3)$
$\lambda 0$-$\alpha\kappa$-$\eta 1$	$\mathscr{O}(\kappa)$	$\mathscr{O}(\tau\kappa)$	$\mathscr{O}(\kappa)$	$\mathscr{O}(\tau^2\kappa)$	$\mathscr{O}(\tau^4\kappa)$	$\mathscr{O}(\tau\kappa)$
$\lambda 0$-$\alpha 1$-$\eta 0$	$\mathscr{O}(\tau)$	$\mathscr{O}(\tau)$	$\mathscr{O}(1)$	$\mathscr{O}(\tau)$	$\mathscr{O}(\tau^6)$	$\mathscr{O}(\tau^2)$
$\lambda 0$-$\alpha 1$-$\eta\kappa$	$\mathscr{O}(\kappa^2)$	$\mathscr{O}(\tau\kappa^2)$	$\mathscr{O}(\kappa^2)$	$\mathscr{O}(\tau\kappa^2)$	$\mathscr{O}(\tau^5\kappa)$	$\mathscr{O}(\tau\kappa^2)$
$\lambda 0$-$\alpha 1$-$\eta 1$	$\mathscr{O}(\tau^2)$	$\mathscr{O}(\tau)$	$\mathscr{O}(1)$	$\mathscr{O}(\tau)$	$\mathscr{O}(\tau^2)$	$\mathscr{O}(\tau^2)$
$\lambda\kappa$-$\alpha 0$-$\eta 0$	$\mathscr{O}(1)$	$\mathscr{O}(\tau)$	$\mathscr{O}(\tau i_1)$	$\mathscr{O}(\tau i_1^2)$	$\mathscr{O}(\tau\kappa i_1)$	$\mathscr{O}(\tau i_1)$
$\lambda\kappa$-$\alpha 0$-$\eta\kappa$	$\mathscr{O}(i_4)$	$\mathscr{O}(j_4)$	$\mathscr{O}(j_3)$	$\mathscr{O}(\tau\kappa^3)$	$\mathscr{O}(\tau^3\kappa^3)$	$\mathscr{O}(\tau\kappa^4)$
$\lambda\kappa$-$\alpha 0$-$\eta 1$	$\mathscr{O}(\kappa^2)$	$\mathscr{O}(j_2)$	$\mathscr{O}(\tau i_1)$	$\mathscr{O}(\tau^2\kappa)$	$\mathscr{O}(\tau^4\kappa)$	$\mathscr{O}(\tau\kappa^2)$
$\lambda\kappa$-$\alpha\kappa$-$\eta 0$	$\mathscr{O}(\kappa)$	$\mathscr{O}(\tau\kappa^2)$	$\mathscr{O}(\kappa)$	$\mathscr{O}(\tau\kappa)$	$\mathscr{O}(\tau^4\kappa^2)$	$\mathscr{O}(\tau^2\kappa i_1)$
$\lambda\kappa$-$\alpha\kappa$-$\eta\kappa$	$\mathscr{O}(\kappa i_3)$	$\mathscr{O}(j_4)$	$\mathscr{O}(\kappa^3)$	$\mathscr{O}(\tau\kappa^3)$	$\mathscr{O}(\tau^3\kappa^4)$	$\mathscr{O}(\tau\kappa^4)$
$\lambda\kappa$-$\alpha\kappa$-$\eta 1$	$\mathscr{O}(\kappa^3)$	$\mathscr{O}(j_3)$	$\mathscr{O}(\kappa)$	$\mathscr{O}(\tau^2\kappa^2)$	$\mathscr{O}(\tau^3\kappa^3)$	$\mathscr{O}(\tau\kappa^3)$
$\lambda\kappa$-$\alpha 1$-$\eta 0$	$\mathscr{O}(\tau\kappa)$	$\mathscr{O}(\tau i_1)$	$\mathscr{O}(1)$	$\mathscr{O}(\tau)$	$\mathscr{O}(\tau^5\kappa i_1)$	$\mathscr{O}(\tau^2 i_1)$
$\lambda\kappa$-$\alpha 1$-$\eta\kappa$	$\mathscr{O}(\kappa^3)$	$\mathscr{O}(j_3)$	$\mathscr{O}(\kappa^2)$	$\mathscr{O}(\tau\kappa^2)$	$\mathscr{O}(\tau^3\kappa^4)$	$\mathscr{O}(\tau\kappa^3)$
$\lambda\kappa$-$\alpha 1$-$\eta 1$	$\mathscr{O}\left(\tau\left[\kappa^2 i_1 - \tau\right]\right)$	$\mathscr{O}(\tau\kappa^2)$	$\mathscr{O}(1)$	$\mathscr{O}(\tau\kappa^2 i_1)$	$\mathscr{O}(\tau\kappa^2 i_1)$	$\mathscr{O}(\tau^2\kappa i_1)$
$\lambda 1$-$\alpha 0$-$\eta 0$	$\mathscr{O}(1)$	$\mathscr{O}(\tau)$	$\mathscr{O}(\tau)$	$\mathscr{O}(\tau^2)$	$\mathscr{O}(\tau^2)$	$\mathscr{O}(\tau)$
$\lambda 1$-$\alpha 0$-$\eta\kappa$	$\mathscr{O}(1)$	$\mathscr{O}(\tau\kappa^2)$	$\mathscr{O}(\tau\kappa^2)$	$\mathscr{O}(\tau^2\kappa^2)$	$\mathscr{O}(\tau^4\kappa)$	$\mathscr{O}(\tau^3\kappa^2)$
$\lambda 1$-$\alpha 0$-$\eta 1$	no shock	no shock	no shock	no shock	no shock	no shock
$\lambda 1$-$\alpha\kappa$-$\eta 0$	$\mathscr{O}(\kappa)$	$\mathscr{O}(\tau i_1)$	$\mathscr{O}(\kappa)$	$\mathscr{O}(\tau\kappa)$	$\mathscr{O}(\tau^4\kappa)$	$\mathscr{O}(\tau^2\kappa)$
$\lambda 1$-$\alpha\kappa$-$\eta\kappa$	$\mathscr{O}(\kappa)$	$\mathscr{O}(j_3)$	$\mathscr{O}(\kappa^3)$	$\mathscr{O}(\tau\kappa^3)$	$\mathscr{O}(\tau^3\kappa^{-1})$	$\mathscr{O}(\tau^2\kappa^3)$
$\lambda 1$-$\alpha\kappa$-$\eta 1$	$\mathscr{O}(\kappa)$	$\mathscr{O}(\tau)$	$\mathscr{O}(\kappa)$	$\mathscr{O}(\tau^4\kappa)$	$\mathscr{O}(\tau^3\kappa)$	$\mathscr{O}(\tau^4\kappa)$
$\lambda 1$-$\alpha 1$-$\eta 0$	$\mathscr{O}(\tau^2)$	$\mathscr{O}(\tau)$	$\mathscr{O}(1)$	$\mathscr{O}(\tau)$	$\mathscr{O}(\tau^3)$	$\mathscr{O}(\tau^2)$
$\lambda 1$-$\alpha 1$-$\eta\kappa$	$\mathscr{O}(\tau^2)$	$\mathscr{O}(\tau)$	$\mathscr{O}(1)$	$\mathscr{O}(\tau^3\kappa^2)$	$\mathscr{O}(\tau^3\kappa^2)$	$\mathscr{O}(\tau^3\kappa^2)$
$\lambda 1$-$\alpha 1$-$\eta 1$	no shock	no shock	no shock	no shock	no shock	no shock

Table A.11 Scaling analysis of post-shock velocity components for $\bar{M}_{(U)} = \mathscr{O}(1)$, $\hat{\mathbf{r}} = -\hat{\mathbf{e}}_2$, $\tau_\theta = \mathscr{O}(\tau)$. Only the dominant terms are shown. $i_n \equiv (1-\kappa^n)$.

Case Code	$\frac{\bar{v}_1}{\lvert\bar{\mathbf{V}}_{(U)}\rvert}$	$\frac{\bar{v}_2}{\lvert\bar{\mathbf{V}}_{(U)}\rvert}$	$\frac{\bar{v}_3}{\lvert\bar{\mathbf{V}}_{(U)}\rvert}$	$\frac{\tilde{v}_1}{\lvert\bar{\mathbf{V}}_{(U)}\rvert}$	$\frac{\tilde{v}_2}{\lvert\bar{\mathbf{V}}_{(U)}\rvert}$	$\frac{\tilde{v}_3}{\lvert\bar{\mathbf{V}}_{(U)}\rvert}$
$\lambda 0$-$\alpha 0$-$\eta 0$	no shock	no shock	no shock	no shock	no shock	no shock
$\lambda 0$-$\alpha 0$-$\eta\kappa$	no shock	no shock	no shock	no shock	no shock	no shock
$\lambda 0$-$\alpha 0$-$\eta 1$	$\mathscr{O}(1)$	$\mathscr{O}(\tau)$	$\mathscr{O}(\tau)$	$\mathscr{O}(\tau^2)$	$\mathscr{O}(\tau^3)$	$\mathscr{O}(\tau^3)$
$\lambda 0$-$\alpha\kappa$-$\eta 0$	no shock	no shock	no shock	no shock	no shock	no shock
$\lambda 0$-$\alpha\kappa$-$\eta\kappa$	no shock	no shock	no shock	no shock	no shock	no shock
$\lambda 0$-$\alpha\kappa$-$\eta 1$	no shock	no shock	no shock	no shock	no shock	no shock
$\lambda 0$-$\alpha 1$-$\eta 0$	$\mathscr{O}(\tau^2)$	$\mathscr{O}(\tau)$	$\mathscr{O}(1)$	$\mathscr{O}(\tau^3)$	$\mathscr{O}(\tau^4)$	$\mathscr{O}(\tau^2)$
$\lambda 0$-$\alpha 1$-$\eta\kappa$	no shock	no shock	no shock	no shock	no shock	no shock
$\lambda 0$-$\alpha 1$-$\eta 1$	no shock	no shock	no shock	no shock	no shock	no shock
$\lambda\kappa$-$\alpha 0$-$\eta 0$	no shock	no shock	no shock	no shock	no shock	no shock
$\lambda\kappa$-$\alpha 0$-$\eta\kappa$	no shock	no shock	no shock	no shock	no shock	no shock
$\lambda\kappa$-$\alpha 0$-$\eta 1$	no shock	no shock	no shock	no shock	no shock	no shock
$\lambda\kappa$-$\alpha\kappa$-$\eta 0$	no shock	no shock	no shock	no shock	no shock	no shock
$\lambda\kappa$-$\alpha\kappa$-$\eta\kappa$	no shock	no shock	no shock	no shock	no shock	no shock
$\lambda\kappa$-$\alpha\kappa$-$\eta 1$	no shock	no shock	no shock	no shock	no shock	no shock
$\lambda\kappa$-$\alpha 1$-$\eta 0$	$\mathscr{O}(\tau^2)$	$\mathscr{O}(\tau)$	$\mathscr{O}(1)$	$\mathscr{O}(\tau^3)$	$\mathscr{O}(\tau^3)$	$\mathscr{O}(\tau^2 i_1)$
$\lambda\kappa$-$\alpha 1$-$\eta\kappa$	no shock	no shock	no shock	no shock	no shock	no shock
$\lambda\kappa$-$\alpha 1$-$\eta 1$	no shock	no shock	no shock	no shock	no shock	no shock
$\lambda 1$-$\alpha 0$-$\eta 0$	no shock	no shock	no shock	no shock	no shock	no shock
$\lambda 1$-$\alpha 0$-$\eta\kappa$	no shock	no shock	no shock	no shock	no shock	no shock
$\lambda 1$-$\alpha 0$-$\eta 1$	no shock	no shock	no shock	no shock	no shock	no shock
$\lambda 1$-$\alpha\kappa$-$\eta 0$	no shock	no shock	no shock	no shock	no shock	no shock
$\lambda 1$-$\alpha\kappa$-$\eta\kappa$	no shock	no shock	no shock	no shock	no shock	no shock
$\lambda 1$-$\alpha\kappa$-$\eta 1$	no shock	no shock	no shock	no shock	no shock	no shock
$\lambda 1$-$\alpha 1$-$\eta 0$	$\mathscr{O}(\tau^2)$	$\mathscr{O}(\tau)$	$\mathscr{O}(1)$	$\mathscr{O}(\tau^3)$	$\mathscr{O}(\tau^3)$	$\mathscr{O}(\tau^2)$
$\lambda 1$-$\alpha 1$-$\eta\kappa$	no shock	no shock	no shock	no shock	no shock	no shock
$\lambda 1$-$\alpha 1$-$\eta 1$	no shock	no shock	no shock	no shock	no shock	no shock

Table A.12 Scaling analysis of post-shock velocity components for $\bar{M}_{(U)} = \mathscr{O}\left(\kappa^{-2}\right)$, $\hat{\mathbf{r}} = -\hat{\mathbf{e}}_2$, $\tau_\theta = \mathscr{O}(\tau)$. Only the dominant terms are shown. $i_n \equiv \left(1-\kappa^4\right)$, $j_n \equiv \left(\kappa^n - \tau\right)$.

Case Code	$\frac{\bar{v}_1}{\lvert\bar{\mathbf{V}}_{(U)}\rvert}$	$\frac{\bar{v}_2}{\lvert\bar{\mathbf{V}}_{(U)}\rvert}$	$\frac{\bar{v}_3}{\lvert\bar{\mathbf{V}}_{(U)}\rvert}$	$\frac{\tilde{v}_1}{\lvert\bar{\mathbf{V}}_{(U)}\rvert}$	$\frac{\tilde{v}_2}{\lvert\bar{\mathbf{V}}_{(U)}\rvert}$	$\frac{\tilde{v}_3}{\lvert\bar{\mathbf{V}}_{(U)}\rvert}$
$\lambda 0$-$\alpha 0$-$\eta 0$	no shock	no shock	no shock	no shock	no shock	no shock
$\lambda 0$-$\alpha 0$-$\eta\kappa$	$\mathscr{O}(i_4)$	$\mathscr{O}(\tau i_4)$	$\mathscr{O}(j_4)$	$\mathscr{O}\left(\tau\kappa^4\right)$	$\mathscr{O}\left(\tau^2\kappa^4\right)$	$\mathscr{O}\left(\kappa^4\right)$
$\lambda 0$-$\alpha 0$-$\eta 1$	$\mathscr{O}\left(\kappa^4\right)$	$\mathscr{O}\left(\tau\kappa^4\right)$	$\mathscr{O}\left(\tau\kappa^4\right)$	$\mathscr{O}\left(\tau^2 i_4\right)$	$\mathscr{O}\left(\tau^3\kappa^4\right)$	$\mathscr{O}(\tau i_4)$
$\lambda 0$-$\alpha\kappa$-$\eta 0$	$\mathscr{O}(\kappa)$	$\mathscr{O}(\tau)$	$\mathscr{O}\left(\kappa^3\right)$	$\mathscr{O}\left(\tau\kappa^3\right)$	$\mathscr{O}\left(\tau^3\kappa^3\right)$	$\mathscr{O}\left(\tau\kappa^3\right)$
$\lambda 0$-$\alpha\kappa$-$\eta\kappa$	$\mathscr{O}(\kappa)$	$\mathscr{O}(\tau)$	$\mathscr{O}(\kappa)$	$\mathscr{O}\left(\tau^2\kappa^3\right)$	$\mathscr{O}\left(\tau^3\kappa^3\right)$	$\mathscr{O}\left(\tau^2\kappa^3\right)$
$\lambda 0$-$\alpha\kappa$-$\eta 1$	$\mathscr{O}\left(\kappa^3\right)$	$\mathscr{O}(\tau i_3)$	$\mathscr{O}(\kappa)$	$\mathscr{O}\left(\tau\kappa^3\right)$	$\mathscr{O}\left(\tau^2\kappa^3\right)$	$\mathscr{O}\left(\tau\kappa^3\right)$
$\lambda 0$-$\alpha 1$-$\eta 0$	$\mathscr{O}(\tau i_4)$	$\mathscr{O}(\tau)$	$\mathscr{O}\left(\kappa^4\right)$	$\mathscr{O}(\tau i_4)$	$\mathscr{O}\left(\tau^4\kappa^4\right)$	$\mathscr{O}\left(\tau^2 i_4\right)$
$\lambda 0$-$\alpha 1$-$\eta\kappa$	$\mathscr{O}\left(\kappa^4\right)$	$\mathscr{O}(\tau i_4)$	$\mathscr{O}(i_4)$	$\mathscr{O}\left(\tau^2\kappa^3\right)$	$\mathscr{O}\left(\tau^3\kappa^3\right)$	$\mathscr{O}\left(\tau\kappa^3\right)$
$\lambda 0$-$\alpha 1$-$\eta 1$	no shock	no shock	no shock	no shock	no shock	no shock
$\lambda\kappa$-$\alpha 0$-$\eta 0$	no shock	no shock	no shock	no shock	no shock	no shock
$\lambda\kappa$-$\alpha 0$-$\eta\kappa$	$\mathscr{O}(1)$	$\mathscr{O}(\tau i_4)$	$\mathscr{O}\left(\tau\kappa^2\right)$	$\mathscr{O}\left(\tau\kappa^3\right)$	$\mathscr{O}\left(\tau\kappa^3\right)$	$\mathscr{O}\left(\tau\kappa^2\right)$
$\lambda\kappa$-$\alpha 0$-$\eta 1$	$\mathscr{O}(i_4)$	$\mathscr{O}(l)$	$\mathscr{O}(\tau i_3)$	$\mathscr{O}\left(\tau^2\kappa^3\right)$	$\mathscr{O}\left(\tau^2\kappa^3\right)$	$\mathscr{O}\left(\tau\kappa^4\right)$
$\lambda\kappa$-$\alpha\kappa$-$\eta 0$	$\mathscr{O}(\kappa)$	$\mathscr{O}(\tau i_4)$	$\mathscr{O}\left(\kappa^3\right)$	$\mathscr{O}\left(\tau\kappa^3\right)$	$\mathscr{O}\left(\tau^2\kappa^4\right)$	$\mathscr{O}\left(\tau\kappa^3\right)$
$\lambda\kappa$-$\alpha\kappa$-$\eta\kappa$	$\mathscr{O}(\kappa i_4)$	$\mathscr{O}(j_5)$	$\mathscr{O}(\kappa i_4)$	$\mathscr{O}\left(\tau\kappa^4\right)$	$\mathscr{O}\left(\tau\kappa^4 i_1\right)$	$\mathscr{O}\left(\tau\kappa^3 i_1\right)$
$\lambda\kappa$-$\alpha\kappa$-$\eta 1$	$\mathscr{O}(\kappa)$	$\mathscr{O}(\tau)$	$\mathscr{O}(\kappa)$	$\mathscr{O}\left(\tau\kappa^3\right)$	$\mathscr{O}\left(\tau\kappa^3\right)$	$\mathscr{O}\left(\tau^2\kappa^2\right)$
$\lambda\kappa$-$\alpha 1$-$\eta 0$	$\mathscr{O}(\tau\kappa i_4)$	$\mathscr{O}(\tau[1-\kappa i_4])$	$\mathscr{O}\left(\kappa^4\right)$	$\mathscr{O}(\tau i_4)$	$\mathscr{O}\left(\tau^3\kappa^5 i_1\right)$	$\mathscr{O}\left(\tau^2 i_4\right)$
$\lambda\kappa$-$\alpha 1$-$\eta\kappa$	$\mathscr{O}\left(\kappa^5\right)$	$\mathscr{O}(j_5)$	$\mathscr{O}(i_4)$	$\mathscr{O}\left(\tau\kappa^4\right)$	$\mathscr{O}\left(\tau\kappa^6\right)$	$\mathscr{O}\left(\tau\kappa^5\right)$
$\lambda\kappa$-$\alpha 1$-$\eta 1$	no shock	no shock	no shock	no shock	no shock	no shock
$\lambda 1$-$\alpha 0$-$\eta 0$	no shock	no shock	no shock	no shock	no shock	no shock
$\lambda 1$-$\alpha 0$-$\eta\kappa$	no shock	no shock	no shock	no shock	no shock	no shock
$\lambda 1$-$\alpha 0$-$\eta 1$	no shock	no shock	no shock	no shock	no shock	no shock
$\lambda 1$-$\alpha\kappa$-$\eta 0$	$\mathscr{O}(\kappa)$	$\mathscr{O}(\tau i_1)$	$\mathscr{O}\left(\kappa^3\right)$	$\mathscr{O}\left(\tau\kappa^3\right)$	$\mathscr{O}\left(\tau^2\kappa^3\right)$	$\mathscr{O}\left(\tau\kappa^3\right)$
$\lambda 1$-$\alpha\kappa$-$\eta\kappa$	$\mathscr{O}(\kappa)$	$\mathscr{O}\left(\tau\kappa^2\right)$	$\mathscr{O}(\kappa)$	$\mathscr{O}\left(\tau^2\kappa^2 i_1\right)$	$\mathscr{O}\left(\tau\kappa^3\right)$	$\mathscr{O}\left(\tau\kappa^3\right)$
$\lambda 1$-$\alpha\kappa$-$\eta 1$	no shock	no shock	no shock	no shock	no shock	no shock
$\lambda 1$-$\alpha 1$-$\eta 0$	$\mathscr{O}\left(\tau^2\kappa^4\right)$	$\mathscr{O}\left(\tau\kappa^4\right)$	$\mathscr{O}\left(\kappa^4\right)$	$\mathscr{O}(\tau)$	$\mathscr{O}\left(\tau^3\right)$	$\mathscr{O}\left(\tau^2\right)$
$\lambda 1$-$\alpha 1$-$\eta\kappa$	$\mathscr{O}(\tau j_4)$	$\mathscr{O}(j_4)$	$\mathscr{O}(i_4)$	$\mathscr{O}\left(\tau\kappa^4\right)$	$\mathscr{O}\left(\tau^3\kappa^4\right)$	$\mathscr{O}\left(\tau^2\kappa^4\right)$
$\lambda 1$-$\alpha 1$-$\eta 1$	no shock	no shock	no shock	no shock	no shock	no shock

Table A.13 Scaling analysis of post-shock velocity components for $\bar{M}_{(U)} = \mathscr{O}\left(\tau^{-1}\right)$, $\hat{\mathbf{r}} = -\hat{\mathbf{e}}_2$, $\tau_\theta = \mathscr{O}(\tau)$. Only the dominant terms are shown. $i_n \equiv (1-\kappa^n)$, $j_n \equiv (\kappa^n - \tau)$.

Case Code	$\frac{\bar{v}_1}{\lvert\bar{\mathbf{V}}_{(U)}\rvert}$	$\frac{\bar{v}_2}{\lvert\bar{\mathbf{V}}_{(U)}\rvert}$	$\frac{\bar{v}_3}{\lvert\bar{\mathbf{V}}_{(U)}\rvert}$	$\frac{\tilde{v}_1}{\lvert\bar{\mathbf{V}}_{(U)}\rvert}$	$\frac{\tilde{v}_2}{\lvert\bar{\mathbf{V}}_{(U)}\rvert}$	$\frac{\tilde{v}_3}{\lvert\bar{\mathbf{V}}_{(U)}\rvert}$
$\lambda 0$-$\alpha 0$-$\eta 0$	$\mathscr{O}(1)$	$\mathscr{O}(\tau)$	$\mathscr{O}(\tau)$	$\mathscr{O}\left(\tau^2\right)$	$\mathscr{O}\left(\tau^3\right)$	$\mathscr{O}(\tau)$
$\lambda 0$-$\alpha 0$-$\eta\kappa$	$\mathscr{O}\left(\kappa^2\right)$	$\mathscr{O}\left(\tau\kappa^2\right)$	$\mathscr{O}(j_2)$	$\mathscr{O}\left(\tau\kappa^2\right)$	$\mathscr{O}\left(\tau^4\kappa^2\right)$	$\mathscr{O}\left(\tau\kappa^2\right)$
$\lambda 0$-$\alpha 0$-$\eta 1$	$\mathscr{O}(1)$	$\mathscr{O}(\tau)$	$\mathscr{O}(\tau)$	$\mathscr{O}\left(\tau^2\right)$	$\mathscr{O}\left(\tau^3\right)$	$\mathscr{O}(\tau)$
$\lambda 0$-$\alpha\kappa$-$\eta 0$	$\mathscr{O}(\kappa)$	$\mathscr{O}(\tau)$	$\mathscr{O}(\kappa)$	$\mathscr{O}(\tau\kappa)$	$\mathscr{O}\left(\tau^5\kappa^3\right)$	$\mathscr{O}\left(\tau^2\kappa\right)$
$\lambda 0$-$\alpha\kappa$-$\eta\kappa$	$\mathscr{O}\left(\kappa^3\right)$	$\mathscr{O}(\tau i_3)$	$\mathscr{O}\left(\kappa^3\right)$	$\mathscr{O}\left(\tau\kappa^3\right)$	$\mathscr{O}\left(\tau^5\kappa^3\right)$	$\mathscr{O}\left(\tau\kappa^3\right)$
$\lambda 0$-$\alpha\kappa$-$\eta 1$	$\mathscr{O}(\kappa)$	$\mathscr{O}(\tau\kappa)$	$\mathscr{O}(\kappa)$	$\mathscr{O}\left(\tau^2\kappa\right)$	$\mathscr{O}\left(\tau^4\kappa\right)$	$\mathscr{O}(\tau\kappa)$
$\lambda 0$-$\alpha 1$-$\eta 0$	$\mathscr{O}(\tau)$	$\mathscr{O}(\tau)$	$\mathscr{O}(1)$	$\mathscr{O}(\tau)$	$\mathscr{O}\left(\tau^6\right)$	$\mathscr{O}\left(\tau^2\right)$
$\lambda 0$-$\alpha 1$-$\eta\kappa$	$\mathscr{O}\left(\kappa^2\right)$	$\mathscr{O}\left(\tau\kappa^2\right)$	$\mathscr{O}\left(\kappa^2\right)$	$\mathscr{O}\left(\tau\kappa^2\right)$	$\mathscr{O}\left(\tau^5\kappa\right)$	$\mathscr{O}\left(\tau\kappa^2\right)$
$\lambda 0$-$\alpha 1$-$\eta 1$	$\mathscr{O}\left(\tau^2\right)$	$\mathscr{O}(\tau)$	$\mathscr{O}(1)$	$\mathscr{O}(\tau)$	$\mathscr{O}\left(\tau^2\right)$	$\mathscr{O}\left(\tau^2\right)$
$\lambda\kappa$-$\alpha 0$-$\eta 0$	$\mathscr{O}(1)$	$\mathscr{O}(\tau)$	$\mathscr{O}(\tau i_1)$	$\mathscr{O}\left(\tau i_1^2\right)$	$\mathscr{O}(\tau\kappa i_1)$	$\mathscr{O}(\tau i_1)$
$\lambda\kappa$-$\alpha 0$-$\eta\kappa$	$\mathscr{O}(i_4)$	$\mathscr{O}(j_4)$	$\mathscr{O}(j_3)$	$\mathscr{O}\left(\tau\kappa^3\right)$	$\mathscr{O}\left(\tau^3\kappa^3\right)$	$\mathscr{O}\left(\tau\kappa^4\right)$
$\lambda\kappa$-$\alpha 0$-$\eta 1$	$\mathscr{O}\left(\kappa^2\right)$	$\mathscr{O}(j_2)$	$\mathscr{O}(\tau i_1)$	$\mathscr{O}\left(\tau^2\kappa\right)$	$\mathscr{O}\left(\tau^4\kappa\right)$	$\mathscr{O}\left(\tau\kappa^2\right)$
$\lambda\kappa$-$\alpha\kappa$-$\eta 0$	$\mathscr{O}(\kappa)$	$\mathscr{O}\left(\tau\kappa^2\right)$	$\mathscr{O}(\kappa)$	$\mathscr{O}(\tau\kappa)$	$\mathscr{O}\left(\tau^4\kappa^2\right)$	$\mathscr{O}\left(\tau^2\kappa i_1\right)$
$\lambda\kappa$-$\alpha\kappa$-$\eta\kappa$	$\mathscr{O}(\kappa i_3)$	$\mathscr{O}(j_4)$	$\mathscr{O}\left(\kappa^3\right)$	$\mathscr{O}\left(\tau\kappa^3\right)$	$\mathscr{O}\left(\tau^3\kappa^4\right)$	$\mathscr{O}\left(\tau\kappa^4\right)$
$\lambda\kappa$-$\alpha\kappa$-$\eta 1$	$\mathscr{O}\left(\kappa^3\right)$	$\mathscr{O}(j_3)$	$\mathscr{O}(\kappa)$	$\mathscr{O}\left(\tau^2\kappa^2\right)$	$\mathscr{O}\left(\tau^3\kappa^3\right)$	$\mathscr{O}\left(\tau\kappa^3\right)$
$\lambda\kappa$-$\alpha 1$-$\eta 0$	$\mathscr{O}(\tau\kappa)$	$\mathscr{O}(\tau i_1)$	$\mathscr{O}(1)$	$\mathscr{O}(\tau)$	$\mathscr{O}\left(\tau^5\kappa i_1\right)$	$\mathscr{O}\left(\tau^2 i_1\right)$
$\lambda\kappa$-$\alpha 1$-$\eta\kappa$	$\mathscr{O}\left(\kappa^3\right)$	$\mathscr{O}(j_3)$	$\mathscr{O}\left(\kappa^2\right)$	$\mathscr{O}\left(\tau\kappa^2\right)$	$\mathscr{O}\left(\tau^3\kappa^4\right)$	$\mathscr{O}\left(\tau\kappa^3\right)$
$\lambda\kappa$-$\alpha 1$-$\eta 1$	$\mathscr{O}\left(\tau\left[\kappa^2 i_1 - \tau\right]\right)$	$\mathscr{O}\left(\tau\kappa^2\right)$	$\mathscr{O}(1)$	$\mathscr{O}\left(\tau\kappa^2 i_1\right)$	$\mathscr{O}\left(\tau\kappa^2 i_1\right)$	$\mathscr{O}\left(\tau^2\kappa i_1\right)$
$\lambda 1$-$\alpha 0$-$\eta 0$	$\mathscr{O}(1)$	$\mathscr{O}(\tau)$	$\mathscr{O}(\tau)$	$\mathscr{O}\left(\tau^2\right)$	$\mathscr{O}\left(\tau^2\right)$	$\mathscr{O}(\tau)$
$\lambda 1$-$\alpha 0$-$\eta\kappa$	$\mathscr{O}(1)$	$\mathscr{O}\left(\tau\kappa^2\right)$	$\mathscr{O}\left(\tau\kappa^2\right)$	$\mathscr{O}\left(\tau^2\kappa^2\right)$	$\mathscr{O}\left(\tau^4\kappa\right)$	$\mathscr{O}\left(\tau^3\kappa^2\right)$
$\lambda 1$-$\alpha 0$-$\eta 1$	no shock	no shock	no shock	no shock	no shock	no shock
$\lambda 1$-$\alpha\kappa$-$\eta 0$	$\mathscr{O}(\kappa)$	$\mathscr{O}(\tau i_1)$	$\mathscr{O}(\kappa)$	$\mathscr{O}(\tau\kappa)$	$\mathscr{O}\left(\tau^4\kappa\right)$	$\mathscr{O}\left(\tau^2\kappa\right)$
$\lambda 1$-$\alpha\kappa$-$\eta\kappa$	$\mathscr{O}(\kappa)$	$\mathscr{O}(j_3)$	$\mathscr{O}\left(\kappa^3\right)$	$\mathscr{O}\left(\tau\kappa^3\right)$	$\mathscr{O}\left(\tau^3\kappa^{-1}\right)$	$\mathscr{O}\left(\tau^2\kappa^3\right)$
$\lambda 1$-$\alpha\kappa$-$\eta 1$	$\mathscr{O}(\kappa)$	$\mathscr{O}(\tau)$	$\mathscr{O}(\kappa)$	$\mathscr{O}\left(\tau^4\kappa\right)$	$\mathscr{O}\left(\tau^3\kappa\right)$	$\mathscr{O}\left(\tau^4\kappa\right)$
$\lambda 1$-$\alpha 1$-$\eta 0$	$\mathscr{O}\left(\tau^2\right)$	$\mathscr{O}(\tau)$	$\mathscr{O}(1)$	$\mathscr{O}(\tau)$	$\mathscr{O}\left(\tau^3\right)$	$\mathscr{O}\left(\tau^2\right)$
$\lambda 1$-$\alpha 1$-$\eta\kappa$	$\mathscr{O}\left(\tau^2\right)$	$\mathscr{O}(\tau)$	$\mathscr{O}(1)$	$\mathscr{O}\left(\tau^3\kappa^2\right)$	$\mathscr{O}\left(\tau^3\kappa^2\right)$	$\mathscr{O}\left(\tau^3\kappa^2\right)$
$\lambda 1$-$\alpha 1$-$\eta 1$	no shock	no shock	no shock	no shock	no shock	no shock